POLISH SOCIETY OF THEORETICAL AND APPLIED MECHANICS

JOURNAL OF THEORETICAL AND APPLIED MECHANICS

No. 4 • Vol 55

Quarterly

WARSAW, OCTOBER 2017

JOURNAL OF THEORETICAL AND APPLIED MECHANICS
(until 1997 Mechanika Teoretyczna i Stosowana, ISSN 0079-3701)

Beginning with Vol 45, No. 1, 2007, *Journal of Theoretical and Applied Mechanics* (JTAM) has been selected for coverage in Thomson Reuters products and custom information services. Now it is indexed and abstracted in the following:

- **Science Citation Index Expanded** (also known as SciSearch®)
- **Journal Citation Reports/Science Edition**

* * * * *

Editorial Office

Al. Armii Ludowej 16, room 650
00-637 Warszawa, Poland
phone (+48 22) 825 7180, (+48) 664 099 345, e-mail: biuro@ptmts.org.pl

www.ptmts.org.pl/jtam.html

* * * * *

Publication supported by Ministry of Science and Higher Education of Poland

(Journal of Theoretical and Applied Mechanics: 1) digitalizacja publikacji i monografii naukowych w celu zapewnienia i utrzymania otwartego dostępu do nich przez sieć Internet, 2) stworzenie anglojęzycznych wersji wydawanych publikacji, 3) wdrożenie procedur zabezpieczających oryginalność publikacji naukowych oraz zastosowane techniki zabezpieczeń – są finansowane w ramach umowy 715/P-DUN/2017 ze środków Ministra Nauki i Szkolnictwa Wyższego przeznaczonych na działalność upowszechniającą naukę)

JOURNAL OF THEORETICAL AND APPLIED MECHANICS
55, 4, pp. 1113-1126, Warsaw 2017
DOI: 10.15632/jtam-pl.55.4.1113

NUMERICAL IMPLEMENTATION OF FINITE STRAIN ELASTO-PLASTICITY WITHOUT YIELD SURFACE

Cyprian Suchocki

Warsaw University of Life Sciences, Department of Fundamental Engineering, Warsaw, Poland
e-mail: cyprian_suchocki@sggw.pl

In the present study, the finite element (FE) implementation of elasto-plasticity without a yield surface is discussed. For that purpose, the method of perturbing the deformation gradient tensor is employed to calculate approximate tangent moduli. The development of a user subroutine that enables one to use the proposed model within the FE program ABAQUS is covered. A number of exemplary numerical simulations is conducted in order to check the performance of this subroutine. Material parameter values determined for different materials are utilized. Finally, the presented constitutive equation is examined upon its ability to capture the shear-softening process.

Keywords: constitutive equation, tangent moduli, UMAT, plasticity

1. Introduction

In this study, the finite element (FE) implementation of a plasticity theory is discussed, which does not introduce neither the yield surface nor the split of strain measures into elastic and plastic components. The basic concepts of the considered framework were first introduced as a part of a viscoplastic constitutive model for polymeric materials, cf Suchocki (2015). Further research proved applicability of the proposed theory to model the material response of metals (Suchocki and Skoczylas, 2016). However, in the case of metallic materials, correct numerical implementation of the considered class of constitutive equations requires a completely different approach from the one used in polymer modeling. This new treatment employs the perturbed deformation gradient method and is discussed in detail further in this work.

The proposed framework of constitutive modeling is a special case of the theory of plasticity whose basic assumptions were introduced by Pipkin and Rivlin (1965). However, the concept of an intrinsic time adopted therein and defined as the arclength in the nine-dimensional strain space has been slightly modified for the purpose of present considerations (cf Suchocki, 2015; Suchocki and Skoczylas, 2016). The fictitious time is utilized to build a functional of the deformation history which determines the material stress response and is analogous to the history functional known from the viscoelasticity theory (e.g. Holzapfel, 2010). The whole constitutive model is written in terms of tensorial internal state variables whose change with time is determined by proper evolution equations.

The FE implementation of the flow theory of plasticity based on the Huber-Mises-Hencky (HMH) yield condition (e.g. Olesiak, 1975) has been a subject of research for a long time. Various concepts of numerical integration have been proposed for the HMH flow plasticity such as radial return algorithms, see for instance Simo and Hughes (2000). These algorithms are rather costly in terms of numerical computations. In each iteration of the Newton-Raphson (N-R) procedure, the criterion of material plastic flow has to be checked. If a plastic deformation occurs, another N-R iterative process has to be initiated in order to calculate the increment of the equivalent

plastic strain. Nevertheless, the numerical algorithms and codes for the HMH flow plasticity have been optimized for decades and are considerably well established nowadays.

The FE implementation of plasticity theories which do not introduce a yield surface attracted rather little attention over the years. Lee (1995) discussed numerical implementation of the endochronic theory of plasticity that was developed by Valanis (1971a,b). Kästner *et al.* (2012) developed and implemented into the finite element method (FEM) a viscoplastic constitutive model which contained an elasto-plastic component similar to the endochronic formulation by Valanis. Both aforementioned approaches referred to the small strain domain. The constitutive equation proposed by Kästner *et al.* (2012) was further extended to the finite strain range by Alkas Yonan *et al.* (2013) using the spatial description in the deformed configuration of material continuum. The FE implementation was discussed as well. A viscoplastic model containing an elasto-plastic term without a yield condition was also proposed and implemented into FEM by Suchocki (2015). This model was formulated in the reference configuration using the material description and presents itself a generalization of the hyperelasticity theory. The approximation of the Material Jacobian (MJ) tensor proposed by Suchocki (2015) proved to be accurate enough for the purpose of modeling the mechanical response of polymers. However, application of the same constitutive modeling framework to metallic materials results in much higher values of the model constants. Consequently, it was noticed that a more accurate approximation of the MJ is required in order to describe the mechanical behavior of metals.

In the present work, the perturbed deformation gradient method proposed by Sun *et al.* (2008) is utilized to implement into FEM the constitutive equation of elasto-plasticity without the yield surface, cf Suchocki an Skoczylas (2016). The implementation of the model into the FE program ABAQUS is facilitated by taking advantage of the user subroutine UMAT (UserMATerial). The presented framework can also be adapted to other FE packages. The accuracy of the implementation is checked using numerous FE simulations performed for different material parameter values. The simplified approach which can be used for the modeling of polymeric materials such as polyethylene, for instance, is briefly discussed as well. The ability of the proposed constitutive model to describe the shear-softening process (e.g. Kowalewski and Szymczak, 2009) is investigated. Finally, an exemplary simulation is conducted to check the performance of the user subroutine for the case of nonhomogenous stress and strain states.

2. Basic notions

The stored elastic energy function $W(\mathbf{C})$ is assumed in the decoupled form (e.g. Holzapfel, 2010)

$$W(\mathbf{C}) = U(J) + \overline{W}(\overline{\mathbf{C}}) \tag{2.1}$$

where $U(J)$ and $\overline{W}(\overline{\mathbf{C}})$ are the volumetric and isochoric components, respectively. The multiplicative split of the deformation gradient $\mathbf{F}$ is utilized, i.e.

$$\mathbf{F} = \mathbf{F}_{vol}\overline{\mathbf{F}} \qquad J = \det \mathbf{F} \qquad \mathbf{F}_{vol} = J^{\frac{1}{3}}\mathbf{1} \qquad \overline{\mathbf{F}} = J^{-\frac{1}{3}}\mathbf{F} \tag{2.2}$$

which enables one to define the isochoric right Cauchy-Green (C-G) deformation tensor $\overline{\mathbf{C}}$ with a set of algebraic invariants, i.e.

$$\overline{\mathbf{C}} = \overline{\mathbf{F}}^{\mathrm{T}}\overline{\mathbf{F}} = J^{-\frac{2}{3}}\mathbf{C} \qquad \bar{I}_1 = \operatorname{tr}\overline{\mathbf{C}} \qquad \bar{I}_2 = \frac{1}{2}[(\operatorname{tr}\overline{\mathbf{C}})^2 - \operatorname{tr}\overline{\mathbf{C}}^2] \qquad \bar{I}_3 = \det\overline{\mathbf{C}} = 1 \tag{2.3}$$

The total second Piola-Kirchhoff (P-K) stress $\mathbf{S}$ is assumed to be the sum of the elastic component $\mathbf{S}_0$ and the tensorial internal state variables $\widetilde{\mathbf{H}}_k$ $(k = 1, 2, \ldots, N)$ which account for the inelastic effects (cf Suchocki and Skoczylas, 2016), thus

$$\mathbf{S} = \mathbf{S}_0 + \sum_{k=1}^{N} \widetilde{\mathbf{H}}_k \qquad \mathbf{S}_0 = \mathbf{S}_0^{vol} + \mathbf{S}_0^{iso}$$
$$\mathbf{S}_0^{vol} = Jp\mathbf{C}^{-1} \qquad \mathbf{S}_0^{iso} = J^{-\frac{2}{3}}\,\mathrm{DEV}\,[\overline{\mathbf{S}}] \tag{2.4}$$

where

$$p = \frac{\partial U}{\partial J} \qquad \overline{\mathbf{S}} = 2\frac{\partial \overline{W}}{\partial \overline{\mathbf{C}}}\Big|_{\overline{\mathbf{C}}=\overline{\mathbf{C}}^{\mathrm{T}}} \qquad \mathrm{DEV}\,[\overline{\mathbf{S}}] = \overline{\mathbf{S}} - \frac{1}{3}(\overline{\mathbf{S}}\cdot\overline{\mathbf{C}})\overline{\mathbf{C}}^{-1} \tag{2.5}$$

The change of each of the internal state variables is governed by a separate evolution equation, i.e.

$$\dot{\widetilde{\mathbf{H}}}_k + \frac{1}{\widetilde{D}_k M(|\dot{\overline{\mathbf{C}}}|)}\widetilde{\mathbf{H}}_k = \gamma_k \dot{\mathbf{S}}_0^{iso} \qquad k = 1, 2, \ldots, N \tag{2.6}$$

with

$$M(|\dot{\overline{\mathbf{C}}}|) = \bar{J}_2^{-\frac{1}{2}} \qquad \bar{J}_2 = \mathrm{tr}\,\dot{\overline{\mathbf{C}}}^2 \tag{2.7}$$

whereas $\widetilde{D}_k$ and γ_k are the material parameters $k = 1, 2, \ldots, N$.

3. Finite element implementation

For the purpose of numerical implementation, the considered constitutive model has to be discretized and further linearized, i.e. expressed as a linear relation between the finite increments of stress and strain. Below both formulations are presented.

3.1. Discretized constitutive equation

According to Eqs. $(2.4)_1$ and $(2.4)_2$, for the time increment $n+1$, the total second P-K stress is given as

$$\mathbf{S}_{n+1} = \mathbf{S}_{0\,n+1} + \sum_{k=1}^{N} \widetilde{\mathbf{H}}_{k\,n+1} \qquad \mathbf{S}_{0\,n+1} = \mathbf{S}_{0\,n+1}^{vol} + \mathbf{S}_{0\,n+1}^{iso} \tag{3.1}$$

with the internal state variables being determined from the discretized evolution equations, i.e.

$$\widetilde{\mathbf{H}}_{k\,n+1} = \frac{\left(1 - \frac{1}{\widetilde{D}_k}\frac{\Delta z_{n+1}}{2}\right)\widetilde{\mathbf{H}}_{k\,n} + \gamma_k(\mathbf{S}_{0\,n+1}^{iso} - \mathbf{S}_{0\,n}^{iso})}{1 + \frac{1}{\widetilde{D}_k}\frac{\Delta z_{n+1}}{2}} \qquad k = 1, 2, \ldots, N \tag{3.2}$$

where Δz_{n+1} is the increment of arclength, namely

$$\Delta z_{n+1} = \sqrt{\Delta\overline{\mathbf{C}}_{n+1} \cdot \Delta\overline{\mathbf{C}}_{n+1}} \tag{3.3}$$

The recurrence-update formula defined by Eq. (3.2) has been obtained by applying the central difference rule to Eq. (2.6), cf Suchocki (2015).

3.2. Linearized constitutive model

Taking the directional derivative on Eq. $(3.1)_1$ yields

$$\Delta\mathbf{S}_{n+1} = \boldsymbol{\mathcal{C}}^{e-p}_{n+1} \cdot \frac{1}{2}\Delta\mathbf{C}_{n+1} \qquad \boldsymbol{\mathcal{C}}^{e-p}_{n+1} = 2\frac{\partial \mathbf{S}_{n+1}}{\partial \mathbf{C}_{n+1}}\Big|_{\mathbf{C}_{n+1}=\mathbf{C}^{\mathrm{T}}_{n+1}} \tag{3.4}$$

with $\boldsymbol{\mathcal{C}}^{e-p}_{n+1}$ being the fourth-order elasto-plastic stiffness tensor. Pushing Eq. $(3.4)_1$ forward to the current configuration leads to the incremental rate equation

$$\boldsymbol{\tau}^{\nabla}_{n+1} = J_{n+1}\boldsymbol{\mathcal{C}}^{MJ}_{n+1} \cdot \Delta\mathbf{D}_{n+1} \tag{3.5}$$

where the incremental Zaremba-Jaumann (Z-J) rate of the Kirchhoff stress $\boldsymbol{\tau}_{n+1}$ is given as

$$\boldsymbol{\tau}^{\nabla}_{n+1} = \Delta\boldsymbol{\tau}_{n+1} - \Delta\mathbf{W}_{n+1}\boldsymbol{\tau}_{n+1} - \boldsymbol{\tau}_{n+1}\Delta\mathbf{W}^{\mathrm{T}}_{n+1} \qquad \boldsymbol{\tau}_{n+1} = \mathbf{F}_{n+1}\mathbf{S}_{n+1}\mathbf{F}^{\mathrm{T}}_{n+1} \tag{3.6}$$

The increments of the spin tensor $\mathbf{W}_{n+1}$, the strain rate tensor $\mathbf{D}_{n+1}$ and the deformation gradient $\mathbf{F}_{n+1}$ are defined by the following formulas

$$\begin{aligned}
\Delta\mathbf{W}_{n+1} &= \frac{1}{2}[\Delta\mathbf{F}_{n+1}\mathbf{F}^{-1}_{n+1} - (\Delta\mathbf{F}_{n+1}\mathbf{F}^{-1}_{n+1})^{\mathrm{T}}] \\
\Delta\mathbf{D}_{n+1} &= \frac{1}{2}[\Delta\mathbf{F}_{n+1}\mathbf{F}^{-1}_{n+1} + (\Delta\mathbf{F}_{n+1}\mathbf{F}^{-1}_{n+1})^{\mathrm{T}}] \\
\Delta\mathbf{F}_{n+1} &= \mathbf{F}_{n+1}\mathbf{F}^{-1}_{n}
\end{aligned} \tag{3.7}$$

whereas the MJ tensor takes the form

$$\boldsymbol{\mathcal{C}}^{MJ}_{n+1} = \frac{1}{J_{n+1}}(\boldsymbol{\mathcal{C}}^{\tau c}_{n+1} + \boldsymbol{\mathcal{I}}_{n+1}) \tag{3.8}$$

with

$$\begin{aligned}
\boldsymbol{\mathcal{C}}^{\tau c}_{n+1} &= (F_{iP}F_{jQ}F_{kR}F_{lS}\mathcal{C}^{e-p}_{PQRS})_{n+1}\mathbf{e}_i \otimes \mathbf{e}_j \otimes \mathbf{e}_k \otimes \mathbf{e}_l \\
\boldsymbol{\mathcal{I}}_{n+1} &= \frac{1}{2}(\delta_{ik}\tau_{jl} + \tau_{ik}\delta_{jl} + \delta_{il}\tau_{jk} + \tau_{il}\delta_{jk})_{n+1}\mathbf{e}_i \otimes \mathbf{e}_j \otimes \mathbf{e}_k \otimes \mathbf{e}_l
\end{aligned} \tag{3.9}$$

where $\{\mathbf{e}_k\}$ $(k = 1, 2, 3)$ is a Cartesian base in the current configuration. For the class of constitutive equations considered in this work, it is not possible to find an analytical, closed-form equation determining the MJ tensor. Thus, approximation methods have to be employed.

3.3. Approximate formula for Material Jacobian

Inserting Eq. $(3.1)_1$ into Eq. $(3.4)_2$ yields

$$\boldsymbol{\mathcal{C}}^{e-p}_{n+1} = 2\frac{\partial \mathbf{S}_{n+1}}{\partial \mathbf{C}_{n+1}}\Big|_{\mathbf{C}_{n+1}=\mathbf{C}^{\mathrm{T}}_{n+1}} = 2\frac{\partial \mathbf{S}_{0\,n+1}}{\partial \mathbf{C}_{n+1}}\Big|_{\mathbf{C}_{n+1}=\mathbf{C}^{\mathrm{T}}_{n+1}} + \sum_{k=1}^{M} 2\frac{\partial \widetilde{\mathbf{H}}_{k\,n+1}}{\partial \mathbf{C}_{n+1}}\Big|_{\mathbf{C}_{n+1}=\mathbf{C}^{\mathrm{T}}_{n+1}} \tag{3.10}$$

where, according to $(3.1)_2$, the elasticity tensor $\boldsymbol{\mathcal{C}}_{0\,n+1}$ is given as

$$\begin{aligned}
\boldsymbol{\mathcal{C}}_{0\,n+1} &= 2\frac{\partial \mathbf{S}_{0\,n+1}}{\partial \mathbf{C}_{n+1}}\Big|_{\mathbf{C}_{n+1}=\mathbf{C}^{\mathrm{T}}_{n+1}} = 2\frac{\partial \mathbf{S}^{vol}_{0\,n+1}}{\partial \mathbf{C}_{n+1}}\Big|_{\mathbf{C}_{n+1}=\mathbf{C}^{\mathrm{T}}_{n+1}} + 2\frac{\partial \mathbf{S}^{iso}_{0\,n+1}}{\partial \mathbf{C}_{n+1}}\Big|_{\mathbf{C}_{n+1}=\mathbf{C}^{\mathrm{T}}_{n+1}} \\
&= \boldsymbol{\mathcal{C}}^{vol}_{0\,n+1} + \boldsymbol{\mathcal{C}}^{iso}_{0\,n+1}
\end{aligned} \tag{3.11}$$

In general, utilizing Eq. (3.2) for calculation of $2\frac{\partial \widetilde{\mathbf{H}}_{k\,n+1}}{\partial \mathbf{C}_{n+1}}\big|_{\mathbf{C}_{n+1}=\mathbf{C}^{\mathrm{T}}_{n+1}}$ derivatives $(k = 1, 2, \ldots, N)$ leads the approximate elasto-plastic stiffness tensor $\boldsymbol{\mathcal{C}}^{e-p}_{n+1}$ to the loss of certain symmetries which

are required for a material to be initially isotropic. This fact was previously highlighted by Kästner *et al.* (2012) for the case of infinitesimal strains. However, for small values of constants γ_k ($k = 1, 2, \ldots, N$), the following approximation provides a good accuracy and preserves the initial material isotropy, i.e.

$$2\frac{\partial \widetilde{\mathbf{H}}_{k\,n+1}}{\partial \mathbf{C}_{n+1}}\bigg|_{\mathbf{C}_{n+1}=\mathbf{C}_{n+1}^{\mathrm{T}}} \approx \gamma_k\Big(1+\frac{\Delta z_{n+1}}{2\widetilde{D}_k}\Big)^{-1}\boldsymbol{\mathcal{C}}_{0\,n+1}^{iso} \tag{3.12}$$

Substitution of Eqs (3.11) and (3.12) into Eq. (3.10) leads to the formula

$$\boldsymbol{\mathcal{C}}_{n+1}^{e-p} = \boldsymbol{\mathcal{C}}_{0\,n+1}^{vol} + \Big[1+\sum_{k=1}^{N}\gamma_k\Big(1+\frac{\Delta z_{n+1}}{2\widetilde{D}_k}\Big)^{-1}\Big]\boldsymbol{\mathcal{C}}_{0\,n+1}^{iso} \tag{3.13}$$

An analogous result can be found for the small strain formulation, cf Kästner *et al.* (2012). By pushing Eq. (3.13) forward to the current configuration, the stiffness tensor associated with the convected rate of the Kirchhoff stress is found, i.e.

$$\boldsymbol{\mathcal{C}}_{n+1}^{\tau c} = \boldsymbol{\mathcal{C}}_{n+1}^{vol} + \Big[1+\sum_{k=1}^{N}\gamma_k\Big(1+\frac{\Delta z_{n+1}}{2\widetilde{D}_k}\Big)^{-1}\Big]\boldsymbol{\mathcal{C}}_{n+1}^{iso} \tag{3.14}$$

By inserting Eq. (3.14) into Eq. (3.8), the required form of the MJ is obtained. The discretized form of the constitutive equation along with the approximate MJ have been implemented into the FE program ABAQUS by utilizing the user subroutine UMAT written in FORTRAN 77 (cf Hibbit *et al.*, 2008).

3.4. Application to polymeric materials

Below the accuracy of MJ approximation defined by Eq. (3.14) is tested for the material constants that have been determined for ultra-high molecular weigth polyethylene (UHMWPE) using the previously developed parameter evaluation algorithm (Suchocki and Skoczylas, 2016), cf Table 1. The isochoric stored-energy function $\overline{W}$ is chosen in the form proposed by Knowles (1977), whereas the volumetic function U is assumed in the form used by Sussman and Bathe (1987), i.e.

$$\overline{W} = \frac{\mu}{2b}\Big\{\Big[1+\frac{b}{\kappa}\Big(\bar{I}_1-3\Big)\Big]^{\kappa}-1\Big\} \qquad U = \frac{1}{D_1}(J-1)^2 \tag{3.15}$$

Furthermore, it is assumed that the inelastic effects are modeled by a single internal variable ($N = 1$).

Table 1. Material constitutive parameters

Material	μ [MPa]	b [–]	κ [–]	D_1 [MPa^{-1}]	γ_1 [–]	$\widetilde{D}_1$ [–]
UHMWPE	62.042	3.63	0.25	3.3E-8	2.83	29E-3
Cast iron	665.16	-	-	3.3E-8	57.40	22E-3
Brass	703.48	-	-	1E-5	48.92	92E-4
WCL	1249.54	-	-	1E-5	31.73	34E-3
Inconel	1114.68	-	-	3.3E-8	83.43	34E-4

The test simulation involves a polymeric 1 mm×1 mm×1 mm block undergoing ramp loading and unloading (cf Fig. 1). The excitation is kinematic in the form of a prescribed displacement $\Delta\mathbf{u}_1$ of the cube frontal face along direction "1". This results in the stretch ratios λ_1 and λ_2 in direction "1" and perpendicular directions "2" and "3", respectively. The boundary conditions

along with the undeformed and deformed configurations are illustrated in Fig. 1. The polymeric block is first meshed using a single C3D8H[1] element. The simulations are then repeated with the mesh of 125 elements with the same results. The tests have been performed for both positive and negative magnitude of $\Delta\mathbf{u}_1$ (elongation and shortening, respectively).

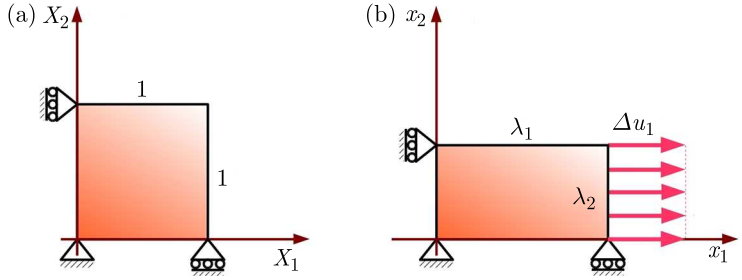

Fig. 1. Uniaxial tension-compression simulation: (a) undeformed FE, (b) deformed FE

In order to verify the results obtained in FE simulations, a Scilab program has been utilized which enables one to solve the one-dimensional process equations. This program is based on the previously presented scalar equation system, cf Suchocki and Skoczylas (2016). As it can be seen in Fig. 2, the ABAQUS UMAT and Scilab results are in an excellent agreement for both tension and compression which allows one to conclude that for small values of γ_k constants ($k = 1, 2, \ldots, N$) Eq. (3.14) provides an accurate approximation of the elasto-plastic stiffness.

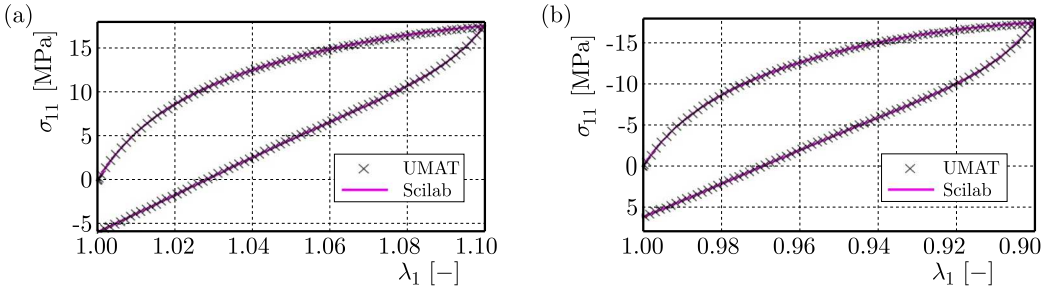

Fig. 2. Polymeric block undergoing: (a) ramp tensions with unloading, (b) ramp compression with unloading

3.5. Perturbed deformation gradient approach

For the group of metallic materials, the model parameters reach considerably high values, which makes approximate Eq. (3.14) inaccurate. Thus, the method of computing the approximate tangent moduli is utilized which is based on a perturbation of the deformation gradient tensor. This technique was originally proposed by Miehe (1996) and was further extended by Sun *et al.* (2008).

The perturbed deformation gradient tensor in the time increment $n+1$ is defined as

$$\widehat{\mathbf{F}}^{(kl)}_{n+1} = \mathbf{F}_{n+1} + \Delta\mathbf{F}^{(kl)}_{n+1} \tag{3.16}$$

where

$$\Delta\mathbf{F}^{(kl)}_{n+1} = \frac{\varepsilon}{2}(\mathbf{e}_k \otimes \mathbf{e}_l\mathbf{F}_{n+1} + \mathbf{e}_l \otimes \mathbf{e}_k\mathbf{F}_{n+1}) \tag{3.17}$$

with ε being the perturbation parameter. The increments of the strain rate tensor $\mathbf{D}_{n+1}$ and the spin tensor $\mathbf{W}_{n+1}$ due to the deformation gradient increment $\Delta\mathbf{F}^{(kl)}_{n+1}$ are given by the following relationships

[1]Cubic, three-dimensional, 8 nodes, hybrid.

$$\begin{aligned}\Delta\mathbf{D}_{n+1}^{(kl)} &= \frac{1}{2}[\Delta\mathbf{F}_{n+1}^{(kl)}\mathbf{F}_{n+1}^{-1} + (\Delta\mathbf{F}_{n+1}^{(kl)}\mathbf{F}_{n+1}^{-1})^{\mathrm{T}}]\\ \Delta\mathbf{W}_{n+1}^{(kl)} &= \frac{1}{2}[\Delta\mathbf{F}_{n+1}^{(kl)}\mathbf{F}_{n+1}^{-1} - (\Delta\mathbf{F}_{n+1}^{(kl)}\mathbf{F}_{n+1}^{-1})^{\mathrm{T}}]\end{aligned} \tag{3.18}$$

Inserting Eq. (3.17) into Eqs (3.18) and performing the computations results in

$$\Delta\mathbf{D}_{n+1}^{(kl)} = \frac{\varepsilon}{2}(\mathbf{e}_k\otimes\mathbf{e}_l + \mathbf{e}_l\otimes\mathbf{e}_k) \qquad \Delta\mathbf{W}_{n+1}^{(kl)} = \mathbf{0} \tag{3.19}$$

The increment of the Kirchhoff stress $\boldsymbol{\tau}_{n+1}$ is approximated by a finite difference, i.e.

$$\Delta\boldsymbol{\tau}_{n+1} \approx \boldsymbol{\tau}_{n+1}(\widehat{\mathbf{F}}_{n+1}^{(kl)}) - \boldsymbol{\tau}_{n+1}(\mathbf{F}_{n+1}) \tag{3.20}$$

Substitution of Eqs (3.19) and Eq. (3.20) into Eqs (3.5) and $(3.6)_1$ yields

$$\boldsymbol{\tau}_{n+1}(\widehat{\mathbf{F}}_{n+1}^{(kl)}) - \boldsymbol{\tau}_{n+1}(\mathbf{F}_{n+1}) \approx J_{n+1}\boldsymbol{\mathcal{C}}_{n+1}^{MJ}\cdot\frac{\varepsilon}{2}(\mathbf{e}_k\otimes\mathbf{e}_l + \mathbf{e}_l\otimes\mathbf{e}_k) \tag{3.21}$$

which, in turn, leads to the approximate formula for the components of MJ

$$\mathcal{C}_{ijkl}^{MJ} = \frac{1}{J_{n+1}\varepsilon}[\boldsymbol{\tau}_{n+1}(\widehat{\mathbf{F}}_{n+1}^{(kl)}) - \boldsymbol{\tau}_{n+1}(\mathbf{F}_{n+1})]_{ij} \tag{3.22}$$

In order to compute all 21 independent components of $\boldsymbol{\mathcal{C}}_{n+1}^{MJ}$, the deformation gradient tensor has to be perturbed for 6 times. During the entire procedure, the parameter ε is held constant with its value being prescribed by the programmer.

The framework presented above has been utilized to implement the proposed constitutive equation of elasto-plasticity into the FE package ABAQUS. A proper user subroutine UMAT written in FORTRAN 77 was used for that purpose, cf Hibbit *et al.* (2008). In the case of all the calculations described in this work ε = 1E-8 was assumed as recommended by Sun *et al.* (2008).

3.6. User subroutine UMAT

The perturbed deformation gradient method requires calculation of the Kirchhoff stress tensor components for a number of different deformation gradients. Thus, in order to shorten the UMAT code, a separate subroutine CALCSTRESS computing the stress tensor has been written and is called within the main code whenever it is necessary to compute the stress. The user subroutine is then used to simulate the mechanical response of metals. The structure of the code is depicted in the attached scheme.

4. Application to metallic materials

For the purpose of modeling the constitutive response of metals, it has been assumed that the isochoric stored energy had the form of neo-Hooke function, i.e.

$$\overline{W} = \frac{\mu}{2}(\bar{I}_1 - 3) \tag{4.1}$$

with the volumetric energy component given by Eq. $(3.15)_2$ which reflects a linear relationship between the pressure and the relative volume change. A more detailed description of the volumetric material response can be achieved by the adjustment of a more sophisticated volumetric energy U (cf Doll and Schweizerhof, 2000). However, such an approach would require a more thorough experimental study.

The material parameter evaluation algorithm developed by Suchocki and Skoczylas (2016) has been utilized to determine the constant values for: cast iron, brass, WCL steel and Inconel.

Algorithm for the implementation in Abaqus

Subroutine UMAT(input: $\mathbf{F}_{n+1}$, STATEV, PROPS; output: $\boldsymbol{\sigma}_{n+1}$, $\boldsymbol{\mathcal{C}}^{MJ}_{n+1}$)

1. Calculate transformation Jacobian $J_{n+1} = \det \mathbf{F}_{n+1}$
2. Extract STATEV, i.e. $\mathbf{S}^{iso}_{0\,n}$, $\widetilde{\mathbf{H}}_{k\,n}$, $\overline{\mathbf{C}}_n$ $(k = 1, 2, \ldots, N)$
3. Calculate Cauchy stress: **Call** CALCSTRESS, $\boldsymbol{\sigma}_{n+1} = J^{-1}_{n+1}\boldsymbol{\tau}_{n+1}$

   Subroutine CALCSTRESS(input: $\mathbf{F}_{n+1}$, J_{n+1}, STATEV, PROPS; output: $\boldsymbol{\tau}_{n+1}$)

   (a) Calculate strain measures from current increment

   $$\mathbf{C}_{n+1} = \mathbf{F}^{\mathrm{T}}_{n+1}\mathbf{F}_{n+1} \qquad \overline{\mathbf{C}}_{n+1} = J^{-\frac{2}{3}}_{n+1}\mathbf{C}_{n+1}$$

   (b) Calculate elastic stresses from current increment

   $$\mathbf{S}^{vol}_{0\,n+1} = J_{n+1}p_{n+1}\mathbf{C}^{-1}_{n+1} \qquad p_{n+1} = \partial_{J_{n+1}}U(J_{n+1})$$
   $$\mathbf{S}^{iso}_{0\,n+1} = J^{-\frac{2}{3}}_{n+1}\,\mathrm{DEV}\,[\overline{\mathbf{S}}_{n+1}] \qquad \overline{\mathbf{S}}_{n+1} = 2\partial_{\overline{\mathbf{C}}_{n+1}}\overline{W}(\overline{\mathbf{C}}_{n+1})\big|_{\overline{\mathbf{C}}_{n+1}=\overline{\mathbf{C}}^{\mathrm{T}}_{n+1}}$$
   $$\mathbf{S}_{0\,n+1} = \mathbf{S}^{vol}_{0\,n+1} + \mathbf{S}^{iso}_{0\,n+1}$$

   (c) Update internal state variables $(k = 1, 2, \ldots, N)$

   $$\Delta z_{n+1} = \sqrt{\Delta\overline{\mathbf{C}}_{n+1} \cdot \Delta\overline{\mathbf{C}}_{n+1}} \qquad \Delta\overline{\mathbf{C}}_{n+1} = \overline{\mathbf{C}}_{n+1} - \overline{\mathbf{C}}_n$$
   $$\widetilde{\mathbf{H}}_{k\,n+1} = \frac{\left(1 - \frac{1}{\widetilde{D}_k}\frac{\Delta z_{n+1}}{2}\right)\widetilde{\mathbf{H}}_{k\,n} + \gamma_k(\mathbf{S}^{iso}_{0\,n+1} - \mathbf{S}^{iso}_{0\,n})}{1 + \frac{1}{\widetilde{D}_k}\frac{\Delta z_{n+1}}{2}}$$

   (d) Calculate total stress from current increment

   $$\mathbf{S}_{n+1} = \mathbf{S}_{0\,n+1} + \sum_{k=1}^{M}\widetilde{\mathbf{H}}_{k\,n+1} \qquad \boldsymbol{\tau}_{n+1} = \mathbf{F}_{n+1}\mathbf{S}_{n+1}\mathbf{F}^{\mathrm{T}}_{n+1}$$

4. Calculate elastic-plastic stiffness: **Call** CALCTANGENT

   Subroutine CALCTANGENT(input: $\mathbf{F}_{n+1}$, J_{n+1}, STATEV, PROPS, $\boldsymbol{\tau}_{n+1}$; output: $\boldsymbol{\mathcal{C}}^{MJ}_{n+1}$)
   For prescribed ij and rs:

   (a) **Call** DEFGRAD

   Subroutine DEFGRAD(input: $\mathbf{F}_{n+1}$, rs; output: $\widehat{\mathbf{F}}^{(rs)}_{n+1}$)

   i. Calculate deformation gradient increment

   $$\Delta\mathbf{F}^{(rs)}_{n+1} = \frac{\varepsilon}{2}(F_{sL}\mathbf{e}_r \otimes \mathbf{e}_L + F_{rL}\mathbf{e}_s \otimes \mathbf{e}_L)$$

   ii. Calculate perturbed deformation gradient

   $$\widehat{\mathbf{F}}^{(rs)}_{n+1} = \mathbf{F}_{n+1} + \Delta\mathbf{F}^{(rs)}_{n+1}$$

   (b) **Call** CALCSTRESS ($\widehat{\mathbf{F}}^{(rs)}_{n+1}$ as input deformation gradient)

   (c) Calculate Material Jacobian components:

   $$\mathcal{C}^{MJ}_{ijrs} = \frac{1}{J_{n+1}\varepsilon}\left[\boldsymbol{\tau}_{n+1}(\widehat{\mathbf{F}}^{(rs)}_{n+1}) - \boldsymbol{\tau}_{n+1}(\mathbf{F}_{n+1})\right]_{ij}$$

5. Store $\mathbf{S}^{iso}_{0\,n+1}$, $\widetilde{\mathbf{H}}_{k\,n+1}$, $\overline{\mathbf{C}}_{n+1}$ in STATEV $(k = 1, 2, \ldots, N)$

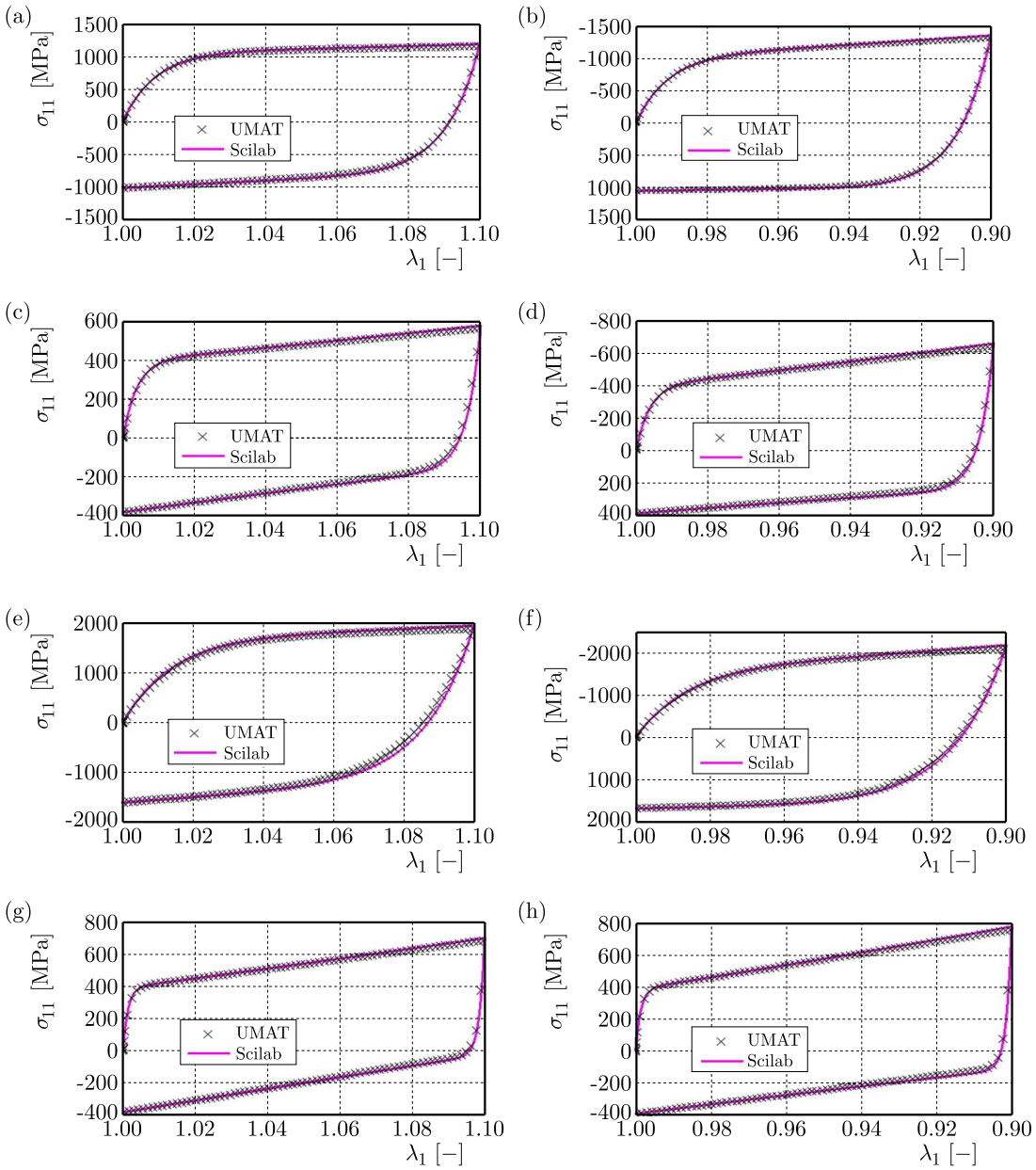

Fig. 3. Metal block undergoing ramp loading-unloading: (a) cast iron tension, (b) cast iron compression, (c) brass tension, (d) brass compression, (e) WCL tension, (f) WCL compression, (g) Inconel tension, (h) Inconel compression

The parameter values have been gathered in Table 1. In simple tension experiments, metals usually act like incompressible materials after reaching the axial strain value of 0.5% with their Poisson's ratio close to 0.5 (e.g. Kozłowska, 2011). Thus, the incompressibility condition is well established within the theory of plasticity. In order to account for the material near incompressibility of cast iron and Inconel, the hybrid elements C3D8H have been used during numerical simulations. In order to check the performance of the UMAT code in the presence of a certain amount of compressibility, $D_1 =\sim$ 1E-5 MPa^{-1} has been set for brass and WCL steel. In the case of the last two materials, ordinary cubic elements C3D8 were utilized.

For each of the considered materials ramp loading/unloading processes have been simulated. Both tension and compression tests have been considered. The boundary conditions are depicted in Fig. 1. In parallel to the FE simulations, every considered process has been independently simulated in Scilab by direct integration of the one-dimensional process equations (cf

Suchocki and Skoczylas, 2016). An excellent agreement has been found between ABAQUS and Scilab predictions which is depicted in Fig. 3 and allows one to conclude that the utilized MJ approximation method provides satisfying accuracy.

5. Comparison to HMH plasticity

In order to highlight the benefits of the proposed formulation of elasto-plasticity, a comparative study has been conducted. The material parameters of the HMH plasticity with isotropic hardening were determined for brass using the same experimental data that were utilized to evaluate the constants of the proposed new constitutive equation.

The determined parameters of the HMH plasticity were defined in ABAQUS to perform a simulation of ramp tension with unloading. The large strain formulation was utilized by setting on the NLGEOM option. Again, the boundary conditions illustrated in Fig. 1 were used. The results along with the list of material constants can be seen in Fig. 4a. The flow plasticity model provides an accurate description of the monotonic loading process, however, at the price of defining 16 material parameters (Fig. 4b). No Bauschinger effect has been observed.

(a)

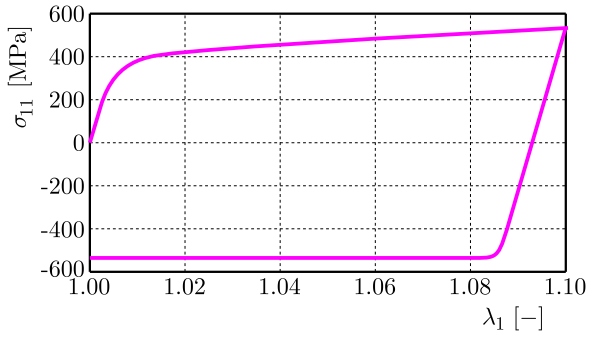

(b)

E [MPa]		ν [–]
84298		0.36
i	$\sigma_y(e_i^p)$	e_i^p
1	218	0
2	311	0.00141
3	374	0.004
4	402	0.00729
5	430	0.0193
6	470	0.0412
7	538	0.0935

Fig. 4. HMH plasticity model for brass: (a) ramp tension-compression response, (b) material parameters

In the next step, the HMH flow plasticity and the proposed elasto-plastic model have been compared in their ability to describe the shear-softening process (e.g. Kowalewski and Szymczak, 2009). For that purpose, FE simulations were prepared in which a brass block with the dimensions 1 mm×1 mm×1 mm was undergoing simultaneous elongation and shear deformation. The initial configuration of the block can be seen in Fig. 5d. The simulation was divided into two stages, i.e. uniaxial tensile prestrain (stage one) and combined tension and shear (stage two). For the first stage of the simulation, the following boundary conditions have been assumed (cf Fig. 5e):

1. The displacement in "1" direction is set to zero on the face $ABCD$.
2. The displacement in "2" direction is set to zero on the face $AA'BB'$.
3. The displacement in "3" direction is set to zero on the face $BB'CC'$.
4. On the face $A'B'C'D'$, a ramp displacement in "1" direction is defined with the maximum value $\Delta u_1/2 = 0.0275\,\text{mm}$.

The uniaxial deformation phase ends when $t = t_0$ (Fig. 5e). For the second stage of the simulation the boundary conditions listed below are assumed:

1. The displacement in "1" direction is set to zero on the edge DC.
2. The zero displacement is set for the point B.

3. The displacements in "1" and "2" directions are set to zero for the point A.

4. The zero displacement in "3" direction is set for the edge $B'C'$.

5. The displacements in "1" and "2" directions are imposed on the face $A'B'C'D'$. The displacement in "1" direction is assumed to increase linearly strating from the initial value $\Delta u_1/2 = 0.0275\,\text{mm}$ up to the maximum value $\Delta u_1 = 0.055\,\text{mm}$. The displacement in "2" direction is given as a triangle periodic function (Fig. 5a).

The deformed cube at the time instant $t \in \langle t_0; t_1 \rangle$ can be seen in Fig. 5f. The axial stress response obtained for the HMH plasticity is depicted in Fig. 5b. The axial stress generated for the present constitutive model (Fig. 5c) is in a better agreement with the experimental measurements (e.g. Kowalewski and Szymczak 2009) than the predictions of the classical flow theory.

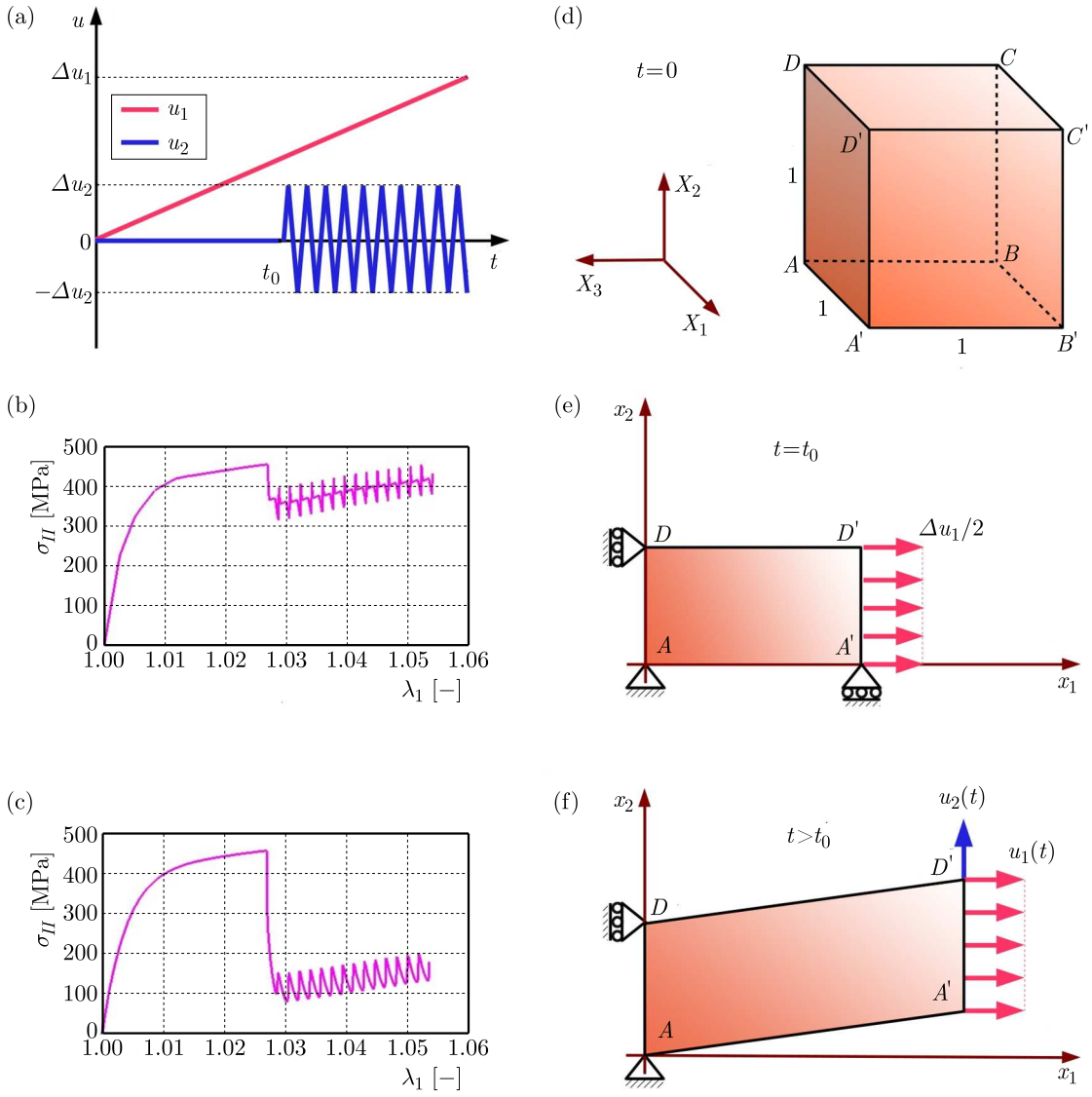

Fig. 5. Combined elongation and shear deformation: (a) displacement functions, (b) shear softening (HMH plasticity), (c) shear softening (UMAT), (d) undeformed cube, (e) deformed cube at the end of stage 1 of the deformation process, (f) deformed cube during stage 2 of the deformation process

6. Simulation of nonhomogenous deformation process

In order to check the performance of the UMAT code in the case of nonhomogenous deformations, a cylinder loaded by the internal pressure has been analyzed. The boundary conditions and cylinder dimensions are depicted in Fig. 6a. Due to the axial symmetry of this problem, only a quarter of the cylinder was taken into account. The FE mesh used C3D8 brick elements and can be seen in Fig. 6b. The loading pressure p was defined to increase linearly until the value of 470 MPa was reached. Subsequently, the unloading process began. A residual stress and strain states remained in the cylinder after the unloading. The material parameter values determined for the Inconel alloy (supersaturated) were utilized (Table 1). The results of FE simulation are gathered in Fig. 7.

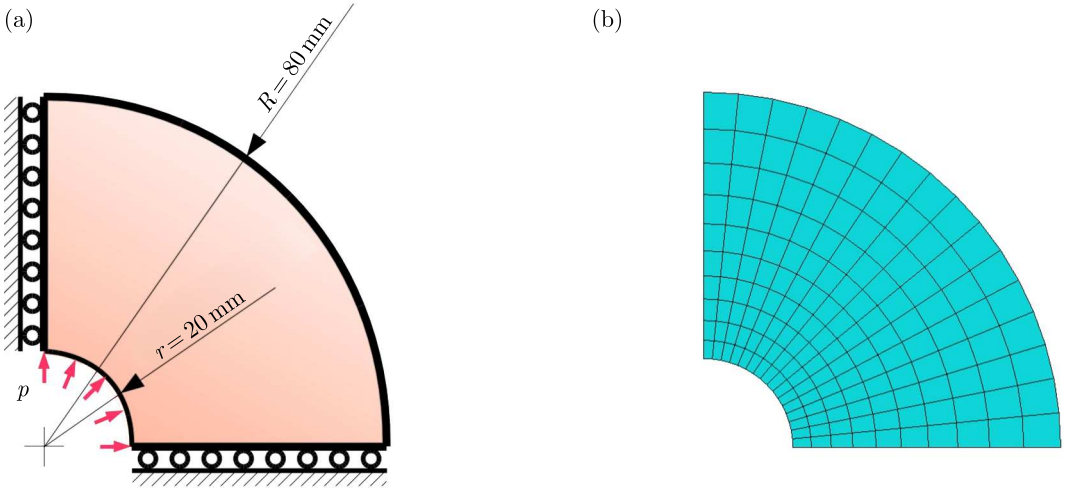

Fig. 6. Cylinder loaded by internal pressure: (a) boundary conditions, (b) FE mesh

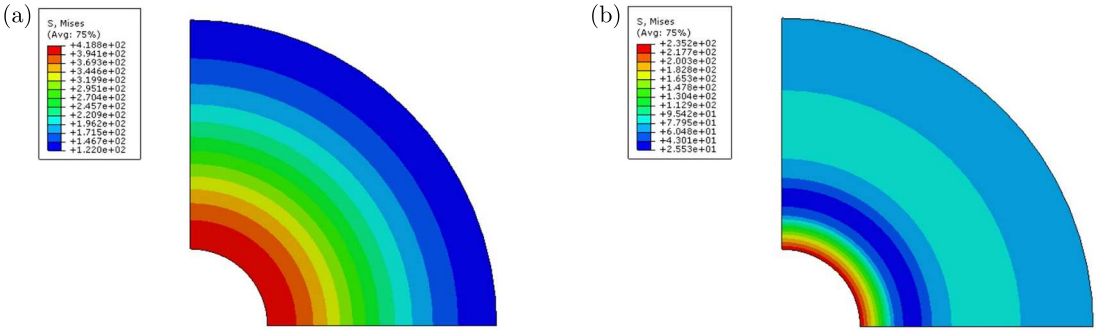

Fig. 7. FE simulation results: (a) HMH stress, (b) HMH residual stress

7. Conclusions

In this work, the FE implementation of the elasto-plasticity without the yield surface is discussed. As it is illustrated, in the case of metals, the proposed elasto-plastic model can be implemented into FEM by utilizing the perturbed deformation gradient method. It should be emphasized that the presented framework of modeling is universal in the sense that it provides a uniform constitutive description for both metals and polymers. Furthermore, the number of the material parameters required to be determined is considerably small. The proposed model

uses 4 constants to describe the mechanical behavior of brass, whereas the HMH flow plasticity needed determination of 16 parameters. The developed constitutive model is capable of describing the Bauschinger effect and shear-softening effects that the classical plasticity fails to capture accurately. What is more, the computation cost turns out to be smaller in the case of using the proposed elastic-plastic model. Further improvement in this matter can be expected after the developed user subroutine is thoroughly optimized.

Acknowledgement
This work was supported by project PBS III/246715/NCBiR.

References

1. Alkas Yonan S., Soyarslan C., Haupt P., Kwiatkowski L., Tekkaya A.E., 2013, A simple finite strain non-linear visco-plastic model for thermoplastics and its application to the simulation of incremental cold forming of polyvinylchloride (PVC), *International Journal of Mechanical Sciences*, **66**, 192-201
2. Doll S., Schweizerhof K., 2000, On the development of vlumetric strain energy functions, *Journal of Applied Mechanics*, **67**, 17-21
3. Hibbit B., Karlsson B., Sorensen P., 2008, *ABAQUS Theory Manual*, Hibbit, Karlsson & Sorensen Inc.
4. Holzapfel G.A., 2010, *Nonlinear Solid Mechanics*, John Wiley & Sons Ltd., New York
5. Kästner M., Obst M., Brummund J., Thielsch K., Ulbricht V., 2012, Inelastic material behavior of polymers – Experimental characterization, formulation and implementation of a material model, *Mechanics of Materials*, **52**, 40-57
6. Knowles J. K., 1977, The finite anti-plane shear field near the tip of a crack for a class of incompressible elastic solids, *International Journal of Fracture*, **13**, 5, 611-639
7. Kowalewski Z.L., Szymczak T., 2009, Variation of mechanical parameters of engineering materials under tension due to cyclic deformation by torsion, *Engineering Transactions*, **57**, 113-123
8. Kozłowska B., 2011, Experimental strain and stress analysis in the process of formation and evolution of elastic-plastic zones in construtions (in Polish), *Scientific Surveys of Warsaw University of Technology, Mechanics*, **239**
9. Lee C.F., 1995, Recent finite element applications of the incremental endochronic plasticity, *International Journal of Plasticity*, **11**, 843-865
10. Miehe C., 1996, Numerical computation of alghoritmic (consistent) tangent moduli in large-strain computational inelasticity, *Computer Methods in Applied Mechanics and Engineering*, **134**, 223-240
11. Olesiak Z., 1975, On Huber-Mises yield condition (in Polish), *Mechanika Teoretyczna i Stosowana*, **13**, 523-528
12. Pipkin A.C., Rivlin R.S., 1965, Mechanics of rate-independent materials, *ZAMP*, **16**, 313-327
13. Simo J.C., Hughes T.J.R., 2000, *Computational Inelasticity*, Springer Verlag Inc., New York
14. Suchocki C., 2015, An internal-state-variable based viscoelastic-plastic model for polymers, *Journal of Theoretical and Applied Mechanics*, **53**, 593-604
15. Suchocki C., Skoczylas P., 2016, Finite strain formulation of elasto-plasticity without yield surface: theory, parameter identification and applications, *Journal of Theoretical and Applied Mechanics*, **54**, 731-742
16. Sun W., Chaikof E.L., Levenston M.E., 2008, Numerical approximation of tangent moduli for finite element implementations of nonlinear hyperelastic material models, *Journal of Biomechanical Engineering*, **130**, 061003-1 – 061003-7

17. Sussman T., Bathe K.J., 1987, A finite element formulation for nonlinear incompressible hyperelastic and inelastic analysis, *Computers and Structures*, **26**, 357-409

18. Valanis K.C., 1971a, A theory of viscoplasticity without a yield surface, Part I: General theory, *Archives of Mechanics*, **23**, 517-534

19. Valanis K.C., 1971b, A theory of viscoplasticity without a yield surface, Part II: Application to mechanical behavior of metals, *Archives of Mechanics*, **23**, 535-551

Manuscript received October 8, 2016; accepted for print February 15, 2017

JOURNAL OF THEORETICAL AND APPLIED MECHANICS
55, 4, pp. 1127-1139, Warsaw 2017
DOI: 10.15632/jtam-pl.55.4.1127

A MULTI-SPRING MODEL FOR BUCKLING ANALYSIS OF CRACKED TIMOSHENKO NANOBEAMS BASED ON MODIFIED COUPLE STRESS THEORY

Majid Akbarzadeh Khorshidi, Mahmoud Shariati
Ferdowsi University of Mashhad, Department of Mechanical Engineering, Mashhad, Iran
e-mail: mshariati44@um.ac.ir

This paper develops a cracked nanobeam model and presents buckling analysis of this developed model based on a modified couple stress theory. The Timoshenko beam theory and simply supported boundary conditions are considered. This nonclassical model contains a material length scale parameter and can interpret the size effect. The cracked nanobeam is modeled as two segments connected by two equivalent springs (longitudinal and rotational). This model promotes discontinuity in rotation of the beam and additionally considers discontinuity in longitudinal displacement due to presence of the crack. Therefore, this multi-spring model can consider coupled effects between the axial force and bending moment at the cracked section. The generalized differential quadrature (GDQ) method is employed to discretize the governing differential equations, boundary and continuity conditions. The influences of crack location, crack severity, material length scale parameter and flexibility constants of the presented spring model on the critical buckling load are studied.

Keywords: buckling, crack, modified couple stress theory, Timoshenko nanobeam, spring model

1. Introduction

Many applicable structures have been used in micro- and nano-scale dimensions. Size effects are significant in the mechanical behavior of these structures. Since the classical continuum mechanics cannot predict the size effect, some size-dependent continuum theories have been developed to capture the size effect using some material length scale parameters. These parameters are related to inherent properties of materials, which become considerable in small scale structures. In view of the difficulties in determining these internal parameters, non-classical continuum theories involving only one material length scale parameter are desirable. A modified couple stress theory has been proposed by Yang *et al.* (2012). This theory uses only one material length scale parameter to capture the size-dependent behavior of structures and employs only the symmetric part of the couple stress tensor as a suitable measure of the continuum micro-rotation. Many studies have been done on the static and dynamic behavior of nanostructures based on the modified couple stress theory. Here we focuse on the static and dynamic behavior of the micro/nanobeams specially on the buckling of the nanobeams.

Park and Gao (2006, 2008) formulated a modified couple stress based model for the Euler-Bernoulli beam and that model was extended by Ma *et al.* (2008) for the Timoshenko beam using Hamilton's principle. Also, a microstructure dependent non-classical Reddy-Levinson beam model was developed by Ma *et al.* (2010), and the difference between the results obtained from the non-classical and the classical models was illustrated for static bending and free vibration. Simsek (2010) proposed analytical and numerical solution procedures for vibration of an embedded microbeam under action of a moving microparticle and studied the influences of the material length scale parameter, Poisson's ratio, velocity of the microparticle and the elastic

medium constant on the maximum dynamic deflections of the microbeam. A size-dependent nonlinear Euler-Bernoulli beam model was presented by Xia *et al.* (2010). They studied nonlinear size-dependent static bending, postbuckling and the free vibration of beams, and Asghari *et al.* (2010) developed their model for Timoshenko beam theory. Ke and Wang (2011) investigated dynamic stability of FGM Timoshenko microbeams and showed the significance of the size effect on dynamic stability. Buckling analysis of microbeams with higher order theories and general boundary conditions was investigated by Mohammad-Abadi and Daneshmehr (2014). They revealed accuracy of the GDQ method for that modified couple stress based size-dependent buckling problem. Also, Mohammad-Abadi and Daneshmehr (2015) developed vibration analysis of composite laminated beams in order of microns using the GDQ method. Akbarzadeh Khorshidi and Shariati (2016b) presented a comprehensive solution for free vibration of a shear deformable S-FGM nanobeam by the GDQ method. Dehrouyeh-Semnani *et al.* (2015) investigated dynamic characteristics of axially moving Timoshenko microbeams using Hamilton's principle and Galerkin's method. An exact solution for prediction of postbuckling behavior of shear deformable nanobeams was presented by Akbarzadeh Khorshidi and Shariati (2015). Also, Akbarzadeh Khorshidi and Shariati (2016a) investigated the propagation of the stress wave in a shear deformable nanobeam and evaluated the effects of shear deformation, material length scale parameter and Poisson's ratio on the phase velocity of it.

It is well known that cracks increase flexibility of a structure. Therefore, the presence of a crack leads to reduction of the stiffness of a structure. So, a simple and accurate model should be used to determine this reduction in stiffness. For this reason, the cracked beam is modeled as two segments connected by means of massless springs (Freund and Herrmann, 1976; Adams *et al.*, 1978). Rice and Levy (1972) viewed the plate as a strictly two dimensional continuum with a local reduction in bending and extensional stiffness along the crack line. This model, which has become known as the line spring model for surface flaws, was also discussed in detail by Rice (1972). Most of the studies which have been recently done utilized an equivalent massless rotational spring at the cracked section. Thus, at the cracked section, a discontinuity in rotation due to bending must be considered. This model has been extensively used for vibration, buckling and postbuckling analyses of cracked structures like cracked beams. Chaudhari and Maiti (2000) presented a method of modelling for transverse vibrations of geometrically segmented slender cracked beams. Lele and Maiti (2002) studied transverse vibration of short beams to detect the location of a crack. Yang and Chen (2008) investigated free vibration and elastic buckling of beams made of FGMs containing three open edge cracks. Ke *et al.* (2009) studied the postbuckling response of edge cracked FG Timoshenko beams. Also, there are many other research works in the context of cracked structures by using the equivalent spring model, see for instance, Chati *et al.* (1997), Krawczuk *et al.* (2003), El Bikiri *et al.* (2006), Kitipornchai *et al.* (2009), Yan *et al.* (2011). But, these models cannot satisfy the multiple discontinuities at the cracked section. Loya *et al.* (2006) considered a rotational and an extensional spring at the cracked section for bending vibration of a Timoshenko cracked beam. Thus, in addition to the discontinuity in rotation due to bending, a discontinuity in the transverse deflection due to shearing has been also defined at the cracked section. However, the contribution of the extensional spring to the strain energy of the system is small in comparison with that of the rotational spring, nevertheless, this discontinuity has been considered for coherency with the general derivation of compliance for cracked beams (Okamura *et al.*, 1973; Tharp, 1987).

There are a few studies on cracked micro/nanostructures, which are mostly different types of vibration analyses of cracked nanobeams based on a nonclassical continuum theory by means of the rotational spring model. Flexural vibrations of cracked nanobeams based on the theory of nonlocal elasticity applied to Euler-Bernouilli beams was studied by Loya *et al.* (2009). They proposed a model containing a rotational and a longitudinal elastic spring at the cracked section and defined compatibility relations of this model. This model presents a discontinuity in the

rotation and a discontinuity in the longitudinal displacement. But, they simplified their model to one spring only (rotational spring) by some assumptions, and many authors followed them for free transverse vibration analyses of cracked nanobeams (Hasheminejad *et al.*, 2011; Torabi and Nafar Dastgerdi, 2012; Hosseini-Hashemi *et al.*, 2014). Of course, those assumptions can be acceptable for free transverse vibration. Also, Hsu *et al.* (2011) investigated longitudinal frequency of a cracked nanobeam by means of the longitudinal spring model. They expressed continuity conditions as a relation between the longitudinal displacement and axial force, and nelegted the discontinuity in rotation. Also, Loya *et al.* (2014) analysed torsional vibrations of a nanorod with a circumferential crack using a nonlocal elasticity model. They utilized a torsional elastic spring at the cracked section to consider additional strain energy due to the presence of the crack, so, a discontinuity in the torsion angle of the rod at the cracked section is introduced. Therefore, an appropriate model can be selected to simulate the influence of the crack based on the type of analysis and the applied loadings.

This paper makes one of the first attempts to investigate the buckling of cracked nanobeams based on a modified couple stress theory. This modified couple stress based Timoshenko beam model contains a material length scale parameter and can interpret the size effect. The present model considers coupled effects between the axial force and bending moment using a longitudinal and a rotational spring at the cracked section. Govrning equations are derived by using the principle of minimum potential energy. The Generalized Differential Quadrature (GDQ) method is employed to solve the governing differential equations. Then the critical buckling loads for different crack locations, crack severities and ratios of the material length scale parameter to thickness are computed, and the obtained results are compared with those corresponding to the classical beam model.

2. Formulation

2.1. Modified couple stress theory

In this Section, a modified couple stress theory (Yang *et al.*, 2012) with only one material length scale parameter is employed to capture the size effect. According to this theory, the strain energy U in an isotropic linear elastic beam under an axial compressive load P at both ends is defined as (Mohammad-Abadi and Daneshmehr, 2014)

$$U = \frac{1}{2}\int\limits_{\Omega}(\sigma_{ij}\delta\varepsilon_{ij} + m_{ij}\delta\chi_{ij})\,dv - \frac{1}{2}\int\limits_{0}^{L} P\Big(\frac{\partial w}{\partial x}\Big)^2\,dx \qquad i,j = 1,2,3 \tag{2.1}$$

where $\boldsymbol{\varepsilon}$, $\boldsymbol{\sigma}$, $\boldsymbol{\chi}$ and $\mathbf{m}$ are the strain tensor, Cauchy stress tensor, symmetric curvature tensor and the deviatoric part of the couple stress tensor, respectively. These tensors are defined as

$$\begin{aligned} \varepsilon_{ij} &= \frac{1}{2}(\nabla\mathbf{u} + (\nabla\mathbf{u})^{\mathrm{T}}) = \frac{1}{2}(u_{i,j} + u_{j,i}) \qquad & \sigma_{ij} &= \lambda\,\mathrm{tr}\,(\varepsilon_{ii})\delta_{ij} + 2\mu\varepsilon_{ij} \\ \chi_{ij} &= \frac{1}{2}(\nabla\theta + (\nabla\theta)^{\mathrm{T}}) = \tfrac{1}{2}(\theta_{i,j} + \theta_{j,i}) \qquad & m_{ij} &= 2\ell^2\mu\chi_{ij} \end{aligned} \tag{2.2}$$

where ℓ is the material length scale parameter which is mathematically the square root of the ratio of the modulus of curvature to the modulus of shear and is physically a property measuring the effect of couple stress (Park and Gao, 2006; Ma *et al.*, 2008). This parameter can be determined from torsion tests of slim cylinders of different diameters or bending tests of thin beams of different thickness. Also, λ and μ are Lame's constants and are defined as

$$\lambda = \frac{\nu E}{(1+\nu)(1-2\nu)} \qquad \mu = \frac{E}{2(1+\nu)} \tag{2.3}$$

where E is Young's modulus and ν is Poisson's ratio. The rotation vector $\boldsymbol{\theta}$ is given as

$$\theta = \frac{1}{2}\,\mathrm{curl}\,(\mathbf{u}) \tag{2.4}$$

2.2. Displacement field

Consider a beam of length L, width b and thickness h. The Timoshenko beam theory is employed to describe the effect of shear deformation. According to the rectangular Cartesian coordinate system shown in Fig. 1, where the x-axis is coincident with the centroidal axis of the undeformed beam, the y-axis is the neutral axis and the z-axis is the symmetry axis, the displacement field in a Timoshenko beam is described as

$$u_1 = u(x,t) - z\varphi(x,t) \qquad u_2 = 0 \qquad u_3 = w(x,t) \tag{2.5}$$

where u_1, u_2 and u_3 are, respectively, the x-, y- and z-components of the displacement vector $\mathbf{u}$, u and w are, respectively, the x- and z-components of the displacement vector of a point located on the beam axis, and φ is the angle of rotation of the cross-section.

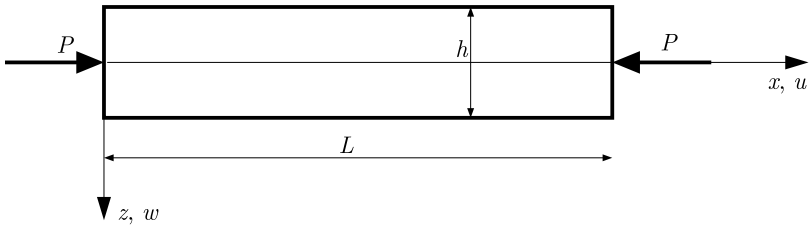

Fig. 1. Beam configuration and coordinate system

From Eqs. $(2.2)_1$ and (2.5), the nonzero strains are given as

$$\varepsilon_{xx} = \frac{\partial u_1}{\partial x} = \frac{\partial u}{\partial x} - z\frac{\partial \varphi}{\partial x} \qquad \varepsilon_{xz} = \frac{1}{2}\Big(\frac{\partial u_1}{\partial z} + \frac{\partial w}{\partial x}\Big) = \frac{1}{2}\Big(\frac{\partial w}{\partial x} - \varphi\Big) \tag{2.6}$$

and from Eqs. $(2.2)_2$ and (2.5), the nonzero stresses are given as

$$\begin{aligned} \sigma_{xx} &= (\lambda + 2\mu)\varepsilon_{xx} = (\lambda + 2\mu)\Big(\frac{\partial u}{\partial x} - z\frac{\partial \varphi}{\partial x}\Big) \\ \sigma_{xz} &= 2\mu\varepsilon_{xz} = \mu\Big(\frac{\partial w}{\partial x} - \varphi\Big) \end{aligned} \tag{2.7}$$

Using Eqs. (2.4) and (2.5), the nonzero component of the rotation vector is obtained as

$$\theta_y = -\frac{1}{2}\Big(\varphi + \frac{\partial w}{\partial x}\Big) \tag{2.8}$$

and from Eqs. $(2.2)_{3,4}$ and (2.8), we have

$$\chi_{xy} = -\frac{1}{4}\Big(\frac{\partial \varphi}{\partial x} + \frac{\partial^2 w}{\partial x^2}\Big) \qquad m_{xy} = -\frac{1}{2}\ell^2\mu\Big(\frac{\partial \varphi}{\partial x} + \frac{\partial^2 w}{\partial x^2}\Big) \tag{2.9}$$

2.3. Governing equations

Substituting Eqs. (2.6), (2.7) and (2.9) into Eq. (2.1), the total strain energy of the Timoshenko nanobeam is achieved. Then, using the principle of minimum potential energy and

fundamental lemma of the calculus of variation, the governing equations of the Timoshenko nanobeam in terms of displacements are obtained as

$$\begin{aligned}
&(\lambda+2\mu)A\frac{\partial^2 u}{\partial x^2}=0\\
&K_s\mu A\Big(\frac{\partial^2 w}{\partial x^2}-\frac{\partial\varphi}{\partial x}\Big)-\frac{1}{4}\ell^2\mu A\Big(\frac{\partial^4 w}{\partial x^4}+\frac{\partial^3\varphi}{\partial x^3}\Big)-P\frac{\partial^2 w}{\partial x^2}=0\\
&K_s\mu A\Big(\frac{\partial w}{\partial x}-\varphi\Big)+\frac{1}{4}\ell^2\mu A\Big(\frac{\partial^3 w}{\partial x^3}+\frac{\partial^2\varphi}{\partial x^2}\Big)+(\lambda+2\mu)I\frac{\partial^2\varphi}{\partial x^2}=0
\end{aligned}\tag{2.10}$$

where A and I are, respectively, the beam cross-sectional area and the second moment of cross--sectional area. Also, K_s is the Timoshenko shear coefficient which is introduced as a correction factor to account for the non-uniformity of the shear strain over the beam cross-section (Park and Gao, 2006) and is defined with Poisson's ratio as $K_s=(5+5\nu)/(6+5\nu)$.

Note that all of the body forces and body couples are neglected in this study. Therefore, the governing equations presented in Eqs. (2.10) are identical to those given by Mohammad-Abadi and Daneshmehr (2014).

the boundary conditions for a simply supported beam are stated as

$$u=w=Y=M=0 \qquad \text{at} \qquad x=0,L \tag{2.11}$$

where Y is the couple moment, which is a resultant of the couple stress component mxy. Also, M is the conventional bending moment. These moments are defined as

$$Y=\int_A m_{xy}\,dA=\frac{1}{2}\ell^2\mu A\Big(\frac{\partial^2 w}{\partial x^2}+\frac{\partial\varphi}{\partial x}\Big) \qquad M=\int_A \sigma_{xx}z\,dA=(\lambda+2\mu)I\frac{\partial\varphi}{\partial x} \tag{2.12}$$

So, the boundary conditions defined in Eq. (2.11), can be writen as

$$u=w=\frac{\partial\varphi}{\partial x}=\frac{\partial^2 w}{\partial x^2}=0 \qquad \text{at} \qquad x=0,L \tag{2.13}$$

2.4. Cracked nanobeam model

Consider a crack at a distance $L_c(e=L_c/L)$ at the left end of the beam (Fig. 2). It is assumed that the crack is perpendicular to the beam surface and always remains open. As shown in Fig. 2, the cracked beam is modeled as two segments connected by two massless elastic springs (longitudinal and rotational) (Loya *et al.*, 2009). This modeling promotes flexibility at the cracked section and introduces discontinuity in rotation and discontinuity in longitudinal displacement of the beam, which are proportional to coupled effects of the axial force and bending moment. Therefore, the continuity conditions are developed for the Timoshenko nanobeam as (at $x=L_c$)

$$\begin{aligned}
&w_1=w_2 \qquad N_1=N_2 \qquad M_1=M_2\\
&Q_1-P\varphi_1=Q_2-P\varphi_2 \qquad \varphi_2-\varphi_1\propto f(N,M) \qquad u_2-u_1\propto g(N,M)
\end{aligned}\tag{2.14}$$

where subscripts 1 and 2 refer to the left segment and right segment of the beam divided by the crack. Also, N and Q are, respectively, the axial force and the shear force, which are defined as

$$N=\int_A \sigma_{xx}\,dA=(\lambda+2\mu)A\frac{\partial u}{\partial x} \qquad Q=\int_A \sigma_{xz}\,dA=K_s\mu A\Big(\frac{\partial w}{\partial x}-\varphi\Big) \tag{2.15}$$

Using Eqs. (2.12) and (2.15), the continuity conditions can be written as (at $x = L_c$)

$$\begin{aligned}
&w_1 = w_2 \qquad \frac{\partial u_1}{\partial x} = \frac{\partial u_2}{\partial x} \qquad \frac{\partial \varphi_1}{\partial x} = \frac{\partial \varphi_2}{\partial x} \\
&K_s \mu A\Big(\frac{\partial w_1}{\partial x} - \frac{\partial w_2}{\partial x} + \varphi_2 - \varphi_1\Big) = P(\varphi_1 - \varphi_2) \\
&\varphi_2 - \varphi_1 = K_{MM}\frac{\partial \varphi}{\partial x} + K_{MN}\frac{\partial u}{\partial x} \qquad u_2 - u_1 = K_{NN}\frac{\partial u}{\partial x} + K_{NM}\frac{\partial \varphi}{\partial x}
\end{aligned} \tag{2.16}$$

where K_{MM}, K_{MN}, K_{NM} and K_{NN} are the flexibility constants and in nondimensional forms they are given as $k_1 = K_{MM}/L$, $k_2 = K_{MN}/L$, $k_3 = K_{NN}/L$, $k_4 = K_{NM}/L$.

Then, governing equations (2.10) must be applied for each segment ($r = 1, 2$) of the cracked beam, so, we have

$$\begin{aligned}
&(\lambda + 2\mu)A\frac{\partial^2 u_r}{\partial x_r^2} = 0 \\
&K_s \mu A\Big(\frac{\partial^2 w_r}{\partial x_r^2} - \frac{\partial \varphi_r}{\partial x_r}\Big) - \frac{1}{4}\ell^2 \mu A\Big(\frac{\partial^4 w_r}{\partial x_r^4} + \frac{\partial^3 \varphi_r}{\partial x_r^3}\Big) - P\frac{\partial^2 w_r}{\partial x_r^2} = 0 \\
&K_s \mu A\Big(\frac{\partial w_r}{\partial x_r} - \varphi_r\Big) + \frac{1}{4}\ell^2 \mu A\Big(\frac{\partial^3 w_r}{\partial x_r^3} + \frac{\partial^2 \varphi_r}{\partial x_r^2}\Big) + (\lambda + 2\mu)I\frac{\partial^2 \varphi_r}{\partial x_r^2} = 0
\end{aligned} \tag{2.17}$$

where $0 \leqslant x_1 \leqslant L_1$ and $L_1 \leqslant x_2 \leqslant L$.

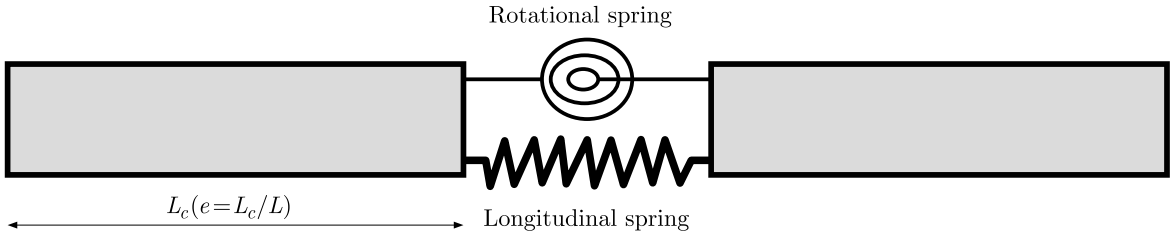

Fig. 2. Model of the cracked beam

3. Solution procedure

The GDQ method (Shu, 1991; Bellman *et al.*, 1972; Shu and Du, 1997) is employed to discretize the governing equations, boundary conditions and continuity conditions, therefore, the differential equations are simplified to algebraic equations. In this method, the region is discretized into several sample points. The sample points are obtained as

$$x_i = \frac{1}{2}\Big(1 - \cos\frac{(i-1)\pi}{N-1}\Big) \qquad i = 1, 2, \ldots, N \tag{3.1}$$

According to the GDQ method (to find details, see Akbarzadeh Khorshidi and Shariati, 2016b; Shu and Du, 1997), governing equations (2.17) are discretized as

$$(\lambda + 2\mu)A\sum_{j=1}^{N} c_{ij}^{(2)} u_r(x_j) = 0 \tag{3.2}$$

and

$$
\begin{aligned}
&K_s\mu A\Big(\sum_{j=1}^{N} c_{ij}^{(2)} w_r(x_j) - \sum_{j=1}^{N} c_{ij}^{(1)} \varphi_r(x_j)\Big) - \frac{1}{4}\ell^2\mu A\Big(\sum_{j=1}^{N} c_{ij}^{(4)} w_r(x_j) + \sum_{j=1}^{N} c_{ij}^{(3)} \varphi_r(x_j)\Big) \\
&\quad - P\Big(\sum_{j=1}^{N} c_{ij}^{(2)} w_r(x_j)\Big) = 0 \\
&K_s\mu A\Big(\sum_{j=1}^{N} c_{ij}^{(1)} w_r(x_j) - \varphi_r(x_j)\Big) + \frac{1}{4}\ell^2\mu A\Big(\sum_{j=1}^{N} c_{ij}^{(3)} w_r(x_j) + \sum_{j=1}^{N} c_{ij}^{(2)} \varphi_r(x_j)\Big) \\
&\quad + (\lambda + 2\mu) I\Big(\sum_{j=1}^{N} c_{ij}^{(2)} \varphi_r(x_j)\Big) = 0
\end{aligned}
\tag{3.3}
$$

where $i, j = 1, \ldots, N$ and $c_{ij}^{(n)}$ is the weighting coefficient which can be found from the recursive formula (Akbarzadeh Khorshidi and Shariati, 2016b; Shu and Du, 1997).

The discretized boundary conditions are expressed as

$$
\begin{aligned}
&u_1(x_1) = w_1(x_1) = \sum_{j=1}^{N} c_{1j}^{(1)} \varphi_1(x_j) = \sum_{j=1}^{N} c_{1j}^{(2)} w_1(x_j) = 0 \\
&u_2(x_N) = w_2(x_N) = \sum_{j=1}^{N} c_{Nj}^{(1)} \varphi_2(x_j) = \sum_{j=1}^{N} c_{Nj}^{(2)} w_2(x_j) = 0
\end{aligned}
\tag{3.4}
$$

also, continuity conditions (2.16) are discretized as

$$
\begin{aligned}
&w_1(x_N) = w_2(x_1) \qquad \sum_{j=1}^{N} c_{Nj}^{(1)} u_1(x_j) = \sum_{j=1}^{N} c_{1j}^{(1)} u_2(x_j) \\
&\sum_{j=1}^{N} c_{Nj}^{(1)} \varphi_1(x_j) = \sum_{j=1}^{N} c_{1j}^{(1)} \varphi_2(x_j) \\
&K_s\mu A\Big(\sum_{j=1}^{N} c_{Nj}^{(1)} w_1(x_j) - \sum_{j=1}^{N} c_{1j}^{(1)} w_2(x_j) + \varphi_2(x_1) - \varphi_1(x_N)\Big) = P\Big(\varphi_1(x_N) - \varphi_2(x_1)\Big) \\
&\varphi_2(x_1) - \varphi_1(x_N) = K_{MM} \sum_{j=1}^{N} c_{Nj}^{(1)} \varphi_1(x_j) + K_{MN} \sum_{j=1}^{N} c_{Nj}^{(1)} u_1(x_j) \\
&u_2(x_1) - u_1(x_N) = K_{NM} \sum_{j=1}^{N} c_{Nj}^{(1)} u_1(x_j) + K_{NN} \sum_{j=1}^{N} c_{Nj}^{(1)} \varphi_1(x_j)
\end{aligned}
\tag{3.5}
$$

Using discretized equations (3.2)-(3.5), a set of algebraic equations is established, and by solving the eigenvalue problem, the critical buckling load of cracked nanobeams is obtained.

4. Results and discussion

This Section presents the influence of crack location, crack severity and material length scale parameter to thickness ratio on the nondimensional critical buckling load of simply supported cracked nanobeams. The nondimensional critical buckling load is defined as $\overline{P} = P_{cr}L^2/EI$. To validate the presented results, the critical buckling load of an intact microbram is compared with the obtained results by Mohammad-Abadi and Daneshmehr (2014). An excellent agreement is shown in Table 1.

Table 1. Nondimensional critical buckling load $\overline{P}$ of intact microbeams ($E = 1.44\,\text{GPa}$, $L = 20h$, $\ell = 17.6\,\mu\text{m}$, $b = 2\,\text{h}$, $\nu = 0.38$)

	h [μm]			
	17.6	52.8	88	123.2
Ref. [25]	60.3571	22.9608	19.9491	19.1188
Present paper	60.4853	22.9962	19.9795	19.1479

Ref. [25] – Mohammad-Abadi and Daneshmehr (2014)

To present a parametric study, a Timoshenko beam with $L = 20h$, $b = 2h$ and $\nu = 0.38$ with simply supported boundary conditions and an open edge crack is considered. The effects of the flexibility constants k_1, k_2, k_3 and k_4 are shown in Tables 2-5. These tables present nondimensional critical buckling loads for different flexibility constants. As mentioned, this study introduces local flexibility by means of four constants which relate discontinuities of the cracked section with the axial force and bending moment. Therefore, different conditions of these four constants state different crack severities. It is found that the flexibility constant related to the bending moment k_1 is more effective on the buckling behavior of the cracked nanobeam than the other constants. In fact, the discontinuity in rotation due to bending has a great effect on the local flexibility introduced by the crack. However, the other constants k_2, k_3 and k_4 have a scant influence on the local flexibility, but this influence becomes larger when the crack severity is increased (Tables 3-5). Also, the crossover flexibility constants caused by the coupled effects between the axial force and bending moment (k_2 and k_4) have similar influences on the critical buckling load (Tables 3 and 5).

Table 2. Effect of k_1 on the nondimensional critical buckling load $\overline{P}$ ($\ell/h = 1$ and $e = 0.5$)

k_1	$k_2 = k_3 = k_4 = 0$	$k_2 = k_3 = k_4 = 0.5$	$k_2 = k_3 = k_4 = 1$	$k_2 = k_3 = k_4 = 2$
0	60.4853	59.4491	58.4024	55.5903
0.25	40.3538	39.7141	39.0139	37.1375
0.5	29.0547	28.5334	28.0332	26.6845
1	18.8317	18.1148	17.7901	16.9438
2	10.7610	9.8532	9.6804	9.2153

Table 3. Effect of k_2 on the nondimensional critical buckling load $\overline{P}$ ($\ell/h = 1$ and $e = 0.5$)

k_2	$k_1 = k_3 = k_4 = 0$	$k_1 = k_3 = k_4 = 0.5$	$k_1 = k_3 = k_4 = 1$	$k_1 = k_3 = k_4 = 2$
0	60.4853	28.3580	18.3580	9.9372
0.25	60.4853	28.6881	18.2012	9.8551
0.5	60.4853	28.5334	18.0786	9.7668
1	60.4852	28.2029	17.7901	9.5905
2	60.4852	27.5220	17.1818	9.2153

Figure 3 shows the effect of the material length scale parameter to thickness ratio ℓ/h on the critical buckling load of Timoshenko cracked nanobeams. It is observed that the critical buckling load increases as ℓ/h increases, and this increase is decreased by the growing severity of the crack. Note that $\ell/h = 0$ virtually indicates the results obtained from the classical continuum theory which neglects the couple stress effect.

The effects of crack location on the critical buckling load of simply supported nanobeams for different crack severities and ℓ/h ratios are respectively demonstrated in Figs. 4 and 5. The critical buckling load is sensitive to crack location and is decreased when the crack gets near to

Table 4. Effect of k_3 on the nondimensional critical buckling load $\overline{P}$ ($\ell/h = 1$ and $e = 0.5$)

k_3	$k_1 = k_2 = k_4 = 0$	$k_1 = k_2 = k_4 = 0.5$	$k_1 = k_2 = k_4 = 1$	$k_1 = k_2 = k_4 = 2$
0	60.4853	28.6977	18.4197	11.1871
0.25	60.4853	28.6128	18.2461	10.5983
0.5	60.4853	28.5334	18.0981	10.1732
1	60.4852	28.4527	17.7901	9.6471
2	60.4852	27.3721	17.5985	9.2153

Table 5. Effect of k_4 on the nondimensional critical buckling load $\overline{P}$ ($\ell/h = 1$ and $e = 0.5$)

k_4	$k_1 = k_2 = k_3 = 0$	$k_1 = k_2 = k_3 = 0.5$	$k_1 = k_2 = k_3 = 1$	$k_1 = k_2 = k_3 = 2$
0	60.4853	28.8544	18.3579	9.9384
0.25	60.4853	28.6879	18.2010	9.8552
0.5	60.4853	28.5334	18.0787	9.7673
1	60.4852	28.2045	17.7901	9.5911
2	60.4851	27.5220	17.1817	9.2153

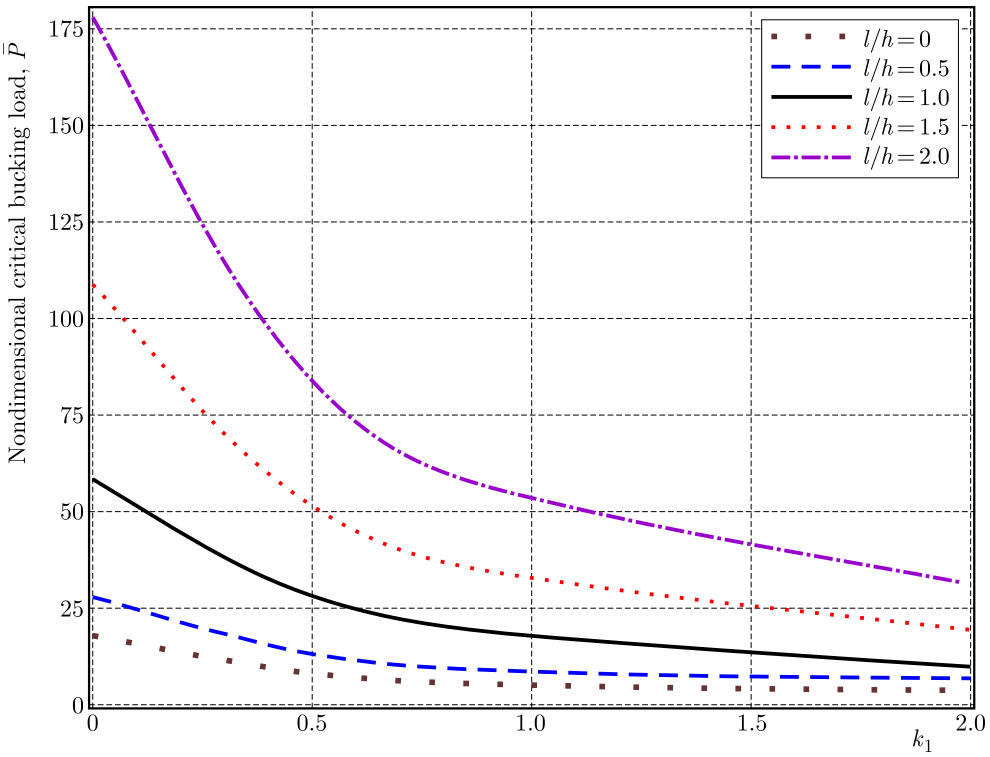

Fig. 3. Effects of ℓ/h ratio and crack severity on the nondimensional critical buckling load ($k_2 = k_3 = k_4 = 1$ and $e = 0.5$)

beam midpoint. Also, the influence of the crack tends to be very small as the crack gets closer to the beam ends. By increasing the crack severity, the effect of crack location is increased; in other words, the crack severity is more effective when the crack is located at the midpoint of the beam ($e = 0.5$). Figure 5 indicates that the effect of crack location increases as the ℓ/h increases. Also, it is found that the ℓ/h ratio at different crack locations has different effects on the critical buckling load of cracked nanobeams, but these effects get similar when the crack gets near to the midpoint.

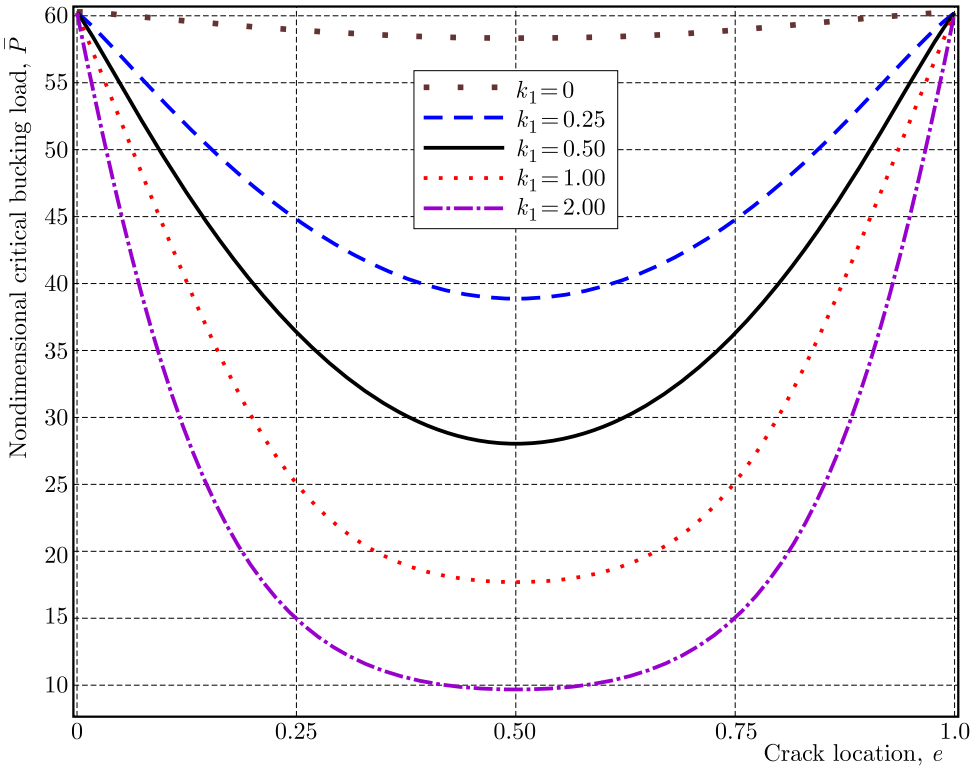

Fig. 4. Effects of crack location and crack severity on the nondimensional critical buckling load ($k_2 = k_3 = k_4 = 1$ and $\ell/h = 1$)

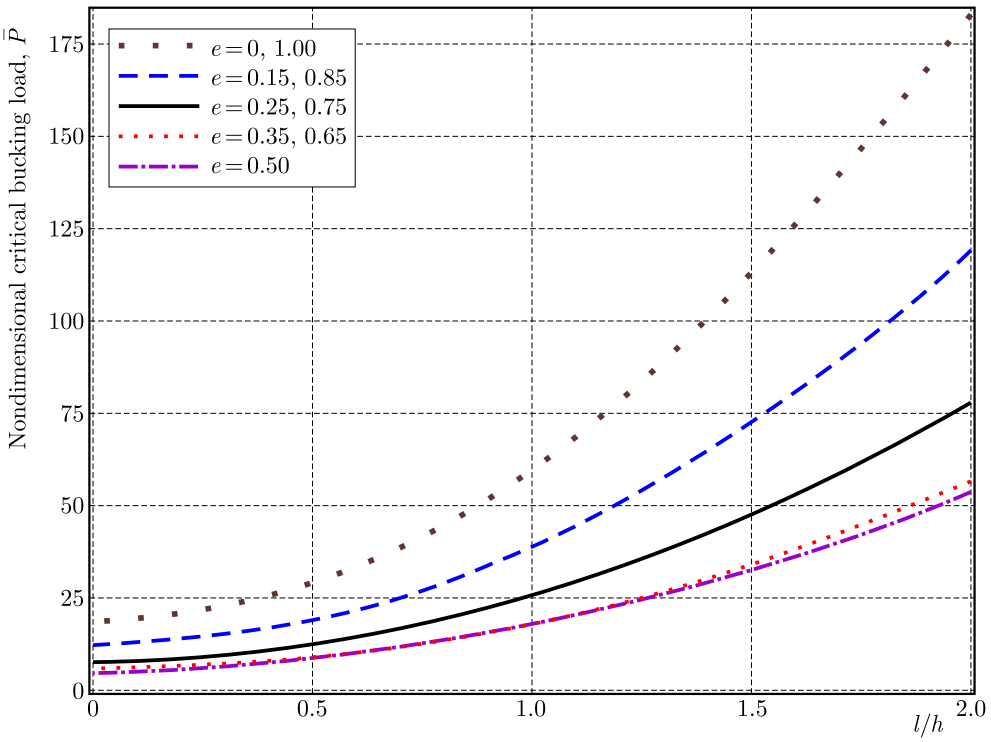

Fig. 5. Effects of crack location and ℓ/h ratio on the nondimensional critical buckling load ($k_1 = k_2 = k_3 = k_4 = 1$)

5. Conclusion

The buckling behavior of cracked nanobeams is studied within the framework of Timoshenko beam theory anda modified couple stress theory. A material length scale parameter is used to capture the size effect. The crack is modeled as two massless elastic springs (rotational and longitudinal) which promote discontinuities at the cracked section. This study employs four flexibility constants which introduce crack severity by two discontinuities which are proportional to the bending moment and axial force transmitted through the cracked section. The principle of minimum potential energy is employed to derive the governing differential equations which are discretized using the GDQ method. The effects of crack severity, crack location and material length scale parameter to thickness ratio are studied.

The obtained results show that the first flexibility constant which connects the discontinuity in rotation with the bending moment makes the main part of the crack severity. The material length scale parameter to thickness ratio ℓ/h considerably affects the value of the critical buckling load which increases as the ℓ/h increases. The influence of ℓ/h is stronger at lower crack severities, in a general manner, reduction of the crack effects (crack severity and location) leads to a decrease in the influence of ℓ/h. The critical buckling loads are significantly affected by crack location and are continuously decreased when the crack gets near to the midpoint of the nanobeam. Also, the crack location is more effective at high crack severities and ℓ/h ratios.

References

1. Adams R.D., Cawley P., Pye C.J., Stone B.J., 1978, A vibration technique for non-destructive assessing the integrity of structures, *Journal of Mechanical Engineering Science*, **20**, 93-100
2. Akbarzadeh Khorshidi M., Shariati M., 2015, A modified couple stress theory for postbuckling analysis of Timoshenko and Reddy-Levinson single-walled carbon nanobeams, *Journal of Solid Mechanics*, **7**, 4, 364-373
3. Akbarzadeh Khorshidi M., Shariati M., 2016a, An investigation of stress wave propagation in a shear deformable nanobeam based on modified couple stress theory, *Waves in Random and Complex Media*, **26**, 243-258, DOI: 10.1080/17455030.2015.1137375
4. Akbarzadeh Khorshidi M., Shariati M., 2016b, Free vibration analysis of sigmoid functionally graded nanobeams based on a modified couple stress theory with general shear deformation theory, *Journal of the Brazilian Society of Mechanical Sciences and Engineering*, **38**, 2607-261, DOI: 10.1007/s40430-015-0388-3
5. Asghari M., Kahrobaiyan M.H., Ahmadian M.T., 2010, A nonlinear Timoshenko beam formulation based on the modified couple stress theory, *International Journal of Engineering Science*, **48**, 1749-1761, DOI: 10.1016/j.ijengsci.2010.09.025
6. Bellman R., Kashef B.G., Casti J., 1972, Differential quadrature: a technique for the rapid solution of nonlinear partial differential equations, *Journal of Computer and Physics*, **10**, 40-52
7. Chati M., Rand R., Mukherjee S., 1007, Modal analysis of a cracked beam, *Journal of Sound and Vibration*, **207**, 2, 249-270
8. Chaudhari T.D., Maiti S.K., 2000, A study of vibration of geometrically segmented beams with and without crack, *International Journal of Solids and Structures*, **37**, 761-779
9. Dehrouyeh-Semnani A.M., Dehrouyeh M., Zafari-Koloukhi H., Ghamami M., 2015, Size-dependent frequency and stability characteristics of axially moving microbeams based on modified couple stress theory, *International Journal of Engineering Science*, **97**, 98-112, DOI: 10.1016/j.ijengsci.2015.09.003
10. El Bikri K., Benamar R., Bennouna M.M., 2006, Geometrically non-linear free vibrations of clamped-clamped beams with an edge crack, *Computers and Structures*, **84**, 485-502, DOI: 10.1016/j.compstruc.2005.09.030

11. Freund L.B., Herrmann G., 1978, Dynamic fracture of a beam or plate in plane bending, *Journal of Applied Mechanic*, **76-APM-15**, 112

12. Hasheminejad S.M., Gheshlaghi B., Mirzai Y., Abbasion S., 2011, Free transverse vibrations of cracked nanobeams with surface effects, *Thin Solid Films*, **519**, 2477-2482, DOI: 10.1016/j.tsf.2010.12.143

13. Hosseini-Hashemi Sh., Fakher M., Nazemnezhad R., Sotoude Haghighi M.H., 2014, Dynamic behavior of thin and thick cracked nanobeams incorporating surface effects, *Composites: Part B*, **61**, 66-72, DOI: 10.1016/j.compositesb.2014.01.031

14. Hsu J.Ch., Lee H.L., Chang W.J., 2011, Longitudinal vibration of cracked nanobeams using nonlocal elasticity theory, *Current Applied Physics*, **11**, 1384-1388, DOI: 10.1016/j.cap.2011.04.026

15. Ke L.L., Wang Y.Sh., 2011, Size effect on dynamic stability of functionally graded microbeams based on a modified couple stress theory, *Composite Structures*, **93**, 342-350, DOI: 10.1016/j.compstruct.2010.09.008

16. Ke L.L., Yang J., Kitipornchai S., 2009, Postbuckling analysis of edge cracked functionally graded Timoshenko beams under end shortening, *Composite Structures*, **90**, 152-160, DOI: 10.1016/j.compstruct.2009.03.003

17. Kitipornchai S., Ke L.L., Yang J., Xiang Y., 2009, Nonlinear vibration of edge cracked functionally graded Timoshenko beams, *Journal of Sound and Vibration*, **324**, 962-982, DOI: 10.1016/j.jsv.2009.02.023

18. Krawczuk M., Palacz M., Ostachowicz W., 2003, The dynamic analysis of cracked Timoshenko beams by spectral element method, *Journal of Sound and Vibration*, **264**, 1139-1153

19. Lele S.P., Maiti S.K., 2002, Modelling of transverse vibration of short beams for crack detection and measurement of crack extension, *Journal of Sound and Vibration*, **257**, 3, 559-583, DOI: 10.1006/jsvi.5059

20. Loya J.A., Aranda-Ruiz J., Fernandez-Saez J., 2014, Torsion of cracked nanorods using a nonlocal elasticity model, *Journal of Physics D: Applied Physics*, **47**, 115304, DOI: 10.1088/0022-3727/47/11/115304

21. Loya J., Lopez-Puente J., Zaera R., Fernandez-Saez J., 2009, Free transverse vibrations of cracked nanobeams using a nonlocal elasticity model, *Journal of Applied Physics*, **105**, 044309, DOI: 10.1063/1.3068370

22. Loya J.A., Rubio L., Fernandez-Saez J., 2006, Natural frequencies for bending vibrations of Timoshenko cracked beams, *Journal of Sound and Vibration*, **290**, 640-653, DOI: 10.1016/j.jsv.2005.04.005

23. Ma H.M., Gao X.-L., Reddy J.N., 2008, A microstructure-dependent Timoshenko beam model based on a modified couple stress theory, *Journal of the Mechanics and Physics of Solids*, **56**, 3379-3391, DOI: 10.1016/j.jmps.2008.09.007

24. Ma H.M., Gao X.-L., Reddy J.N., 2010, A nonclassical Reddy-Levinson beam model based on a modified couple stress theory, *Journal for Multiscale Computational Engineering*, **8**, 2, 167-180

25. Mohammad-Abadi M., Daneshmehr A.R., 2014, Size dependent buckling analysis of microbeams based on modified couple stress theory with high order theories and general boundary conditions, *International Journal of Engineering Science*, **74**, 1-14, DOI: 10.1016/j.ijengsci.2013.08.010

26. Mohammad-Abadi M., Daneshmehr A.R., 2015, Modified couple stress theory applied to dynamic analysis of composite laminated beams by considering different beam theories, *International Journal of Engineering Science*, **87**, 83-102, DOI: 10.1016/j.ijengsci.2014.11.003

27. Okamura H., Watanabe K., Takano T., 1973, Applications of compliance concept in fracture mechanics, [In:] *Progress in Flaw Growth and Fracture Toughness Testing*, 536, J.G. Kaufman (Edit.), American Society for Testing and Materials, Philadelphia, 423-438

28. Park S.K., Gao X.-L., 2006, Bernoulli-Euler beam model based on a modified couple stress theory, *Journal Micromechanics and Microengineering*, **16**, 2355-2359

29. Park S.K., Gao X.-L., 2008, Variational formulation of a modified couple stress theory and its application to a simple shear problem, *Zeitschrift für angewandte Mathematik und Physik*, **59**, 904-917

30. Rice J.R., 1972, The line spring model for surface flaws, [In:] *The Surface Crack*, Swedlow J.L. (Edit.), ASME, New York

31. Rice J.R., Levy N., 1972, The part-through surface crack in an elastic plate, *Journal of Applied Mechanics*, **39**, *Trans. ASME, Series E*, **94**, 185-194

32. Shu C., 1991, Generalized differential-integral quadrature and application to the simulation of incompressible viscous flows including parallel computation, Ph.D. Thesis, University of Glasgow

33. Shu C., Du H., 1997, Implement of clamped and simply supported boundary conditions in the GDQ free vibration analysis of beams and plates, *International Journal of Solids and Structures*, **19**, 59-68

34. Simsek M., 2010, Dynamic analysis of an embedded microbeam carrying a moving microparticle based on the modified couple stress theory, *International Journal of Engineering Science*, **48**, 1721-1732, DOI: 10.1016/j.ijengsci.2010.09.027

35. Tharp T., 1987, A finite element for edge-cracked beam columns, *International Journal for Numerical Methods in Engineering*, **24**, 1941-1950

36. Torabi K., Nafar Dastgerdi J., 2012, An analytical method for free vibration analysis of Timoshenko beam theory applied to cracked nanobeams using a nonlocal elasticity model, *Thin Solid Films*, **520**, 6595-6602, DOI: 10.1016/j.tsf.2012.06.063

37. Xia W., Wang L., Yin L., 2010, Nonlinear non-classical microscale beams: Static bending, post-buckling and free vibration, *International Journal of Engineering Science*, **48**, 12, 2044-2053, DOI: 10.1016/j.ijengsci.2010.04.010

38. Yan T., Kitipornchai S., Yang J., 2011, Parametric instability of functionally graded beams with an open edge crack under axial pulsating excitation, *Composite Structures*, **93**, 1801-1808, DOI: 10.1016/j.compstruct.2011.01.019

39. Yang F., Chong A.M., Lam D.C.C., Tong P., 2012, Couple stress based strain gradient theory of elasticity, *International Journal of Solids and Structures*, **39**, 2731-2743, DOI: 10.1016/S0020--7683(02)00152-X

40. Yang J., Chen Y., 2008, Free vibration and buckling analyses of functionally graded beams with edge cracks, *Composite Structures*, **83**, 48-60, DOI: 10.1016/j.compstruct.2007.03.006

Manuscript received February 6, 2017; accepted for print April 14, 2017

JOURNAL OF THEORETICAL AND APPLIED MECHANICS
55, 4, pp. 1141-1153, Warsaw 2017
DOI: 10.15632/jtam-pl.55.4.1141

ANALYSIS OF CONTROLLED MOLECULAR DYNAMIC FLOW IN A CHANNEL WITH NON-EQUAL INLET AND OUTLET CROSS-SECTIONAL AREAS

Hamed R. Najafi, S.M. Hossein Karimian

Department of Aerospace Engineering, Amirkabir University of Technology, Tehran, Iran

e-mail: hamedramezani@aut.ac.ir; hkarim@aut.ac.ir

Thermo-fluid properties are required for numerical modeling of nano/micro devices. These properties are mostly obtained from the results of molecular dynamics (MD) simulations. Therefore, efforts have been made to develop methods for numerical evaluation of fluid properties such as pressure and velocity. One of the main challenges faced by numerical simulations is to simulate steady molecular flow in channels with non-equal inlet and outlet boundaries. Currently, periodic boundary conditions at the inlet and outlet boundaries are an inevitable condition in many steady flow molecular dynamics simulations. As a result, a nano-channel with different cross sectional areas at the inlet and outlet could not be simulated easily. Here, a method is presented to generate and control steady molecular flow in a nano-channel with different cross sectional areas at the inlet and outlet. The presented method has been applied to a converging-diverging channel, and its performance has been studied through qualitative and quantitative representation of flow properties.

Keywords: molecular dynamics, nano-channel, steady flow, non-equal inlet and outlet, pressure

1. Introduction

Flow behavior at micro and nano scales has been the subject of interest in the recent years. As a typical reduced-size fluid flow system, flow in a nanochannel can demonstrate different aspects of nanofluid systems. Therefore, several investigations have been focused on the simulation of nanochannel flows (Mi and Chwang, 2003).

Molecular Dynamics (MD) is a deterministic method to calculate the position of molecules and their dynamic properties. Different potential functions have been introduced to represent molecular forces in MD simulations (see for example Leach, 1999; Sadus, 2002). Extracting macroscopic properties such as velocity, temperature and pressure from microscopic data has also been a challenging issue (Allen and Tildesley, 1987; Karniadakis *et al.*, 2002; Karimian *et al.*, 2011).

In earlier studies, the characterization of domain boundaries was not of the primary importance and thus they were treated as simple as possible. In most of the cases, therefore, periodic boundary conditions were used in MD simulations (Stillinger and Rahman, 1974; Travis and Evans, 1977; Koplik *et al.*, 1989; Travis and Gubbins, 2000; Nagayama and Cheng, 2004). However, due to the rapid advancement of computational facilities in the recent years, new problems with more complex boundaries have become a subject of MD simulations. As a result, implementation of realistic boundary conditions in MD simulation is now the center of attention, especially in the field of fluid mechanics (Sun and Ebner, 1992; Huang *et al.*, 2004; Hanasaki and Nakatani, 2006; Huang *et al.*, 2006).

One of the MD applications today that can practically be very beneficial is to present a method for simulation of a specific known or predefined flow in a nanochannel with non-equal

inlet and outlet cross-sectional areas. Different approaches can be found in the literature to create flow fields in a nanochannel. The most simple and straightforward method is to implement an external force or acceleration to move molecules in a specified direction (Koplik *et al.*, 1988; Fan *et al.*, 2002; Ziarani and Mohamad, 2005; Sofos *et al.*, 2009; Kamali and Kharazmi, 2011). Other than this, some has used motion of a piston or plate upstream of the inlet to create flow in nanotubes (Huang *et al.*, 2004, 2006; Hanasaki and Nakatani, 2006). Implementation of flow gradients such as the temperature gradient can also be used to create nanoflow (Han, 2008; Liu and Li, 2010; Darbandi *et al.*, 2011; Bao *et al.*, 2015). In addition to these methods, in another method, wall motion has been used to create molecular flow in nanochannels (Zhang *et al.*, 2009; Kim *et al.*, 2010).

Implementation of a periodic boundary condition at the inlet and outlet is inevitable in all the above-mentioned methods except for the second one in which a piston upstream of the inlet is used to move the molecules. However, the disadvantage of this approach is that the solution is limited to the period at which the piston moves in its stroke. Also, since additional molecules are to be taken into account in stroke space upstream of the inlet, extra computational efforts are required in this method.

While all of the above-mentioned methods achieve the goal of creating molecular flow in nanochannels, they fail to model steady flow in a channel with different inlet and outlet cross--sectional areas since they use a periodic boundary condition at the inlet and outlet. Also, none of the above methods offers a proper approach to produce specific known or predefined flow in nanochannels. Therefore, the main objective of present study is to investigate flow behavior in a channel of non-equal inlet and outlet cross-sectional areas with controllable flow. In the following sections, we first introduce the calculation method used here to evaluate macroscopic properties in nanoflow. Then we will discuss details about the nanoflow controlled by a temperature gradient. Finally, we introduce a method to solve molecular dynamic flow in a non-equal inlet and outlet cross-sectional-area channel controlled by the temperature gradient.

Finally, a short review on boundary conditions is required since they are implemented on the nanotube wall. The most common option is to model the walls by two rows of molecules. The wall molecules are allowed to oscillate about their initial positions where they are fixed. This is set up either by assigning heavy weights to the wall molecules (Koplik *et al.*, 1988), rescaling the velocity of wall molecules to their initial values (Huang *et al.*, 2004), or using fictitious springs (Fan *et al.*, 2002; Huang *et al.*, 2006; Sofos *et al.*, 2009; Branam and Micci, 2009; Kamali and Kharazmi, 2011). Meanwhile, some studies can be found where walls are modeled differently. An example of such investigations is the study of Ziarani and Mohamad (2005), where the walls were modeled as reflective. The investigation of wall boundary conditions is not the subject of the present study, and the interested scientists are encouraged to refer to the literature for more details. As will be described later, two rows of molecules that are allowed to oscillate about their initial fixed positions represent channel walls.

2. Pressure and temperature formula in molecular dynamics

In this paper, the Non-Equilibrium Molecular Dynamics (NEMD) technique is used to simulate flow of Argon. In molecular dynamics, positions of molecules are determined using Newton's second law. Intermolecular forces are calculated using Lennard-Jones 12-6 potential equation (Rapaport, 2004) with a small correction by truncating at the cut-off distance and shifting to eliminate the discontinuity (Leach, 1999)

$$V(r_{ij}) = \begin{cases} 4\varepsilon\Big[\Big(\dfrac{\sigma}{r_{ij}}\Big)^{12} - \Big(\dfrac{\sigma}{r_{ij}}\Big)^{6} - \Big(\dfrac{\sigma}{r_c}\Big)^{12} + \Big(\dfrac{\sigma}{r_c}\Big)^{6}\Big] & \text{for} \quad r_{ij} \leqslant r_c \\ 0 & \text{for} \quad r_{ij} > r_c \end{cases} \tag{2.1}$$

where r_{ij} is the intermolecular distance between atoms i and j, ε is the energy scale. We choose a cut-off distance of $r_c = 2.5\sigma$ herein, which has commonly been used in other studies to simulate Argon flow (Koplik *et al.*, 1989; Priezjev, 2007; Sofos *et al.*, 2009; Bao *et al.*, 2015). σ is the finite distance at which the intermolecular potential is zero, and it is equal to molecular diameter in the hard sphere model. In this paper, wall and fluid molecules are formed from the same material. Therefore, all interaction between wall molecules, fluid molecules or wall-fluid molecules follows the above equation with Argon constants.

In a macroscopic analysis, pressure is calculated solely based on the virial equation of state. In a microscopic system however, pressure is calculated from the virial equation of state on all atoms plus the summation of intermolecular forces multiplied by the corresponding distances between them. For pair-additive force fields, the fluid pressure P can be estimated through the virial equation of state given below (Allen and Tildesly, 1987)

$$P = \frac{Nk_BT}{V} + \frac{1}{3V}\sum_{i=1}^{N}\sum_{j>i}^{N} r_{ij} f_{ij} \tag{2.2}$$

where N is the number of molecules in the computational domain, k_B is Boltzmann's constant, and V and T are volume and temperature of the computational domain, respectively. r_{ij} is the distance between two interacting molecules i and j, and f_{ij} is the force of molecule j acting on molecule i. The first term in Eq. (2.2) is called the kinetic term and contains temperature of the computational domain. In a microscopic view, temperature is defined as

$$T = \frac{m}{3Nk_B}\sum_{n=1}^{N}\sum_{i=1}^{3}(V_{ni} - \overline{V}_i)^2 \tag{2.3}$$

where n denotes the molecule number in the domain, $i = 1, 2, 3$ denotes the x, y and z components of the atomic velocity $\mathbf{V}_n$, $\overline{V}_i$ is the i-th component of the mean flow velocity $\overline{\mathbf{V}}$, and m is the atom mass. Mean velocity can be obtained from each of the several averaging methods like SAM (Tysanner and Garcia, 2004), CAM (Tysanner and Garcia, 2005) or SMC (Karimian *et al.*, 2011) which reduces statistical errors in its calculation. In the present study, the SMC method is used to calculate mean velocity. The velocity difference within parentheses that represents instantaneous velocity due to thermal fluctuations is called virial velocity.

The pressure calculation method defined by Eqs. (2.2) and (2.3) has been implemented in an in-house MD code developed in FORTRAN to extract pressure values from the results of MD simulations. This code has been used in authors' previous studies, where its accuracy in calculation of macroscopic properties was demonstrated (Karimian *et al.*, 2011; Karimian and Namvar, 2012; Namvar and Karimian, 2012; Karimian and Izadi, 2013; Hasheminasab and Karimian, 2015; Najafi and Karimian, 2016).

It should be noted that in regions near the boundary, all of the molecules including those outside domain boundary should be taken into account within their cut-off region. This is crucial for correct calculation of pressure (Najafi and Karimian, 2016).

3. Controlling flow with the temperature gradient in a channel with non-equal inlet and outlet cross-sectional area

In (Najafi and Karimian, 2016), it was shown that uniform flow of molecules can be created by enforcing two macroscopic properties such as temperature and mean flow velocity at a control point; e.g. at a bin. Najafi and Karimian (2016) also showed that flow of molecules with a gradient of flow properties, such as temperature, can be created if one flow property is defined on an additional control point as well. In fact, they were able to set up a desired periodic flow. In

the present study, we would like to apply the approach of Najafi and Karimian to set up a desired flow field in a channel with non-equal inlet and outlet cross-sectional areas. To investigate this idea, the following test case is defined.

Geometry of the nano channel considered here is a non-symmetric converging-diverging channel with length of 126.525 Å, inlet cross-sectional area of 36.15 Å×36.15 Å, outlet cross-sectional area of 29.05 Å×36.15 Å, and ratio of throat to inlet cross-sectional areas of 0.6, as shown in Fig. 1. Seven bins with equal lengths of 18.075 Å are located along the channel. Note that the bin length cannot be very small. In this case, a sufficient number of molecules will not exist in each bin and, therefore, fluctuations will appear in the calculated properties. On the other hand, although smooth results are obtained in larger bins with a moderate number of molecules, they cannot represent local properties accurately. More details about the effect of bin size on sampling and averaging can be found in (Karimian and Izadi, 2013). Wall molecules in bin 1 are arranged in a straight line. From the beginning of bin 2 to the end of bin 7, the wall molecules are located on a half-sinusoidal profile. The throat of this channel is located at the boundary of bins 5 and 6 that is 90.375 Å from the inlet. The wall profile of bins 6 and 7 is in symmetry with that of bins 5 and 4. This non-symmetric channel is in fact the first part of a fully symmetric converging-diverging channel with a length of 180.75 Å. As mentioned above, the desired flow field can be developed in this channel by enforcing temperature and mean velocity at bin 2, and temperature at bin 7.

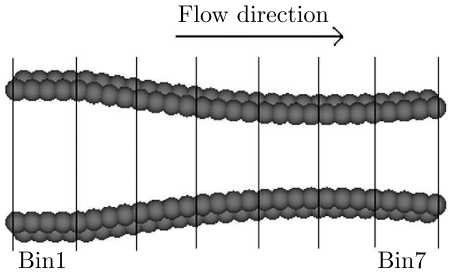

Fig. 1. Non-symmetric channel with 7 bins along the x direction and different inlet and outlet cross-sectional areas

In order to verify our results, we need to know the solution of molecular flow in this channel for the desired values of mean velocity and temperatures at these two bins. For this purpose, we can assume that the above-defined non-symmetric channel is a part of the symmetric converging-diverging channel for which its solution is available. In this case, the solution of the non-symmetric channel would be equal to the solution of this symmetric channel in its first 126.525 Å provided that values of mean velocity and temperatures extracted from the solution of the symmetric converging-diverging channel are enforced at bins 2 and 7.

Therefore, we first solve molecular flow in a 180.75 Å length symmetric converging-diverging channel, which has the exact wall profile of our test case in its first 126.525 Å. A schematic of this channel with its initial configuration of molecules is shown in Fig. 2. This symmetric channel is solved with the periodic boundary condition, and has exactly the same 7 bins of our test case plus 3 extra bins in its 54.225 Å extended part. Obviously, this symmetric converging-diverging channel has an inlet/outlet cross-sectional area of 36.15 Å×36.15 Å, and the ratio of throat to inlet cross-sectional areas of 0.6.

This channel contains mono-atomic molecules of Argon gas with an atomic diameter of $\sigma = 3.4$ Å and energy parameter of $\varepsilon = 1.67 \cdot 10^{-21}$ J. Argon molecules are initially arranged in a FCC lattice form. Solution starts from the initial temperature of 120 K and zero mean velocity. The periodic boundary condition is applied in the x and z directions. In the y direction, the channel is restricted at each side by two rows of fluid molecules as channel walls. Wall molecules are allowed to oscillate about their initial fixed positions. Temperature of the wall molecules

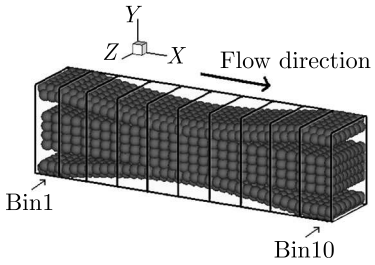

Fig. 2. Schematic of molecule positions in the symmetric converging-diverging channel with 1062 fluid molecules and 1092 wall molecules

is maintained at 120 K by scaling of the molecule velocities. This channel contains 1062 flow molecules (N) and 1092 wall molecules (N_w). As seen in Fig. 2, the flow molecules are initialized over the channel in a rectangular cube. Each wall has 546 molecules, arranged in a FCC lattice form in a half-sinusoidal profile. Thus, molecular densities of the wall and fluid are 2237.79 kg/m^3 and 1108.18 kg/m^3, respectively. Low amplitude oscillations of the wall molecules, managed by a spring stiffness coefficient of 5000 N/m, decrease the possibility of molecule escape from the domain boundaries.

The equation of motion is integrated over time with time steps of 10^{-16} s using the Verlet scheme (Verlet, 1967). Note that the time step value should be chosen appropriately. Very small time steps increase computational cost and solution time, and large time steps may cause solution divergence. The solution domain is divided into 10 equal bins. The solution is preceded for 15 000 000 time steps to reach equilibrium.

During the solution, temperature of 300 K and mean velocity of 20 m/s are continuously enforced in the second bin. At each time step, mean velocity in this bin is modified by adding the difference between desired and calculated mean velocities to the velocity of each molecule inside the bin. In a similar fashion, temperature in the bin is updated by rescaling the virial velocity of molecules at each time step. The SMC averaging method (Karimian *et al.*, 2011) is applied to calculate pressure and velocity at each time step using Eq. (2.2). Pressure, mean flow velocity, molecular density and temperature variations along the channel are shown in Fig. 3. Convergence rates of velocity and temperature in the bins are shown in Fig. 4.

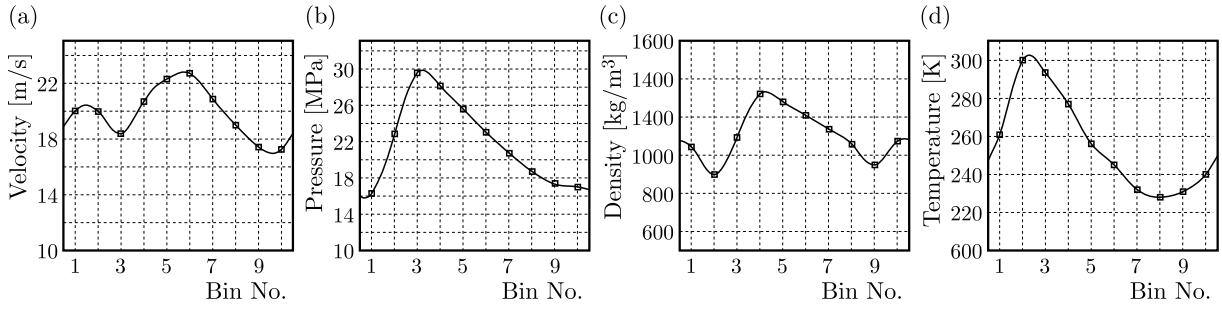

Fig. 3. Variations of flow properties along the symmetric converging-diverging channel generated by enforcement of temperature and mean velocity in bin 2, (a) velocity, (b) pressure and (c) molecular density (d) temperature

It can be seen in Fig. 3a that the mean flow velocity increases through the channel from the inlet to throat and, after that, decreases towards the end of the channel. The throat of this channel is located between bins 5 and 6. Velocity enforcement at bin 2 results in molecules to be driven towards the flow direction and leave the bin. Therefore, this bin would have the least molecular density. Higher concentration of molecules in bin 3 leads to lower velocities and higher pressures at this bin.

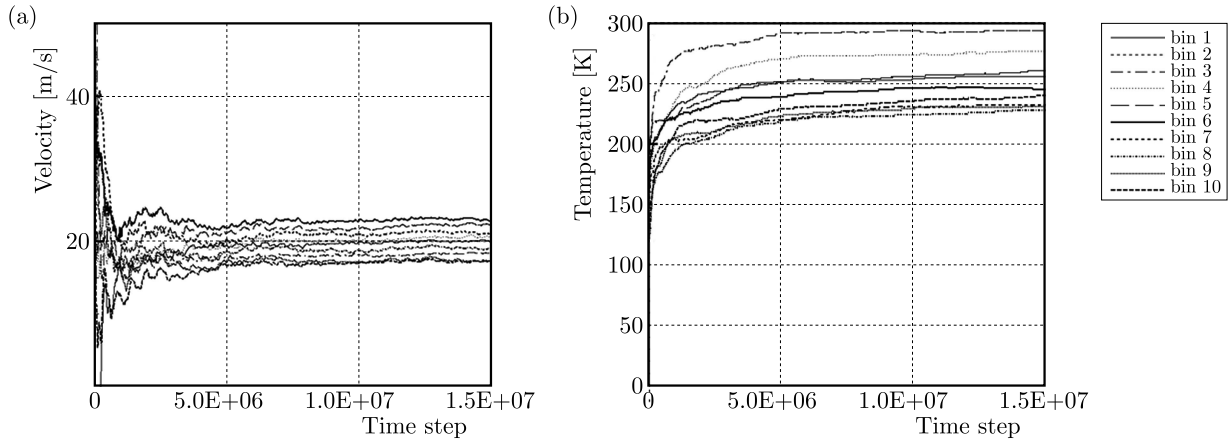

Fig. 4. Convergence rates of: (a) velocity and (b) temperature, along the symmetric converging-diverging channel generated by enforcement of temperature and mean velocity in bin 2

As shown in Fig. 3c, the highest value of molecular density occurs in bin 4 before the throat. Temperature decreases from the control bin through the end of the channel, and the minimum temperature occurs in bin 8. The temperature setting at the control bin influences upstream bins at lower flow velocities. So the temperature rise could be observed in bins 1, 9 and 10. According to Eq. (2.2), the pressure increases with temperature only through the first term while the effect of molecular density appears in both terms, giving the temperature the dominant role in determining the pressure value and its variation. Therefore, the highest pressure has occurred at bin 3 near the highest temperature bin, as can be seen in Fig. 3b. It should be noted that the flow energy decreases through the channel by restricting and scaling temperature of wall molecules to a fixed value.

As mentioned before, these results will be used to verify the solution of our test case with non-equal inlet and outlet cross-sectional areas, defined in Fig. 1. This non-symmetric channel includes 7 bins. The equation of motion is integrated over time with time steps of $\Delta t = 10^{-16}$ second using the Verlet scheme. The solution proceeds for 15 000 000 time steps to reach equilibrium. Similar to the symmetric channel flow, temperature of 300 K and mean velocity of 20 m/s are continuously enforced in the second bin. In addition, temperature of 234 K is enforced at the outlet of the channel in bin 7. This temperature has been extracted from the solution of the symmetric converging-diverging channel introduced in Fig. 3. There are 756 wall molecules and 803 fluid molecules between bins 1 to 7 which are equal to those in the same bins of the symmetric converging-diverging channel at the equilibrium. The number of molecules is not changed during the solution. This means that for each molecule leaving the end of the channel, either it should return back into the channel at the inlet or one molecule should be inserted into the domain at the inlet. Insertion of molecules into the domain creates drastic intermolecular forces and change the internal energy in the domain. Such instantaneous forces sometimes cause unexpected disorder in the motion of molecules, which normally results in divergence of the solution. Some methods have been presented to perform the insertion process with minimum changes in the domain internal energy (Sun and Ebner, 1992; Li *et al.*, 1998). In those methods however, inserted molecules may overlap with other molecules and, therefore, due to high internal forces between them, one or both of them may be ejected out of the domain.

Due to difficulties associated with insertion of molecules at the inlet, it has been decided to use a periodic boundary condition at the inlet and outlet of the channel. In this case, every molecule that leaves the solution domain at the outlet will be returned back into the solution domain at the inlet without any difficulty. However, the problem is that cross-sectional areas of the inlet and outlet are not equal to each other. To resolve this problem, the molecules leaving

the outlet of the non-symmetric channel will be sent into an adaption zone which expands the flow cross-sectional area from the outlet of the non-symmetric channel to an area equal to the inlet cross-sectional area of the channel, i.e. from area of 29.05 Å×36.15 Å, to an area of 36.15 Å×36.15 Å. Note that the periodic boundary condition is applied between the outlet of the non-symmetric channel and the inlet of the adaption zone, and also between the outlet of the adaption zone and the inlet of the non-symmetric channel. Different profiles can be designed for the wall geometry in this zone; this will be discussed later in this Section. But we know that the best option is to select a wall profile similar to the part of the symmetric converging-diverging channel that has been cut off from it, i.e. a part of the channel with bins 8 to 10, as shown in Fig. 5. This adaption zone, denoted by 1st, is filled with 259 Argon molecules to bring the number of mono-atomic Argon molecules to 1062 in the solution domain. Results obtained from the numerical solution of molecular flow in the non-symmetric channel are compared with the results of the symmetric converging-diverging channel in Fig. 6.

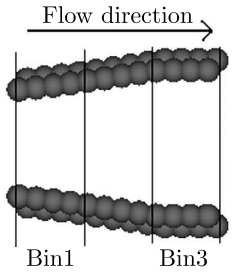

Fig. 5. 1st adaptation zone with 3 bins along the x direction

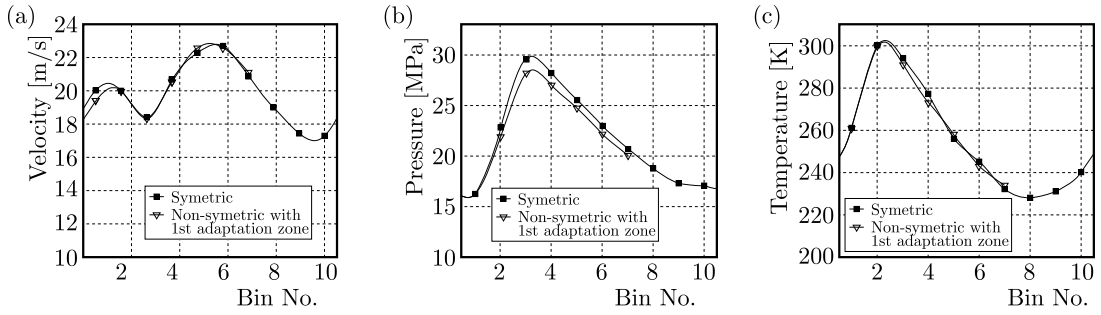

Fig. 6. Variations of flow properties along the non-symmetric channel with temperature of 300 K and mean velocity of 20 m/s at bin 2 and temperature of 234 K at bin 7 in comparison to those of the symmetric channel, (a) mean flow velocity, (b) pressure, and (c) temperature

As shown in Fig. 6, the agreement between results obtained from the solutions of symmetric and non-symmetric channels is excellent, except for the pressure variation. Note that since temperature of bin 7 is set up to 234 K by rescaling of the Virial velocity of molecules in this bin at each time step, the arrangement of molecules in this bin will be changed in comparison to that of the symmetric converging-diverging channel. Due to this rearrangement of molecules in bin 7, temperature variation is slightly underestimated. As noted before, temperature has the main role in the determination of pressure. Therefore, rearrangement of molecules in bin 7 has affected pressure through both terms of Eq. (2.2). As a result, a small difference between the results of pressure depicted in Fig. 6b is inevitable. Therefore, we have been able to generate specific flow in a channel with non-equal inlet and outlet cross-sectional areas by enforcement of temperature and mean velocity at one bin, e.g. bin 2 here, and temperature at another bin, e.g. bin 7 here.

In order to produce extra validation data for comparison purposes, molecular flow of Argon in the symmetric converging-diverging channel of Fig. 2 has been solved for two additional

conditions at bin 2: (a) temperature of 300 K and mean velocity of 50 m/s, and (b) temperature of 300 K and mean velocity of 100 m/s. Other settings of these two numerical solutions are exactly the same as those of the first solution with temperature of 300 K and mean velocity of 20 m/s. Solutions of cases (a) and (b) indicate that temperature of bin 7 in these two cases reaches 263 K and 279 K, respectively. Now, once again molecular flow is solved in the non-symmetric channel, having enforced temperature and mean velocity at bin 2, and extracted temperature at bin 7. All other settings of the solution are as before. Comparison of pressure, mean flow velocity, molecular density and temperature variations along the non-symmetric channel with those of the symmetric converging-diverging channel are shown in Fig. 7.

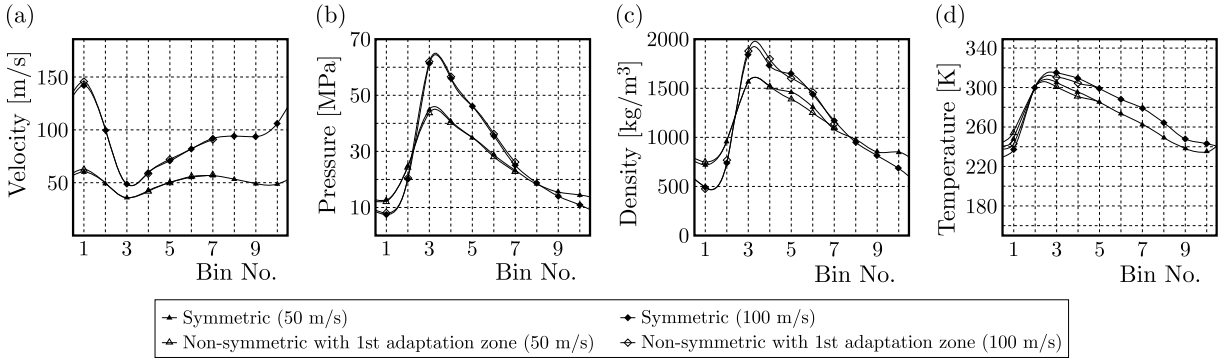

Fig. 7. Comparison of velocity, pressure, molecular density and temperature along the non-symmetric channel with those of the symmetric converging-diverging channel for two cases of (a) temperature of 300 K and mean velocities of 50 m/s at bin 2 and temperatures of 263 K at bin 7, and (b) temperature of 300 K and mean velocities of 100 m/s at bin 2 and temperatures of 279 K at bin 7

Variation of the mean flow velocity along the channel shows a slightly different trend at 100 m/s in comparison to 50 m/s case as seen in Fig. 7a. Due to the accumulation of molecules in the throat region, the mean velocity of molecules decreases in the throat upstream for both cases. Downstream the throat however, molecules gain velocity as a result of less concentration in this region. It could be seen in Fig. 7b that pressure increases with molecular density upstream the throat. In this region, higher temperature has also caused the pressure to increase, according to Eq. (2.2). The agreement between the results of the symmetric and non-symmetric channels is more realized at higher mean flow velocities. Therefore, it is clear that the presented method is more accurate at higher velocities of mean flow.

Again, comparison of the results in Fig. 7 proved that the presented approach has been able to generate specific flow in the channel with non-equal inlet and outlet cross-sectional areas by enforcement of temperature and mean velocity at one bin, and temperature at another bin if a proper adaption zone is used. In order to generalize this approach, it is needed to investigate the effect of adaption-zone geometry on the results. It is significant to demonstrate that the presented approach is mainly independent of the shape of the adaption zone. The adaption zone is characterized by its length, its wall slopes at the inlet and outlet, and cross-sectional areas at the inlet and outlet. For any channel, the latter one is fixed, i.e. from inlet of 29.05 Å×36.15 Å to outlet of 36.15 Å×36.15 Å. Therefore, we define test cases to investigate the effect of other two parameters, i.e. length and slope of the adaption zone.

First, two different adaption zones shown in Fig. 8 are investigated. Test case (b) where mean flow velocity of 100 m/s is enforced at bin 2 is solved with these adaption zones. The adaptation zones proposed in Figs. 8a and 8b as 2nd and 3rd geometries include three and two bins, respectively; i.e. equal to 54.225 Å and 36.15 Å in length, respectively. In both cases, the slope of the wall profile is 0.196 in the first bin, and is zero in the other bins.

The number of fluid molecules in the 2nd and 3rd adaptation zones of Figs. 8a and Fig. 8b are equal to 259 and 153, respectively. The number of molecules in the geometries has been selected

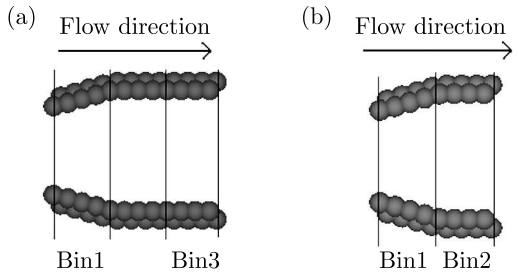

Fig. 8. Modified adaptation zones: (a) 2nd geometry (b) 3rd geometry

based on the average density of molecules in the non-symmetric channel. Therefore, the added number of molecules is proportional to the adaptation zone volume. The results obtained from these two solutions are compared with those obtained from the symmetric converging-diverging channel and from the non-symmetric channel with the 1st adaption zone in Fig. 9.

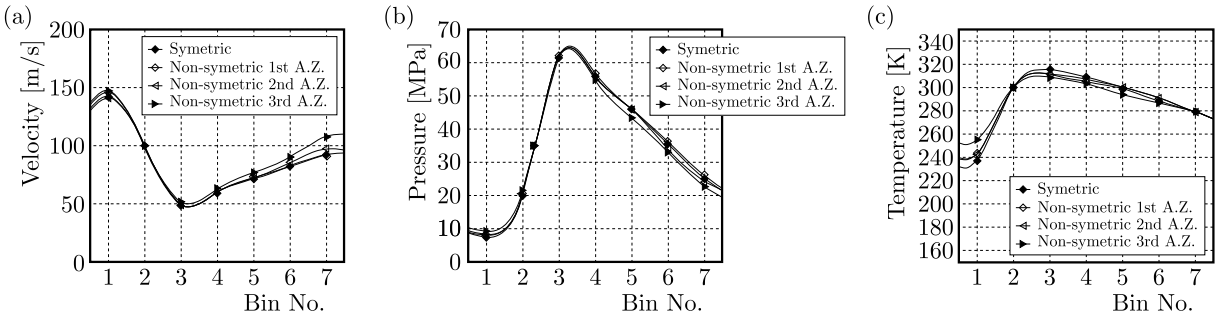

Fig. 9. Comparison of velocity, pressure and temperature variations of flow variables along the non-symmetric channel generated by temperature of 300 K and mean velocity of 100 m/s at bin 2 and temperatures of 279 K at bin 7 with 1st, 2nd, and 3rd adaption zones, with those of the symmetric channel

In comparison to the results of the symmetric channel and those obtained using the 1st adaption zone, both adaption zones have predicted flow properties very well, however, between the 2nd and 3rd adaptation zones, the 2nd adaption zone leads to a better estimation of flow properties. We believe that this is due to the facts that 1) the slope of the 2nd adaption zone from the inlet to outlet is smoother than that of the 3rd adaption zone, and 2) length of the 2nd adaption zone is longer. But we would like to have an adaption zone with small length in order to minimize computational cost. For this purpose, two additional adaption zones denoted by fourth (4th) and fifth (5th), with 36.15 Å in length are defined. Lengths of both adaption zones are equal to the 3rd adaption zone. The 4th adaption zone shown in Fig. 10a has a smoother wall slope. From the beginning of the first bin up to the middle of the second bin, the wall slope is constant and equal to 0.13, i.e. with an angle of 7.4°. From the middle of the second bin, the slope of the wall is set equal to zero. The 5th adaption zone shown in Fig. 10b will be introduced after analysis of the results obtained from the 4th adaption zone. The number of fluid molecules in both adaptation zones is equal to 259.

Having solved molecular flow in the non-symmetric channel using the 4th adaption zone with temperature of 300 K and mean velocity of 100 m/s at bin 2 and temperatures of 279 K at bin 7, its results are compared with the results of the symmetric channel and those of the non-symmetric channel with the 2nd and 3rd adaption zones in Fig. 11. Having compared with the results of the symmetric channel, results of Fig. 11 show that using the 4th adaptation zone, the flow properties are estimated better than when the 3rd adaptation zone is used. We believe that this is due to the fact that the wall of the 4th adaption zone has a lower wall slope. This once again proves that the adaption zone with smoother wall profiles are preferred. Note that

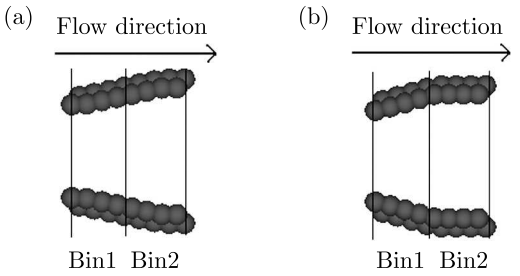

Fig. 10. (a) 4th adaptation zone (b) 5th adaptation zone

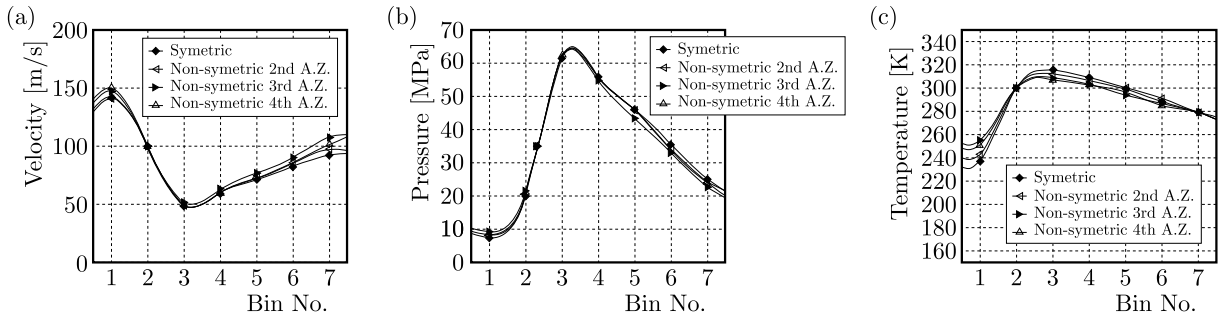

Fig. 11. Comparison of velocity, pressure and temperature along the non-symmetric channel generated by temperature of 300 K and mean velocity of 100 m/s at bin 2 and temperatures of 279 K at bin 7 with 2nd, 3rd and 4th adaption zones, with those of the symmetric channel

based on Fig. 11, although the results obtained using the 4th adaption zone do not give a better estimation of flow properties in comparison to the results obtained using the 2nd adaptation zone, it costs computationally less since it is shorter in length.

Careful inspection of the 4th adaption zone reveals that the slope of this adaptation zone at its inlet is very close to the slope of the non-symmetric channel at its outlet. Therefore, to achieve more correct results, it is necessary to match the inlet slope of the adaptation zone with the outlet slope of the non-symmetric channel.

To account for these requirements, it is proposed to generate the wall profile of the adaption zone with a 3rd degree (cubic) polynomial which will have an inlet slope equal to the outlet slope of the non-symmetric channel and an outlet slope equal to the inlet slope of the non-symmetric channel. Two other constants of the cubic polynomial are determined by the definition of the beginning and the end coordinates of the adaption zone. This profile that has length equal to that of the 4th adaption zone (2 bins) is shown in Fig. 10b. The previous flow simulation is repeated but using the 5th adaption zone. The results of this simulation including variation of velocity, pressure and temperature along the channel are shown in Fig. 12.

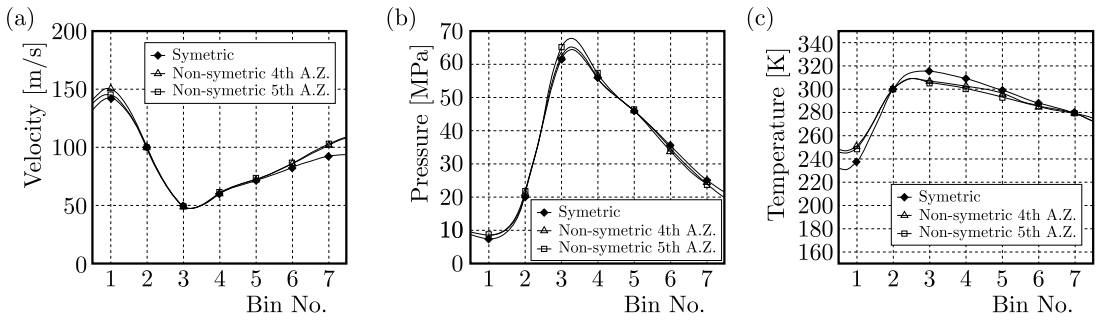

Fig. 12. Comparison between variations of flow variables along the non-symmetric channel generated by temperature of 300 K and mean velocity of 100 m/s at bin 2 and temperatures of 279 K at bin 7 with 4th and 5th adaptation zones, (a) velocity, (b) pressure and (c) temperature

As seen in Fig. 12, the results obtained using the 4th and 5th adaptation zones are very similar to each other. Especially, accurate results have been achieved at the end of the nozzle.

To show that this method does not depend on the number of molecules, the previous flow simulations are repeated with 200 more and fewer molecules in the symmetric nanochannel and the same trend is observed with the adaptation zones in variation of velocity, pressure and temperature.

4. Conclusion

In this paper, it is shown that flow can be generated and controlled in a channel with different inlet and outlet cross sections by setting temperature at two different regions and mean flow velocity at one of these regions. In a channel with non-equal inlet and outlet, periodic boundary conditions cannot be implemented. Therefore, to handle this difficulty, an adaption zone is used to computationally expand the outlet of the channel to a cross sectional area equal to its inlet. This adaption zone should have the following specifications to result in a more accurate flow prediction.

- Length: If its length is too short then the accuracy of estimated flow properties along the channel with variable cross-sectional area decreases. On the other hand, if the length of the channel is too long, then the cost of computation will raise. In the non-symmetric converging-diverging channel, for instance, the making use of the adaptation zone with length and wall profile similar to the part that has been cut off from it, results in a more accurate estimation of flow properties.
- Slope at junctions: To achieve more accurate results, it is necessary to set the inlet slope of the adaption zone equal to the outlet slope of the channel, and also to set the outlet slope of the adaption zone equal to the inlet slope of the channel.
- Wall profile: A 3rd degree (cubic) polynomial is used for the wall profile of the adaption zone. With this profile, slopes at the inlet and outlet, and also length of the adaption zone can be fixed to the desired values and, therefore, guarantee a smooth wall profile. Note that the slope of the channel inlet (and thus the adaption zone outlet) is preferred to be zero.

References

1. Allen M.P., Tildesley D.J., 1987, *Computer Simulation of Liquids*, Oxford, New York
2. Bao F., Huang Y., Zhang Y., Lin J., 2015, Investigation of pressure-driven gas flows in nanoscale channels using molecular dynamics simulation, *Microfluid Nanofluid*, **18**, 1075-1084
3. Branam R.D., Micci M.M., 2009, Comparison of wall models for the molecular dynamics simulation of microflows, *Nanoscale and Microscale Thermophysical Engineering*, **13**, 1-12
4. Darbandi M., Abbassi H.R., Khaledi Alidusti R., Sabouri M., 2011, *Molecular Dynamics Simulation of Nano Channel as Nanopumps*, ICNMM, Edmonton, Alberta, Canada
5. Fan X.J., Nhan P.T., Ng T.Y„ Xu D., 2002, Molecular dynamics simulation of a liquid in a complex nano channel flow, *Physics of Fluids*, **14**, 3, 1146-1153
6. Han M., 2008, Thermally-driven nanoscale pump by molecular dynamics simulation, *Journal of Mechanical Science and Technology*, **22**, 157-165
7. Hanasaki I., Nakatani A., 2006, Fluidized piston model for molecular dynamics simulations of hydrodynamics flow, *Modelling and Simulation in Materials Science and Engineering*, **14**, S9-S20

8. Hasheminasab S.M., Karimian S.M.H., 2015, New indirect method for calculation of flow forces in molecular dynamics simulation, *Journal of Molecular Liquids*, **206**, 183-189

9. Huang C., Choi P.Y.K., Nandakumar K., Kostiuk L.W., 2006, Molecular dynamics simulation of a pressure-driven liquid transport process in a cylindrical nanopore using two self-adjusting plates, *Journal of Chemical Physics*, **124**, 234701

10. Huang C., Nandakumar K., Kwok D.Y., 2004, Non-equilibrium injection flow in a nanometer capillary channel, *ICMENS'04*, 374-378

11. Kamali R., Kharazmi A., 2011, Molecular dynamics simulation of surface roughness effects on nanoscale flows, *International Journal of Thermal Science*, **50**, 3, 226-232

12. Karimian S.M.H., Izadi S., 2013, Bin size determination for the measurement of mean flow velocity in molecular dynamics simulation, *International Journal for Numerical Methods in Fluids*, **71**, 7, 930-938

13. Karimian S.M.H., Izadi S., Barati Farimani A., 2011, A study on the measurement of mean velocity and its convergence in molecular dynamics simulations, *International Journal for Numerical Methods in Fluids*, **67**, 12, 2130-2140

14. Karimian S.M.H., Namvar S., 2012, Implementation of SMC averaging method in a channeled molecular flow of liquids and gases, *Journal of Physics: Conference Series*, **362**, 01, 2029

15. Karniadakis G.E., Beskok A., Aluru N., 2002, *Micro Flows and Nano Flows*, Springer, New York, 641-648

16. Kim B.H., Beskok A., Cagin T., 2010, Viscous heating in nanoscale shear driven liquid flows, *Microfluid Nanofluid*, **9**, 31-40

17. Koplik J., Banavar J., Willemsen J., 1988, Molecular dynamics of Poiseuille flow and moving contact lines, *Physical Review Letters*, **60**, 1282-1285

18. Koplik J., Banavar J.R., Willemsen J.F., 1989, Molecular dynamics of fluid flow at solid surfaces, *Physics of Fluids A*, **1**, 781-794

19. Leach A.R., 1999, *Molecular Modeling: Principles and Applications*, Longman

20. Li J., Liao D., Yip S., 1998, Coupling continuum to molecular-dynamics simulation: reflecting particle method and the field estimator, *Physical Review E*, **57**, 6, 7259-7267

21. Liu C., Li Z., 2010, Molecular dynamics simulation of composite nanochannels as nanopumps driven by symmetric temperature gradients, *Physical Review Letters*, **105**, 174501

22. Mi X.B., Chwang A. T., 2003, Molecular dynamics simulations of nanochannel flows at low Reynolds numbers, *Molecules*, **8**, 193-206

23. Nagayama G., Cheng P., 2004, Effects of interface wettability on microscale flow by molecular dynamics simulation, *International Journal of Heat and Mass Transfer*, **47**, 501-513

24. Najafi H.R., Karimian S.M.H., 2016, Analysis of pressure behavior in a temperature controlled molecular dynamic flow, *Journal of Theoretical and Applied Mechanics*, **54**, 3, 881-892

25. Namvar S., Karimian S.M.H., 2012, Detailed investigation on the effect of wall spring stiffness on velocity profile in molecular dynamics simulation, *Journal of Physics: Conference Series*, **362**, 01, 2039

26. Priezjev N.V., 2007, Effect of surface roughness on rate-dependent slip in simple fluids, *Journal of Chemical Physics*, **127**, 144708

27. Rapaport D.C., 2004, *The Art of Molecular Dynamics Simulation*, Cambridge University Press

28. Sadus R.J., 2002, *Molecular Simulation of Fluids: Theory, Algorithms and Object-Orientation*, Elsevier

29. Sofos F., Karakasidas T.E., Liakopoulos A., 2009, Non-equilibrium molecular dynamics investigation of parameters affecting planar nanochannel flows, *Contemporary Engineering Sciences*, **2**, 6, 283-298

30. Stillinger F.H., Rahman A., 1974, Improved simulation of liquids water by molecular dynamics, *Journal of Chemical Physics*, **60**, 1545-1557

31. Sun M., Ebner C., 1992, Molecular-dynamics simulation of compressible fluid flow in two--dimensional channels, *Physical Review A*, **46**, 4813

32. Travis K.P., Evans D.J., 1997, Molecular spin in a fluid undergoing Poiseille flow, *Physical Review E*, **55**, 1566-1572

33. Travis K.P., Gubbins K.E., 2000, Poiseuille flow of Lennard-Jones fluids in narrow slit pores, *Journal of Chemical Physics*, **112**, 1984-1994

34. Tysanner M.W., Garcia A.L., 2004, Measurement bias of fluid velocity in molecular simulations, *Journal of Computational Physics*, **196**, 173-183

35. Tysanner M.W., Garcia A.L., 2005, Non-equilibrium behavior of equilibrium reservoirs in molecular simulations, *International Journal of Numerical Methods in Fluids*, **2050**, 1-12

36. Verlet L., 1967, Computer "experiments" on classical fluids. I. Thermodynamical properties of Lennard-Jones molecules, *Physical Review*, **159**, 98

37. Zhang Z.Q., Zhang H.W., Ye H.F., 2009, Pressure-driven flow in parallel-plate nanochannels, *Applied Physics Letters*, **95**, 154101

38. Ziarani A.S., Mohamad A.A., 2005, A molecular dynamics study of perturbed Poiseulle flow in a nanochannel, *Microfluid Nanofluid*, **2**, 12-20

Manuscript received November 30, 2016; accepted for print April 15, 2017

JOURNAL OF THEORETICAL AND APPLIED MECHANICS
55, 4, pp. 1155-1165, Warsaw 2017
DOI: 10.15632/jtam-pl.55.4.1155

THERMAL CREEP STRESS AND STRAIN ANALYSIS IN A NON-HOMOGENEOUS SPHERICAL SHELL

Pankaj Thakur

Department of Mathematics, Faculty of Science and Technology, ICFAI University Baddi, Solan, India
e-mail: pankaj_thakur15@yahoo.co.in; dr_pankajthakur@yahoo.com

Satya Bir Singh

Department of Mathematics, Punjabi University Patiala, Punjab, India; e-mail: sbsingh69@yahoo.com

D.S. Pathania

Department of Mathematics, Guru Nanak Dev Engineering College, Ludhiana, Punjab, India
e-mail: despathania@yahoo.com

Gaurav Verma

Research Scholar, IKG Punjab Technical University Kapurthala, Punjab, India; e-amil: gkdon85@gmail.com

The purpose of this paper is to present study of thermal creep stress and strain rates in a non-homogeneous spherical shell by using Seth's transition theory. Seth's transition theory is applied to the problem of creep stresses and strain rates in the non-homogeneous spherical shell under steady-state temperature. Neither the yield criterion nor the associated flow rule is assumed here. With the introduction of thermal effect, values of circumferential stress decrease at the external surface as well as internal surface of the spherical shell. It means that the temperature dependent materials minimize the possibility of fracture at the internal surface of the spherical shell. The model proposed in this paper is used commonly as a design of chemical and oil plants, industrial gases and stream turbines, high speed structures involving aerodynamic heating.

Keywords: stress, strain rates, thermal, spherical shell, non-homogeneous

1. Introduction

Spherical shell structures have found widespread use in modern technology such as design of chemical and oil plants, accumulator shells, pressure vessel for industrial gases or media transportation of high-pressurized fluids and piping of nuclear containment, high speed structures involving aerodynamic heating, submerged undersea structures, earth sheltered domes, and the like. These spherical systems are effective from the perspectives of both structural and architectural design. In many of these cases, the spherical shells have to operate under severe mechanical and thermal loads causing significant creep and thus reducing its service life. The collapse or damage is initiated by creep, shrinkage and thermal effects, or from their interaction with structures that both experience or do not experience environmental degradation. Consequently, demand for strengthening and upgrading the existing concrete structures, because of damage caused by long-term effects and excessive structural deformations, has been recognized. However, before the application of costly strengthening techniques, understanding of nonlinear long-term behaviour of the existing and new spherical shells is essential, and the development of suitable and reliable theoretical approaches for their analysis and safety assessment is required. Creep effects generally increase deformations of a shell structure even under room temperatures, and are usually only considered to affect behaviour at the service ability limit states. Therefore, the analysis of

long term steady state creep deformations of shells is very important in these applications (Hamed *et al.*, 2010; Kashkoli and Nejad, 2014). Due to the occurrence of these creep deformations, non-homogeneous materials are widely used in the engineering applications. Non-homogeneous materials are a specific class of composite materials known as functionally graded materials (FGM) in which constituents are graded in one or more direction with continuous variation to achieve desired properties. The smooth grading of the constituents result in better thermal properties, higher fracture toughness, improved residual stress distribution and reduced stress intensity factors. These properties allow non-homogeneous structures to withstand high pressure under elevated thermal environment. Therefore, the analysis of non-homogeneity in the spherical shell through a mathematical model by taking one and all the complexities into consideration is the major concern of researchers (Kar and Panda, 2016). Some degree of non-homogeneity is present in a wide class of materials such as hot rolled metals, magnesium and aluminum alloys. Non-homogenity can also be introduced by a certain external field which is a thermal gradient material as the elastic moduli of the materials vary with temperature (Olszak, 1960). Penny (1967) obtained the effects of creep in spherical shells by analysis similar to the corresponding elastic ones described here. Miller (1995) evaluated solutions for stresses and displacements in a thick spherical shell subjected to internal and external pressure loads. You *et al.* (2005) presented an accurate model to carry out elastic analysis of thick-walled spherical pressure vessels subjected to internal pressure. Kellogg and King (1997) developed a finite element model of convection in a spherical axisymmetric shell that we use to simulate upwelling thermal plumes in the mantle. Thakur (2011) analyzed creep transition stresses of a thick isotropic spherical shell by finitesimal deformation under steady state of temperature and internal pressure by using Seth's transition theory. Seth's transition theory does not acquire any assumptions like the yield condition, incompressibility condition, and thus poses and solves a more general problem from which cases pertaining to the above assumptions can be worked out. This theory utilizes the concept of a generalized strain measure and asymptotic solution at critical points or turning points of differential equations defining the deformed field and has been successfully applied to a large number of problems (Seth, 1962, 1966; Thakur, 2011, 2014; Thakur *et al.*, 2016, 2017). Seth (1962) defined the concept of generalized strain measures as

$$e_{ii} = \int_0^{\overset{A}{e_{ii}}} \left(1 - 2\,\overset{A}{e_{ii}}\right)^{\frac{n}{2}-1} d\,\overset{A}{e_{ii}} = \frac{1}{n}\left[1 - \left(1 - 2\,\overset{A}{e_{ii}}\right)^{\frac{n}{2}}\right] \qquad i = 1,2,3 \tag{1.1}$$

where n is the measure and $\overset{A}{e_{ii}}$ are the Almansi finite strain components. For $n = -2, -1, 0, 1, 2$ it gives the Cauchy, Green Hencky, Swainger and Almansi measures respectively. Non-homogeneity in a spherical shell has been taken as the compressibility of the material as

$$C = C_0 r^{-k} \tag{1.2}$$

where $a \leqslant r \leqslant b$, C_0 and k are real constants.

2. Governing equations

We consider a spherical shell whose internal and external radii are a and b, respectively, and is subjected to uniform internal pressure p_i of gradually increasing magnitude and temperature Θ_0 applied to the internal surface $r = a$ as shown in Fig. 1. The components of displacement in spherical co-ordinates are given by (Seth, 1962, 1966)

$$u = r(1-\beta) \qquad v = 0 \qquad w = 0 \tag{2.1}$$

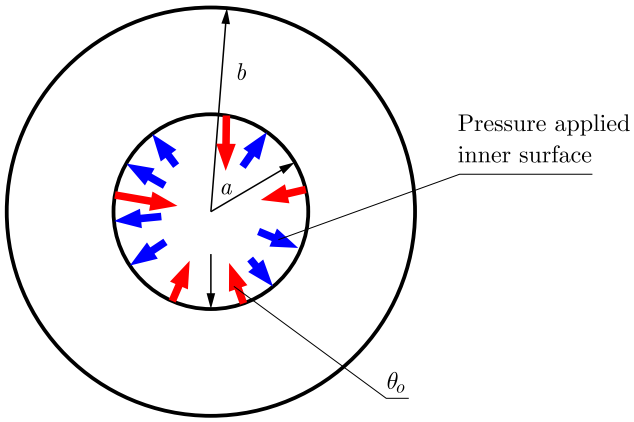

Fig. 1. Geometry of the spherical shell

where u, v, w are displacement components, β is a position function depending on r.

The generalized components of strain are given by Seth (1966)

$$e_{rr} = \frac{1}{n}[1-(r\beta'+\beta)^n] \qquad e_{\theta\theta} = \frac{1}{n}(1-\beta^n) = e_{\varphi\varphi} \qquad e_{r\theta} = e_{\theta\varphi} = e_{\varphi r} = 0 \tag{2.2}$$

where n is the measure and $\beta' = d\beta/dr$.

Stress-strain relation. The stress-strain relations for a thermo-elastic isotropic material are given by (Parkus, 1976)

$$T_{ij} = \lambda\delta_{ij}I_1 + 2\mu e_{ij} - \xi\Theta\delta_{ij}T_{ij} \qquad i,j = 1,2,3 \tag{2.3}$$

where T_{ij} are stress components and e_{ij} is strain component, λ and μ are Lame's constants, $I_1 = e_{kk}$ is the first strain invariant, δ_{ij} is Kronecker's delta, $\xi = \alpha(3\lambda+2\mu)$, α being the coefficient of thermal expansion, and Θ is temperature. Further, Θ has to satisfy

$$\nabla^2\Theta = 0 \tag{2.4}$$

Substituting the strain components from Eq. (2.2) in Eq. (2.3), the stresses are obtained as

$$\begin{aligned} T_{rr} &= \frac{2\mu}{n}[1-(r\beta'+\beta)^n] + \frac{\lambda}{n}[3-(r\beta'+\beta)^n - 2\beta^n] - \xi\Theta \\ T_{\theta\theta} &= T_{\varphi\varphi} = \frac{2\mu}{n}(1-\beta^n) + \frac{\lambda}{n}[3-(r\beta'+\beta)^n - 2\beta^n] - \xi\Theta \\ T_{r\theta} &= T_{\theta\varphi} = T_{\varphi r} = 0 \end{aligned} \tag{2.5}$$

Equation of equilibrium. The radial equilibrium of an element of the spherical shell requires

$$\frac{dT_{rr}}{dr} + \frac{2}{r}(T_{rr} - T_{\theta\theta}) = 0 \tag{2.6}$$

where T_{rr} and $T_{\theta\theta}$ are the radial and hoop stresses, respectively.

Boundary conditions. The temperature satisfying Laplace equation (2.4) with boundary conditions

$$\begin{aligned} &\Theta = \Theta_0 \quad \wedge \quad T_{rr} = -p_i \qquad \text{at} \quad r = a \\ &\Theta = 0 \quad \wedge \quad T_{rr} = 0 \qquad \text{at} \quad r = b \end{aligned} \tag{2.7}$$

where Θ_0 is constant, is given by (Parkus, 1976)

$$\Theta = \frac{\Theta_0 \log(r/b)}{\log(a/b)} \tag{2.8}$$

Critical points or turning points. Using Eq. (2.5) in Eq. (2.6), we get a non-linear differential equation in β as

$$nP(P+1)^{n-1}\beta^{n+1}\frac{dP}{d\beta} = \Big(\frac{\mu'}{\mu} - \frac{C'}{C}\Big)\{3-2C-\beta^n[2(1-C)+(1+P)^n]\} - 2C'r(1-\beta^n) \\ - n\beta^n P[2(1-C)+(1+P)^n] + 2C\beta^n[1-(1+P)^n] - \frac{nC\overline{\Theta}_0}{2\mu\beta^n}\Big(\xi + r\xi'\log\frac{r}{b}\Big) \tag{2.9}$$

where $\overline{\Theta}_0 = \Theta_0/\log(a/b)$, $C = 2\mu/\lambda + 2\mu$ and $r\beta' = \beta P$ (P is a function of β and β is a function of r only). The transition or turning points of β in Eq. (2.9)) are $P \to -1$ and $P \to \pm\infty$.

3. Analytical solution

For finding thermal creep stresses and strain rates, the transition function is taken through the principal stress difference (see Seth, 1962, 1966; Thakur, 2011, 2014; Thakur *et al.*, 2016, 2017) at the transition point $P \to -1$. We define the transition function ψ as

$$\psi = T_{rr} - T_{\theta\theta} = \frac{2\mu\beta^n}{n}[1-(P+1)^n] \tag{3.1}$$

where ψ is a function of r only, and ψ is the dimension.

Taking logarithmic differentiation of Eq. (3.1) with respect to r and substituting the value of $dP/d\beta$ from Eq. (2.9), we get

$$\frac{d\log\psi}{dr} = \frac{np}{r} + \frac{\mu'}{\mu} - \frac{1}{r\beta^n[1-(1+P)^n]}\Bigg[r\Big(\frac{\mu'}{\mu} - \frac{C'}{C}\Big)\{3-2C-\beta^n[2(1-C)+(1+P)^n]\} \\ - 2rC'(1-\beta^n) - n\beta^n P[2(1-C)+(1+P)^n] \\ + 2C\beta^n[1-(1+P)^n] - \frac{nC\overline{\Theta}}{2\mu}\Big(\xi + r\xi'\log\frac{r}{b}\Big)\Bigg] \tag{3.2}$$

Taking asymptotic value of Eq. (3.2) at $P \to -1$, we get

$$\frac{d}{dr}(\log\psi) = \frac{3\mu'}{\mu} - \frac{2C'}{C} - \frac{3n}{r} + X \tag{3.3}$$

where

$$X = \frac{2(n-1)C}{r} - \frac{2C\mu'}{\mu} + \frac{2C'}{\beta^n} - \Big(\frac{\mu'}{\mu} - \frac{C'}{C}\Big)\frac{3-2C}{\beta^n} + \frac{nC\overline{\Theta}_0}{2\mu r\beta^n}\Big(\xi + r\xi'\log\frac{r}{b}\Big)$$

Integrating equation (3.3), we get

$$\psi = A\frac{\mu^3}{C^2r^{3n}}\exp(h) \tag{3.4}$$

where $h = \int X\,dr$ and A is a constant of integration, which can be determined from the boundary condition. From Eq. (3.1) and Eq. (3.4), we have

$$T_{rr} - T_{\theta\theta} = A\frac{2r\mu^3}{2C^2r^{3n+1}}\exp(h) = \frac{ArH}{2} \tag{3.5}$$

where

$$H = \frac{2\mu^3}{C^2r^{3n+1}}\exp(h)$$

Substituting Eq. (3.5) in Eq. (2.6) and integrating, we get

$$T_{rr} = B - A \int H \, dr \tag{3.6}$$

where B is a constant of integration, which can be determined from the boundary condition and asymptotic value of β as $P \to -1$ is D/r, with D being a constant.

Using boundary condition Eq. (2.7) in Eq. (3.6), we get

$$A = -\frac{p_i}{\int\limits_a^b H \, dr} \qquad B = -\frac{p_i}{\int\limits_a^b H \, dr} \int H \, dr \tag{3.7}$$

where p_i is pressure at the inner surface of the spherical shell. Using the integration constants A and B in Eq. (3.6), we get

$$T_{rr} = \frac{p_i}{\int\limits_a^b H \, dr} \int\limits_r^b H \, dr \tag{3.8}$$

Substituting Eq. (3.8) into Eq. (3.5), we get

$$T_{\theta\theta} = T_{\varphi\varphi} = \frac{p_i}{\int\limits_a^b H \, dr} \Big(\int\limits_r^b H \, dr + \frac{rH}{2} \Big) \tag{3.9}$$

We introduce non-homogeneity in the spherical shell due to variable compressibility as given in Eq. (1.2), then Eq. (3.8) and Eq. (3.9) become

$$T_{rr} = \frac{p_i}{\int\limits_a^b H \, dr} \int\limits_r^b H_1 \, dr \qquad T_{\theta\theta} = T_{\varphi\varphi} = \frac{p_i}{\int\limits_a^b H_1 \, dr} \Big(\int\limits_r^b H_1 \, dr + \frac{rH_1}{2} \Big) \tag{3.10}$$

where T_{rr}, $T_{\theta\theta}$ are radial and circumferential stresses, and

$$H_1 = \frac{2\mu^3}{C^2 r^{3n+1}} \exp(h_1) = \frac{r^{-(3n+k+1)}}{4(1 - C_0 r^{-k})^3} \exp(h_1)$$

$$h_1 = -\frac{2(n-1)}{k} C_0 r^{-k} - \frac{2kC_0 r^{n-k}}{D^n (n-k)} + \frac{kC_0}{D^n} \int \frac{r^{n-k-1}(3 - 2C_0) r^{-k}}{1 - C_0 (bR)^{-k}} \, dr + 2 \log(1 - C_0 r^{-k})$$

$$+ \frac{\alpha n \overline{\Theta}_0}{D^n} \int (1 - C_0 r^{-k}) \Big(3 + \frac{C_0 r^{-k}}{1 - C_0 r^{-k}} - \frac{kC_0 r^{-k} \log(r/b)}{1 - C_0 r^{-k}} \Big) r^{n-1} \, dr$$

$$C' = -kC_0 r^{-k-1} \qquad \frac{\mu'}{\mu} = \frac{C'}{C(1 - C)}$$

Equations $(3.10)_{1,2}$ give thermal creep stresses for a spherical shell made of a non-homogeneous material under steady-state temperature. We introduce the following non-dimensional components as: $R = r/b$, $R_0 = a/b$, $\sigma_{rr} = \tau_{rr}/p_i$, $\sigma_{\theta\theta} = \tau_{\theta\theta}/p_i$ and $\alpha\Theta_0 = \Theta_1$. Equations $(3.10)_{1,2}$ in non-dimensional form become

$$\sigma_{rr} = \frac{\int\limits_R^1 H_2 \, dR}{\int\limits_{R_0}^1 H_2 \, dr} \qquad \sigma_{\theta\theta} = \sigma_{\varphi\varphi} = \frac{1}{\int\limits_{R_0}^1 H_2 \, dR} \Big(\int\limits_R^1 H_2 \, dR + \frac{RH_2}{2} \Big) \tag{3.11}$$

where

$$H_2 = \frac{(bR)^{-(3n+k+1)} C_0 \lambda^3}{4(1 - C_0 b^{-k} R^{-k})^3} \exp(h_2)$$

$$h_2 = -\frac{2(n-1)}{k} C_0 (bR)^{-k} - \frac{2kC_0 (bR)^{n-k}}{D^n (n-k)} + \frac{kC_0 b^{n-k}}{D^n} \int \frac{R^{n-k-1}(3 - 2C_0) R^{-k}}{1 - C_0 (bR)^{-k}}\, dR + 2\log(1 - C_0 b^{-k} R^{-k}) + \frac{n\Theta_1}{D^n \ln R_0} \int (1 - C_0 b^{-k} R^{-k}) \Big(3 + \frac{C_0 (bR)^{-k}}{1 - C_0 b^{-k} R^{-k}} - \frac{kC_0 (bR)^{-k} \log R}{1 - C_0 b^{-k} R^{-k}}\Big) R^{n-1}\, dR$$

Particular case: In the absence of temperature gradient (i.e. $\Theta_1 = 0$), Eqs. (3.11), become

$$\sigma_{rr} = \frac{\int_R^1 H_2^*\, dR}{\int_{R_0}^1 H_2^*\, dR} \qquad \sigma_{\theta\theta} = \sigma_{\varphi\varphi} = \frac{1}{\int_{R_0}^1 H_2^*\, dR} \Big(\int_R^1 H_2^*\, dR + \frac{R H_2^*}{2} \Big) \tag{3.12}$$

where

$$H_2^* = \frac{(bR)^{-(3n+k+1)} C_0 \lambda^3}{4(1 - C_0 b^{-k} R^{-k})^3} \exp(h_2^*)$$

$$h_2^* = -\frac{2(n-1)}{k} C_0 (bR)^{-k} - \frac{2kC_0 (bR)^{n-k}}{D^n (n-k)} + \frac{kC_0 b^{n-k}}{D^n} \int \frac{R^{n-k-1}(3 - 2C_0) R^{-k}}{1 - C_0 (bR)^{-k}}\, dR + 2\log(1 - C_0 b^{-k} R^{-k})$$

4. Estimation of creep parameters

When the creep sets in, the strains should be replaced by strain rates, then stress-strain relations are given (Sokolnikoff, 1946; Parkus, 1976)

$$e_{ij} = \frac{1+\nu}{E} T_{ij} - \frac{\nu}{E} \delta_{ij} T + \alpha\Theta \tag{4.1}$$

where e_{ij} is the strain component and $T = T_{ii}$ is the first stress invariant and $\nu = (1-C)/(2-C)$ is Poisson's ratio. Differentiating Eq. (2.2) with respect to time t, we get

$$\dot{e}_{\theta\theta} = -\beta^{n-1} \dot{\beta} \tag{4.2}$$

For Swainger measure (i.e. $n = 1$), Eq. (4.2) become

$$\dot{\varepsilon}_{\theta\theta} = \dot{\beta} \tag{4.3}$$

where $\dot{\varepsilon}_{\theta\theta}$ is the Swainger strain measure. From Eq. (3.1), the transition value β is given at the transition point $P \to -1$ by

$$\beta = \Big(\frac{n}{2\mu}\Big)^{\frac{1}{n}} (T_{rr} - T_{\theta\theta})^{\frac{1}{n}} \tag{4.4}$$

Using Eqs. (4.2)-(4.4) in Eq. (4.1), we get

$$\begin{aligned} &\dot{\varepsilon}_{rr} = m(\sigma_{rr} - \nu\sigma_{\theta\theta} + \alpha\Theta) \qquad \dot{\varepsilon}_{\theta\theta} = m(\sigma_{\theta\theta} - \nu\sigma_{rr} + \alpha\Theta) \\ &\dot{\varepsilon}_{\varphi\varphi} = -m[\nu(\sigma_{rr} + \sigma_{\theta\theta}) + \alpha\Theta] \end{aligned} \tag{4.5}$$

where $\dot{\varepsilon}_{rr}$, $\dot{\varepsilon}_{\theta\theta}$ and $\dot{\varepsilon}_{\varphi\varphi}$ are strain rates, σ_{rr}, $\sigma_{\theta\theta}$ are stress components and $m = [n(\sigma_r - \sigma_\theta)(1+\nu)]^{\frac{1}{n}-1}$. These are the constitutive equations used by Odquist (1974) for finding the creep stresses, provided we put $n = 1/N$ and N is the measure.

5. Numerical results and discussion

For calculating creep stresses and strain rates on the basis of the above analysis, the following values have been taken, $\nu = 0.5$ (incompressible material $C_0 = 0$), $\nu = 0.42857$ (compressible material $C_0 = 0.25$) and 0.333 (compressible material $C_0 = 0.50$), $n = 1/3$, $1/5$, $1/7$ (i.e. $N = 3$, 5, 7), thermal expansion coefficient $\alpha = 5.0 \cdot 10^{-5}\,\mathrm{deg\,F^{-1}}$ for Methyl Methacrylate (Levitsky and Shaffer, 1975) and $\Theta_1 = \alpha\Theta_0 = 0$ and 0.5, $D = 1$. In classical theory, the measure N is equal to $1/n$. The definite integrals in Eqs. (3.11) have been evaluated by using Simpson's rule. From Figs. 2-4, curves are presented between stresses along the radii ratio $R = r/b$ in the spherical shell made of compressible as well as incompressible materials for $k = -1$, 0, 1. It can be seen form Figs. 2 and 3 that the circumferential stresses are maximum at the external surface for $n = 1/7$ and $k = -1$, 0 for a compressible material as compared to the incompressible material. From Fig. 4, the circumferential stress is maximum at the internal surface for non-homogeneity $k = 1$. The non-homogeneity increases the values of circumferential stress (i.e. $k = -1$, 0), but reverse the result for $k = 1$.

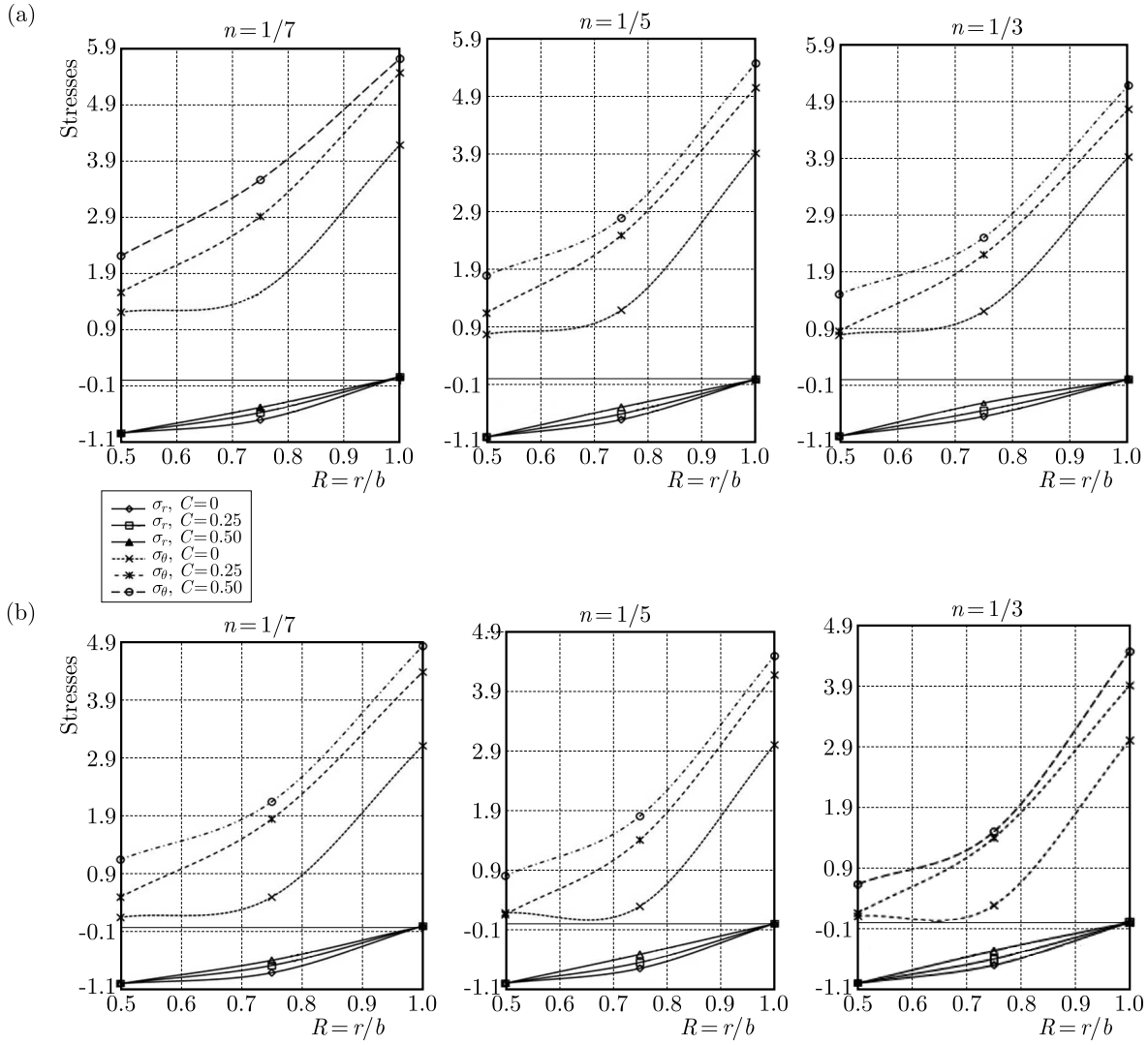

Fig. 2. Creep stresses in a non-homogeneous ($k = -1$) spherical shell along the radii ratio $R = r/b$; (a) without temperature, (b) for temperature $\Theta_1 = 0.5$

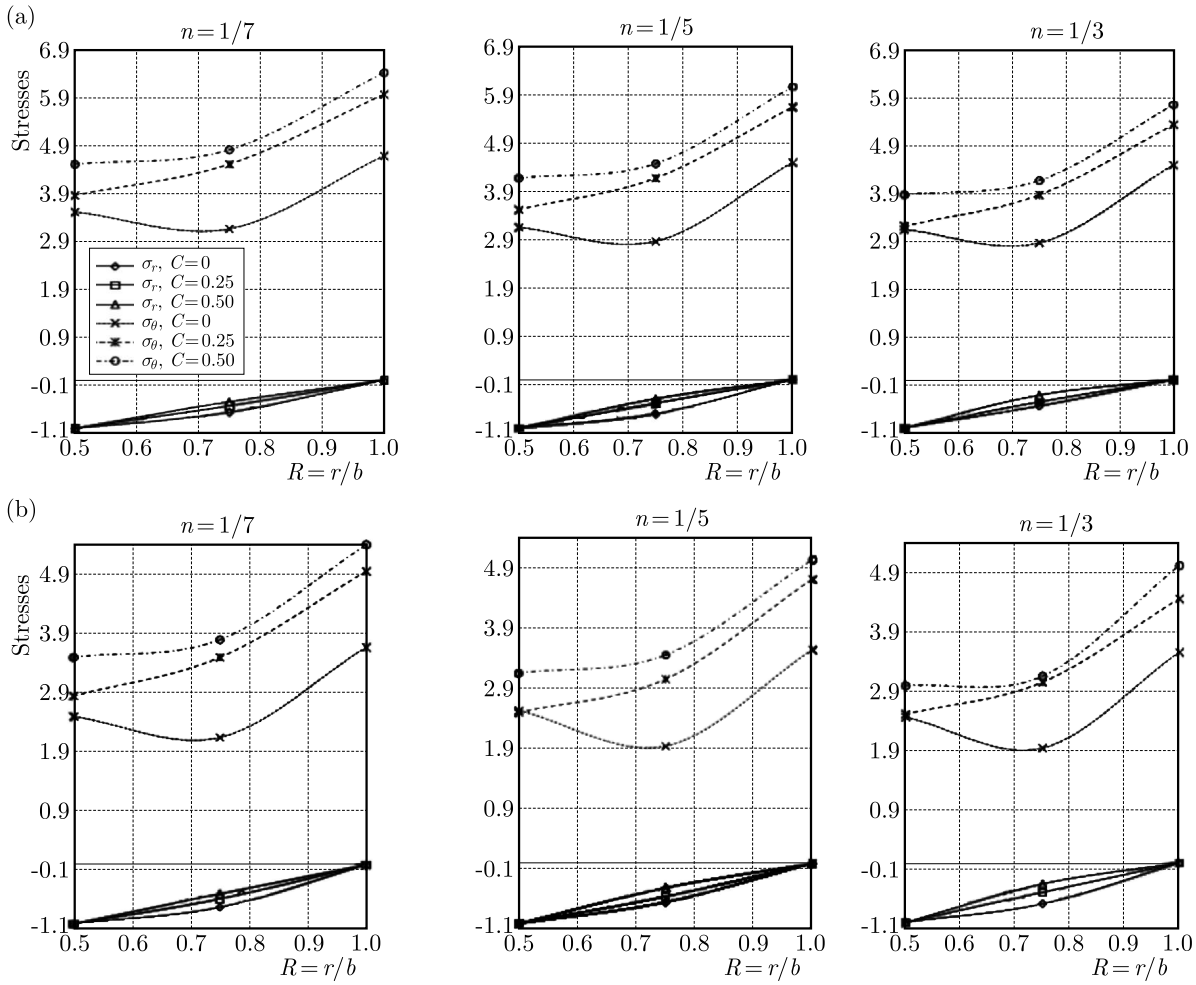

Fig. 3. Creep stresses in a non-homogeneous ($k = 0$) spherical shell along the radii ratio $R = r/b$; (a) without temperature, (b) for temperature $\Theta_1 = 0.5$

With the introduction of a temperature gradient, the values of circumferential stress are decreased at the external surface as well as internal surface of the spherical shell for different values of non-homogeneity. It means that temperature dependent materials minimize the possibility of fracture at the internal surface of the spherical shell. From (Fig. 5), curves are produced between strain rates along the radii ratio $R = r/b$ for the spherical shell made of compressible material $C = 0.25$, i.e. saturated clay for $k = -1$, 0, 1. It can be seen that the strain rates are maximum at the external surface for $k = -1$, 0 and reverse in the case $k = 1$. With the introduction of a temperature gradient, the strain rates decrease at the internal surface as well as the external surface. It means that the temperature dependent materials minimize the possibility of fracture at the internal surface of the spherical shell.

Acknowledgment

The authors are grateful to the referee for his critical comments which led to a significant improvement of the paper.

References

1. Hamed E., Bradford M.A., Gilbert R.I., 2010, Nonlinear long-term behaviour of spherical shallow thin-walled concrete shells of revolution, *International Journal of Solids and Structures*, **47**, 2, 204-215

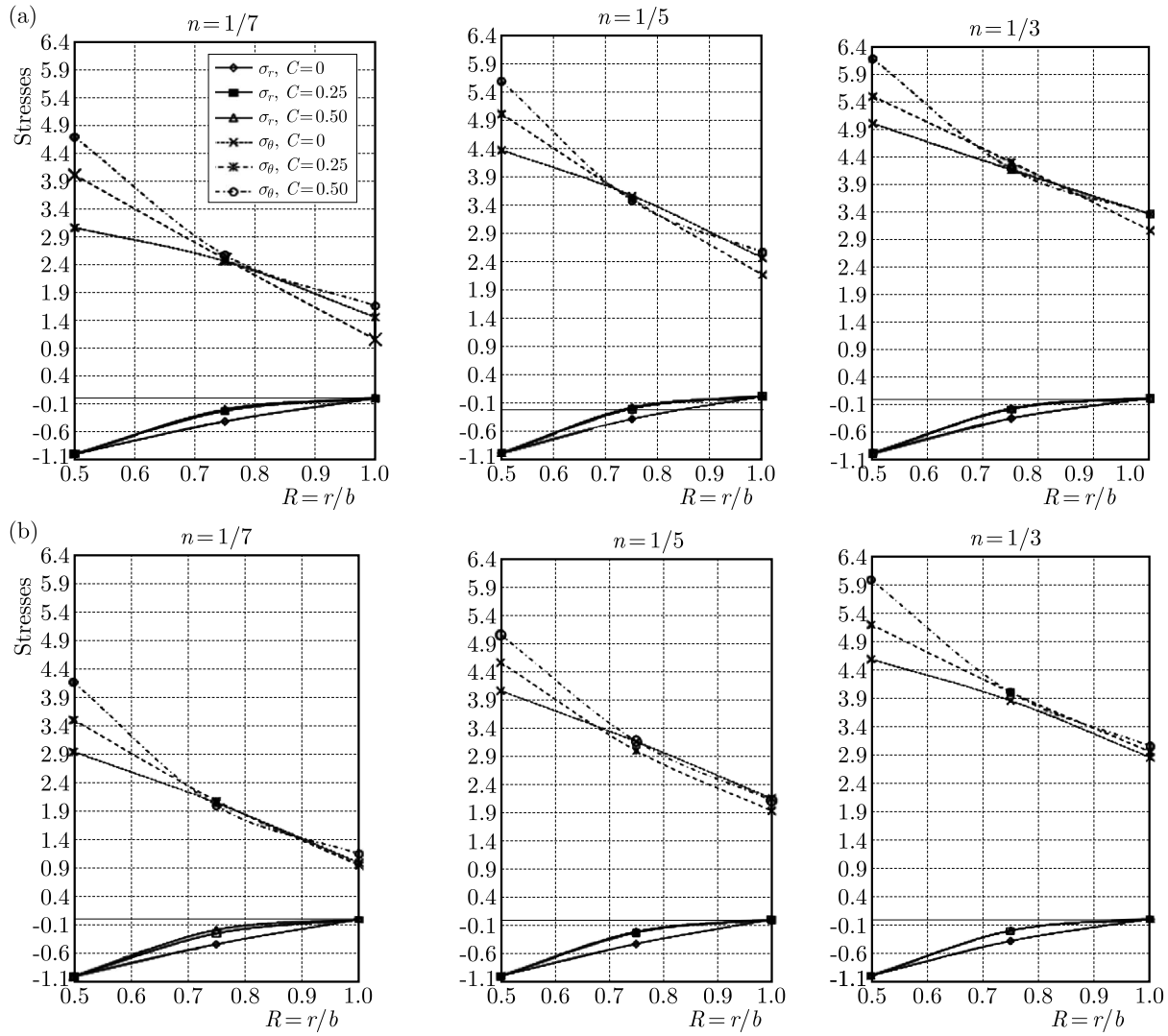

Fig. 4. Creep stresses in a non-homogeneous ($k = 1$) spherical shell along the radii ratio $R = r/b$; (a) without temperature, (b) for temperature $\Theta_1 = 0.5$

2. Kar V.R., Panda S.K., 2016, Nonlinear thermo-mechanical deformation behaviour of P-FGM shallow spherical shell panel, *Chinese Journal of Aeronautics*, **29**, 1, 173-183

3. Kashkoli M.D., Nejad M.Z., 2014, Effect of heat flux on creep stresses of thick walled cylindrical pressure vessels, *Journal of Applied Research and Technology*, **12**, 3, 585-597

4. Kellogg L.H., King S.D., 1997, The effect of temperature dependent viscosity on the structure of new plumes in the mantle: Results of a finite element model in a spherical, axisymmetric shell, *Earth and Planetary Science Letters*, **148**, 1/2, 13-26

5. Levitsky M., Shaffer, B.W., 1975, Residual thermal stresses in a solid sphere from a thermo-setting material, *Journal of Applied Mechanics, Transactions of ASME*, **42**, 3, 651-655

6. Miller G.K., 1995, Stresses in a spherical pressure vessel undergoing creep and dimensional changes, *International Journal of Solids and Structures*, **32**, 14, 2077-2093

7. Odquist F.K.G., 1974, *Mathematical Theory of Creep and Creep Rupture*, Clarendon Press, Oxford

8. Olszak W., 1960, Non-homogeneity in elasticity and plasticity, *ZAMM*, **40**, 10/11, 522-523

9. Parkus H., 1976, *Thermo-Elasticity*, Springer-Verlag Wien, New York, USA

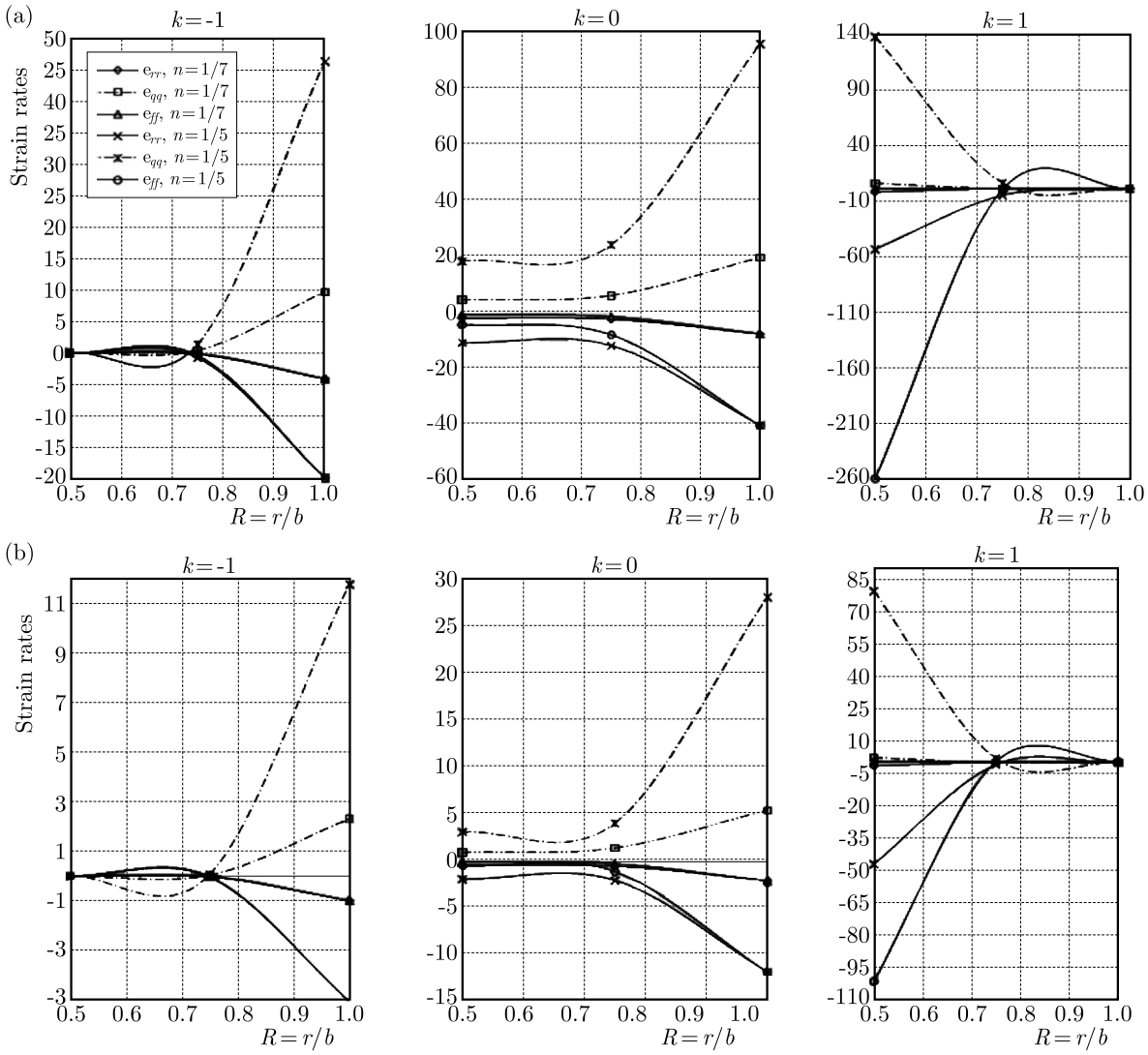

Fig. 5. Strain rates in a non-homogeneous spherical shell along the radii ratio $R = r/b$ for $C = 0.25$; (a) without temperature $\Theta_1 = 0$, (b) for temperature $\Theta_1 = 0.5$

10. Penny R.K., 1967, The creep of spherical shells containing discontinuities, *International Journal of Mechanical Sciences*, **9**, 6, 373-388

11. Seth B.R., 1962, Transition theory of elastic-plastic deformation, creep and relaxation, *Nature*, **195**, 896-897, DOI: 10.1038/195896a0

12. Seth B. R., 1966, Measure concept in mechanics, *International Journal of Non-Linear Mechanics*, **1**, 1, 35-40

13. Sokolnikoff I.S., 1946, *Mathematical Theory of Elasticity*, 1st edition, Mc-Graw Hill Book Company, Inc., New York, 60-76

14. Thakur P., 2011, Creep transition stresses of a thick isotropic spherical shell by finitesimal deformation under steady state of temperature and internal pressure, *Thermal Science*, **15**, 2, S157-S165

15. Thakur P., 2014, Steady thermal stress and strain rates in a circular cylinder with non-homogeneous compressibility subjected to thermal load, *Thermal Science*, **18**, 1, S81-S92

16. Thakur P., Singh S.B., Kaur J., 2016, Thermal creep stresses and strain rates in a circular disc with shaft having variable density, *Engineering Computation*, **33**, 3, 698-712

17. Thakur P., Gupta N., Singh S.B., 2017, Creep strain rates analysis in cylinder under temperature gradient for different material, *Engineering Computations*, **34**, 3, DOI: 10.1108/EC-05-2016--0159

18. You L.H., Zhang J.J., You X.Y., 2005, Elastic analysis of internally pressurized thick-walled spherical pressure vessels of functionally graded materials, *International Journal of Pressure Vessels and Piping*, **82**, 5, 347-354

Manuscript received December 2, 2016; accepted for print April 15, 2017

JOURNAL OF THEORETICAL AND APPLIED MECHANICS
55, 4, pp. 1167-1179, Warsaw 2017
DOI: 10.15632/jtam-pl.55.4.1167

BANDGAP PROPERTIES IN LOCALLY RESONANT PHONONIC CRYSTAL DOUBLE PANEL STRUCTURES WITH PERIODICALLY ATTACHED PILLARS

Denghui Qian, Zhiyu Shi

State Key Laboratory of Mechanics and Control of Mechanical Structures, College of Aerospace Engineering, Nanjing University of Aeronautics and Astronautics, Nanjing, Jiangsu, China

e-mail: qdhsd318@163.com; zyshi@nuaa.edu.cn (correspongding author)

The locally resonant (LR) phononic crystal double panel structure made of a two-dimensional periodic array of a two-component cylindrical LR pillar connected between the upper and lower plates is proposed, and the bandgap properties of the structure are investigated theoretically in this paper. The band structures, displacement fields of eigenmodes and transmission power spectrums of the corresponding 8×8 finite structure are calculated by the finite element method. Numerical results and further analysis demonstrate that a band gap with a low starting frequency and a wide band width is opened by the coupling between dominant vibrations of the pillars and plate modes of the upper and lower plates when the vibration source and the receiver are considered on different sides of the structure. By comparing the band structures and displacement fields of the double panel and those of the single plate with the same parameters, many common characteristics are displayed. Then, the influence of geometrical parameters on the band gap are studied and understood with the help of a simple 'spring-mass' model.

Keywords: bandgap property, phononic crystal double panel, band structure, displacement field, transmission power spectrum

1. Introduction

Due to the advantageous sound-insulated property, double panels are extensively used as the containment structures in many areas such as marine, transport, aerospace engineering and civil construction projects (Carnael and Fuller, 2004; Pietrzko and Mao, 1992). As it is well-known, vibrations are mostly propagated along containment structures from vibration sources, and structural noises are produced by radiation of the vibrations. The proposition of the phononic crystal concept provides a new idea for the investigation on theory about vibration insulation and noise reduction. Over the past two decades, the propagation of elastic waves in phononic crystals has attracted a lot of attention which mainly focuses on calculation methods and bandgap properties, but the application researches particularly on the field of vibration insulation and noise reduction are still immature. Brag scattering (Saindou *et al.*, 2002; Sigalas and Economou, 1992; Vasseur *et al.*, 2002; Zhang *et al.*, 2003) and locally resonant (Goffaux *et al.*, 2004; Hirsekorn *et al.*, 2004; Ho *et al.*, 2003; Liu *et al.*, 2000) are developed as the two main mechanisms for the creation of band gaps, in which the frequency range of band gaps based on the first mechanism is almost two orders of magnitude higher than that based on the second mechanism (Liu *et al.*, 20007). Hence, the studies on double panel structures with the design idea of locally resonant phononic crystal introduced provide a new idea for restraining structural vibration and reducing noise in the unmanageable low frequency region (Hsu, 2011; Oudich *et al.*, 2011; Qian and Shi, 2017; Xiao *et al.*, 2017) of some industrial products.

For now, bandgap properties of double panel structures with the design idea of a locally resonant phononic crystal introduced have rarely been studied. However, such an idea has been widely implemented in single plates recently. By etching holes periodically in a solid matrix plate and then filling them with scatters, the so-called filled-in system is formed. By stubbing resonant units periodically onto free surfaces of the plate, a stubbed-on system is formed (Ma *et al.*, 2014). Hsu and Wu (2007) and Xiao *et al.* (2008) investigated vibration of band gaps of epoxy base plates with filled-in rubber resonant units and filled-in rubber-coated heavy mass resonant units by using the plane wave expansion method, respectively. Similarly, the three-component and two-component stubbed-on systems constructed by periodically depositing rubber stubs with and without Pb capped on the surface of the base plate were studied by using the finite element method by Oudich *et al.* (2010). Besides, Xiao *et al.* (2012) researched flexural wave propagation and vibration transmission in a locally resonant thin plate with a two-dimensional periodic array of attached spring-mass resonators, which can be regarded as a simplified model of the stubbed-on system. Zhao *et al.* (2016) proposed a double-vibrator (rubber-steel-rubber-steel layers) three-component pillared PC plate on the basis of the traditional uni-vibrator (rubber-steel layers) three-component pillared PC plate and studied propagation characteristics of band gaps of flexural vibration and longitudinal vibration in the two-layer stubbed-on system. By revisiting the filled-in and stubbed-on structures, Ma *et al.* (2014) proposed a new structure with three-layered spherical resonant units, which opens a large sub-wavelength full band gap. By combining the filled-in and stubbed-on units, Li *et al.* (2015) investigated propagation characteristics of Lamb waves in a locally resonant phononic crystal single plate with the combined resonant unit. Based on this, Li *et al.* (2016) further researched the expansion of locally resonant complete band gaps in two-dimensional phononic crystals using a double-sided stubbed composite PC plate with composite stubs. Recently, Qian and Shi (2016) investigated the propagation characteristics of flexural waves in the locally resonant phononic crystal double panel structure made of a two-dimensional periodic array of a spring-mass resonator surrounded by n springs connected between the upper and lower plates.

In this paper, we investigate propagation characteristics of flexural vibration and longitudinal vibration in a locally resonant double panel structure consisting of a two-layer uniform thin plate with periodically attached cylindrical LR pillars in the cavity. At first, the band structures, displacement fields of eigenmodes and transmission power spectrums of the corresponding finite structure are calculated to study the formation mechanisms of the band gap. Then, a comparison between the band structure of the double panel and that of the single plate with the same parameters is displayed. Further, the influence of the geometrical parameters such as height of the rubber layer in the pillar, height of the Pb layer, radius of the pillar, thickness of the base plate and the lattice constant on the band gap of the proposed structure are discussed.

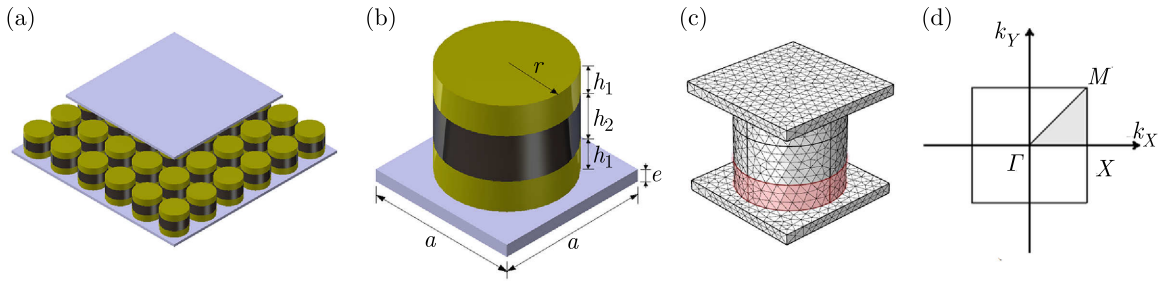

Fig. 1. (a) The LR phononic crystal double panel structure with periodically attached pillars, (b) its unit cell (upper plate is ignored), a is the lattice constant, e is thickness of the base plates, r is radius of the pillar, h_1 is height of rubber layer in the pillar, and h_2 is height of Pb layer in the pillar, (c) meshing of the unit cell, (d) and the irreducible first Brillouin zone (1BZ)

2. Model and method

As shown in Fig.1a, the studied system is constructed by periodically depositing the two--component cylindrical LR pillars squarely onto the surfaces of the upper and lower thin plates. The material of the first and last layers in the pillar is rubber, and the materials of the plates and the middle layer in the pillar are epoxy and Pb, respectively. The lattice constant, thickness of the base plates, radius of the pillar, and heights of different layers in the pillar in a unit cell are denoted by a, e, r, h_1 and h_2, which can be seen in Fig. 1b. Table 1 displays the material parameters used in the calculation, and all materials are assumed to be elastically isotropic.

Table 1. Material parameters used in calculations

Material	Mass density [kg/m^3]	Young's modulus [10^{10} N/m^2]	Poission's ratio
Epoxy	1180	0.435	0.368
Rubber	1300	1.175e-5	0.469
Pb	11600	4.08	0.37

The band structure of the proposed system is calculated by the finite element method (FEM), which is implemented by adopting the commercial software, COMSOL Multiphysics. For the mesh elements, the default tetrahedral mesh provided by the software is used and the meshing of the unit cell is shown in Fig. 1c. From the figure, we can see only that one unit cell is taken into consideration, which can be attributed to the periodicity of the structure. The stress-free boundary conditions are applied to the free surfaces, and the periodic boundary conditions according to the Bloch-Floquet theorem are used for the interfaces between the nearest unit cells (Hsu and Wu, 2007; Xiao *et al.*, 2008)

$$u_i(x+a, y+a) = u_i(x,y)\mathrm{e}^{-\mathrm{i}(k_x a + k_y a)} \qquad i = x, y, z \tag{2.1}$$

where u_i denotes the elastic displacement along the x-, y- and z-direction, respectively, when i equals to x, y and z; k_x and k_y are components of the Bloch wave vector limited in the irreducible first Brillouin zone (1BZ), as shown in Fig. 1d.

3. Numerical results and analyses

3.1. Band structures, eigenmodes and transmission power spectrums

In this Section, the band structure of the proposed double panel structure is calculated, as shown in Fig. 2b. The parameters are as follows: $a = 0.1\,\mathrm{m}$, $e = 0.005\,\mathrm{m}$, $r = 0.04\,\mathrm{m}$, $h_1 = 0.01\,\mathrm{m}$, and $h_2 = 0.03\,\mathrm{m}$. To verify the accuracy of the calculated result, the transmission power spectrums of the flexural vibration and the longitudinal vibration in the corresponding finite system are displayed in Figs. 2a and 2c, separately. In this work, the finite double panel structure is made of 8×8 unit cells and the excitation point is picked on one end of the lower plate as well as the response point is picked on the other end of the upper plate, as shown in Fig. 3.

From Fig. 2b, a narrow complete band gap is observed between 72 Hz and 83 Hz. But from Figs. 2a and 2c, the frequency range of the attenuation in the transmission power spectrum is very wide no matter the finite structure is vibrated flexurally or longitudinally, which should have matched well with the frequency range of the band gap. To find more attenuation characteristics, both the response point and the excitation point are picked on the lower plate, and the transmission power spectrum of the longitudinal vibration is shown in Fig. 2d. From it,

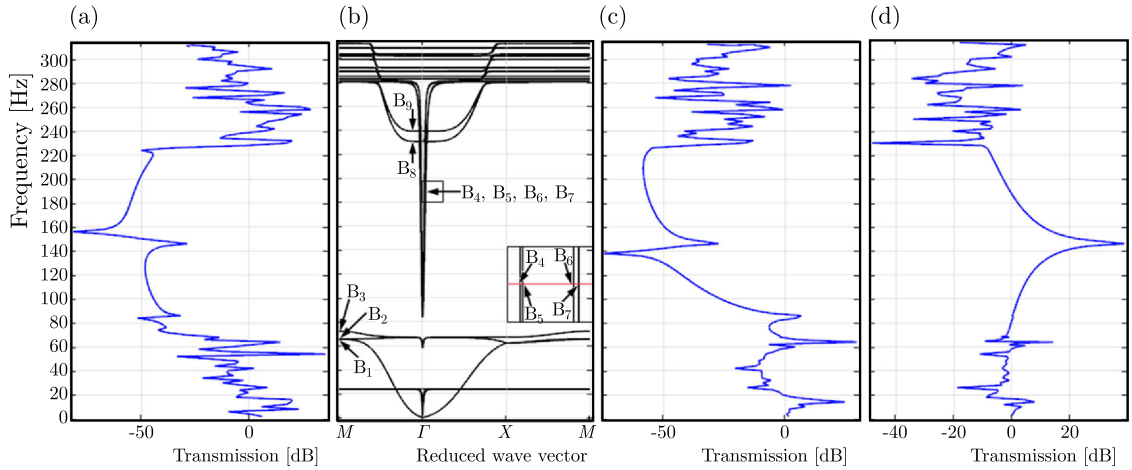

Fig. 2. Band structure of the proposed double panel structure and transmission power spectrums of the corresponding finite 8×8 system: (a) transmission power spectrum of flexural vibration when the response point and excitation point are picked on different plates; (b) band structure; (c) transmission power spectrum of longitudinal vibration when the response point and excitation point are picked on different plates; (d) transmission power spectrum of longitudinal vibration when both the response and excitation point are picked on the same plate

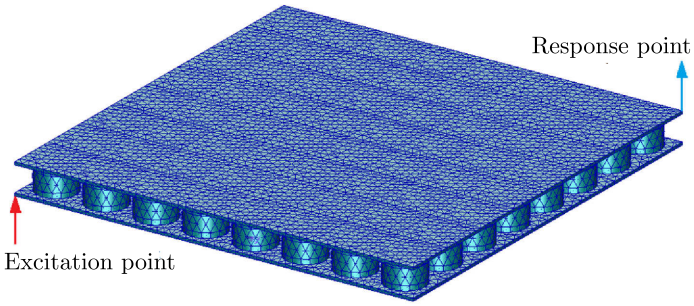

Fig. 3. Meshing of the finite locally resonant double panel structure made of 8×8 unit cells

hardly any frequency range of the attenuation can be observed. To reveal the mechanisms of typical phenomena displayed in transmission power spectrums of the locally resonant double panel structure, the displacement fields of the eigenmodes labeled in Fig. 2b are shown in Fig. 4.

For modes B_3, B_8 and B_9, the dominant vibration translating along the z direction couples with the out-of-plane plate mode of the upper and lower plates. In mode B_3, the vibration energy is concentrated in the pillar with two plates static. Both in modes B_8 and B_9, the middle Pb layer of the pillar acts as a stationary layer. What is opposite, the two base plates achieve dynamic balance in the inverse flexural vibration in mode B_8 while the uniform flexural vibration of the two plates achieve dynamic balance in mode B_9, based on which, modes B_8 and B_9 are called as the symmetric flexural vibration mode and antisymmetric flexural vibration mode, respectively. As a result of the coupling, a partial flexural vibration band gap between B_3 and B_8 with a frequency interval 72 Hz-230 Hz is opened, which is why the big attenuation exists in the transmission power spectrum of the flexural vibration, as shown in Fig. 2a.

For modes B_1 and B_2, the dominant vibration rotating in the xy plane couples with the out-of-plane shear deformation of the upper and lower plates. Both modes B_1 and B_2 concentrate the vibration energy in the pillar with the two stationary plates. As for modes B_4-B_7, they can be treated as the result of the coupling between the dominant vibration translating in the xy plane and the in-plane shear deformation of the upper and lower plates. In all the four modes, the middle Pb layer of the pillar keeps stationary. Meanwhile, the uniform longitudinal

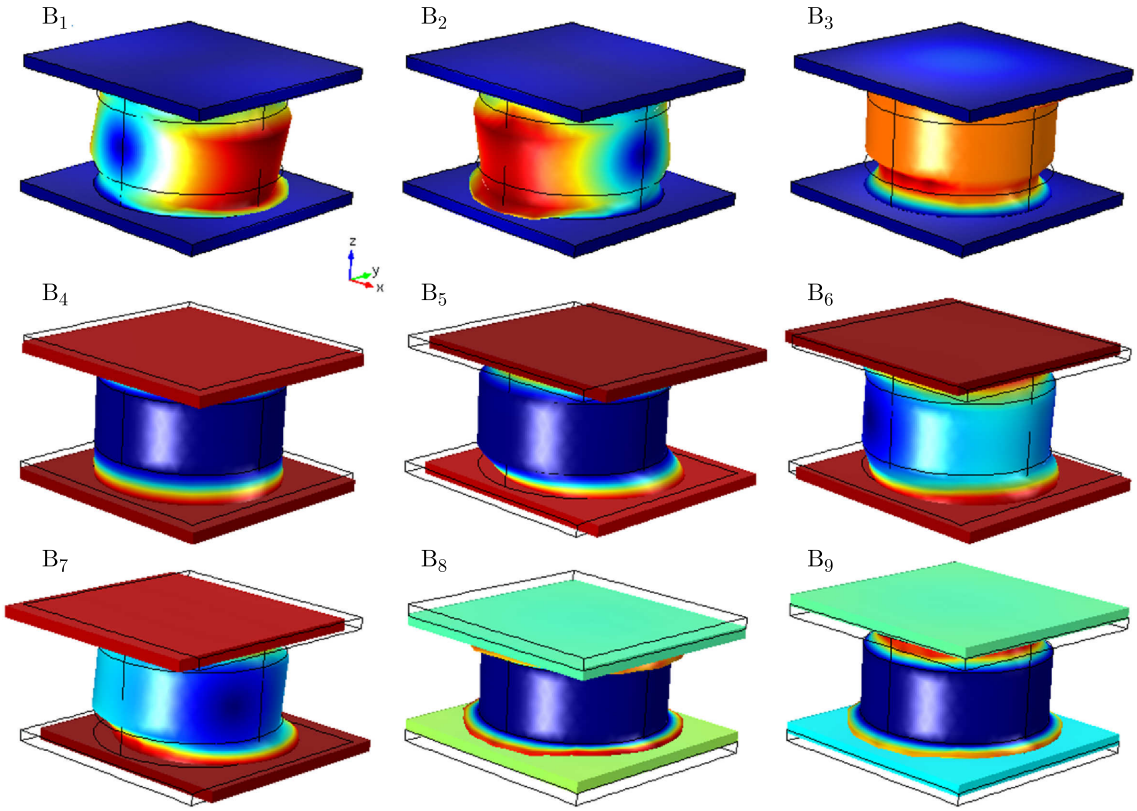

Fig. 4. The displacement fields of eigenmodes labeled in Fig. 2b

vibration of the lower and upper plates achieve dynamic balance in mode B_4 and B_5 while the two plates achieve dynamic balance in the inverse longitudinal vibration in mode B_6 and B_7. Similarly, modes B_4-B_5 and modes B_6-B_7 are called as the antisymmetric longitudinal vibration mode and symmetric longitudinal vibration mode, respectively. As a result of the couplings, a partial longitudinal vibration band gap with a frequency interval 66 Hz-83 Hz is opened. The corresponding attenuations existing in the transmission power spectrums of the longitudinal vibration shown in Figs. 2c and 2d are not obvious, which is consistent with the phenomenon described in (Xiao *et al.*, 2008).

What should be noted is that the vibration of the upper plate is weakened because the vibration phases of the upper plate in the antisymmetric longitudinal vibration mode B_4 and the symmetric longitudinal vibration mode B_6 are inverse, as well as in B_5 and B_7. Based on this, the big attenuation displayed in the transmission spectrum of the longitudinal vibration shown in Fig. 2c can be understood. Meanwhile, the attenuation is absent in Fig. 2d because the lower plate vibrates strongly with the uniform phase. To further illustrate the attenuation characteristic, Fig. 5 shows a view of the vibration mode of the frequency located inside the frequency range of the attenuation. The calculation model is shown in Fig. 3. Here, the displacement excitation along three directions is imposed on the excitation point and the frequency is chosen as $f = 140$ Hz. From Fig. 5, when both flexural and longitudinal excitations are imposed on the lower plate, none of the flexural and longitudinal vibrations can be propagated along the upper plate while only the longitudinal vibration can be propagated along the lower plate. In consequence, if the vibration source and the response area are on different sides of the double panel structure, the band gap with the starting frequency (higher frequency between B_2 and B_3) and cutoff frequency B_8 can be regarded as complete with the wide frequency range of attenuation in both flexural and longitudinal vibrations of the corresponding finite structure.

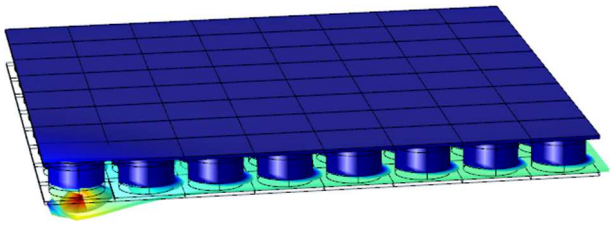

Fig. 5. The vibration mode of the frequency located inside the frequency range of attenuation ($f = 140\,\mathrm{Hz}$)

3.2. Comparison of double panel and single plate

When the upper plate and the upper rubber layer of the pillar are taken away in Fig. 1b, the unit cell of the locally resonant single plate is formed. The band structure of the single plate is shown in Fig. 6a, where the parameters are same as those in the example shown in Fig. 2. To ease the comparison, the band structure of the locally resonant double panel, which is been shown in Fig. 2b, is replotted in Fig. 6b. In addition, the displacement fields of the eigenmodes labeled in Fig. 6a are shown in Fig. 7.

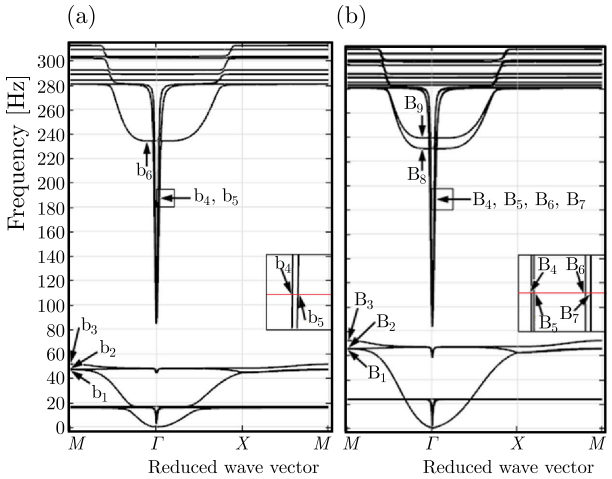

Fig. 6. Band structures of (a) the locally resonant single plate and (b) the locally resonant double panel with the same parameters

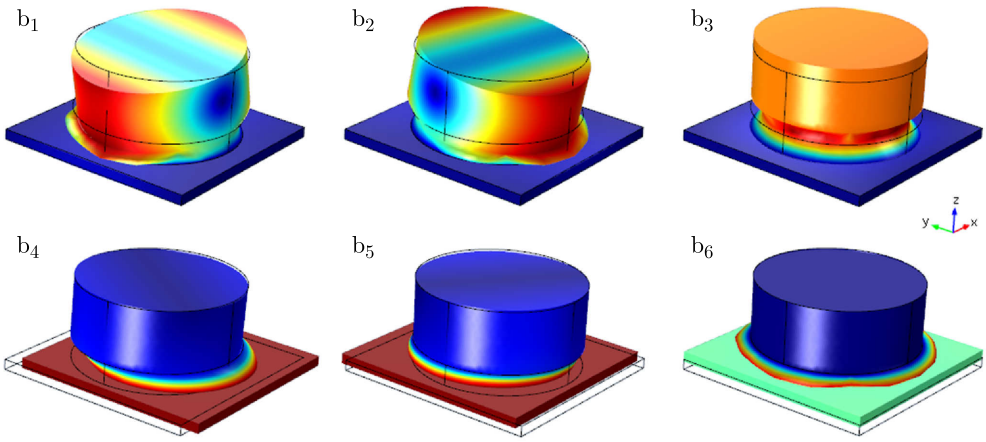

Fig. 7. The displacement fields of eigenmodes labeled in Fig. 6a

Similarly, the coupling between the dominant vibration translating along the z direction and the out-of-plane plate mode of the base plate as shown in modes b_3 and b_6 opens a partial flexural vibration band gap. Meanwhile, both the coupling between the dominant vibration rotating in the xy plane and the out-of-plane shear deformation of base plate as shown in modes b_1 and b_2 and the coupling between the dominant vibration translating in the xy plane and the in-plane shear deformation of the base plate as shown in modes b_5 open a partial longitudinal vibration band gap. As a result, a narrow complete band gap is opened in both flexural and longitudinal vibrations.

For modes B_1-B_3 and b_1-b_3, the base plates in all of them remain still and the dominant vibrations displayed in B_1 and b_1, dominant vibrations displayed in B_2 and b_2 as well as the dominant vibrations displayed in B_3 and b_3 are consistent, respectively. Here, the mass-spring models as shown in Fig. 8 are applied to help one to understand the vibration modes, which (a) and (b) with eigen frequencies $\sqrt{k/m}$ and $\sqrt{2k/m}$ are regarded as simplified models of the vibrations in modes b_1-b_3 and B_1-B_3, respectively. According to such an analysis, the frequencies of modes B_1-B_3 should be $\sqrt{2}$ times larger than those of modes b_1-b_3. From Fig. 6, the frequencies of modes B_1-B_3 are 65.3 Hz, 65.6 Hz and 72 Hz, and the frequencies of modes b_1-b_3 are 46.9 Hz, 47.2 Hz and 51 Hz, which matches very well with $f_{B_1-B_3} = \sqrt{2} f_{b_1-b_3}$.

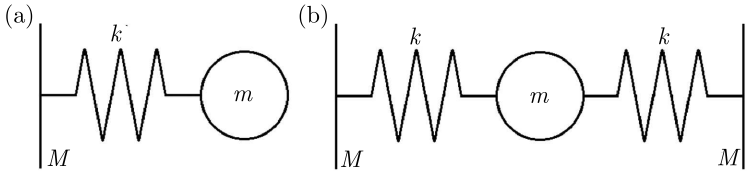

Fig. 8. The simplified mass-spring models applied to help understanding the vibration modes in (a) the single plate and (b) double panel

For modes B_4-B_9 and b_4-b_6, the middle Pb layer of the pillar in all of them stays stationary and the vibration modes displayed in B_4, B_6 and b_4, vibration modes displayed in B_5, B_7 and b_5 as well as vibration modes displayed in B_8, B_9 and b_6 are consistent, respectively. For each set of the corresponding vibration modes, the lower plate vibrates in the same direction as shown in the displacement fields. What should be noted is that the two vibration modes of the double panel are corresponding to each vibration mode of the single plate, which can be attributed to the effect of the upper plate. Besides, the vibration directions of the upper plate in the two different vibration modes of the double panel are opposite. Similarly, the mass-spring models shown in Fig. 8 can also be used to help understanding the vibration modes. Here, the mass m is static and both the vibrations of the two base plates M shown in Fig. 8b can be treated as vibration of the single plate shown in Fig. 8a. Therefore, both the eigenfrequencies of the two models are the same $\sqrt{k/M}$. From Fig. 6, the highest frequencies of the bands traveling modes B_4-B_9 are 280 Hz, 280 Hz, 281 Hz, 281 Hz, 282 Hz, 285 Hz and the highest frequencies of the bands traveling modes b_4-b_6 are 281 Hz, 281 Hz and 284 Hz, which matches quite well with the analysis above. But in the low frequency range of the bands, traveling modes B_4-B_9, the middle Pb layer in the pillar cannot remain absolute still like in the high frequency range. The vibration amplitudes of the upper and lower plates have slight differences and the two vibration modes in the double panel corresponding to that of the single plate are not entirely same as shown in Fig. 4, so the bands traveling B_4-B_5, B_6-B_7 and B_8-B_9 are all divided unlike in the high frequency range, which can be understood as the division of the bands traveling b_4, b_5 and b_6 in the single plate, respectively.

In general, the band structures of the double panel and the single plate have much in common, and the overall trends between them displayed in Fig. 6 are similar. In addition, some pairs of the bands in the double panel structure can be treated as the division of the corresponding bands in the single plate. But the particular property displayed in the band structure of the

double panel that a wide complete band gap is opened when the excitation and response areas are on different sides of the structure is incomparable.

3.3. Influence of parameters on the band gap

As is well known, the vibration source and the receiver are on the opposite sides of the double panel commonly. Thus, the band gap formed by B_2, B_3 and B_8 is considered and investigated below. To get the band gap with a low starting frequency and a wide band width, some geometrical parameters are picked to analyze the influences on the band gap. Here, the height of the rubber layer in the pillar h_1, height of the Pb layer in the pillar h_2, radius of the pillar r, thickness of the base plate e and the lattice constant a are chosen as the influencing parameters. During the study, the rest parameters are same as those in the example shown in Fig. 2a while considering the influence of one parameter on the starting frequency f_s (B_2 or B_3), cutoff frequency f_c (B_8) and band width f_w.

Figure 9 shows the influence of height of the rubber layer h_1 on f_2, f_3, f_8 and f_w. In the figure, f_w equals to the difference between f_8 and f_3 as f_2 is always located under f_3. In addition, both f_3 and f_8 decrease with an increase in h_1, which can be understood by the model shown in Fig. 8b. In the model, the rubber layers are simplified as springs and f_3 and f_8 can be described by $\sqrt{2k/m}$ and $\sqrt{k/M}$ qualitatively. Because the equivalent spring stiffness k decreases with an increase in h_1, f_3 and f_8 decrease with an increase in height of the rubber layer. In addition, the equivalent mass of the Pb layer m is larger than the equivalent mass of the base plate M obviously, so the slope of f_3 is smaller than that of f_8 from $\sqrt{2k/m}$ and $\sqrt{k/M}$ as shown in Fig. 9, which leads f_w to decrease with an increase in h_1 as shown in Fig. 9.

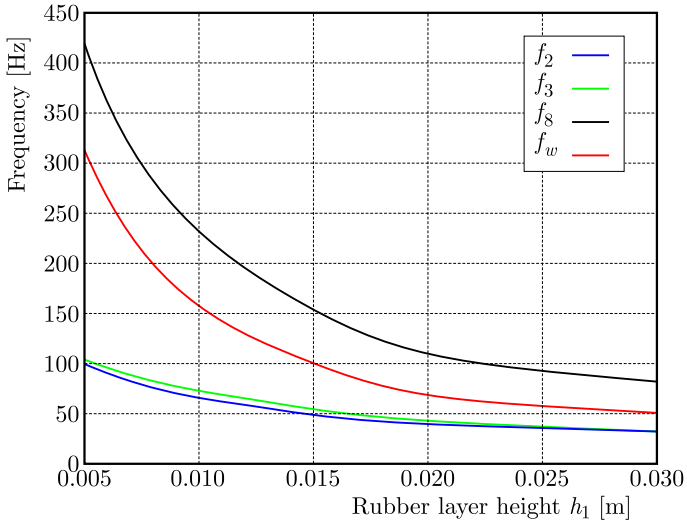

Fig. 9. The influence of the height of the rubber layer in the pillar h_1 on f_2, f_3, f_8 and f_w

Figure 10 shows the influence of the height of the Pb layer h_2 on f_2, f_3, f_8 and f_w. In the figure, f_w also equals to the difference between f_8 and f_3. Moreover, both f_2 and f_3 decrease with an increase in h_2 because the equivalent mass of the Pb layer m in the simplified model shown in Fig. 8b is proportional to h_2. f_8 keeps nearly constant because the Pb layer is static in the vibration mode shown in Fig. 4. The variation trends of f_3 and f_8 lead to an increase in f_w with an increase in h_2 as shown in the figure.

Figure 11 shows the influence of the radius of the pillar r on f_2, f_3, f_8 and f_w. In the figure, f_w is obtained by the difference between f_8 and f_3 as f_2 is always under f_3. Both f_2 and f_3 increase slowly with an increase in r, which can be attributed to an increase in the equivalent spring stiffness k and the equivalent mass m with an increase in r, and the larger slope of k than

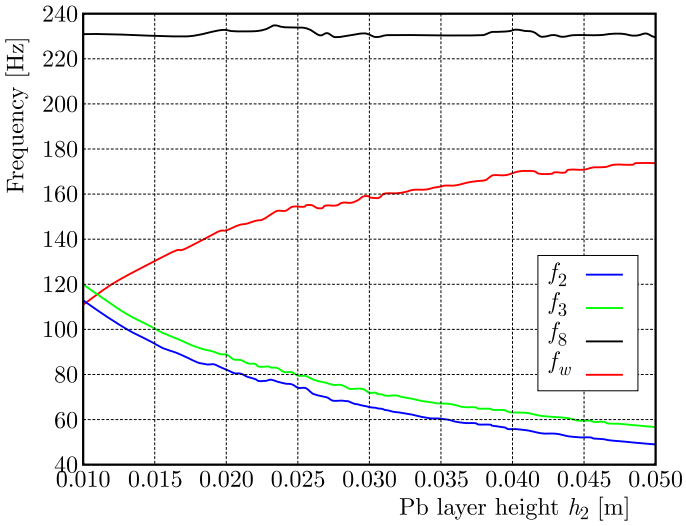

Fig. 10. The influences of the height of the Pb layer in the pillar h_2 on f_2, f_3, f_8 and f_w

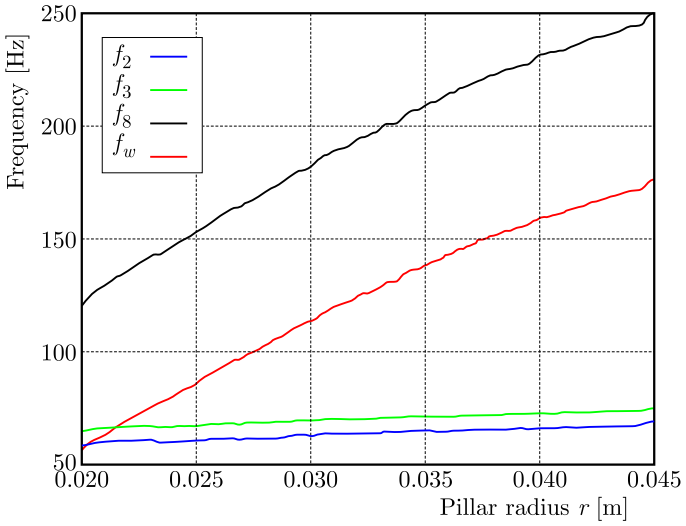

Fig. 11. The influences of the radius of the pillar r on f_2, f_3, f_8 and f_w

that of m. Besides, f_8 increases rapidly with an increase in r because the Pb layer is static here and only an increase in k makes the slope of f_8 large. Hence, the rapid increase of f_8 and slow increase of f_3 lead f_w to increase with an increase in r.

Figure 12 shows the influence of the thickness of the base plates e on f_2, f_3, f_8 and f_w. f_w is obtained by the difference between f_8 and the maximum of f_2 and f_3. From the figure, f_2 is larger when e is less than $3.42 \cdot 10^{-3}$ m and f_3 is larger when e is greater than $3.42 \cdot 10^{-3}$ m. Both f_2 and f_3 increase with an increase in e, which can be understood well with the help of Fig. 13. Figure 13 shows the displacement fields of modes B_2 and B_3 when e takes the value of 0.003 m and 0.007 m, respectively. From the figure, the base plates are vibrated but not absolutely static, and the vibration mode of the base plate is more easily displayed when e equals to 0.003 m because of the smaller stiffness. Hence, the equivalent spring stiffness k in the simplified model shown in Fig. 8b can be treated as a combined effect of both the base plates and the rubber layer in the pillar. Because the stiffness of the base plate increases with an increase in e, the equivalent spring stiffness k increases, which results in an increase in f_2 and f_3. In addition, f_8 decreases with an increase in e because the equivalent mass of the base plate M increases with an increase in e. As a result, the decrease of f_8 and the increase of f_2 and f_3 lead f_w to decrease with an increase in e.

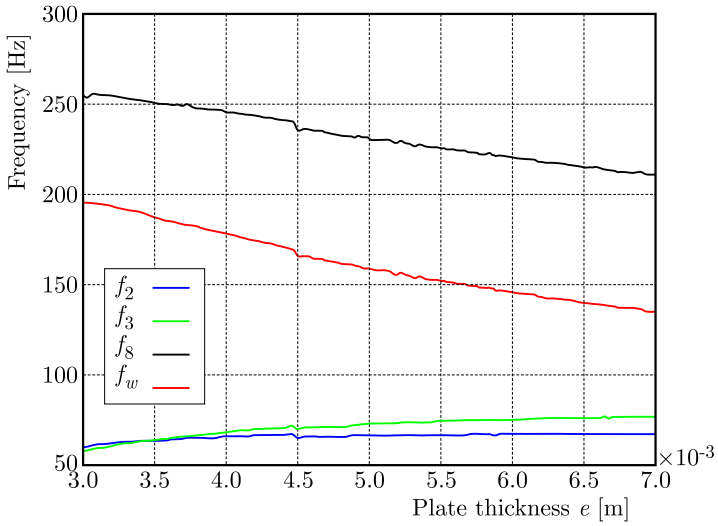

Fig. 12. The influences of the thickness of the base plates e on f_2, f_3, f_8 and f_w

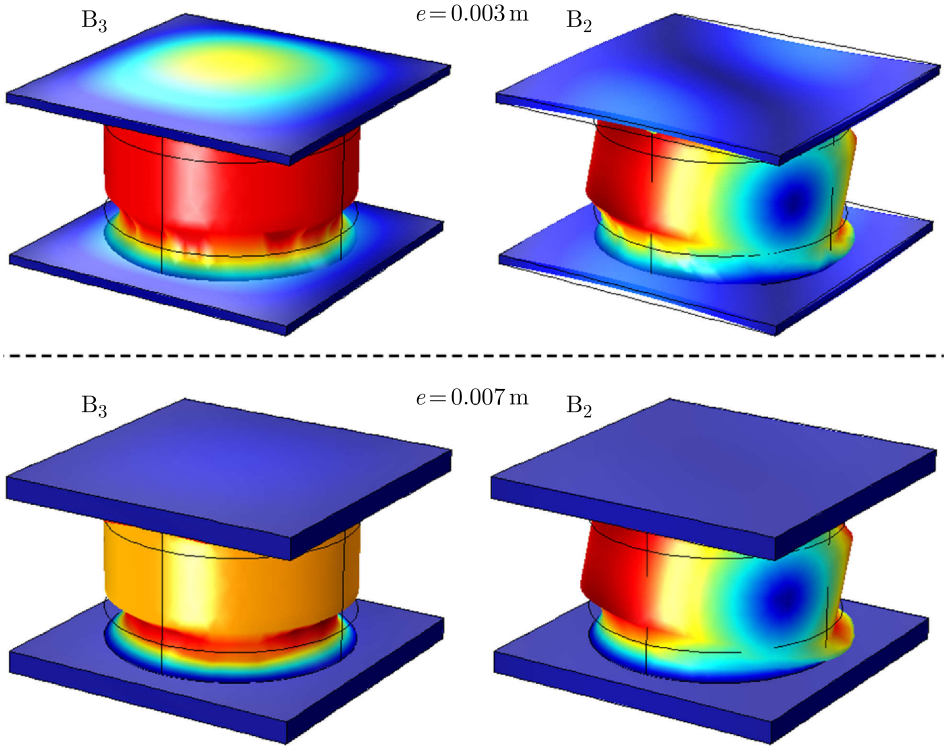

Fig. 13. The displacement fields of modes B_2 and B_3 when e takes the value of 0.003 m and 0.007 m, respectively

Figure 14 shows the influence of the lattice constant a on f_2, f_3, f_8 and f_w. f_w is obtained by the difference between f_8 and the maximum of f_2 and f_3. From the figure, f_3 is larger when a is less than 0.132 m and f_2 is larger when a is greater than 0.132 m. f_2 keeps almost constant and f_3 decreases with an increase in a, which can also be understood with the help of the displacement fields of modes B_2 and B_3 when a takes the value of 0.085 m and 0.2 m, respectively, as shown in Fig. 15. From the figure, what can be concluded is that the stiffness of the base plate decreases with an increase in a. Besides, the variation of the stiffness of the base plate in mode B_2 is not big by comparing the displacement fields of modes B_2 when a equals to 0.085 m and 0.2 m separately. Hence, the variation trends of f_2 and f_3 are explained. In addition,

f_8 decreases with an increase in a because the equivalent mass of the base plate M increases with an increase in e. As a result, the rapid decrease of f_8 and the slow decrease of f_2 and f_3 shown in Fig. 14 lead f_w to decrease with an increase in a.

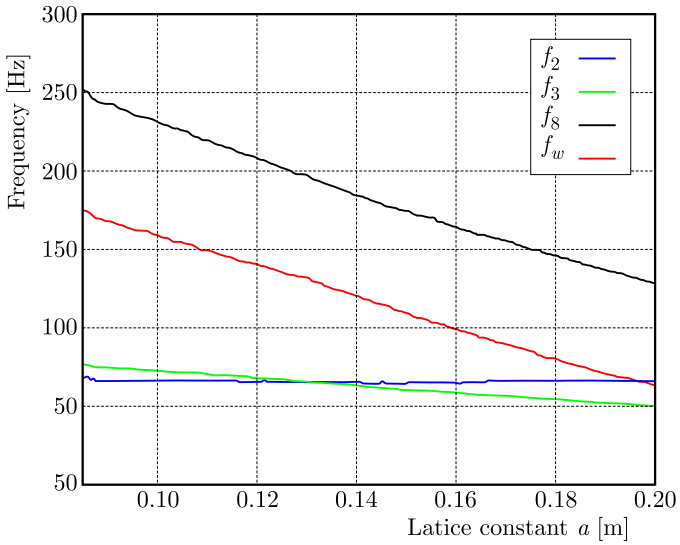

Fig. 14. The influences of the lattice constant a on f_2, f_3, f_8 and f_w

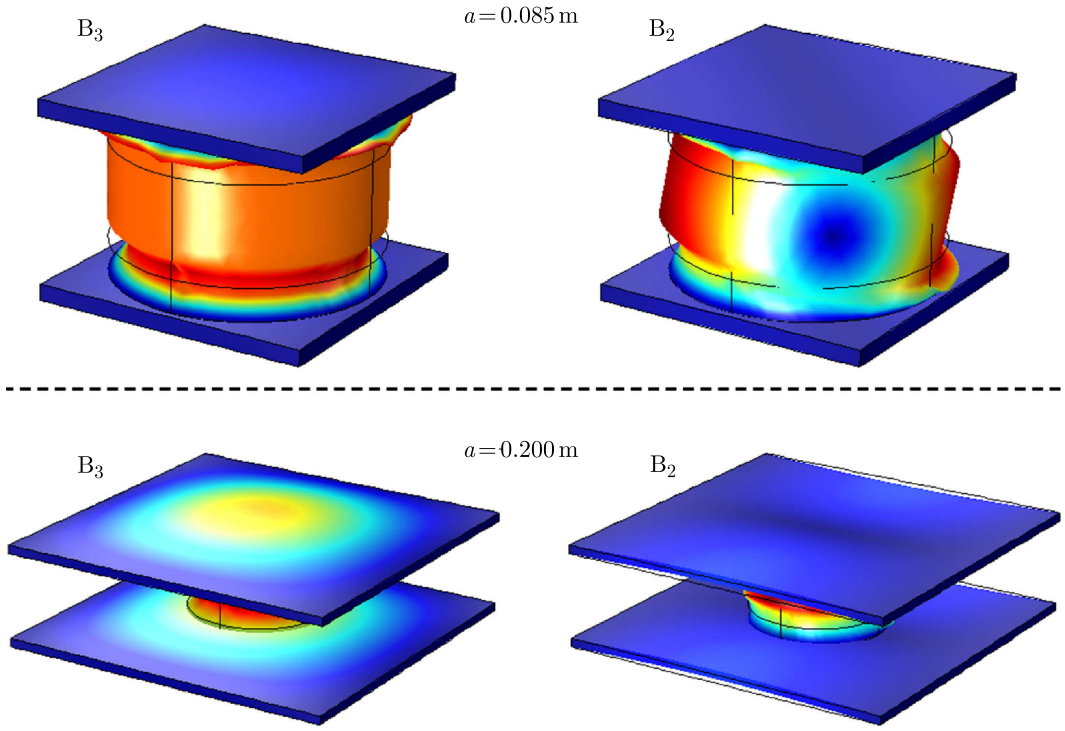

Fig. 15. The displacement fields of modes B_2 and B_3 when a takes the value of 0.08 5m and 0.2 m, respectively

4. Conclusions

In this paper, we propose a three-component pillared phononic crystal double panel structure and study the bandgap properties of the structure by applying the finite element method. A complete band gap with a low starting frequency and a wide band width is opened according

to the band structure and the transmission power spectrums when the vibration source and the receiver are on different sides of the structure, and the formation mechanisms of the band gap is revealed according to the displacement fields of the eigenmodes. By comparing the band structure of the double panel and that of the single plate, the bands of the double panel can be treated as the division of the corresponding bands of the single plate by the effect of the upper and lower plates. Besides, the influence of height of the rubber layer in the pillar, height of the Pb layer in the pillar, radius of the pillar, thickness of the base plate and the lattice constant on the band gap are studied and understood. In general, by increasing the height of the Pb layer or decreasing the thickness of the base plate, the starting frequency and band width of the band gap gets lower and wider. By decreasing the height of the rubber layer, the band width of the band gap gets wider, but increases the starting frequency. By increasing the radius of the pillar or decreasing the lattice constant, the band width of the band gap also gets wider, and the change in the starting frequency is not big. All the results of the investigation provide a new idea for restraining the vibration and reducing the noise of the low frequency region in the double panel structure.

Acknowledgments

This research has been supported by the National Natural Science Foundation of China through Grant No. 11172131, the Research Fund of State Key Laboratory of Mechanics and Control of Mechanical Structures (Nanjing University of Aeronautics and Astronautics) (Grant No. 0515G01) and the Foundation Research Project of Jiangsu Province (The Natural Science Fund No. 2015003-01).

References

1. Carneal J.P., Fuller C.R., 2004, An analytical and experimental investigation of active structural acoustic control of noise transmission through double panel systems, *Journal of Sound and Vibration*, **272**, 3-5, 749-771
2. Goffaux C., Sánchez-Dehesa J., Lambin P., 2004, Comparison of the sound attenuation efficiency of locally resonant materials and elastic band-gap structures, *Physical Review B*, **70**, 18, 184302
3. Hirsekorn M., Delsanto P.P., Batra N.K., Matic P., 2004, Modelling and simulation of acoustic wave propagation in locally resonant sonic materials, *Ultrasonics*, **42**, 1, 231-235
4. Ho K.M., Cheng C.K., Yang Z., Zhang X.X., Sheng P., 2003, Broadband locally resonant sonic shields, *Applied Physics Letters*, **83**, 26, 5566-5568
5. Hsu J.C., 2011, Local resonances-induced low-frequency band gaps in two-dimensional phononic crystal slabs with periodic stepped resonators, *Journal of Physics D, Applied Physics*, **44**, 5, 55401-55409
6. Hsu J.C., Wu T.T., 2007, Lamb waves in binary locally resonant phononic plates with two-dimensional lattices, *Applied Physics Letters*, **90**, 20, 201904-201904-3
7. Li S., Chen T., Wang X., Li Y., Chen W., 2016, Expansion of lower-frequency locally resonant band gaps using a double-sided stubbed composite phononic crystals plate with composite stubs, *Physics Letters A*, **380**, 25-26, 2167-2172
8. Li Y., Chen T., Wang X., Xi Y., Liang Q., 2015, Enlargement of locally resonant sonic band gap by using composite plate-type acoustic metamaterial, *Physics Letters A*, **379**, 5, 412-416
9. Liu Z., Zhang X., Mao Y., Zhu Y., Yang Z., Chan C.T., Sheng P., 2000, Locally resonant sonic materials, *Science*, **289**, 5485, 1734-1736
10. Ma J., Hou Z., Assouar B.M., 2014, Opening a large full phononic band gap in thin elastic plate with resonant units, *Journal of Applied Physics*, **115**, 9, 093508-093508-5

11. Oudich M., Li Y., Assouar B.M., Hou Z., 2010, A sonic band gap based on the locally resonant phononic plates with stubs, *New Journal of Physics*, **12**, 2, 201-206

12. Oudich M., Senesi M., Assouar M.B., Ruzenne M., Sun J.-H., Vincent B., Hou Z., Wu T.-T., 2011, Experimental evidence of locally resonant sonic band gap in two-dimensional phononic stubbed plates, *Physical Review B*, **84**, 16, 667-673

13. Pietrzko S.J., Mao Q., 2008, New results in active and passive control of sound transmission through double wall structures, *Aerospace Science and Technology*, **12**, 1, 42-53

14. Qian D., Shi Z., 2016, Bandgap properties in locally resonant phononic crystal double panel structures with periodically attached spring-mass resonators, *Physics Letters A*, **380**, 41, 3319-3325

15. Qian D„ Shi Z., 2017, Using PWE/FE method to calculate the band structures of the semi-infinite beam-like PCs: Periodic in z-direction and finite in x-y plane, *Physics Letters A*, **381**, 17, 1516-1524

16. Sainidou R., Stefanou N., Psarobas I.E., Modinos A., 2002, Scattering of elastic waves by a periodic monolayer of spheres, *Physical Review B*, **66**, 2, 024303

17. Sigalas M.M., Economou E.N., 1992, Elastic and acoustic wave band structure, *Journal of Sound and Vibration*, **158**, 2, 377-382

18. Vasseur J.O., Deymier P.A., Khelif A., Lambin Ph., Djafari-Rouhani B., Akjouj A., Dobrzynski L., Fettouhi N., Zemmouri J., 2002, Phononic crystal with low filling fraction and absolute acoustic band gap in the audible frequency range: A theoretical and experimental study, *Physical Review E*, **65**, 5, 056608

19. Xiao W., Zeng G.W., Cheng Y.S., 2008, Flexural vibration band gaps in a thin plate containing a periodic array of hemmed discs, *Applied Acoustics*, **69**, 3, 255-261

20. Xiao Y., Wen J., Wen X., 2012, Flexural wave band gaps in locally resonant thin plates with periodically attached spring-mass resonators, *Journal of Physics D, Applied Physics*, **45**, 19, 195401-195412

21. Zhang X., Liu Z., Liu Y., Wu F., 2003, Elastic wave band gaps for three-dimensional phononic crystals with two structural units, *Physics Letters A*, **313**, 5, 455-460

22. Zhao H.J., Guo H.W., Gao M.X., Liu R.-Q., Deng Z.-Q., 2016, Vibration band gaps in double-vibrator pillared phononic crystal plate, *Journal of Applied Physics*, **119**, 1, 377

Manuscript received February 14, 2017; accepted for print April 18, 2017

JOURNAL OF THEORETICAL AND APPLIED MECHANICS
55, 4, pp. 1181-1192, Warsaw 2017
DOI: 10.15632/jtam-pl.55.4.1181

FRICTIONAL CONTACT OF TWO SOLIDS WITH A PERIODICALLY GROOVED SURFACE IN THE PRESENCE OF AN IDEAL GAS IN INTERFACE GAPS

Nataliya Malanchuk, Bogdan Slobodyan, Rostyslav Martynyak
Pidstryhach Institute for Applied Problems of Mechanics and Mathematics, NASU, Lviv, Ukraine
e-mail: labmtd@iapmm.lviv.ua

The frictional contact between two solids, one of which having a periodically grooved surface, under the action of normal and shear load is investigated. The interface between the contacting solids consists of a periodic array of gas-filled gaps and a periodic array of contact regions, where stick-slip contact occurs. The corresponding plane contact problem is reduced to a set of two singular integral equations. A solution to the contact problem is obtained for a certain shape of the grooves. The analysis of dependences of contact parameters of the solids on the applied load and gas pressure is carried out.

Keywords: stick-slip contact, periodically grooved surface, gas pressure

1. Introduction

The surface microtexturing, which consists in forming regularly (periodically) arranged grooves of the same shape on a surface of a solid, is one way of improving performance of joints. A regular surface texture may be generated by several methods (Etsion, 2004; Greco *et al.*, 2009; Nakano *et al.*, 2007; Schreck and Zum Gahr, 2005; Stepien, 2011): laser texturing, precise diamond turning, rolling, embossing, etching, vibrorolling, abrasive jet machining, micro electrical discharge machining, grinding. When periodically grooved surfaces are placed in contact, periodically arranged intercontact gaps occur at the interface. These gaps are usually filled with some substance (a natural substance (gas, liquid), a substance used for functional purposes (grease, coolant) or a biological fluid (synovia)). The effect of the interstitial medium filling the gaps of different nature on mechanical behavior of bodies was investigated by Kit *et al.* (2009), Machyshyn and Nagórko (2003), Martynyak and Slobodyan (2009), Evtushenko and Sulim (1981), Kaczyński and Monastyrskyy (2004), Monastyrskyy and Kaczyński (2007).

The contact between microtextured surfaces is usually realized not only under normal load, but also under shear load. This shear load may cause partial slip of surfaces, and the filler of the gaps may have some effect on propagation of the slip zones. However, the existing studies of stick-slip contact (Ciavarella, 1998a,b; Chang *et al.*, 1984; Block and Keer, 2008; Hills *et al.*, 2016; Goryacheva and Martynyak, 2014) do not consider this effect.

When contacting solids are subjected to heating, thermal deformations can also cause partial slip of surfaces. The thermally induced partial slip of a rigid flat-ended punch and an elastic half-space with different temperatures was investigated in (Pauk, 2007). The thermoelastic stick-slip contact problem for two semi-infinite solids in the presence of a single thermoinsulated gap at the interface was studied in (Malanchuk *et al.*, 2011). The effect of thermal conductivity of a medium filling the interface gaps on partial slip between a textured half-space and a flat half-space, which was caused by an imposed heat flow, was studied in (Chumak *et al.*, 2014).

The goal of this research is to investigate partial slip between a half-space with a periodically grooved surface and a flat half-space, which is caused by the applied shear load, taking into

account pressure of an ideal gas in the interface gaps. The stick-slip contact between a surface with a single groove and a flat surface in the presence of an ideal gas in the interface gap was previously studied in (Slobodyan *et al.*, 2014). The model of partial slip between a periodically grooved surface and a flat one was presented in (Slobodyan *et al.*, 2016). However, that model did not take into account the effect of the interstitial medium.

2. Statement of the problem

Consider the contact between two isotropic elastic half-spaces made of an identical material under plane strain conditions. The upper solid D_2 has a flat surface. The surface of the lower solid D_1 has an array of grooves of width $2b$ spaced with the period d ($d > 2b$). The shape of each groove is described by a smooth function $r(x)$ ($r(x) \ll b$, $r'(x) \ll 1$, $r(\pm b) = 0$, $r'(\pm b) = 0$). The solids are successively loaded by normal and shear loads. At the first stage of loading, the solids are pressed together by a monotonically increasing nominal pressure $p_n = P/d$ applied at infinity, where P denotes the normal force per one period. The compressive load is assumed to vary quasistatically. Due to the regular surface texture of the lower solid, the interface consists of a periodic array of gaps and a periodic array of contacts. The width $2a$ ($a < b$) and height $h(x)$ of the interface gaps are unknown and decrease monotonically with an increase of the nominal pressure. The gaps are filled with an equal amount of the ideal gas, whose pressure P_1 changes during the loading. The relation between the gas pressure P_l and gas volume $V = l\int_{-a}^{a} h(x)\,dx$ is described by the ideal gas law

$$P_1 V = \frac{m_1}{\mu} RT \tag{2.1}$$

where m_1 is mass of the gas, μ is molar mass of the gas, T is gas temperature, R is the ideal gas constant, $R = 8.3145\,\mathrm{JK^{-1}mol^{-1}}$ and $l = 1\,\mathrm{m}$.

The shear displacements of the contacting surfaces due to the normal load are the same because of identity of the materials. The shear stresses do not, therefore, arise at the interface and the slip of the solids does not occur at the first loading phase. At the second loading phase, the normal load is held fixed and the bodies are subjected to the action of the nominal shear loading $s_n = S/d$ applied at infinity (Fig. 1). Here, S denotes the shear force per one period. According to the Coulomb-Amontons law, the surfaces of the bodies are in stick until the contact shear stress τ_{xy} is less than the contact pressure $|\sigma_y|$ multiplied by the friction coefficient f ($\tau_{xy} < f|\sigma_y|$). The applied shear force leads to the frictional slip of the contacting surfaces in the regions $(-c + kd, -a + kd)$, $(a + kd, c + kd)$, which, due to symmetry of the problem with respect to y-axis, are located symmetrically relative to the origin of each gap, $k = 0, \pm1, \pm2, \ldots$. In the slip zones, $\tau_{xy} = f|\sigma_y|$. The direction of slip is indicated by arrows in Fig. 1.

Denote $I_k^i = [-i + kd, i + kd]$, $J_k^i = [-d/2 + kd, -i + kd] \cup [i + kd, d/2 + kd]$, $i = a, b, c$, $Y_k^{c,a} = [-c + kd, -a + kd] \cup [a + kd, c + kd]$, hereinafter $k = 0, \pm1, \pm2, \ldots$.

The boundary conditions are:

— at the gaps ($x \in I_k^a$)

$$\begin{aligned} &\sigma_y^-(x,0) = \sigma_y^+(x,0) \qquad && \sigma_y^-(x,0) = -P_1 \\ &\tau_{xy}^-(x,0) = \tau_{xy}^+(x,0) && \tau_{xy}^-(x,0) = 0 \end{aligned} \tag{2.2}$$

— in the slip zones ($x \in Y_k^{c,a}$)

$$\begin{aligned} &\sigma_y^-(x,0) = \sigma_y^+(x,0) \qquad && \tau_{xy}^-(x,0) = \tau_{xy}^+(x,0) \qquad && v^-(x,0) - v^+(x,0) = -r(x) \\ &\tau_{xy}^-(x,0) = -f\sigma_y^-(x,0) \end{aligned} \tag{2.3}$$

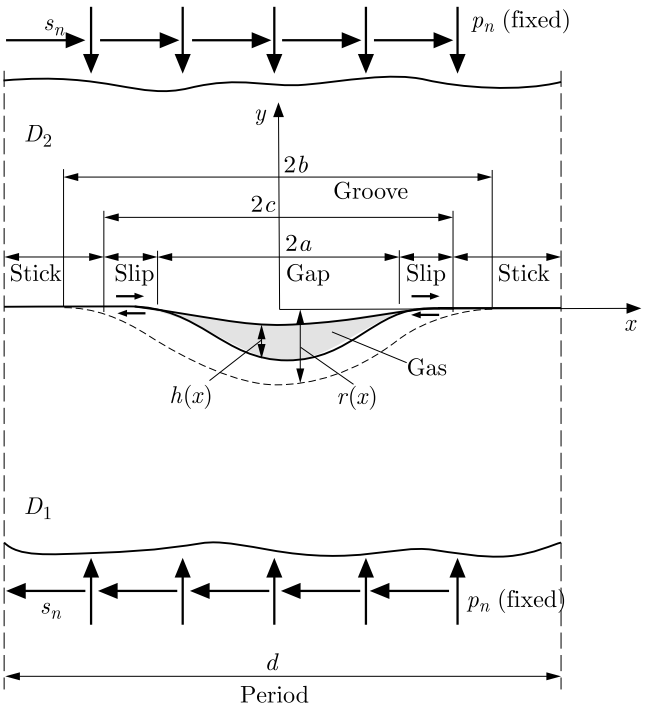

Fig. 1. Contact of the solids (within one period)

— in the stick zones ($x \in J_k^c$)

$$\sigma_y^-(x,0) = \sigma_y^+(x,0) \qquad \tau_{xy}^-(x,0) = \tau_{xy}^+(x,0) \qquad v^-(x,0) - v^+(x,0) = -r(x) \tag{2.4}$$

— at infinity

$$\sigma_y(x,\pm\infty) = -p_n \qquad \sigma_x(x,\pm\infty) = 0 \qquad \tau_{xy}(x,\pm\infty) = s_n \tag{2.5}$$

Here, $r(x) = 0$ when $x \in J_k^b$, $\sigma_y(x,y)$, $\sigma_x(x,y)$, $\tau_{xy}(x,y)$ are stress components, $u(x,y)$, $v(x,y)$ are displacement components, superscripts + and − denote the boundary values of the functions on the x-axis in the upper and lower solid, respectively.

Note that because of identity of the contacting materials, the frictional slip does not influence the normal contact stress and width as well as and height of the gaps.

3. Solution to the problem

Let us represent the stresses and displacements in both solids throughout three functions: height of the grooves $r(x)$, height of the gaps $h(x)$, and relative tangential shift of the solids surfaces $U(x) = u^-(x,0) - u^+(x,0)$ (Slobodyan *et al.*, 2014; Muskhelishvili, 1953)

$$\begin{aligned}
&\sigma_x + \sigma_y = 4\mathrm{Re}[\Phi_j(z)] - p_n \\
&\sigma_y - \mathrm{i}\tau_{xy} = \Phi_j(z) - \Phi_j(\overline{z}) + (z-\overline{z})\overline{\Phi_j'(z)} - p_n - \mathrm{i}s_n \\
&2G(u' + \mathrm{i}v') = (3-4\nu)\Phi_j(z) + \Phi_j(\overline{z}) - (z-\overline{z})\overline{\Phi_j'(z)} + \nu p_n + \mathrm{i}s_n \\
&\Phi_1(z) = -\Phi_2(z) = \frac{(-1)^{j+1}G}{4\pi(1-\nu)} \sum_{k=-\infty}^{\infty} \left(\mathrm{i} \int_{-c+kd}^{c+kd} \frac{U'(t)\,dt}{t-z} + \int_{-a+kd}^{a+kd} \frac{h'(t)\,dt}{t-z} + \int_{-b+kd}^{b+kd} \frac{r'(t)\,dt}{t-z} \right) \\
&z \in D_j \qquad j = 1,2
\end{aligned} \tag{3.1}$$

where $U(x) = 0$ when $x \in J_k^c$, $z = x + \mathrm{i}y$, $\mathrm{i} = \sqrt{-1}$, ν is Poisson's ratio, G is the shear modulus.

Representations (3.1) have been constructed so that they satisfy boundary conditions $(2.3)_1$, (2.4) and (2.5). Taking into account the periodicity of the functions $U(x)$, $h(x)$ and $r(x)$ (Schmueser and Comninou, 1979), the complex functions $\Phi_1(z)$, $\Phi_2(z)$ can be rewritten as

$$\begin{aligned}\Phi_1(z) &= \frac{(-1)^{j+1}G}{4d(1-\nu)}\left(\mathrm{i}\int_{-c}^{c} U'(t)\cot\frac{\pi(t-z)}{d}\,dt + \int_{-a}^{a} h'(t)\cot\frac{\pi(t-z)}{d}\,dt\right.\\ &\quad\left.+\int_{-b}^{b} r'(t)\cot\frac{\pi(t-z)}{d}\,dt\right)\\ \Phi_2(z) &= -\Phi_1(z) \qquad z\in D_j \qquad j=1,2\end{aligned} \tag{3.2}$$

The normal and shear stresses at the interface $y=0$ calculated from expressions (3.1), are

$$\begin{aligned}N(x) &= \sigma_y(x,0) = \frac{G}{2d(1-\nu)}\left(\int_{-b}^{b} r'(t)\cot\frac{\pi(t-z)}{d}\,dt + \int_{-a}^{a} h'(t)\cot\frac{\pi(t-z)}{d}\,dt\right) - p_n\\ S(x) &= \tau_{xy}(x,0) = -\frac{G}{2d(1-\nu)}\int_{-c}^{c} U'(t)\cot\frac{\pi(t-z)}{d}\,dt + s_n\end{aligned} \tag{3.3}$$

In order to satisfy boundary condition $(2.2)_1$, we substitute $(3.3)_1$ into $(2.2)_1$, which leads to a singular integral equation

$$\frac{1}{d}\int_{-a}^{a} h'(t)\cot\frac{\pi(t-x)}{d}\,dt = -\frac{1}{d}\int_{-b}^{b} r'(t)\cot\frac{\pi(t-x)}{d}\,dt + \frac{2(1-\nu)}{G}(p_n - P_1) \qquad |x|\leqslant a \tag{3.4}$$

From boundary conditions $(2.2)_2$ and $(2.3)_2$, and expression $(3.3)_2$, we obtain a singular integral equation for the function $U'(x)$

$$\begin{aligned}&\frac{1}{d}\int_{-c}^{c} U'(t)\cot\frac{\pi(t-x)}{d}\,dt = \frac{2(1-\nu)s_n}{G}\\ &+\begin{cases} 0 & x\in I_k^a\\ f\left(\dfrac{1}{d}\displaystyle\int_{-a}^{a} h'(t)\cot\dfrac{\pi(t-x)}{d}\,dt + \dfrac{1}{d}\displaystyle\int_{-b}^{b} r'(t)\cot\dfrac{\pi(t-x)}{d}\,dt\right) & \\ \quad -\dfrac{2(1-\nu)f}{G}(p_n-P_1) & x\in Y_k^{c,a}\end{cases}\end{aligned} \tag{3.5}$$

As a result, we get a set of two singular integral equations with the Hilbert kernel for the functions $h'(x)$ and $U'(x)$.

It is obvious from Eq. (3.5) that the gas pressure P_1 influences the relative tangential shift $U(x)$ of the contacting surfaces.

The functions $h(x)$ and $U(x)$ satisfy the conditions

$$\begin{aligned} h(\pm a) &= 0 \qquad & h'(\pm a) &= 0\\ U(\pm c) &= 0 \qquad & U'(\pm c) &= 0\end{aligned} \tag{3.6}$$

The first condition in $(3.6)_1$ means that the gaps between the solids vanish in the contact regions. The second condition in $(3.6)_1$ represents smooth closure of the gaps at $x=\pm a$ and

ensures that the normal contact stress is bounded at $x = \pm a$. The first condition in $(3.6)_2$ follows from the continuity of shear displacements of the contacting surfaces. The second condition in $(3.6)_2$ ensures that the shear stress is bounded at the edges of the slip zones $x = \pm c$.

By changing variables $\xi = \tan(\pi x/d)$, $\eta = \tan(\pi t/d)$, $\alpha = \tan(\pi a/d)$, $\beta = \tan(\pi b/d)$, $\gamma = \tan(\pi c/d)$, we reduce set (3.4), (3.5) to a set of singular integral equations with the Cauchy kernel

$$\int\limits_{-\alpha}^{\alpha} \frac{h'(\eta)\,d\eta}{\eta-\xi} = -\int\limits_{-\beta}^{\beta} \frac{r'(\eta)\,d\eta}{\eta-\xi} + \frac{2d(1-\nu)}{G(1+\xi^2)}(p_n - P_1) \qquad |\xi| \leqslant \alpha$$

$$\int\limits_{-\gamma}^{\gamma} \frac{U'(\eta)\,d\eta}{\eta-\xi} = \frac{2d(1-\nu)s_n}{G(1+\xi^2)} + \begin{cases} 0 & |\xi| \leqslant \alpha \\ f\left(\displaystyle\int\limits_{-\alpha}^{\alpha} \frac{h'(\eta)\,d\eta}{\eta-\xi} + \int\limits_{-\beta}^{\beta} \frac{r'(\eta)\,d\eta}{\eta-\xi}\right) & \\ \quad - \dfrac{2d(1-\nu)f}{G(1+\xi^2)}(p_n - P_1) & \alpha \leqslant |\xi| \leqslant \gamma \end{cases} \tag{3.7}$$

In the new variables, conditions (3.6) have the form

$$\begin{aligned} &h(\pm\alpha) = 0 \qquad && h'(\pm\alpha) = 0 \\ &U(\pm\gamma) = 0 \qquad && U'(\pm\gamma) = 0 \end{aligned} \tag{3.8}$$

To solve set (3.7), the function $r(x)$, which describes the shape of the grooves, should be specified. We preset it as follows: $r(x) = -r_0\Big(1 - \tan^2(\pi x/d)/\tan^2(\pi b/d)\Big)^{3/2}$, $x \in I_k^b$, where r_0 is the maximum depth of the grooves, and $0 < r_0 \ll b$. In the new variables, the shape of the grooves is $r(\xi) = -r_0(1 - \xi^2/\beta^2)^{3/2}$, $|\xi| < \beta$.

In accordance with the second condition in $(3.8)_1$, we find a solution to Eq. $(3.7)_1$ that is bounded at $\xi = \pm\alpha$. The bounded solution of a singular integral equation with the Cauchy kernel is possible only if the right-hand side of the equation satisfies the consistency condition (Muskhelishvili, 1953) for Eq. $(3.7)_1$

$$\int\limits_{-\alpha}^{\alpha} \Big[\frac{-3r_0\pi}{\beta}\Big(\frac{1}{2} - \frac{\xi^2}{\beta^2}\Big) + \frac{2d(1-\nu)(p_n - P_1)}{G(1+\xi^2)}\Big)\frac{d\xi}{\sqrt{\alpha^2-\xi^2}} = 0 \tag{3.9}$$

Carrying out integrations, Eq. (3.9) reduces to an equation that relates the semi-width α of the gaps to the applied nominal pressure p_n

$$\frac{3r_0\pi}{\beta}\Big(\frac{\alpha^2}{\beta^2} - 1\Big) + \frac{4d(1-\nu)(p_n - P_1)}{G\sqrt{1+\alpha^2}} = 0 \tag{3.10}$$

The bounded solution (Muskhelishvili, 1953) of Eq. $(3.7)_1$ is

$$h'(\xi) = \xi\sqrt{\alpha^2-\xi^2}\Big(-\frac{3r_0}{\beta^3} + \frac{2d(1-\nu)(p_n - P_1)}{\pi G\sqrt{1+\alpha^2}(1+\xi^2)}\Big) \qquad |\xi| \leqslant \alpha \tag{3.11}$$

Integration of Eq. (3.11) from $-\alpha$ to ξ in view of the first condition in $(3.8)_1$ gives the gaps height ($|\xi| \leqslant \alpha$)

$$h(\xi) = r_0\sqrt{\Big(\frac{\alpha^2}{\beta^2} - \frac{\xi^2}{\beta^2}\Big)^3} + \frac{d(1-\nu)(p_n - P_1)}{\pi G}\left(\frac{2\sqrt{\alpha^2-\xi^2}}{\sqrt{1+\alpha^2}} - \ln\left|\frac{\sqrt{1+\alpha^2} + \sqrt{\alpha^2-\xi^2}}{\sqrt{1+\alpha^2} - \sqrt{\alpha^2-\xi^2}}\right|\right) \tag{3.12}$$

Substituting Eq. (3.12) into the formula for gas volume and carrying out integration, ideal gas law (2.1) can be rewritten as

$$P_1\Big[\frac{\pi r_0}{\beta^3}\Big(\sqrt{(1+\alpha^2)^3}-1-\frac{3}{2}\alpha^2\Big)+\frac{d(1-\nu)(p_n-P_1)}{G}\Big(2-\frac{2}{\sqrt{1+\alpha^2}}-\ln(1+\alpha^2)\Big)\Big]=\frac{m_1}{\mu}RT \tag{3.13}$$

Note that the function $h(\xi)$ includes two unknown parameters: the parameter α and gas pressure P_1. For determination of these parameters, we use (3.10) and (3.13). Since Eqs. (3.10) and (3.13) are nonlinear with respect to α and the difference $p_n - P_1$ appears in both equations, the following technique is proposed for solving set (3.10), (3.13):

i) the external load p_n is assumed to be unknown, while the gaps width α is set from the range $0 < \alpha \leqslant \beta$;

ii) the difference between the external load p_n and the gas pressure P_1 is then determined from Eq. (3.10) as

$$p_n - P_1 = \frac{3\pi G r_0\sqrt{1+\alpha^2}}{4(1-\nu)\beta^3 d}(\beta^2-\alpha^2) \tag{3.14}$$

the gas pressure P_1 is then obtained from Eq. (3.13) after substituting (3.14) for $p_n - P_1$

$$P_1 = \frac{\beta^3 m_1 RT}{2\pi\mu r_0}\left((\sqrt{1+\alpha^2}-1)(3\beta^2+2)-\frac{\sqrt{\alpha^2+1}}{2}[2\alpha^2+3(\beta^2-\alpha^2)\ln(1+\alpha^2)]\right)^{-1}$$

iii) once the gas pressure P_1 for a given value of α is known, the external load p_n is calculated from Eq. (3.10) as

$$p_n = P_1 + \frac{3\pi G r_0\sqrt{1+\alpha^2}}{4(1-\nu)\beta^3 d}(\beta^2-\alpha^2)$$

Substituting Eq. (3.11) into Eq. $(3.3)_1$, we find the normal contact stress:

— for $\alpha \leqslant |\xi| \leqslant \beta$

$$N(\xi) = \frac{3\pi G r_0(1+\xi^2)}{4d(1-\nu)\beta^3}\left(\frac{\sqrt{1+\alpha^2}+|\xi|\sqrt{\xi^2-\alpha^2}}{1+\xi^2}(\beta^2-\alpha^2)-2|\xi|\sqrt{\xi^2-\alpha^2}\right)-p_n \tag{3.15}$$

— for $|\xi| \geqslant \beta$

$$N(\xi) = \frac{3\pi G r_0(1+\xi^2)}{4d(1-\nu)\beta^3}\left[\frac{\sqrt{1+\alpha^2}+|\xi|\sqrt{\xi^2-\alpha^2}}{1+\xi^2}(\beta^2-\alpha^2)+2|\xi|\Big(\sqrt{\xi^2-\beta^2}-\sqrt{\xi^2-\alpha^2}\Big)\right]-p_n \tag{3.16}$$

By taking Eqs. (3.15) and (3.16) into account, Eq. $(3.7)_2$ appears as follows

$$\int_{-\gamma}^{\gamma}\frac{U'(\eta)\,d\eta}{\eta-\xi} = \frac{2d(1-\nu)s_n}{G(1+\xi^2)} + L(\xi) \qquad |\xi| \leqslant \gamma \tag{3.17}$$

where

$$L(\xi) \equiv \begin{cases} 0 & |\xi| \leqslant \alpha \\ F(\xi) & \alpha \leqslant |\xi| \leqslant \gamma \end{cases}$$

$$F(\xi) = \begin{cases} \dfrac{3fr_0\pi}{2\beta^3}\left(\dfrac{\sqrt{1+\alpha^2}+|\xi|\sqrt{\xi^2-\alpha^2}}{1+\xi^2}(\beta^2-\alpha^2) - 2|\xi|\sqrt{\xi^2-\alpha^2}\right) - fp_n & \xi \leqslant \beta \\ \dfrac{3fr_0\pi}{2\beta^3}\left(\dfrac{\sqrt{1+\alpha^2}+|\xi|\sqrt{\xi^2-\alpha^2}}{1+\xi^2}(\beta^2-\alpha^2)\right. & \\ \quad \left. + 2|\xi|\Big(\sqrt{\xi^2-\beta^2}-\sqrt{\xi^2-\alpha^2}\Big)\right) - fp_n & \xi > \beta \end{cases}$$

Since conditions $(3.8)_2$ must be met, we find a solution to Eq. (3.17) that is bounded at $\xi = \pm\gamma$. The solution to singular integral equation (3.17) is (Muskhelishvili, 1953)

$$U'(\xi) = \frac{2d(1-\nu)s_n\xi\sqrt{\gamma^2-\xi^2}}{\pi G\sqrt{1+\gamma^2}(1+\xi^2)} - \frac{\sqrt{\gamma^2-\xi^2}}{\pi^2}\int\limits_{-\gamma}^{\gamma}\frac{L(\eta)\,d\eta}{\sqrt{\gamma^2-\eta^2}(\eta-\xi)} \qquad |\xi| \leqslant \gamma \tag{3.18}$$

Using a piecewise constant approximation of the function $L(\xi)$ for evaluation of the integral in the right-hand side of Eq. (3.18), we obtain

$$U'(\xi) = \frac{2d(1-\nu)s_n\xi\sqrt{\gamma^2-\xi^2}}{\pi G(1+\xi^2)\sqrt{1+\gamma^2}} + \frac{1}{2\pi^2}\sum_{j=0}^{m-1} L_j\big(\Gamma(\gamma,\xi,\zeta_{j+1}) - \Gamma(\gamma,\xi,\zeta_j)\big) \qquad |\xi| \leqslant \gamma \tag{3.19}$$

where $\zeta_j = -\gamma + 2j\gamma/m$, $j = 1, 2, \ldots, m$ are nodes of the approximation; L_j are the nodal values of the function $L(\xi)$, that is $L_j = L(\zeta_j)$, $j = 1, 2, \ldots, m$; and

$$\Gamma(\gamma,\xi,\zeta) = \ln\frac{\gamma^2 - \xi\zeta + \sqrt{(\gamma^2-\xi^2)(\gamma^2-\zeta^2)}}{\gamma^2 - \xi\zeta - \sqrt{(\gamma^2-\xi^2)(\gamma^2-\zeta^2)}}$$

Integration of Eq. (3.19) from $-\gamma$ to ξ in view of the first condition in Eq. $(3.8)_2$ gives the relative tangential shift

$$\begin{aligned} U(\xi) = {} & \frac{d(1-\nu)s_n}{\pi G}\left(\ln\left|\frac{\sqrt{1+\gamma^2}-\sqrt{\gamma^2-\xi^2}}{\sqrt{1+\gamma^2}+\sqrt{\gamma^2-\xi^2}}\right| + \frac{2\sqrt{\gamma^2-\xi^2}}{\sqrt{1+\gamma^2}}\right) \\ & + \frac{1}{\pi^2}\sum_{j=0}^{m-1} L_j\Big\{(\xi-\zeta_{j+1})\Gamma(\gamma,\xi,\zeta_{j+1}) - (\xi-\zeta_j)\Gamma(\gamma,\xi,\zeta_j) \\ & + 2\Big(\sqrt{\gamma^2-\zeta_{j+1}^2}-\sqrt{\gamma^2-\zeta_j^2}\Big)\Big[\arcsin\Big(\frac{\xi}{\gamma}\Big) + \frac{\pi}{2}\Big]\Big\} \qquad |\xi| \leqslant \gamma \end{aligned} \tag{3.20}$$

By setting $\xi = \gamma$ in Eq. (3.20) and in view of the first condition in Eq. $(3.8)_2$, we obtain an equation for width γ of the slip zones

$$\frac{2d(1-\nu)s_n}{G\sqrt{1+\gamma^2}} + \frac{1}{\pi^2}\sum_{j=0}^{m-1} L_j\Big(\sqrt{\gamma^2-\zeta_{j+1}^2}-\sqrt{\gamma^2-\zeta_j^2}\Big) = 0 \tag{3.21}$$

This equation is solved numerically. Substituting Eq. (3.19) into Eq. $(3.3)_2$ and performing some integrations, we find shear contact stresses in the stick zones ($|\xi| \geqslant \gamma$)

$$\begin{aligned} S(\xi) = {} & \frac{s_n}{\sqrt{1+\gamma^2}}\Big(\xi^2+1-|\xi|\sqrt{\xi^2-\gamma^2}\Big) + \frac{G}{2d(1-\nu)\pi}(\xi^2+1) \\ & \cdot\sum_{j=0}^{m-1} L_j\Big[\arcsin\Big(\frac{\zeta_{j+1}}{\gamma}\Big) - \arcsin\Big(\frac{\zeta_j}{\gamma}\Big) - \arcsin\Big(\frac{\xi\zeta_{j+1}-\gamma^2}{\gamma(\xi-\zeta_{j+1})}\Big) + \arcsin\Big(\frac{\xi\zeta_j-\gamma^2}{\gamma(\xi-\zeta_j)}\Big)\Big] \end{aligned} \tag{3.22}$$

As $d \to \infty$, we obtain results for the single groove (Slobodyan *et al.*, 2014). By putting in Eqs. (3.10)-(3.12) and (3.15)-(3.22) $m_1 = 0$, we obtain results for the frictional contact interaction between two solids, one of which having a regular surface texture in form of periodically arranged grooves, in the case when the gaps do not contain a filler (Slobodyan *et al.*, 2016).

4. Numerical results and discussion

The obtained results are illustrated in Figs. 2-6, where the dimensionless parameters $\overline{x} = x/d$, $\overline{a} = a/d$, $\overline{b} = b/d$, $\overline{c} = c/d$, $\overline{r} = r/d$, $\overline{h} = h/d$, $\overline{U} = U/d$, $\overline{\sigma}_y = 4\sigma_y(1-\nu)G^{-1}$, $\overline{\tau}_{xy} = 4\tau_{xy}(1-\nu)G^{-1}$, $\overline{p}_n = 4p_n(1-\nu)G^{-1}$, $\overline{s}_n = 4s_n(1-\nu)G^{-1}$, $\overline{P}_1 = 4P_1(1-\nu)G^{-1}$, $\overline{m}_1 = m_1 RT\mu^{-1}d^{-1}$ are introduced. The maximum depth of the grooves $\overline{r}_0$ is taken to be 10^{-3}, the half-width of the grooves $\overline{b} = 0.3$, and the friction coefficient $f = 0.1$.

The nonlinear dependence of the half-width $\overline{a}$ of the gaps on the applied pressure $\overline{p}_n$ is given in Fig. 2. The half-width $\overline{a}$ of the gaps decreases with an increase in the applied pressure $\overline{p}_n$.

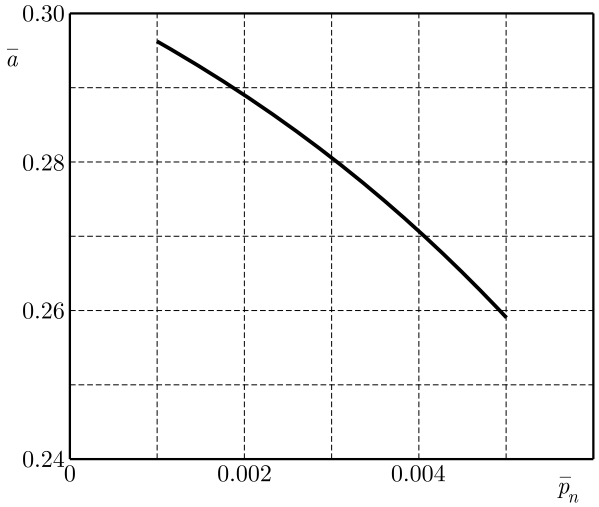

Fig. 2. Dependence of the half-width $\overline{a}$ of the gaps on the applied pressure $\overline{p}_n$

Figure 3a shows height of the gaps for different values of the applied pressure $\overline{p}_n$. The height $\overline{h}$ of the gaps decreases with the increasing nominal pressure and has its maximum value in the center of the gap. The height $\overline{h}$ of the gaps for different values of the gas mass $\overline{m}_1$ is given in Fig. 3b, where $\overline{p}_n = 0.003$. The curve for $\overline{m}_1 = 0$ corresponds to the case of gaps without a filler. As seen in the figure, $\overline{h}$ is the largest in the case of filled gaps and increases with increasing $\overline{m}_1$.

Figure 4a shows the dependence of the half-width $\overline{c}$ of the slip zones on the shear load $\overline{s}_n$ for different values of the applied pressure $\overline{p}_n$. If the edge of the slip zone is located within the groove ($\overline{a} < \overline{c} < \overline{b}$), then this dependence is nonlinear. If the edge of the slip zone exceeds the bounds of the groove ($\overline{c} > \overline{b}$), then this dependence is almost linear. The width $\overline{c}$ of the slip zones monotonically increases with the increasing shear load $\overline{s}_n$.

The rate of the increase of $\overline{c}$ with a change of $\overline{s}_n$ is greater for smaller values of $\overline{p}_n$. The curves $\overline{c} = \overline{c}(\overline{s}_n)$ have specific kinks at the points $\overline{c} = \overline{b} = 0.3$ (the right/left end of the right/left slip zone reaches the right/left end of the groove). If $\overline{c} > \overline{b}$, then the slope of curves $\overline{c} = \overline{c}(\overline{s}_n)$ increases significantly. This effect can be explained by the fact that the normal contact stress has its maximum value at the edges of the grooves and rapidly decreases in the region beyond the grooves (see Fig. 6a). The dependence of the half-width $\overline{c}$ of the slip zones on the gas mass $\overline{m}_1$ is given in Fig. 4b, where $\overline{p}_n = 0.003$. As seen in the figure, for a fixed $\overline{s}_n$, $\overline{c}$ is the smallest in the case of gaps without a filler (the curve that corresponds to $\overline{m}_1 = 0$) and increases with increasing $\overline{m}_1$ (curves that correspond to $\overline{m}_1 = 8 \cdot 10^{-7}$, $\overline{m}_1 = 9 \cdot 10^{-7}$, $\overline{m}_1 = 10^{-6}$).

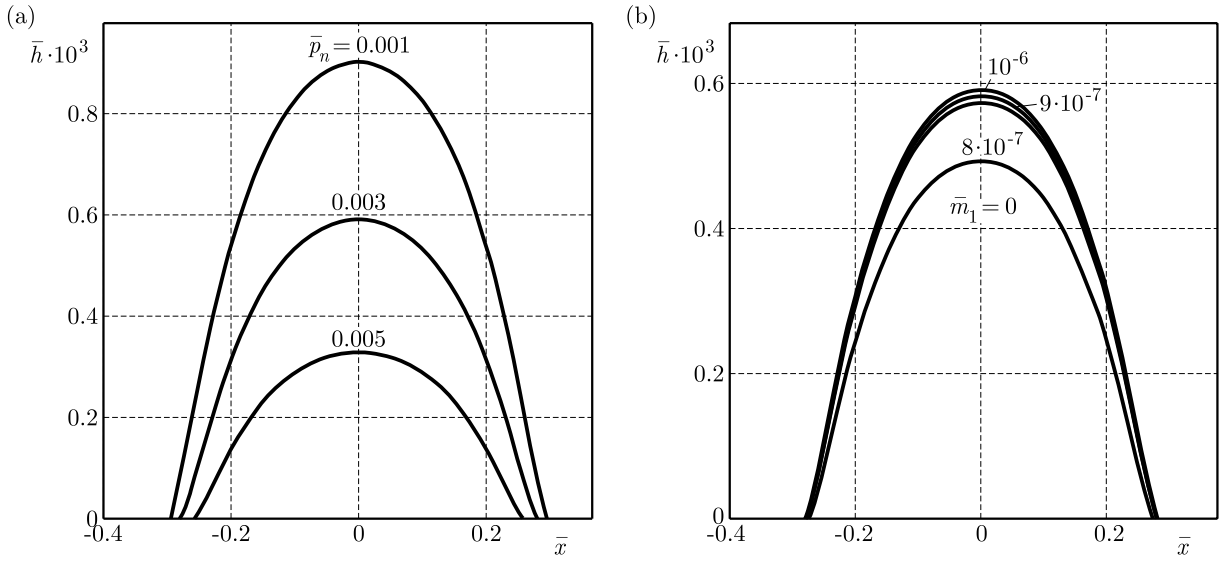

Fig. 3. The height $\overline{h}$ of the gaps

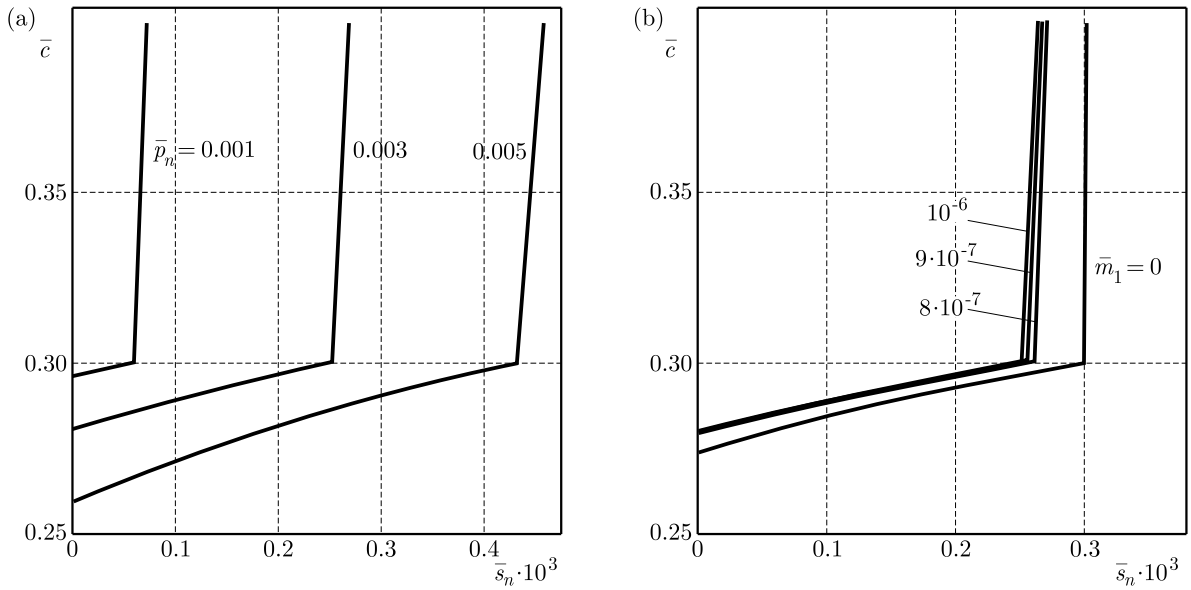

Fig. 4. Dependence of the half-width $\overline{c}$ of the slip zones on the shear load $\overline{s}_n$

Figure 5a shows the relative tangential shift $\overline{U}$ of the surfaces within one period for different values of the applied pressure $\overline{p}_n$. The relative tangential shift $\overline{U}$ of the surfaces increases with the increasing applied pressure $\overline{p}_n$ and has its maximum value in the center of the grooves. At the gaps, the relative tangential shift $\overline{U}$ is larger than in the slip zones. The relative tangential shift $\overline{U}$ of the surfaces within one period for four values of the gas mass $\overline{m}_1$ $(0;\ 8\cdot 10^{-7};\ 9\cdot 10^{-7};\ 10^{-6})$ is given in Fig. 5b, where $\overline{p}_n = 0.001$. The relative tangential shift $\overline{U}$ is smallest in the case of gaps without the filler (the curve that corresponds to $\overline{m}_1 = 0$) and increases with increasing $\overline{m}_1$ (curves that correspond to $\overline{m}_1 = 8\cdot 10^{-7}$, $\overline{m}_1 = 9\cdot 10^{-7}$, $\overline{m}_1 = 10^{-6}$).

Figure 6a shows the distribution of the contact normal stress $\overline{\sigma}_y$ for different values of the nominal pressure $\overline{p}_n$. The magnitude of the contact normal stress $|\overline{\sigma}_y|$ increases with the increasing nominal pressure $\overline{p}_n$ and has its maximum value at the edges of the grooves ($\overline{x} = \overline{b} = \pm 0.3$). As required by boundary condition $(2.2)_1$, $\sigma_y^{\pm} = -P_1$ at the surfaces of the gaps. Beyond the grooves, the contact normal stress monotonically decreases.

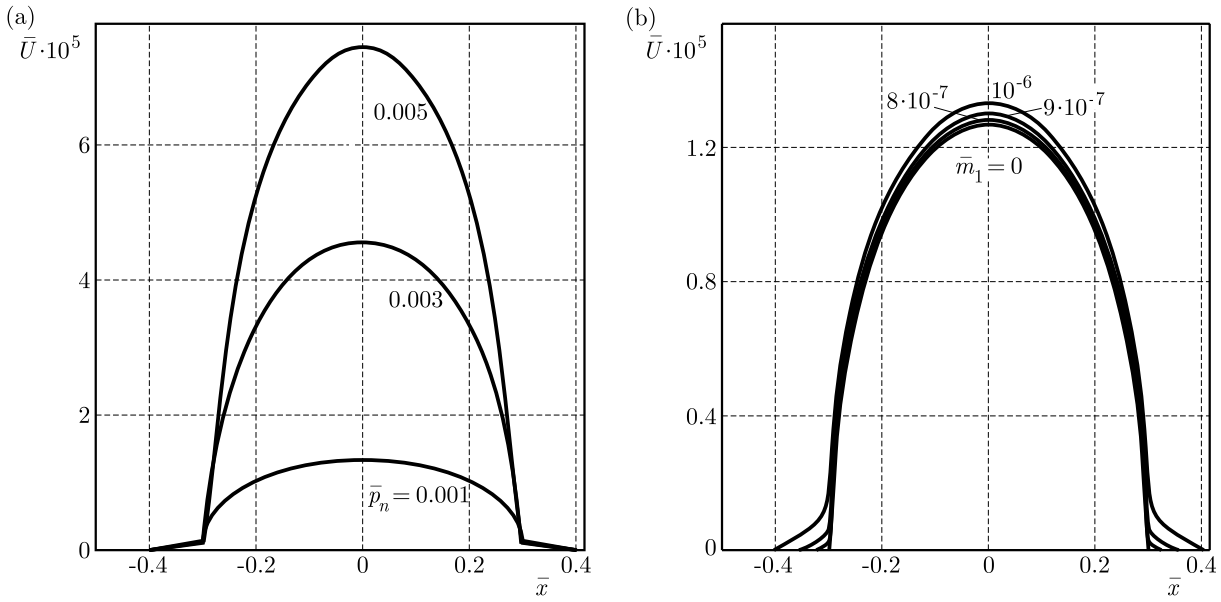

Fig. 5. The relative tangential shift $\overline{U}$ of the surfaces

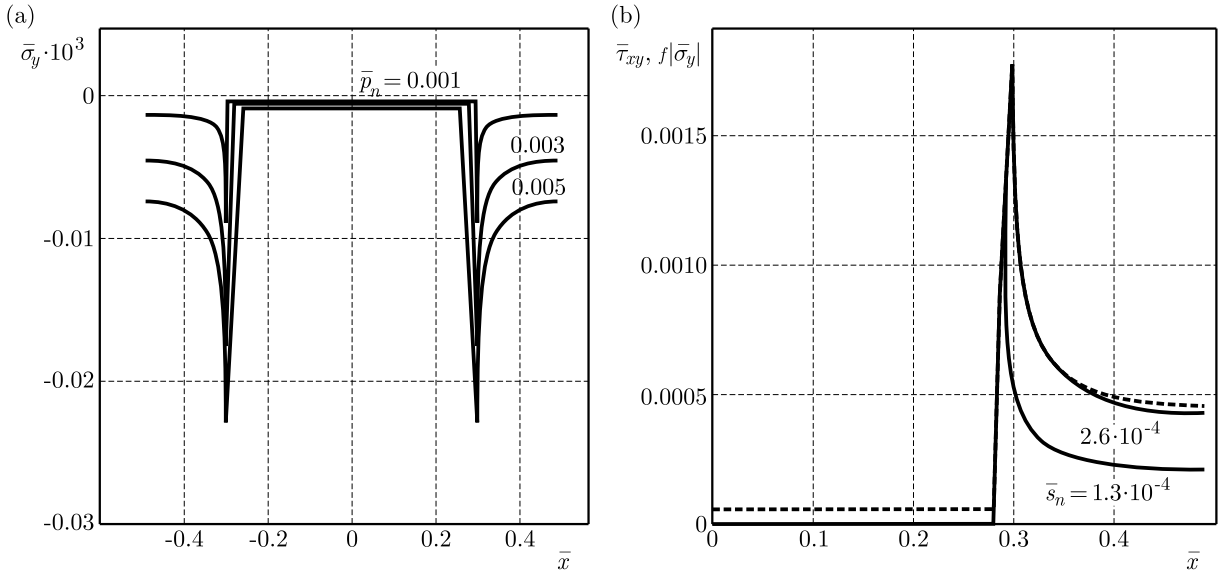

Fig. 6. Distribution of the stresses

The distributions of the shear contact stress $\overline{\tau}_{xy}$ (solid curves) and the normal contact stress $f|\overline{\sigma}_y|$ multiplied by the friction coefficient (dashed curve) are given in Fig. 6b. The solid curves are plotted for two values of the shear load $\overline{s}_n$. For $\overline{s}_n = 1.3 \cdot 10^{-4}$; $2.6 \cdot 10^{-4}$, the corresponding values of $\overline{c}$ are 0.28; 0.35. The shear contact stress $\overline{\tau}_{xy}$ increases with the increasing shear load $\overline{s}_n$. The stress $\overline{\tau}_{xy}$ has the maximum value at $\overline{x} = \pm\overline{c}$ (the ends of the slip zones) if the applied shear load $\overline{s}_n$ is such that slip occurs within the grooves ($\overline{c} < \overline{b}$) (the curve that corresponds to $\overline{s}_n = 1.3 \cdot 10^{-4}$), and at $\overline{x} = \pm\overline{b}$ (the ends of the grooves) if the applied shear load $\overline{s}_n$ is such that slip extends outside the grooves ($\overline{c} \geqslant \overline{b}$) (the curve that corresponds to $\overline{s}_n = 2.6 \cdot 10^{-4}$). At the surfaces of the gaps, $\overline{\tau}_{xy} = 0$ and $f|\overline{\sigma}_y| = fP_1$. As required by boundary condition $(2.3)_2$, the solid curves coincide with the dashed curve in the slip zones. Outside the slip zones, $\overline{\tau}_{xy}$ is less than $f|\overline{\sigma}_y|$ (the solid curves lie below the dashed curve).

5. Conclusions

The contact problem for two half-spaces of the same material under sequential application of the nominal pressure and nominal shear stress has been considered. One of the contacting surfaces is textured in form of periodically arranged grooves, and the other is flat. Partial slip of the surfaces of the solids is induced by shear load, and the first points to slip are the ends of each gap. The contact problem has been solved for the case when the interface gaps are filled with the ideal gas. Analysis of contact parameters of the contact pair on the applied load has been carried out. It has been shown that the half-width and height of the gaps decrease when the nominal pressure increases. The height of the gaps is the largest in the case of filled gaps and increases with the increasing mass of the gas, and has the maximum value in the center of the gaps. The normal contact stress increases with the increasing nominal pressure and has the maximum value at the edges of grooves. The width of the slip zones, relative tangential shift of the surfaces and shear contact stress increase with the increasing shear load. For a fixed load, the relative tangential shift and width of the slip zones is the smallest in the case of gaps without the filler and increases with the increasing gas mass. The shear contact stress has the maximum value at the ends of the slip zones if the applied shear load is such that slip occurs within the grooves and at the ends of the grooves if the applied shear load is such that slip extends outside the grooves.

References

1. Block J.M., Keer L.M., 2008, Periodic contact problems in plane elasticity, *Journal of Mechanics of Materials and Structures*, **3**, 7, 1207-1237
2. Chang F.-K., Comninou M., Sheppard S., Barber J.R., 1984, The subsurface crack under conditions of slip and stick caused by a surface normal force, *ASME Journal of Applied Mechanics*, **51**, 311-316
3. Chumak K., Malanchuk N., Martynyak R., 2014, Partial slip contact problem for solids with regular surface texture assuming thermal insulation or thermal permeability of interface gaps, *International Journal of Mechanical Sciences*, **84**, 138-146
4. Ciavarella M., 1998a, The generalized Cattaneo partial slip plane contact problem. I – Theory, *International Journal of Solids and Structures*, **35**, 18, 2349-2362
5. Ciavarella M., 1998b, The generalized Cattaneo partial slip plane contact problem. II – Examples, *International Journal of Solids and Structures*, **35**, 18, 2363-2378
6. Etsion I., 2004, Improving tribological performance of mechanical components by laser surface texturing, *Tribology Letters*, **17**, 4, 733-737
7. Evtushenko A.A., Sulim G.T., 1981, Stress concentration near a cavity filled with a liquid, *Materials Science*, **16**, 6, 546-549
8. Goryacheva I.G., Martynyak R.M., 2014, Contact problems for textured surfaces involving frictional effects, *Proceedings of the Institution of Mechanical Engineers, Part J: Journal of Engineering Tribology*, **228**, 7, 707-716
9. Greco A., Raphaelson S., Ehmann K., Wang Q.J., Lin C., 2009, Surface texturing of tribological interfaces using the vibromechanical texturing method, *ASME Journal of Manufacturing Science and Engineering*, **131**, 6, 061005-1–061005-8
10. Hills D.A., Fleury R.M.N., Dini D., 2016, Partial slip incomplete contacts under constant normal load and subject to periodic loading, *International Journal of Mechanical Sciences*, **108-109**, 115-121

11. Kaczyński A., Monastyrskyy B., 2004, On the problem of some interface defect filled with a compressible fluid in a periodic stratified medium, *Journal of Theoretical and Applied Mechanics*, **42**, 1, 41-57

12. Kit G.S., Martynyak R.M., Machishin I.M., 2009, The effect of a fluid in the contact gap on the stress state of conjugate bodies, *International Applied Mechanics*, **39**, 3, 292-299

13. Machyshyn I., Nagórko W., 2003, Interaction between a stratified elastic half-space and an irregular base allowing for the intercontact gas, *Journal of Theoretical and Applied Mechanics*, **41**, 2, 271-288

14. Malanchuk N., Martynyak R., Monastyrskyy B., 2011, Thermally induced local slip of contacting solids in vicinity of surface groove, *International Journal of Solids and Structures*, **48**, 11/12, 1791-1797

15. Martynyak R.M., Slobodyan B.S., 2009, Contact of elastic half spaces in the presence of an elliptic gap filled with liquid, *Materials Science*, **45**, 1, 62-66

16. Monastyrskyy B., Kaczyński A., 2007, The elasticity problem for a stratified semi-infinite medium containing a penny-shaped crack filled with a gas, *Acta Mechanica et Automatica*, **1**, 1, 63-66

17. Muskhelishvili N.I., 1953, *Singular Integral Equations: Boundary Problems of Function Theory and Their Application to Mathematical Physics*, P. Noordhoff, N.V. Groningen

18. Nakano M., Korenaga A., Korenaga A., Miyake K., Murakami T., Ando Y., Usami H., Sasaki S., 2007, Applying micro-texture to cast iron surfaces to reduce the friction coefficient under lubricated conditions, *Tribology Letters*, **28**, 2, 131-137

19. Pauk V., 2007, Plane contact of hot flat-ended punch and thermoelastic half-space involving finite friction, *ASME Journal of Applied Mechanics*, **74**, 6, 1172-1177

20. Schmueser D., Comninou M., 1979, The periodic array of interface cracks and their interaction, *International Journal of Solids and Structures*, **15**, 12, 927-934

21. Schreck S., Zum Gahr K.-H., 2005, Laser-assisted structuring of ceramic and steel surfaces for improving tribological properties, *Applied Surface Science*, **247**, 1-4, 616-622

22. Slobodyan B.S., Lyashenko B.A., Malanchuk N.I., Marchuk V.E., Martynyak R.M., 2016, Modeling of contact interaction of periodically textured bodies with regard for frictional slip, *Journal of Mathematical Sciences*, **215**, 1, 110-120

23. Slobodyan B.S., Malanchuk N.I., Martynyak R.M., Lyashenko B.A., Marchuk V.E., 2014, Local sliding of elastic bodies in the presence of gas in the intercontact gap, *Materials Science*, **50**, 2, 261-268

24. Stepien P., 2011, Deterministic and stochastic components of regular surface texture generated by a special grinding process, *Wear*, **271**, 3/4, 514-518

Manuscript received April 4, 2017; accepted for print April 24, 2017

JOURNAL OF THEORETICAL AND APPLIED MECHANICS
55, 4, pp. 1193-1203, Warsaw 2017
DOI: 10.15632/jtam-pl.55.4.1193

POWER SPECTRUM OPTIMIZATION IN THE DESIGN OF MULTISINE MANOEUVRE FOR IDENTIFICATION PURPOSES

Piotr Lichota, Joanna Szulczyk
Warsaw University of Technology, Institute of Aeronautics and Applied Mechanics, Poland
e-mail: plichota@meil.pw.edu.pl; jszulczyk@meil.pw.edu.pl
Daniel Agudelo Noreña, Felipe A. Vallejo Monsalve
Universidad de San Buenaventura, Bogotá, Colombia
e-mail: dagudelon@gmail.com; fvallejo@usbbog.edu.co

In this paper, two sets of multisine signals are designed for system identification purposes. The first one is obtained without any information about system dynamics. In the second case, the *a priori* information is given in terms of dimensional stability and control derivatives. Magnitude Bode plots are obtained to design the multisine power spectrum that is optimized afterwards. A genetic algorithm with linear ranking, uniform crossover and mutation operator has been employed for that purpose. Both designed manoeuvres are used to excite the aircraft model, and then system identification is performed. The estimated parameters are obtained by applying two methods: Equation Error and Output Error. The comparison of both investigated cases in terms of accuracy and manoeuvre time is presented afterwards.

Keywords: flight dynamics, optimal input design, multisine excitations, system identification, least squares, maximum likelihood

1. Introduction

System identification (Sys-ID) techniques play an important role in the development of high-quality aircraft-simulation models from flight-test data (Grauer, 2016; Albisser *et al.*, 2017; Viana, 2016). The main purpose of those approaches is to develop a mathematical model of the aircraft. To achieve this aim, an adequate input has to be designed in order to obtain dynamic characteristics of the object from flight tests.

The research on this topic started in the 1960s when Levin (1960) made the first systematic attempt at obtaining optimal inputs. Later, in the late 60s, Nahi and Wallis (1969) made a significant step by using an optimality criterion to design inputs in the time domain. Since then the use of optimality criteria was a great deal of interest and was investigated by, e.g., Fedorov (1972), Kalaba and Springarn (1982) or Goodwin and Payne (1997). At first, designed inputs were used for manoeuvres in which only one flight control was deflected. Further investigation made by, e.g., Wells and Ramachadran (1977) or Morelli and Klein (1990) showed that designing sets of excitations in which flight-control surfaces were deflected simultaneously was also possible. Even though, none of the theoretical developments seemed to be fully adapted for solving complex issues. Some recent progress has been made in applying numerical algorithms and incorporating them with other tools to design optimal inputs (Seren *et al.*, 2006, 2013; Lichota, 2016; Lichota *et al.*, 2017).

To shorten the time of the flight test campaign, multisine excitations that allow simultaneous flight control deflections can be used. Planning manoeuvres with those inputs requires the designing of their power spectrum. In our study, a genetic algorithm has been used to optimize

that energy distribution. The main purpose is to improve the input effectiveness by maximizing the power stored in certain harmonics.

The organization of this article is as follows. First, we describe the process of designing multisine signals for simultaneous aileron and elevator deflections. That section is divided into two parts. In the first one, a method for designing the inputs without *a priori* knowledge of the object is presented. In the second part, the optimization process (based on the available information of the aircraft dynamics) that leads to obtaining energy optimized multisine excitations is described. Parameter estimation methods used for estimating stability and control derivatives from the model response are presented in the next Section. Comparison of inputs in terms of manoeuvre time and Sys-ID accuracy is shown thereafter. The paper closes with a short summary of conclusions.

2. Multisine input design

One of the approaches that allows one to shorten the time spent during flight tests in order to reduce the total cost of the Sys-ID process is to design a manoeuvre with simultaneous flight control deflections. Multisine input signals that are mutually orthogonal in the time and frequency domain can be easily designed for those purposes. To achieve this aim different harmonics need to be assigned to each flight control (Morelli, 2009)

$$u = \sum_{k=1}^{M} A_k \sin(2\pi f_k t + \phi_k) \tag{2.1}$$

where f_k are consecutive harmonic frequencies, A_k is the amplitude of k-th harmonic, ϕ_k is the phase shift angle and t denotes time.

2.1. Uniform power spectrum

When there is no knowledge about the aircraft dynamics, it should be assumed that the same amount of information can be obtained from each power spectrum component. Therefore, the amplitude of each harmonic is designed for the energy content that is uniformly distributed along the frequency range of interest

$$A_{j,k} = A_j \sqrt{p_{j,k}} \tag{2.2}$$

where $p_{j,k}$ is the power of the k-th harmonic component assigned to the j-th flight control.

To increase the efficiency of the input signal, the phase shift angles ϕ_k have to be adjusted by minimizing the Relative Peak Factor

$$RPF(u_j) = \frac{\max(u_j) - \min(u_j)}{2\sqrt{2} rms(u_j)} \tag{2.3}$$

Initial values of the phase angles are obtained by using the Schroeder formula (Schroeder, 1970)

$$\phi_{j,k} = \phi_{j,k-1} + 2\pi(f_{j,k-1} - f_{j,k})\frac{k-1}{M_j}T \tag{2.4}$$

The Nelder-Mead simplex algorithm (Lagarias *et al.*, 1998) has been used to minimize the non-linear cost function.

In order to obtain non-corellated inputs, even harmonics have been assigned to the elevator and the rest of the set to the ailerons. The first harmonic is omitted due to signal optimization which is performed later, therefore the lowest frequency is 0.1 Hz. The total set is sampled with a resolution of 0.05 Hz and the upper bound of the frequency range of interest is set to 2 Hz. Moreover, to start and finish the control vector with zero amplitude, each input signal is shifted along the time axis. As a result, we obtain a control vector **u** shown in Fig. 1.

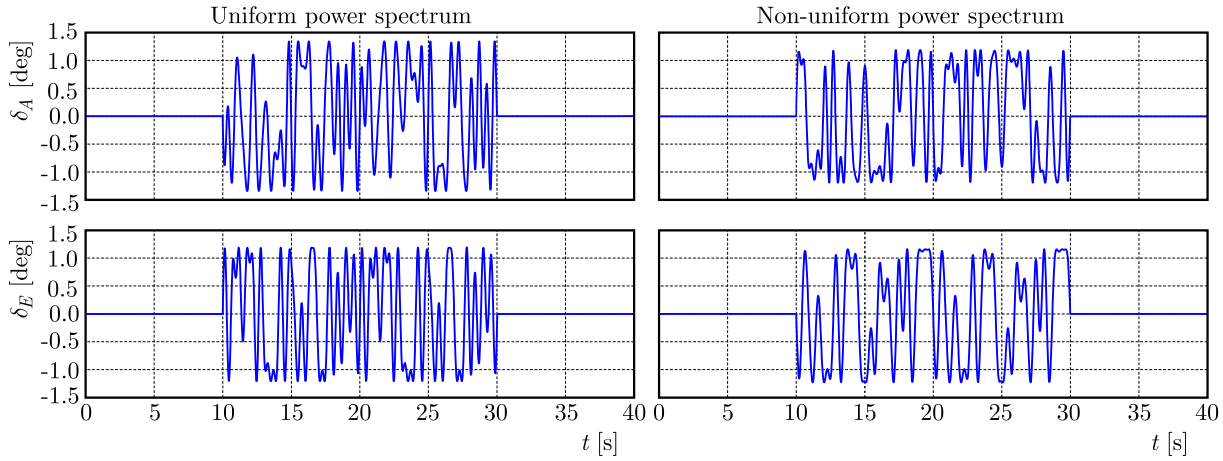

Fig. 1. Multisine input signals

2.2. Non-uniform power spectrum

In the second case, the multisine inputs are designed by including the *a priori* knowledge of the system dynamics. The initial information is given in terms of dimensional stability and control derivatives. Improvement of the signals efficiency is achieved by using the *a priori* knowledge in order to design a power spectrum with the energy that is maximized at significant frequencies. To select the frequencies at which more power should be stored, the magnitude Bode plots for all aerodynamic force and moment components are created. One of the Bode plots used for the reference power spectrum design is presented in Fig. 2.

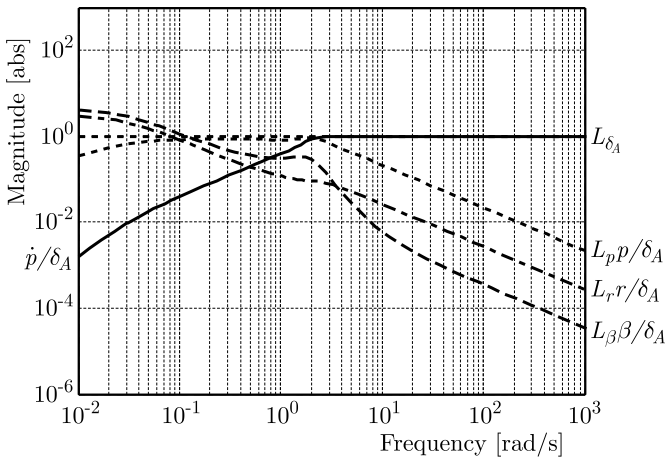

Fig. 2. Rolling moment Bode plot for aileron deflection

The reference power spectrum designed on the Bode plots base and Marchand method (Marchand, 1974) is showed in Fig. 3.

In order to optimize the design, the power stored at different harmonics is adjusted by introducing weighting factors so that the energy distribution minimizing the RPF maximizes the input efficiency.

A genetic algorithm with linear ranking, uniform crossing and 5% mutation probability has been used to obtain the final values of the weighting factors. We chose the genetic algorithm for optimization because the cost function has multiple local minima and the search space is large. Due to mutual orthogonality of the multisine inputs, this procedure is performed separately for each control surface. The obtained optimized power spectrum shown in Fig. 4 is used later to design the control vector **u** that is presented in Fig. 1.

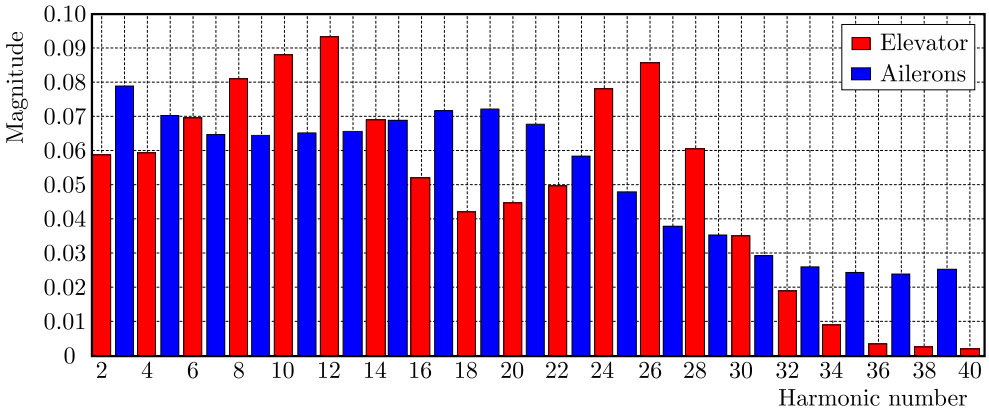

Fig. 3. Reference Power Spectrum

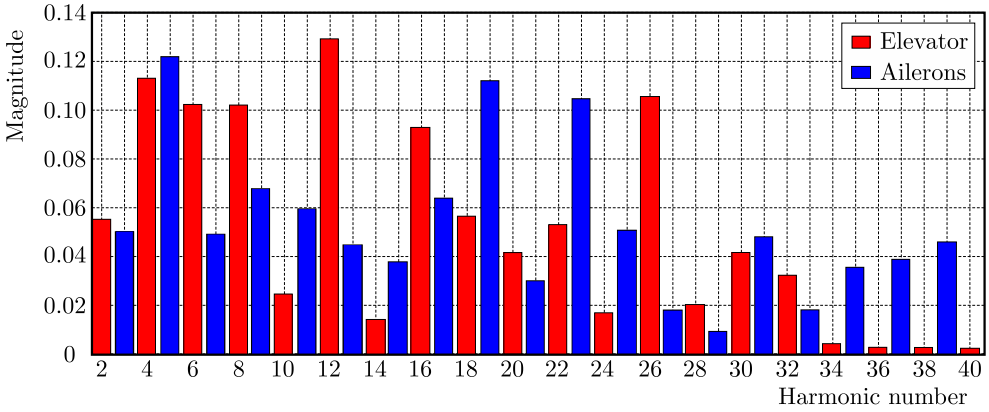

Fig. 4. Optimized Power Spectrum

3. System identification

The general aim of the parametric Sys-ID is to determine an adequate mathematical model which contains unknown values of certain system coefficients that have to be obtained indirectly from measured data. To achieve this goal, specific experiments have to be done in order to excite the system sufficiently and register inputs and object responses. From the modelling aspect, it means that determined equations must provide the model response $\mathbf{y}$ which matches adequately the measured system response $\mathbf{z}$.

In this paper, to perform the Sys-ID experiment, simultaneous multsine inputs for both investigated cases are used as excitations for a transport aircraft model with cross-coupling derivatives. To perform parameter estimation, the input signals (elevator and ailerons deflections) and aircraft response (longitudinal velocity, angle of attack, sideslip angle, roll, pitch, yaw rates, roll and pitch angles and linear acceleration components) are recorded. As the signals are corrupted with measurement noise, a 15-th point low-pass digital filter is used (Kendall *et al.*, 1983)

$$y_n = \frac{1}{320}(-3u_{n-7} - 6u_{n-6} - 5u_{n-5} + 3u_{n-4} + 21u_{n-3} + 46u_{n-2} + 67u_{n-1} + 74u_n + 67u_{n+1} + 46u_{n+2} + 21u_{n+3} + 3u_{n+4} - 5u_{n+5} - 6u_{n+6} - 3u_{n+7}) \tag{3.1}$$

3.1. Equation Error Method

Multiple different approaches can be used to perform the aircraft Sys-ID, e.g., Equation Error Methods, Output Error Methods, Filter Error Methods or Artificial Neural Networks. Equation

Error Methods minimize the cost function defined directly by the input-output equation. Among this class, the Ordinary Least Squares (OLS) is the most popular due to its mathematical simplicity

$$\mathbf{Y} = \mathbf{X}\boldsymbol{\Theta} + \boldsymbol{\epsilon} \tag{3.2}$$

where $\mathbf{Y}$ are dependent variables, $\boldsymbol{\Theta}$ denotes unknown parameters, $\boldsymbol{\epsilon}$ represent equation errors and $\mathbf{X}$ are independent variables. To obtain the estimates, the cost function which is the sum of the squares of the residuals is minimized

$$J(\boldsymbol{\Theta}) = \frac{1}{2}\sum_{k=1}^{N}\boldsymbol{\epsilon}^2(k) = \frac{1}{2}[\mathbf{Y} - \mathbf{X}\boldsymbol{\Theta}]^{\mathrm{T}}[\mathbf{Y} - \mathbf{X}\boldsymbol{\Theta}] \tag{3.3}$$

where k are discrete time points indices.

As a result, the estimates of the unknown parameters are given by

$$\widehat{\boldsymbol{\Theta}} = (\mathbf{X}^{\mathrm{T}}\mathbf{X})^{-1}\mathbf{X}^{\mathrm{T}}\mathbf{Y} \tag{3.4}$$

The block schematic of the OLS is presented in Fig. 5.

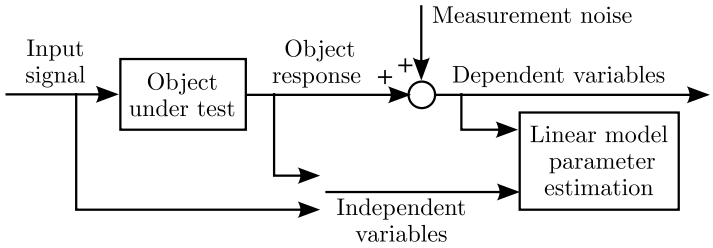

Fig. 5. Block schematic of the Least Squares Method

Before using the OLS to estimate stability and control derivatives, a data preprocessing step is performed. It is required to differentiate selected measured object responses and eliminate biases from the signals. To increase the accuracy of the estimates by eliminating parameters that have no physical meaning, Eq. (3.2) is solved independently for each output signal. In the parameter estimation process, the backward elimination is used to determine the model structure.

3.2. Output Error Method

After performing the Sys-ID using the OLS it turned out that the obtained results are not satisfying. Regardless of the excitations set, the absolute relative error is considered too high for N_r. When the identification experiment is designed without *a priori* knowledge M_u, M_q and N_β are estimated with large uncertainty. When the *a priori* information is included, it is observed for N_p.

As the estimates are biased due to measurement noise in the registered signals, to increase accuracy of the estimates, the Output Error Method (OEM) is used. This approach is the most widely applied Sys-ID technique. The main reason for its popularity is its good representation of a natural formulation for a dynamic system. The block schematic of the OEM is shown in Fig. 6.

The OEM used in this study is based on the Maximum Likelihood Estimation (MLE), therefore it seeks for maximizing the probability of observing the measured responses for model parameters (Jategaonkar, 2015)

$$\widehat{\boldsymbol{\Theta}} = \arg\max_{\boldsymbol{\Theta}} p(\mathbf{z}|\boldsymbol{\Theta}) \tag{3.5}$$

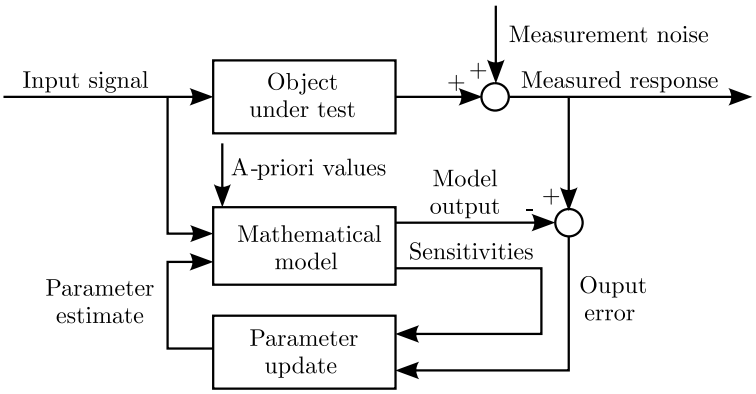

Fig. 6. Block schematic of the Output Error Method

where $\mathbf{z}$ denotes the measured response, $\boldsymbol{\Theta}$ are model parameters and the hat symbol stands for the estimates. To obtain the estimates, the cost function which is negative log-likelihood, has been minimized

$$\mathcal{L}(\boldsymbol{\Theta}|\mathbf{z}) = \frac{1}{2}\sum_{k=1}^{N}[\mathbf{z}(t_k) - \mathbf{y}(t_k)]^{\mathrm{T}}\mathbf{R}^{-1}[\mathbf{z}(t_k) - \mathbf{y}(t_k)] + \frac{nN}{2}\ln(2\pi) + \frac{N}{2}\ln(\det(\mathbf{R})) \tag{3.6}$$

where t_k is the discrete time at the k-th point, $k = 1, \ldots, N$, $\mathbf{R}$ is the measurement noise covariance matrix and n denotes the number of model outputs. The unknown measurement covariance matrix $\mathbf{R}$ is estimated from

$$\widehat{\mathbf{R}} = \frac{1}{N}\sum_{k=1}^{N}[\mathbf{z}(t_k) - \mathbf{y}(t_k)][\mathbf{z}(t_k) - \mathbf{y}(t_k)]^{\mathrm{T}} \tag{3.7}$$

Substituting the measurement covariance matrix into Eq. (3.6) and neglecting the constant terms allows one to simplify the cost function to the form given by

$$J(\boldsymbol{\Theta}) = \prod_{l=1}^{m}\frac{1}{N}\sum_{k=1}^{N}\left(z_i(t_k) - y_i(t_k)\right)^2 \tag{3.8}$$

where $l = 1, \ldots, m$ is the number of system outputs.

Similarly to the OLS, when the MLE is applied, backward elimination is used to determine the model structure.

4. Results

To determine if including the *a priori* knowledge in the multisine inputs design improves the identification experiment, several criteria are used. For that purpose, deviations from the trim condition, magnitude coherence function and estimates accuracy are investigated.

4.1. Manoeuvre analysis

To increase the model efficiency designed manoeuvres should allow the aircraft to remain close to the equilibrium point in which it is excited, and the time spent to perform a flight experiment should be minimized. Small deviations from the trim conditions decrease the stabilization time, so the next manoeuvre can be performed faster.

Deviations of various flight parameters from the equilibrium point for both investigated cases are presented in Fig. 7. From the cross-plot, it can be seen that the dispersion of the motion

parameters from their initial values are slightly smaller for the uniform power spectrum. It leads to a conclusion that designing the inputs by only optimizing their power spectrum does not result in shortening the manoeuvre time. Nevertheless, the obtained deviations from the trim point are small for both cases. This means that both designs are short in time in comparison to the conventional approach, and even the global aerodynamic parameter estimation can be performed.

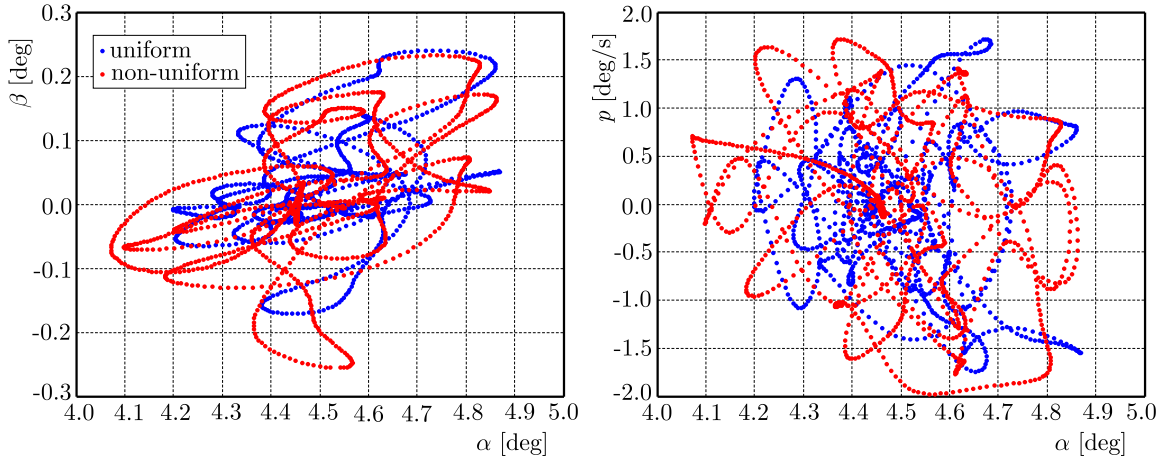

Fig. 7. Cross-plots of flight parameters

To asses the amount of information that can be obtained from a specific manoeuvre, the magnitude squared coherence function (known as coherence) can be used (Young and Patton, 1988) as it is a measure of the linear dependence between the input and output signals

$$\Gamma_{xy}^2(f_k) = \frac{|G_{xy}(f_k)|^2}{G_{xx}(f_k)G_{yy}(f_k)} \tag{4.1}$$

where G_{xy}, G_{xx}, G_{yy} are cross, input and output spectral densities.

When there is an ideal linear dependency between the input and output signal, the coherence equals 1, whilst 0 means that there is no dependence between those signals. Typically, a value above 0.6 provides a good object response mapping for multi-output systems (Tischler and Remple, 2012).

Coherence for the roll rate due to ailerons and pitch rate due to elevator deflection for both investigated designs is shown in Fig. 8. In our study, we observed that the coherence obtained for both manoeuvres is comparable. As it can be seen from the plots, the coherence is almost 1 in the whole frequency range when the elevator is deflected, and over 0.6 when the ailerons are used. For the roll rate due to ailerons deflection, the design with the *a priori* knowledge is slightly better in the low frequency range, however both manoeuvres provide sufficient amount of information as the coherence is above the assumed threshold.

4.2. Estimates accuracy

After the whole data set containing excitations (aileron δ_A and elevator deflections δ_E) and model response (longitudinal velocity u, angle of attack α, sideslip angle β, angular rates p, q, r, attitude angles ϕ, θ and linear acceleration components a_x, a_y, a_z) has been collected and filtered, Sys-ID is performed. The OLS are used for that purpose. To obtain a mathematical model of the object, the recorded signals are preprocessed and the backward elimination is used to determine the model structure. To compare the results obtained for both manoeuvres (uniform and non-uniform power spectrum), an absolute relative error for each aerodynamic coefficient is evaluated. The obtained outcomes are presented in Table 1.

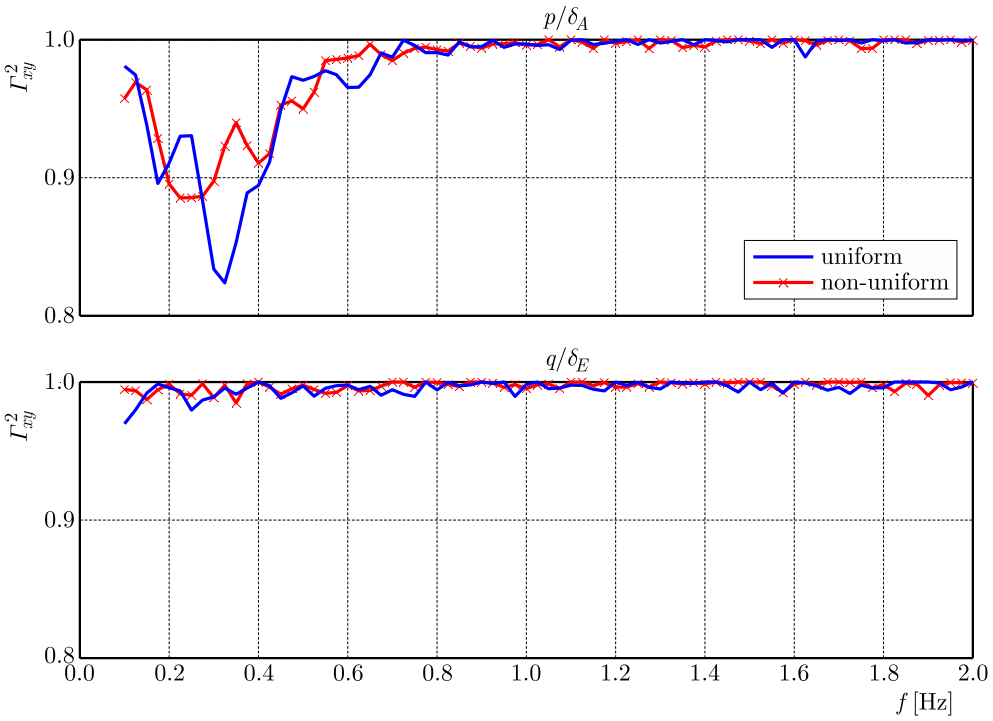

Fig. 8. Coherence function

Table 1. Absolute relative error for Equation Error Method, [%]

Name	Uniform	Optimized	Name	Uniform	Optimized
X_α	2.74	1.35	L_β	2.03	2.89
Z_α	5.07	5.42	L_p	7.33	4.55
M_u	16.29	8.83	L_r	3.64	1.42
M_α	6.13	3.68	L_{δ_A}	1.14	0.83
M_q	13.31	8.58	N_α	0.06	1.23
M_{δ_E}	2.26	1.72	N_β	10.51	6.23
Y_β	0.15	0.36	N_p	6.29	14.47
Y_p	0.23	0.03	N_r	31.35	34.18
Y_r	1.09	0.02	N_{δ_A}	2.88	4.13
Y_{δ_A}	0.03	0.05			

From Table 1 it can be observed that the absolute relative error values are high for both investigated cases. It could be caused by the fact that there is a measurement noise in the registered signals. As it was mentioned earlier, the Sys-ID is performed again using a more sophisticated method, which is the MLE, because it allows one to include the measurement noise. The outcomes are presented in Table. 2.

Table 2 shows that the parameters are estimated with high accuracy in both cases. It can be seen that the non-uniform power spectrum allows one to evaluate slightly better the outcomes. On the other hand, one has to have in mind that for a non-uniform case, additional computational time has to be spent to perform power spectrum optimization. The results of the Sys-ID performed using the MLE in form of lateral and longitudinal acceleration time histories are presented in Fig. 9.

In the plots, the recorded object response obtained for both sets of the input signals is represented by blue lines, whilst the red lines with black markers show the results of the Sys-ID process. Almost an ideal match between the measurements for all flight parameters is observed

Table 2. Absolute relative error for Output Error Method, [%]

Name	Uniform	Optimized	Name	Uniform	Optimized
X_α	0.3346	0.2409	L_α	1.8495	1.8454
Z_α	0.3134	0.2233	L_β	0.1540	0.0573
Z_{δ_E}	2.1896	0.8917	L_p	0.1689	0.1440
M_u	0.5759	0.1646	L_r	0.3220	0.0698
M_α	0.0598	0.1160	L_{δ_A}	0.1409	0.1221
M_q	0.3982	0.0529	N_α	0.0205	0.0304
M_{δ_E}	0.2597	0.0846	N_β	0.0369	0.0471
Y_β	0.0568	0.0228	N_p	0.2287	0.0540
Y_p	0.2089	0.3757	N_r	0.0329	0.0748
Y_r	0.1619	0.0261	N_{δ_R}	0.2930	0.0426
Y_{δ_R}	0.3917	0.3380			

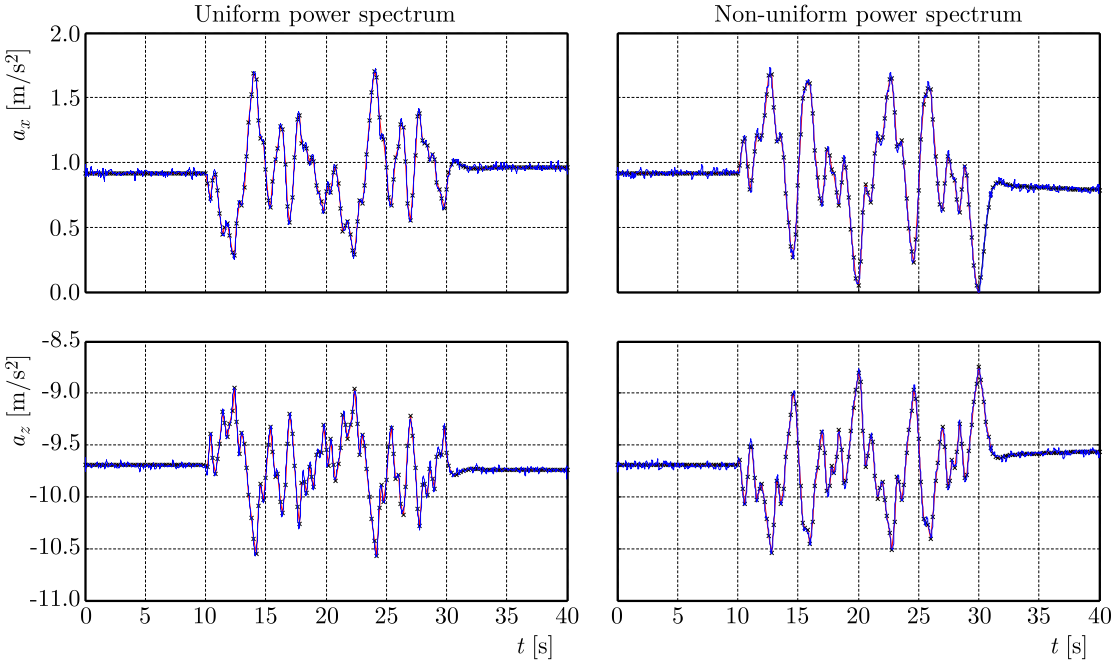

Fig. 9. Time histories for MLE

for both cases. The flight parameters time history plots confirm also our previous conclusion regarding the stabilization time, i.e. when the uniform power spectrum has been used, the aircraft returned to the trim point slightly faster. Moreover, if the non-uniform energy distribution has been selected, a new equilibrium point was reached.

5. Conclusions

In this paper, it is shown how to design multisine input signals with *a priori* information of the system dynamics in order to improve the Sys-ID accuracy. Two types of multisine excitations are used in our investigation.

In the first case, the input signals are obtained without any information of the aircraft dynamics. However, for the majority of Sys-ID tests, there is an *a priori* knowledge of aerodynamic coefficients provided that can be used to improve the excitations effectiveness. In our study, this

knowledge is given in terms of dimensional stability and control derivatives. Those parameters are used to obtain magnitude Bode plots that allow one to design an optimized input energy distribution. In order to achieve this aim, a genetic algorithm has bee used. The obtained non-uniform power spectrum has been used later to design multisine signals.

The model is excited with both sets of inputs, and the Sys-ID is performed for both cases separately. For estimating the stability and control derivatives, two methods are used: Equation Error and Output Error. The model parameters obtained from the OLS are biased as the approach is not resistant to the measurement noise in the independent variables. The second method allows one to obtain stability and control derivatives with a very high accuracy. On the basis of those outcomes, it is found that both manoeuvres allow one to obtain accurate estimates. Almost an ideal match between the results and measurements is observed. Introducing the *a priori* information in the manoeuvre design enables evaluation of slightly better estimates.

However, when the initial knowledge of the system dynamics is not included, a slightly shorter time required for stabilization is observed. Nevertheless, in both cases the time that is required for performing the experiment is greatly reduced in comparison to the conventional approach, so both designs lower the overall cost of the Sys-ID process. The only noticeable drawback of the novel approach is that an additional time has to be spent on performing the energy distribution optimization.

Acknowledgement

This work has been supported by the Universidad de San Buenaventura in Colombia, Bogota and Deutsches Zentrum für Luft- und Raumfahrt e.V., Flugsystemtechnik Institut, Braunschweig, Germany.

References

1. Albisser M., Dobre S., Berner C., Thomassin M., Garnier H., 2017, Aerodynamic coefficient identification of a space vehicle from multiple free-flight tests, *Journal of Spacecraft and Rockets*, in press, DOI: 10.2514/1.A33587
2. Fedorov V.V., 1972, *Theory of Optimal Experiments*, Probability and Mathematical Statistics, Acade, New York, USA
3. Goodwin G.C., Payne R.L., 1977, *Dynamic System Identification: Experiment Design and Data Analysis*, Academic Press Inc., New York, USA
4. Grauer J.A., 2016, Aircraft fault detection using real-time frequency response estimation, *AIAA Guidance, Navigation, and Control Conference*, San Diego, USA, AIAA 20160372, DOI: 10.2514/6.2016-0372
5. Jategaonkar R.V., 2015, *Flight Vehicle System Identification: A Time Domain Methodology*, 2nd ed., Progess in Astronautics and Aeronautics, AIAA, Reston, USA, DOI: 10.2514/4.102790
6. Kalaba R.E., Springarn K., 1982, *Control, Identification and Input Optimization*, Mathematical Concepts and Methods in Science and Engineering, Plenum Press, New York, USA, DOI: 10.1007/978-1-4684-7662-0
7. Kendall M.G., Stuart A., Ord J.K., 1983, *The Advanced Theory of Statistics*, 4th ed., Vol. 3, Charles Griffin (Edit.), London, UK, DOI: 10.1002/for.3980040310
8. Lagarias J.C., Reeds J.A., Wright M.H., Wright P.E., 1998, Convergence properties of the Nelder-Mead simplex method in low dimensions, *SIAM Journal of Optimization*, **9**, 1, 112147, DOI: 10.1137/S1052623496303470
9. Levin M.J., 1960, Optimum estimation of impulse response in the presence of noise, *IRE Transactions on Circuit Theory*, **7**, 1, 5056, DOI: 10.1109/TCT.1960.1086622
10. Lichota P., 2016, Inclusion of the D-optimality in multisine manoeuvre design for aircraft parameter estimation, *Journal of Theoretical and Applied Mechanics*, **54**, 1, 8798, DOI: 10.15632/jtam-pl.54.1.87

11. Lichota P., Sibilski K., Ohme P., 2017, D-optimal simultaneous multistep excitations for aircraft parameter estimation, *Journal of Aircraft*, in press, DOI: 10.2514/1.C033794

12. Marchand M., 1974, Untersuchung der Bestimmbarkeit von Fleugzeugderivativen aus Flugversuchen, DLR, Report DFVLR-IB 154-74/32, Braunschweig, Germany

13. Morelli E.A., 2009, Flight test experiment design for characterizing stability and control of hypersonic vehicles, *Journal of Guidance, Control and Dynamics*, **32**, 3, 949959, DOI: 10.2514/1.37092

14. Morelli E.A., Klein V., 1990, Optimal input design for aircraft parameter estimation using dynamic programming principles, *AIAA Atmospheric Flight Mechanics Conference*, Portland, USA, DOI: 10.2514/6.1990-2801

15. Nahi N.E., Wallis D.E.J., 1969, Optimal inputs for parameter estimation in dynamic systems with white observation noise, *Proceedings of Joint Automatic Control Conference*, 506512

16. Schroeder M., 1970, Synthesis of low-peak-factor signals and binary sequences with low autocorrelation, *IEEE Transactions on Information Theory*, **16**, 1, 8589, DOI: 10.1109/tit.1970.1054411

17. Seren C., Bommier F., Verdier L., Bucharles A., Alazard D., 2006, Optimal experiment and input design for flight test protocol optimization, *AIAA Athmospheric Flight Mechanics Conference*, Keystone, USA, DOI: 10.2514/6.2006-6280

18. Seren C., Hardier G., Roos C., 2013, Swarm intelligence and system identification: a hybrid discrete jumping frogs algorithm for optimal input design, *3rd IFAC International Conference on Intelligent Control*, Chengdu, China

19. Tischler M.B., Remple R.K., 2012, *Aircraft and Rotorcraft System Identification*, 2nd ed., AIAA Education Series, AIAA, Washington D.C., USA, DOI: 10.2514/4.868207

20. Viana M.V.P., 2016, Time-domain system identification of rigid-body multipoint loads model, *AIAA Atmospheric Flight Mechanics Conference*, Washington D.C., USA, AIAA 20163706, DOI: 10.2514/6.2016-3706

21. Wells W.R., Ramachandran S., 1977, Multiple control input design for identification of light aircraft, *IEEE Transactions on Automatic Control*, **22**, 985987, DOI: 10.1109/TAC.1977.1101653

22. Young P., Patton R.J., 1988, Frequency domain identification of remotely-piloted helicopter dynamics using frequency-sweep and Schroeder-phased test signals, *AIAA Atmospheric Flight Mechanics Conference*, Minneapolis, USA, AIAA 884349CP, DOI: 10.2514/6.1988-4349

Manuscript received February 27, 2017; accepted for print May 4, 2017

JOURNAL OF THEORETICAL AND APPLIED MECHANICS
55, 4, pp. 1205-1217, Warsaw 2017
DOI: 10.15632/jtam-pl.55.4.1205

AN EXPERIMENTAL STUDY ON THE SHEAR STRENGTH OF SFRC BEAMS WITHOUT STIRRUPS

Guray Arslan, Riza Secer Orkun Keskin, Semih Ulusoy
Yildiz Technical University, Department of Civil Engineering, Istanbul, Turkey
e-mail: aguray@yildiz.edu.tr; okeskin@yildiz.edu.tr; smhulusoy@gmail.com

The use of steel fibers in reinforced concrete (RC) structural members aims at the improvement of mechanical properties of such members. This study focuses on shear strength characteristics of steel fiber reinforced concrete (SFRC) beams without stirrups. Test specimens consisting of three RC and ten SFRC beams without stirrups have been tested under three-point loading in order to investigate the effects of fiber content and shear span-to--effective depth ratio on the shear strength. Furthermore, an equation developed previously for predicting the ultimate shear strength of SFRC beams without stirrups is proposed to predict the diagonal cracking strength of SFRC beams without stirrups.

Keywords: steel fiber, reinforced concrete, shear strength, beam

1. Introduction

Concrete is a brittle material that has a relatively low tensile strength. This makes reinforced concrete (RC) beams without any shear reinforcement vulnerable to shear failure. Such brittle materials have been reinforced by using various types of fibers since ancient times. A substantial amount of research has been carried out to investigate the use of steel fibers for enhancing mechanical properties of concrete over the last half century (ACI, 1996). The focus of this study is on shear strength characteristics of low- and normal-strength steel fiber reinforced concrete (SFRC) beams without stirrups. It has been shown through experimental studies that the use of steel fibers improves those characteristics significantly (Batson *et al.*, 1972; Kadir and Saeed, 1986; Mansur *et al.*, 1986; Uomoto *et al.*, 1986; Lim *et al.*, 1987; Narayanan and Darwish, 1987; Li *et al.*, 1992; Swamy *et al.*, 1993; Noghabai, 2000; Kwak *et al.*, 2002; Rosenbusch and Teutsch, 2002; Dupont and Vandewalle, 2003; Cucchiara *et al.*, 2004; Parra-Montesinos, 2006; Parra-Montesinos *et al.*, 2006; Dinh *et al.*, 2010; Ding *et al.*, 2011; Aoude *et al.*, 2012; Minelli and Plizzari, 2013; Minelli *et al.*, 2014; Sahoo and Sharma, 2014; Shoaib *et al.*, 2014; Singh and Jain, 2014; Sahoo *et al.*, 2015). Besides, various studies have been conducted to develop an accurate model for predicting the shear strength of SFRC beams without stirrups (Sharma, 1986; Narayanan and Darwish, 1987; Ashour *et al.*, 1992, Swamy *et al.*, 1993; Imam *et al.*, 1997, Khuntia *et al.* 1999; Kwak *et al.*, 2002; RILEM, 2003; Yakoub, 2011; Gandomi *et al.*, 2011; Dinh *et al.*, 2011; Arslan, 2014). Despite these studies, SFRC has not yet achieved a widespread structural use. It is essential to increase the experimental database for both verifying the current models and developing more accurate ones.

The objective of this study is to investigate shear strength characteristics of low- and normal--strength SFRC beams without stirrups experimentally. A total of thirteen specimens, three of which being RC and the others SFRC beams, have been tested under three-point loading in order to examine the effects of volume fraction of steel fibers V_f and shear span-to-effective depth ratio a/d on the shear strength of SFRC beams without stirrups. Furthermore, the ultimate shear strengths and diagonal cracking strengths of test specimens have been predicted by using

a number of equations available in the literature, and a comparison of those predictions is presented. A modified version of the equation proposed by Arslan (2014) for predicting the ultimate shear strength of SFRC beams without stirrups is suggested for predicting the diagonal cracking strength of SFRC beams without stirrups.

2. Experimental program

Test specimens consisting of three RC and ten SFRC beams have been divided into three groups as A2.5, A3.5 and A4.5 series based on the shear span-to-effective depth ratio. The beams of A2.5 series have a shear span-to-effective depth ratio of 2.5, which is usually defined as the lower limit for slender RC beams without stirrups. The shear span-to-effective depth ratios of the beams of A3.5 and A4.5 series have been chosen as 3.5 and 4.5, respectively, in order to observe shear failure resulting from diagonal tension. The geometrical properties of test specimens are shown in Fig. 1. All beams have the same cross-section of 150 mm by 230 mm with an effective depth of 200 mm. The beams of A2.5 series are 1400 mm long, whereas the beams of A3.5 and A4.5 series are 2200 mm long.

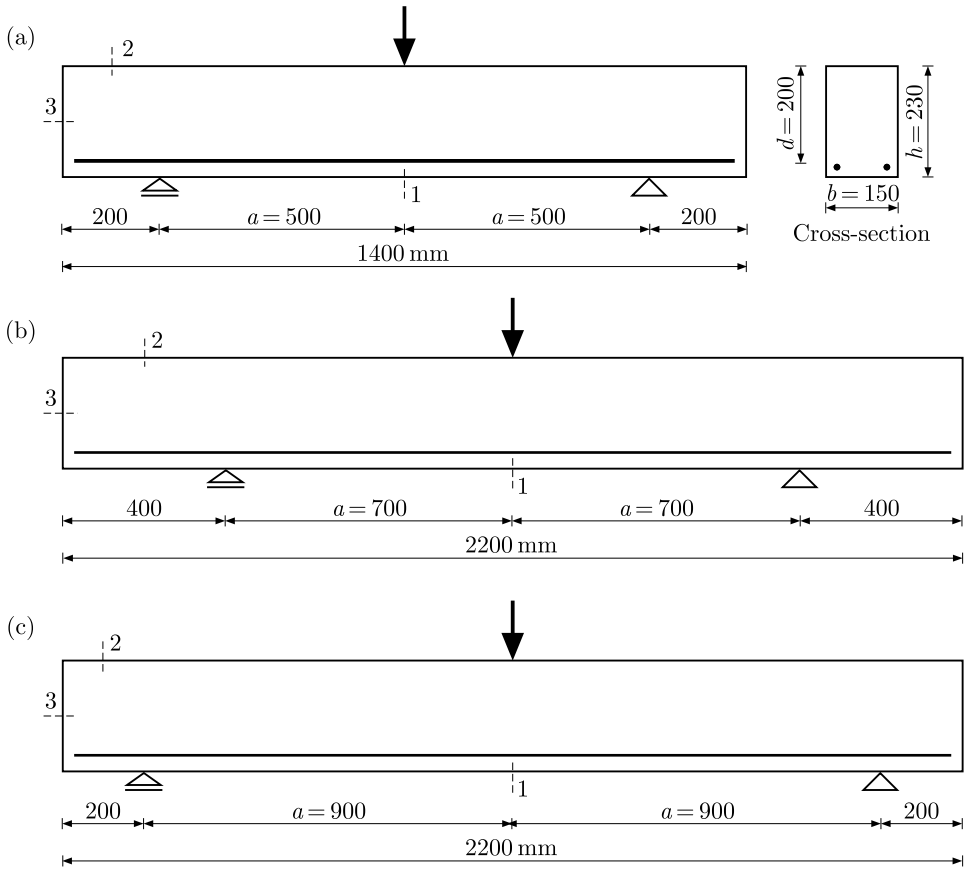

Fig. 1. Configuration and geometry of test specimens; (a) A2.5 series, (b) A3.5 series, (c) A4.5 series

A longitudinal reinforcement ratio ρ of 1.34% has been chosen to avoid any premature flexural failure. Two deformed (S420 grade) steel bars of 16 mm diameter were used as the longitudinal reinforcement for all beams. Hooked-end steel fibers with a length L_f of 30 mm and a nominal diameter D_f of 0.55 mm, resulting in an aspect ratio L_f/D_f of 54.5, were used as the only shear reinforcement. Each group of test specimens includes beams with the volume fraction of steel fibers ranging from 0.0% to 3.0%.

A specimen label consists of a combination of letters and numbers. Each label starts with an "A" followed by 2.5, 3.5 or 4.5 to designate the shear span-to-effective depth ratio and continues with an "F" to indicate the volume fraction of steel fibers followed by 1.0, 2.0 or 3.0 to designate the volume fraction of steel fibers. For example, a beam having a shear span-to--effective depth ratio of 3.5 with a volume fraction of steel fibers equal to 1.0% is labeled as A3.5F1.0. The specimens labeled as A2.5R, A3.5R and A4.5R are the reference beams that do not contain any steel fibers.

Table 1. Properties of test specimens

Test specimen	f_c [MPa]	V_f [%]	a/d	l [mm]
A2.5R	39.00	0.0	2.5	1400
A2.5F1.0a	33.68	1.0		
A2.5F1.0b	24.53	1.0		
A2.5F2.0	21.43	2.0		
A2.5F3.0	9.77	3.0		
A3.5R	31.52	0.0	3.5	2200
A3.5F1.0	20.21	1.0		
A3.5F2.0	21.43	2.0		
A3.5F3.0	27.91	3.0		
A4.5R	41.82	0.0	4.5	2200
A4.5F1.0	24.53	1.0		
A4.5F2.0	21.43	2.0		
A4.5F3.0	27.91	3.0		

The properties of test specimens are summarized in Table 1, where f_c is the concrete compressive cylinder strength and l is the length of test specimen. All specimens have been cast with the concrete mix given in Table 2. The concrete compressive strength of each specimen has been determined by using either 150×150×150 mm cube or 100×100 mm cylinder samples. The concrete compressive strength of A2.5F3.0 is notably low compared to the others. This might have been occurred due to poor mixing and/or compacting of concrete leading to a relatively low concrete compressive strength.

Table 2. Concrete mix

Materials	A2.5R, A2.5F3.0, A3.5R, A3.5F3.0, A4.5R, A4.5F3.0	A2.5F1.0a, A2.5F1.0b, A2.5F2.0, A3.5F1.0, A3.5F2.0, A4.5F1.0, A4.5F2.0
	Mixture proportions [kg/m^3]	
0-5 mm crushed sand	1180	1150
5-12 mm crushed stone	721	310
12-22 mm crushed stone	–	470
Fly ash (40% of binder)	80	90
Cement CEMI 42.5R	240	220
Water/binder	0.55	0.55
Superplasticizer	3.20	3.10

A load-controlled test procedure has been followed such that all specimens were incrementally loaded up to the failure. After each load increment, the deflections were measured by means of linear variable differential transducers (LVDTs) placed at locations 1, 2 and 3 shown in Fig. 1, and the crack pattern was monitored visually throughout the test.

3. Experimental results

At the early stages of loading, fine vertical cracks were observed in the vicinity of mid-span of each beam. With the increasing load, new flexural cracks formed away the mid-span. With a further increase in the load, the flexural cracks started then to propagate diagonally towards the applied load and additional diagonal cracks began to form farther away the mid-span. The failure mechanisms of test specimens except for A4.5F2.0 and A4.5F3.0 were characterized by a wide diagonal crack. It was observed that (i) the failure mechanisms were controlled by an increased shear strength and the dowel effect, and reduced crack spacing and crack width resulting from the crack-bridging ability of steel fibers, and (ii) the specimens exhibited large deflections at failure. The crack patterns of test specimens at failure are shown in Fig. 2.

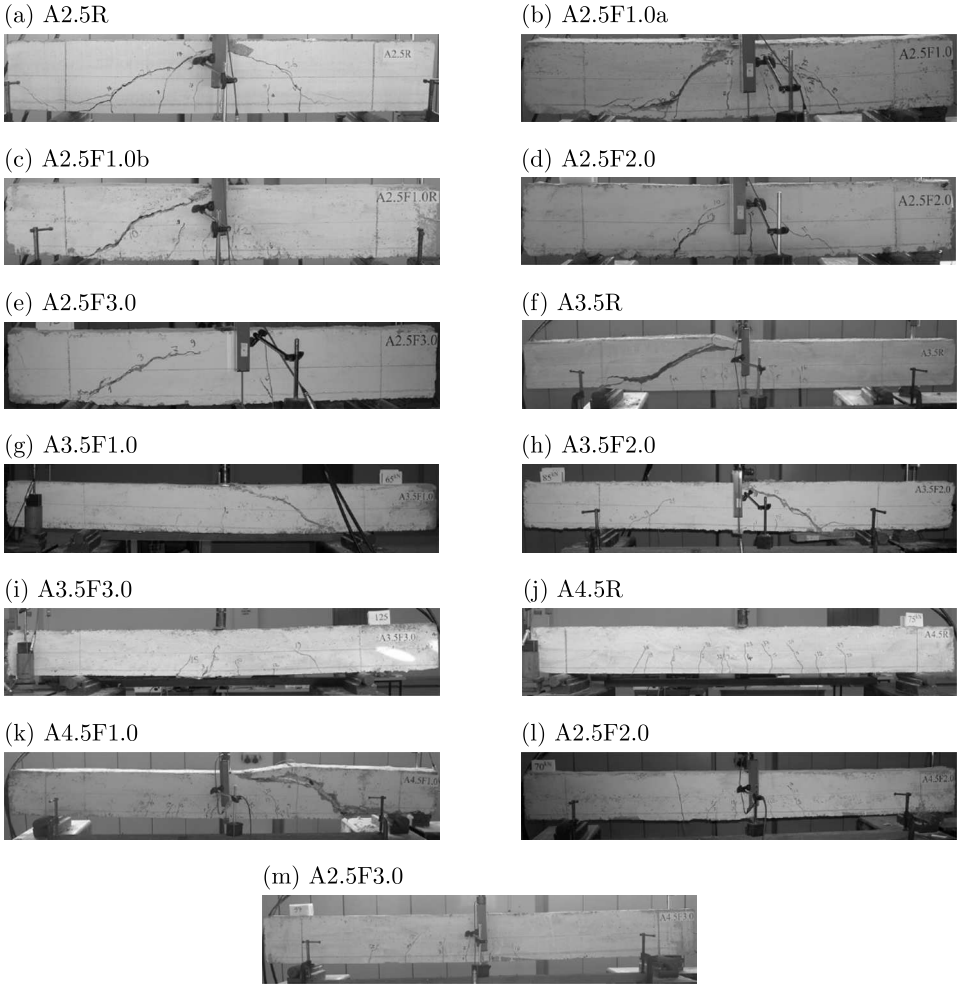

Fig. 2. Crack patterns of test specimens

It is usually assumed that the diagonal tension failure of an RC beam without stirrups initiates when the principal tensile stresses within the shear span exceed the tensile strength of concrete and a diagonal crack propagates through the beam web. In the studies of Arslan (2008, 2012) and Arslan and Polat (2013), a diagonal crack is defined as a major inclined crack extending from the level of the longitudinal reinforcement towards the applied load, and the load at the growth of the first inclined crack is termed as the diagonal cracking load. The diagonal cracking load P_{cr}, the mid-span deflection at diagonal cracking δ_{cr}, the ultimate load P_u, the ultimate mid-span deflection δ_u, the diagonal cracking strength v_{cr} and the ultimate shear strength v_u for each test specimen are given in Table 3, where the diagonal cracking strength and the ultimate

shear strength are the diagonal cracking load and the ultimate load divided by the product of beam thickness b_w and effective depth, respectively. The load-deflection curves of all specimens are plotted in Fig. 3.

Table 3. Experimental results

Test specimen	P_{cr} [kN]	δ_{cr} [mm]	P_u [kN]	δ_u [mm]	v_{cr} [MPa]	v_u [MPa]	δ_u/δ_{cr}	v_u/v_{cr}
A2.5R	65	1.23	81	1.89	1.08	1.35	1.54	1.25
A2.5F1.0a	85	4.31	130	6.69	1.42	2.17	1.55	1.53
A2.5F1.0b	70	4.41	88	5.71	1.17	1.47	1.29	1.26
A2.5F2.0	70	2.75	100	5.09	1.17	1.67	1.85	1.43
A2.5F3.0	60	4.90	78	7.79	1.00	1.30	1.59	1.30
A3.5R	60	2.81	62	2.83	1.00	1.03	1.01	1.03
A3.5F1.0	55	2.80	65	4.26	0.92	1.08	1.52	1.17
A3.5F2.0	60	3.08	85	6.36	1.00	1.42	2.06	1.42
A3.5F3.0	95	5.09	117	6.83	1.58	1.95	1.34	1.23
A4.5R	60	5.51	76	7.37	1.00	1.27	1.34	1.27
A4.5F1.0	60	4.60	85	8.70	1.00	1.42	1.89	1.42
A4.5F2.0*	45	8.54	70	15.35	0.75	1.17	1.80	1.56
A4.5F3.0**	–	–	97	18.63	–	1.62	–	–

* Failed in shear-flexure; ** failed in flexure

3.1. Influence of volume fraction of steel fibers

Experimental results given in Table 3 and Fig. 3 clearly show that the use of steel fibers improved the shear strength and deformation capacity considerably. In the case of A2.5 series, the use of steel fibers in the amounts of 1.0% and 2.0% by volume increased the ultimate shear strength by 9% and 23%, respectively, and increased the deflection capacity 3.02 and 2.69 times, respectively. It is to be noted that increasing the volume fraction of steel fibers from 1.0% to 2.0% for approximately the same concrete compressive strength (A2.5F1.0b and A2.5F2.0) increased the ultimate shear strength by 14% but did not increase the deflection capacity. A2.5F3.0 cannot be compared directly since its concrete compressive strength is significantly low. In the case of A3.5 series, an increase in the ultimate shear strength due to the use of steel fibers in the amounts of 1.0%, 2.0% and 3.0% is 5%, 37% and 89%, respectively, and the deflection capacity is increased 1.51, 2.25 and 2.41 times, respectively.

For a better understanding of the effect of fiber content on the shear strength, the normalized maximum shear stress against the volume fraction of steel fibers for each beam is plotted in Fig. 4. It is clearly observed that the normalized maximum shear stress increases with the fiber content in the case of A2.5 and A3.5 series. A similar trend cannot be observed in the case of A4.5 series since A4.5F2.0 and A4.5F3.0 failed in flexure.

Even though the use of steel fibers enhanced the shear strengths and deformation capacities of the beams considerably, it was still not able to change the failure mechanisms of the beams of A2.5 and A3.5 series. On the other hand, the use of steel fibers in the amount of 3.0% in the case of A4.5 series both increased the shear strength and the deformation capacity by 28% and 152%, respectively, and changed the failure mode from shear to flexure. It is to be noted that a high volume fraction of steel fibers, i.e. 3.0%, was required to prevent the shear failure and use the flexural capacity. However, it may not be practical to work with a concrete mix having such a high volume fraction of steel fibers. Instead, steel fibers can be used together with a limited amount of stirrups to modify the failure mode.

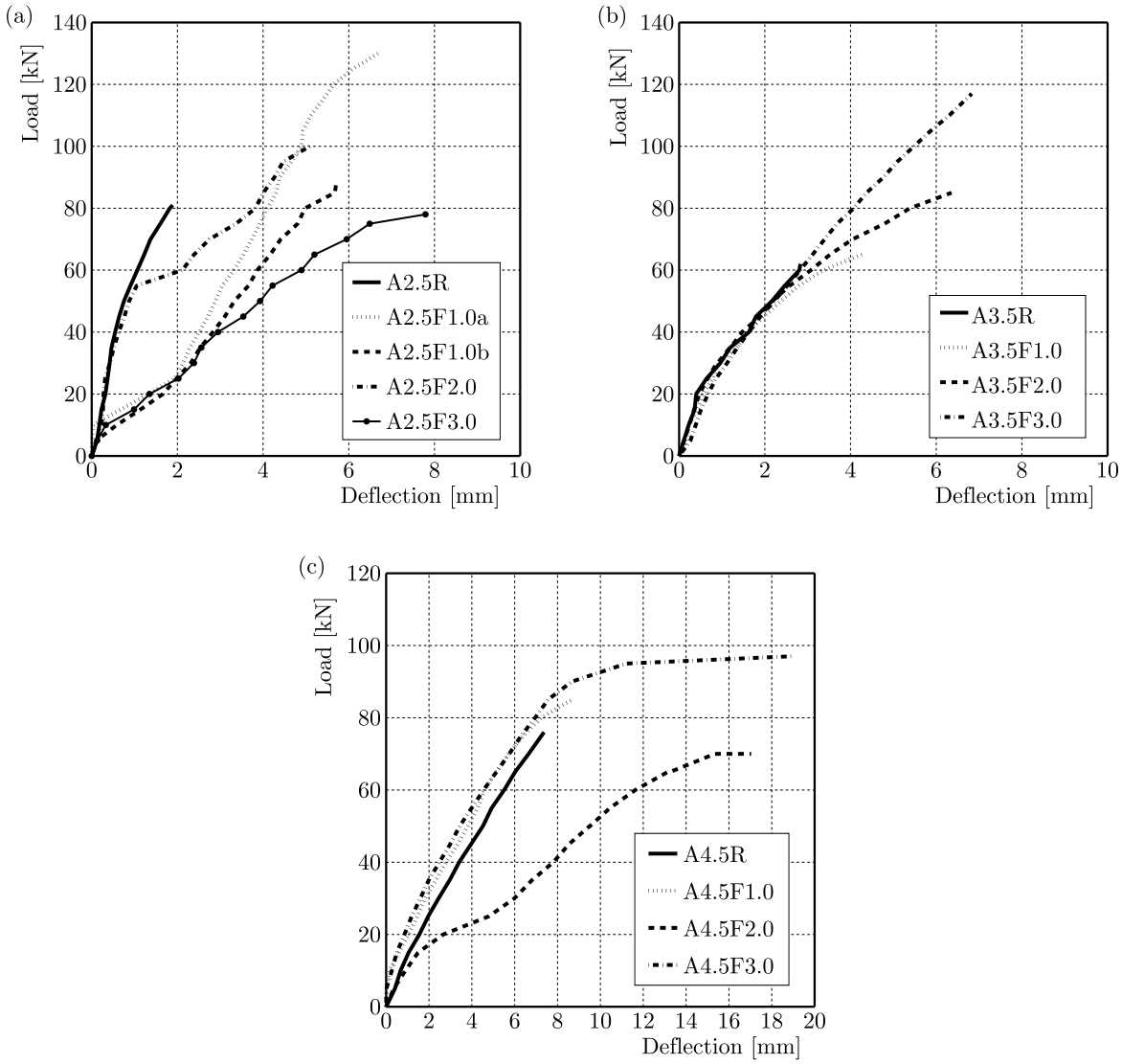

Fig. 3. Load-deflection curves; (a) A2.5 series, (b) A3.5 series, (c) A4.5 series

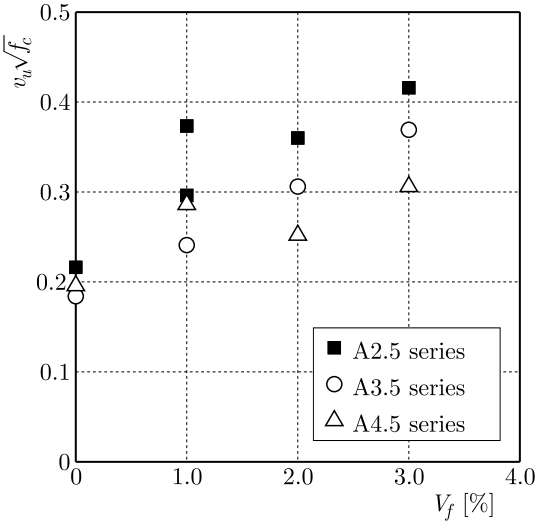

Fig. 4. Normalized maximum shear stress vs. fiber content

It is observed in Table 3 that the ratio of the ultimate shear strength to the diagonal cracking strength increases with the volume fraction of steel fibers up to 2.0% for the beams of all three series, but decreases with an increase in the volume fraction of steel fibers from 2.0% to 3.0% for the beams of A2.5 and A3.5 series. A4.5F3.0 exhibited flexural failure and the diagonal cracking was not observed in this specimen.

3.2. Influence of shear span-to-effective depth ratio

It can be seen in Table 3 that the diagonal cracking strength decreases with the increasing shear span-to-effective depth ratio as a result of the increased flexural moment and the associated principal stresses and the diminishing arching effect. The shear span-to-effective depth ratio eventually affects the ultimate shear strength. As expected for the reference beams, the ultimate shear strength of A2.5R, which has the smallest shear span-to-effective depth ratio, is greater than that of the other reference beams; however it has a smaller deflection capacity. A similar relationship between the beams with the volume fraction of steel fibers of 2.0% is observed. A2.5F2.0 has a greater load carrying capacity and a smaller deflection capacity than A3.5F2.0 and A4.5F2.0 do.

It is observed that increase in the deflection capacity decreases with the increasing shear span-to-effective depth ratio for a given fiber content. The deflection capacities of A2.5F1.0b, A3.5F1.0 and A4.5F1.0 are 3.02, 1.51 and 1.18 times those of A2.5R, A3.5R and A4.5R, respectively. The use of steel fibers in the amount of 2.0% by volume resulted in deflection capacities 2.69, 2.25 and 2.08 times those of the reference specimens for A2.5F2.0, A3.5F2.0 and A4.5F2.0, respectively. Experimental results manifest that it is essential to consider the effect of shear span-to-effective depth ratio in predicting the shear strength of SFRC beams, as done by Sharma (1986), Narayanan and Darwish (1987), Ashour *et al.* (1992), Imam *et al.* (1997), Kwak *et al.* (2002), Gandomi *et al.* (2011) and Arslan (2014).

4. Predicting the shear strengths of test specimens

A number of equations proposed for predicting the ultimate shear strength and diagonal cracking strength of SFRC beams without stirrups are considered. The statistical evaluations of the equations considered within the scope of this study are available in the work of Arslan (2014). In this study, the equations are used only for predicting the ultimate shear strength and diagonal cracking strength of test specimens.

4.1. The equations for ultimate shear strength

Sharma (1986) proposed a simple empirical equation for predicting the ultimate shear strength of SFRC beams without stirrups. The equation, which is recommended by ACI (1988) (v_u in MPA), is

$$v_u = k f_{ct} \Big(\frac{d}{a}\Big)^{0.25} \tag{4.1}$$

where f_{ct} is the concrete tensile strength, $k = 1$ if f_{ct} is obtained by a direct tension test, $k = 2/3$ if f_{ct} is obtained by an indirect tension test and $k = 4/9$ if f_{ct} is obtained by using the modulus of rupture or $f_{ct} = 0.79\sqrt{f_c}$.

Narayanan and Darwish (1987) proposed an empirical equation as

$$v_u = e\Big(0.24 f_{sp} + 80\rho\frac{d}{a}\Big) + v_b \tag{4.2}$$

where $e = 1.0$ for $a/d > 2.8$ and $e = 2.8d/a$ for $a/d \leqslant 2.8$, $f_{sp} = f_{cuf}/(20 - \sqrt{F}) + 0.7 + \sqrt{F}$ is the computed value of split-cylinder strength of fiber concrete, f_{cuf} is the cube strength of fiber reinforced concrete, $F = (L_f/D_f)V_f d_f$ is the fiber factor (d_f is the fiber bond factor that is 0.5 for round, 0.75 for crimped and 1.0 for indented fibers), $v_b = 0.41\tau F$ is the pull-out strength of fibers along the inclined crack and τ is the average fiber matrix interfacial bond stress equal to 4.15 MPa.

Ashour *et al.* (1992) revised the equations given by the ACI 318 code (ACI, 2014) and Zsutty (1971) for predicting the ultimate shear strength of RC beams without stirrups in order to propose two empirical equations for SFRC beams with $a/d \geqslant 2.5$ as

$$v_u = \left(0.7\sqrt{f_c} + F\right)\frac{d}{a} + 17.2\rho\frac{d}{a} \qquad v_u = \left(2.11\sqrt[3]{f_c} + 7F\right)\sqrt[3]{\rho\frac{d}{a}} \tag{4.3}$$

respectively.

Swamy *et al.* (1993) proposed an equation based on the truss model as

$$v_u = 0.37\tau V_f\frac{L_f}{D_f} + 0.167\sqrt{f_c} \tag{4.4}$$

where τ is assumed to be 4.15 MPa as suggested by Narayanan and Darwish (1987).

Imam *et al.* (1997) modified the equation that Bazant and Sun (1987) had developed to predict the ultimate shear strength of RC beams without stirrups to propose the relationship

$$v_u = 0.6\frac{1 + \sqrt{5.08/d_a}}{\sqrt{1 + d/25d_a}}\sqrt[3]{\rho(1 + 4F)}\left(f_c^{0.44} + 275\sqrt{\frac{\rho(1 + 4F)}{(a/d)^5}}\right) \tag{4.5}$$

where d_a is the maximum aggregate size and d_f is 0.5 for smooth, 0.9 for deformed and 1.0 for hooked fibers.

Khuntia *et al.* (1999) proposed the following equation

$$v_u = (0.167 + 0.25F)\sqrt{f_c} \tag{4.6}$$

where d_f is 2/3 for plain and round, 1.0 for hooked or crimped fibers.

Kwak *et al.* (2002) developed an equation by using the form of the equation proposed by Zsutty (1971) combined with an additional term accounting for the contribution of steel fibers and proposed two versions of the equation with different constants as

$$v_u = 2.1ef_{sp}^{0.7}\left(\rho\frac{d}{a}\right)^{0.22} + 0.8v_b^{0.97} \tag{4.7}$$

where $e = 1.0$ for $a/d > 3.5$ and $e = 3.5d/a$ for $a/d \leqslant 3.5$, and

$$v_u = 3.7e\sqrt[3]{f_{sp}^2}\sqrt[3]{\rho\frac{d}{a}} + 0.8v_b \tag{4.8}$$

where $e = 1.0$ for $a/d > 3.4$ and $e = 3.4d/a$ for $a/d \leqslant 3.4$.

According to RILEM (2003), the ultimate shear strength of SFRC beams without stirrups is calculated as

$$v_{Rd,3} = 0.12k\sqrt[3]{100\rho f_c} + 0.7k_f k_1\tau_{fd} \tag{4.9}$$

where $k = 1 + \sqrt{200/d} \leqslant 2$ (d is in mm), $\rho \leqslant 0.02$, k_f is a factor considering the contribution of flanges in a T-section and is equal to 1 for rectangular sections, $k_1 = 1 + \sqrt{200/d} \leqslant 2$ (d is

in mm), $\tau_{fd} = 0.12 f_{Rk,4}$ is the design value of increase in shear strength due to steel fibers and $f_{Rk,4}$ is the characteristic residual strength for the ultimate limit state.

Yakoub (2011) used an expression developed for predicting the contribution of steel fibers to the shear strength of SFRC beams to modify the equations given by Bazant and Kim (1984) and CSA A23.3-04 (CSA, 2004). The resulting equations for $a/d \geqslant 2.5$ are

$$\begin{aligned} v_u &= 0.83\xi \sqrt[3]{\rho}\left(\sqrt{f_c} + 249.28\sqrt{\frac{\rho}{(a/d)^5}}\right) + 0.162F\sqrt{f_c} \\ v_u &= \beta\sqrt{f_c}(1 + 0.70F) \end{aligned} \tag{4.10}$$

respectively, where $\xi = 1/\sqrt{1 + d/(25da)}$ is the aggregate size effect factor, $\beta = [0.4/(1 + 1500\varepsilon_x)][1300/(1000 + s_{xe})]$ (s_{xe} is in mm), $\varepsilon_x = (M/d_v + V)/(2E_s A_s)$ is the longitudinal strain at the mid-depth of the beam web, M and V are the external failure moment and shear acting on the section, respectively, d_v is the flexural lever arm equal to $0.9d$ or $0.72h$ (h is the beam height), whichever is greater, $s_{xe} = 35s_x/(16 + d_a) \geqslant 0.85s_x$ is the equivalent crack spacing factor that accounts for the maximum aggregate size effects on the shear strength, s_x is the crack spacing parameter that accounts for the crack spacing at the mid-depth of the beam and d_f is 0.79 for sheared, 0.83 for crimped, 0.89 for duoform, 0.91 for rounded, 0.92 for indented cut wire and 1.00 for hooked fibers.

Gandomi *et al.* (2011) developed a nonlinear model by means of linear genetic programming as

$$v_u = 2\frac{d}{a}(\rho f_c + v_b) + 2\frac{d}{a}\frac{\rho}{(288\rho - 11)^4} + 2 \tag{4.11}$$

Dinh *et al.* (2011) proposed an equation as the summation of the shear stress carried across the compression zone and the vertical component of the diagonal tension resistance provided by steel fibers, such that

$$v_u = 0.13\rho f_y + 1.2\sqrt[4]{\frac{V_f}{0.0075}}\left(1 - \frac{c}{d}\right) \tag{4.12}$$

where f_y is the yield strength of flexural reinforcement and c is depth of the compression zone, which can be simply taken as $0.1h$.

Arslan (2014) proposed an equation by considering the influences of the shear span-to--effective depth ratio, dowel strength of tensile reinforcement and contribution of steel fibers to the shear strength as

$$v_u = \left(0.2\sqrt[3]{f_c^2}\frac{c}{d} + \sqrt{\rho(1 + 4F)f_c}\right)\sqrt[3]{\frac{3}{a/d}} \tag{4.13}$$

where $(c/d)^2 + (600\rho/f_c)(c/d) - 600\rho/f_c = 0$.

4.2. The predictions for ultimate shear strength

The ultimate shear strengths of test specimens excluding the reference beams (A2.5R, A3.5R and A4.5R), A4.5F2.0 and A4.5F3.0 – since they failed in shear-flexure and flexure, respectively – have been predicted by using Eqs. (4.1)-(4.13) and the predictions were compared with the experimental values. The mean value (MV), standard deviation (SD) and coefficient of variation (COV) of the ratios of the experimental values to the corresponding predictions are given in Table 4.

Table 4. Statistics of the ratios of the experimental values to the predictions

The model	MV	SD	COV
Sharma (1986)	1.241	0.186	0.150
Narayanan and Darwish (1987)	0.593	0.183	0.309
Ashour *et al.* (1992), Eq. $(4.3)_1$	0.504	0.186	0.369
Ashour *et al.* (1992), Eq. $(4.3)_2$	0.783	0.214	0.274
Swamy *et al.* (1993)	0.734	0.239	0.326
Imam *et al.* (1997)	0.633	0.201	0.317
Khuntia *et al.* (1999)	0.853	0.192	0.225
Kwak *et al.* (2002), Eq. (4.7)	0.543	0.128	0.235
Kwak *et al.* (2002), Eq. (4.8)	0.574	0.145	0.253
RILEM (2003)	1.361	0.227	0.167
Yakoub (2011), Eq. $(4.10)_1$	0.858	0.126	0.147
Yakoub (2011), Eq. $(4.10)_2$	1.342	0.329	0.246
Gandomi *et al.* (2011)	0.480	0.116	0.242
Dinh *et al.* (2011)	0.725	0.172	0.238
Arslan (2014)	0.833	0.098	0.118

The equations proposed by Sharma (1986), RILEM (2003) and Yakoub (2011) (Eq. $(4.10)_2$) underestimate the ultimate shear strengths of test specimens involved in this study, whereas the ones proposed by Narayanan and Darwish (1987), Ashour *et al.* (1992) (Eq. $(4.3)_1$), Imam *et al.* (1997), Kwak *et al.* (2002) and Gandomi *et al.* (2011) largely overestimate the experimental values. It is observed from the statistics given in Table 4 that the equation proposed by Yakoub (2011) (Eq. $(4.10)_2$) and Arslan (2014) provide the most accurate predictions for the specimens involved in this study, where as the predictions of the equation of Arslan (2014) are slightly better. The ratios of the experimental values to the corresponding predictions of the equation of Arslan (2014) have a mean value of 0.833 with the lowest coefficient of variation equal to 0.118.

4.3. The equations for diagonal cracking strength

Narayanan and Darwish (1987) proposed an empirical equation for predicting the diagonal cracking strength as

$$v_{cr} = 0.24 f_{sp} + 20\rho\frac{d}{a} + 0.5F \tag{4.14}$$

Kwak *et al.* (2002) proposed an equation by following a procedure similar to the one followed for developing Eqs. (4.7) and (4.8) as

$$v_{cr} = 3\sqrt[3]{f_{sp}^2}\sqrt[3]{\rho\frac{d}{a}} \tag{4.15}$$

The equation proposed by Arslan (2014) and given in Eq. (4.13) has been modified by introducing a strength reduction factor of 0.6, which was obtained through a regression analysis undertaken to identify the strength reduction factor in calculating the diagonal cracking strength of SFRC slender beams without stirrups by using the results of existing experimental data. The resulting equation is

$$v_u = 0.6\Big(0.2\sqrt[3]{f_c^2}3\frac{c}{d} + \sqrt{\rho(1+4F)f_c}\Big)\sqrt[3]{\frac{3}{a/d}} \tag{4.16}$$

4.4. The predictions for diagonal cracking strength

The diagonal cracking strengths of test specimens containing steel fibers excluding A4.5F3.0 that failed in flexure have been predicted by using Eqs. (4.14)-(4.16). The mean value, standard deviation and coefficient of variation of the ratios of the experimental values to the corresponding predictions are given in Table 5. It is observed from Table 5 that Eq. (4.16) performed better in predicting the diagonal cracking strengths of the considered test specimens than the other equations do. The ratios of the experimental values to the corresponding predictions obtained from Eq. (4.16) have a mean value of 1.032 with the lowest coefficient of variation equal to 0.079.

Table 5. Statistics of the ratios of the experimental values to the predictions

The model	MV	SD	COV
Eq. (4.16)	1.032	0.082	0.079
Narayanan and Darwish (1987)	0.899	0.166	0.185
Kwak *et al.* (2002)	1.102	0.131	0.119

5. Conclusion

An experimental study has been conducted to investigate shear strength characteristics of low- and normal-strength SFRC slender beams without stirrups. The fact that the use of steel fibers improves the ultimate shear strength, diagonal cracking strength and ductility significantly is justified based on the following observations.

- The use of steel fibers with volume fractions of 1.0% and 2.0% increased the ultimate shear strength by 9% and 23%, respectively, in the case of a shear span-to-effective depth ratio of 2.5 and by 5% and 37%, respectively, in the case of a shear span-to-effective depth ratio of 3.5.
- The use of steel fibers in an amount of 3.0% was not able to change the failure mode of test specimens with a shear span-to-effective depth ratio of either 2.5 or 3.5, but it made the beam with a shear span-to-effective depth ratio of 4.5 fail in flexure instead of shear. However, it is to be noted that 3.0% may not be a practical volume fraction in the context of workability of a concrete mix. The use of steel fibers with a limited amount of stirrups can be a more practical way to modify the failure mode.
- The ratio of the ultimate shear strength to the diagonal cracking strength increased with the volume fraction of steel fibers up to 2.0% for all series of beams.
- The diagonal cracking strength decreased with the increasing shear span-to-effective depth ratio, which eventually affected the ultimate shear strength. This implies that it is essential to consider the effect of shear span-to-effective depth ratio in predicting the shear strength of SFRC beams.
- The use of steel fibers increased the deflection capacities significantly in all cases.

Besides the experimental study, the ultimate shear strengths and diagonal cracking strengths of SFRC beams involved in the experimental study were predicted by various equations available in the literature. Among the fifteen equations considered for predicting the ultimate shear strength of SFRC beams without stirrups, the equation proposed by Arslan (2014) had the best performance. The equation of Arslan (2014) was modified to predict the diagonal cracking strengths of SFRC beams involved in this study by introducing a strength reduction factor equal to 0.6. The modified equation had a better performance than those of the other two considered equations. Since the number of test specimens was limited, the modified version of the equation of Arslan (2014) should be verified with more data.

References

1. ACI (American Concrete Institute), 1988, *ACI 544.4R-88: Design Considerations for Steel Fiber Reinforced Concrete (Reapproved 1999)*, ACI, Farmington Hills, MI, USA
2. ACI, 1996, *ACI 544.1R-96: State-of-the-Art Report on Fiber Reinforced Concrete (Reapproved 2009)*, ACI, Farmington Hills, MI, USA
3. ACI, 2014, *ACI 318-14: Building Code Requirements for Structural Concrete and Commentary*, ACI, Farmington Hills, MI, USA
4. Aoude H., Belghiti M., Cook W.D., Mitchell D., 2012, Response of steel fiber-reinforced concrete beams with and without stirrups, *ACI Structural Journal*, **109**, 3, 359-367
5. Arslan G., 2008, Cracking shear strength of RC slender beams without web reinforcement, *Journal of Civil Engineering and Management*, **14**, 3, 177-182
6. Arslan G., 2012, Diagonal tension failure of RC beams without stirrups, *Journal of Civil Engineering and Management*, **18**, 2, 217-226
7. Arslan G., 2014, Shear strength of steel fiber reinforced concrete (SFRC) slender beams, *KSCE Journal of Civil Engineering*, **18**, 2, 587-594
8. Arslan G., Polat Z., 2013, Contribution of concrete to shear strength of RC beams failing in shear, *Journal of Civil Engineering and Management*, **19**, 3, 400-408
9. Ashour S.A., Hasanain G.S., Wafa F.F., 1992, Shear behavior of high-strength fiber reinforced concrete beams, *ACI Structural Journal*, **89**, 2, 176-184
10. Batson G., Jenkins E., Spatney R., 1972, Steel fibers as shear reinforcement in beams, *ACI Journal Proceedings*, **69**, 10, 640-644
11. Bazant Z.P., Kim J.K., 1984, Size effect in shear failure of longitudinally reinforced beams, *ACI Journal Proceedings*, **81**, 5, 456-468
12. Bazant Z.P., Sun H.H., 1987, Size effect in diagonal shear failure: influence of aggregate size and stirrups, *ACI Materials Journal*, **84**, 4, 259-272
13. CSA (Canadian Standard Association), 2004, *CSA A23.3-04: Design For Concrete Structures*, Toronto, ON, Canada
14. Cucchiara C., La Mendola L., Papia M., 2004, Effectiveness of stirrups and steel fibres as shear reinforcement, *Cement and Concrete Composites*, **26**, 7, 777-786
15. Ding Y., You Z., Jalali S., 2011, The composite effect of steel fibres and stirrups on the shear behaviour of beams using self-consolidating concrete, *Engineering Structures*, **33**, 1, 107-117
16. Dinh H.H., Parra-Montesinos G.J., Wight J.K., 2010, Shear behavior of steel fiber-reinforced concrete beams without stirrup reinforcement, *ACI Structural Journal*, **107**, 5, 597-606
17. Dinh H.H., Parra-Montesinos G.J., Wight J.K., 2011, Shear strength model for steel fiber reinforced concrete beams without stirrup reinforcement, *ASCE Journal of Structural Engineering*, **137**, 10, 1039-1051
18. Dupont D., Vandewalle L., 2003, Shear capacity of concrete beams containing longitudinal reinforcement and steel fibers, *ACI Special Publication*, **216**, 6, 79-94
19. Gandomi A.H., Alavi A.H., Yun G.J., 2011, Nonlinear modeling of shear strength of SFRC beams using linear genetic programming, *Structural Engineering and Mechanics*, **38**, 1, 1-25
20. Imam M., Vandewalle L., Mortelmans F., 1994, Shear capacity of steel fiber high-strength concrete beams, *SP-149: Proceedings of the ACI International Conference on High Performance Concrete*, Singapore
21. Kadir M.R.A., Saeed J.A., 1986, Shear strength of fiber reinforced concrete beams, *Engineering and Technology Journal, The Scientific Journal of the University of Technology*, **4**, 3, 98-112

22. Khuntia M., Stojadinovic B., Goel S.C., 1999, Shear strength of normal and high-strength fiber reinforced concrete beams without stirrups, *ACI Structural Journal*, **96**, 2, 282-289

23. Kwak Y.K., Eberhard M.O., Kim W.S., Kim J., 2002, Shear strength of steel fiber-reinforced concrete beams without stirrups, *ACI Structural Journal*, **99**, 4, 530-538

24. Li V.C., Ward R., Hamza A.M., 1992, Steel and synthetic fibers as shear reinforcement, *ACI Materials Journal*, **89**, 5, 499-508

25. Lim T.Y., Paramasivam P., Lee S.L., 1987, Shear and moment capacity of reinforced steel-fiber-concrete beams, *Magazine of Concrete Research*, **39**, 140, 148-160

26. Mansur M.A., Ong K.C.G., Paramasivam P., 1986, Shear strength of fibrous concrete beams without stirrups, *ASCE Journal of Structural Engineering*, **112**, 9, 2066-2079

27. Minelli F., Plizzari G.A., 2013, On the effectiveness of steel fibers as shear reinforcement, *ACI Structural Journal*, **110**, 3, 379-390

28. Minelli F., Conforti A., Cuenca E., Plizzari G.A., 2014, Are steel fibres able to mitigate or eliminate size effect in shear?, *Materials and Structures*, **47**, 3,459-473

29. Narayanan R., Darwish I.Y.S., 1987, Use of steel fibers as shear reinforcement, *ACI Structural Journal*, **84**, 3, 216-227

30. Noghabai K., 2000, Beams of fibrous concrete in shear and bending: experiment and model, *ASCE Journal of Structural Engineering*, **126**, 2, 243-251

31. Parra-Montesinos G.J., 2006, Shear strength of beams with deformed steel fibers, *Concrete International*, **28**, 11, 57-66

32. Parra-Montesinos G.J., Wight J.K., Dinh H.H., Libbrecht A., Padilla C., 2006, *Shear Strength of Fiber Reinforced Concrete Beams without Stirrups*, Report No. UMCEE 06-04, University of Michigan, Ann Arbor, MI, USA

33. RILEM, 2003, RILEM TC 162-TDF: Test and design methods for steel fibre reinforced concrete, stress-strain design method: final recommendation, *Materials and Structures*, **36**, 8, 560-567

34. Rosenbusch J., Teutsch M., 2002, *Trial Beams in Shear*, Brite/Euram Project 97-4163, Final Report, Sub Task 4.2., Technical University of Braunschweig, Germany

35. Sahoo D.R., Sharma A., 2014, Effect of steel fiber content on behavior of concrete beams with and without stirrups, *ACI Structural Journal*, **111**, 5, 1157-1166

36. Sahoo D.R., Maran K., Kumar A., 2015, Effect of steel and synthetic fibers on shear strength of RC beams without shear stirrups, *Construction and Building Materials*, **83**, 150-158

37. Sharma A.K., 1986, Shear strength of steel fiber reinforced concrete beams, *ACI Journal Proceedings*, **83**, 4, 624-628

38. Shoaib A., Lubell A.S., Bindiganavile V.S., 2014, Size effect in shear for steel fiber-reinforced concrete members without stirrups, *ACI Structural Journal*, **111**, 5, 1081-1090

39. Singh B., Jain K., 2014, An appraisal of steel fibres as minimum shear reinforcement in concrete beams, *ACI Structural Journal*, **111**, 5, 1191-1202

40. Swamy R.N., Jones R., Chiam A.T.P., 1993, Influence of steel fibers on the shear resistance of lightweight concrete I-beams, *ACI Structural Journal*, **90**, 1, 103-114

41. Uomoto T., Weerarathe R.K., Furukoshi H., Fujino H., 1986, Shear strength of reinforced concrete beams with fiber reinforcement, *Proceedings: Third International RILEM Symposium on Developments in Fiber Reinforced Cement and Concrete*, Sheffield, England, July, 313-325.

42. Yakoub H.E., 2011, Shear stress prediction: steel fiber-reinforced concrete beams without stirrups, *ACI Structural Journal*, **108**, 3, 304-314

43. Zsutty T., 1971, Shear strength prediction for separate categories of simple beam tests, *ACI Journal Proceedings*, **68**, 2, 138-143

Manuscript received January 19, 2017; accepted for print May 9, 2017

JOURNAL OF THEORETICAL AND APPLIED MECHANICS
55, 4, pp. 1219-1233, Warsaw 2017
DOI: 10.15632/jtam-pl.55.4.1219

EXPERIMENTAL AND NUMERICAL ANALYSIS OF ALUMINUM ALLOY AW5005 BEHAVIOR SUBJECTED TO TENSION AND PERFORATION UNDER DYNAMIC LOADING

Amine Bendarma
Poznan University of Technology, Institute of Structural Engineering, Poznań, Poland, and Universiapolis, Ecole Polytechnique d'Agadir Bab Al Madina, Qr Tilila, Agadir, Morocco
e-mail: b.amine@e-polytechnique.ma

Tomasz Jankowiak, Tomasz Łodygowski
Poznan University of Technology, Institute of Structural Engineering, Poznań, Poland
e-mail: tomasz.jankowiak@put.poznan.pl; tomasz.lodygowski@put.poznan.pl

Alexis Rusinek
Laboratory of Mechanics, Biomechanics, Polymers and Structures (LaBPS), National Engineering School of Metz (ENIM), Metz, France; e-mail: alexis.rusinek@univ-lorraine.fr

Maciej Klósak
Universiapolis, Ecole Polytechnique d'Agadir Bab Al Madina, Qr Tilila, Agadir, Morocco, and The International University of Logistics and Transport in Wrocław, Poland
e-mail: klosak@e-polytechnique.ma

The paper describes mechanical behavior of aluminum alloy AW5005 (EN AW5005) under impact loading. The work is focused on tensile tests and the process of perforation of aluminum alloy AW5005 sheets. Experimental, analytical and numerical investigations are carried out to analyse in details the perforation process. Based on these approaches, ballistic properties of the structure impacted by a conical nose shape projectile are studied. Different failure criteria are discussed, coupling numerical and experimental analyses for a wide range of strain rates. Optimization method functions are used to identify the parameters of the failure criteria. Finally, good correlation is obtained between the numerical and experimental results for both tension and perforation tests.

Keywords: aluminum alloy, AW5005, ballistic behavior, failure criterion

1. Introduction

In this paper, a study on aluminum alloy AW5005 behavior is reported. This alloy contains nominally 0.8% magnesium and it presents a medium strength, good weldability and good corrosion resistance in marine atmospheres. The metallurgical state of the aluminum alloy used in this work is as received. It has a lower density and an excellent thermal conductivity compared to other aluminum alloys. It is the most commonly used type of aluminum in sheet and plate forms (Kulekci, 2014).

The ballistic behavior and resistance of aluminum sheet plates is strongly dependent on the material behavior under dynamic loading. The ballistic properties of the structure are intensely related to the material behavior and to the interaction between the projectile and a thin aluminum target during the perforation process. Therefore, to find expected curves, many dynamic constitutive relations have been studied in several works. For instance, Johnson and Cook (1983) proposed a dynamic constitutive relation based on a phenomenological approach. The model has

been often used in impact and perforation problems analysis. Verleysen *et al.* (2011) investigated the effect of strain rate on the forming behavior of sheet metals and described stress-strain curves of the material using the Johnson-cook model. Erice *et al.* (2014) presented a coupled elastoplastic-damage constitutive model to simulate the failure behavior of inconel plates. Rusinek and Rodríguez-Martínez (2009) provided two extensions of the original Rusinek-Klepaczko constitutive relation (Rusinek and Klepaczko, 2001) in order to define the behavior of aluminum alloys at wide ranges of strain rates and temperatures showing a negative strain rate sensitivity. Børvik *et al.* (2009) studied the influence of a modified Johnson-Cook constitutive relation using numerical simulations of steel plate perforation. Jankowiak *et al.* (2013) considered perforation of different configurations: mild steel and sandwich plates. The effectiveness of these kinds of structures was checked. The authors also presented the effect of strain rate sensitivity models (Johnson-Cook and Rusinek-Klepaczko) on the ballistic curve. Additionally, several effects were considered: strain hardening, yield stress and projectile mass. Based on these results, it was possible to optimize the structure and find the right plate thickness to prevent its perforation. The sandwich configuration containing two sheets of steel is less efficient than a monolithic steel sheet of an equivalent total thickness. It was proven that thickness of the target had an important effect on the ballistic performance. This analysis can be used for the present AW5005 structure optimization. Kpenyigba *et al.* (2013) and Rusinek *et al.* (2008) studied the influence of the projectile nose shape (conical, blunt and hemispherical) and the projectile diameter on ballistic properties and failure modes of thin steel targets. In order to simulate the behavior of impacted and perforated structures, the finite element method with an explicit time integration procedure was an effective technique (Kpenyigba *et al.*, 2013; Rusinek *et al.*, 2008; Rusinek and Rodríguez-Martínez, 2008; Quinney and Taylor, 1937; Xue and Belytschko, 2010). Numerical simulations, in particular by the FE method, are also effective supplements for theoretical and experimental investigations which were carried out to analyze the dynamic behavior of impacted structures.

In order to determine mechanical characteristics of the material in quasi-static conditions, tensile tests have been carried out according to the methodology discussed in (Zhong *et al.*, 2016).

2. Experimental approach

There are little references about this material, especially concerning mechanical properties of this specific aluminum alloy. However, Kulekci (2014) published that the yield strength is equal to 45 MPa and the tensile strength is 110 MPa. Additionally, it is described that the elongation of this alloy is close to 15%. In the present paper, a tensile test is used to calibrate the material behavior. The specimen is machined from a 1.0 mm thickness aluminum sheet. The dimensions of the specimen are presented in Fig. 1. Additionally, the perforation test is used to describe ballistic properties of the material and failure modes for the conical projectile nose shape see Fig. 4. Compression using a sandwich specimen (Zhong *et al.*, 2015) and shear tests (Rusinek and Klepaczko, 2001; Bao and Wierzbicki, 2004) also reports for this material but it is out of scope of this analysis.

2.1. Tensile test

Quasi-static uniaxial tensile tests of AW5005 aluminum have been performed using a conventional hydraulic machine. The dimensions of the flat dumbbell-shaped specimen are shown in Fig. 1 (Zhong *et al.*, 2016). The first part of the specimen is embedded on 40 mm while the other end of the specimen is fixed to the mobile crosshead. The loading force and the displacement are recorded during the tests for the imposed velocity.

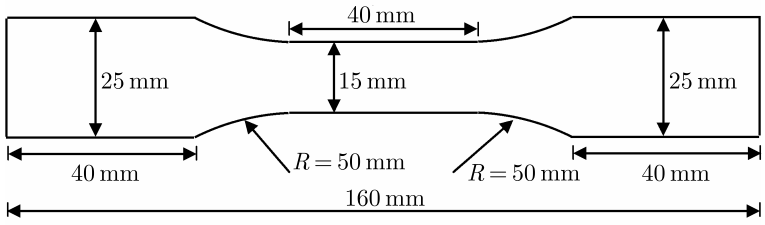

Fig. 1. Dimensions of the tensile specimens

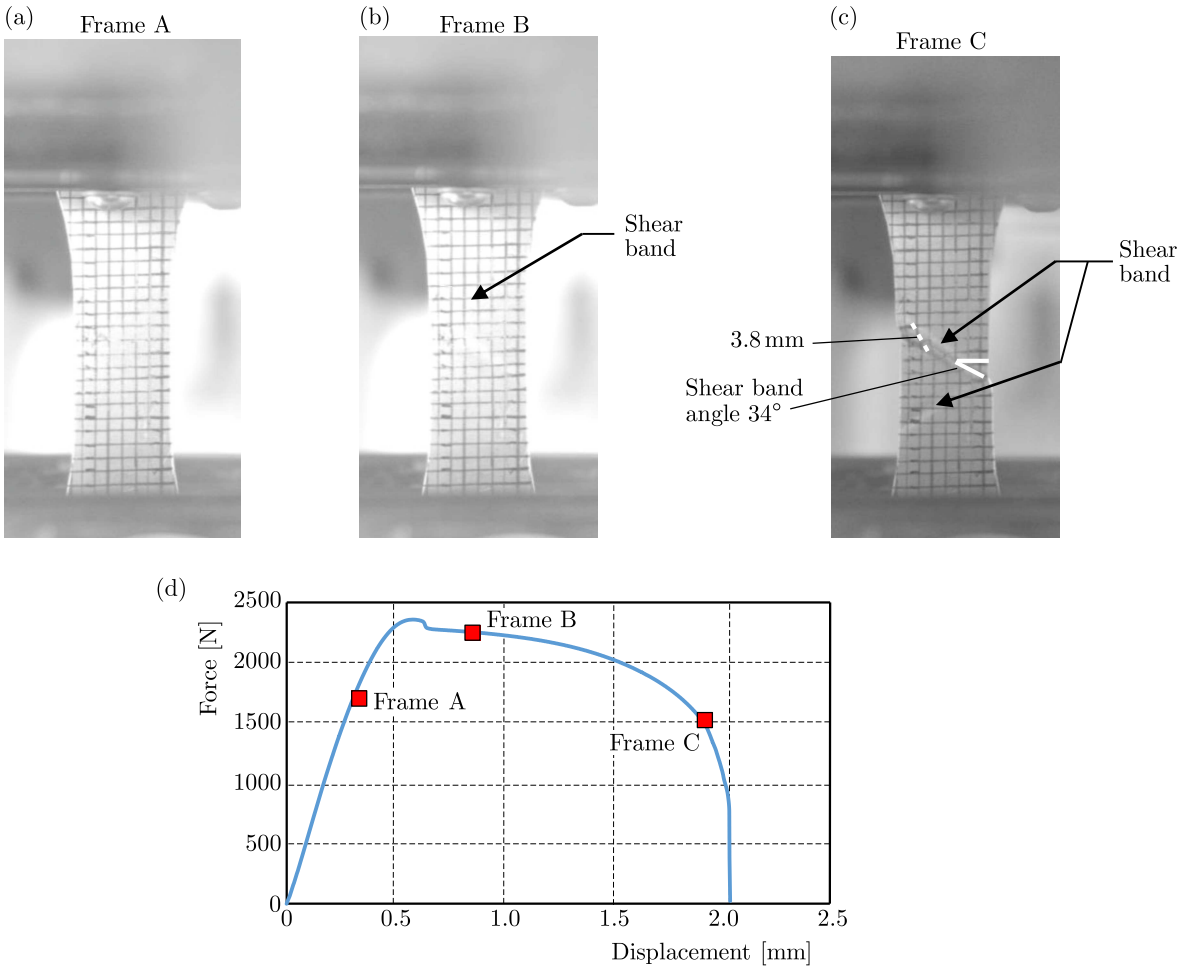

Fig. 2. Description of kinematic failure for three selected time points: (a) homogeneous deformation, elastic part, (b) strain localization $\varepsilon = 0.015$, (c) shear band before failure $\varepsilon = 0.045$, (d) force versus displacement curve for strain rate of $0.001\,\mathrm{s}^{-1}$

During the tests, an inclined fracture plane occurs along thickness of the specimens and a shear failure zone is observed along the oblique direction as Fig. 2 shows. The shear fracture is the main failure mode for AW5005 aluminum alloy subjected to quasi-static tension. A camera has been used to investigate the specimen behavior during quasi-static tensile tests. The results are given in Fig. 2 for a strain rate equal to $0.001\,\mathrm{s}^{-1}$. A set of perpendicular lines is drawn on the specimen surface with a gap of 2.25 mm between them. The tension process is recorded to estimate local deformation along the specimen loaded in tension. The failure process is presented together with the force displacement curve in Fig. 2. The analysis of the three frames A, B and C has allowed one to report the failure development of the specimen. On the frame A, the tensile process starts and the force is increasing together with the displacement. By coupling

the force and displacement measurements obtained using the hydraulic machine and the displacement observed from the camera measurement, the behavior can be defined. After the force reaches the maximum level, the process of tensile plastic strains localization starts as reported on the frame B. Finally, the plastic strain localizes, see the frame C. If the local critical failure strain is reached, a crack is formed and the measured force decreases to zero. Using local strain measurements, it is observed that the local nominal strains before the failure is close to 0.55 compared to the global strain which equals 0.1.

The quasi-static tensile tests are performed for four different strain rates, i.e. 0.001, 0.01, 0.1 and 0.15 s^{-1}. The resulting stress-strain curves are presented in Fig. 3. The experimental tests show that there is no strain rate sensitivity for aluminum alloy AW5005 behavior in the range of the strain rate used, but there is a significant difference in terms of ductility. The macroscopic true strains values at failure varies from 0.042 to 0.1. It is also observed that the ductility increases with the strain rate, Fig. 3. It shows that the average yield strength of the AW5005 aluminum is close to 147 MPa.

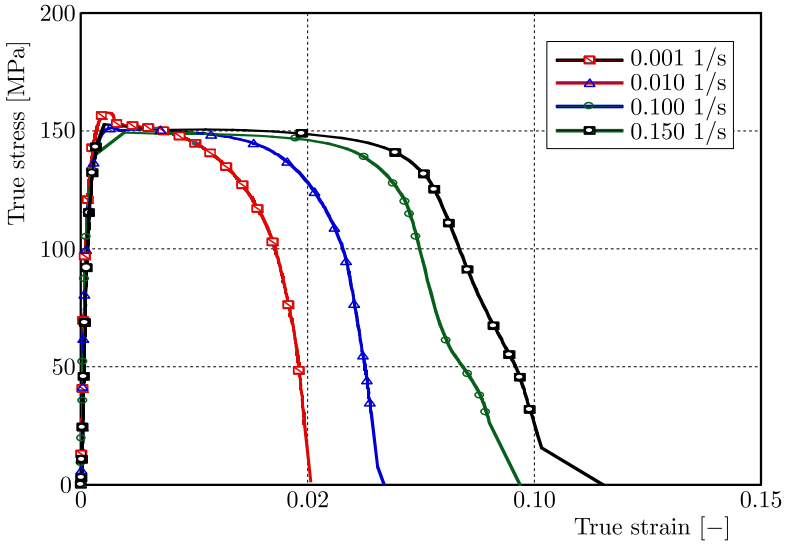

Fig. 3. Stress-strain curves for different strain rates at room temperature, aluminum AW5005

2.2. Perforation test

This part describes the mechanical behavior of aluminum sheets under impact loading. Experimental, analytical and numerical investigations have been carried out to analyze in details the perforation process (Kpenyigba *et al.*, 2013). A wide range of impact velocities from 40 to 180 m/s has been covered during the tests. A conical projectile with an angle of 72° has 13 mm in diameter and the plate is 1.0 mm thick. The active part of the specimen during perforation is presented in Fig. 4.

The projectile is launched using a pneumatic gas gun, it accelerates in the tube to reach the initial impact velocity V_0. Then, the projectile impacts the alumium sheet with partial or complete perforation depending on quantity of kinetic energy delivered to the tested plate. At the end, the residual velocity V_R of the projectile is measured after the projectile perforates the plate. Laser sensors are used to measure the initial velocity and a laser barrier for the residual velocities of the projectile during perforation. The projectile mass m_p is 28 g. The material used for machining the projectile is maraging steel with heat treatment to reach the yield stress of the projectile of 2 GPa. Therefore, the projectile is assumed as rigid during the perforation process (Kpenyigba *et al.*, 2013). The results in terms of the ballistic curve V_R-V_0 are reported in Fig. 5a.

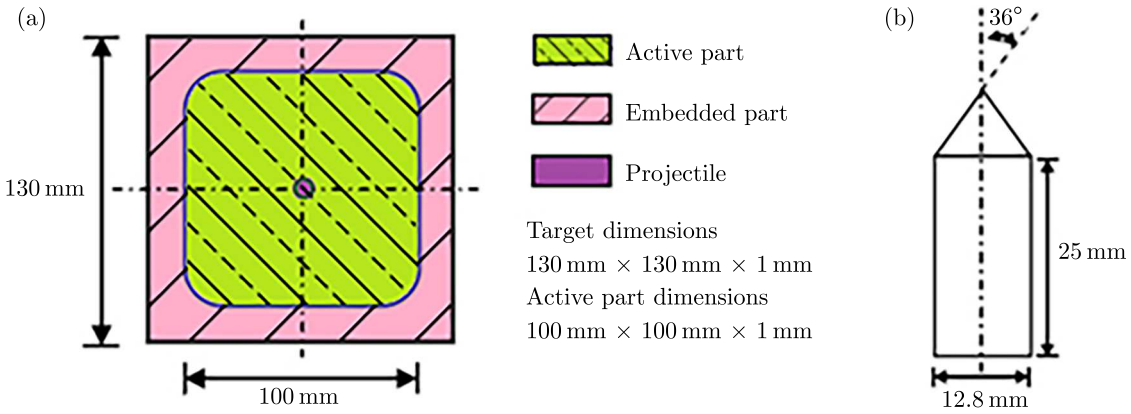

Fig. 4. Dimensions of the projectile and target used during perforation tests

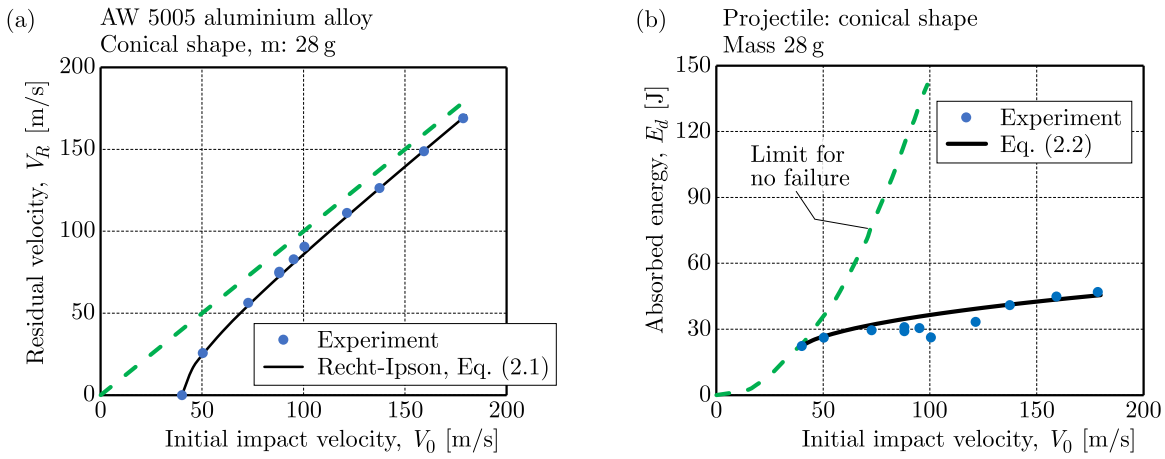

Fig. 5. (a) Ballistic curve obtained during perforation and determination of ballistic limit, (b) energy absorbed by plate during impact test, determination of failure energy

The residual velocity of the projectile can be calculated using the following equation proposed by Recht and Ipson (1963)

$$V_R = (V_0^\kappa - V_B^\kappa)^{\frac{1}{\kappa}} \tag{2.1}$$

where V_0 is the initial velocity and V_B is the ballistic velocity. In the above equation, the constants V_B is equal to 40 m/s, and κ is the ballistic curve shape parameter equal to 1.65.

The energy absorbed by the plate E_d can be calculated using the following equation

$$E_d = \frac{m_P}{2}(V_0^2 - V_R^2) \tag{2.2}$$

The difference of the initial and residual kinetic energy can be calculated using the experimental data, then based on the Recht-Ipson approximation, the energy absorbed by the plate can be calculated, see Fig. 5b. Using Eq. (2.2), the minimum energy to perforate is 28 J ($m_P = 28$ g and $V_0 = V_B = 40$ m/s).

In Fig. 6, for the initial impact velocity of $V_0 = 85$ m/s, the failure pattern is presented with four petals for the residual velocity of $V_R = 66.5$ m/s. The same failure is observed for $V_0 = 132.3$ m/s with $V_R = 120.2$ m/s, respectively. The number of petals is equal to 4 in the whole range of impact velocities, i.e. from 40 to 180 m/s. A complete description concerning the number of petals depending on the projectile shape and the failure mode was published and discussed in details in (Atkins and Liu, 1998).

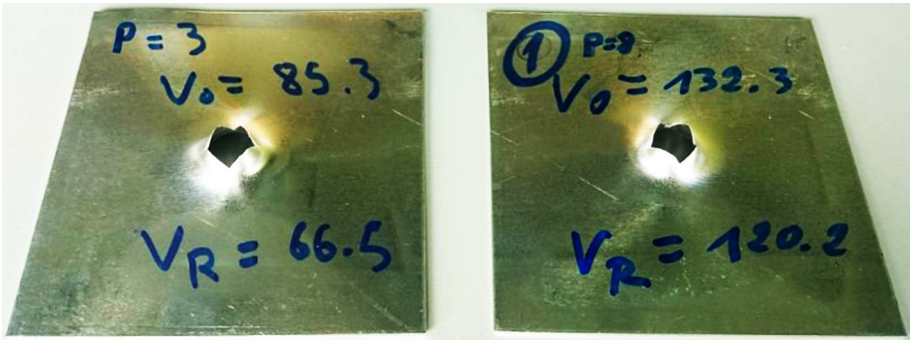

Fig. 6. Experimental observation of failure patterns, $V_0 = 85.3\,\mathrm{m/s}$ and $132.3\,\mathrm{m/s}$

3. Johnson-Cook material model

Using experimental tests, the parameters of the Johnson-Cook (JC) model (Johnson and Cook, 1983) have been identified and used to simulate tension and perforation tests. The thermo--viscoplastic behavior of AW5005 aluminum alloy is defined as follows

$$\sigma = (A + B\varepsilon_{pl}^{n})\Big(1 + C\ln\frac{\dot{\varepsilon}_{pl}}{\dot{\varepsilon}_0}\Big)(1 - T^{*m}) \tag{3.1}$$

where A is the yield stress, B and n are strain hardening coefficients, C is the strain rate sensitivity coefficient, $\dot{\varepsilon}_0$ is the strain rate reference value and m is the temperature sensitivity parameter. In this work, isothermal conditions are assumed. Therefore, the last term of the JC model related to the non-dimensional temperature T^* is not considered. All numerical simulations are done at room temperature $T = 300\,\mathrm{K}$.

The material constants are obtained by experimental tests. The parameter C has been calculated using the presented experimental tests for a quasi-static loading (strain rates from 0.001 to $0.15\,\mathrm{s}^{-1}$). In this range small strain rates sensitivity has been observed. The optimization using the minimum least square method gives the value of C equal to 0.003. These constants are shown in Table 1.

Table 1. Material parameters for the Johnson-Cook model

A [MPa]	B [MPa]	n [–]	C [–]
147	60	0.9	0.003

In order to define the material behavior completely, a failure criterion was proposed by Johnson and Cook (1985). When mixed with their classical constitutive law, Eq. (3.1), it enabled one to reflect failure modes of structures or materials.

The Johnson-Cook failure model is applied widely because of the simplicity of formulation. A number of material parameters that are available in literature were provided by Johnson and Holmquist (1989). However, Johnson and Cook only determined the positive range of the stress triaxiality based on some tensile tests and shear tests, and no small or negative values of stress triaxiality were expressed. In order to effectively apply the Johnson-Cook fracture model, researchers extended the model in different ways. Liu *et al.* (2014) proved that the Johnson-Cook fracture model can be used as damage initiation coupled with damage evolution in metal cutting simulations. Moreover, the damage evolution combines two different fracture modes effects.

In Fig. 7, the progressive damage model is used for aluminum alloy. The description includes the elastic part with E_0 (part *a*-*b*) and the plasticity range (*b*-*c*). The damage initiation with the JC criterion can be expressed by Eq. (3.2) (*c*). Along the line (*c*-*e*), the damage variable evolution grows from 0 to the maximum degradation ratio D_{max} (*d*), therefore, stiffness of the material is

degraded and reduced to $(1-D)E_0$ where D is the damage variable and E_0 is the initial Young modulus. The damage evolution is described by mesh-independent measurements (displacement at failure and damage energy dissipation) in the model. A linear evolution damage rule is used by defining a value of displacement at failure u_f (e). Thus, the maximum degradation of stiffness as well as the maximum damage have been taken finally as the failure criterion (d). The element after reaching the failure criterion is deleted from the mesh in simulation.

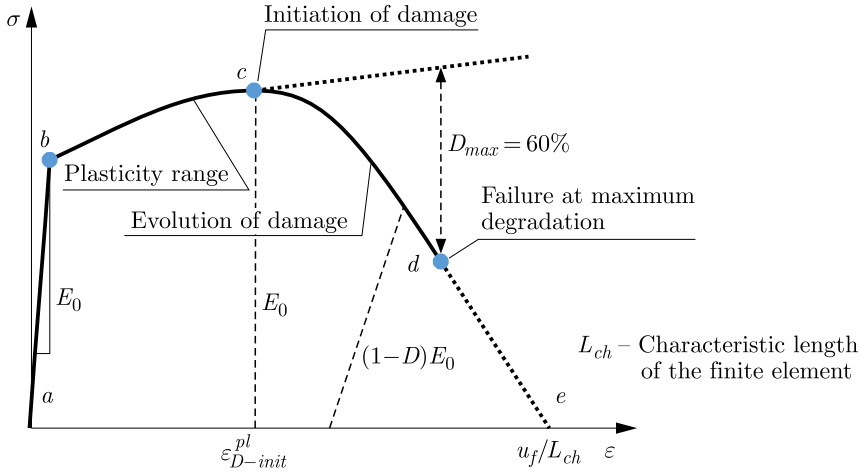

Fig. 7. Schematic representation of tensile test data in stress-displacement space for elastic-plastic materials (ABAQUS, 2011)

The Johnson-Cook damage initiation model (Johnson and Cook, 1985; Johnson and Holmquist, 1989) describes the strain at damage initiation $\varepsilon^{pl}_{D-init}$ including effects of the stress triaxiality, strain rate and temperature, as shown in the following equation

$$\varepsilon^{pl}_{D-init} = [d_1 + d_2 \exp(-d_3\eta)]\Big(1 + d_4 \ln\frac{\dot{\varepsilon}}{\dot{\varepsilon}_0}\Big)(1 + d_5 T^*) \tag{3.2}$$

where d_1, d_2, d_3, d_4, d_5 are material parameters, η is the stress triaxiality factor, $\dot{\varepsilon}_0$ is the reference strain rate and T^* is the non-dimensional temperature. The first bracket in Eq. (3.2) concerns the influence of the stress triaxiality factor on the value of strain at damage initiation $\varepsilon^{pl}_{D-init}$. The value of the first bracket decreases as the stress triaxiality factor increases. The second bracket represents the influence of the strain rate on that value, while the third one represents the effect of thermal softening.

Table 2. Failure parameters for tension and perforation

Test	Tensile test				Perforation test	
	1 ($0.001\,\mathrm{s}^{-1}$)	4 ($0.01\,\mathrm{s}^{-1}$)	3 ($0.1\,\mathrm{s}^{-1}$)	4 ($0.15\,\mathrm{s}^{-1}$)	$10^3\,\mathrm{s}^{-1}$	$10^4\,\mathrm{s}^{-1}$
Damage initiation strain $\varepsilon^{pl}_{D-init}$	0.008	0.03	0.08	0.12	0.9	0.96
Displacement at failure u_f	0.0008 m					
Max. degradation D_{max}	0.6					

By using those analytical approaches coupled to experiment results, the failure parameters have been deduced and used in the numerical model for both traction and perforation tests. They are presented in Table 2. The tensile test values are obtained from experiments, whereas the perforation test values are obtained using a numerical analysis and available literature data for similar materials (Jankowiak *et al.*, 2013, 2014; Kpenyigba *et al.*, 2013). The strain rates for perforation tests $\dot{\varepsilon} = 1000\,\mathrm{s}^{-1}$ and $\dot{\varepsilon} = 10000\,\mathrm{s}^{-1}$ correspond to initial impact velocities V_0 of 120 m/s and 180 m/s, respectively. They have been observed locally using numerical simulations.

4. Numerical approach

Numerical models are built using Abaqus/Explicit. The tests using this numerical model are conducted at different strain rates in quasi-static and dynamic conditions with impact velocities up to 180 m/s. The shell element type S4R with 8 degrees of freedom and 4 nodes with reduced integration (ABAQUS, 2011) have been used. The same element type with the element size of 0.5 mm×0.5 mm has been proposed for tension and perforation analysis as presented in Fig. 9a. The effectiveness of such elements for this type of analysis was previously proved by Ambati and Lorenzis (2016), Amiri *et al.* (2014), Elnasri and Zhao (2016).

In order to extend experimental results, some other thickness of the aluminum plate has been added for both tensile and perforation simulations, therefore, thicknesses of 1.0 mm and 1.5 mm have been used.

4.1. Modelling procedures of tensile and perforation tests

In order to verify the Johnson-Cook constitutive and failure models, tension and perforation tests have been simulated using Abaqus/Explicit version 6.14.

4.1.1. Tensile test

The aim of this numerical analysis has been to reproduce experimental results by checking the observed failure mode. The constitutive parameters have been identified based on the experimental tests. The constants are reported in Table 1. The number of elements used for meshing is 16356, and 16731 is the total number of nodes. The distribution of the equivalent plastic strains called PEEQ in Abaqus is presented in Fig. 8b.

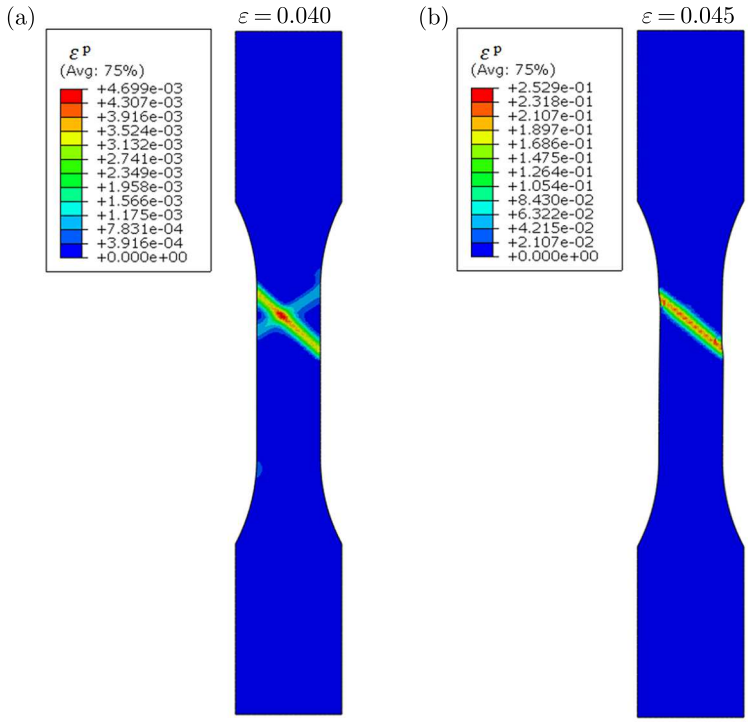

Fig. 8. Numerical simulation of tensile test, (a) equivalent plastic strain distribution for macroscopic strain equal to $\varepsilon = 0.04$, (b) equivalent plastic strain distribution for macroscopic strain $\varepsilon = 0.045$

The numerical simulations are in agreement with experimental observations where the failure mode is by shearing, see Fig. 2c.

4.1.2. Perforation test

The optimal mesh has been obtained using a convergence method (stability of the results without mesh dependency). The mesh is denser in the projectile-plate contact zone, thickness of the plate in this area is 1.0 mm and the velocity is defined in predefined fields with the range of impact velocities from 40 to 180 m/s as conceded in the experiment. This model contains 6048 elements in the central part of impact and 6161 using the same element size (0.5 mm×0.5 mm).

The ballistic curves are reported in the following Section and compared to the experimental results. The interior zone of the model allows one to initiate the process of crack propagation in a precise way. The projectile behavior has been defined as rigid, because a kinematic coupling constraint (rigid body) has been applied to avoid deformation of the projectile. The friction coefficient is assumed to be equal to 0.2.

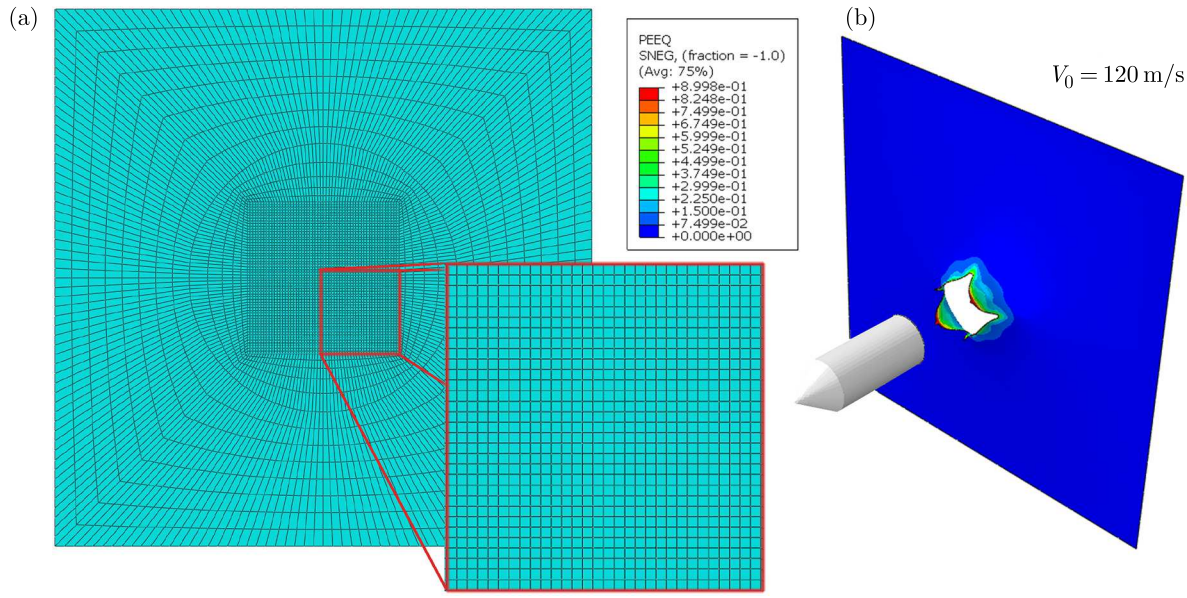

Fig. 9. Numerical model used during numerical simulations and mesh density distribution: (a) mesh, (b) equivalent plastic strain distribution for macroscopic strain ε

A decrease of the number of petals with a nose angle of 72° has been observed when the value of failure strain is changed. An analytical model for prediction of the number of petals proposed by Atkins and Liu (1998) has been used and confirmed by FE simulations.

4.2. Failure criterion model

4.3. Model I (Johnson-Cook model)

Using values illustrated in Table 2, the parameters are used to identify the Johnson-Cook damage initiation model. The triaxiality dependent part is neglected because the triaxiality in all cases is 1/3. The influence of temperature is also ignored since there is no effect on all strain rates captured by the temperature camera that have been used during the tests. The final equation used to determine the Johnson-Cook damage initiation strain $\varepsilon^{pl}_{D-init}$ as a function of strain rates $\dot{\varepsilon}$ corresponding to aluminum alloy is

$$\varepsilon^{pl}_{D-init} = [d_1]\Big[1 + d_4 \ln \frac{\dot{\varepsilon}}{\dot{\varepsilon}_0}\Big] \tag{4.1}$$

In order to determine the parameters d_1, d_4, an algorithm with Matlab optimization using Eq. (4.1) has been developed, and the adopted values are presented in Table 3.

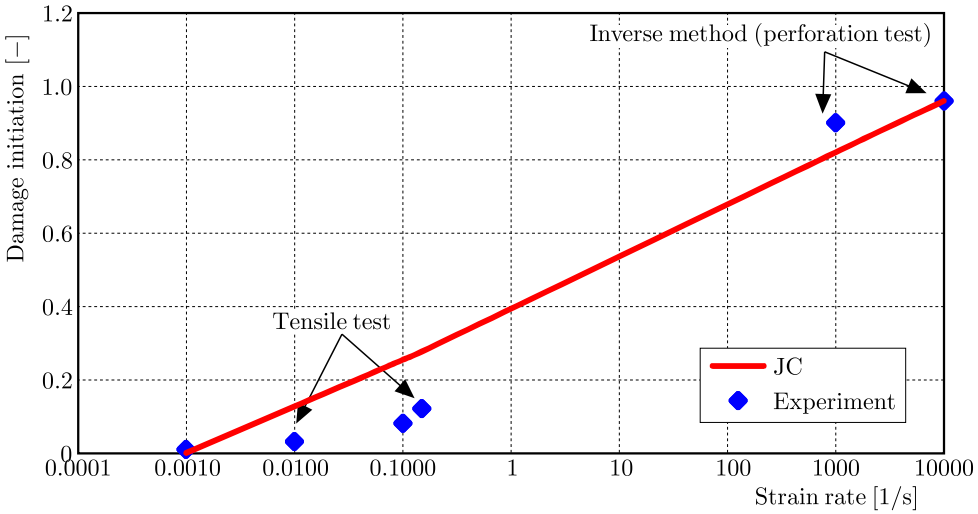

Fig. 10. Plot of damage initiation strain versus plastic strain rate using Model I JC), Eq. (4.1)

For tensile tests cases 2, 3 and 4, the damage initiation Johnson-Cook model gives too high values of the initial damage strain because it is linear in the interval of the strain rate. Finally, the global behavior in space stress-strain is too ductile, therefore, another approach has been proposed.

4.3.1. Failure modeling using optimized Model II

Another function has been proposed to better fit the damage initiation model. This function (Eq. (4.2)) contains three constants E, F and G to be determined by using an optimization algorithm. The constants are reported in Table 3

$$\varepsilon_{D-init}^{pl} = G\frac{\exp(E+F\dot{\varepsilon})}{1+\exp(E+F\dot{\varepsilon})} \tag{4.2}$$

As demonstrated in Fig. 11, there is a good correlation between the fitted curve, the experimental and numerical values, however, there is still a bit of miss-match between some points in the middle of the curve.

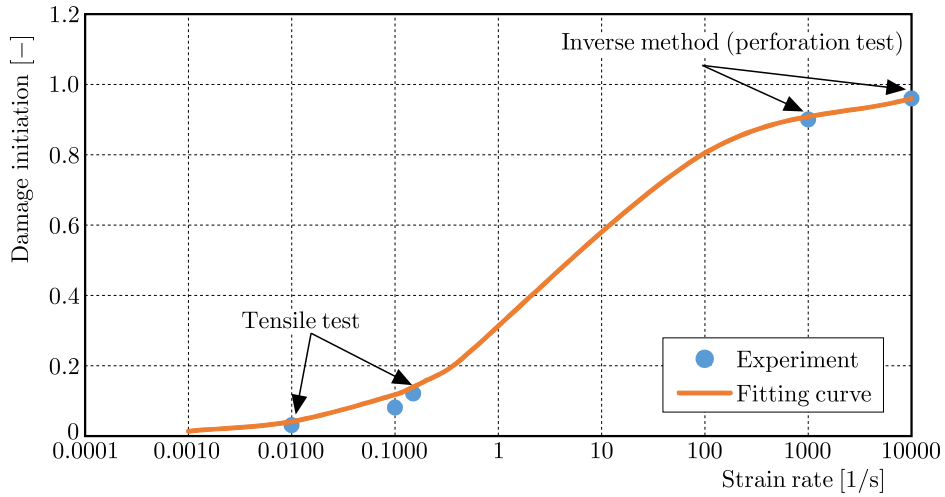

Fig. 11. Plot of damage initiation strain versus plastic strain rate using optimized Model II, Eq. (4.2)

4.3.2. Failure modeling using Model III

The next damage initiation criterion (Eq. (4.3)) is defined with two glued functions with four constants H, I, J and K. Using an optimization method, a good correlation in a wide range of strain rates is obtained (see Fig. 12)

$$\varepsilon^{pl}_{D-init} = \begin{cases} f(\dot{\varepsilon}) = H \exp(I \log_{10} \dot{\varepsilon}) & \text{if} \quad \dot{\varepsilon} \leqslant \dot{\varepsilon}_{transmition} \\ g(\dot{\varepsilon}) = J - K \exp(\log_{10} \dot{\varepsilon}) & \text{if} \quad \dot{\varepsilon} \geqslant \dot{\varepsilon}_{transmition} \end{cases} \tag{4.3}$$

The estimated constants are reported in Table 3 with $\dot{\varepsilon}_{transmition} = 1\,\mathrm{s}^{-1}$.

Table 3. Parameters for failure models

Model I (JC)		Model II			Model III			
d_1 [–]	d_4 [–]	E [–]	F [–]	G [–]	H [–]	I [–]	J [–]	K [–]
0.007	78.722	−0.89	1.13	1.0085	−0.398	1.4523	1.0085	0.6647

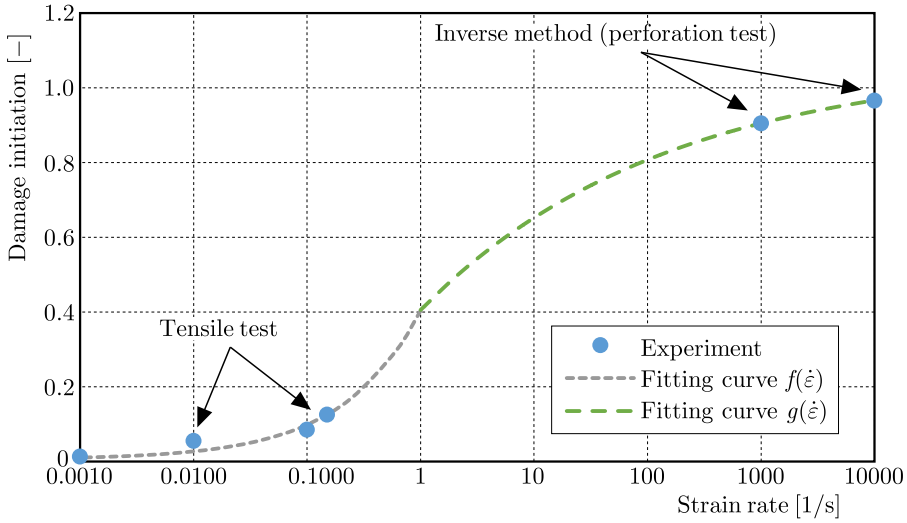

Fig. 12. Plot of failure strain versus plastic strain rate using optimized Model III

5. Comparison of numerical and experimental results

5.1. Tensile test comparisons

A comparison has been made between three initiation damage models using test number 3. As it is presented in Fig. 13, the best results are obtained with Model III. This is why this model has been adopted for an other analysis.

Initiation damage Model III has been implemented into the numerical model and then compared with the experimental data for different strain rates (0.001, 0.01, 0.1 and $0.15\,\mathrm{s}^{-1}$). The results are shown in Fig. 14.

As it might be seen in Fig. 15, there is a good correlation between the experimental and numerical results. In the case of test 3, the numerical model has demonstrated more ductile behavior at the failure start, whereas for test 4, it has revealed ductility at the terminal phase of failure.

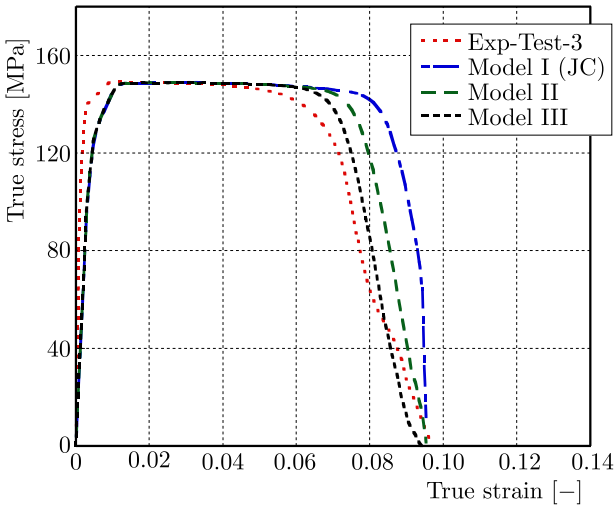

Fig. 13. Comparison between experimental and numerical curves using 3 failure criteria

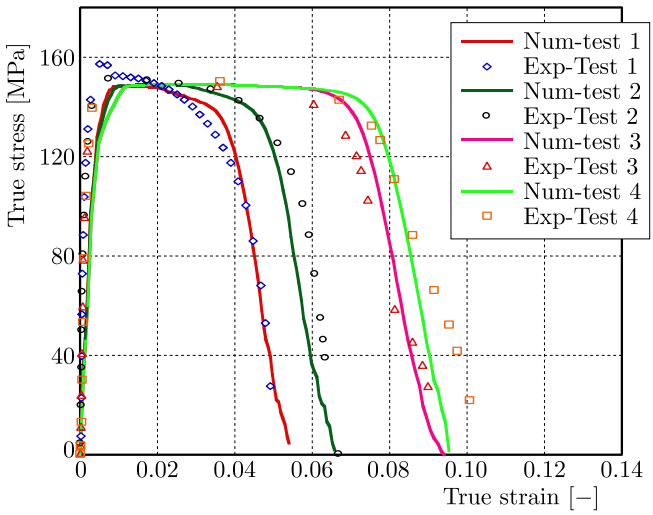

Fig. 14. Comparison between experimental and numerical curves using optimized initiation damage model (Model III)

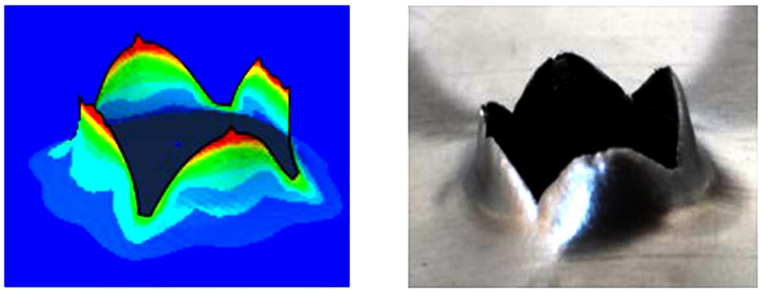

Fig. 15. Numerical result for conical projectile shape, $V_0 = 120\,\mathrm{m/s}$, comparison between experiments and simulations

5.2. Perforation test comparison

During this study, the same model (Model III) has been used to compare the numerical and experimental results in the dynamic field using the perforation process in Abaqus/Explicit with a wide range of impact velocities from 40 to 180 m/s and with target thicknesses of 1.0 and

1.5 mm. As it is shown in Fig. 15, the number of petals is the same as in the experiments, four petals are observed. It was reported in (Atkins and Liu, 1989; Landkof and Goldsmith, 1985) that the number of petals N observed during dynamic perforation coupled to a conical projectile shape was related to the nose angle ϕ. In this work, one angle (72°) has been used to analyze the results. In (Kpenyigba *et al.*, 2013) during the analysis of results it was observed that generally the number of petals N decreased when the projectile angle $\phi/2$ increased.

Figure 16 contains both the experimental and the numerical results of simulations with the same interval of velocity. Damage initiation criterion Model III has been used to verify the correlation between the numerical curve and the experiment. There is a good correlation between the experimental and numerical results which adds to the credibility of correctness of the failure criterion model. It can be observed that for thicker plates than 1.5 mm, the value of the ballistic limit is shifted from 40 m/s to 50 m/s.

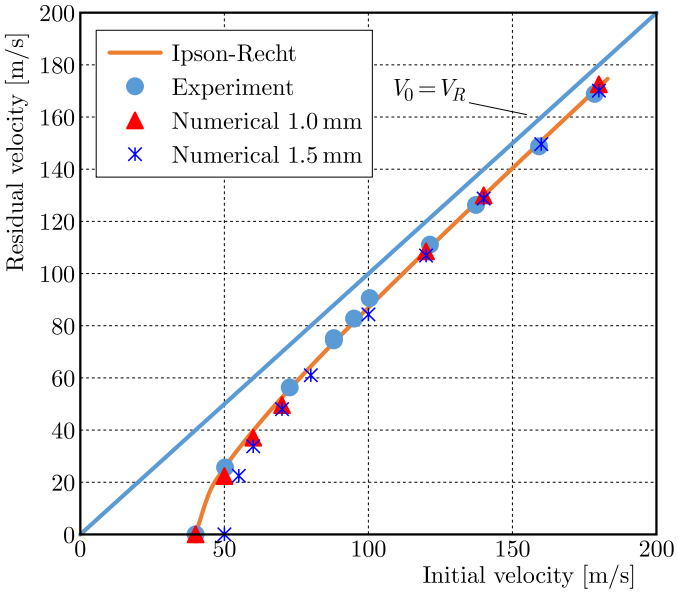

Fig. 16. The ballistic curve in experiment and in simulation

6. Conclusions

Mechanical characteristics of new aluminum alloy AW5005 have been investigated. The identification of material parameters has been done using the coupling of the simulation and experimental techniques. Additionally, three damage initiation criteria have been used in numerical modelling for both tension and perforation simulations. A good agreement has been observed between the experimental results and FE simulations in terms of the stress-strain curve and ballistic curves as well as the energy absorbed. It confirms the correctness of the damage initiation criterion.

The future work will investigate the behavior of a composite material in form of a sandwich structure with two plates of aluminum (AW5005) and one internal layer of polyethylene.

References

1. ABAQUS, Abaqus/Explicit User's Manuals, version 6.11, 2011
2. Ambati M., De Lorenzis L., 2016, Phase-field modeling of brittle and ductile fracture in shells with isogeometric NURBS-based solid-shell elements, *Computer Methods in Applied Mechanics and Engineering*, DOI: 10.1016/j.cma.2016.02.017

3. Amiri F., Millán D., Shen Y., Rabczuk T., Arroyo M., 2014, Phase-field modeling of fracture in linear thin shells, *Theoretical and Applied Fracture Mechanics*, **69**, 102-109

4. Atkins A.G., Liu J.H., 1998, Necking and radial cracking around perforations in thin sheets at normal incidence, *International Journal of Impact Engineering*, **21**, 521-539

5. Bao Y., Wierzbicki T., 2004, On fracture locus in the equivalent strain and stress triaxiality space, *International Journal of Mechanical Sciences*, **46**, 81-98

6. Børvik T., Hopperstad O.S., Langseth M., Malo K.A., 2003, Effect of target thickness in blunt projectile penetration of Weldox 460 E steel plates, *International Journal of Impact Engineering*, **28**, 413-464

7. Børvik T., Dey S., Clausen A.H., 2009, Perforation resistance of five different high-strength steel plates subjected to small-arms projectiles, *International Journal of Impact Engineering*, **36**, 948-964

8. Elnasri I., Zhao H., 2016, Impact perforation of sandwich panels with aluminum foam core: a numerical and analytical study, *International Journal of Impact Engineering*, **96**, 50-60

9. Erice B., Pérez-Martín M.J., Gálvez F., 2014, An experimental and numerical study of ductile failure under quasi-static and impact loadings of Inconel 718 nickel-base superalloy, *International Journal of Impact Engineering*, **69**, 11-24

10. Hancock J.W., Mackenzie A.C., 1976, On the mechanisms of ductile failure in high-strength steels subjected to multi-axial stress-states, *Journal of the Mechanics and Physics of Solids*, **24**, 147-160

11. Jankowiak T., Rusinek A., Kpenyigba K.M., Pesci R., 2014, Ballistic behavior of steel sheet subjected to impact and perforation, *Steel and Composite Structures*, **16**, 595-609

12. Jankowiak T., Rusinek A., Wood P., 2013, A numerical analysis of the dynamic behavior of sheet steel perforated by a conical projectile under ballistic conditions, *Finite Elements in Analysis and Design*, **65**, 39-49

13. Johnson G.R., Cook W.H., 1983, A constitutive model and data for metals subjected to large strains, high strain rates and high temperatures, *Proceedings of the 7th International Symposium on Ballistics*, **21**, 541-547

14. Johnson G.R., Cook W.H., 1985, Fracture characteristics of three metals subjected to various strains, strain rates, temperatures and pressures, *Engineering Fracture Mechanics*, **21**, 1, 31-48

15. Johnson G.R., Holmquist T.J., 1989, Test data and computational strength and fracture model constants for 23 materials subjected to large strains, high strain rates, and high temperatures. Los Alamos National Laboratory, Los Alamos, NM, Report No. LA-11463-MS

16. Kpenyigba K.M., Jankowiak T., Rusinek A., Pesci R., 2013, Influence of projectile shape on dynamic behavior of steel sheet subjected to impact and perforation, *Thin-Walled Structures*, **65**, 93-104

17. Kulekci M.K., 2014, Effect of the process parameters on tensile shear strength of friction stir spot welded aluminum alloy (EN AW5005), *Archives of Metallurgy and Materials*, **59**, 221-224

18. Landkof, B., Goldsmith, W., 1985, Petalling of thin, metallic plates during penetration by cylindro-conical projectiles, *International Journal of Solids and Structures*, **21**, 245-266

19. Liu J., Bai Y., Xu C., 2014, Evaluation of ductile fracture models in finite element simulation of metal cutting processes, *Journal of Manufacturing Science and Engineering*, **136**, 011010

20. Quinney H., Taylor G.I., 1937, The emission of the latent energy due to previous cold working when a metal is heated, *Proceedings of the Royal Society of London. Series A, Mathematical and Physical Sciences*, 157-181

21. Recht R.F., Ipson T.W., 1963, Ballistic perforation dynamics, *Journal of Applied Mechanics*, **30**, 384-390

22. Rusinek A., Klepaczko J.R., 2001, Shear testing of a sheet steel at wide range of strain rates and a constitutive relation with strain-rate and temperature dependence of the flow stress, *International Journal of Plasticity*, **17**, 87-115

23. Rusinek A., Rodríguez-Martínez J.A., 2009, Thermo-viscoplastic constitutive relation for aluminum alloys, modeling of negative strain rate sensitivity and viscous drag effects, *Materials and Design*, **30**, 4377-4390

24. Rusinek A., Rodríguez-Martínez J.A., Arias A., Klepaczko J.R., López-Puente J., 2008, Influence of conical projectile diameter on perpendicular impact of thin steel plate, *Engineering Fracture Mechanics*, **75**, 2946-2967

25. Verleysen P., Peirs J., Van Slycken J., Faes K., Duchene L., 2011, Effect of strain rate on the forming behaviour of sheet metals, *Journal of Materials Processing Technology*, **211**, 1457-1464

26. Zhong W.Z., Rusinek A., Jankowiak T., Abed F., Bernier R., Sutter G., 2015, Influence of interfacial friction and specimen configuration in Split Hopkinson Pressure Bar system, *Tribology International*, **90**, 1-14

27. Xue L., Mock W., Belytschko T., 2010, Penetration of DH-36 steel plates with and without polyurea coating, *Mechanics of Materials*, **42**, 981-1003

28. Zhong W.Z., Mbarek I.A., Rusinek A., Bernier R., Jankowiak T., Sutter G., 2016, Development of an experimental set-up for dynamic force measurements during impact and perforation, coupling to numerical simulations, *International Journal of Impact Engineering*, **91**, 102-115

Manuscript received January 3, 2017; accepted for print May 9, 2017

JOURNAL OF THEORETICAL AND APPLIED MECHANICS
55, 4, pp. 1235-1244, Warsaw 2017
DOI: 10.15632/jtam-pl.55.4.1235

ON THE CHOICE OF THICKNESS OF THE CEMENT MANTLE IN CEMENTED HIP ARTHROPLASTY

Ievgen Levadnyi

Lodz University of Technology, Department of Automation, Biomechanics and Mechatronics, Łódź, Poland
e-mail: evgenabaqus@gmail.com

Jan Awrejcewicz

Lodz University of Technology, Department of Automation, Biomechanics and Mechatronics, Łódź, Poland, and Warsaw University of Technology, Institute of Vehicles, Warszawa, Poland; e-mail: jan.awrejcewicz@p.lodz.pl

Alexander Loskutov

Dnipropetrovsk State Medical Academy, Department of Orthopaedics and Traumatology, Dnipropetrovsk, Ukraine
e-mail: loskutovae@ukr.net

Olga Szymanowska

Lodz University of Technology, Department of Automation, Biomechanics and Mechatronics, Łódź, Poland
e-mail: olga.szymanowska@p.lodz.pl

Recommendations for the optimal thickness of the cement mantle in cemented hip arthroplasty are outlined based on the results obtained with the finite element method. The investigations show that distal femur cement thickness higher than 2 mm positively affects mechanical behaviour of the cement mantle and can be useful in reducing stress-strain levels in the distal part of the femur what leads to prevention of development of a stress-shielding effect. The results of the study can contribute to the success of long-term implants.

Keywords: total hip replacement, bone cement, femur, stress state, finite elements method

1. Introduction

Nowadays, hip replacement is one of the most common and effective surgical methods for treatment of musculoskeletal system diseases and restoration of motion of the hip joint (Jenkins *et al.*, 2013). Since 1959, by virtue of the work of Sir John Charnley (Charnley, 1960), numerous researchers working on the fixation in arthroplasty have used bone cement to fasten implants. Such a fixation of the prosthesis is advantageous in the case of a wide medullary canal of femur, osteoporosis, bone dysplasia, and consequences of mechanical injuries of hip and has been also traditionally used for femoral revision (Sullivan *et al.*, 1994; Davis *et al.*, 2003; Warth *et al.*, 2014). Furthermore, cement fixation allows for a reduction of a rehabilitation period.

In the case of a cemented stem endoprosthesis of the hip joint, an important role is played by both strong bond between the implant surface and the bone cement as well as stable mechanical interaction between the cement and bone tissue. During the long-term use of the prosthesis, various difficulties, which can lead to aseptic loosening of the prosthesis and also to partial or complete loss of functionality of the whole system, occur (Huiskes, 1993; Bhambri and Gilbertson, 1995; Kroell *et al.*, 2009). The above-mentioned conditions are usually observed in patients who have an overly active lifestyle or suffer from osteoporosis and/or overweight. They may also occur if the implant is incorrectly installed or if thickness of the cement mantle is wrongly chosen (Gunn *et al.*, 2012), what results from low skills of a surgeon.

It is of particular importance to properly choose thickness of the cement mantle while implanting a hip joint endoprosthesis, since too thin cement mantle may contribute to cracking of the cement, which, in turn, may lead to aseptic loosening of the implant. The complete absence of the mantle may lead to wear of bone (the so-called stress shielding effect) due to micro friction. On the other hand, too thick cement mantle will poorly transfer the load to the bone, which can lead to the bone atrophy and lysis. Thus, correctly chosen thickness of the cement mantle and proper positioning of the stem of the hip joint endoprosthesis in the medullary canal should ensure a long-term implant success.

However, the optimal thickness of the cement mantle has not been defined. Typically, its selection is the surgeon's responsibility and depends on the surgeon experience (Shah and Porter, 2005). In this regard, the development of a biomechanical rationale for the choice of the optimal cement mantle thickness in the cemented hip replacement is a compelling and urgent task, which will improve the outcome of treatment and increase durability of the prosthesis.

Currently, numerical simulation (especially the finite element method (FEM)) is one of the most effective and informative methods of research of problems related to biomechanics. By virtue of the FEM, it is possible to avoid difficulties associated with the use of analytical methods for calculation of the stress-strain state of biomechanical systems and, most importantly, to obtain high accuracy of results (Yamako *et al.*, 2014).

The aim of this study is to analyse the stress state arising in a bone-cement-implant system with different sizes of tapered stems, depending on the thickness of the cement mantle. Such an analysis will contribute to finding the rationale for the size of the implant to avoid fatigue fracture of the cement and to provide even distribution of stress in the bone.

2. Materials and methods

For the analysis, a three-dimensional model of femur has been developed using computed tomography (CT), which is a method allowing creation of highly accurate models of organs. CT provides information on the shape and properties of soft and bone tissue, giving almost an in vivo model. The algorithm of generation of a three-dimensional geometric model of the femur includes several steps. At first, CT images of the patient are downloaded for subsequent segmentation of the object. The segmentation is performed based on the obtained axial projections of the object, using the selection as a separate mask. Then, a STF file with the 3D object made on the mask is created. In the third step, the quality of the model is improved by employing various surface smoothing functions. Eventually, mechanical characteristics of femur are found by calculating analytical dependences between the Hounsfield units (HU) obtained from the computed tomograms (Fig. 1). Hounsfield units determine the dependence between radiographic density of the femur tissue, presented in arbitrary units (Cann, 1988; Peng *et al.*, 2006), the actual bone density ρ [g/cm^3], and the elastic modulus E [MPa] (Yosibash *et al.*, 2007; Helgason *et al.*, 2008; Khan *et al.*, 2014). One can find numerous relationships between bone density and HU for different bone types. In our study, the relationship $\rho = 1 + 7.185 \cdot 10^{-4} \cdot \mathrm{HU}$ (Peng *et al.*, 2006; Laz *et al.*, 2007; Snethen, 2013; Pérez *et al.*, 2014) is used. Material properties of cortical and cancellous bone have been assigned according to the equations proposed by Wirtz *et al.* (2000)

$$E\ [\mathrm{MPa}] = E(\rho) = \begin{cases} 2065^{3.09} & \text{if} \quad \rho > 1.2\,\mathrm{g/cm^3} \quad \text{(cortical bone)} \\ 1904^{1.64} & \text{if} \quad \rho \leqslant 1.2\,\mathrm{g/cm^3} \quad \text{(cancellous bone)} \end{cases}$$

Poisson's ratio is assumed to be 0.3 for the whole analysed bone (Wirtz *et al.*, 2000).

The model used in this work has the shape and size of an ORTAN® tapered femoral component (Ukraine). In general, such implants consist of two elements: a stem and a ball head (Fig. 2b). The stem comprises four parts, including cervical (2), head (1), metaphyseal (3), and

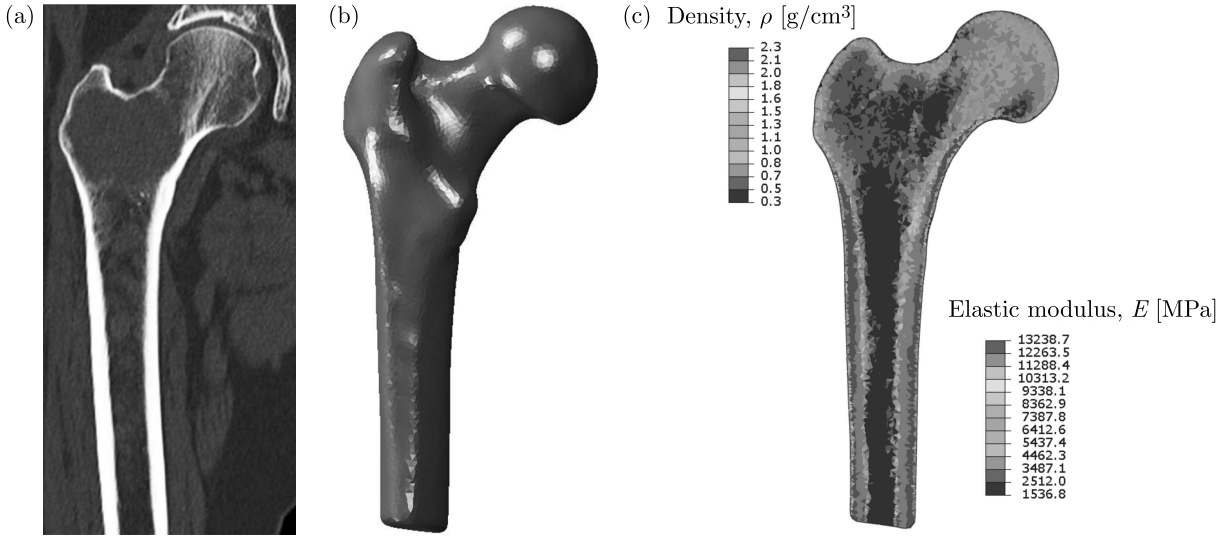

Fig. 1. Three-dimensional femur model created from CT images: (a) CT image, (b) solid geometry of the bone, (c) distribution of material properties: density ρ [g/cm^3] and elastic modulus E [MPa] in the cross section of proximal femur

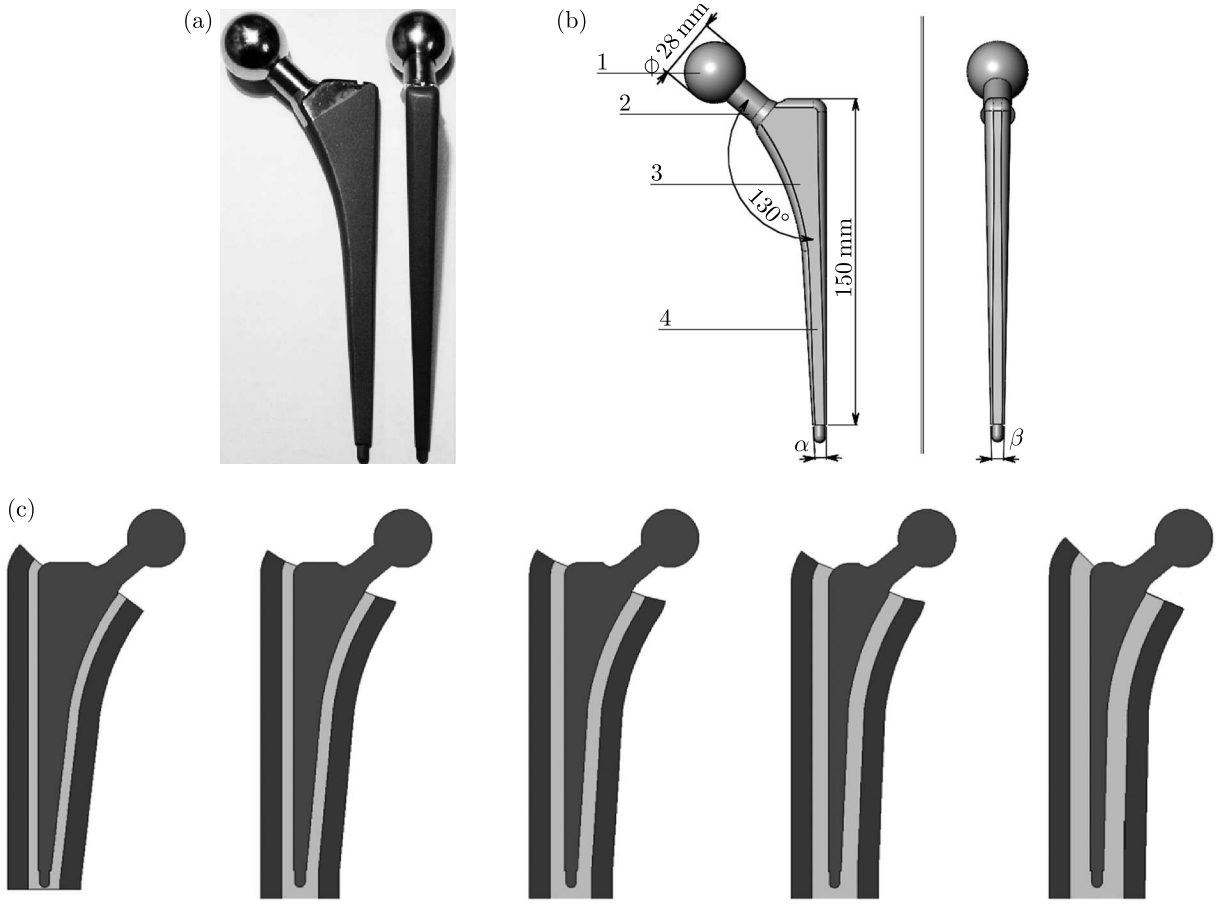

Fig. 2. Size 1 tapered stem hip endoprosthesis: (a) photograph of the implant; (b) 3D model used in numerical simulations (1 – head, 2 – cervical part at an angle of 130° to the stem; 3 – metaphyseal part and 4 – diaphyseal part); (c) geometric model of cemented endoprosthesis with thickness of cement mantle (light grey) equal to 1, 2, 3, 4 and 5 mm, respectively

diaphyseal (4) ones. Cervical part (2), which is used to install head (1), has a form of a (Morse) cone. The stem of the prosthesis is wedge-shaped with an angle α to the sagittal plane and β to the frontal plane. For this type of endoprosthesis, the cervico-diaphyseal angle is equal to 130°. The diameter of the head of the hip joint endoprosthesis is 28 mm. Wedge-shaped metaphyseal part (3) contributes to stability and strength of fixation of the stem in the bone and resists subsidence of the stem prosthesis. Distal part of the stem (4) has a conical shape and is jammed in the front-rear direction. In the developed model, the femoral component has physical properties of stainless steel (316L) with Young's modulus $E = 200$ GPa and Poisson's ratio 0.3.

In this paper, we consider several possible variations of installation of stems with different sizes in the bone cement that fills the medullary canal of femur. Owing to varying implant thickness, the thickness of the cement mantle is changed in a range between 1 mm and 5 mm (Fig. 2c). Young's modulus of the cement equals 2.5 GPa and Poisson's ratio is 0.29. All contact surfaces of the cement mantle are assumed to be perfectly bonded to the surrounding bone. Contact between the implant and the cement is modelled using a surface-to-surface contact algorithm (in Abaqus software) with the Coulomb stick-slip model of friction with the friction coefficient equal to 0.25, simulating the surface finish for the stem, consistent with the surface finish of the ORTAN® stems. The cement mantle is assumed to be fixed to the surrounding cortical and trabecular bone.

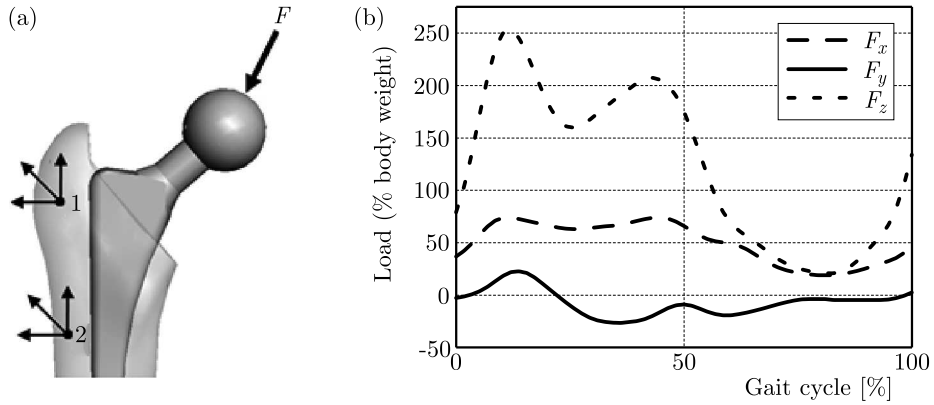

Fig. 3. Load cases: (a) hip contact force acting from the acetabular cup to the implant head of the magnitude **F** and its components F_x (frontal axis), F_y (sagittal axis) and F_z (vertical axis); numbers 1 and 2 indicate points where the muscle forces act; (b) values of components F_x, F_y, and F_z of the contact force **F** in percentage of the body weight [% BW] during normal walking

Table 1. Physiological loading conditions on the lateral surface of femur during normal walking

Muscle	Load component [N]			Initial point
	X	Y	Z	
Abductor	406	30.1	605.5	1
Tensor fascia lata, proximal part	50.4	81.2	92.4	1
Tensor fascia lata, distal part	−3.5	−4.9	−133	1
Vastus lateralis	−6.3	129.5	−650.3	2

The contact load, acting from acetabulum to the head of the endoprosthesis, can be represented as a principal vector **F**, which can be decomposed into three components acting along axes of the local Cartesian coordinate system associated with the centre of the prosthesis head. The force **F** and its components are presented in Fig. 3a. The dependence between F_x, F_y, and F_z (expressed in percentage of the body weight) during a normal gait cycle is shown in Fig. 3b (Bergmann *et al.*, 2001; Bergmann, 2008; Levadnyi *et al.*, 2017). According to the plot,

the maximum values of the components F_x, F_y, and F_z are equal to: $F_x = 0.743Q$, $F_y = 0.254Q$, $F_z = 2.649Q$, respectively, where Q is the weight of a human body (for body mass assumed to be 70 kg and the acceleration of gravity 9.81 m/s^2). In this case, the load acting on the femoral head equals: $F_x = 510.2$ N, $F_y = 174.4$ N, $F_z = 1918.1$ N. In addition, the forces acting on the bone surface in muscle attachment sites have been also taken into account (Table 1) (Heller *et al.*, 2005).

The finite element models of the bone-cement-implant system used in this study contain 1100123 3D solid four-node tetrahedral elements. For all elements of the system, length of the edge of mesh elements equals 1 mm.

3. Results

In Figs. 4-6, the distributions and values of the equivalent von Mises stress in the bone-cement--hip implant system are reported for different thicknesses of the cement mantle and stem sizes. The curve number corresponds to thickness of the cement mantle in mm.

As shown, the stresses in bones are smaller if thinner stems are used, and bigger in the case of thicker implants. The results show that an increase in the stem thickness and the corresponding decrease in the cement mantle yield a stress increase in the distal part of femur. The maximum bone stresses are found on the medial side of femur, in the vicinity of the distal end of the stem. If the cement mantle thickness is equal to 1 to 2 mm, there is a high concentration of stresses on the medial side of femur, in the contact zone of the distal stem and the cortical bone (Fig. 4). This can lead to development of the stress shielding effect and hypertrophy of femur. An increase

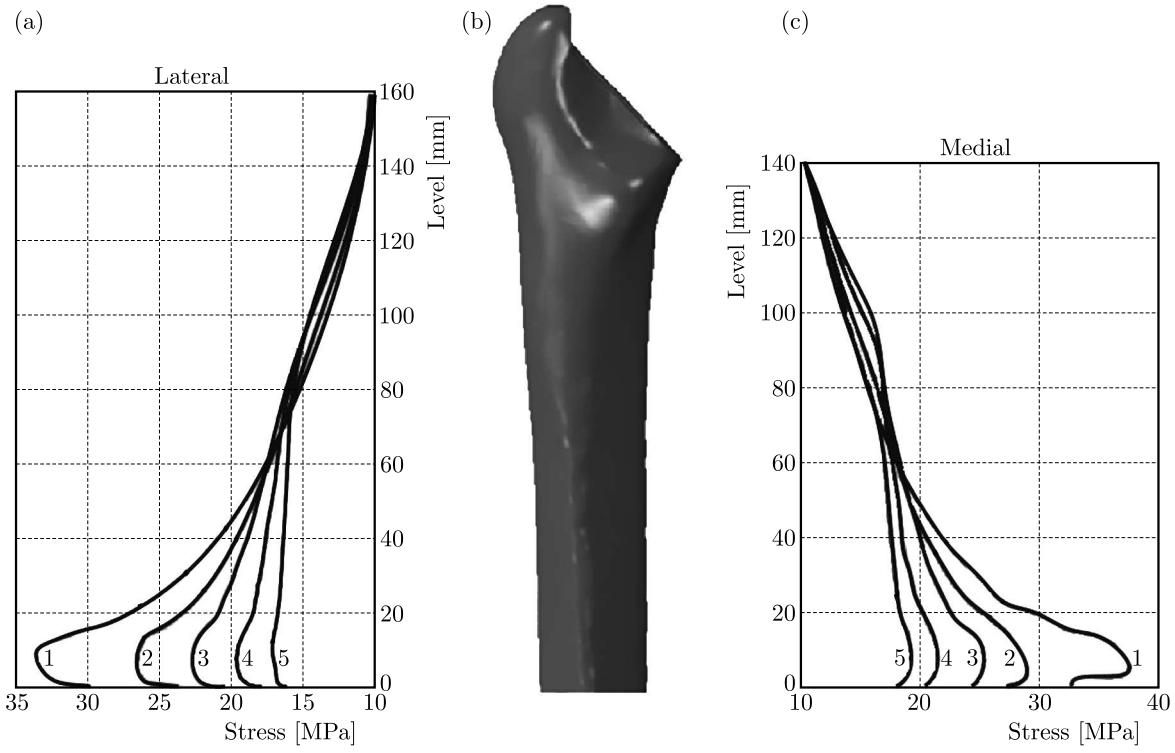

Fig. 4. (a) Distribution of the maximum equivalent stress on the lateral side of the femur depending on thickness of the cement mantle, (b) femur model, (c) distribution of the maximum equivalent stress on the medial side of the femur depending on thickness of the cement mantle

in thickness of the cement mantle causes a decrease in stresses in the distal part of the bone. If the thickness of the cement mantle ranges from 3.5 to 5 mm, the stress values (tensile) on the

lateral side and stress values (compression) on the medial side of the bone are evenly distributed excluding excessive stress concentration (Fig. 4).

For thickness of the cement mantle between 1 and 1.5 mm, a peak stress is observed in the distal part. Its value exceeds the limit of durability of the bone cement (Fig. 5). In such a case, the cement mantle will not be able to ensure long-term functioning of the system, and hence there is a greater likelihood of loosening of the femoral component. According to the results, an increase in thickness of the cement mantle leads to reduction of stresses in the distal part of the cement mantle. Taking into account that, according to the manufacturers, the fatigue limit of bone cements is 8-10 MPa (Kunh, 2000), a cement mantle thicker than 1.5 mm provides satisfactory conditions for functioning of the prosthesis under functional loads. Notice that while analysing the stress-strain state of the cement mantle, it is necessary to take into account stresses that occur on the lateral side (tensile stresses), since mechanical properties of the cement in tension are 9 times lower than those of the cement in compression.

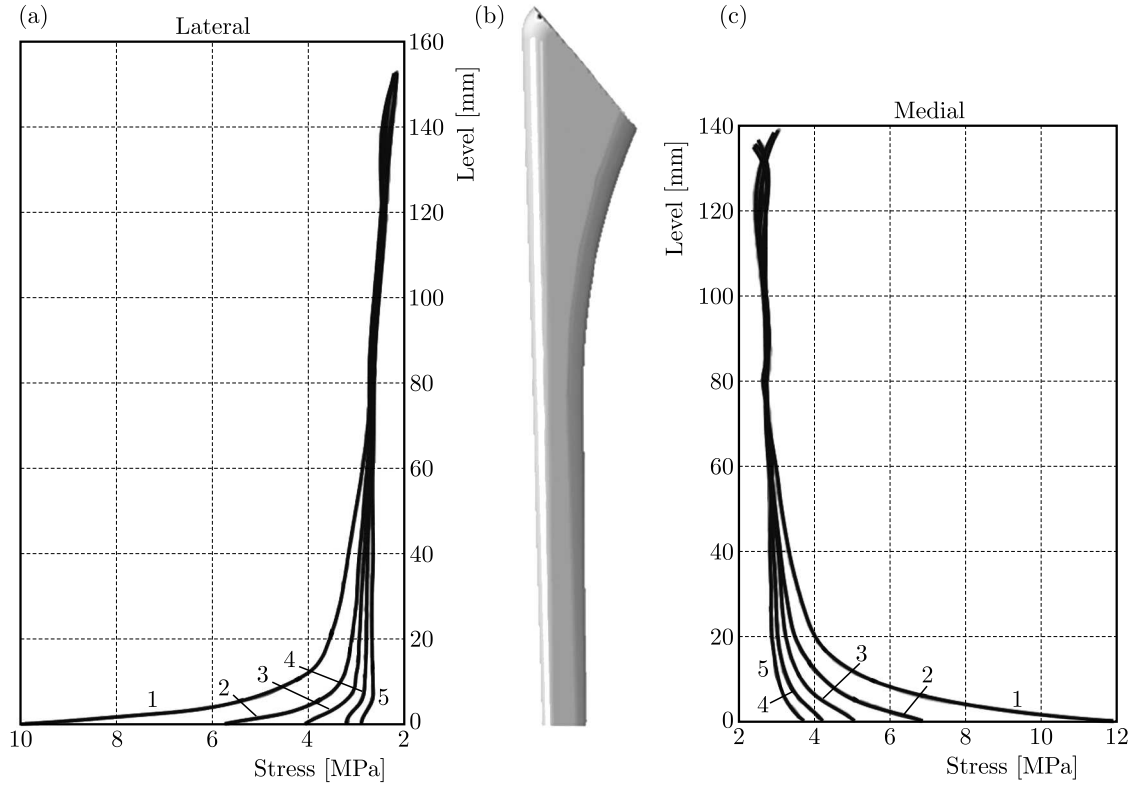

Fig. 5. (a) distribution of the maximum equivalent stress on the lateral side of the cement mantle depending on its thickness, (b) cement mantle model, (c) distribution of the maximum equivalent stress on the medial side of the cement mantle depending on its thickness

The stress-strain state of the stem is determined by a combination of the bending moment acting in the frontal plane and compression forces acting in the axial direction. The results show that the maximum stresses in the implant are found on the medial side, in the vicinity of the distal end of the stem of the prosthesis (Fig. 6). In general, the calculation results indicate that, regardless of the size of the endoprosthesis, the maximum implant stress does not exceed the yield strength of the material, and all implants are in the state of elastic deformation. This means that stresses in the material of implants under the functional loads are not dangerous to the structure of the implant. In this case, the dangerous stress value is assumed to be greater than the fatigue strength of 316L stainless steel, which is usually used to manufacture implants, this is greater than about 250 MPa (Maruyama *et al.*, 2011). Thus, the use of these structures provides a sufficient safety margin. However, the above observations are valid only for correct

implantation of the prosthesis in femur. In the case of incorrect installation or presence of defects, pores, cracks, gaps, or distortions in the bone, implant or cement mantle, an increase in the stresses near the concentrator is observed, which causes fatigue failure of components or loss of stability of the system.

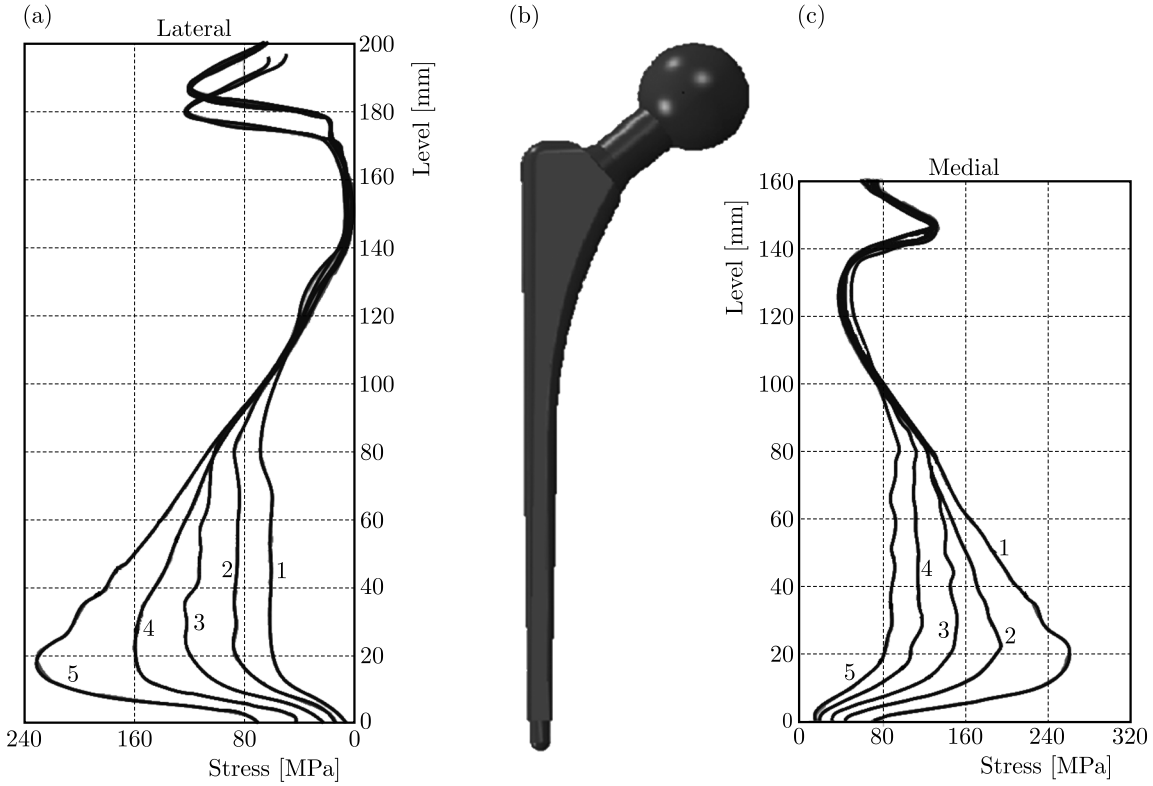

Fig. 6. (a) distribution of the maximum equivalent stress on the lateral side of the stem depending on thickness of the cement mantle, (b) model of the stem, (c) distribution of the maximum equivalent stress on the medial side of the stem depending on thickness of the cement mantle

4. Discussion

Improved cementing techniques and stem positioning are considered to be crucial factors for a long-term implant success. One of the methods used by researchers aimed at improving the orthopedic clinical practice is the finite element method, which is also applied in the present study.

For all considered thicknesses of the cement mantle under the action of functional loads, intensity and distribution of stresses have been obtained for both medial and lateral sides. The stress-strain state of the stem, cement mantle, and femur have been determined by combining the bending moment acting in the frontal plane and compression forces acting in the axial direction. As described in Section 3, the longitudinal tensile stress acts on the lateral side and the cervical part of the stem, cement mantle and bone, while compressive stresses are present on the medial side. The values of tensile stress in the cement mantle and femur are smaller than the values of the compressive stress.

The results have shown that changes in the cement mantle thickness around cemented femoral components can lead to significant changes in the stress-strain state of bone-cement-femoral component systems. For instance, an increase in the cement mantle thickness from 2 to 5 mm has led to a 47% reduction in stress in the distal medial strain gage and a 50% reduction in

the distal lateral cement stress. This data is an experimental verification of the results from finite-element modeling reported by Estok *et al.* (1991), in which a 45-55% reduction in peak distal cement strains was obtained by increasing cement mantle thickness from 2.5 to 5 mm and keeping the prosthesis diameter constant. A subsequent computational study by Lee *et al.* (1994) showed a reduction in peak tensile cement stresses by 45% when the cement mantle thickness was increased from 2 to 5 mm by means of reducing the prosthesis diameter. Also Fisher *et al.* (1997) conducted an experiment with two different sizes of cobalt-chromium stems and proved that in the case of increasing the cement mantle thickness from 2.4 to 3.7 mm, substantial strain reductions in the distal cement (40-49%) were observed.

In our work, the numerical simulation results have also shown that thickness of the cement mantle affects only the distal part of the cement mantle and does not affect the proximal one. Thus, one may conclude that the cement mantle should not be of the same thickness throughout the medullary canal of femur. Instead, to provide satisfactory conditions of functioning of the prosthesis under action of functional loads, the cement mantle should not be thicker than 1 mm in the proximal part of the femur. At the same time, most of the cement should be located in the distal part. The above-mentioned conditions should be ensured: 1) satisfactory conditions of functioning of the prosthesis, 2) even distribution of stresses in the bone (stresses concentration can be avoided). According to outcomes of this study, a slightly thicker cement mantle (up to 3 mm) can be useful in reducing stress-strain levels around cemented femoral components. To thicken the cement mantle, either a smaller stem can be used or the femoral medullary canal can be expanded in the distal femur.

5. Conclusions

To obtain reliable results of the finite element analysis, models of both femur and endoprosthesis have been generated. The size, shape, material physicomechanical properties, and values of physical load of the models obtained for numerical simulations are the same as of real objects.

It has been found that, since all system elements work under cyclic load, the stress analysis should be conducted for comparison of the occurred stresses in the system components and the limit durability of the material from which the elements are made of. It has been also detected that when the bone cement in distal parts is thicker than 3 mm, the load acting on tissue in the distal part of femur is significantly reduced. On the other hand, in the proximal part of femur, thickness of the cement mantle should not be smaller than 1.5 mm to ensure satisfactory conditions for functioning of the prosthesis under action of functional loads. What should be also emphasized, stresses in the stem of the endoprosthesis, regardless of thickness of the cement mantle, are lower than the fatigue strength of 316L steel used in hip implants, and thus fatigue fractures of stems are unlikely to occur.

Acknowledgment

The work has been supported by the National Science Centre of Poland under the grant OPUS 9 No. 2015/17/B/ST8/01700 for years 2016-2018.

References

1. Bergmann G., Deuretzbacher G., Heller M., Graichen F., Rohlmann A., Strauss J., Duda G.N., 2001, Hip contact forces and gait patterns from routine activities, *Journal of Biomechanics*, **34**, 7, 859-871

2. Bergmann G. (Ed.), 2008, *OrthoLoad database*, Charité-Universitätsmedizin Berlin, www.OrthoLoad.com, Accessed on December 10, 2016

3. Bhambri S.K., Gilbertson L.N., 1995, Micromechanisms of fatigue crack initiation and propagation in bone cements, *Journal of Biomedical Materials Research*, **29**, 2, 233-237
4. Cann, C., 1998, Quantitative CT for determination of bone mineral density: a review, *Journal of Radiology*, **166**, 509-522
5. Charnley J., 1960, Surgery of the hip joint, *British Medical Journal*, **1**, 821-826
6. Devis C.M., Berry D.J., Harmsen W.S., 2003, Cemented revision of failed uncemented femoral components of total hip arthroplasty, *The Journal of Bone and Joint Surgery*, **85-A**, 7, 1264-1269
7. Estok D.M., Harrigan T.P., Harris W.H., 1991, Finite element analysis of cement strains at the tip of an idealized cemented femoral component, *Transactions of Orthopaedic Research Society*, **16**, 504
8. Fisher D.A., Tsang A.C., Paydar N., Milionis S., Turner C.H., 1997, Cement-mantle thickness affects cement strains in total hip replacement, *Journal of Biomechanics*, **30**, 11-12, 1173-1177
9. Gunn E, Gundapaneni D, Goswami T., 2012, Effect of cement fill ratio in loosening of hip implants, *Biomatter*, **2**, 2, 87-93
10. Helgason B. Perilli E. Schileo E. Taddei F. Brynjolfsson S. Viceconti M., 2008, Mathematical relationships between bone density and mechanical properties: a literature review, *Journal of Clinical Biomechanics*, **23**, 1, 135-146
11. Heller M.O., Bergmann G., Kassi J.-P., Claes L., Haas N.P., Duda G.N., 2005, Determination of muscle loading at the hip joint for use in pre-clinical testing, *Journal of Biomechanics*, **38**, 5, 1155-1163
12. Huiskes R., 1993, Mechanical failure in total hip arthroplasty with cement, *The Journal of Current Orthopaedics*, **7**, 239-247
13. Jenkins P.J., Clement N.D., Hamilton D.F., Gaston P., Patton J.T., Howie C.R., 2013, Predicting the cost-effectiveness of total hip and knee replacement: a health economic analysis, *The Bone and Joint Journal*, **95-B**, 115-121
14. Khan S.N., Warkhedkar R.M., Shyam A.K., 2014, Analysis of Hounsfield unit of human bones for strength evaluation, *Procedia Materials Science*, **6** (2014), 512-519
15. Kroell A., Beaulé P., Krismer M., Behensky H., Stoeckl B., Biedermann R., 2009, Aseptic stem loosening in primary THA: migration analysis of cemented and cementless fixation, *Journal of International Orthopaedics*, **33**, 6, 1501-1505
16. Kuhn K., 2000, *Bone Cements: Up-To-Date Comparison of Physical and Chemical Properties of Commercial Materials*, Springer, Berlin
17. Laz P.J., Stowe J.Q., Baldwin M.A., Petrella A.J., Rullkoetter P.J., 2007, Incorporating uncertainty in mechanical properties for finite element-based evaluation of bone mechanics, *Journal of Biomechanics*, **40**, 2831-2836
18. Lee I.Y., Skinner H.B., Keyak J.H., 1994, Effects of variation of prosthesis size on cement stress at the tip of a femoral implant, *Journal of Biomedical Materials Research*, **28**, 1055-1066
19. Levadnyi I., Awrejcewicz J., Fagundes-Goethel M., Loskutov A., 2017, Influence of the fixation region of a press-fit hip endoprosthesis on the stress-strain state of the "bone-implant" system, *Computers in Biology and Medicine*, **84**, 195-204
20. Maruyama N., Mori D., Hiromoto S., Kanazawa K., Nakamura M., 2011, Fatigue strength of 316L-type stainless steel in simulated body fluids, *Journal of Corrosion Science*, **53**, 2222-2227
21. Peng L., Bai J., Zeng X., Zhou Y., 2006, Comparison of isotropic and orthotropic material property assignments on femoral finite element models under two loading conditions, *Journal of Medical Engineering and Physics*, **28**, 3, 227-233

22. Pérez M.A., Venditoli P.-A., Lavigne M., Nuño N., 2014, Bone remodeling in the resurfaced femoral head: Effect of cement mantle thickness and interface characteristics, *Medical Engineering and Physics*, **36**, 2, 185-195

23. Shah N., Porter M., 2005, Evolution of cemented stems, *Journal of Orthopedics*, **28**, 8, 819-825

24. Snethen K., 2013, A computed tomography-based model of the infant hip anatomy for dynamic finite element analysis of hip dysplasia biomechanics, *HIM 1990-2015*, 1465

25. Sullivan P.M., Mackenzie J.R., Callaghan J.J., Johnston R.C., 1994, Total hip arthroplasty with cement in patients who are less than fifty years old. A sixteen to twenty-two-year follow-up study, *The Journal of Bone and Joint Surgery*, **76**, 6, 863-869

26. Warth L.C., Callaghan J.J., Liu S.S., Klaassen A.L., Goetz D.D., Johnston R.C., 2014, Thirty-five-year results after Charnley total hip arthroplasty in patients less than fifty years old. A concise follow-up of previous reports, *The Journal of Bone and Joint Surgery. American Volume*, **96**, 21, 1814-1819

27. Wirtz D.C., Schiffers N., Pandorf T., Radermacher K., Weichert D., Forst R., 2000, Critical evaluation of known bone material properties to realize anisotropic FE-simulation of the proximal femur, *Journal of Biomechanics*, **33**, 10, 1325-1330

28. Yamako G., Chosa E., Zhao X., Totoribe K., Watanabe S., Sakamoto T., Nakane N., 2014, Load-transfer analysis after insertion of cementless anatomical femoral stem using pre- and post-operative CT images based patient – specific finite element analysis, *Medical Engineering and Physics*, **36**, 694-700

29. Yosibash Z., Trabelsi N., Milgrom C., 2007, Reliable simulations of the human proximal femur by high-order finite element analysis validated by experimental observations, *Journal of Biomechanics*, **40**, 16, 3688-3699

Manuscript received February 6, 2017; accepted for print May 10, 2017

JOURNAL OF THEORETICAL AND APPLIED MECHANICS
55, 4, pp. 1245-1256, Warsaw 2017
DOI: 10.15632/jtam-pl.55.4.1245

ANALYSIS OF VIBRATION TRANSFER CHARACTERISTICS OF VEHICLE SUSPENSION SYSTEM EMPLOYING INERTER

Yujie Shen, Long Chen, Yanling Liu, Xiaoliang Zhang
School of Automotive and Traffic Engineering, Jiangsu University, Zhenjiang, China
e-mail: shenliang6018@163.com; chenlong@ujs.edu.cn; liuyl@ujs.edu.cn; zxl1979@ujs.edu.cn

In this paper, the force transfer mechanism of three mechanical elements "inerter, spring and damper" is analyzed based on the "force-current" analogy theory. The vibration isolation performance of the two types of simple three-element vehicle suspensions S1 (inerter is in parallel with damper) and S2 (inerter is in series with damper) are studied. The dual--mass system model of the suspensions is built by means of using the mechanical impedance method. The influence of parameters variation on vibration transfer characteristics is also investigated.

Keywords: vehicle, suspension, inerter, vibration analysis

1. Introduction

The vehicle suspension is a general term for power transmission device located between wheels and axles. The performance of suspension has a great impact on the vehicle ride comfort, handle and stability (Rajamani, 2012). There are three types of vehicle suspensions including passive suspension, semi-active (Eltantawie, 2012; Huang *et al.*, 2013; Tudon-Martinez *et al.*, 2013) and active suspension (Hac, 1992; Roh and Park, 1999; Youn and Hac, 2006). Recently, a new type of vehicle suspension employing an inerter has drawn the attention of scholars.

The inerter (Smith, 2002) is a newly proposed two-terminal element. It has a characteristic that the force applying to the two terminals is proportional to relative acceleration. The dynamic equation is

$$F = b(\dot{v}_1 - \dot{v}_2) \tag{1.1}$$

where F is the force applying to the two terminals, v_1, v_2 are velocities of the two terminals, b is the inertance, the unit is kg.

In the "force-current" analogy between mechanical circuit and electric circuit, the mass, spring and damper correspond to capacitor, inductor and resistor. There is a restriction in the mass element for its one-terminal property, so that the capacitor should be grounded. With the birth of the inerter, the mechanical circuit mass element is replaced by the inerter corresponding to the capacitor in an electric circuit. Also, the traditional mechanical spring-damper network performance can be improved by inclusion of the inerter and has been widely used in vehicle suspensions (Smith and Wang, 2004; Papageorgiou and Smith, 2006; Kuznetsov *et al.*, 2011; Hu *et al.*, 2014; Wang and Chan, 2011), train suspensions (Wang *et al.*, 2009; Wang and Liao, 2010), building suspensions (Wang *et al.*, 2010) and the steering compensation for high-performance motorcycles (Evangelou *et al.*, 2004).

The earliest types of inerters are rack-and-pinion and ball-screw inerters (Papageorgiou and Smith, 2005). Experiments were also carried out to verify the effectiveness of mechanical inerters. Furthermore, the influence of the inerter on natural frequencies of vibration systems

was investigated (Chen *et al.*, 2014) to demonstrate that the inerter can reduce the natural frequencies of the vibration system. The benefits of semi-active suspensions with inerters were investigated by Zhang and Mehdi (2012). It was also observed that the inerter and spring force were in anti-phase to each other (Ming *et al.*, 2014), but the force transfer mechanism of the three elements and the influence of the parameters on the vibration transfer characteristics of the vehicle suspension remained unknown.

This paper intends to study the force transfer mechanism of the inerter, spring and damper based on the "force-current" analogy, and to investigate the effectiveness of the mechanical network compromising the inerter. Meanwhile, vibration transfer characteristics of the vehicle suspension are also studied to draw some conclusions. The paper is arranged as follows:

In Section 2, the force transfer mechanism of the three types of elements is analyzed. Then, a single mass model is built in Section 3 to demonstrate the effectiveness of the new mechanical network compromising the inerter from the perspective of the force transferred in suspension. In order to analyze the influence of variable parameters on the vibration transfer characteristics, a dual mass model is built in Section 4, and the effect is studied in Section 5. At last, some conclusions are drawn in Section 6.

2. Force transfer mechanism of the three elements

The force and velocity in a mechanical field correspond to the current and voltage in an electric field. The force and current are both "through-variables" while velocity and voltage are both "across-variables". In the current transfer process, it is known that the current phase is ahead of the voltage phase between two terminals of the capacitor. But for the inductor, the voltage phase is ahead of the current phase. In the mechanical element, the direction of the force between two terminals of an inerter is always opposite to that of the spring (Ming *et al.*, 2014). In the following, the force transfer mechanism of the three elements will be studied. Figure 1 shows the force transfer model of the three elements, where q_0 is displacement of the input, k_0 is stiffness, b_0 is inertance, c_0 is damping coefficient.

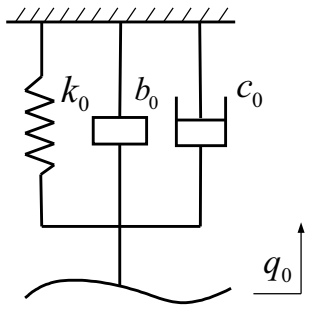

Fig. 1. Force transfer model

The force between the two terminals of the spring, inerter and damper f_k, f_b, and f_c are

$$f_k = k_0 q_0 \qquad f_b = b_0 \ddot{q}_0 \qquad f_c = c_0 \dot{q}_0 \tag{2.1}$$

when q_0 is set as

$$q_0 = A\sin(wt) \tag{2.2}$$

where A is the amplitude equal to 0.1 m and w is the circle frequency set as 2π. The velocity between the two terminals is

$$\dot{q}_0 = Aw\cos(wt) \tag{2.3}$$

In simulation, $k_0 = 10\,\mathrm{N/m}$, $c_0 = 1.5\,\mathrm{N\,s/m}$, $b_0 = 0.1\,\mathrm{kg}$.

Figures 2a to 2c show the force and velocity of the two terminals of the spring, inerter, and damper.

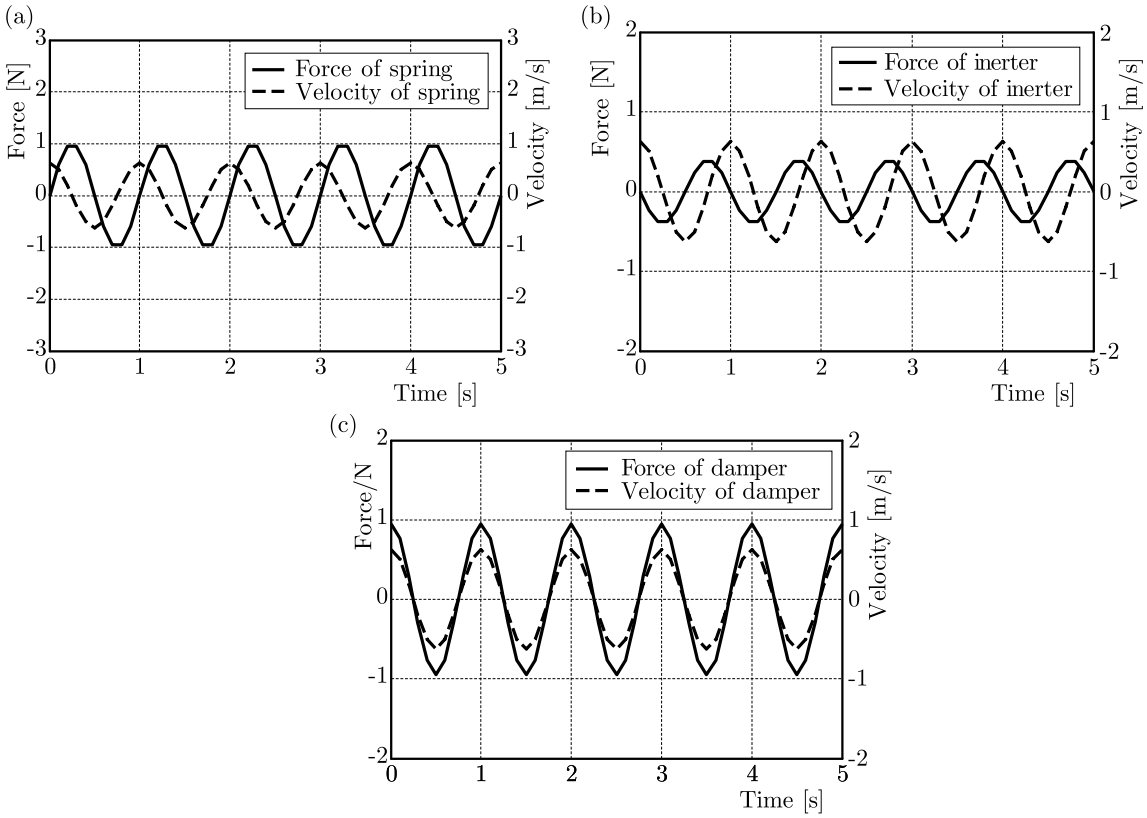

Fig. 2. Force and velocity of the two terminals of (a) the spring, (b) the inerter, (c) the damper

It can be seen that the velocity phase of the spring is ahead of the force phase, which is consistent with the relationships between the voltage and current phase of the inductor. For inerter, the force phase is ahead of the velocity phase which is consistent with the relationships between the current phase and the voltage phase of the capacitor. The force phase is always synchronous with the velocity phase, which is consistent with the relationships between the current phase and the voltage phase of the resistor. The analysis above demonstrates the effectiveness of the "force-current" analogy again.

3. Single mass system model

There are many types of vehicle suspensions employing the inerter. In this paper, two types of a simple three-element vehicle suspension are investigated. Both of them have a spring to bear the sprung mass. For S1 suspension, the inerter is in parallel with the damper. For S2 suspension, the inerter is in series with the damper. Two types of the suspension structures and the traditional passive suspension S0 compromising parallel "spring and damper" are shown in Fig. 3 (z, z_1, z_2 are displacements of the mass, q, q_1, q_2 are displacements of the input, z_b is displacement of the inerter, k, k_1, k_2 are stiffnesses of springs, c, c_1, c_2 are damping coefficients, b_1, b_2 are inertances).

The force in S0 is

$$f_{S_0} = f_k + f_c = k(q - z) + c(\dot{q} - \dot{z}) \tag{3.1}$$

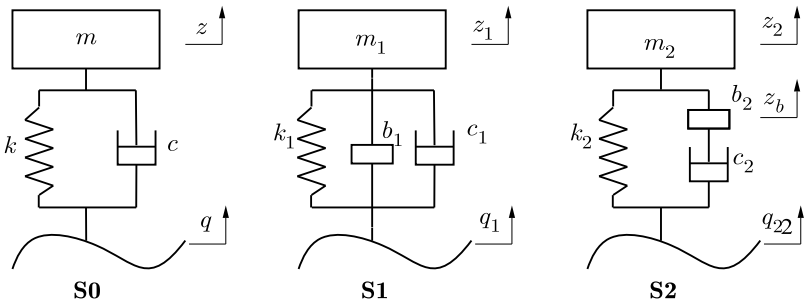

Fig. 3. Three types of the suspension structure

The force in S1 is

$$f_{S_1} = f_k + f_b + f_c = k_1(q_1 - z_1) + b_1(\ddot{q}_1 - \ddot{z}_1) + c(\dot{q}_1 - \dot{z}_1) \tag{3.2}$$

The force in S2 is

$$f_{S_2} = f_k + b_2(\ddot{z}_b - \ddot{z}_2) \tag{3.3}$$

where

$$b_2(\ddot{z}_b - \ddot{z}_2) = c_2(\dot{q}_2 - \dot{z}_b) \tag{3.4}$$

Assuming the λ is

$$\lambda = \frac{w}{w_0} \qquad w_0 = \sqrt{\frac{k}{m}} \tag{3.5}$$

The model parameters are all kept the same, see Table 1.

Table 1. Model parameters

Parameters	Value
Sprung mass m, m_1, m_2 [kg]	320
Stiffness k, k_1, k_2 [kN/m]	15
Inertance b_1, b_2 [kg]	10
Damping coefficient c, c_1, c_2 [N s/m]	1095

The input displacement is also set as a sine wave with an amplitude of 0.1 m. Figure 4 shows the amplitude ratio of the force in S1 and S2 with S0.

The solid line corresponds to the constant value of 1. When the amplitude of the ratio of the force in the suspension structure is less than 1, it indicates that the vibration isolation performance is superior to the traditional passive suspension. In the range from 0 to 8 of λ, both ratios S1 and S2 are less than 1, which means that their vibration isolation performance is superior to the traditional passive suspension in low frequency. The amplitude of ratio of S1 is becoming larger than 1 with an increase in λ but for S2, the amplitude of the ratio is always less than 1. It can be inferred that the vibration isolation performance of the mechanical circuit is improved in the low frequency by involving of the inerter element, which is consistent with the capacitor function to block the low frequency current. Also, suspension S2 has a superior isolation performance with respect to S1 and is more suitable for vehicle suspension design.

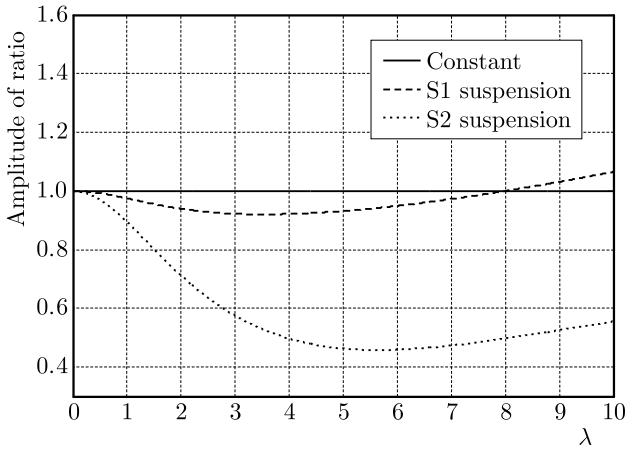

Fig. 4. Amplitude ratio of the force

4. Dual-mass system model

In the "force-current" analogy, the spring, damper and inerter have the same forms of dynamic equations like the inductor, resistor and capacitor. So, the impedances of the spring, damper and inerter also have the same forms of k/s, c and bs, just like the electric impedance $1/(Ls)$, Cs and $1/R$ of inductor, resistor and capacitor, where k is stiffness of the spring, c is the damping coefficient, b is the inertance, L is the inductance coefficient, C is the capacitance coefficient, R is the resistance coefficient. Analysis of vibration transfer characteristics in the frequency domain can become more convenient by using the impedance methods. A dual mass system model compromising the sprung and unsprung mass is built in Fig. 5, where m_s is the sprung mass, m_u is the unsprung mass, k_t is the stiffness of the tire, z_s is the displacement of the sprung mass, z_u is the displacement of the unsprung mass, z_r is the displacement of the road input, $T(s)$ is the velocity impedance of the suspension.

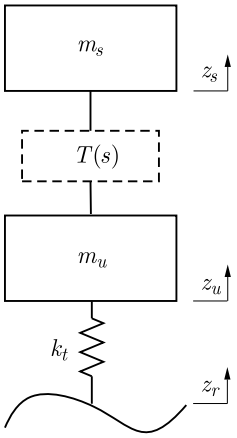

Fig. 5. Dual mass system

The dynamic model is

$$\begin{aligned} &m_s s^2 Z_s + sT(s)(Z_s - Z_u) = 0 \\ &m_u s^2 Z_u - sT(s)(Z_s - Z_u) + k_t(Z_u - Z_r) = 0 \end{aligned} \tag{4.1}$$

where Z_s, Z_u and Z_r are the Laplace transforms of z_s, z_u and z_r and:

— for S1

$$T_1(s) = \frac{k_1}{s} + b_1 s + c_1 \tag{4.2}$$

— for S2

$$T_2(s) = \frac{k_2}{s} + \frac{1}{\frac{1}{b_2 s} + \frac{1}{c_2}} \tag{4.3}$$

So, the gain of the body acceleration is

$$H(s)_{\ddot{z}_s \sim z_r} = \frac{Z_s}{Z_r} s^2 = \frac{T(s) k_t s^2}{[m_s s + T(s)][m_u s^2 + sT(s) + k_t] - sT^2(s)} \tag{4.4}$$

The gain of the suspension deflection is

$$H(s)_{(z_s - z_u) \sim z_r} = \frac{Z_s - Z_u}{Z_r} = \frac{-m_s s k_t}{[m_s s + T(s)][m_u s^2 + sT(s) + k_t] - sT^2(s)} \tag{4.5}$$

The gain of the dynamic tire load is

$$H(s)_{(z_u - z_r) k_t \sim z_r} = \frac{Z_u - Z_r}{Z_r} k_t = \Big(\frac{[m_s s + T(s)] k_t}{[m_s s + T(s)][m_u s^2 + sT(s) + k_t] - sT^2(s)} - 1 \Big) k_t \tag{4.6}$$

In simulation, the parameters of the suspensions are optimized by using a genetic algorithm. The model parameters are shown in Table 2. In order to show the performance of the vehicle suspension employing the inerter, a traditional passive suspension (stiffness is 22 kN/m and damping coefficient is 1000 N s/m) is set as a comparison object.

Table 2. Simulation parameters

Parameters	Values
Sprung mass m_s [kg]	320
Unsprung mass m_u [kg]	45
Stiffness of tire k_t [kN/m]	190
Stiffness of S1 k_1 [kN/m]	28
Damping coefficient of S1 c_1 [N s/m]	2800
Inertance of S1 b_1 [kg]	20
Stiffness of S2 k_2 [kN/m]	22
Damping coefficient of S1 c_2 [N s/m]	1300
Inertance of S2 b_2 [kg]	500

The other parameters are remained unchanged in order to analyze the effect of one parameter. The variation of the parameters are shown in Table 3.

Table 3. Parameters

	b_1 [kg]	b_2 [kg]	c_1 [kN s/m]	c_2 [kN s/m]	k_1 [kN/m]	k_2 [kN/m]
Value	20	500	2.8	1.3	28	22
+6dB	40	1000	5.6	2.6	56	44
-6dB	10	250	1.4	0.65	14	11

5. Analysis of vibration transfer characteristics

5.1. Effect of variable stiffness

Firstly, the damping coefficient and the inertance remain unchanged. Figures 6-8 show the gains of body acceleration, suspension deflection and dynamic tire load of variable stiffness. The red line represents passive suspension S0 while the blue and green lines represent S1 and S2 suspensions. The direction of the arrows means an increase of the stiffness.

In Fig. 6, it can be seen that both the gains of the body acceleration of S1 and S2 become larger and even beyond S0 with an increase of the stiffness in low frequency. But in high frequency, the gains become smaller and slightly lower than S0 in S1 while become larger and higher than S0 in S2. Furthermore, both their resonance frequencies become larger with an increase of stiffness.

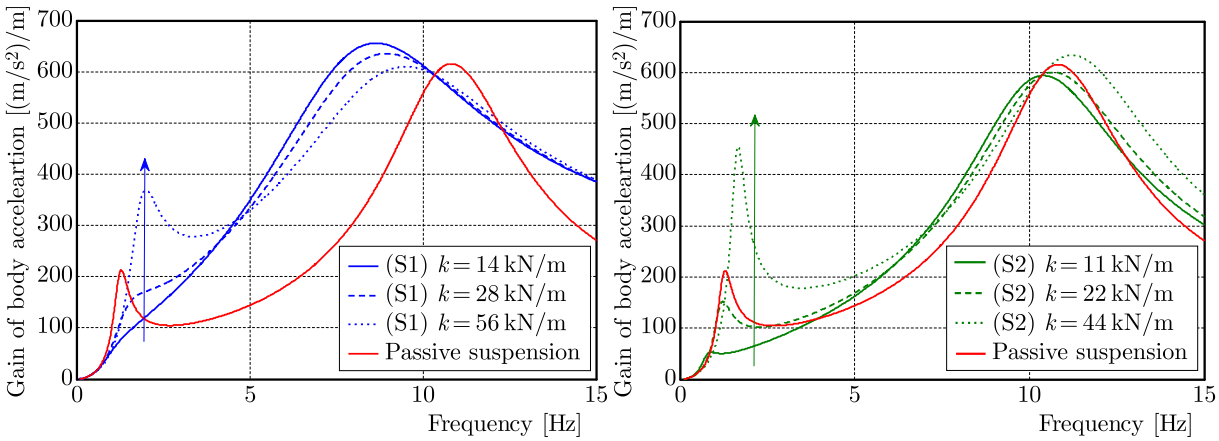

Fig. 6. Gains of body acceleration of variable stiffness

Figure 7 shows the gains of suspension deflection of variable stiffness. Both their gains and resonance frequencies become larger with an increase of stiffness except for the gains in high frequency. Note that all the peak values of S1 and S2 are smaller than S0 except for S2 where $k = 44\,\mathrm{kN/m}$. At last, the gains of dynamic tire load of variable stiffness are shown in Fig. 8.

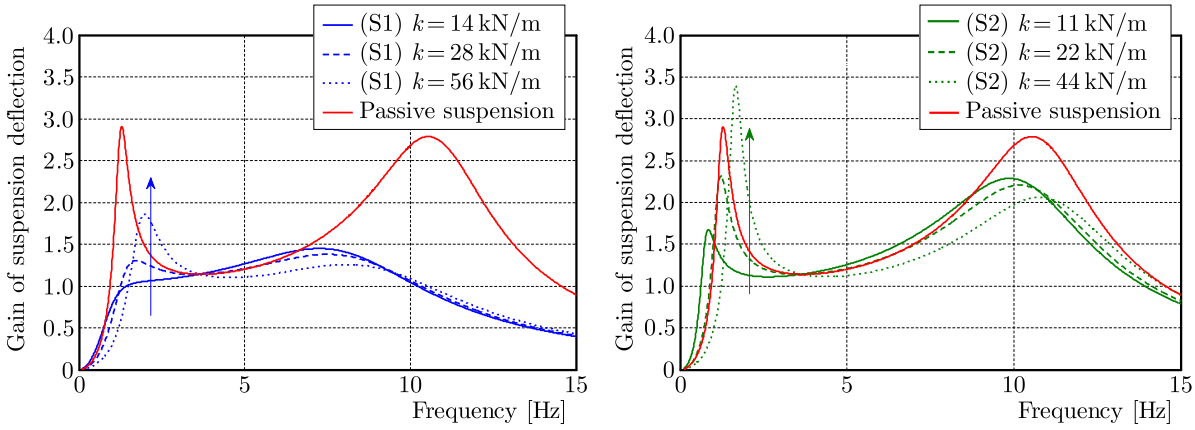

Fig. 7. Gains of suspension deflection of variable stiffness

It can be seen that the trends are all consistent with the suspension deflection that their gains become larger in low frequency and become smaller in high frequency. Compared with the passive suspension, the peak value in low frequency becomes larger than S0 but always smaller

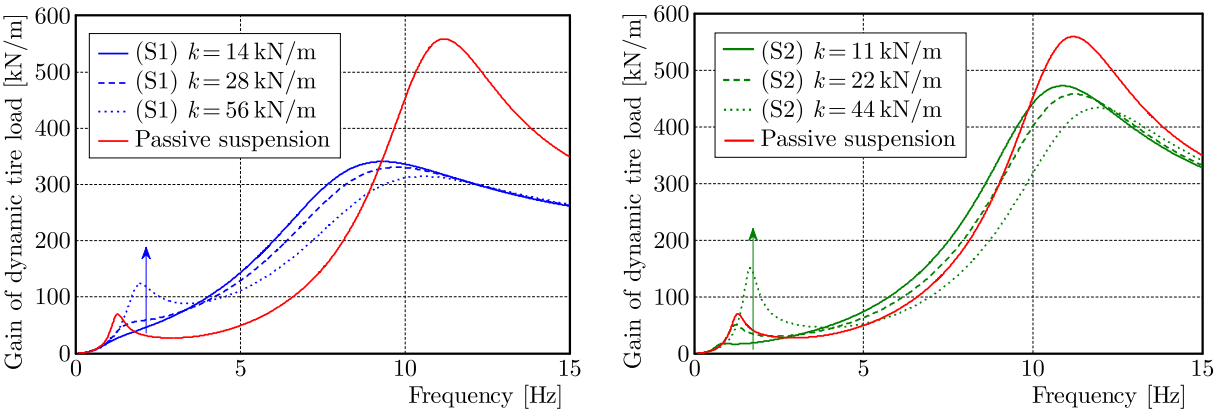

Fig. 8. Gains of dynamic tire load of variable stiffness

than S0 in high frequency. Both the resonance frequencies become larger with an increase of stiffness.

It can be concluded that the gains of S1 and S2 become larger in low frequency and become smaller in high frequency except for the gains of body acceleration of S2 with an increase of stiffness. Both their resonance frequencies become larger with an increase of stiffness.

5.2. Effect of variable damping coefficient

Then, the stiffness and the inertance remain unchanged. Figures 9-11 show the gains of body acceleration, suspension deflection and dynamic tire load of variable damping coefficient. The red line represents passive suspension S0 while the blue and green lines represent S1 and S2 suspensions. The direction of the arrows means an increase of the damping coefficient.

It can be seen that both the gains of the body acceleration become smaller than S0 at the original two resonance frequencies with an increase of the damping coefficient. Furthermore, the original two resonances change to one resonance.

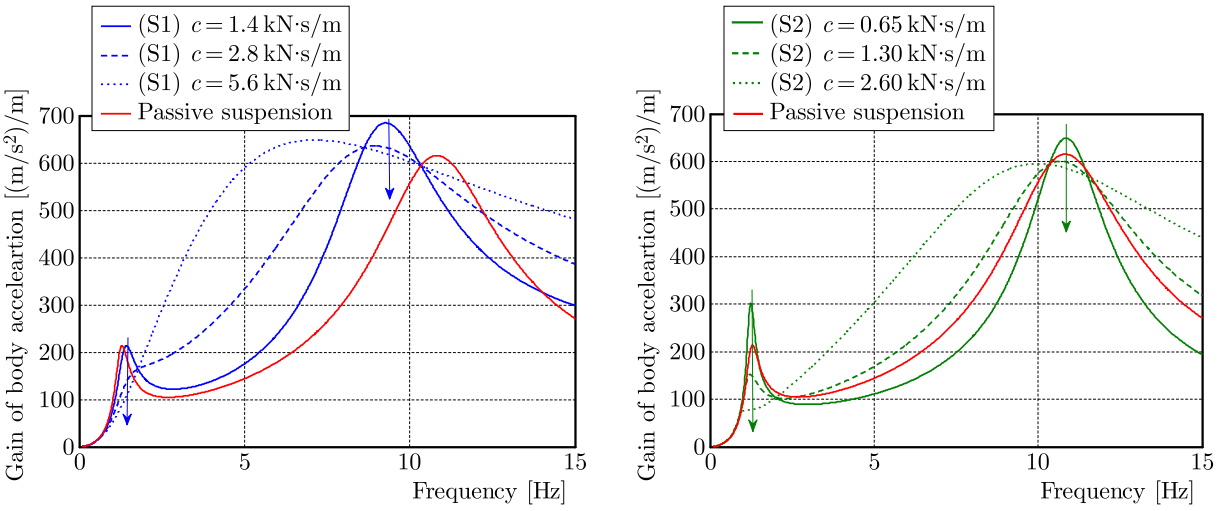

Fig. 9. Gains of body acceleration of variable damping coefficient

Figure 10 shows the gains of suspension deflection of the variable damping coefficient. The trends are consistent with the body acceleration that their gains become smaller than S0 at the original two resonance frequencies with an increase of the damping coefficient. At the same time, the original two resonances change to one resonance. At last, the gains of dynamic tire load of the variable damping coefficient are shown in Fig. 11.

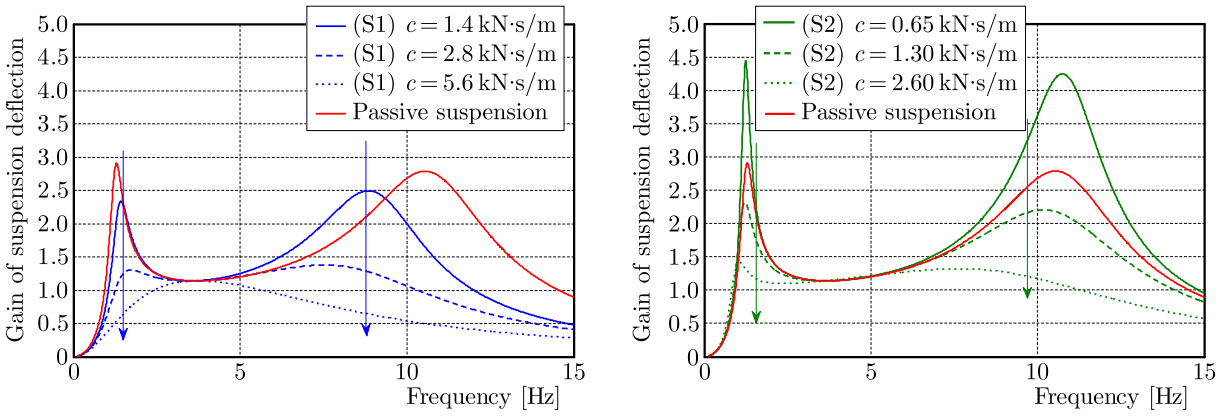

Fig. 10. Gains of suspension deflection of variable damping coefficient

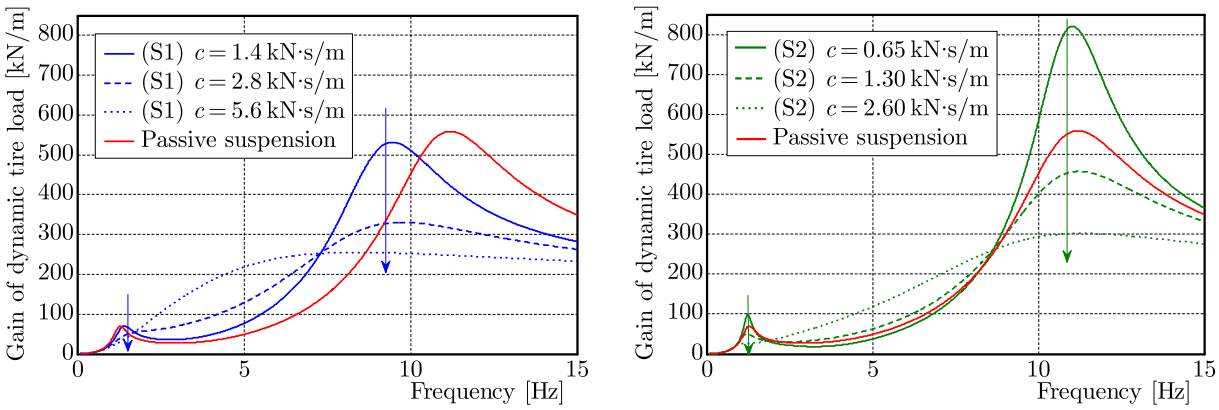

Fig. 11. Gains of dynamic tire load of variable damping coefficient

It can be seen that the trends are all consistent with the suspension deflection and body acceleration that their gains become smaller than S0 at the original two resonance frequencies, The original two resonances change to one resonance with an increase of the damping coefficient.

It can be concluded that the gains of S1 and S2 have the same trends that their gains become smaller than S0 at the original two resonance frequencies, and the original two resonances change to one resonance with an increase of the damping coefficient.

5.3. Effect with variable inertance

Lastly, the stiffness and the damping coefficient remain unchanged. Figures 12-14 show the gains of body acceleration, suspension deflection and dynamic tire load of variable inertance. The red line represents passive suspension S0 while the blue and green lines represent S1 and S2 suspensions. The direction of the arrows means an increase of the inertance.

It can be seen that both the gains of the body acceleration of S1 and S2 become smaller than S0 in low frequency, and the resonance frequencies become smaller in S1 while become larger in S2 with an increase of inertance. But in high frequency, the gains of S1 become larger than S0 and the resonance frequencies become smaller while there is no obvious change in S2.

Figure 13 shows the gains of suspension deflection of variable inertance. The trends are consistent with the body acceleration that both the gains become smaller than S0 in low frequency and the resonance frequencies become smaller in S1 while become larger in S2 with an increase of the inertance. But in high frequency, the gains of S1 become larger but still less than S0, and the resonance frequencies become smaller while there is no obvious change in S2. At last, the gains of dynamic tire load of variable inertance are shown in Fig. 14.

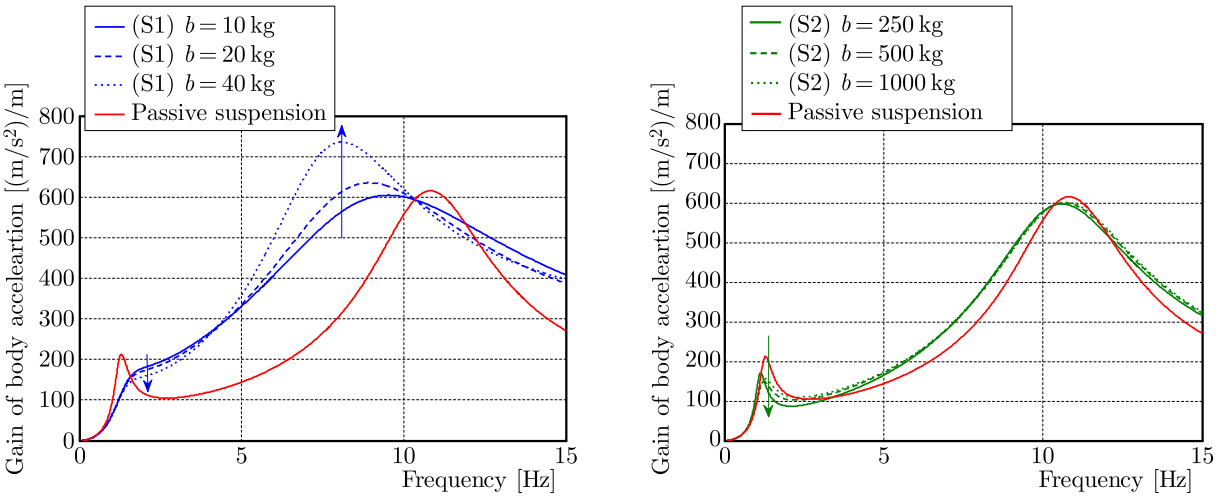

Fig. 12. Gains of body acceleration of variable inertance

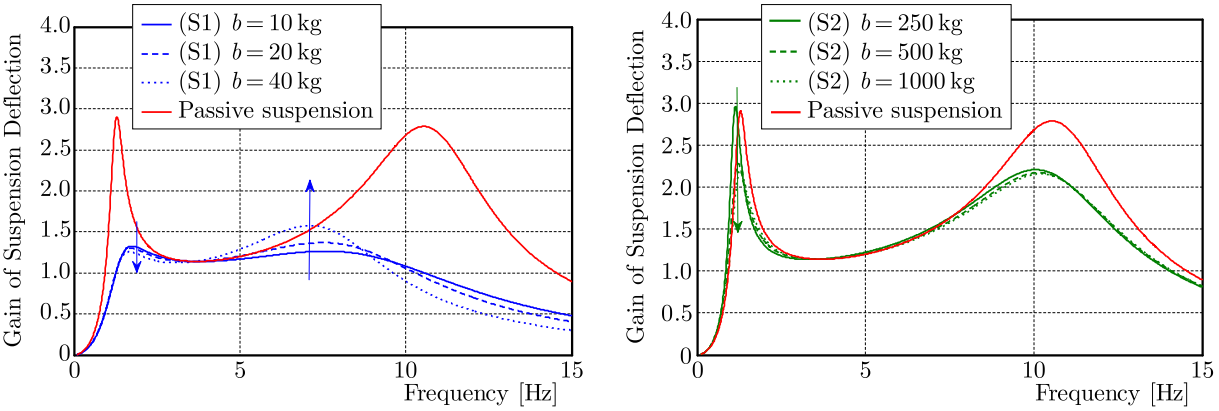

Fig. 13. Gains of suspension deflection of variable inertance

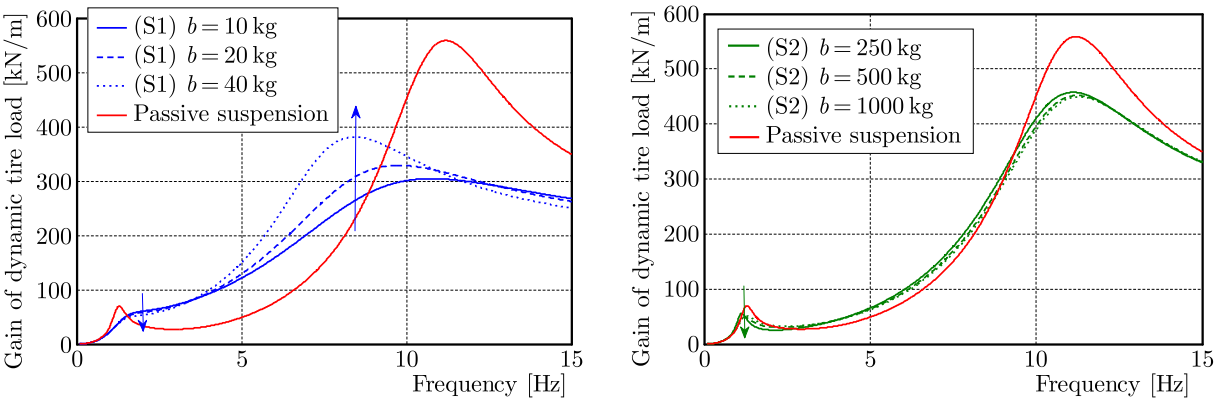

Fig. 14. Gains of dynamic tire load of variable inertance

It can be seen that the trends are all consistent with the suspension deflection and body acceleration that both of the gains become smaller than S0 in low frequency and the resonance frequencies become smaller slightly in S1 while become larger slightly in S2 with an increase of inertance. But in high frequency, the gains of S1 become larger but still less than S0, and the resonance frequencies become smaller while there is no obvious change in S2.

It can be concluded that the gains of S1 and S2 have the same trends that both the gains become smaller than S0 in low frequency and the resonance frequencies become smaller in S1

while become larger in S2 with an increase of inertance. But in high frequency, the gains of S1 become larger but still less than S0 except for the body acceleration where $b = 20\,\text{kg}$ and $40\,\text{kg}$, and the resonance frequencies become smaller while there is no obvious change in S2.

6. Conclusion

In this paper, the force transfer mechanism of the three types of mechanical elements, i.e. the inerter, spring and damper are analyzed. A "force-current" analogy is further demonstrated that the force phase is ahead of the velocity phase in the inerter, the velocity phase is ahead of the force phase in the spring, while the force phase is always synchronous with the velocity phase in the damper. Then, the vibration isolation performance of S1 and S2 suspensions are deemed improved by compromising the inerter in low frequency from the prospective of the force transferred. At last, the dual-mass model of the suspension is built by means of the impedance method. The velocity impedances of the mechanical elements are used in frequency analysis for they have the same forms of dynamic equations of the electric elements according to the "force--current" analogy. The influences on the vibration transfer characteristics of the parameters variation are investigated. The conclusions are drawn that the gains of S1 and S2 become larger in low frequency and become smaller in high frequency, except for the gain of body acceleration in S2 with an increase of stiffness. Both their resonance frequencies become larger with an increase of stiffness. For the damping coefficient, the gains of S1 and S2 have the same trends that their gains become smaller at the original two resonance frequencies, and the original two resonances change to one resonance with an increase of the damping coefficient. With an increase of inertance, the gains of S1 and S2 have the same trend that both the gains become smaller in low frequency and the resonance frequencies becomes smaller in S1 while become larger in S2. But in high frequency, the gains of S1 become larger and the resonance frequencies become smaller while there is no obvious change in S2.

Acknowledgement

This work is supported by the National Natural Science Foundation of China (Grant No. 51405202), Scientific Research Innovation Projects of Jiangsu Province (Grant No. KYLX15_1081), China Postdoctoral Science Foundation (Grant No. 2014M561591), the "Six Talent Peaks" high-level project of Jiangsu Province (Grant No. 2014-JNHB-023) Yujie Shen is also supported by the China Scholarship Council.

References

1. Chen M.Z.Q., Hu Y.L., Huang L.X., 2014, Influence of inerter on natural frequencies of vibration systems, *Journal of Sound and Vibration*, **333**, 7, 1874-1887
2. Eltantawie M.A., 2012, Decentralized neuro-fuzzy control for half car with semi-active suspension system, *International Journal of Automotive Technology*, **13**, 3, 423-431
3. Evangelou S., Limebeer D.J.N., Sharp R.S., 2004, Steering compensation for high performance motorcycles, *Proceedings of the 43rd IEEE Conference on Design and Control*, 749-754
4. Hac A., 1992, Optimal linear preview control of active vehicle suspension, *Vehicle System Dynamics*, **21**, 1, 167-195
5. Huang C., Chen L., Yuan C.C., Jiang H.B., 2013, Non-linear modelling and control of semi-active suspensions with variable damping, *Vehicle System Dynamics*, **51**, 10, 1568-1587
6. Hu Y.L., Chen M.Z.Q., Shu Z., 2014, Passive vehicle suspensions employing inerters with multiple performance requirements, *Journal of Sound and Vibration*, **333**, 8, 2212-2225

7. Kuznetsov A., Mammadov M., Sultan I., 2011, Optimization of improved suspension system with inerter device of the quarter-car model in vibration analysis, *Archive of Applied Mechanics*, **81**, 10, 1427-1437

8. Ming F.S., Rahizar R., Wan N.L.W.M., 2014, Vehicle suspension with parallel inerter: effectiveness in improving vibration isolation, *Journal of Vibroengineering*, **16**, 1, 255-265

9. Papageorgiou C., Smith M.C., 2005, Laboratory experimental testing of inerters, *Proceedings of the 44th IEEE Conference on Decision and Control, and the European Control Conference*, 3351-3356

10. Papageorgiou C., Smith M.C., 2006, Positive real synthesis using matrix inequalities for mechanical networks: application to vehicle suspension, *IEEE Transactions on Control System Technology*, **14**, 3, 423-434

11. Rajamani R., 2012, *Vehicle Dynamics and Control*, Springer, New York

12. Roh H., Park Y., 1999, Stochastic optimal preview control of an active vehicle suspension, *Journal of Sound and Vibration*, **220**, 2, 313-330

13. Smith M.C., Wang F.C., 2004, Performance benefits in passive vehicle suspensions employing inerters, *Vehicle System Dynamics*, **42**, 4, 235-257

14. Smith M.C., 2002, Synthesis of mechanical networks: the inerter, *IEEE Transactions on Automatic Control*, **47**, 10, 1648-1662

15. Tudon-Martinez J., Fergani S., Verrier S., Sename O., Dugard L., Morales--Menendez R., Ramirez-Mendoza R.A., 2013, Road adaptive semi-active suspension in an automotive vehicle using an LPV controller, *Advances in Automotive Control*, **7**, 231-236

16. Wang F.C., Chan H., 2011, Vehicle suspension with a mechatronic network strut, *Vehicle System Dynamics*, **49**, 5, 811-830

17. Wang F.C., Hong M.F., Chen C.W., 2010, Building suspension with inerters, *Proceedings of the Institution of Mechanical Engineers, Part C: Journal of Mechanical Engineering Science*, **224**, 8, 1605-1616

18. Wang F.C., Liao M. K., 2010, The lateral stability of train suspension systems employing inerters, *Vehicle System Dynamics*, **48**, 5, 619-643

19. Wang F.C., Liao M.K., Liao B.H., 2009, The performance improvements of train suspension systems with mechanical networks, *Vehicle System Dynamics*, **47**, 7, 805-830

20. Youn I., Hac A., 2006, Preview control of active suspension with integral action, *International Journal of Automotive Technology*, **7**, 5, 547-554

21. Zhang X.J., Mehdi A., 2012, On the benefits of semi-active suspensions with inerters, *Shock and Vibration*, **19**, 257-272

Manuscript received November 15, 2016; accepted for print May 11, 2017

JOURNAL OF THEORETICAL AND APPLIED MECHANICS
55, 4, pp. 1257-1268, Warsaw 2017
DOI: 10.15632/jtam-pl.55.4.1257

EFFECTS OF THE COMPOSITE STACKING SEQUENCE ON THE FAILURE LOAD OF THE SINGLE LAP BONDED JOINT

Mohamed Mokhtari

Laboratoire de la Recherche en Technologie de Fabrication Mécanique, Ecole Nationale Polytechnique of Oran, Oran, Algeria; e-mail: mokhtarimohamed44@yahoo.fr

Kouider Madani

Laboratoire Mécanique Physique des Matériaux (LMPM), University of Sidi Bel Abbes, Sidi Bel Abbes, Algeria e-mail: koumad10@yahoo.fr

Habib Benzaama

Laboratoire de Biomécanique Appliquée et de Biomatériaux, Ecole Nationale Polytechnique of Oran, Oran, Algeria e-mail: habenza@yahoo.fr

Stephanie Malarino

Laboratoire des Sciences de l'Ingénieur pour l'Environnement, Université de La Rochelle, La Rochelle, Cedex, France e-mail: stephanie.mallarino@univ-lr.fr

Composite materials are widely used in aircraft structures, their relative rigidity/weight confers their advantage over metal structures, and the stacking sequence plays an important role for their use. The objective of this work is to analyze by the finite element method the mechanical behavior of a single lap joint of composite/composite type under a tensile load. In order to see the effects on the failure load, two basic parameters are taken into consideration; the stacking sequence of composite and thickness of each layer constituting the composite. Calculation of the failure load is made numerically with the ABAQUS code using the developed technique of VCCT (Virtual Crack Closure Technique) based on fracture mechanics. Finally, the influence of the bonding defect on the failure load is analyzed. The results clearly show the importance of optimizing fiber orientation and hence the stacking sequence for proper use of composite in bonded assemblies.

Keywords: Virtual Crack Closure Technique (VCCT), laminate sequence, single lap joint, bonding defect

1. Introduction

Single lap joints are widely used, in particular, in aeronautics. Their main problem is the non--uniform stress distribution in the adhesive joint. These stresses are concentrated at the edges of the adhesive. This concentration is usually due to misalignment of two forces that engender creation of additional stresses at the edges of the bending moment, which causes subsequent joint failure. The behavior analysis of the assembly leads directly to the analysis of mechanical behavior of the adhesive by determination of stresses in the adhesive joint and the adhesive/composite interface.

Several authors analyze stresses in the adhesive by analytical methods, see Adams *et al.* (1986), to estimate the response of the adhesive against the applied load. Others have extended their research to analyze the stress distribution by numerical methods, Tsai *et al.* (1995), to vary more mechanical and geometric parameters influencing the adhesive durability. The effect of the nature of materials to be assembled on the bonding strength of single lap joints is still not fully

understood. Conventional elastic analyzes predict that the resistance increases with strength of the adherent, and experimental results confirm this.

The analysis of breakdown of composite laminate or composite bonded joints is essential to ensure a long structure life, see Shiming *et al.* (2011), Ray and Majamuder (2014) and Liu *et al.* (2015). It has led researchers to use more effective methods, namely the Virtual Crack Closure Technique (VCCT), the eXtended Finite Element Methods (XFEM) and the Cohesive Zone Method (CZM).

The Virtual Crack Closure Technique (VCCT) is a well-established method for calculating the energy release rate (ERR) when analysing fracture problems through the finite element method (FEM). The technique is based on the numerical implementation of Irwin (1958). The crack closure integral was first proposed for two-dimensional problems by Rybicki and Kanninen (1977), and later extended to three-dimensional problems by Shivakumar *et al.* (1988). In the recent years, the VCCT has gained great popularity in the study of mixed-mode fracture problems such as delamination of composite materials and interfacial fracture between dissimilar materials. In these cases, the VCCT is used to compute not only the total ERR, but also the contributions of three fracture modes (I or opening, II or sliding and III or tearing) Krueger (2004).

A comprehensive review of VCCT formulae for different element types was given by Krueger (2004) and Whitcomb (1989) who were first to introduce the use of the VCCT to determine ERR for circular delamination. Since then, a lot of numerical analyses have been performed by using this technique, many of them dealing with initiations and growth of delamination, see Mukherjee *et al.* (1994), others with growth evolution, Klug *et al.* (1996).

The Virtual Crack Closure Technique (VCCT) is a fracture analysis method that is typically used when plastic dissipation does not exist. More recently, several researchers have developed this method in their failure analysis in composite structures, namely composite materials and bonded assemblies.

Delamination can be assimilated to a fracture process between anisotropic layers (interlaminar damage). Thus, fracture mechanics principles by Janssen *et al.* (2004) can be used to study behaviour of composite structures in presence of interlaminar damage and to determine conditions for the initiation and growth of delamination. If the delamination growth process is considered as a crack propagation phenomenon, fracture mechanics concepts can be generally transferred to the analysis of delaminated composite structures. The propagation of a crack is possible when the energy released for a unit width and length of the fracture surface (named Strain Energy Release Rate, G) is equal to a threshold level or fracture toughness, characteristic for each material, see Janssen Zuidema *et al.* (2004).

Jokinen *et al.* (2015) studied the applicability of VCCT for crack growth analyses of a bonded joint with a ductile adhesive and self-similar crack growth. Their analyses were performed for a Double Cantilever Beam (DCB) specimen with epoxy adhesive. Their force-displacement curve matched well with the experimental data.

Shokrieh *et al.* (2012) proposed new finite element methods for modeling the crack growth taking into account the Timoshenko beam element with only displacement degrees of freedom addressed for laminated composite beams. Then, they proposed a finite element procedure for simulation of mode I delamination growth in symmetric multidirectional double cantilever beam (DCB) specimens based on the fracture mechanics using the above-mentioned element. A variable strain energy release rate was used instead of constant initiation fracture toughness. The strain energy release rate was computed using Virtual Crack Closure Technique (VCCT) method. Their results of the finite element simulation corresponded well with the experimental data available in the literature.

Ahn and Woo (2015) presented in their paper the p-convergent partial discrete-layer elements with the Virtual Crack Closure Technique (VCCT) for delamination analysis of laminated com-

posite plates. The proposed element could be formulated by suitable dimensional reduction from a three-dimensional solid to a two-dimensional plate. The three-dimensional VCCT was also slightly modified to incorporate with the proposed elements and estimate the energy release rate. Then for fracture analysis, the efficiency of their proposed approach was demonstrated with the help of two additional problems such as the double cantilever beam test and the orthotropic laminated square plate with interior delamination.

The objective of this study is to analyze numerically the effect of composite stacking sequence on the resistance of an assembly of composite/composite type. Six stacking sequences for the laminate have been selected in order to see the effect of fiber orientation on the failure load of the joint. Different values of fracture energy of the adhesive have been proposed in order to see their effect on the assembly failure load value. The thickness effect of the composite ply on the assembly failure load value has been highlighted. For this, four thickness values of various layers of the composite have been studied, namely, 0.125, 0.2, 0.25 and 0.3 mm, and that for each stacking sequence of laminate plates. The analysis of the numerical results show that the failure load increases as the laminated plate has high strength.

2. Description of model geometry and material properties

The objective of this study is to determine, by a three-dimensional numerical analysis, the failure load for a single lap joint of composite/composite type under tensile load as shown in Fig. 1. The dimensions of the two substrates and the adhesive are shown in Table 1. The composite is of carbon/epoxy type. Its mechanical properties are shown in Table 2.

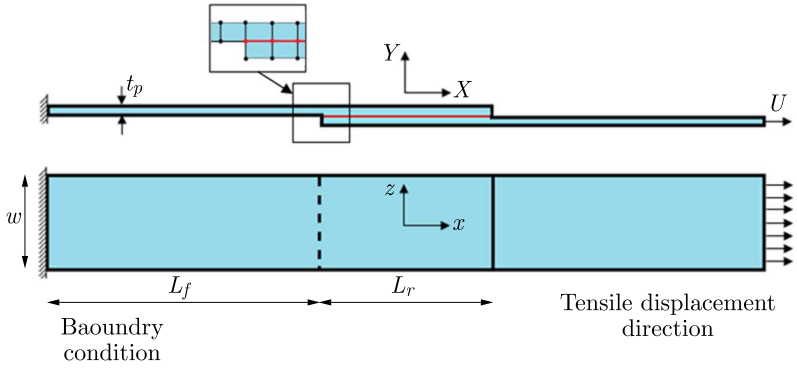

Fig. 1. Single lap joint geometry

Table 1. Dimensions of different layers of a single lap joint

Thickness of lower and upper parent laminate	$t_p = 2\,\text{mm}$
Free length of parent laminate	$L_f = 60\,\text{mm}$
Overlap length	$L_r = 20\,\text{mm}$
Wide of parent laminate	$w = 15\,\text{mm}$
Applied tensile displacement	$U = 2\,\text{mm}$

Table 2. Mechanical properties of the used laminates, Campilho *et al.* (2005)

$E_1 = 1.09\text{E+}05\,\text{MPa}$	$\nu_{12} = 0.342$	$G_{12} = 4315\,\text{MPa}$
$E_2 = 8819\,\text{MPa}$	$\nu_{13} = 0.342$	$G_{13} = 4315\,\text{MPa}$
$E_3 = 8819\,\text{MPa}$	$\nu_{23} = 0.380$	$G_{23} = 3200\,\text{MPa}$

E – Young's modulus, ν – Poisson's ratio, G – shear modulus

The adhesive used for bonding is Araldite 420, its tensile curve is represented in Fig. 2. The different mechanical properties of the adhesive are given in Table 3 and taken directly from the literature, see de Moura *et al.* (2006). This adhesive is used also in the aerospace industry given its important mechanical characteristics.

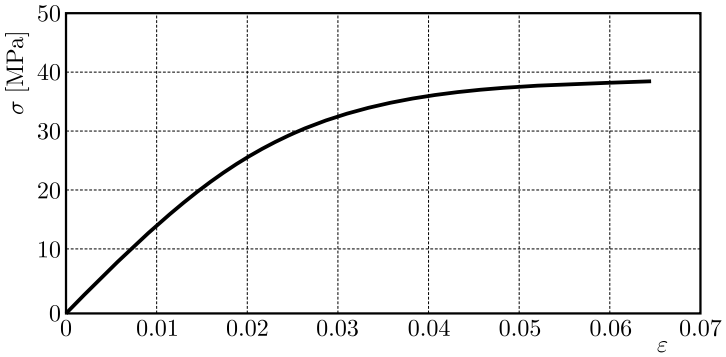

Fig. 2. Stress-strain relationship of Araldite®420adhesive (de Moura *et al.*, 2006)

Table 3. Elastic, strength and fracture properties of the used adhesive (de Moura *et al.*, 2006); $\sigma u_{,I}$, $\sigma u_{,II}$ – local strength in mode I and II, respectively, G_{IC}, G_{IIC} – critical strain energy release rate in mode I and II, respectively

Elastic	Strength	Fracture energy
$E = 1850\,\text{MPa}$	$\sigma u_{,I} = 40\,\text{MPa}$	$G_{IC} = 0.3\,\text{N/mm}$
$\nu = 0.3$	$\sigma u_{,II} = 24.1\,\text{MPa}$	$G_{IIC} = 0.6\,\text{N/mm}$

Different ply orientations of the composite adherent are considered in this study to investigate their effect on the failure load. The value of θ (orientation angle) is measured from the longitudinal direction of the structure (x-axis) and varied from 0° to 90° (Table 4). Then, in the second case, a change of thickness of the layer which has fiber orientation except for 0° and 90° (Fig. 3) is introduced. All layers have the same matrix (epoxy) and the same fiber materials (carbon).

The numbers $1, 2, \ldots, 6$ show the laminate type chosen in the x-axis of different curves. The laminate type is presented in Table 4.

Table 4. Different ply orientations used in analyses (Campilho *et al.*, 2005)

Laminate 1 – $(0_8)_S$	Laminate 4 – $(0_2/45_2/45_2/90_2)_S$
Laminate 2 – $(0_2/15_2/-15_2/90_2)_S$	Laminate 5 – $(0_2/60_2/-60_2/902)_S$
Laminate 3 – $(0_2/30_2/-30_2/902)_S$	Laminate 6 – $(0_2/75_2/-75_2/90_2)_S$

To simulate the crack onset and it is growth as well as to obtain the failure load associated with delamination of the bonded area, linear behaviour of the materials has been assumed using shell elements and a 4-node plain part. Figure 6 shows a detail of the mesh used at the lower and upper bonded edge. The adhesive has been modeled as an interface where it is necessary to introduce the mechanical parameters listed in Table 2. The delamination has been modeled between the lower and upper plate using two superimposed shell elements with contact constraint defined to prevent penetration of the elements.

The debonding has been simulated in the finite element model by maintaining merged nodes on the two adjacent faces of the overlap region (adhesive/composite). It is necessary to have an appropriate number of the mesh member in the overlap region since this modeling approach is based on the number of nodes. When the number of nodes increases, the failure load value decreases to a steady value regardless of the increase in the number of nodes (approximately

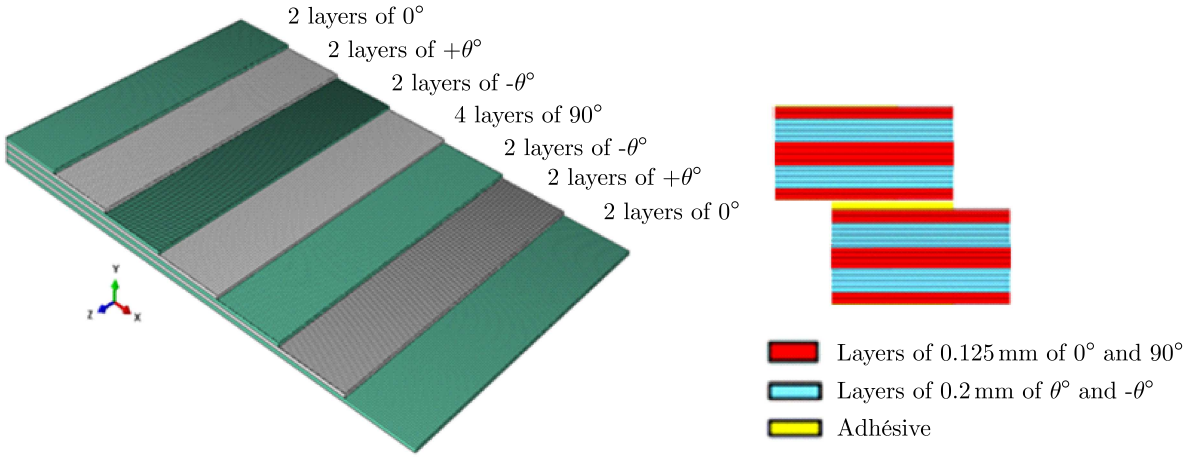

Fig. 3. Stacking sequence as function of layer thickness

6800 nodes in the overlapping area). However, the interlaminate failure of the plate has not been considered in this analysis in order to promote only the separation between plates as it was verified by several authors (Adkins and Pipes, 1988; Kumar *et al.*, 2006).

Delamination is merely debonding between two adjacent parts of the same structure along thickness. This debonding can be simulated in the finite element method by maintaining not merged nodes on two adjacent faces of the volumes or surfaces representing respectively two sublaminates (Fig. 4).

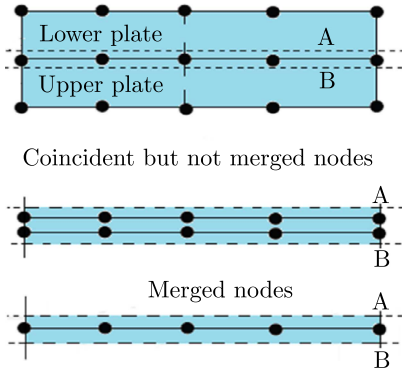

Fig. 4. Delamination simulated by maintaining not merged nodes with identical coordinates belonging to adjacent elements

The two layers of elements are tied at the interface during the loading. It should also be noted that some concerns have been raised, mainly related to the convergence of the model by introducing regular viscosity for an adequate time increment.

The interfacial properties which ensure the adhesion between the laminate plates are assigned to the nodes, the more the node number increases, the more the interfacial energy decreases to an optimal number when the separation energy is independent of the number of nodes (see Fig. 5).

3. Effect of stacking sequence and layers thickness of the laminate plate

In bonded assemblies, the stress distribution in the adhesive joint is heterogeneous. The edges are always overstretched while the heart of the adhesive is generally inactive. Whether participants

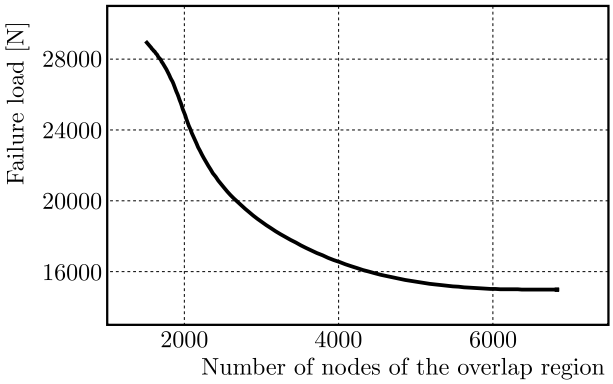

Fig. 5. Mesh convergence of the merged nodes in the interface using VCCT

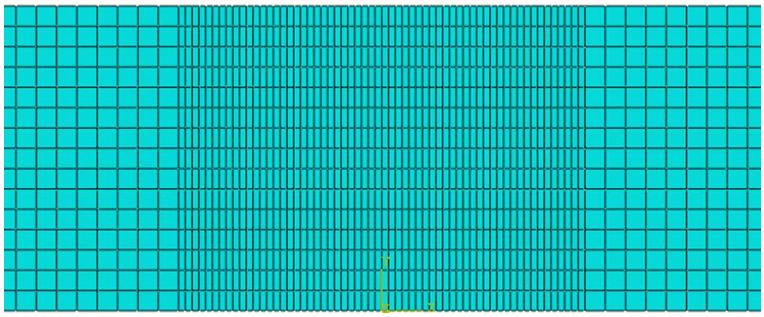

Fig. 6. Detail of the mesh at the bonded region

(composite) are too rigid, much of the applied load is transmitted to the adhesive layer and the fracture will be located at the edges of the adhesive.

The finite element analysis allows one to simulate the traction-separation of a single lap joint using the VCCT method.

A change in fiber orientation of the composite modifies its resistance and, therefore, minimizes the charge transfer to the adhesive. The objective is to see how the stiffness of the composite (stacking sequence) can affect the fracture load value of the overall assembly.

Interface finite elements are placed at the same locations to enable simulation of the crack onset and its growth, and predict the joint strength under the mixed failure mode. In all cases, an interfacial failure has been observed. Failure onset occurs at the interface starting in the borders of the covering surface. This fact is explained by highly pronounced stresses (shear and peel peaks) at these locations. This overstress peak becomes wider in the presence of defect bonding, especially at the edges of the adhesive.

Figure 7 presents the fracture load for different stacking sequences of the laminate composite. According to the analysis results in Fig. 7, the failure load is controlled by the rigidity of the assembled plates and the bonding surface.

In our analysis, the stiffness is not only due to the composite (Mokhtari *et al.*, 2013; Campilho *et al.*, 2005), but it is the composite/adhesive/composite stiffness. Figure 7 shows the composite/adhesive/composite stiffness during loading for each laminate.

For a unidirectional composite in which individual layers have the same orientation of the fibers and parallel to the direction of the applied load, the stiffness of the composite is very elevated and, therefore, the structure (composite/adhesive/composite) gets a minimum ductility ensuring a high failure load and a minimum displacement. However, if the plates are less rigid, the displacement is greater and, therefore. the tensile strength is less important.

So the failure load is controlled by the rigidity of the assembled plate. The more ductile the plates are, the greater is the elongation and, therefore, the lower is the failure load. In our

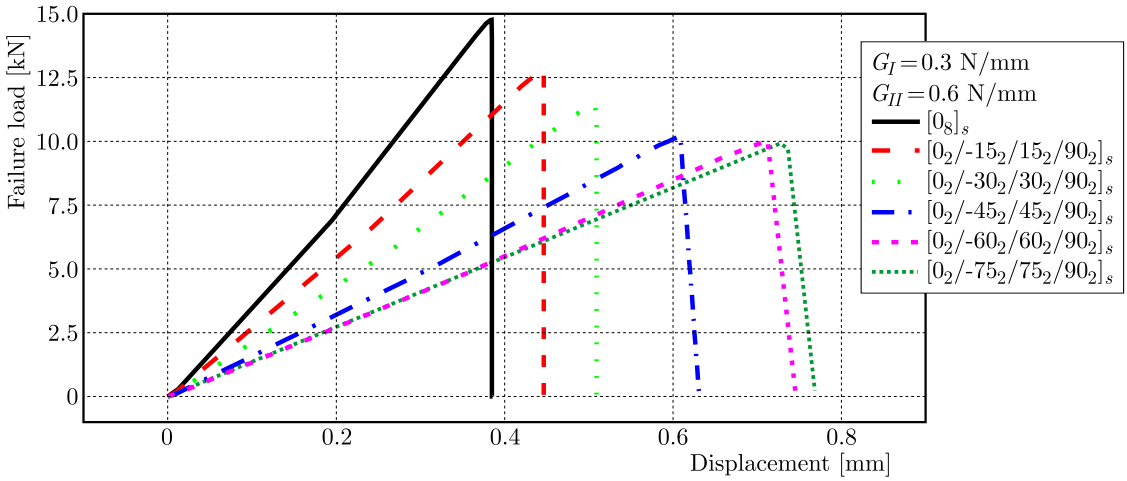

Fig. 7. Failure load-displacement curves for different stacking sequences of Carbon-Epoxy laminate

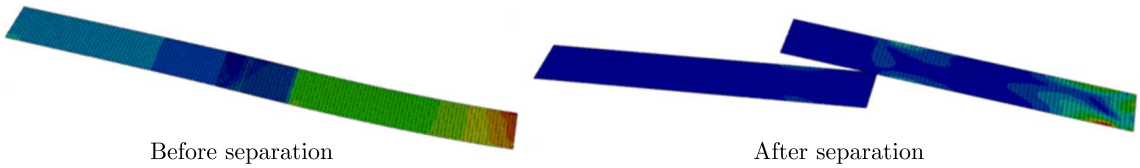

Fig. 8. Interfacial failure of the bonded joint

study, the stiffness of the plates is explained by orientation of the fibers relative to the loading axis (stacking sequence effect), which also explains the rapid separation with the load failure. However, for laminate 2, 3 and 4, the stacking sequence have some effect on the results in contrast to laminates 5 $(0_2/60_2/-60_2/90_2)_S$ and 6 $(0_2/75_2/-75_2/90_2)_S$, where the results are very similar, so the effect is much less.

A change in the composite fiber orientation modifies its mechanical properties which affects directly the charge transfer to the adhesive and thus the assembly rupture. If thickness of the plies forming the composite is changed, the composite is consolidated gradually and hence its section increases. Therefore, more energy is necessary to deform the assembly and thus fracture load will be higher. The more ply thickness increases, the more the separation force increases, and this applies to all stacking sequences.

4. Effect of fracture energy and layers thickness of the laminate plate

Different composite bonded systems can have significantly different fracture energies (Varughese and Mukherjee, 1997). So, it is appropriate to investigate whether variation of this parameter will affect the predicted failure mechanisms and loads. The fracture energies G_I and G_{II} are varied but the ratio of G_I to G_{II} is kept constant. Other parameters are fixed at the baseline values given in Tables 3. Figure 9 summarizes the effect of fracture energy on the predicted tensile failure load.

From Figs. 10 and 11, it should be noted that if the fracture energy increases, the assembly resistance becomes higher, leading to a longer lifetime. The magnitude of this resistance varies with the variation of the stacking sequence specifically with fiber orientation. The combination of high breaking energy and stacking sequence for which the fiber orientation is less than 45° gives the assembly with high fracture load.

Changing the thickness of the composite ply generates a great resistance to the composite and thus difficult transfer load to the adhesive and, therefore, high fracture load.

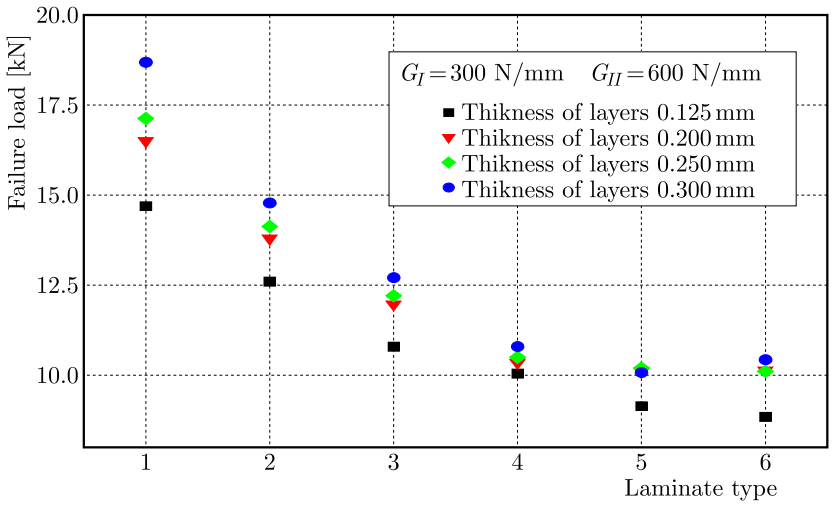

Fig. 9. Failure load as a function of layer thickness for each stacking sequence

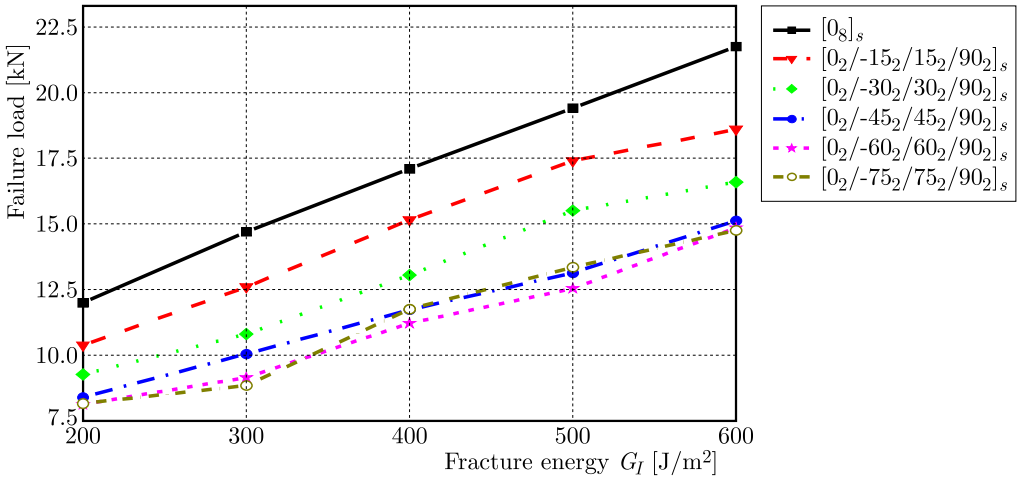

Fig. 10. Failure load as a function of fracture energy for different stacking sequences (ply thickness of 0.125 mm)

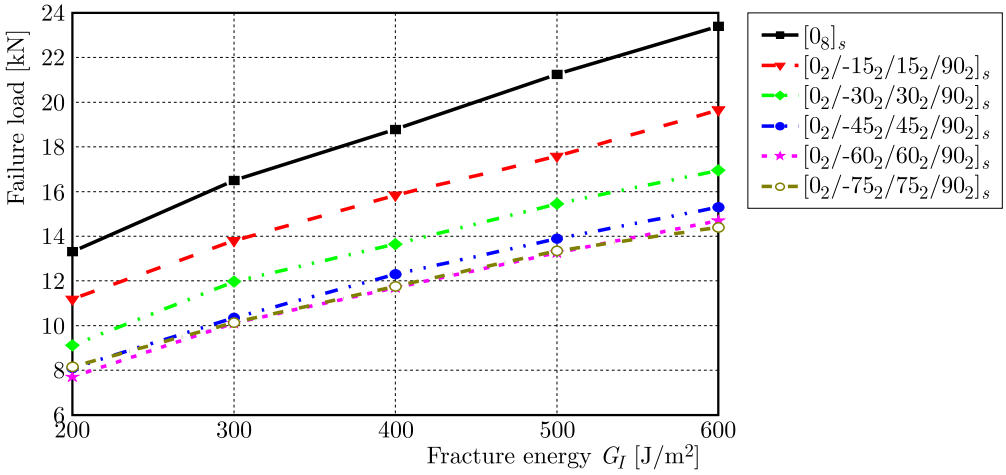

Fig. 11. Failure load as a function of fracture energy for different stacking sequences (ply thickness of 0.2 mm)

5. Effect of bonding defect on the failure load

Most of the research in the bonding area has not considered the presence of bonding defects in numerical calculations. However, at the end of the stage of implementation of bonded joints, various defects are likely to be created at different areas of the overlap length. The presence of porosities in the adhesive joint can be created due to volatile compounds evaporation and/or the existence of trapped air bubbles during the curing. It is obvious that these types of defects are prime areas for degradation of the interface by introduction of water or oxygen. More recently, Karachalios *et al.* (2013), Shishesaz and Bavi (2013), and Benchiha and Mandi (2015) analyzed the resistance of a bonded lap joint in the presence of defect by experimental, numerical and analytical methods. Their results showed that the resistance of the assembly was associated to the position and size of the defect.

In this part of the work, the effect of presence of a circular defect (diameter of 2 mm) is studied for seven different possible positions (Fig. 12).

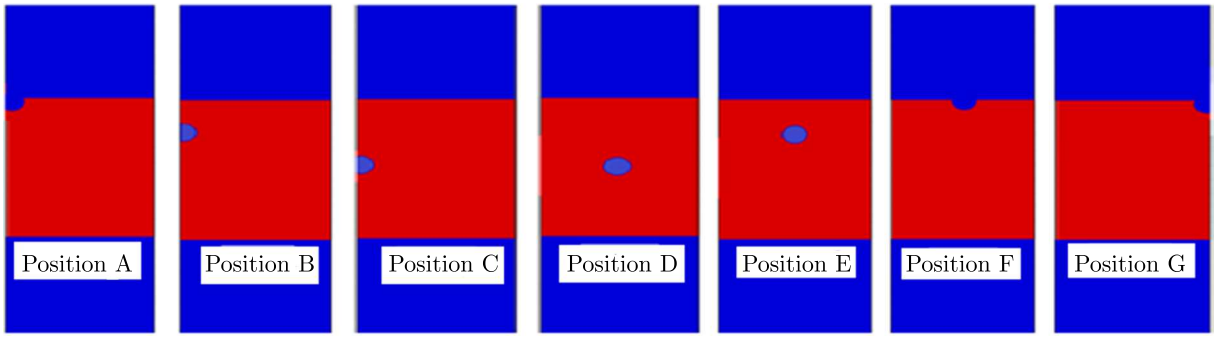

Fig. 12. Different positions of defect

Figure 13 shows the mesh for each defect position. The results of the value of the breaking load are very sensitive to the mesh since the method is based on the number of nodes at the level of the overlap zone. It is also important to ensure the same mesh for the plates, especially at the position of the defect. For all cases, it has been observed that separation of two plates begins at the defect location, especially when the latter is placed near the free edge.

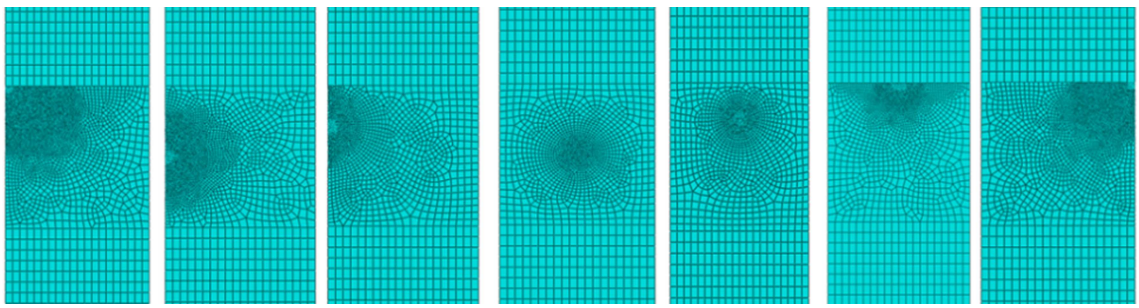

Fig. 13. Detail of the mesh at the region of the bond area for different positions of defects

The architecture of the mesh follows the location of the defect, and the number of nodes is checked at each analysis. Figure 5 illustrates the effect of the number of nodes on the results.

If the defect is in the middle of the adhesive (position D), the breaking strength value will not be affected by this position, but by the stacking sequence.

If the defect is on the free edge of the adhesive, it may have a more serious effect on the breaking strength value, leading to easy separation of the two substrates. If the material stiffness

is high and the defect is on the free edge of the adhesive, the value of the failure load decreases considerably (the case of stacking sequence and orientation of fibers less than 45°).

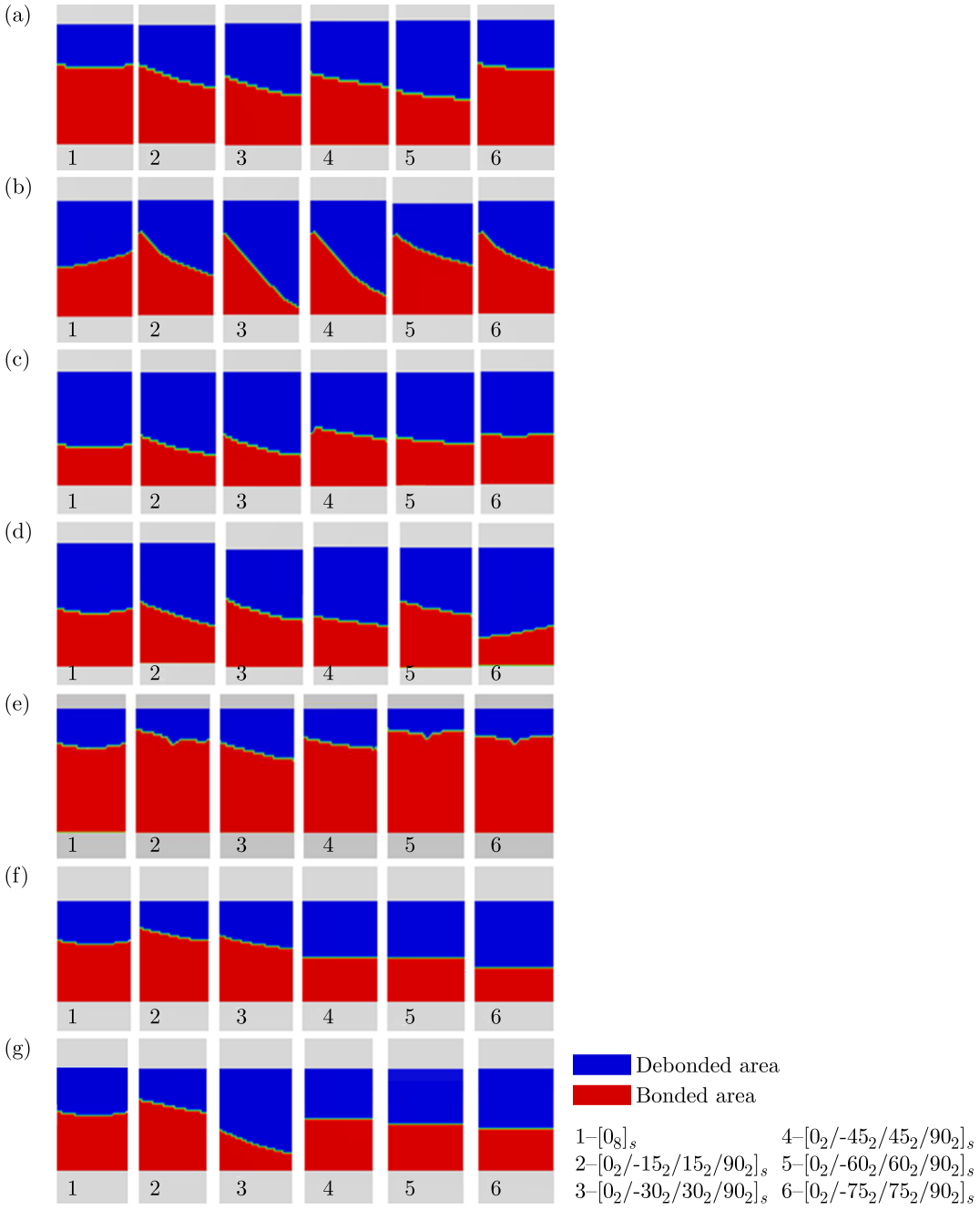

Fig. 14. Debonding area as a function of the stacking sequence and different positions of defects

Figure 15 shows that the defect presence decreases the fracture load. This decrease is remarkable for stack 0° (laminate1) and becomes smaller with the increasing angle of fiber orientation. Therefore, the plate rigidity in the loading direction focuses the defect effect on the separation load, when comparing the effect of defect position. We find that it is more pronounced and may go up until 1KN except for some stacks $(0_2/75_2/-75_2/90_2)$ and $(0_2/75_2/-75_2/90_2)$. Figure 15 presents delaminations paths for different bonding defect positions and stacking sequences. The delamination path depends both of the defect position and the stacking sequence.

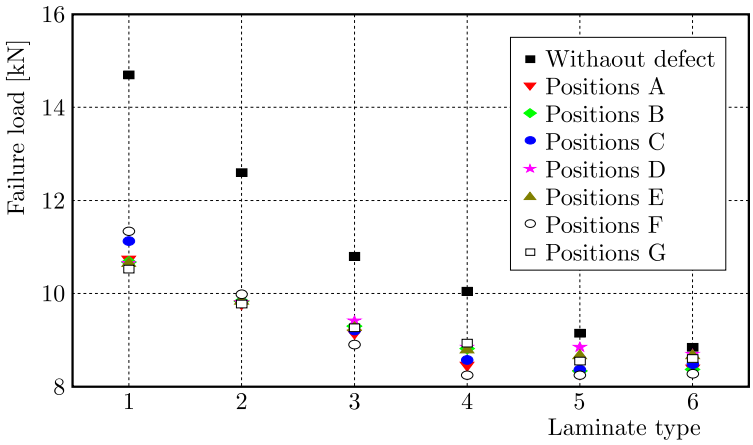

Fig. 15. Failure load as a function of different positions of defects for each stacking sequence

6. Conclusion

This study has been focused on numerical simulation based on the Virtual Crack Closure Technique (VCCT) of a single lap joint with and without the presence of the bonding defect. The following conclusions could be deduced from the obtained results:

- VCCT technique has been used to estimate the failure load value of two composite substrates.
- The failure load value is directly related to stiffness of the material. If the material is more rigid, the failure load value is elevated, but the displacement decreases.
- An increase in thickness of different layers increases rigidity of the composite plate and, consequently, increases the failure load.
- Fiber orientation plays a crucial role on the composite mechanical properties. If the fiber orientation is parallel to the traction direction, the composite acquires high rigidity and, therefore, a significant failure load.
- If the fiber orientation angle exceeds 45°, the material stiffness decreases and the elongation is more important for the plates in the longitudinal axis of the load, which decreases the failure load.
- If energy separation G_I increases, the failure load increases.
- The failure load considerably decreases with variation of the adhesive separation energy and stacking sequence of the composite if the adhesive has a bonding defect.

References

1. Adams R., Atkins R., Harris J., Kinloch A., 1986, Stress analysis and failure properties of carbon-fibre reinforced plastic/steel double lap-joint, *Journal of Ahdesives*, **20**, 29-30
2. Adkins D.W., Pipes R.B., 1988, Tensile behaviour of bonded scarf joints between composite adherend, *Proceedings of the Fourth Japan – US Conference on Composite Materials*, 845-854
3. Ahn J.S., Woo K.S., 2015, Delamination of laminated composite plates by p-convergent partial discrete-layer elements with VCCT, *Mechanics Research Communications*, **66**, June, 60-69
4. Benchiha A., Madani K., 2015, Influence of the presence of defects on the stresses shear distribution in the adhesive layer for the single-lap bonded joint, *Structural Engineering and Mechanics*, **53**, 5, 1017-1030
5. Campilho R., de Moura M.F.S.F, Domingues J.J.M.S., 2005, Modelling single and double-lap repairs on composite materials, *Composites Science and Technology*, **65**, 1948

6. De Moura M.F.S.F., Daniaud R., Magalhães A.G., 2006, Simulation of mechanical behaviour of composite bonded joints containing strip defects, *International Journal of Adhesion and Adhesives*, **26**, 464-473
7. Irwin G.R., 1958, Fracture, [In:] *Handbuch der Physik*, Flugge S., (Ed.), vol. VI, Springer, Berlin, 551-590
8. Janssen M., Zuidema J., Wanhill R.J.H., 2004, *Fracture Mechanics*, Spon Press Taylor & Francis, ISBN 0415346223
9. Jokinen J., Wallin M., Saarela O., 2015, Applicability of VCCT in mode I loading of yielding adhesively bonded joints - a case study, *International Journal of Adhesion and Adhesives*, **62**, October, 85-91
10. Karachalios E.F., Adams R.D., da Silva L.F.M., 2013, Strength of single lap joints with artificial defects, *International Journal of Adhesion and Adhesives*, **45**, 69-76
11. Klug J., Wu X., Sun C.T., 1996, Efficient modeling of postbuckling delamination growth in composite laminates using plate elements, *AIAA Journal*, **34**, 178-184
12. Krueger R., 2004, The virtual crack closure technique: history, approach and applications, *Applied Mechanics Reviews*, **57**, 2, 109-143
13. Kumar S.B., Sridhar I., Sivashanker S., Osiyemi S.O., Bag A., 2006, Tensile failure of adhesively bonded CFRP composite scarf joints, *Materials Science and Engineering B*, **132**, 113-120
14. Liu L., Zhang J., Wang H., Guan Z., 2015, Mechanical behavior of the composite curved laminates in practical applications, *Steel and Composite Structures*, **19**, 5
15. Mokhtari M., Madani K., Belhouari M., Touzain S., Feaugas X., Ratwani M., 2013, Effects of composite adherent properties on stresses in double lap bonded joints, *International Journal of Mechanics and Materials in Design*, **44**, 633-639
16. Mukherjee Y.X., Gulrajani S.N., Mukherjee S., Netravali A.N., 1994, A numerical and experimental study of delaminated layered composites, *Applied Mechanics Reviews*, **28**, 837-870
17. Ray C., Majamuder S., 2014, Failure analysis of composite plates under static and dynamic loading, *Structural Engineering and Mechanics*, **52**, 1
18. Rybicki E.F., Kanninen M.F., 1977, A finite element calculation of stress intensity factors by a modified crack closure integral, *Engineering Fracture Mechanics*, **9**, 931-938
19. Shiming C., Xiaoyu S., Zihao Q., 2011, Shear bond failure in composite slabs – a detailed experimental study, *Steel and Composite Structures*, **11**, 3
20. Shishesaz M., Bavi N., 2013, Shear stress distribution in adhesive layers of a double-lap joint with void or bond separation, *Journal of Adhesion Science and Technology*, **27**, 11, 1197-1225
21. Shivakumar K.N., Tan P.W., Newman J.C., 1988, A virtual crack-closure technique for calculating stress intensity factors for cracked three dimensional bodies, *International Journal of Fracture*, **36**, R43-R50
22. Shokrieh M.M., Rajabpour-Shirazi H., Heidari-Rarani M., Haghpanahi M., 2012, Simulation of mode I delamination propagation in multidirectional composites with R-curve effects using VCCT method, *Computational Materials Science*, **65**, December, 66-73
23. Tsai M., Morton J., Matthews F., 1995, Experimental and numerical studies of a laminated composite single-lap adhesive joint, *Journal of Composite Materials*, **29**, 1254-1275
24. Varughese B., Mukherjee A., 1997, Ply drop-off in layered composites-evaluation of design parameters, [In:] *Computational Structural Mechanics*, Allied Publishers Ltd., 473-482
25. Whitcomb J.D., 1989, Three-dimensional analysis of a postbuckled embedded delamination, *Journal of Composite Materials*, **23**, 862-889

Manuscript received March 2, 2017; accepted for print May 14, 2017

JOURNAL OF THEORETICAL AND APPLIED MECHANICS
55, 4, pp. 1269-1278, Warsaw 2017
DOI: 10.15632/jtam-pl.55.4.1269

COMPARISON OF BAYESIAN AND OTHER APPROACHES TO THE ESTIMATION OF FATIGUE CRACK GROWTH RATE FROM 2D TEXTURAL FEATURES

Matej Mojzeš, Jaromír Kukal

Czech Technical University in Prague, Faculty of Nuclear Sciences and Physical Engineering, Department of Software Engineering, Prague, Czech Republic

e-mail: mojzemat@fjfi.cvut.cz

Hynek Lauschmann

Czech Technical University in Prague, Faculty of Nuclear Sciences and Physical Engineering, Department of Materials, Prague, Czech Republic

The fatigue crack growth rate can be explained using features of the surface of a structure. Among other methods, linear regression can be used to explain crack growth velocity. Non-linear transformations of fracture surface texture features may be useful as explanatory variables. Nonetheless, the number of derived explanatory variables increases very quickly, and it is very important to select only few of the best performing ones and prevent overfitting at the same time. To perform selection of the explanatory variables, it is necessary to assess quality of the given sub-model. We use fractographic data to study performance of different information criteria and statistical tests as means of the sub-model quality measurement. Furthermore, to address overfitting, we provide recommendations based on a cross-validation analysis. Among other conclusions, we suggest the Bayesian Information Criterion, which favours sub-models fitting the data considerably well and does not lose the capability to generalize at the same time.

Keywords: quantitative fractography, optimization, heuristic, linear regression, sub-model selection

1. Introduction

One of the tasks of quantitative fractography consists of modelling the relation between the fatigue crack growth rate (CGR) and textural features of images of fatigue fracture surfaces as explained in (Lauschmann and Siska, 2012; Nadbal *et al.*, 2008; Lauschmann *et al.*, 2006). For this purpose, e.g. a multilinear regression model (Sekeresova and Lauschmann, 2008; Kunz *et al.*, 2010) or a neural network may be used. Of these two, the neural network allows us to analyze and describe the structure of the obtained modeland better imagine the textural subset which is mutually related with the CGR (Lauschmann and Goldsmith, 2009).

The parameters of the respective regression model may be estimated using the least squares method. However, in real-world applications, the basic linear model is not flexible enough to fit the data. This can be solved by adding terms defined by non-linear functions of the basic features, e.g. logarithm, square root, etc. However, adding such features is soon limited by the given number of images.

According to Lauschmann and Goldsmith (2009), one possible way around this limitation is a two-phase stepwise regression with the first stage being bottom-up stepwise regression beginning with a constant model and terminating at a given overfitting level p_0. In each iteration, a new explanatory variable is included – the one which maximally decreases the sum of squares of residui. The second stage is top-down stepwise regression beginning with the final sub-model

from the first stage and terminating at the given final overfitting level p_F. In this procedure, an explanatory variable is selected for the elimination via the Wald test on a selected critical level.

While keeping in mind the relevant motivation for this problem, we suggest that instead of the stepwise regression, an alternative statistical approach based on the method of sub--model multiple testing may provide better results (Mojzeš *et al.*, 2012). There is a vast set of possible criteria that evaluate the quality of a given sub-model and are to be minimized. Further in the paper, we elaborate on the selection and assessment of some of the criteria. They are are interesting in the fractographic context, but may be applied generally to multi-parametric recognition as well.

2. Material and methods

2.1. Linear model

Denote by v_j the crack growth rate assigned to the j-th image of the fracture surface, and by f_{uj} the set of image features. The multilinear model in its basic form is based on the formula

$$\log_{10} v_j \approx c_0 + \sum_u c_u f_{uj} \tag{2.1}$$

Parameters c_u can be estimated by the least squares method. Since the linear model is not flexible enough to fit the data, we may add different non-linear functions of basic features and, therefore, modify the model to the following form

$$\log_{10} v_j \approx c_0 + \sum_q c_q h_q \tag{2.2}$$

where h are selected from an extended set of features containing the features f_u and a selection of their basic non-linear functions, e.g.

$$\{h_v\} \subset \mathbf{P} \cup \mathbf{Q} \cup \mathbf{R} \tag{2.3}$$

where

$$\mathbf{P} = \{f_u\} \qquad \mathbf{Q} = \{\log_{10} f_u, f_u^{-1}, f_u^{1/2}, f_u^2\}, \qquad \mathbf{R} = \{F_{uv}, F_{uv}^{-1}, F_{uv}^{1/2}, F_{uv}^2 \,|\, u > v\} \tag{2.4}$$

where $F_{uv} = f_u f_v$.

The next task will consist of defining a specific methodology on how to select and assess a distinct combination of explanatory variables, i.e. how to select the best sub-model from the extended feature set.

2.2. Sub-model selection

A sub-model should be considered a nested subset of the full model consisting of all the variables from the extended feature set. There are two extreme cases: the first is the full model and the second one corresponds to the constant model.

Let $n \in \mathbb{N}$ be the length of v (i.e. the number of observations), $m \in \mathbb{N}$ the extended feature set cardinality and $k \in \{0, 1, \ldots, m\}$ the number of explanatory extended feature set variables used in the sub-model. Also, let $\mathbf{c} = [c_0, c_1, \ldots, c_k]$ be the vector representing sub-model coefficients calculated solving Eq. (2.2). This vector can be divided into $\mathbf{c}_{red} = [c_1, c_2, \ldots, c_k]$ as its significant part and $\mathbf{c}_0 = [c_0]$ as the constant term coefficient.

Furthermore, we may express the sum of squares for the optimum $\mathbf{c}$ of a given sub-model as SSQ and SSQ_0 as the sum of squares for $\mathbf{c}_0$. Lastly, we will use the sub-model error defined as

$$s_e^2 = \frac{SSQ}{n - k - 1} \tag{2.5}$$

2.3. Data description

The methods developed in this paper will be applied to fatigue fracture surfaces of three laboratory specimens of the heat-resistant steel P92. Compact tension specimens (Fig. 1) (Lauschmann *et al.*, 2011) were loaded in air at 20°C by constant sinusoidal cycles with parameters of the external force according to Table 1. The loading frequency was lowered in steps from 13 Hz to 4 Hz in the final stage.

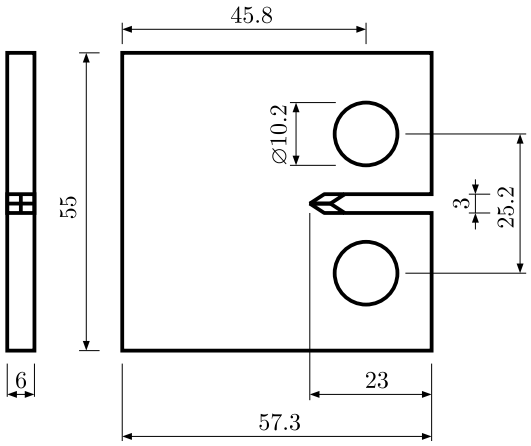

Fig. 1. Compact tension specimen

Table 1. External force parameters

Specimen	F_{min} [N]	F_{max} [N]
1	140	3300
2	2000	4800
3	3300	5500

The fatigue crack surfaces were documented using SEM with magnification 200×, real field of view was 0.6 mm×0.45 mm (examples in Fig. 2). The sequence of images was located in the middle of the crack surface along the same axis according to which the crack length was measured (Fig. 3). The recorded areas were mutually shifted by 0.4 mm. The direction of crack growth in the images was bottom-up. Digital representation in 1200×1600 pixels and 256 brightness values was used. The estimates of CGR were computed from frequently repeated records of the crack length. The course of the CGR related to the crack length was estimated, and every image was assigned a value of the CGR pertinent to its middle.

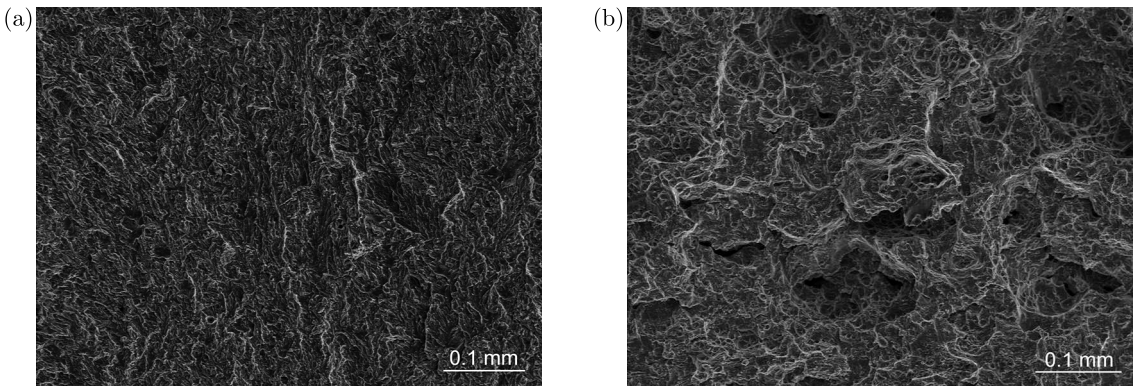

Fig. 2. Examples of SEM pictures of fracture surface; (a) low crack growth rate, (b) high crack growth rate

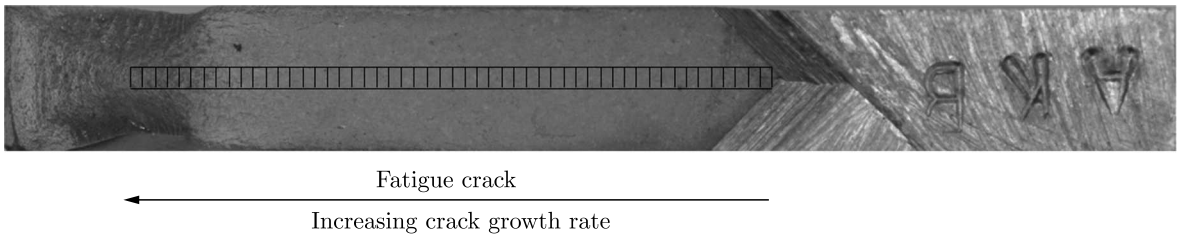

Fig. 3. Layout of snaps in crack surface (schematic plot)

For image textural features, energies of a 2D discrete wavelet transform were taken (Lauschmann and Goldsmith, 2009). Decomposition using the Type 3 Daubechies wavelet at 8 levels was computed by Matlab function `wavedec2`. The energy is the mean square of wavelet coefficients for a given level and direction.

The basic sequence of features, $x_1, x_2, \ldots, x_{24}$, may be regarded as a set of $H_1, V_1, D_1, \ldots, H_8, V_8, D_8$ where H_j, V_j, D_j are wavelet decomposition energies at the j-th level in the horizontal, vertical and diagonal directions. The vector y represents decimal logarithm of the crack growth rate $y = \log_{10} v$.

The analysed data consisted of $n = 162$ observations and a total of 1224 features in the expanded feature set. It comprises:

- basic linear features $\mathbf{P}$, $\mathrm{card}(\mathbf{P}) = 24$,
- non-linear transformations of the basic features $\mathbf{Q}$, $\mathrm{card}(\mathbf{Q}) = 96$,
- dot product transformations of the basic features $\mathbf{R}$, $\mathrm{card}(\mathbf{R}) = 1104$,

as stated in (2.3).

To minimize potential numerical errors when working with the data, input data standardization was implemented as follows

$$x_k = \frac{h_k - \mathrm{E}h}{\sqrt{\mathrm{D}h}} \tag{2.6}$$

using Eh and Dh as the mean value and dispersion of the explanatory data.

Last, but not least – apart from the significance of the data, we can make use also of physical distribution of the data in the given data set, which is divided randomly into three separate groups. This will be especially useful when dealing with the cross-validation.

2.4. Selection heuristic

Searching for the best available sub-model is a binary optimization task that can be defined as minimization of the objective function f: $\mathbf{D} \to \mathbb{R}$ where

$$\mathbf{D} = \{\mathbf{x} \in \{0,1\}^m \mid \mathbf{0} \leqslant \mathbf{x} \leqslant \mathbf{1}\} \tag{2.7}$$

is the binary domain. Here, the binary vector $\mathbf{x}$ is directly representing utilization of the extended feature set, i.e. its components that are equal to "one" are included in the corresponding sub-model. Therefore, $\mathbf{0}$ refers to the constant model, and $\mathbf{1}$ to the full model.

Furthermore, suppose that we have an acceptable value of the objective function f^*. Then, we can define a set of solutions, the goal set, as

$$\mathbf{G} = \{\mathbf{x} \in \mathbf{D} \mid f(\mathbf{x}) \leqslant f^*\} \tag{2.8}$$

where

$$f^* \geqslant \min\{f(\mathbf{x}) \mid \mathbf{x} \in \mathbf{D}\} \tag{2.9}$$

For that purpose, we may utilize some of the well-known heuristic algorithms. We have chosen physically motivated Fast Simulated Annealing (FSA) (Kvasnička *et al.*, 2000) with reputable efficiency in the case of integer optimization tasks. FSA performs mutation on the ring neighbourhood

$$N(\mathbf{x}) = \{\mathbf{y} \in \mathbf{D} \,|\, \|\mathbf{y} - \mathbf{x}\|_1 = 1\} \tag{2.10}$$

Beginning with $k = 0$, $T_k > 0$ and the initial solution vector generated by uniform distribution $\mathbf{x}_0 \sim U(\mathbf{D})$, we perform FSA mutation as a uniformly generated random binary vector $\mathbf{y}_k \sim U(N(\mathbf{x}_k))$. Using $\eta_k \sim U([-1, +1])$, we set

$$\mathbf{x}_{k+1} = \begin{cases} \mathbf{y}_k & \text{for} \quad f(\mathbf{y}_k) < f(\mathbf{x}_k) + T_k \tan \dfrac{\pi\eta}{2} \\ \mathbf{x}_k & \text{for} \quad f(\mathbf{y}_k) \geqslant f(\mathbf{x}_k) + T_k \tan \dfrac{\pi\eta}{2} \end{cases} \tag{2.11}$$

until a solution from the goal set is found, or the pre-defined number of objective function evaluations is exhausted. The cooling strategy is represented by a non-increasing sequence of positive temperatures T_k.

We have been inspired by the increased efficiency of hybrid heuristics in the case of combination of a differential evolution and the steepest descent (Tvrdík and Křivý, 2011). And since the previously defined set of optimization problems has many local minima, we have enhanced the FSA algorithm by a hybrid part – the steepest descent, which may increase the probability of reaching the global optimum.

In our approach to hybrid heuristic optimization, instead of $f(\mathbf{x})$ optimization, we optimize $g(\mathbf{x}) = f(\mathbf{h})$ where $\mathbf{x} = \mathbf{x}_0$, $\mathbf{h} = \mathbf{x}_H$ are the first and last members of any series $\{\mathbf{x}_k\}_{k=0}^{H}$ satisfying $\mathbf{x}_j \in N(\mathbf{x}_{j-1})$, $f(\mathbf{x}_j) < f(\mathbf{x}_{j-1})$ for $j = 1, \ldots, H$. This means $\mathbf{h}$ is the best solution in terms of the steepest descent heuristic. Before any problem solution vector is evaluated, its nearest local neighbourhood is iteratively searched for a better solution until no further advance in terms of the objective function can be made (or until a pre-defined maximum number of local evaluations is exceeded).

This way we were able to set a higher temperature T_0 and use a more benevolent cooling strategy. In other words, the algorithm is able to prevent getting stuck in a local minimum and still not lose the ability to fine-tune a given solution. Thus the FSA performance, on this specific task, has been improved.

2.5. Cross-validation

Having the data divided into three distinct groups allows us to perform strong cross-validation to assess how the results of a specific criterion will generalize to an independent data set.

We will perform the optimization on two out of three groups (training groups) and validate the analysis on the remaining third group (verification group). To improve the overall consistency, multiple rounds of cross-validation will be performed using different permutations of the data sets, and the verification results will be aggregated over the rounds.

As the goodness of fit measure we propose to use R as the correlation coefficient between the original data and the data proposed by the respective sub-model. However, during the optimization itself, we will use the original objective function based on the minimization of the $CRIT$ value.

3. Theory of sub-model selection

At this point, we should choose some of many possibilities for testing sub-model quality. We have selected a few of them in accordance with (Mojzeš *et al.*, 2016) that can be divided in two sets, based on the concepts they are based on. The first one comprises traditional statistical tests and the criterion that will reflect the quality of a sub-model will be the logarithm of the p_{value}. On the other hand, the second set contains different statistical information criteria regarding selection of the model. In the latter case, we are simply minimizing the value of the selected information criterion.

3.1. Sub-model testing

Here, we test significance of a sub-model described by its $\mathbf{c}_{red}$. Respective hypotheses are defined as

$$H_0: \quad \mathbf{c}_{red} = \mathbf{0}$$
$$H_1: \quad \mathbf{c}_{red} \neq \mathbf{0}$$

and the R-square as well as the Wald test are used for their testing.

R-*square test*

In order to use R^2 for the analysis of the sub-model and constant model, according to the variance analysis (Wooldridge, 2002), we must define the stochastic variable F

$$F = \frac{SSQ_0 - SSQ}{SSQ} \frac{n-k-1}{k} \tag{3.1}$$

Here F belongs to $\mathrm{F}_{k,n-k-1}$ and the respective $p_{value} = 1 - \mathrm{F}_{k,n-k-1}(F)$.

Wald test

Alternatively, to test sub-model hypotheses via the Wald test (Anděl, 1978), the variable Z has to be used

$$Z = \frac{1}{k s_e^2} \mathbf{c}^{\mathrm{T}} \mathbf{W}^{-1} \mathbf{c} \tag{3.2}$$

The matrix $\mathbf{W}$ is a result of $(\mathbf{X}^{\mathrm{T}}\mathbf{X})^{-1}$ without the first row and column. Finally, Z has the distribution $\mathrm{F}_{k,n-k-1}$ and $p_{value} = 1 - \mathrm{F}_{k,n-k-1}(Z)$.

Lastly, for both tests, the resulting sub-model quality criterion can be defined as

$$CRIT = \log_{10} p_{value} \tag{3.3}$$

to be minimized. Due to the fact that values of p_{value} may get very close to zero, it is necessary to avoid potential numerical issues and express p_{value} in terms of an incomplete gamma distribution.

3.2. Information criteria

Another approach to the assessment of the sub-model quality is based on statistical information criteria. The selected criteria are presented in order from the least stringent one.

Wilks Information Criterion

Ralston and Rabinowitz (2001) according to Wilks (1962) recommend searching for a sub-model having the minimal error s_e^2. The corresponding logarithmic form, consistent with the following criteria, can be defined as

$$WIC = n \ln s_e^2 \tag{3.4}$$

In this basic criterion, k (i.e. the number of explanatory variables included in the sub-model) is already indirectly penalizing the information quality.

Akaike Information Criterion

Furthermore, an additional penalty for adding more explanatory variables is included in the Akaike criterion measuring relative goodness of the sub-model (Akaike, 1974) denoted as

$$AIC = WIC + 2k \tag{3.5}$$

Bayesian Information Criterion

Bayesian criterion (Schwarz, 1978) prevents overfitting even more by generating a stronger penalty for extra explanatory variables. Following the existing terminology, the criterion may be defined as

$$BIC = WIC + k \ln n \tag{3.6}$$

for $n \geqslant 8$.

As opposed to the logarithm of p_{value}, the final $CRIT$ to be minimized is directly equal to values of the information criteria.

4. Results and discussion

4.1. Heuristic optimization

In order to compare the results achieved with the hybrid heuristic to the stepwise alternative, we have implemented a traditional stepwise approach (Mojzeš *et al.*, 2012). Despite using only 125 variables (basic linear and non-linear transformations, **P** and **Q**) the heuristic sub-model optimization approach was superior to the stepwise approach based on the best correlation coefficient found.

Table 2 aggregates the best results achieved with the current, much more computationally demanding, data. In multiple runs of the heuristic optimization, we were able to obtain even better values of the correlation coefficient. Still, as the ultimate target should be the ability to generalize the independent data set, we will draw final conclusions based on the following cross-validation.

4.2. Cross-validation

The full data set has been divided into three groups of data, each having 59 (Group I), 53 (Group II) and 50 (Group III) observations. For each permutation of training and verification groups the hybrid heuristic optimize the sub-model to make the model fit the training data as well as possible according to the respective method. The same settings and conditions were used as in the case of the full data set without cross-validation. The detailed results are organized

Table 2. Optimal sub-model quality and features using hybrid heuristic

Method	*CRIT*	R	k_{opt}	Term								
				f_u	$f_u^{1/2}$	f_u^2	f_u^{-1}	$\log_{10} f_u$	F_{uv}	$F_{uv}^{1/2}$	F_{uv}^2	F_{uv}^{-1}
F-test	−117.92	0.9909	27	0	0	0	0	0	7	4	11	5
Wald test	−100.29	0.9839	15	0	0	0	1	0	1	3	7	3
WIC	−1099.00	0.9993	88	1	1	4	1	1	14	19	22	25
AIC	−927.03	0.9992	82	0	1	2	1	0	20	19	18	21
BIC	−626.86	0.9871	20	0	0	1	0	1	1	2	13	2

Table 3. Cross-validation results

Method	Training groups	*CRIT*	R_{train}	R_{verify}	k_{opt}
R^2 test	I+II	−86.72	0.9970	0.5937	34
R^2 test	II+III	−76.70	0.9900	0.5785	13
R^2 test	I+III	−79.29	0.9924	0.9594	22
Wald test	I+II	−74.29	0.9867	0.8624	10
Wald test	II+III	−71.34	0.9848	0.6661	5
Wald test	I+III	−66.24	0.9854	0.9476	13
WIC	I+II	−736.29	0.9991	0.4471	55
WIC	II+III	−804.83	0.9997	0.5214	61
WIC	I+III	−716.25	0.9993	0.8286	63
AIC	I+II	−619.41	0.9988	0.8292	48
AIC	II+III	−674.31	0.9996	0.1351	56
AIC	I+III	−584.22	0.9987	0.9229	48
BIC	I+II	−479.12	0.9984	0.6896	45
BIC	II+III	−500.70	0.9995	0.3800	53
BIC	I+III	−430.91	0.9926	0.9574	21

in Table 3. The most important results are in the column of the correlation coefficient R_{verify} which measures the quality of the fit on the verification data set.

These results are aggregated using the mean of respective methods and, furthermore, expanded by comparing the data composed from distinct verification data sets to the original one in Table 4. Also, the results of composed cross-validation are depicted in Fig. 4 as log-log plots of measured and predicted CGRs. The predicted data are distinguished by group symbols $(\times, +, \circ)$. The results of WIC and AIC are the worst ones, since the outliers had to be omitted to enable the plotting. As can be seen, the Wald approach and BIC criterion offer the best results.

Table 4. Cross-validation summary

Method	Mean R	Composed R
R^2 test	0.7105	0.7043
Wald test	0.8254	0.7702
WIC	0.5990	0.5320
AIC	0.6291	0.3281
BIC	0.6757	0.6096

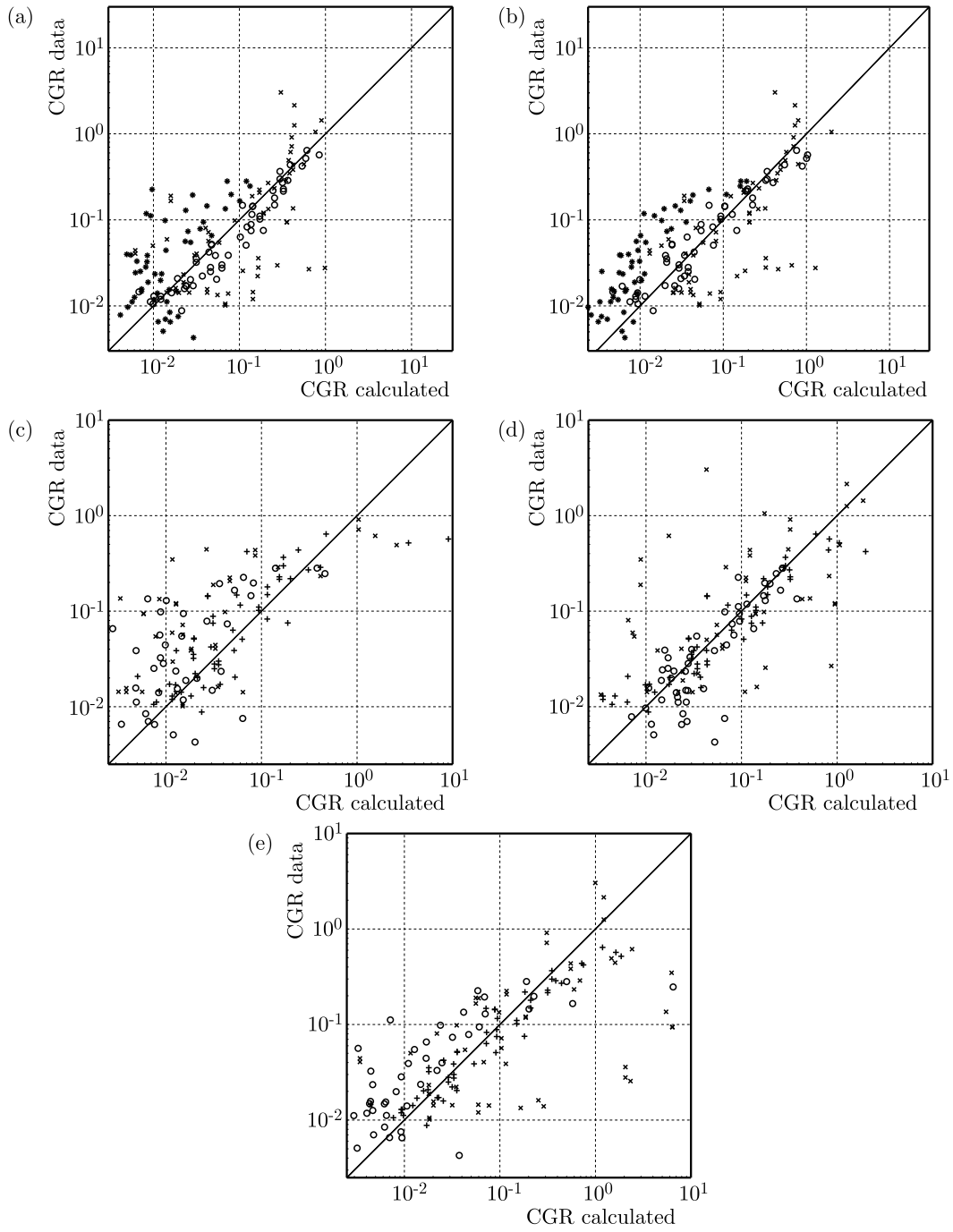

Fig. 4. Prediction of Crack Growth Rate (CGR) using various techniques of sub-model selection (× representing data in group I, + in group II, and ∘ in group III)

5. Conclusions

The benefits of the solution described above are considerable. Nearly an unlimited set of explanatory variables may be offered without any respect to the original number of observations in a given case. Very good models have been obtained also in previously unsolvable cases with a very small number of observations.

Of course, the final result is mostly dependent on the approach of sub-model selection. As it is apparent from the results of cross-validation, and also based on our experience, we are recommending BIC, Wald test and potentially also R^2 test and WIC. Nevertheless, there are significant differences between these four and, more specifically, we are suggesting:

- BIC as a universal criterion,
- Wald test as a well balanced criterion, similar to BIC,
- R^2 test as a legitimate criterion with respect to the variance analysis approach,
- WIC as a criterion that leads to considerable adherence to the data, however, as opposed to other criteria, lacks the ability of generalization.

Acknowledgement
This paper was created under the support of grant OHK4-165/11 CTU in Prague.

References

1. Akaike H., 1974, A new look at the statistical model identification, *IEEE Transactions on Automatic Control*, **AC-19**, 716-723
2. Anděl J., 1978, *Mathematical Statistics* (in Czech), SNTL/Alfa, Praha
3. Kunz J., Kovarik O., Lauschmann H., Siegl J., Augustin P., 2010, Fractographic reconstitution of fatigue crack growth in integrally stiffened panels, *FATIGUE 2010*, **2**, 1711-1720
4. Kvasnička V., Pospíchal J., Tiňo P., 2000, *Evolutionary Algorithms* (in Slovak), STU Bratislava
5. Lauschmann H., Goldsmith N., 2009, Textural fractography of fatigue fractures, [In:] *Fatigue Crack Growth: Mechanics, Behavior and Prediction*, A.F. Lignelli (Edit.), Nova Science Publishers, Inc., 125-166
6. Lauschmann H., Kunz J., Kovařík O., 2011, Analyzing crack growth rate in steel P92 (in Czech), Research report V-KMAT-839/11, FNSPE CTU Prague
7. Lauschmann H., Siegl J., Sumbera J., Siska F., Nedbal I., 2006, An unifying concept for fatigue: The reference crack growth rate, *Materials Characterization*, **56**, 257-265
8. Lauschmann H., Siska F., 2012, The reference texture: A proposal of a physical explanation, *International Journal of Fatigue*, **43**, 120-127
9. Mojzeš M., Klimt M., Kukal J., 2016, Feature selection via competitive levy flights, *2016 International Joint Conference on Neural Networks (IJCNN)*
10. Mojzeš M., Kukal J., Lauschmann H., 2012, Sub-model testing in fractographic analysis, *Proceedings of Mendel 2012 Soft Computing Conference*, Brno University Technology Press, 350-355
11. Nedbal I., Lauschmann H., Siegl J., Kunz J., 2008, Fractographic reconstitution of fatigue crack history – Part II, *Fatigue and Fracture of Engineering Materials and Structures*, **31**, 177-183
12. Ralston A., Rabinowitz P., 2001, *A First Course in Numerical Analysis*, Courier Dover Publications
13. Sekeresova Z., Lauschmann H., 2008, Multi-fractal features of fatigue crack surfaces in relation to crack growth rate, *Materials Structure and Micromechanics of Fracture V*, **567-568**, 129-132
14. Schwarz G., 1978, Estimating the dimension of a model, *Annals of Statistics*, **6**, 461-464
15. Tvrdík J., Křivý I., 2011, Hybrid adaptive differential evolution in partitional clustering, *Proceedings of 17th International Conference on Soft Computing, Mendel 2011*, VUT Brno, Brno, 1-8
16. Wilks S.S., 1962, *Mathematical Statistics*, John Wiley & Sons, Inc., New York
17. Wooldridge J.M., 2002, *Econometric Analysis of Cross Section and Panel Data*, Cambridge, MA: MIT Press

Manuscript received February 14, 2017; accepted for print May 16, 2017

JOURNAL OF THEORETICAL AND APPLIED MECHANICS
55, 4, pp. 1279-1283, Warsaw 2017
DOI: 10.15632/jtam-pl.55.4.1279

TORSION OF A CIRCULAR ANISOTROPIC BEAM WITH TWO LINEAR CRACKS WEAKENED WITH A CIRCULAR CAVITY

Etimad Bayramoğlu Eyvazov, Mecit Öge
Bartın University, Faculty of Engineering, Department of Mechanical Engineering, Bartın, Turkey
e-mail: mecitoge@bartin.edu.tr; mecitoge@yahoo.com

Various components made of anisotropic materials (plast-mass, glass material, etc.) have been widely used in the production of modern mechanisms and machinery. Precise calculation of these elements, constituting the design, holds great importance. In general, fracture and distribution are essential issues in safety calculations. In this study, torsion of a beam with an S oblast having outer and inner constraints as L_2 and L_1 circles with R_2 and R_1 radii, respectively, is investigated.

Keywords: anisotropic medium, orthotropic beams, isotropic beams, affine connections, conformal mapping functions

1. Introduction

There is no study available in the literature a solution of the mentioned in the abstract cases, since the contour L_1 is void of the mapping function. In this study, the solution of the problem is presented with numerical values.

Here, torsion of an area limited with an outer circle L_2 with radius R_2 and inner circle L_1 with radius R_1, having two linear cracks, is investigated. The coordinates of the end points of these cracks are taken as $\pm e$. Volumetric forces are neglected.

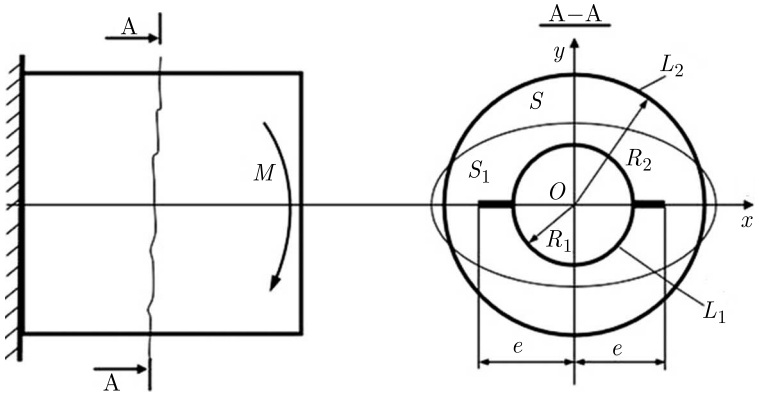

Fig. 1. Anisotropic beam and its cross-section after affine transformation

The beam is twisted by means of a torsional moment applied to the edges (Fig. 1). Here, the coordinate origin is taken as the center of cross-section. The beam is assumed to be made of a homogeneous anisotropic material. At least one elastic plane of symmetry is available on each point of the beam. In this case, all stresses except τ_{xz} and τ_{yz} are zero.

As known (Kosmodamianskii, 1976; Lethniskii, 1971; Kuliyev, 1991), solutions to torsion problems related to orthotropic beams are found using the solutions to torsion problems of beams with other cross-sections. In this case, affine connections are used

$$x_1 = x \qquad \text{and} \qquad y_1 = \beta y \tag{1.1}$$

It should be noted that if the affine connection is assumed as below, then the beam will not be orthotropic

$$x_1 = x + \alpha y \qquad \text{and} \qquad y_1 = \beta y \tag{1.2}$$

With expression (1.1), none of the horizontal values in the beam cross-section changes (since the horizontal axis does not change) as for the vertical values (i.e. those on Oy axis), they will either increase or decrease depending on the coefficient β that characterizes anisotropy of the beam.

Thereby, in order to evaluate stresses on orthotropic bars, firstly, the torsion problem of an isotropic beam with S_1 cross-section (which is obtained with affine connection $= x_1$ and $y_1 = \beta y$) should be solved.

According to the previous studies, $\tau_{x_1y_1}$ and $\tau_{y_1z_1}$ stresses are found from the following equation

$$\tau_{x_1z_1} - \mathrm{i}\tau_{y_1z_1} = \mathrm{i}[2F'(z_1) - \overline{z}_1] \tag{1.3}$$

where $\tau_{x_1z_1}$ and $\tau_{y_1z_1}$ are components of the tangential stresses on the cross-section S_1, and i – imaginary unit, $F(z_1)$ is the regular function on the cross-section S_1, $z_1 = x_1 + \mathrm{i}y_1$ and $\overline{z}_1 = x_1 - \mathrm{i}y_1$ are complex variables. $F(z_1)$ is calculated from boundary conditions, i.e., from the states of equilibrium and the equation of deformations on the boundaries.

These boundaries can be written as follows

$$\begin{array}{lll} \varepsilon_x = 0 & \varepsilon_y = 0 & \varepsilon_z = 0 \\ \gamma_{xy} = 0 & \gamma_{xz} = a_{55}\tau_{xz} & \gamma_{yz} = a_{44}\tau_{yz} \end{array}$$

where a_{44} and a_{55} are elastic constants that characterize anisotropy of the material.

Equations (1.1) with affine connections, semi axes of L_2 contour with radius R_2 are transformed into an ellipse $a = x_1$ and $b = \beta y_1$, on the other hand, the contour L_1 with radius R_1 on the Ox axis with two cracks, is transformed into an ellipse with two cracks (here it is assumed that $\beta \neq 1$).

If $\beta < 1$, then the linear values decline along the Oy axis, in the case of $\beta > 1$ the same values increase.

$F(z_1)$ regular function within the enclosed area S_1 can be evaluated using the below given boundary conditions (Kosmodamianskii, 1976; Kuliyev, 1991, 2004; Sherman, 1992)

$$F(z_1) - \overline{F(z_1)} = \mathrm{i}t_1\overline{t}_1 + C_k \tag{1.4}$$

where t_1 are affixes of the points on one of the contours of the cross-section S_1. C_k is an arbitrary constant.

Components of $\tau_{x_1z_1}$ and $\tau_{y_1z_1}$ tangential stresses on characteristic points of the cross--section S_1 can be calculated by equation (1.4) (here, the end points of the cracks are also included).

Afterwards, τ_{xz} and τ_{yz} can be calculated for an orthotropic beam by the following equation (Kosmodamianskii, 1976; Lethniskii, 1971; Kuliyev, 1991)

$$\tau_{xz} = \beta\tau_{x_1z_1} \qquad \tau_{yz} = \tau_{y_1z_1}$$

As indicated by these equations, τ_{yz} and $\tau_{y_1z_1}$ stresses do not vary on isotropic and anisotropic beams. Here, τ_{xz} tangential stress varies depending on the parameter β. It increases or decreases depending on β ($\beta = \sqrt{a_{44}/a_{55}}$).

$F(z_1)$ regular function can be expressed as follows for the contour L_2 within the enclosed S_1 area (Kosmodamianskii, 1976; Kuliyev, 1991, 2004; Sherman, 1992)

$$F(t_2) = \mathrm{i}\sum_{k=0}^{\infty}\alpha_k\Big(\frac{A_2}{t_2}\Big)^k + \mathrm{i}\sum_{k=0}^{\infty} b_k\Big(\frac{t_2}{A_2}\Big)^k \qquad \text{on} \quad L_2 \tag{1.5}$$

where

$$\alpha_k = \sum_{\nu=k-2E(k/2)}^{k\ *}\alpha_\nu L_{(k-\nu)/2} \qquad b_k = \sum_{n=k}^{\infty}\beta_k a^{(2)}_{(n-k)/2} \tag{1.6}$$

$F(z_1)$ function can be defined as follows in the inner L_1 contour (an ellipse with two linear cracks) (Kosmodamianskii, 1976; Kuliyev, 1991; Sherman, 1992)

$$F(t_1) = i\sum_{k=0}^{\infty}\alpha_k\xi_1^{-k} + \mathrm{i}\sum_{k=1}^{\infty}H_1(k)\xi_1^{k} + \mathrm{i}\sum_{k=0}^{\infty}H_2(k)\xi_1^{-k} \qquad \text{on} \quad L_1 \tag{1.7}$$

The following notations are given in equation (1.7)

$$\begin{aligned} &H_1(k) = \sum_{\nu=k}^{\infty} b_\nu\Big(\frac{A_1}{A_2}\Big)^\nu m_1^{\frac{\nu-k}{2}} C_\nu^{\frac{\nu-k}{2}} \qquad H_2(k) = \sum_{\nu=\varepsilon}^{\infty\ *} b_\nu\Big(\frac{A_1}{A_2}\Big)^\nu m_1^{\frac{\nu+k}{2}} C_\nu^{\frac{\nu+k}{2}} \\ &\varepsilon' = \varepsilon + \frac{1}{2}(k+\varepsilon) \qquad \varepsilon = 0 \qquad \varepsilon = 1 \\ &b_k = \sum_{n=k}^{\infty\ *}\beta_n a_{(n-k)/2} \end{aligned} \tag{1.8}$$

The outer circle with contour L_2 (with semi axes $a_2 = R_2$ and $b_2 = \beta R_2$) is mapped on the circle with the unit diameter (equals to 1) using the mapping function (Kosmodamianskii, 1976; Kuliyev, 1991, 2004; Sherman, 1992)

$$t_2 = A_2\Big(\tau + \frac{m_2}{\tau}\Big) \qquad A_2 = \frac{R_2 + \beta R_2}{2} \qquad m_2 = \frac{R_2 - \beta R_2}{R_2 + \beta R_2} \tag{1.9}$$

The inner contour L_1 is mapped onto the circle with the unit diameter (equals to 1) using the mapping function (Kuliyev, 1991, 2004)

$$t_1 = A_1\tau\sum_{n=0}^{\infty}\tau^{-n}\Pi_n \tag{1.10}$$

where

$$\begin{aligned} &A_1 = \frac{R_1 + \beta R_1}{2} \qquad m_1 = \frac{R_1 - \beta R_1}{R_1 + \beta R_1} \\ &\Pi_n = \sum_{k=0}^{\infty}\gamma_{k-1}T_{n-k} \qquad T_n = \sum_{\nu=n-2E(n/2)}^{n\ *} m_1^{\frac{n-\nu}{2}}\gamma_{-1}^{\frac{n-\nu}{2}} l_\nu^{n-\nu} \end{aligned}$$

The inverse functions of (1.9) and (1.10) mapping functions are as bellow (Kosmodamianskii, 1976; Kuliyev, 2004; Sherman, 1992)

$$\xi_2 = \frac{z_2}{A_2}\sum_{n=0}^{\infty}a_n^{(2)}\Big(\frac{A_2}{z_2}\Big)^{2n} \qquad \xi_1 = \chi(z) = \frac{z_1}{A_1}\sum_{n=0}^{\infty}E_k\Big(\frac{A_1}{z_1}\Big)^k \tag{1.11}$$

The coefficients of the serial elements of the analytical functions $F_1(z)$ and $F_2(z)$ can be found using proper boundary conditions given below: (Kosmodamianskii, 1976; Kuliyev, 1991; Sherman, 1992)

$$\begin{aligned} &F_1(t_1) + \overline{F_1(t_1)} = \mathrm{i}\bar{t}_1 + C_1 \\ &F_1(t_2) + \overline{F_1(t_2)} = \mathrm{i}\bar{t}_2 + C_2 \end{aligned} \tag{1.12}$$

where t_1 and t_2 variables are properly found from (1.9) and (1.10) equations.

As we place equations (1.6) and (1.7) into boundary condition (1.12), we obtain a linear algebraic system depending on two unknown coefficients following some mathematical connections and remarks by Kosmodamianskii (1976), Kuliyev (1991, 2004). Here, we proceed with the variable τ since $\tau\overline{\tau} = 1$ on the unit circle)

$$\begin{aligned} &\alpha_k + H_1(k) + H_2(k) = \sum_{n=k}^{\infty} \Pi_{n-k}\Pi \qquad \text{on} \quad L_1 \\ &V_1(k) + V_2(k) + V_3(k) = A_2^2 m_2 \varepsilon \qquad \text{on} \quad L_1 \end{aligned} \tag{1.13}$$

where $V_1(k)$, $V_2(k)$, $V_3(k)$ are respectively found from the following equations (Kuliyev, 1991, 2004)

$$\begin{aligned} &V_1(k) = \sum_{\nu=0}^{k}{}^{*} \Big(\frac{A_1}{A_2}\Big)^k C_{-\nu}^{\frac{k-\nu}{2}} m_2^{\frac{k-\nu}{2}} \alpha_\nu \qquad V_2(k) = \sum_{\nu=k}^{\infty}{}^{*} b_\nu C_\nu^{\frac{k+\nu}{2}} m_2^{\frac{k+\nu}{2}} \\ &V_3(k) = \sum_{\nu=k}^{\infty}{}^{*} b_\nu C_\nu^{\frac{k-\nu}{2}} m_2^{\frac{k-\nu}{2}} \end{aligned} \tag{1.14}$$

From the first terms of these equations, a system of equations is obtained. α_k and β_k are coefficients that can be found using these equations.

This is presented with the following numerical example.

Cross-sectional dimensions of the beam are assumed in accordance with the following ratio for numerical calculations.

1. In the case of $\beta = 1/2$, the semi axes of the outer contour (curvilinear line, the circle with radius R_2) are transformed into the ellipse with semi axes $a_2 = R_2$; $b_2 = \beta R_2$, and the inner contour (the one with two cracks and radius R_1) is transformed into the ellipse with two cracks. The semi axes of such ellipses can be defined as $a_1 = R_1$; $b_1 = \beta R_1$. Accordingly, the problem related with torsion of the beam depending on the parameter β is calculated using the torsion problem of another beam with a different cross section.

Tangential τ_{xz} and τ_{yz} stresses, given in Table 1, are found using equation (1.3).

Table 1. Tangential τ_{xz} and τ_{yz} stresses for choice 1

Choice 1	Points	$\tau_{xz}/(\mu\tau a_2)$	$\tau_{yz}/(\mu\tau a_2)$
$\beta = 1/2$	$z = 0.65$	–	24.58
$a_1 = 2b_1$	$z = 0.70$	–	13.29
$a_1 = 0.25a_2$	$z = 0.75$	–	8.02
	$z = 1.00$	–	2.92
	$z = 0.5\mathrm{i}a_1$	0.548	–
	$z = 0.7\mathrm{i}a_1$	0.141	–
	$z = 1.0\mathrm{i}a_1$	0.118	–

2. In the case of $\beta = 1/2$, $R_2 = 0$. The inner contour transforms into the linear crack with length $l = 2e$; and the outer contour transforms into the ellipse with semi axes $a_2 = R_2$, $b_2 = \beta R_2$. This way, the problem, the subject of the current study, is solved by means of the solution to the torsion problem of the elliptical beam with a central linear crack.

The values of τ_{xz} and τ_{yz} tangential stresses for choice 2 are given in Table 2.

Table 2. Values of τ_{xz} and τ_{yz} tangential stresses

Choice 1	Points	$\tau_{xz}/(\mu\tau a_2)$	$\tau_{yz}/(\mu\tau a_2)$
$\beta = 1/2$	$z = 0.65$	–	14.17
$b_1 = 0$	$z = 0.70$	–	7.76
$a_1 = 0.5a_2$	$z = 0.75$	–	4.77
	$z = 1.00$	–	1.56
	$z = 0.5\mathrm{i}a_1$	-1.01	–
	$z = 0.7\mathrm{i}a_1$	-0.031	–
	$z = 1.0\mathrm{i}a_1$	-0.48	–

2. Conclusion

Calculations of torsion of orthotropic beams can be performed using calculations of isotropic beams with different cross-sections (the cross-section S is obtained with affine connection $x_1 = x$ and $y_1 = \beta y$). Here, the linear values on the x axis do not vary with the varying parameter β), the ones on the y axis increase or decrease in direct proportion with β.

The stresses on orthotropic beams can be calculated using the equations given below ($\tau_{x_1 z_1}$ and $\tau_{y_1 z_1}$ are known)

$$\tau_{xz} = \beta^2 \tau \tau_{x_1 y_1} \qquad \tau_{yz} = \beta \tau \tau_{y_1 z_1} \tag{2.1}$$

References

1. Kosmodamianskii A.S., 1976, *Stress State of Anisotropic Media with Holes and Cavities*, Kiev-Donetsk Vysshaya Shkola, p. 200
2. Kuliyev S.A., 1991, *Two Dimensional Problems of Elasticity Theory*, M. Stroyizdat, p. 352
3. Kuliyev S.A., 2004, *Conformally Mapping Functions of Complex Domains*, Baku Azerneshr, p. 372
4. Lethniskii S.G., 1971, *Torsion of Anisotropic and Inhomogeneous Bars*, M. Nauka, p. 200
5. Sherman D.I., 1992, Solution of planar elasticity problems in anisotropic media, *Prikladnaya Mathematika i Mekhanika*, 180-106

Manuscript received November 10, 2016; accepted for print May 19, 2017

JOURNAL OF THEORETICAL AND APPLIED MECHANICS
55, 4, pp. 1285-1297, Warsaw 2017
DOI: 10.15632/jtam-pl.55.4.1285

PROPERTY IDENTIFICATION OF VISCOELASTIC SOLID MATERIALS IN NOMOGRAMS USING OPTIMIZATION TECHNIQUES

Tiago Lima de Sousa, Ferdinand Kanke, Jucélio Tomás Pereira, Carlos Alberto Bavastri

Parana Federal University, Postgraduate Program in Mechanical Engineering, Curitiba, Brazil

e-mail: tiago.sousa.eng@gmail.com; ferdinand.2k@gmail.com; jucelio.tomas@ufpr.br; bavastri@ufpr.br

Viscoelastic materials have been widely used as devices for vibration control in general. Frequently, dynamic properties of those materials are provided by manufacturers only in a graph form in the frequency domain. This is a recurring problem in industry and academia. Thereby, the goal of this work is to contribute to this important issue which is to obtain the properties of viscoelastic materials from nomograms supplied by the manufacturer. The methodology is based on the digitalization of the nomogram of the material and on the subsequent reading of a set of points from two curves in different temperatures. An optimization problem with simple restrictions is built having characteristic constants of the constitutive models as design variables. The problem is solved by applying a hybrid optimization technique. The results obtained are presented, and prove to be very promising.

Keywords: identification, optimization, viscoelastic materials, Zener fractional model, Wiechert model

1. Introduction

Viscoelastic materials (VEMs) have very common applications as structural components or as elements for mitigating vibrations in vehicular structures, aeronautic structures, rotating axes, etc. (Rao, 2002; Ribeiro *et al.*, 2015). Due to the great variety of applications of this type of materials, in the recent decades there has been an increase in the need for more precise models to describe their mechanical behavior. In this sense, a plenty of works have been presented in the recent years, not only in the frequency domain but also in the time domain.

In this context, among the works in the frequency domain, one can mention Park (2001), and Costa and Ribeiro (2011). In these works, the Wiechert generalized model is used to perform an interconversion of the relaxation modulus function (written in terms of Prony series) from the time domain to the frequency domain, obtaining a complex modulus. In this function, the real part represents the equivalent of the stored modulus in mechanical systems, while the imaginary part represents the equivalent of the loss modulus. Thereby, the authors use optimization techniques for fitting theoretical curves of the loss and storage modulus to the experimental curves. Following the same line, starting from a VEM composite with one-degree-of-freedom system, Lopes *et al.* (2004) proposes an identification methodology based on experimentally measured transmissibility curves of constitutive models based on fractional calculus. Agirre and Elejabarrieta (2010) present an inverse identification method using Laplace transforms, in which a four-parameter fractional model is converted from the time domain to the frequency domain. In order to identify properties of a material, an optimization problem is proposed aiming at minimization of the distance between the theoretical and the experimental values of dynamic response in a clamped beam, in a given frequency range. Likewise, Jrad *et al.* (2013) investigate the VEM's behavior in terms of the dynamic stiffness in the frequency domain using the

Wiechert model. The constants related to springs and dampers of the model are identified. More recently, Jalocha *et al.* (2015) propose a method to identify VEM material parameters, in which the relaxation times are optimized based on numerical integration involving the measured relaxation spectra.

From this brief review of literature, one can observe that different approaches to the characterization of VEMs are based on experimental data. However, one frequently faces the situation in which the user of such a material has access only to the nomogram provided by the manufacturer. That nomogram (exemplified in Fig. 1, for material EAR® C1002) provides a graphic representation for the dynamic modulus and loss factor in a reference temperature, and (using the concept of 'reduced frequency') the possibility of obtaining those variables in other temperatures.

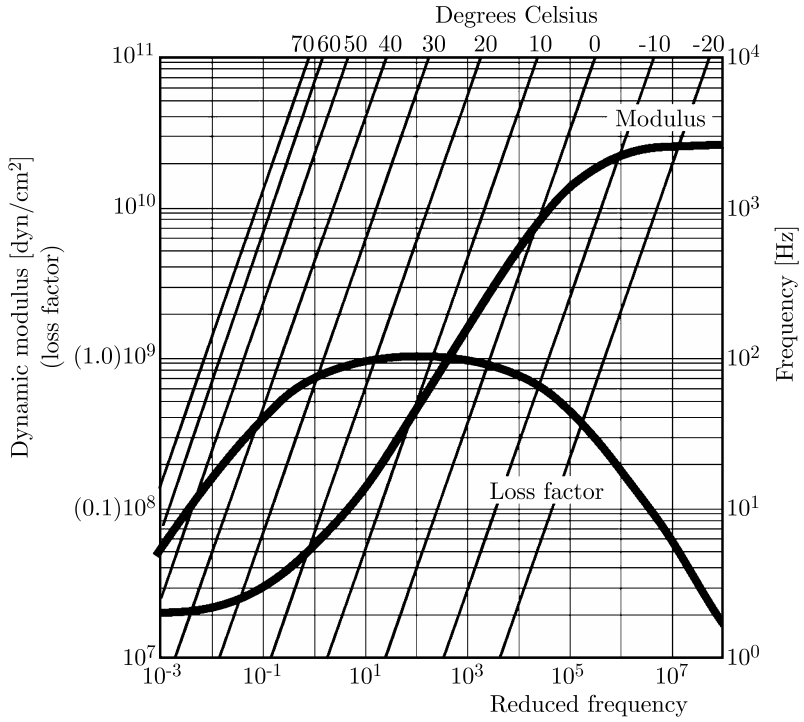

Fig. 1. Material: C1002 – nomogram provided by the EAR® manufacturer

The present work aims at developing and applying a numerical methodology to identify the properties of a linear and thermorheologically simple VEMs based exclusively on nomograms. Such a methodology is based on the digitalization of points of the curves from the nomogram, namely, the dynamic modulus and the loss factor, for different temperatures and frequencies. An objective function to be minimized is defined by taking into account the distance between the theoretical model and the digitized points. The design variables of the optimization process are parameters of the VEM constitutive model. Through mathematical optimization, one minimizes the objective function. However, due to the optimal point being strongly dependent of the initial point in the optimization process, we opt for a hybrid algorithm. In this case, initially a heuristic optimization method, based on the Genetic Algorithm, is used in order to approximate the probable optimum global point ($\mathbf{X}_{GA}$). This point is used as the starting point for an optimization process based on nonlinear programming. This last step aims at generating a better approximation of the global optimum.

2. Models for linear viscoelastic material response

VEMs can be defined as those which present elastic and viscous behavior simultaneously (Brinson and Brinson, 2008; Lemini, 2014). In order to describe their mechanical behavior, various works (Welch *et al.*, 1999; O'Brien *et al.*, 2001; Jrad *et al.*, 2013) make use of rheological models of linear viscoelasticity that consist of combinations of springs and dampers in which the springs represent the elastic part of the behavior and dampers represent its viscous part. Therewith, and associating those elements in series, parallel, series-parallel, etc., various constitutive equations appear, which can be written applying the classical mechanical model or the fractional calculus (Mainardi, 2010). In addition, by interconversion, those models can be defined in time or frequency domains.

2.1. Wiechert constitutive model (classical mechanical model)

Aiming at describing the mechanical behavior of VEMs, Brinson and Brinson (2008) discuss a classical physical model named 'Wiechert model' or 'generalized Maxwell model' (Fig. 2a). The mathematical modeling of this mechanical system in the time domain t, considering the influence of temperature T, creates the relaxation modulus function $E(t,T)$, written in terms of a series of decreasing exponentials, named 'Prony Series', as follows

$$E(t,T) = E_\infty + \sum_{i=1}^{NT} E_i \exp\Big(\frac{-t}{\alpha_T \tau_i}\Big) \tag{2.1}$$

where NT is the total number of terms of that series; E_∞ is a constant named as 'equilibrium modulus', representing the purely elastic response of the material; E_i and τ_i are the elastic constant and the relaxation time, respectively, associated to the i-th component of the Wiechert model (Soussou *et al.*, 1970; Brinson and Brinson, 2008; Suchocki *et al.*, 2013). Additionally, α_T is a constant defined as a shift factor that describes the dependence of the relaxation times in relation to temperature and, in the present work, follows the Williams-Landel-Ferry empirical equation (Williams *et al.*, 1955) given by

$$\log \alpha_T = -\frac{C_1^T (T - T_0)}{C_2^T + (T - T_0)} \tag{2.2}$$

where C_1^T and C_2^T are constants to be determined, which are related to the material properties (Ferry and Stratton, 1960; Ward and Sweeney, 2004; Brinson and Brinson, 2008).

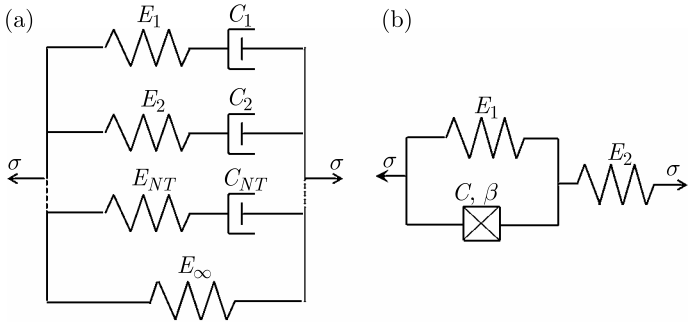

Fig. 2. (a) Wiechert model and (b) fractional Zener model

To analyze the VEMs behavior in the frequency domain, it is common in the literature (Nashif *et al.*, 1985; Honerkamp, 1989; Bavastri, 1997; Park, 2001; Lopes *et al.*, 2004; Jalocha *et al.*, 2015) to rewrite Eq. (2.1) as follows

$$E(\Omega_r) = E_{\mathrm{Re}}(\Omega_r) + \mathrm{i} E_{\mathrm{Im}}(\Omega_r) \tag{2.3}$$

defined as a complex dynamic modulus. The variable Ω_r, defined as the 'reduced frequency', groups temperature effects T and frequency Ω. The reduced frequency can be represented by

$$\Omega_r = \alpha_T \Omega \tag{2.4}$$

It is important to highlight that the real part of Eq. (2.3), defined as the 'storage modulus', is given by

$$E_{\mathrm{Re}}(\Omega_r) = E_\infty + \sum_{i=1}^{NT} \frac{(\Omega_r \tau_i)^2 E_i}{(\Omega_r \tau_i)^2 + 1} \tag{2.5}$$

and the imaginary part, defined as the 'loss modulus', is given by

$$E_{\mathrm{Im}}(\Omega_r) = \sum_{i=1}^{NT} \frac{\Omega_r \tau_i E_i}{(\Omega_r \tau_i)^2 + 1} \tag{2.6}$$

The storage modulus and the loss modulus indicate how much the material behavior approaches the elastic or viscous behavior, respectively. In this case, the loss factor η, is defined as the ratio between the loss and the storage, that is

$$\eta(\Omega_r) = \frac{E_{\mathrm{Im}}(\Omega_r)}{E_{\mathrm{Re}}(\Omega_r)} \tag{2.7}$$

This equation describes the ratio between energies dissipated and stored by the material in a cycle. Consequently, Eq. (2.3) can be written as follows

$$E(\Omega_r) = E_{\mathrm{Re}}(\Omega_r)[1 + \mathrm{i}\eta(\Omega_r)] \tag{2.8}$$

The real storage modulus and the corresponding loss factor are referred to as dynamic properties of the material at issue. Such information is useful, for example, for designing projects in which it is necessary to know the frequencies that results in a greater or lesser energy dissipation.

2.2. The fractional Zener constitutive model

Another mathematical model that describes VEMs behavior is the fractional Zener model (Fig. 2b) whose differential equation of a non-integer order (often named 'fractional order' in the literature) is given by

$$\sigma(t) + \frac{C}{E_1 + E_2} \frac{d^\beta \sigma(t)}{dt^\beta} = \frac{E_1 E_2}{E_1 + E_2} \varepsilon(t) + \frac{E_2 C}{E_1 + E_2} \frac{d^\beta \varepsilon(t)}{dt^\beta} \tag{2.9}$$

where E_1 and E_2 are the stiffness modulus of the elastic elements, C is the viscosity coefficient and β is the non-integer order of differentiation of the Scott-Blair model (Bagley and Torvik, 1986; Mainardi, 2010). Defining the parameters $\overline{E}_0 = E_1 E_2/(E_1 + E_2)$, $r_E = (E_1 + E_2)/E_1$ and $(\tau_a)^\beta = C/(E_1 + E_2)$, it is possible to rewrite Eq. (2.9) as follows

$$\sigma(t) + (\tau_a)^\beta \frac{d^\beta \sigma(t)}{dt^\beta} = \overline{E}_0 \varepsilon(t) + \overline{E}_0 r_E (\tau_a)^\beta \frac{d^\beta \varepsilon(t)}{dt^\beta} \tag{2.10}$$

This mathematical model is known in the literature as a 'four-parameter fractional constitutive model'. Consequently, the relaxation modulus, in the time domain, can be put as follows

$$E(t) = \overline{E}_0 \Big[1 + r_E E_\beta \Big(-\Big(\frac{t}{\tau_a}\Big)^\beta\Big)\Big] \tag{2.11}$$

where $E_\beta(\cdot)$ is the Mittag-Leffler (ML) function of an β order parameter (Mainardi and Spada, 2011).

The ML function, denoted by $E_\beta(z)$ with $\beta > 0$, can be defined by a representation in convergent series in the complex plane $\mathbb{C}$ as follows

$$E_\beta(z) = \sum_{n=0}^{\infty} \frac{z^n}{\Gamma(1+\beta n)} \qquad \beta > 0, \quad z \in (C) \tag{2.12}$$

where Γ is the Euler gamma function. For the convergence of the series of potencies in Eq. (2.12), the parameter β can be complex, since $\mathrm{Re}(\beta) > 0$ (Mainardi, 2010).

To obtain the dynamic modulus in the frequency domain, one can apply the Fourier transform to all terms in Eq. (2.10), producing

$$\sigma(\Omega) + (\tau_a)^\beta (\mathrm{i}\Omega)^\beta \sigma(\Omega) = \overline{E}_0 \varepsilon(\Omega) + E_0 r_E (\tau_a)^\beta (\mathrm{i}\Omega)^\beta \varepsilon(\Omega) \tag{2.13}$$

From Eq. (2.13), one can define the complex modulus of the material, $\overline{E}_c(\Omega)$, as follows

$$\overline{E}_c(\Omega) = \frac{\sigma(\Omega)}{\varepsilon(\Omega)} = \frac{\overline{E}_0 + \overline{E}_0 r_E (\mathrm{i}\tau_a \Omega)^\beta}{1 + (\mathrm{i}\tau_a \Omega)^\beta} \tag{2.14}$$

Regarding the influence of temperature, Eq. (2.14) can be rewritten as a function of the reduced frequency (Pritz, 1996; Cruz, 2004; Lopes *et al.*, 2004; Jalocha *et al.*, 2015) according to

$$\overline{E}_c(\Omega_r) = \frac{\overline{E}_0 + \overline{E}_\infty b_1 (\mathrm{i}\Omega_r)^\beta}{1 + b_1 (\mathrm{i}\Omega_r)^\beta} \tag{2.15}$$

where $\overline{E}_\infty = \overline{E}_0 r_E$ and $b_1 = (\tau_a)^\beta$. Equation (2.15) is the classical model of a four-parameter fractional derivative in the frequency domain, and can be rewritten as follows

$$\overline{E}_c(\Omega_r) = E_{\mathrm{Re}}(\Omega_r) + \mathrm{i} E_{\mathrm{Im}}(\Omega_r) = E_{\mathrm{Re}}(\Omega_r)[1 + \mathrm{i}\eta(\Omega_r)] \tag{2.16}$$

In this case, the storage modulus can be expressed as

$$E_{\mathrm{Re}}(\Omega_r) = \frac{\overline{E}_0 + (\overline{E}_0 + \overline{E}_\infty) b_1 (\Omega_r)^\beta \cos\left(\frac{\beta\pi}{2}\right) + \overline{E}_\infty b_1^2 (\Omega_r)^{2\beta}}{1 + 2 b_1 (\Omega_r)^\beta \cos\left(\frac{\beta\pi}{2}\right) + b_1^2 (\Omega_r)^{2\beta}} \tag{2.17}$$

and the loss factor as

$$\eta(\Omega_r) = \frac{(\overline{E}_\infty - \overline{E}_0) b_1 (\Omega_r)^\beta \sin\left(\frac{\beta\pi}{2}\right)}{\overline{E}_0 + (\overline{E}_0 + \overline{E}_\infty) b_1 (\Omega_r)^\beta \cos\left(\frac{\beta\pi}{2}\right) + \overline{E}_\infty b_1^2 (\Omega_r)^{2\beta}} \tag{2.18}$$

3. Methodology

Starting from the nomogram of a given material, the methodology is based on the digitalization of that image and in the subsequent reading of a set of points on the two characteristic curves of the material (storage modulus and loss factor) in different frequencies and temperatures. Next, the parameters of the theoretical model are identified through minimization, using a hybrid optimization technique, of the relative squared distance between that model and the curves obtained by digitalization. The standard optimization problem is solved based on the corresponding differences between the curves of the storage dynamic modulus R_{qk}^{Re} and the loss factor R_{qk}^{η} in the k-th point $1 \leqslant k \leqslant N_{pt}$ (N_{pt} is the total number of points of each analyzed

curve) and in the q-th temperature $1 \leqslant q \leqslant N_{temp}$ (N_{temp} is the total number of evaluated curves in different temperatures). That is

$$R_{qk}^{\mathrm{Re}} = \frac{E_{\mathrm{Re}}^{Exp}(\Omega_k, T_q) - E_{\mathrm{Re}}(\Omega_k, T_q)}{E_{\mathrm{Re}}^{Exp}(\Omega_k, T_q)} \qquad R_{qk}^{\eta} = \frac{\eta^{Exp}(\Omega_k, T_q) - \eta(\Omega_k, T_q)}{\eta^{Exp}(\Omega_k, T_q)} \tag{3.1}$$

This way, the total relative squared distance R_{T2} is given by

$$R_{T2} = \frac{1}{N_{totalPts}} \sum_{q=1}^{N_{temp}} \sum_{k=1}^{N_{pt}} \left((R_{qk}^{\mathrm{Re}})^2 + (R_{qk}^{\eta})^2 \right) \tag{3.2}$$

where $N_{totalPts}$ is the sum of the total number of all curves. In this case, the goal is to minimize the total relative squared distance. Thus, the standard optimization problem for the Wiechert model is defined as

$$\begin{aligned} &\text{minimize} \quad R_{T2}(\mathbf{x}) : R^{NT+3} \to R \\ &\text{where} \quad \mathbf{x} = (E_\infty, E_i, C_1^T, C_2^T), \quad i = 1, 2, \ldots, NT \\ &\text{with restrictions:} \quad \mathbf{x}^{low} \leqslant \mathbf{x} \leqslant \mathbf{x}^{upp} \end{aligned} \tag{3.3}$$

where the superscripts "low" and "upp" indicate the upper and lower limit values of each design variable.

On the other hand, in the optimization procedure considering the four-parameter fractional Zener model, the optimization problem is written as follows

$$\begin{aligned} &\text{minimize} \quad R_{T2}(\mathbf{x}) : R^6 \to R \\ &\text{where} \quad \mathbf{x} = (\overline{E}_\infty, \overline{E}_0, b_1, \beta, C_1^T, C_2^T) \\ &\text{with restrictions:} \quad \mathbf{x}^{low} \leqslant \mathbf{x} \leqslant \mathbf{x}^{upp} \end{aligned} \tag{3.4}$$

The solution to those problems (Eq. (3.3) or (3.4)) provides the characteristic parameters of VEM under study according to the selected constitutive model.

3.1. Computational structure

The computational implementation of the proposed methodology has been carried out in a MATLAB® environment, as seen in the flowchart presented in Fig. 3.

The characterization procedure is based on a hybrid optimization technique. In that technique, an approximation of the optimal material parameters is initially obtained using Genetic Algorithms (GAs). Next, this result is improved by using a deterministic algorithm of Non-Linear Programming (NLP). In the process of optimization by GA, a sub-routine (ga.m) is used with a population of 5 000 individuals, 500 generations and a 1.0% mutation rate. Moreover, in NLP, a sub-routine (fmincon.m) is used with a maximum number of iterations of 1 000, 1E-11 tolerance and a maximum number of evaluation of the objective function of 10 000.

For the optimization procedure, the simple limits for parameters related to the WLF model, equilibrium modulus, terms of the Prony series and the fractional Zener model are listed in Table 1. Those limits are based on numerical experiments so that the upper and/or lower limits should not be obtained as optimal points.

Regarding the Wiechert model, the relaxation times τ_i, are fixed and defined dividing the interval between the minimum (τ_1) and the maximum (τ_{NT}) relaxation time into equal intervals on a logarithmic scale. This procedure is common in the literature (Honerkamp, 1989; Chen *et al.*, 2000; Soussou *et al.*, 1970; Jalocha *et al.*, 2015). Each material has specific properties and, thus, different time limits of relaxation. In this sense, Table 2 presents different intervals for each material.

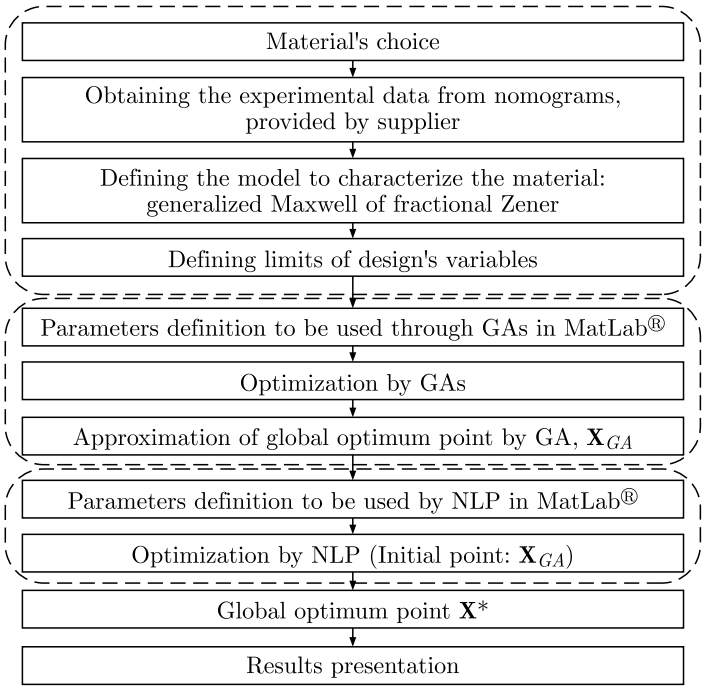

Fig. 3. Computational flowchart implemented in MatLab® environment

Table 1. Interval limits of the material properties used in the optimization process

Model	Variable	Nomenclature	Interval limits
WLF	WLF 1 material constant	C_1^T	$0 \leqslant C_1^T \leqslant 1000$
	WLF 2 material constant	C_2^T [°C]	$0 \leqslant C_2^T \leqslant 2000$
Wiechert	equilibrium modulus	E_∞ [MPa]	$0 \leqslant E_\infty \leqslant 10000$
	Prony series constants	E_i $(i = 1, \ldots, NT)$ [MPa]	$0 \leqslant E_i \leqslant 5000$
Zener fractional	equilibrium modulus	$\overline{E}_\infty$ [MPa]	$10^2 \leqslant \overline{E}_\infty \leqslant 10^5$
	instantaneous modulus	$\overline{E}_0$ [MPa]	$10 \leqslant \overline{E}_0 \leqslant 10^2$
	fractional derivative parameter	b_1	$10^{-5} \leqslant b_1 \leqslant 10^{-2}$
	fractional derivative order	β	$0 < \beta < 1$

Table 2. Relaxation time intervals for each material

Material	Minimum time τ_1	Maximum time τ_{NT}
C1002	10^{-8}	10^3
C2003	10^{-9}	10^3
ISODAMP	10^{-9}	10^3

4. Results

4.1. C1002 – material identification

The proposed methodology is applied to the identification of the EAR® C1002 material using Wiechert constitutive models with 8, 16, 32 Prony terms and the fractional Zener model. One can observe – according to Fig. 4 – that the more Prony terms, the better adjustments are obtained, so much so that above 16 terms there are no significant improvements, evidencing that from that quantity of terms on, it is already possible to describe the dynamic characteristics of the material under study with desired precision. On the other hand, the theoretical curves of

the fractional model adjust almost perfectly to the data, evidencing a good identification of that material model. The results can be seen in Fig. 4d.

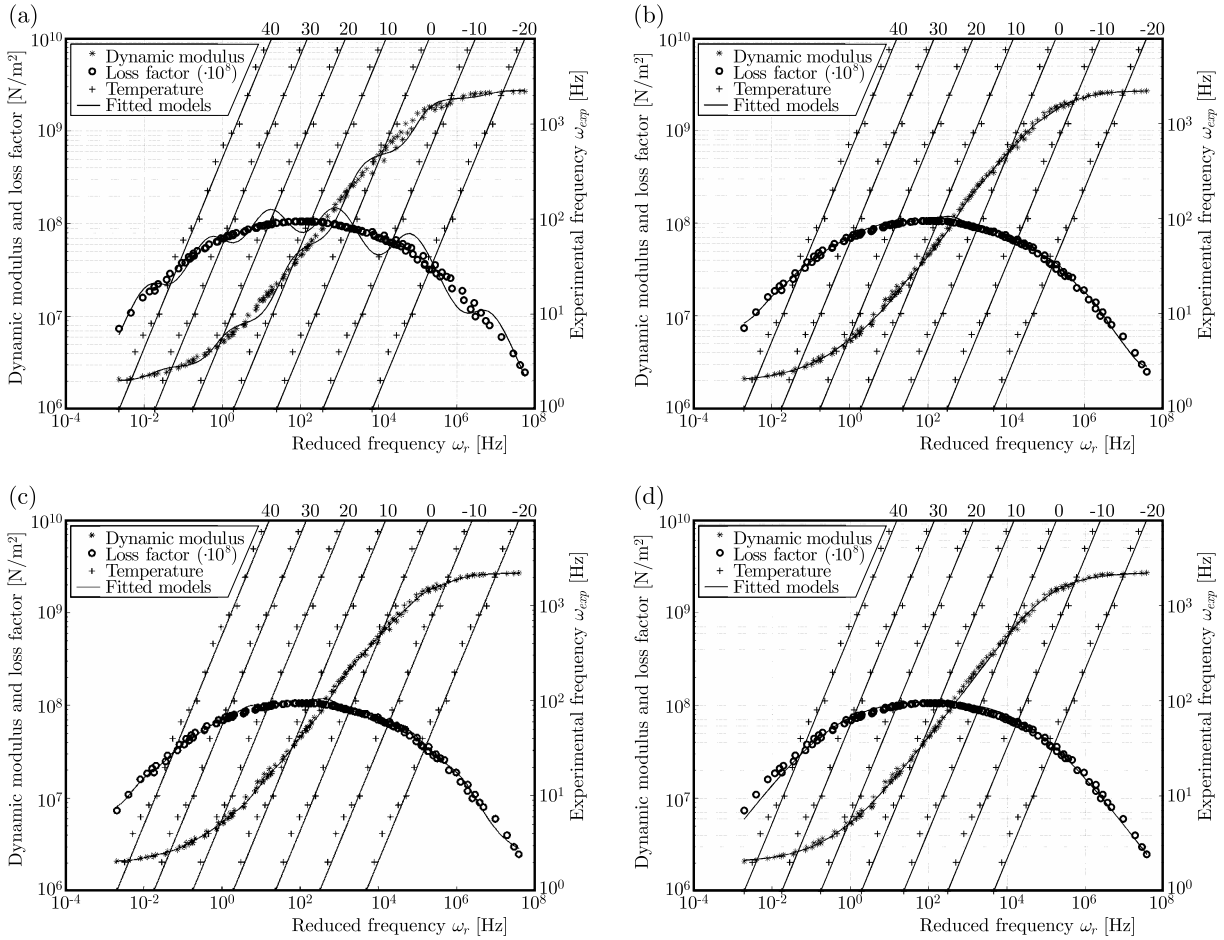

Fig. 4. C1002 identification: (a) 8 Prony terms, (b) 16 Prony terms, (c) 32 Prony terms, (d) fractional Zener model

The parameters obtained for each identification are presented in Table 3 and 4. Analyzing the optimal numerical values of constants C_1^T, C_2^T and E_0, one observes that the results – for the different analyses – are close, evidencing an adequate computational implementation.

Table 3. C1002 parameters obtained by hybrid optimization using the Wiechert model

Number of Prony terms	C_1^T [°C]	C_2^T [°C]	$E_0 = \sum_{i=1}^{NT} E_i$ [MPa]	E_∞ [MPa]	NLP error
8	33.40	317.23	2.54E+3	1.96	5.71E-2
16	35.27	340.77	2.67E+3	1.95	9.30E-3
32	34.75	336.15	2.69E+3	1.95	8.50E-3

Table 4. C1002 parameters using the fractional Zener model

Constants	C_1^T [°C]	C_2^T [°C]	$\overline{E}_\infty$ [MPa]	$\overline{E}_0$ [MPa]	b_1 [s$^\beta$]	β	τ_a [s]	NLP error
Numerical values	34.577	333.037	2.706E+3	1.927	2.089E-3	0.538	1.048E-5	1.225E-2

Furthermore, one must notice that the constant $\overline{E}_\infty$ of the fractional model corresponds to E_0 of the Wiechert model, and $\overline{E}_0$ corresponds to E_∞. Comparing the corresponding values, one notices a good correlation reaffirming that both models characterize precisely the mechanical behavior of that material.

4.2. C2003 – material identification

From the proposed methodology, similar identifications to those carried out with C1002 have been performed, and the graphic results are presented in Fig. 5. The numerical values that characterize the dynamics behavior of that material are shown in Table 5 and 6.

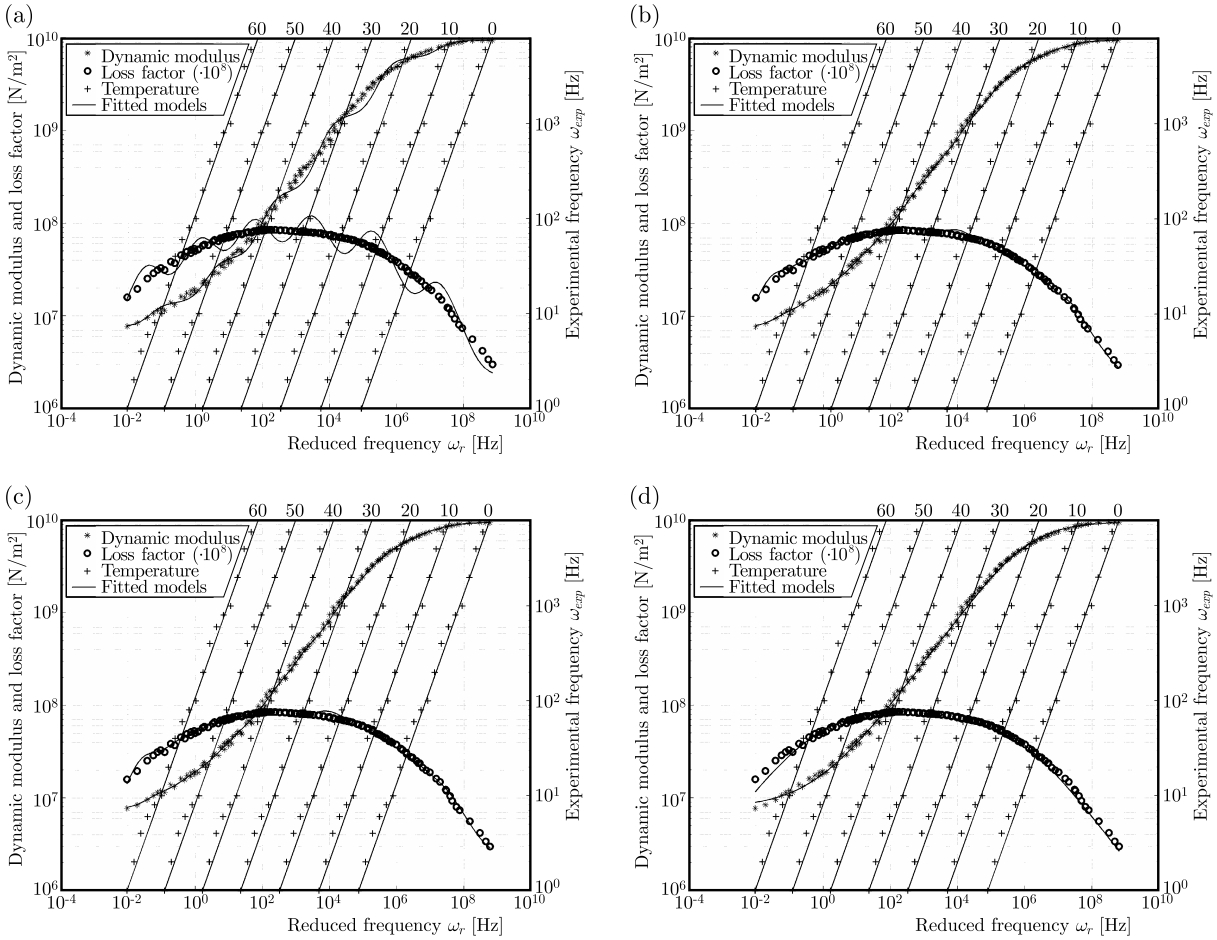

Fig. 5. C2003 identification: (a) 8 Prony terms, (b) 16 Prony terms, (c) 32 Prony terms, (d) fractional Zener model

Table 5. Parameters of C2003 material obtained by hybrid optimization using the Wiechert model

Number of Prony terms	C_1^T [°C]	C_2^T [°C]	$E_0 = \sum_{i=1}^{NT} E_i$ [MPa]	E_∞ [MPa]	NLP error
8	137.16	1165.16	9.30E+3	7.28	7.25E-2
16	178.62	1564.92	9.71E+3	7.17	4.70E-3
32	186.17	1632.68	9.70E+3	7.17	4.20E-3

Table 6. Parameters of material C2003 using the fractional Zener model

Constants	C_1^T [°C]	C_2^T [°C]	$\overline{E}_\infty$ [MPa]	$\overline{E}_0$ [MPa]	b_1 [s$^\beta$]	β	τ_a [s]	NLP error
Numerical values	146.012	1281.529	9.863E+3	6.989	1.593E-3	0.466	9.913E-7	6.54E-3

4.3. Identification of ISODAMP material

The characterization of the EAR® ISODAMP material is performed in a similar way the previous cases. The graphic results are illustrated in Fig. 6. The numerical values of each identification procedure are presented in Table 7 and 8.

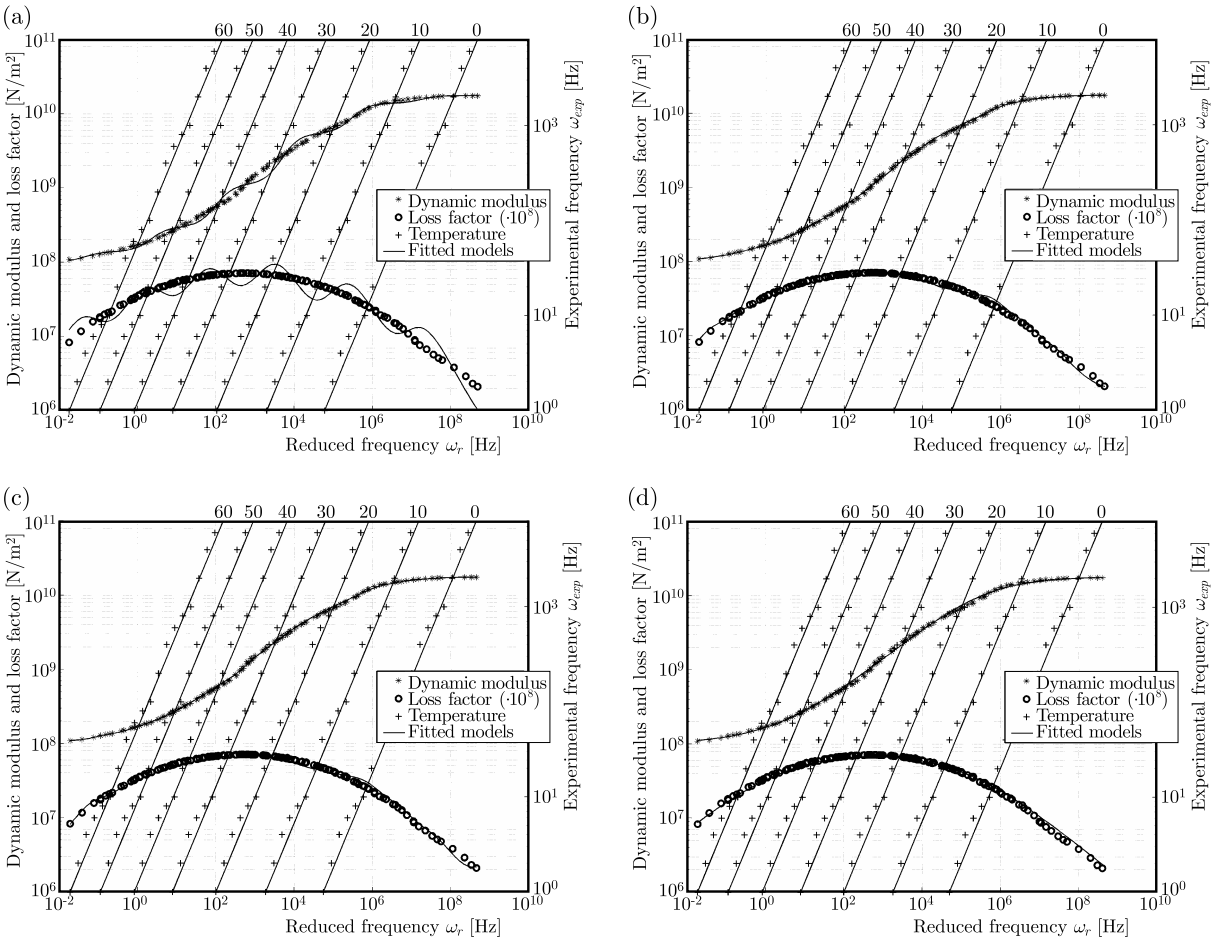

Fig. 6. ISODAMP identification: (a) 8 Prony terms, (b) 16 Prony terms, (c) 32 Prony terms, (d) fractional Zener model

Table 7. ISODAMP parameters obtained by hybrid optimization using the Wiechert model

Number of Prony terms	C_1^T [°C]	C_2^T [°C]	$E_0 = \sum_{i=1}^{NT} E_i$ [MPa]	E_∞ [MPa]	NLP error
8	14.34	153.35	1.68E+4	9.70E+1	6.63E-2
16	14.58	160.42	1.74E+4	9.72E+1	2.90E-3
32	14.56	160.13	1.75E+4	1.01E+2	2.60E-3

Table 8. ISODAMP parameters using the fractional Zener model

Constants	C_1^T [°C]	C_2^T [°C]	$\overline{E}_\infty$ [MPa]	$\overline{E}_0$ [MPa]	b_1 [s$^\beta$]	β	τ_a [s]	NLP error
Numerical values	14.785	162.518	1.757E+4	9.787E+1	4.704E-3	0.443	5.623E-6	3.52E-3

4.4. Relaxation modulus in the time domain

Previously, the parameters characterizing the mechanical behavior of EAR® C1002, C2003 and ISODAMP materials have been obtained. Replacing such parameters in the relaxation modulus, Eq. (2.1), it is possible having a graphic visualization, in the time domain, as illustrated in Fig. 7.

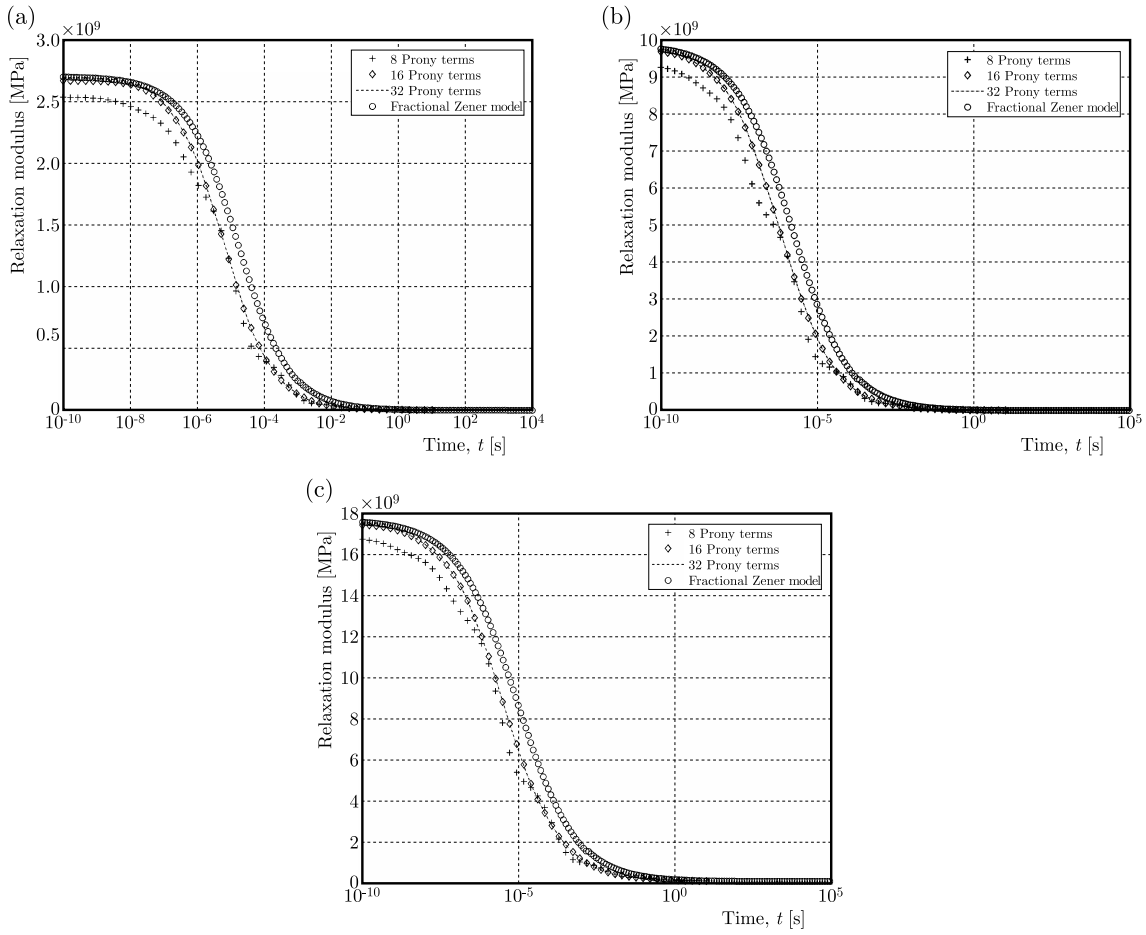

Fig. 7. Relaxation modulus by Wiechert model with increasing Prony terms and using fractional Zener model: (a) C1002, (b) C2003, (c) ISODAMP

5. Final remarks

The main goal of the present work is to obtain material parameters of constitutive models that seek to describe the dynamic modulus and the loss factor. Therefore, one starts from nomograms of EAR® C1002, C2003 and ISODAMP materials provided by their own manufacturer. Using a hybrid optimization technique, identifications are carried out involving the Wiechert model and the fractional Zener derivative model. Regarding the first model, various identifications are

performed using increasing Prony terms. One can observe that the greater is the quantity of Prony terms, the better adjustments are obtained, so that for designs involving those VEMs under study, 16 Prony terms proved to be enough for their characterization. Regarding identification involving the fractional Zener model, more accurate adjustments are obtained not only for the dynamic modulus but also for the loss factor. Besides that, for having less parameters, the fractional Zener model leads to a shorter computational time of the optimization process.

Acknowledgement

T.L. de Sousa thanks the Foundation for Research Support of the State of Amazonas-BR, FAPEAM, for the financial support granted in the form of a scholarship, for doctoral degree, without which it would not have been possible to develop the present work.

References

1. Agirre M.M., Elejabarrieta M.J., 2010, Characterization and modeling of viscoelastically damped sandwich structures, *International Journal of Mechanical Sciences*, **52**, 1225-1233
2. Bagley R.L., Torvik J., 1986, On the fractional calculus model of viscoelastic behavior, *Journal of Rheolology*, **30**, 133-155
3. Bavastri C.A., 1997, Vibration reduction broadband complex structures by viscoelastic neutralizers, Doctoral Thesis, Federal University of Santa Catarina, Santa Catarina, Brazil
4. Brinson H.F., Brinson L.C., 2008, *Polymer Engineering Science and Viscoelasticity: An Introduction*, Springer, New York
5. Chen T., 2000, Determining a Prony series for a viscoelastic material from time varying strain data, *Internal Report, National Technical Information Service – NASA*
6. Costa M.F.P., Ribeiro C., 2011, Parameter estimation of viscoelastic materials: a test case with different optimization strategies, *AIP Conference Proceedings*, **1389**, 771-774
7. Cruz G.A.M., 2004, Optimal design of neutralizing viscoelastic model based on the fractional derivatives, Doctoral thesis, Federal University of Santa Catarina, Santa Catarina, Brazil
8. Ferry J.D., Stratton R.A., 1960, The free volume interpretation of the dependence of viscosities and viscoelastic relaxation times on concentration, pressure, and tensile strain, *Kolloid-Zeitschrift*, **171**, 107-111
9. Honerkamp J., 1989, Ill posed problems in rheology, *Rheologica Acta*, **28**, 363-371
10. Jalocha D., Constantinescu A., Neviere R., 2015, Revisiting the identification of generalized Maxwell models from experimental results, *International Journal of Solids and Structures*, **67-68**, 169-181
11. Jrad H., Dion J.L., Renaud F., Tawfiq I., Haddar M., 2013, Experimental characterization, modeling and parametric identification of the non linear dynamic behavior components, *European Journal of Mechanics A/Solids*, **42**, 176-187
12. Lemini D.G., 2014, *Engineering Viscoelastic*, Springer, New York
13. Lopes E.M.O., Bavastri C.A., Neto J.M.S., Espíndola J.J., 2004, Characterization dynamics in integrated elastomers generalized derivatives, *Proceedings of the III CONEM*, Belem, Brazil
14. Mainardi F., 2010, *Fractional Calculus and Waves in Linear Viscoelasticity – An Introduction to Mathematical Models*, Imperial College Press, London
15. Mainardi F., Spada G., 2011, Creep, relaxation and viscosity properties for basic fractional models in rheology, *The European Physical Journal, Special Topics*, **193**, 133-160
16. Nashif A.D., Jones D., Henderson J., 1985, *Vibration Damping*, Wiley-Interscience, New York

17. O'brien D., Mather P.T., White S.R., 2001, Viscoelastic properties of an epoxy resin during cure, *Journal of Composite Materials*, **35**, 883-904

18. Park S.W., 2001, Analytical modeling of dampers for structural and vibration control, *International Journal of Solids and Structures*, **38**, 8065-8092

19. Pritz T., 1996, Analysis of four-parameter fractional derivative model of real solid materials, *Journal of Sound and Vibration*, **195**, 103-115

20. Rao M.D., 2002, Recent applications of viscoelastic damping for noise control in automobiles and commercial airplanes, *Journal of Sound and Vibration*, **262**, 457-474

21. Ribeiro E.A., Pereira J.T., Bavastri C.A., 2015, Passive vibration control in rotor dynamics: optimization composed support using viscoelastic materials, *Journal of Sound and Vibration*, **351**, 43-56

22. Soussou J.E., Moavenzadeh F., Gradowczyk M.H., 1970, Application of Prony series to linear viscoelasticity, *Transactions of the Society of Rheology*, **14**, 573-584

23. Suchocki C., Pawlikowski M., Skalski K., 2013, Determination of material parameters of quasi-linear viscoelastic rheological model for thermoplastics and resins, *Journal of Theoretical and Applied Mechanics*, **51**, 569-580

24. Ward I.M., Sweeney J., 2004, *An Introduction to the Mechanical Properties of Solid Polymers*, New Jersey, Chichester

25. Welch S.W.J., Rorrer R.A.L., Duren R.G. Jr., 1999, Application of time – based fractional calculus methods to viscoelastic creep and stress relaxation of materials, *Mechanics of Time-Dependent Materials*, **3**, 279-303

26. Williams M.L., Landel R.F., Ferry J.D., 1955, The temperature dependence of relaxation mechanisms in amorphous polymers and other glass-forming liquids, *Journal of the American Chemical Society*, **77**, 3701-3707

Manuscript received December 21, 2016; accepted for print May 22, 2017

JOURNAL OF THEORETICAL AND APPLIED MECHANICS
55, 4, pp. 1299-1312, Warsaw 2017
DOI: 10.15632/jtam-pl.55.4.1299

VIBRATION ANALYSIS OF THREE-LAYERED NANOBEAMS BASED ON NONLOCAL ELASTICITY THEORY

Nouha Kammoun, Hanen Jrad, Slim Bouaziz

Laboratory of Mechanical Modeling and Production (LA2MP), National School of Engineers of Sfax, Tunisia
e-mail: kamoun.noha@gmail.com; hanen.j@gmail.com; slim.bouaziz1@gmail.com

Mohamed Soula

Laboratory of Applied Mechanics and Engineering (LR-May-ENIT), National School of Engineers of Tunis, Tunisia
e-mail: soulamed2003@yahoo.fr

Mohamed Haddar

Laboratory of Mechanical Modeling and Production (LA2MP), National School of Engineers of Sfax, Tunisia
e-mail: mohamed.haddar@enis.rnu.tn

In this paper, the first investigation on free vibration analysis of three-layered nanobeams with the shear effect incorporated in the mid-layer based on the nonlocal theory and both Euler Bernoulli and Timoshenko beams theories is presented. Hamilton's formulation is applied to derive governing equations and edge conditions. In order to solve differential equations of motions and to determine natural frequencies of the proposed three-layered nanobeams with different boundary conditions, the generalized differential quadrature (GDQM) is used. The effect of the nanoscale parameter on the natural frequencies and deflection modes shapes of the three layered-nanobeams is discussed. It appears that the nonlocal effect is important for the natural frequencies of the nanobeams. The results can be pertinent to the design and application of MEMS and NEMS.

Keywords: beams theories, nonlocal elasticity theory, vibration analysis, GDQ method

1. Introduction

In the last few years, scientific researchers have been focusing on nanotechnology and the resulting nano-materials which play key roles in many engineering devices at the nano-scale used in several applications including microactuators, microswtiches, biosensors, nanowires, nanoprobes, ultra-thin films and micro-and nano-electromechanical systems (MEMS and NEMS) studied in works of (Hung and Senturia, 1999; Li *et al.*, 2003; Moser and Gijs, 2007; Pei *et al.*, 2004; Najar *et al.*, 2010). In fact, nano-materials have special mechanical, chemical, electrical, optical and electronic properties. Modeling and analysis of nanostructures including nanobeams, nanofils, carbon and boron-nirtide nanotubes, nanoribbons and nanoplates which are mostly applied MEMS and NEMS, and tracking their mechanical behavior can give truthful and promising results for designing such devices.

Although classical theories of linear and nonlinear vibration of strings and beams at macroscales are well established, the vibration behavior of structures at the nanoscale, which is significantly size dependent, is far from being well understood. In fact, experimental and molecular dynamics simulation results (Bauer *et al.*, 2011) have shown that the small-scale effects in the analysis of mechanical properties of nano- and micro-structures cannot be neglected. Due to being scale-free, the classical continuum theory is unable to accurately detect the static and dynamic mechanical behavior of nano- and micro-structures.

Nonlocal continuum theories of elasticity has found successful applications in nanomechanics including lattice dispersion of elastic waves, wave propagation in composites, dislocation mechanics, fracture mechanics (Peddieson *et al.*, 2003). Nonlocal theories that have been studied in the literature include Eringen's nonlocal elasticity theory (Eringen, 1972), modified couple stress theory of Mindlin (1963), Koiter (1964), and Toupin (1964), and the strain gradient theory (Mindlin, 1965; Lam *et al.*, 2003). Eringen's nonlocal elasticity can be classified into a differential nonlocal form or an integral nonlocal form. Detailed review of both forms is discussed by Lim (2010).

Numerous researchers have studied the mechanical behavior of nano-sized structures based on Eringen's nonlocal elastic theory. Analytical solutions for bending, buckling and vibration of beams using the Euler-Bernoulli, Timoshenko, Reddy, and Levinson beam theories have been developed by Reddy (2007). Analytical study of bending, buckling and vibration response of a Euler-Bernoulli nanobeam was proposed in the work of Thai (2012). Using a meshless method based on collocation with a radial basis, Roque *et al.* (2011) studied static bending, buckling and free vibration behavior of a Timoshenko nanobeam. Considering the perturbation method, free vibration, steady-state resonance and stability of a vibrating nanobeam subjected to a variable axial load was studied by Li *et al.* (2011). Moreover, the finite element method was used by Eltaher (2013) to solve the vibration problem of a Euler-Bernoulli nanobeam. Nonlinear vibration of nanobeams is reported in several works. Reddy (2010) reformulated classical shear deformation beam and plate theories taking into account the von Karman nonlinear strains. The nonlinear pull-in instability of a nanoswitch modeled as an Euler-Bernoulli nanobeam subjected to electrostatic and intermolecular forces and having different boundary conditions was investigated by Mousavi *et al.* (2013) using the differential quadrature method. Later, nonlinear finite element analysis of the Euler-Bernoulli and Timoshenko beam theories with the von Karman nonlinear strains and Eringen's nonlocal model was developed by Reddy and El-Borgi (2014).

The choice of a discretization process is indispensable for obtaining the number of resulting ordinary differential equations. Discretized models are time efficient and can be strongly employed to determine dynamics of systems subject to simple excitations with very small displacements about a given equilibrium point (Shkel, 2006). Finite element lumping of MEMS and NEMS, including complex geometry and using commercial softwares would provide more rigorous results. However, this discretization remains a heavy step in the design procedure, even when using automated size-reduction routines. Furthermore, the dynamic behavior cannot be totally inspected using these models. However, there are other discretization methods, such as the generalized differential quadrature method (GDQM), which approximate the original mechanism by a small number of ordinary differential equations. These techniques preserve the complexity of the system response, due to nonlinearities, in a parameterized model that is well suited for relatively complex geometries. Using this approach, the system dynamics can be precisely modeled using fewer degrees of freedom.

This paper makes the first attempt to investigate vibration of three-layered nanobeams incorporating the mid-layer shear effect based on Eringen's nonlocal theory as well as Euler Bernoulli and Timoshenko beam theories. The nonlocal nanobeam model is developed to capture the size effect in three-layered nanostructures. The governing equations and boundary conditions are derived by using Hamilton's principle. The generalized differential quadrature method (GDQM) is employed to discretize the governing equations which are then solved to obtain natural frequencies and mode shapes of three-layered nanobeams with different edge conditions. The influence of the nonlocal parameter on the vibration of the three-layered nanobeams incorporating the mid-layer shear effect are discussed.

2. Equations of motion and boundary conditions of the nonlocal three-layred nanobeam model

The majority of existing works on nonlocal elasticity are pertaining to the analysis of single nanobeams: nanotubes (Wang *et al.*, 2007; Reddy, 2007; Behera *et al.*, 2014) and nanoribbons (Nazemnezhad *et al.*, 2015). Though mechanical studies of nanobeams may include buckling and vibration of multiple-walled nanotubes and multilayer nanoribbons, the study of discrete multi-layered nanobeams has not been reported in literature.

Recently, Nazemnezhad *et al.* (2016) discussed nonlocal vibration of multi-layer graphene nanoribbons (MLGNRs) incorporating the interlayer shear effect. In fact, multilayer graphene nanoribbons (MLGNRs) are single layers of nanoribbons held together by weak van der Waals (vdWs) forces. According to Nilsson *et al.* (2008) and Hosseini Kordkheili *et al.* (2013), these weak interlayer vdWs bindings induce considerable changes in electrical and mechanical properties of MLGNRs (Nilsson *et al.*, 2008) and (Hosseini Kordkheili *et al.*, 2013) and, consequently, static and dynamic behavior of MLGNRs will change.

Based on the above discussion, in this paper an investigation is carried out to illustrate the small-scale effects in the behavior of a three-layered nanobeam incorporating the interlayer shear effect. The studied nanobeam is constructed of a thin elastic layer sandwiched between two identical elastic layers. The following general assumptions are made when developing governing differential equations of motion in free vibration of a three-layered nanobeam and associated boundary conditions:

- The theory of linear elasticity is applied to all displacements and strains.
- Transverse normal strains in the three layers are negligible.
- There is continuity of displacement at the interfaces between the layers.

Considering Cartesian coordinate system, Fig. 1 shows a three-layered nanobeam of length L. Each layer has its own geometric properties with a subscript i denoting the layer number ($i = 1$ for the top layer). Thus each layer has thickness h_i, width b_i (so that area $A_i = h_i b_i$).

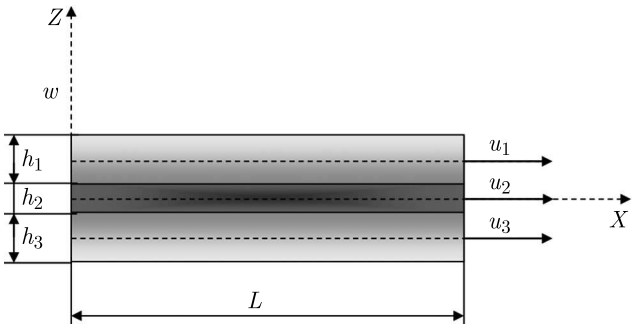

Fig. 1. Schematic configuration for a three-layered nanobeam incorporating the mid-layer shear effect

The system of displacements used is as follows. All three layers have common flexure in the y-direction with the flexural displacement denoted by w. The axial displacement (i.e. displacement in the x-direction) of the mid-plane of each layer is u_i ($i = 1, 2, 3$) which varies linearly through thickness, as shown in Fig. 1.

Assuming that the cross-section of each layer does not rotate so as to be normal to the common flexure, but it necessarily shears at the central layer, we propose to model the upper and lower layers by considering the Euler-Bernoulli beam formulation, and the central layer behavior is captured using the Timoshenko beam formulation taking into account small-scale effects.

According to the Euler-Bernoulli beam theory, the displacement of an arbitrary point of layer (1) and layer (3) of the three-layered nanobeam along the x and z axes denoted by $u_{xi}(x,z,t)$ and $u_{zi}(x,z,t)$, respectively, are:

— for $\frac{h_2}{2} \leqslant z \leqslant \frac{h_2}{2} + h_1$

$$u_{z1}(x,z,t) = w_1(x,t) \qquad u_{x1}(x,z,t) = u_1(x,t) - \Big(z - \frac{h_1+h_2}{2}\Big) w_{,x}(x,t) \tag{2.1}$$

— for $-h_3 - \frac{h_2}{2} \leqslant z \leqslant -\frac{h_2}{2}$

$$u_{z3}(x,z,t) = w_3(x,t) \qquad u_{x3}(x,z,t) = u_3(x,t) - \Big(z + \frac{h_3+h_2}{2}\Big) w_{,x}(x,t) \tag{2.2}$$

where ',' symbolizes differentiation with respect to coordinates and u_1, w_1, and u_3, w_3 are the axial and transverse displacements of an arbitrary point located on the mid-axis of layer (1) and layer (3), respectively, and t is time. It is further assumed for the transverse displacement that $u_{z1} = u_{z2} = u_{z3} = w(x,t)$. For layer (2), the displacement is expressed using the Timoshenko beam theory for the shear effect taken into account

$$u_{z2}(x,z,t) = w(x,t) \qquad u_c(x,z,t) = u_2(x,t) + z\phi(x,t) \qquad -\frac{h_2}{2} \leqslant z \leqslant \frac{h_2}{2} \tag{2.3}$$

where ϕ is rotation of the beam cross-section.

The strain-displacement equations of the three-layered nanobeam are given as follows

$$\begin{aligned} &\varepsilon_{xx}^{(1)} = u_{1,x} - \Big(z - \frac{h_1+h_2}{2}\Big) w_{,xx} && \varepsilon_{xx}^{(2)} = u_{2,x} + z\phi_{,x} \\ &\gamma_{xz}^{(2)} = w_{,x} + \phi && \varepsilon_{xx}^{(3)} = u_{3,x} - \Big(z + \frac{h_3+h_2}{2}\Big) w_{,xx} \end{aligned} \tag{2.4}$$

The strain energy U of the three-layered nanobeam resulting from the advent of variation in the stresses with respect to the initial configuration is given by

$$\begin{aligned} U &= \frac{1}{2} \int_0^L \int_A \left(\sigma_{xx}^{(1)} \varepsilon_{xx}^{(1)} + \sigma_{xx}^{(2)} \varepsilon_{xx}^{(2)} + \sigma_{xz}^{(2)} \gamma_{xz}^{(2)} + \sigma_{xx}^{(3)} \varepsilon_{xx}^{(3)} \right) dA\, dx \\ &= \frac{1}{2} \int_0^L \Big[N_x^{(1)} u_{1,x} + N_x^{(2)} u_{2,x} + N_x^{(3)} u_{3,x} - \left(M_x^{(1)} + M_x^{(3)} \right) w_{,xx} \\ &\quad + M_x^{(2)} \phi_{,x} + Q(w_{,x} + \phi) \Big] \, dx \end{aligned} \tag{2.5}$$

where $N_x^{(i)}$, $M_x^{(i)}$ and Q are the normal resultant force, the bending moment and the transverse shear force for layer (i), respectively. They are obtained from

$$\begin{aligned} &N_x^{(1)} = \int_A \sigma_{xx}^{(1)} \, dA = EA_1 u_{1,x} = A_{11} u_{1,x} && N_x^{(2)} = \int_A \sigma_{xx}^{(2)} \, dA = EA_2 u_{2,x} = A_{12} u_{2,x} \\ &N_x^{(3)} = \int_A \sigma_{xx}^{(3)} \, dA = EA_3 u_{3,x} = A_{13} u_{3,x} && M_x^{(1)} = \int_A \sigma_{xx}^{(1)} z^{(1)} \, dA = b_1 D w_{,xx} = B_{11} w_{,xx} \\ &M_x^{(3)} = \int_A \sigma_{xx}^{(3)} z^{(3)} \, dA = b_3 D w_{,xx} = B_{13} w_{,xx} && M_x^{(2)} = \int_A \sigma_{xx}^{(2)} z \, dA = b_2 D \phi_{,x} = B_{12} \phi_{,x} \\ &Q_x = k_s \int_A \sigma_{xz}^{(2)} \, dA = k_s GA(\phi + w_{,x}) = k_s C_{12}(\phi + w_{,x}) \end{aligned} \tag{2.6}$$

in which A_1, A_2 and A_3 are the cross section areas of layer (1), layer (2) and layer (3), respectively. D is the bending rigidity of the three-layered nanobeam. k_s is the shear correction factor depending on the shape of the cross section of the beam.

The kinetic energy T can be expressed as

$$T = \frac{1}{2}\int_0^L\int_A \rho(\dot{u}_{xi}^2+\dot{u}_{zi}^2)\,dA\,dx = \frac{1}{2}\int_0^L [I_1(\dot{u}_1^2+\dot{w}^2)+I_2(\dot{u}_2^2+\dot{w}^2)+I_3\dot{\phi}^2+I_4(\dot{u}_3^2+\dot{w}^2)]\,dx \quad (2.7)$$

where '.' signifies differentiation with respect to time, $\{I_1, I_2, I_3, I_4\} = \rho\{A_1, A_2, I, A_3\}$ and $A_i = b_i h_i$, $I = b_2 h_2^3/12$.

Using Hamilton's principle ($\int_0^t(\delta T - \delta U)\,dt = 0$), the classical governing equations of the three-layered nanobeam are obtained as follows

$$\begin{aligned} &N_{x,x}^{(1)} = I_1\ddot{u}_1^2 \qquad N_{x,x}^{(2)} = I_2\ddot{u}_2^2 \qquad N_{x,x}^{(3)} = I_4\ddot{u}_3^2 \qquad M_{x,xx}^{(1)} = I_1\ddot{w}^2 \\ &M_{x,x}^{(2)} - Q_x = I_3\ddot{\phi}^2 \qquad Q_{x,x} = I_2\ddot{w}^2 \qquad M_{x,xx}^{(3)} = I_4\ddot{w}^2 \end{aligned} \quad (2.8)$$

Considering a beam-type structure, thicknesses and widths are much smaller than its length. So that, for a beam with transverse motion in the xz-plane, we can assume that the nonlocal behavior is negligible in the thickness direction (Reddy, 2007). Then, nonlocal constitutive relation (2.3) can be approximated to a one-dimensional form expressed as in the following

$$\sigma_{xx} - (e_0a)^2\frac{\partial^2\sigma_{xx}}{\partial x^2} = E\varepsilon_{xx} \qquad \sigma_{xz} - (e_0a)^2\frac{\partial^2\sigma_{xz}}{\partial x^2} = G\gamma_{xz} \quad (2.9)$$

where E and G are respectively the elastic modulus and shear modulus of the beam. e_0a is the scale coefficient revealing the size effect on the response of the structures in the nanosize. e_0 is a material constant, and a and L are the internal and external characteristic lengths of the nanostructures, respectively. $\mu = e_0a/L$ is the nonlocal parameter.

To develop the nonlocal governing equations of motion of the three-layered nanobeam, it is necessary to obtain the nonlocal normal resultant force $N_x^{(i)}$, shear force Q_x and bending moment $M_x^{(i)}$. From Eqs. (2.9) and (2.8), the nonlocal $N_x^{(i)}$, Q_x and $M_x^{(i)}$ are defined as

$$\begin{aligned} &N_x^{(1)} - (e_0a)^2N_{x,xx}^{(1)} = A_{11}u_{1,x} \qquad N_x^{(2)} - (e_0a)^2N_{x,xx}^{(2)} = A_{12}u_{2,x} \\ &N_x^{(3)} - (e_0a)^2N_{x,xx}^{(3)} = A_{13}u_{3,x} \qquad M_x^{(1)} - (e_0a)^2M_{x,xx}^{(1)} = B_{11}w_{,xx} \\ &M_x^{(3)} - (e_0a)^2M_{x,xx}^{(3)} = B_{13}w_{,xx} \qquad M_x^{(2)} - (e_0a)^2M_{x,xx}^{(2)} = B_{12}\phi_{,x} \\ &Q_x - (e_0a)^2Q_{x,xx} = k_sC_{12}(w_{,x}+\phi) \end{aligned} \quad (2.10)$$

By substituting Eq. (2.10), into Eq. (2.8), the explicit expression of the nonlocal normal resultant force $N_x^{(i)}$, shear force Q_x and bending moment $M_x^{(i)}$ can be written as

$$\begin{aligned} &N_x^{(1)} = A_{11}u_{1,x} + (e_0a)^2I_1\ddot{u}_{1,x} \qquad N_x^{(2)} = A_{12}u_{2,x} + (e_0a)^2I_2\ddot{u}_{2,x} \\ &N_x^{(3)} = A_{13}u_{3,x} + (e_0a)^2I_4\ddot{u}_{3,x} \qquad M_x^{(1)} = B_{11}w_{,xx} + (e_0a)^2I_1\ddot{w}_{,x} \\ &M_x^{(3)} = B_{13}w_{,xx} + (e_0a)^2I_4\ddot{w}_{,x} \qquad M_x^{(2)} = B_{12}\phi_{,x} + (e_0a)^2I_3\ddot{\phi}_{,x} \\ &Q_x = k_sC_{12}(w_{,x}+\phi) + (e_0a)^2I_2\ddot{w}_{,x} \end{aligned} \quad (2.11)$$

Then, the nonlocal governing equations of motion of the three-layered nanobeam can be expressed as

$$\begin{aligned} &A_{11}u_{1,xx} = I_1(\ddot{u}_1 - (e_0a)^2\ddot{u}_{1,xx}) \qquad A_{12}u_{2,xx} = I_2(\ddot{u}_2 - (e_0a)^2\ddot{u}_{2,xx}) \\ &A_{13}u_{3,xx} = I_4(\ddot{u}_{3,xx} - (e_0a)^2\ddot{u}_{3,xx}) \qquad B_{12}\phi_{,xx} - k_sC_{12}(w_{,x}+\phi) = I_3(\ddot{\phi} - (e_0a)^2\ddot{\phi}_{,xx}) \\ &(B_{11}+B_{13})w_{,xxxx} + k_sC_{12}(w_{,xx}+\phi_{,x}) = (I_1+I_2+I_4)(\ddot{w} - (e_0a)^2\ddot{w}_{,xx}) \end{aligned} \quad (2.12)$$

3. Non-dimensional form of governing equations of motion of the nonlocal three-layred nanobeam model

The non-dimensionalization procedure has important applications in the analysis of differential equations. In this part, all parameters of the governing equations of motion are changed to a dimensionless form in order to facilitate the resolution process. Considering the following dimensionless parameters as

$$\begin{aligned}
&\xi = \frac{x}{L} \qquad \eta = \frac{L}{H} \qquad \mu = \frac{e_0 a}{L} \qquad \tau = \frac{t}{L}\sqrt{\frac{A_t}{I_t}} \qquad A_t = A_{11} + A_{12} + A_{13} \\
&I_t = I_1 + I_2 + I_4 \qquad H = h_1 + h_2 + h_3 \qquad (U_1, U_2, U_3, W) = \Big(\frac{u_1}{H}, \frac{u_2}{H}, \frac{u_3}{H}, \frac{w}{H}\Big) \\
&\phi^* = \phi \qquad C_{12} = \frac{c_{12}}{A_{12}} \qquad (\overline{A}_{11}, \overline{A}_{12}, \overline{A}_{13}) = \Big(\frac{A_{11}}{A_{11}}, \frac{A_{12}}{A_{12}}, \frac{A_{13}}{A_{13}}\Big) \\
&(\overline{B}_{11}, \overline{B}_{12}, \overline{B}_{13}, \overline{C}_{12}) = \Big(\frac{B_{11}}{A_{11}h_1^2}, \frac{B_{12}}{A_{12}h_2^2}, \frac{B_{13}}{A_{13}h_3^2}, \frac{C_{12}}{A_{12}}\Big) \\
&(\overline{I}_1, \overline{I}_2, \overline{I}_3, \overline{I}_4) = \Big(\frac{I_1}{I_1}, \frac{I_2}{I_2}, \frac{I_3}{I_2 h_2^2}, \frac{I_4}{I_4}\Big)
\end{aligned} \tag{3.1}$$

Governing equation (2.12) can be rewritten taking into account the dimensionless parameters as

$$\begin{aligned}
&\overline{A}_{11}U_{1,\xi\xi} = \overline{I}_1(\ddot{U}_1 - \mu^2\ddot{U}_{1,\xi\xi}) \qquad \overline{A}_{12}U_{2,\xi\xi} = \overline{I}_2(\ddot{U}_2 - \mu^2\ddot{U}_{2,\xi\xi}) \\
&\overline{A}_{13}U_{3,\xi\xi} = \overline{I}_4(\ddot{U}_3 - \mu^2\ddot{U}_{3,\xi\xi}) \qquad \overline{B}_{12}\phi^*_{,\xi\xi} - k_s\overline{C}_{12}\eta(W_{,\xi} + \eta\phi^*) = \overline{I}_3(\ddot{\phi}^* - \mu^2\ddot{\phi}^*_{,\xi\xi}) \\
&(\overline{B}_{11} + \overline{B}_{13})W_{,\xi\xi\xi\xi} + k_s\overline{C}_{12}(W_{,\xi\xi} + \eta\phi^*_{,\xi}) = (\overline{I}_1 + \overline{I}_2 + \overline{I}_4)(\ddot{W} - \mu^2\ddot{W}_{,\xi\xi})
\end{aligned} \tag{3.2}$$

The related edge conditions can also be adjusted in the dimensionless form:

— for a clamped-clamped (C-C) three-layred nanobeam

$$U_1 = U_2 = U_3 = W = \phi^* = 0 \qquad \text{at} \quad \xi = 0, 1 \tag{3.3}$$

— for a simply supported-simply supported (SS-SS) three-layred nanobeam

$$U_1 = U_2 = U_3 = W = \overline{M}_x^{(2)} = 0 \qquad \text{at} \quad \xi = 0, 1 \tag{3.4}$$

— for a clamped-simply supported (C-SS) three-layred nanobeam

$$\begin{aligned}
&U_1 = U_2 = U_3 = W = \phi^* = 0 \qquad \text{at} \quad \xi = 0 \\
&U_1 = U_2 = U_3 = W = \overline{M}_x^{(2)} = 0 \qquad \text{at} \quad \xi = 1
\end{aligned} \tag{3.5}$$

4. Modal discretization

In this part, a reduced order method is used to analyze the behavior of the three-layered nanobeam incorporating the mid-layer shear effect. The derivative terms, in governing equations Eq. (3.2) and related boundary conditions Eqs. (3.3)-(3.5) are discretized by using the Generalized Differential Quadrature Method (GDQM) in order to determine natural frequencies and deflection mode shapes of the three-layred nanobeam. GDQM's main concept is to consider the derivative of a function at a chosen point as a linear weighted sum of the function values at all

of the surrounding sample points in the corresponding domain (Ke and Wang, 2012). Hence, U_1, U_2, U_3, W, ϕ^* and their k-th derivatives regarding ξ can be expressed as

$$\{U_1, U_2, U_3, W, \phi^*\} = \sum_{m=1}^{N} l_m(\xi)\{U_{1m}(\xi_m, t), U_{2m}(\xi_m, t), U_{3m}(\xi_m, t), W_m(\xi_m, t), \phi^*_m(\xi_m, t)\} \tag{4.1}$$

and

$$\frac{\partial^k}{\partial \xi^k}\{U_1, U_2, U_3, W, \phi^*\}\Big|_{\xi=\xi_i} = \sum_{m=1}^{N} C_{im}^{(k)}\{U_{1m}(\xi_m, t), U_{2m}(\xi_m, t), U_{3m}(\xi_m, t), W_m(\xi_m, t), \phi^*_m(\xi_m, t)\} \tag{4.2}$$

where N is the number of grid points dispersed along the beam axis, the nanobeam deflection at the Chebyshev-Gauss-Lobatto grid points ξ_i (Ke and Wang, 2012) is given by

$$\zeta_i = \frac{1}{2}\Big[1 - \cos\frac{\pi(i-1)}{N-1}\Big] \qquad i = 1, 2, \ldots, N \tag{4.3}$$

The Lagrange interpolation polynomials $l_m(\xi)$ are expressed as

$$l_m(\xi) = \frac{R(\xi)}{(\xi - \xi_m)R^{(1)}(\xi)} \qquad R(\xi) = \prod_{m=1}^{N}(\xi - \xi_m) \qquad R^{(1)}(\xi) = \prod_{m=1, m\neq i}^{N}(\xi_i - \xi_m) \tag{4.4}$$

and $C_{im}^{(k)}$ are the weighting coefficients of the k-th order differentiation, which can be determined by employing a set of recurrence formulae through the following equations

$$[D_\xi^{(k)}]_{ij} = C_{ij}^{(k)} = \begin{cases} [I_x]_{ij} & k = 0 \\ \dfrac{R(\xi_i)}{(\xi_i - \xi_m)R(\xi_m)} & i \neq m \wedge i, m = 1, \ldots, N \wedge k = 1 \\ k\Big(C_{im}^{(1)} C_{ii}^{(k-1)} - \dfrac{C_{im}^{(k-1)}}{\zeta_i - \zeta_m}\Big) & i \neq m \wedge m = 1, \ldots, N \wedge k = 2, 3, \ldots, N-1 \\ -\sum\limits_{m=1, m\neq i}^{N} C_{im}^{(k)} & i = m \wedge i, m = 1, \ldots, N \wedge k = 2, 3, \ldots, N-1 \end{cases} \tag{4.5}$$

where $\mathbf{I}_x$ is the $N \times N$ identity matrix.
Considering $\mathbf{U}_1$, $\mathbf{U}_2$, $\mathbf{U}_3$, $\mathbf{W}$ and $\boldsymbol{\phi}^*$ defined as

$$\begin{aligned} &\mathbf{U}_1 = [U_{11}, U_{12}, U_{13}, \ldots, U_{1N}]^{\mathrm{T}} \qquad \mathbf{U}_2 = [U_{21}, U_{22}, U_{23}, \ldots, U_{2N}]^{\mathrm{T}} \\ &\mathbf{U}_3 = [U_{31}, U_{32}, U_{33}, \ldots, U_{3N}]^{\mathrm{T}} \qquad \mathbf{W} = [W_1, W_2, W_3, \ldots, W_N]^{\mathrm{T}} \\ &\boldsymbol{\phi}^* = [\phi_1^*, \phi_2^*, \phi_3^*, \ldots, \phi_N^*]^{\mathrm{T}} \end{aligned} \tag{4.6}$$

and

$$\begin{aligned} &U_{1i} = U_1(\xi_i) \qquad U_{2i} = U_2(\xi_i) \qquad U_{3i} = U_3(\xi_i) \\ &W_i = W(\xi_i) \qquad \phi_i^* = \phi^*(\xi_i) \end{aligned} \tag{4.7}$$

consequently, we obtain discretized governing equations of motion expressed as

$$\mathbf{M}\ddot{\mathbf{X}} + \mathbf{K}\mathbf{X} = \mathbf{0} \tag{4.8}$$

where $\mathbf{X}$, $\mathbf{K}$ and $\mathbf{M}$ denote, respectively, the vector of variables, stiffness matrix and mass matrix defined as

$$\mathbf{X} = \begin{bmatrix} \mathbf{U}_1^{\mathrm{T}} & \mathbf{U}_2^{\mathrm{T}} & \mathbf{U}_3^{\mathrm{T}} & \mathbf{W}^{\mathrm{T}} & \boldsymbol{\phi}^{*\mathrm{T}} \end{bmatrix}^{\mathrm{T}}$$

$$\mathbf{K} = \begin{bmatrix} \overline{A}_{11}C_\xi^{(2)} & 0 & 0 & 0 & 0 \\ 0 & \overline{A}_{12}C_\xi^{(2)} & 0 & 0 & 0 \\ 0 & 0 & \overline{A}_{13}C_\xi^{(2)} & 0 & 0 \\ 0 & 0 & 0 & (\overline{B}_{11}+\overline{B}_{13})C_\xi^{(4)} + k_s\overline{C}_{12}C_\xi^{(2)} & k_s\overline{C}_{12}\eta C_\xi^{(1)} \\ 0 & 0 & 0 & -k_s\overline{C}_{12}C_\xi^{(1)} & \overline{B}_{12}C_\xi^{(2)} - k_s\overline{C}_{12}\eta C_\xi^{(0)} \end{bmatrix}$$

$$\mathbf{M} = \begin{bmatrix} \overline{I}_1 D_\xi & 0 & 0 & 0 & 0 \\ 0 & \overline{I}_1 D_\xi & 0 & 0 & 0 \\ 0 & 0 & \overline{I}_4 D_\xi & 0 & 0 \\ 0 & 0 & 0 & (\overline{I}_1+\overline{I}_2+\overline{I}_4)D_\xi & 0 \\ 0 & 0 & 0 & 0 & \overline{I}_3 D_\xi \end{bmatrix} \tag{4.9}$$

with $D_\xi = C_\xi^(0) - \mu^2 C_\xi^{(2)}$.

Accordingly, the related edge conditions can be handled in the same way. It follows that for a simply supported-simply supported (SS-SS) three-layred nanobeam incorporating the mid-layer shear effect one obtains

$$\begin{aligned} &U_{11} = U_{21} = U_{31} = W_1 = \overline{M}_{x1}^{(2)} = 0 \qquad \text{at} \quad \xi = 0 \\ &U_{1N} = U_{2N} = U_{3N} = W_N = \overline{M}_{xN}^{(2)} = 0 \qquad \text{at} \quad \xi = 1 \end{aligned} \tag{4.10}$$

with

$$\begin{aligned} \overline{M}_{x1}^{(2)} &= \overline{B}_{12}\sum_{m=1}^{N} C_{1m}^{(1)}\overline{\phi}_m + \mu^2\overline{I}_2\sum_{m=1}^{N} C_{1m}^{(1)}\ddot{W}_m \\ \overline{M}_{xN}^{(2)} &= \overline{B}_{12}\sum_{m=1}^{N} C_{Nm}^{(1)}\overline{\phi}_m + \mu^2\overline{I}_2\sum_{m=1}^{N} C_{Nm}^{(1)}\ddot{W}_m \end{aligned} \tag{4.11}$$

5. Results and discussion

In the design of nanostructures, many nano-materials have been used such as carbon nanotubes (CNTs) (Behera *et al.*, 2014) and graphene nanoribbons (GNRs) (Nazemnezhad *et al.*, 2014). The choice of the two nano-materials is based on the superiority of mechanical and electrical properties (Geim, 2009). In fact, these nano-materials have an ultrahigh frequency range up to the terahertz order. In this part, we present numerical results of vibration of the clamped-clamped (–C), simply supported-simply supported (SS-SS) and clamped-simply supported (C-SS) three-layred nanobeam. The three-layred nanobeam is made of bilayer Graphene nanoribbon (BLGNR) with the following material properties $\rho = 2260\,\mathrm{kg\,m^{-3}}$, $G = 4.6\,\mathrm{GPa}$ and $E = 1.06\,\mathrm{TPa}$ (Nazemnezhad *et al.*, 2014) and (Hosseini Kordkheili *et al.*, 2013). The effects of the dimensionless nonlocal parameter μ on vibration frequencies and deflection mode shapes under different boundary conditions are discussed. It is assumed that the length of the nanobeam is $L = 14\,\mathrm{nm}$, thicknesses $h_1 = h_3 = 0.3\,\mathrm{nm}$, $h_2 = 0.1\,\mathrm{nm}$ and the shear correction factor $k_s = 0.563$.

5.1. Comparison and convergence studies

In this Section, behavior of the three-layered nanobeam incorporating the mid-layer shear effect with different end supports are analysed. Table 1 presents the fundamental ω_1 [THz] of the three-layred nanobeam with a different number of elements N used for computing the GDQM with $\mu = 0.2$. It can be seen that the numerical values get similar to each other as N increases, and those with $N = 18$ and 20 are similar for different boundary conditions C-C, SS-SS and C-SS. Therefore, $N = 18$ is employed in all subsequent computing.

Table 1. Fundamental frequency ω_1 [THz] of the C-C, SS-SS and C-SS three-layred nanobeam with different N

N	C-C	SS-SS	C-SS
8	0.93886	0.63522	0.71865
10	0.85984	0.41472	0.60103
14	0.86111	0.43731	0.60156
18	0.86117	0.45077	0.60228
20	0.86117	0.45077	0.60228

Until now, no theoretical simulations, experimental observations and molecular dynamic results on nonlocal three-layred nanobeams are reported that we can examine and compare the present work against. Hence, in order to ensure efficiency and validity of the proposed model, we consider the two following cases.

In fact, if we decrease thickness of the central layer of the beam comparing to the upper and lower layers thicknesses, the shear effect is neglected and the present model can be directly reduced to the nonlocal Euler-Bernoulli beam model.

Further, if we increase thickness of the central layer of the beam comparing to the upper and lower layers thicknesses, the shear effect is prevalent, so that the present model can be considered as the nonlocal Timoshenko beam model.

Moreover, Wang *et al.* (2007) analytically analyzed free vibration of an elastic nanobeam based on the nonlocal theory. Tables 2 and 3 give non-dimensional linear frequencies of single--walled carbon nanotubes based on respectively the nonlocal Euler-Bernouilli and Timoshenko beam model. The analytical results provided by Wang *et al.* (2007) are also given for comparison. Parameters used in this example are taken as (Wang *et al.*, 2007): diameter $d = 0.678\,\text{nm}$, Young's modulus $E = 5.5\,\text{TPa}$, Poisson's ratio $\nu = 0.19$, length of beam $L = 10d$ and shear correction factor $k_s = 0.563$.

Solutions obtained by the proposed model of three-layered nanobeams with the shear effect incorporated in the mid-layer based on nonlocal elasticity theory are in good agreement with the analytical results given by Wang *et al.* (2007) using the nonlocal Euler-Bernoulli and Timoshenko beam theory as well.

5.2. The proposed nanobeam vibration analysis

The effect of the scaling parameter μ on the first four natural frequencies $\omega_1 - \omega_4$ [THz] of the three layred nanobeam incorporating the mid-layer shear effect for different boundary conditions is presented in Fig. 2. It should be mentioned that the nonlocal parameter $\mu = 0$ corresponds to classical nanobeams without the nonlocal effect.

It can be clearly noticed that the nonlocal parameter has a marked effect on the natural frequencies of the three layred nanobeam incorporating the mid-layer shear effect for different edge conditions. Indeed, an increase in the nonlocal parameter leads to a decrease in the natural frequencies. This reduction is more manifested when we consider higher vibration modes. The reduction can be explained by the fact that the nonlocal model may be seen as atoms linked by

Table 2. Dimensionless frequency of single-walled carbon nanotubes based on the nonlocal Euler Bernoulli beam model considering $h_1 = h_3 = 0.3\,\text{nm}$ and $h_2 = 0.078\,\text{nm}$ for different boundary conditions

Frequency parameter	$\mu = 0.1$		$\mu = 0.3$	
	Wang *et al.* (2007)	Present	Wang *et al.* (2007)	Present
C-C				
1	4.5945	4.4958	3.9184	3.7276
2	7.1402	7.1803	5.1963	5.2607
3	9.2583	9.3447	6.2317	6.1826
4	11.016	11.157	7.0482	7.1145
SS-SS				
1	3.0685	3.2293	2.6800	2.7139
2	5.7817	5.4906	4.3013	4.3293
3	8.0400	8.1050	5.4423	5.5188
4	9.9162	10.072	6.3630	6.4189
C-SS				
1	3.8209	3.7139	3.2828	3.3506
2	6.4649	6.4293	4.7668	4.6857
3	8.6517	8.6378	5.4423	5.4614
4	10.469	10.521	6.3630	6.4952

Table 3. Dimensionless frequency of single-walled carbon nanotubes based on the nonlocal Timoshenko beam model considering $h_1 = h_3 = 0.039\,\text{nm}$ and $h_2 = 0.6\,\text{nm}$ for different boundary conditions

Frequency parameter	$\mu = 0.1$		$\mu = 0.3$	
	Wang *et al.* (2007)	Present	Wang *et al.* (2007)	Present
C-C				
1	4.3026	4.2512	3.2420	3.3238
2	6.3507	6.4276	3.9940	4.1702
3	8.1969	7.9274	4.4769	4.4708
4	9.5447	9.1456	5.1131	4.9152
SS-SS				
1	3.0243	3.1423	2.2867	2.4693
2	5.5304	5.7235	3.4037	3.2657
3	7.4699	7.2662	4.1644	4.0209
4	8.9874	8.6490	4.7436	4.5083
C-SS				
1	3.6939	2.9972	2.7471	2.9446
2	6.0348	6.3202	3.7312	3.8269
3	7.8456	7.5816	4.1644	4.2341
4	9.2751	8.8744	4.7436	4.6686

elastic springs while in the case of a local continuum model, the spring is constant and supposed to take the infinite value. Consequently, the presence of the nonlocal effect tends to decrease the stiffness of nanostructures and, hence, decreases the values of frequencies (Reddy 2007; Wang *et al.*, 2007).

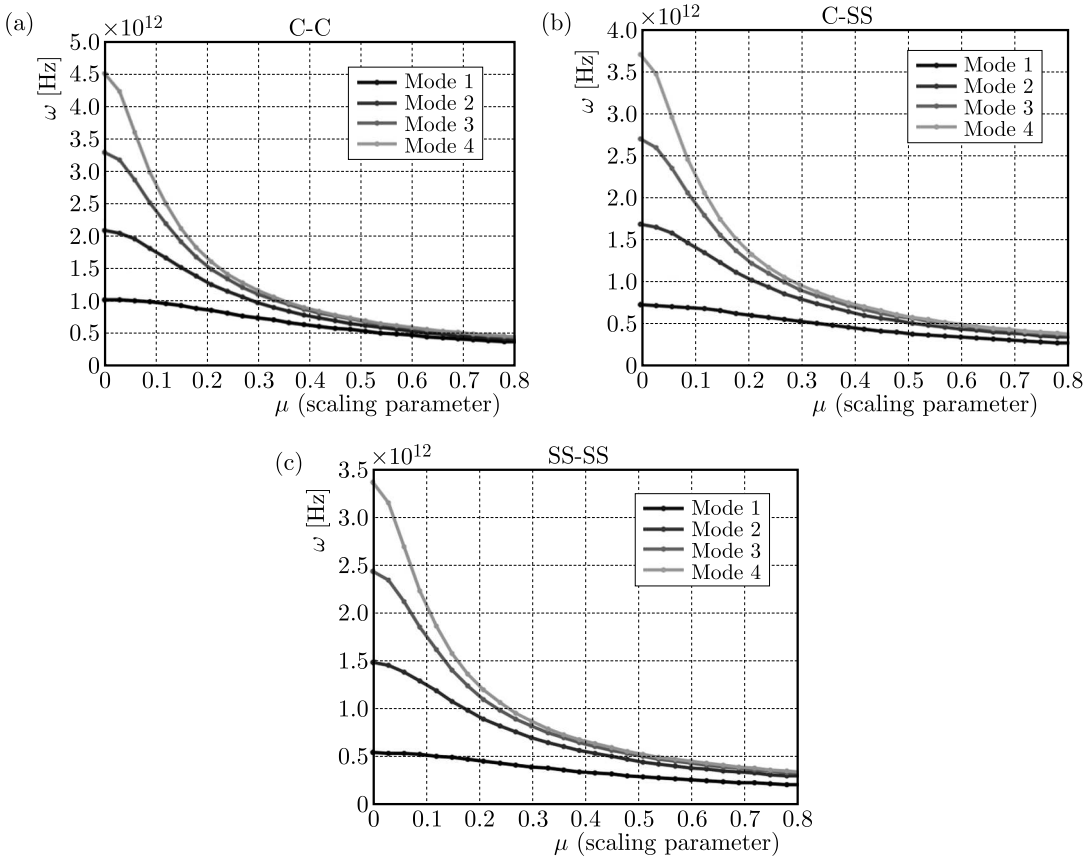

Fig. 2. Effect of the scaling parameter on the first four natural frequencies of three-layered nanobeams for different boundary conditions: (a) C-C, (b) SS-SS, (c) C-SS

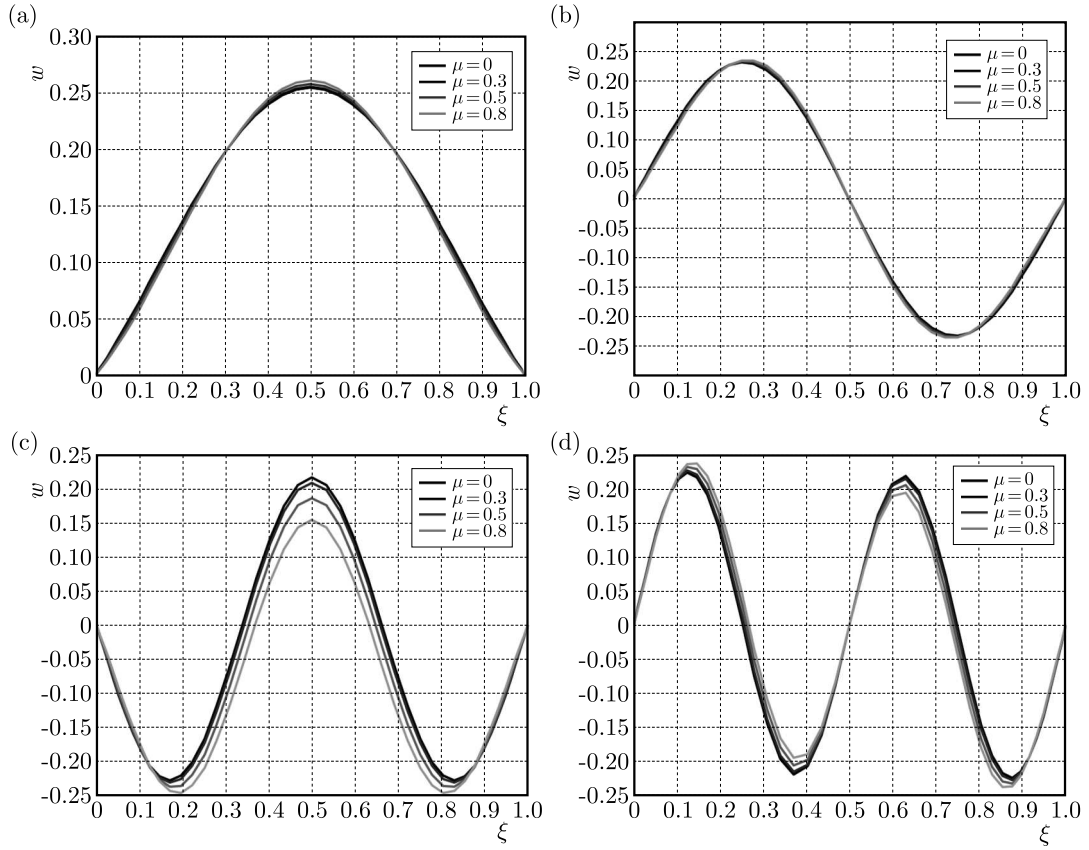

Fig. 3. Effect of the scaling parameter on the first four deflection shapes for C-C three layered nanobeams: (a) first deflection, (b) second deflection, (c) third deflection and (d) fourth deflection

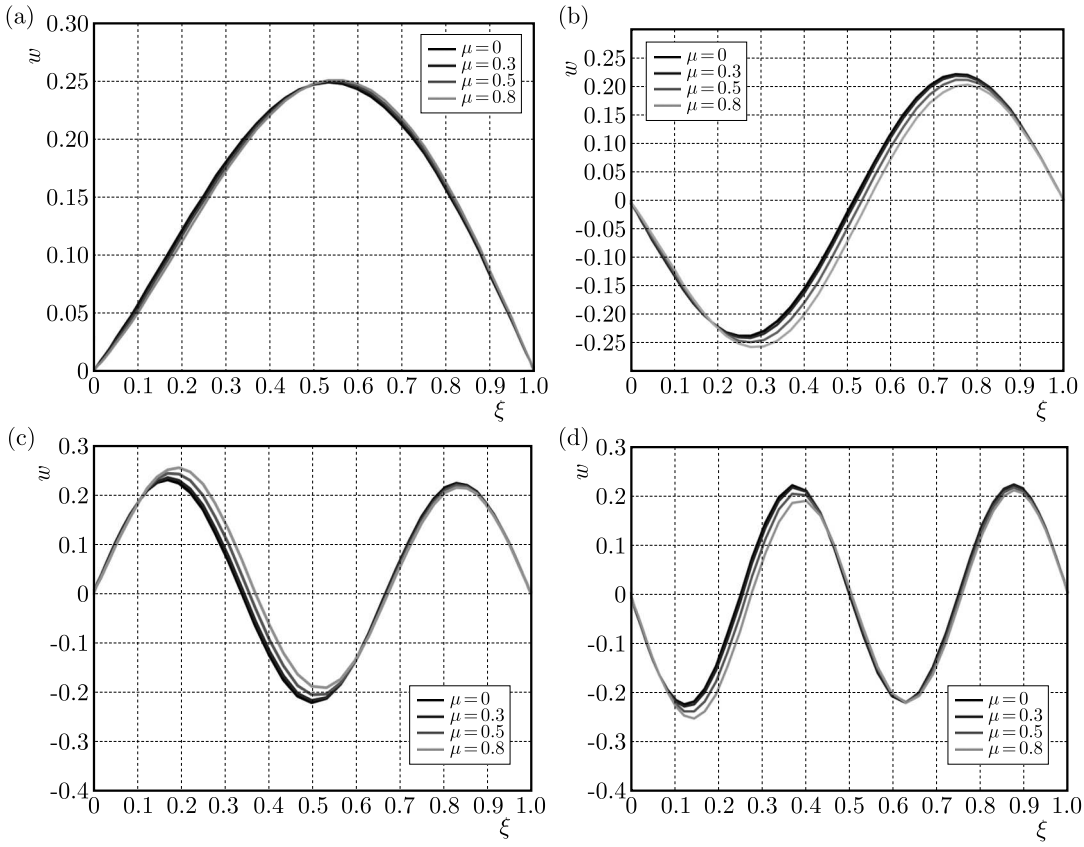

Fig. 4. Effect of the scaling parameter on the first four deflection shapes for C-SS three layered nanobeams: (a) first deflection, (b) second deflection, (c) third deflection and (d) fourth deflection

The C-C nanobeam has higher natural frequencies while the SS-SS has lower natural frequencies since the end support is stronger for the C-C nanobeam and weaker for the SS-SS nanobeam.

Sometimes, the knowledge of higher modes is necessary before finalizing the design of an engineering system. Hence, the first four deflections of nonlocal C-C and C-SS of the proposed three-layred nanobeam are shown respectively in Figs. 3 and 4 for different scaling parameters.

It can be noticed that the deflection mode shapes are affected by an increase in the nonlocal parameter. Deflection graphs of nonlocal C-C and C-SS three-layred nanobeams incorporating the mid-layer shear effect are plotted in this study for different scaling effect parameters to be useful for benchmarking. In fact, by understanding the modes of vibration, we can design structures better in accordance with the need.

6. Conclusion

This paper investigates free vibration of three-layered nanobeams incorporating the mid-layer shear effect based on the nonlocal theory, Euler-Bernoulli and Timoshenko beam theories. The GDQM is employed to obtain natural frequencies and deflection mode shapes of the three-layered nanobeams incorporating the mid-layer shear effect with different end supports. Effects of the scaling parameter on vibration characteristics of the proposed nanobeams model are discussed. The results show that an increase in the nonlocal parameter leads to a decrease in the natural frequencies, and the nonlocal parameter nanobeam has a distinguished effect on the mode shapes for the C-C and C-SS nanobeams, but has a less effect on the mode shapes for the SS-SS of the

proposed nanobeam. Numerical solutions presented herein may be useful to design MEMS and NEMS devices.

References

1. Ansari R., Gholami R., 2016, Size-dependent nonlinear vibrations of first-order shear deformable magneto-electro-thermo elastic nanoplates based on the nonlocal elasticity theory, *International Journal of Applied Mechanics*, **8**, 4, 1650053-1650086
2. Bauer S., Pittrof A., Tsuchiya H., Schmuki P., 2011, Size-effects in TiO2 nanotubes: Diameter dependent anatase/rutile stabilization, *Electrochemistry Communications*, **6**, 538-541
3. Behera L., Chakraverty S., 2014, Free vibration of Euler and Timoshenko nanobeams using boundary characteristic orthogonal polynomials, *Applied Nanoscience*, **3**, 347-358
4. Eltaher M.A., Emam S.A., Mahmoud F.F., 2013, Static and stability analysis of nonlocal functionally graded nanobeams, *Composite Structures*, **96**, 82-88
5. Eringen A.C., 1972, Nonlocal polar elastic continua, *International Journal of Engineering Science*, **10**, 1, 1-16
6. Geim A.K., 2009, *Graphene: Status and Prospects*, Manchester Centre for Mesoscience and Nanotechnology, University of Manchester, Oxford Road M13 9PL, Manchester, UK, **324**, 1-8
7. He J.H., 1999, Homotopy perturbation technique, *Computer Methods in Applied Mechanics and Engineering*, **178**, 257-262
8. Hosseini Kordkheili S.A., Sani H., 2013, Mechanical properties of double-layered graphene sheets, *Computational Materials Science*, **69**, 335-343
9. Hung E.S., Senturia S.D., 1999, Extending the travel range of analog-tuned electrostatic actuators, *Journal of Microelectromechanics Systems*, **8**, 497-505
10. Ke L.L., Wang Y.S., 2012, Thermoelectric-mechanical vibration of piezoelectric nanobeams based on nonlocal theory, *Smart Materials and Structures*, **21**, 1-12
11. Ke L.L., Wang Y.S., 2014, Free vibration of size-dependent magneto-electro-elastic nanobeams based on the nonlocal theory, *Physica E*, **63**, 52-61
12. Koiter W.T., 1964, Couple-stresses in the theory of elasticity: I and II, *Koninklijke Nederlandse Akademie van Wetenschappen* (Royal Netherlands Academy of Arts and Sciences), **67**, 17-44
13. Lam D.C.C., Yang F., Chong A.C.M., Wang J., Tong P., 2003, Experiments and theory in strain gradient elasticity, *Journal of Mechanics and Physics of Solids*, **51**, 1477-1508
14. Li C., Lim C.W., Yu J.L., 2011, Dynamics and stability of transverse vibrations of nonlocal nanobeams with a variable axial load, *Smart Materials and Structures*, **20**
15. Li X., Bhushan B., Takashima K., Baek C.W., Kim Y.K., 2003, Mechanical characterization of micro/nanoscale structures for MEMS/NEMS applications using nanoindentation techniques, *Ultramicroscopy*, **97**, 481-494
16. Lim C.W., 2010, On the truth of nanoscale for nanobeams based on nonlocal elastic stress field theory: equilibrium, governing equation and static deflection, *Applied Mathematics and Mechanics*, **1**, 37-54
17. Mindlin R.D., 1963, Influence of couple-stresses on stress concentrations, *Experimental Mechanics*, **3**, 1-7
18. Mindlin R.D., 1965, Second gradient of strain and surface-tension in linear elasticity, *International Journal of Solids and Structures*, **1**, 217-238
19. Moser Y., Gijs M.A.M., 2007, Miniaturized flexible temperature sensor, *Journal of Microelectromechanical Systems*, **16**, 1349-1354

20. Mousavi T., Bornassi S., Haddadpour H., 2013, The effect of small scale on the pull--in instability of nano-switches using DQM, *International Journal of Solids and Structures*, **50**, 1193-1202

21. Najar F., Nayfeh A.H., Abdel-Rahman E.M., Choura S., El-Borgi S., 2010, Global stability of microbeam-based electrostatic microactuators, *Journal of Vibration and Control*, **16**, 721-748

22. Nazemnezhad R., Hosseini-Hashemi S., 2014, Free vibration analysis of multi-layer graphene nanoribbons incorporating interlayer shear effect via molecular dynamics simulations and nonlocal elasticity, *Physics Letters A*, **44**, 3225-3232

23. Nazemnezhad R., Zare M., 2016, Nonlocal Reddy beam model for free vibration analysis of multilayer nanoribbons incorporating interlayer shear effect, *European Journal of Mechanics – A/Solids*, **55**, 234-242

24. Nilsson J., Neto A.C., Guinea F., Peres N., 2008, Electronic properties of bilayer and multilayer graphene, *Physical Review B*, **78**, 4, 405-434

25. Peddieson J., Buchanan G.R., McNitt R.P., 2003, Application of nonlocal continuum models to nanotechnology, *International Journal of Engineering Science*, **41**, 305-312

26. Pei J., Tian F., Thundat T., 2004, Glucose biosensor based on the microcantilever, *Analytical Chemistry*, **76**, 292-297

27. Reddy J.N., 2007, Nonlocal theories for bending, buckling and vibration of beams, *International Journal of Engineering Science*, **45**, 288-307

28. Reddy J.N., 2010, Nonlocal nonlinear formulations for bending of classical and shear deformation theories of beams and plates, *International Journal of Engineering Science*, **48**, 1507-1518

29. Reddy J.N., El-Borgi S., 2014, Eringen's nonlocal theories of beams accounting for moderate rotations, *International Journal of Engineering Science*, **82**, 159-177

30. Roque C.M.C., Ferreira A.J.M., Reddy J.N., 2011, Analysis of Timoshenko nanobeams with a nonlocal formulation and meshless method, *International Journal of Engineering Science*, **49**, 976-984

31. Shkel A.M., 2006, Type I and Type II micromachined vibratory gyroscopes, *Proceedings of the IEEE/Institute of Navigation Plans*, San Diego, CA, 586-593

32. Simsek M., 2014, Large amplitude free vibration of nanobeams with various boundary conditions based on nonlocal elasticity theory, *Composites: Part B*, **56**, 621-628

33. Thai H.T., 2012, A nonlocal beam theory for bending, buckling, and vibration of nanobeams, *International Journal of Engineering Science*, **52**, 56-64

34. Toupin R.A., 1964, Theories of elasticity with couple-stress, *Archive for Rational Mechanics and Analysis*, **17**, 85-112

35. Wang Q., Wang C.M., 2007, The constitutive relation and small scale parameter of nonlocal continuum mechanics for modelling carbon nanotubes, *Nanotechnology*, **18**, 7

Manuscript received October 16, 2016; accepted for print May 31, 2017

JOURNAL OF THEORETICAL AND APPLIED MECHANICS
55, 4, pp. 1313-1324, Warsaw 2017
DOI: 10.15632/jtam-pl.55.4.1313

NUMERICAL INVESTIGATION OF LOCAL HEAT TRANSFER DISTRIBUTION ON SURFACES WITH A NON-UNIFORM TEMPERATURE UNDER AN ARRAY OF IMPINGING JETS WITH VARIOUS NOZZLE SHAPES

Krzysztof Marzec
Rzeszow University of Technology, Rzeszów, Poland and MTU Aero Engines, Rzeszów, Poland
e-mail: k_marzec@prz.edu.pl
Anna Kucaba-Piętal
Rzeszow University of Technology, Rzeszów, Poland

Numerical calculations of heat transfer characteristics of an impingement cooling system with a non-uniform temperature on a cooled surface using ANSYS CFX have been performed. The influence of a surface heat flux $q_w(x)$ and a nozzle shape on the Nusselt number distribution on the cooled surface has been studied. The setup consisted of a cylindrical plenum with an inline array of ten impingement jets. Cylindrical, convergent divergent shapes of nozzles and linear temperature distribution on the cooled surface have been considered for various heat fluxes $q_w(x)$. Results indicate that geometry of the cylindrical nozzles resulted in the highest Nusselt numbers along the cooled surface. The line of the averaged Nusselt number has a trend to increase in the direction of the flow for the cooling system with increasing values of the surface heat flux $q(x)$. This tendency can be observed for all presented shapes of jets. On the other hand, for decreasing functions of the heat flux $q_w(x)$, the Nusselt number distribution is more uniform. It can be observed for all types of nozzles. Very similar values of the Nusselt number occur especially for the non-uniform heat flux 5000-2500 $\mathrm{W/m^2}$. For constant values of the heat flux $q(x) = 5000\,\mathrm{W/m^2}$, the line of the average Nusselt number has a trend to increase slightly in the direction of the flow. Numerical analysis of different mesh density results in good convergence of the GCI index, what excludes mesh size dependency. The presented study is an extension of the paper (Marzec and Kucaba-Piętal, 2016) and aims at answering the question how the Nusselt number distribution on the cooled surface is affected by various geometries of nozzles for a non-uniform surface heat flux $q_w(x)$.

Keywords: impinging jet, heat transfer, Nusselt number, nozzle shape

1. Introduction

An impingement cooling system is an array of jets with a high velocity fluid which is made to strike a target surface. It is an effective method to generate a high cooling rate on a surface of a hot object. Impingement jets are widely used in many engineering applications for cooling, drying or heating. Many of cooling systems are installed, in particular, in electronic devices, aeronautical and heavy industry equipment and many others. Technological processes are supported by impinging jets. Cooling nozzles are used in various geometrical configurations implementing either a single injector or several parallel jets. Wide application of cooling systems is due to the fact that modern devices and machines operate at very high temperatures. Therefore, usage of impingement cooling systems is mandatory to provide a high rate of heat and mass transfer. In gas turbine engines, impinging jets are applied for cooling turbine blades and casings (Active Clearance Control) (Ahmed *et al.*, 2010; Andreini *et al.*, 2013; Ruiz *et al.*, 2006), which operate at very high temperatures. Besides the high heat transfer, cooling systems reduce fuel consumption of engines. A number of experimental and numerical studies have dealt with the investigation of

the heat transfer between an air jet and a flat surface (Al-Hadhrami *et al.*, 2007, 2010; Mubarak *et al.*, 2011). Many of them are focused on the high Nusselt number delivery (Goordo *et al.*, 2007). Heat transfer rates in the case of impinging jets are affected by various parameters like the Reynolds number, jet to plate spacing, radial distance from a stagnation point, target plate inclination, nozzle geometry, roughness of the target plate and turbulence intensity at the nozzle exit. The majority of studies are experimental ones (Goordo *et al.*, 2007; Nirmalkumar *et al.*, 2011). However, many simulations of impingement cooling systems are numerical (Ee-Mahghany *et al.*, 2012; Żukowski, 2013). It is remarkable that only few are addressed to the problem of cooling a surface with an inhomogeneous distribution of temperature (Tarabsheh *et al.*, 2013; Xu *et al.*, 2014). Such a situation occurs in many technical applications such as photovoltaic cells (Royne *et al.*, 2005). Tarabsheh *et al.* (2013) presented research on the performance of photovoltaic (PV) modules with respect to the non-uniform temperature and proposed various pipe layouts. The operating temperatures of the PV cells are not equal since the temperature of the flowing fluid is different at the inlet and outlet of the cooling pipes. Different geometries of cooling pipes were introduced in order to maximize the PV module efficiency. The results show that implementation of various cooling pipes improved the efficiency of the PV cells. Xu *et al.* (2014) presented a multi-channel cooling experiment which was developed for studying heat removal inside an electronic device. The results showed that the designed multi-channel heat sink structure could control the temperature distribution of the device with multiple heat sources by altering the coolant flow rate and different design of the cooling multi-channel structure. Marzec and Kucaba-Piętal (2014) presented the influence of different geometries of nozzles of an impingement cooling array directed to the flat surface on a flow mechanism and heat transfer at constant temperature on the cooled surface. The obtained results indicate that the usage of various types of nozzles results in different values of the heat transfer coefficient and the Nusselt number along the cooled surface. In turn, Marzec and Kucaba-Piętal (2016) focused on heat transfer characteristics of a cooling system with a non-uniform temperature on the cooled surface. Three decreasing linear functions of a heat flux $q_w(x)$ were reviewed. The most uniform Nusselt number distribution was observed along the cooled surface for the heat flux $q_w(x) = 5000\text{-}2500\ \mathrm{W/m^2}$. Additionally, Marzec and Kucaba-Piętal (2016) investigated heat transfer characteristics for a constant surface heat flux $q_w(x) = 5000\ \mathrm{W/m^2}$. It is worth to note that research work by Marzec and Kucaba-Piętal (2016) was addressed only to the usage of cylindrical nozzles.

This paper presents numerical analysis of the effect of nozzle shape on the heat transfer performance. The cooling surface posses both decreasing and increasing linear temperature distributions. Cylindrical, convergent and divergent geometry of the nozzles are taken into consideration like in the work by Marzec and Kucaba-Piętal (2014). Calculations are performed using Computational Fluid Dynamics (CFD) code Ansys CFX. The k-ω shear stress transport (SST) turbulence model is used in the calculations.

The results show that the line of the averaged Nusselt number has a trend to increase in the direction of the flow for the cooling system with increasing values of the surface heat flux $q_w(x)$. This tendency occurs for all presented shapes of the jets. For the decreasing functions of the heat flux $q_w(x)$, the Nusselt number distribution is more homogenous. It can be observed for all geometries of the nozzles. Very similar values of the Nusselt number occur especially for the non-uniform heat flux $5000\text{-}2500\ \mathrm{W/m^2}$.

2. Problem formulation

The geometry of the numerical setup is presented in Fig. 1. Geometry, fluid, thermal and flow data used for the calculations are the same as in the work by Marzec and Kucaba-Piętal (2016) and are equal to the values presented in Table 1.

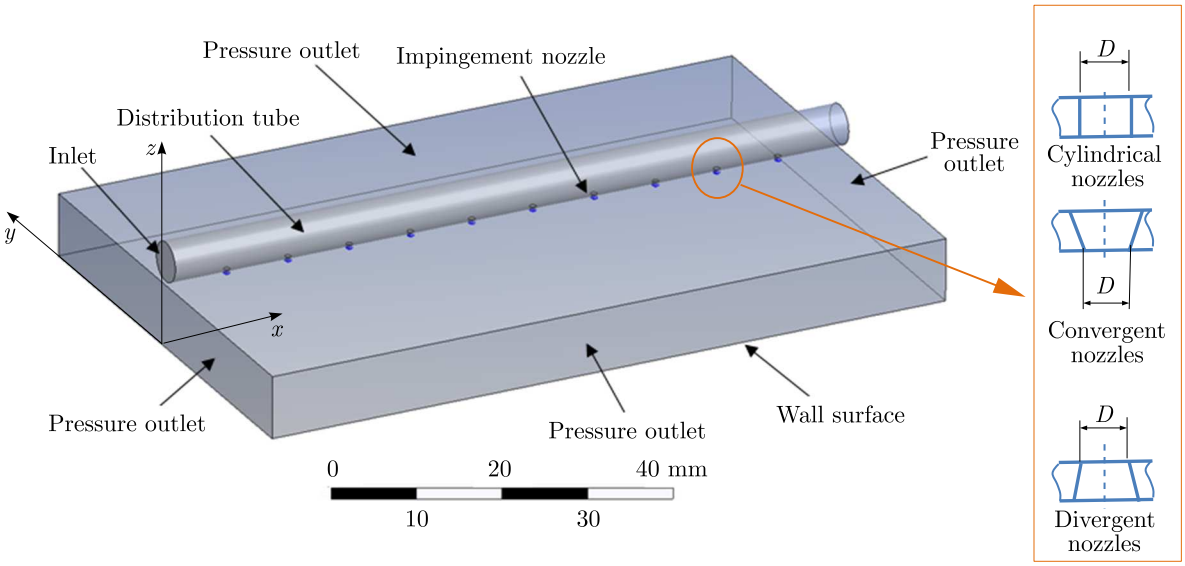

Fig. 1. Investigated computational 3D domain

Table 1. Geometry, fluid data, thermal and flow parameters used for calculations

Symbol	Value	Unit	Description
D	0.8	mm	nozzle diameter
α	30	°	taper angle
z/D	8	–	nozzles exit-plate distance
S/D	8	–	nozzle pitch-diameter ratio
D_T	5	mm	distribution tube inlet diameter
L	88	mm	length of target plate
W	56	mm	width of target plate
T_{jet}	20	°	fluid temperature in jet area
u	14	m/s	inlet air velocity
Re	4800	–	Reynolds number in jet area
ρ	1.17	kg/m^3	air density
k	0.025	W/(mK)	thermal conductivity
μ	$1.8 \cdot 10^{-5}$	Pas	dynamic viscosity

The presented cooling system consists of an array of ten impingement nozzles directed normally to the flat surface. Three different geometries of the nozzles are taken into consideration: cylindrical, convergent and divergent. Geometry of all the jets is based on the study by Royne and Dey (2006). Consequently, for the convergent and divergent nozzles, a taper angle $\alpha = 30°$ is introduced.

Both the left and the right hand side of the system are open to allow the fluid to flow. The fluid is free to expand after impinging the target surface.

Impingement cooling systems (especially gas turbines) have to operate with temperature differences on the cooled casing up to 250°C. Considering this and based on formula from Vinze *et al.* (2016) a heat flux range $q_w(x) = 0\text{-}5000\ \mathrm{W/m^2}$ has been established. To define the influence of the non-uniform heat flux on the results of calculations, four different functions $q_w(x)$ have been defined including the pointed range $q_w(x) = 0\text{-}5000\ \mathrm{W/m^2}$. Both increasing and decreasing values have been taken into account. They are presented in Tables 2 and 3.

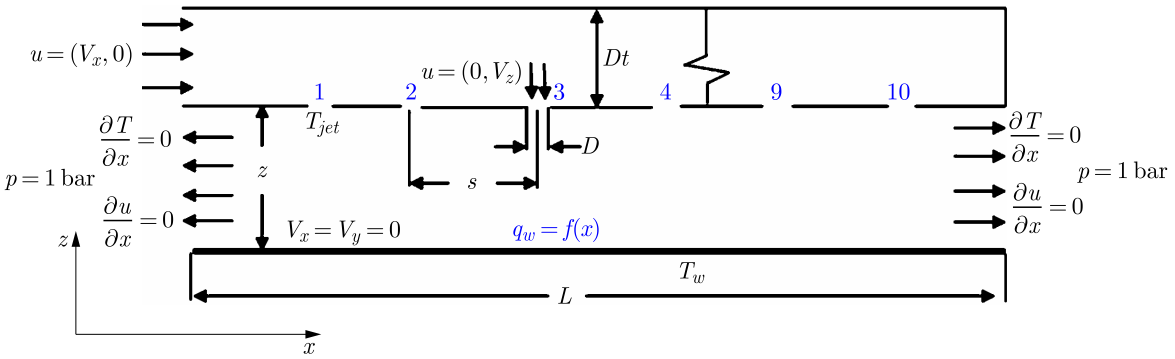

Fig. 2. 2D diagram of the considered problem (Marzec and Kucaba-Piętal, 2016)

Table 2. Cooled surface heat flux $q_w(x)$ representation by increasing linear functions

No.	Heat flux function $q_w(x)$	$q_w(0)$ [W/m^2]	$q_w(88)$ [W/m^2]	Graph of function $q_w(x)$
1	$56.82x$	0	5000	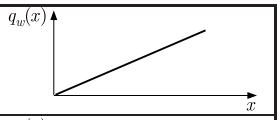
2	$45.45x+1000$	1000	5000	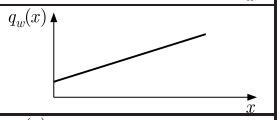
3	$28.41x+2500$	2500	5000	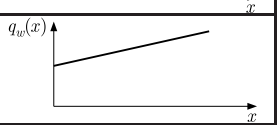

Table 3. Cooled surface heat flux $q_w(x)$ representation by decreasing linear functions

No.	Heat flux function $q_w(x)$	$q_w(0)$ [W/m^2]	$q_w(88)$ [W/m^2]	Graph of function $q_w(x)$
1	$-56.82x+5000$	5000	0	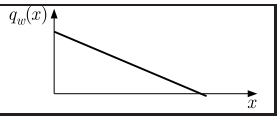
2	$-45.45x+5000$	5000	1000	
3	$-28.41x+5000$	5000	2500	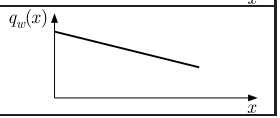

3. Governing correlations

The heat transfer rate measurements along the impingement surface are presented in terms of the Nusselt number as

$$\mathrm{Nu}=\frac{hD}{k} \tag{3.1}$$

where h is the heat transfer coefficient, D is nozzle diameter, and k is conductivity of the fluid. The heat transfer coefficient is defined as

$$h=\frac{q_w}{T_w-T_{jet}} \qquad h=-k\frac{1}{T_{jet}-T_w}\frac{\partial T}{\partial z} \tag{3.2}$$

where q_w is the wall heat flux, T_w is the wall adiabatic temperature, T_{jet} is the jet temperature, $\partial T/\partial z$ gives the temperature gradient component normal to the wall.

In this study, the line averaged Nusselt Number is defined as below

$$\overline{\mathrm{Nu}} = \frac{1}{L}\int_L \mathrm{Nu}(x)\, dx \tag{3.3}$$

where L is the line of the plate parallel to the distribution tube axis.

4. Numerical methods

4.1. Numerical approach

The 3D analysis of the heat transfer characteristics is carried out using Computational Fluid Dynamics (CFD) software Ansys CFX that solves equations of continuity, momentum end energy using the Reynolds-Averaged Navier-Stokes approach (RANS). In the RANS treatment, velocity vectors and other functions (in this case pressure) are split into average values and fluctuations, what can be written as follows (Błoński, 2009)

$$\begin{aligned} u_i(x,y,z,t) &= \overline{u}_i(x,y,z) + u_i'(x,y,z,t) \\ p(x,y,z,t) &= \overline{p}(x,y,z) + p'(x,y,z,t) \end{aligned} \tag{4.1}$$

where $i = 1,2,3$, u_i are velocity vector components, p – pressure.

Based on this approach, the Navier-Stokes equations of continuity and momentum can be written as follows

$$\begin{aligned} &\frac{\partial \overline{u}_j}{\partial x_j} = 0 \\ &\frac{\partial}{\partial x_j}(\rho\overline{u_i u_j}) = -\frac{\partial \overline{p}}{\partial x_i} + \frac{\partial}{\partial x_j}\Big[\Big(\frac{\partial \overline{u}_i}{\partial x_j} + \frac{\partial \overline{u}_j}{\partial x_i}\Big)\Big] + \frac{\partial}{\partial x_j}(-\rho\overline{u_i' u_j'}) \qquad i,j = 1,2,3 \end{aligned} \tag{4.2}$$

The correlations between the velocity fluctuations appearing in the momentum equations act as stresses and are called Reynolds stresses. They are defined as below

$$(-\rho\overline{u_i' u_j'}) = \mu_t\Big(\frac{\partial \overline{u}_i}{\partial x_j} + \frac{\partial \overline{u}_j}{\partial x_i}\Big) - \frac{2}{3}\rho\delta_{ij}k \tag{4.3}$$

where μ_t is turbulent viscosity, k – turbulence kinetic energy

$$k = \frac{1}{2}(\overline{u_i' u_j'}) \tag{4.4}$$

Finally, the Navier-Stokes equations for the stationary and viscous flow of the fluid can be written as follows

$$\begin{aligned} &\frac{\partial}{\partial x_j}(\rho\overline{u_i u_j}) = -\frac{\partial \overline{p}}{\partial x_i} + \frac{\partial}{\partial x_j}\Big[(\mu+\mu_t)\Big(\frac{\partial \overline{u}_i}{\partial x_j} + \frac{\partial \overline{u}_j}{\partial x_i}\Big)\Big] - \frac{2}{3}\frac{\partial}{\partial x_j}(\rho k) \\ &\frac{\partial \overline{u}_j}{\partial x_j} = 0 \end{aligned} \tag{4.5}$$

In the present investigation, the k-ω shear stress transport (SST) turbulence model is used. It combines the k-ω model near the wall and the k-ε model further from the wall. This approach utilizes strengths of each model. SST model is recommended as the best method for the impinging jet heat transfer predictions (Zuckerman and Lior, 2006).

The investigation is limited to the steady state assumption, and dynamic features of the impinging jets are ignored. However, the steady state assumption is able to provide average flow and temperature fields. To validate the numerical technique and the solution procedure, the comparison of numerical results of an impingement cooling system of the surface with a uniform temperature distribution with experimental have been performed and showed satisfying agreement (Marzec and Kucaba-Piętal, 2013).

4.2. Initial and boundary conditions

The velocity of the flow $u = (V_x, V_z)$ at the inlet of the supply tube $V_x = 14\,\mathrm{m/s}$ is constant for the whole analysis and is prescribed to obtain the Reynolds number $\mathrm{Re} = 4800$ in the area of the cylindrical nozzle. Thereby, the Reynolds number is based on the mean velocity at the nozzle and jet diameter D. The outlet boundaries of the calculated domain are represented by opening pressure boundary conditions which permit the fluid to both enter or leave the domain. The ambient pressure is constant at $p = 1\,\mathrm{bar}$. The fluid entering the plenum has total temperature of $T_{jet} = 20°\mathrm{C}$ which corresponds to temperature of the ambient air. The wall and the jet impinged onto have various heat fluxes $q_w(x)$. The walls of the cylindrical plenum are unheated and are modeled as an adiabatic no-slip wall. To simplify the analysis, the steady-state incompressible viscous fluid flow is considered. Moreover, it is assumed that the fluid physical properties are constant and the effect of the gravity and radiation is neglected. The flow field is three-dimensional. The roughness of the tube which contains the flowing fluid is $30\,\mu\mathrm{m}$.

4.3. Numerical grids and numerical accuracy

The geometry of the nozzles supporting the tube and the cooled surface, which were described previously, are taken into account in the grid definition which consists of 1.79 mln elements and 323119 nodes of unstructured tetrahedral grids generated by the Ansys CFX mesher. The influence of the numerical grid density on the results of the heat transfer coefficient and the Nusselt number in the stagnation region is taken into consideration. Four analyses with different cell sizes in the area of the interface (between the air flow and the surface) were performed. To investigate the sensitivity of the numerical results analysis, the Grid Convergence Index GCI (Eq. (4.1)) is calculated (Xu *et al.*, 2014). This is the most frequently used method for estimation of numerical uncertainty, endorsed by ASME Journal of Fluid Engineering (ASME, 2008). The safety factor $F_s = 3$, has been set for two grids comparison. Temperature is the chosen parameter. It is measured in the cooled surface for each grid. The order of convergence is $p = 2$, r^p is the density factor. In the third analysis, $\mathrm{GCI} = 1.3\%$ has been obtained. Therefore, it might be concluded that numerical results for the fine grid are grid independent

$$\mathrm{GCI} = F_s \frac{1}{r^p - 1} \left| \frac{T_{h2} - T_{h1}}{T_{h1}} \right| \cdot 100\% \tag{4.6}$$

5. Results and discussion

This Section presents the analysis of heat transfer characteristics of an array of ten impingement jets directed normally to the flat surface with various ways of the surface heat flux $q_w(x)$ distribution. Beside cylindrical nozzles, the usage of convergent and divergent jets are taken into consideration in terms of heat transfer characteristics with an inhomogeneous distribution of the surface heat flux $q_w(x)$. Flow field characteristics of the impingement cooling system with ten cylindrical nozzles is presented in the work Marzec and Kucaba-Piętal (2016). The optimal system configuration for a given surface heat flux $q_w(x)$ will be determined by the constant mass flow rate, the uniform Nusselt number distribution on the cooled surface and a high rate of

heat transfer. The uniform Nusselt number $\overline{\mathrm{Nu}}$ distribution plays a significant role as it might reduce thermal stresses on the cooled surface. In Fig. 3, the Nusselt number $\overline{\mathrm{Nu}}$ corresponding to the usage of ten cylindrical, convergent and divergent nozzles with the constant heat flux $q_w(x) = 5000\,\mathrm{W/m^2}$ is presented. For the cylindrical nozzles, the usage of a constant heat flux $q_w = 5000\,\mathrm{W/m^2}$ results in the highest averaged Nusselt number $\overline{\mathrm{Nu}} = 4.59$. The usage of convergent and divergent nozzles results in a very similar value of the averaged Nusselt number $\overline{\mathrm{Nu}} = 3.59$ and $\overline{\mathrm{Nu}} = 3.52$, respectively. The lowest values of the heat transfer rate are achieved for divergent nozzles in the area of the first jet. This is caused because of the flow deflection angle. In addition, it can be seen that for all nozzle geometries, the line of the averaged Nusselt number increases slightly in the x direction (along the flow of the distribution tube). The maximum difference between cylindrical, convergent and divergent nozzles, in the Nusselt Number Nu_o is respectively 31.5%, 36% and 42%.

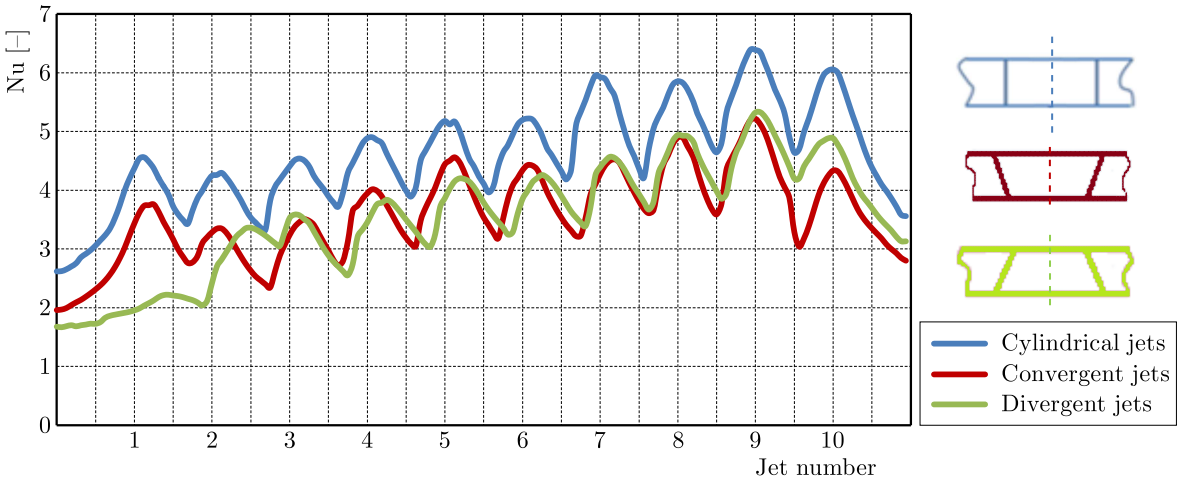

Fig. 3. Area of the averaged Nusselt number $\overline{\mathrm{Nu}}$ for cylindrical, convergent, divergent jets and a constant surface heat flux $q_w = 5000\,\mathrm{W/m^2}$

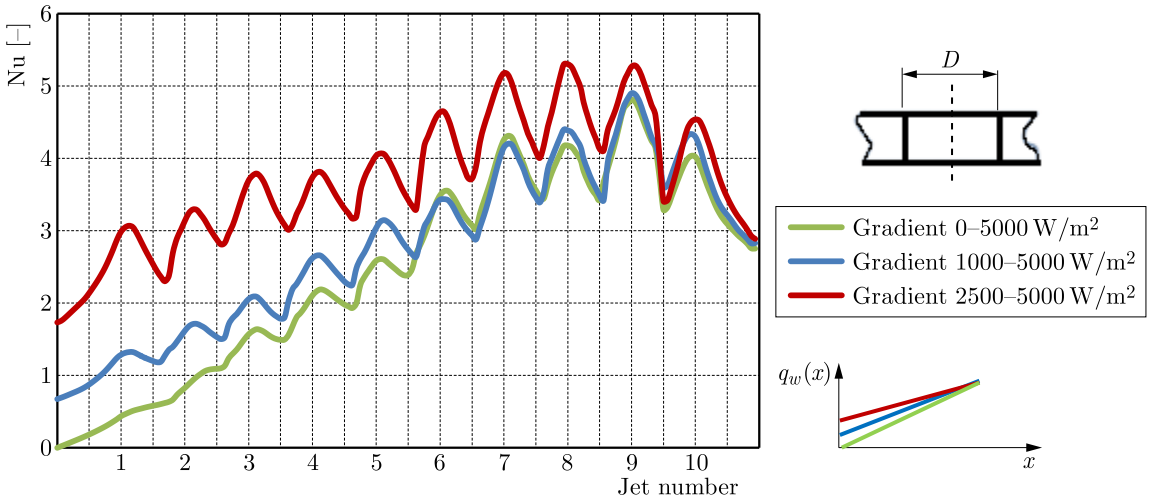

Fig. 4. Area of the averaged Nusselt number $\overline{\mathrm{Nu}}$ for the increasing heat flux $q_w(x)$, cylindrical nozzles

In Fig. 4, the Nusselt number corresponding to the application of ten cylindrical nozzles with the increasing heat flux $q_w(x)$ is presented. The wall, the jet impinged onto, is heated with a heat flux represented by three different linear functions (Table 2). The first one represents the heat flux $q_w = 0\,\mathrm{W/m^2}$ at the beginning of the cooled surface and $q_w = 5000\,\mathrm{W/m^2}$ at the end

of the cooled surface. The second one represents the heat flux $q_w = 1000\text{-}5000\ \mathrm{W/m^2}$. The third one represents the heat flux $q_w = 2500\text{-}5000\ \mathrm{W/m^2}$. It can be seen that the line of the averaged Nusselt number increases in the direction of the flow in the distribution tube for all three heat flux functions. The heat flux distribution $q_w = 2500\text{-}5000\ \mathrm{W/m^2}$ represents the most uniform values of the Nusselt number Nu_o in the stagnation region across all of the jets. The average difference of the Nusselt number Nu_o is 19.8%.

In Fig. 5, the Nusselt number corresponding to making use of ten convergent nozzles with a variable heat flux $q_w(x)$ increasing in the direction of the flow is presented. The wall, the jet impinged onto, is heated with the heat flux represented by three different linear functions (Table 2). The first one represents the heat flux $q_w = 0\ \mathrm{W/m^2}$ at the beginning of the cooled surface and $q_w = 5000\ \mathrm{W/m^2}$ at the end of the cooled surface. The second one represents the heat flux $q_w = 1000\text{-}5000\ \mathrm{W/m^2}$. The third one represents the heat flux $q_w = 2500\text{-}5000\ \mathrm{W/m^2}$. It can be seen that the line of the averaged Nusselt number increases in the direction of the flow in the distribution tube for all three heat flux functions. The heat flux distribution $q_w = 2500\text{-}5000\ \mathrm{W/m^2}$ represents the most uniform values of the Nusselt number Nu_o in the stagnation region across all of the jets. The average difference of the Nusselt number Nu_o is 27.1%.

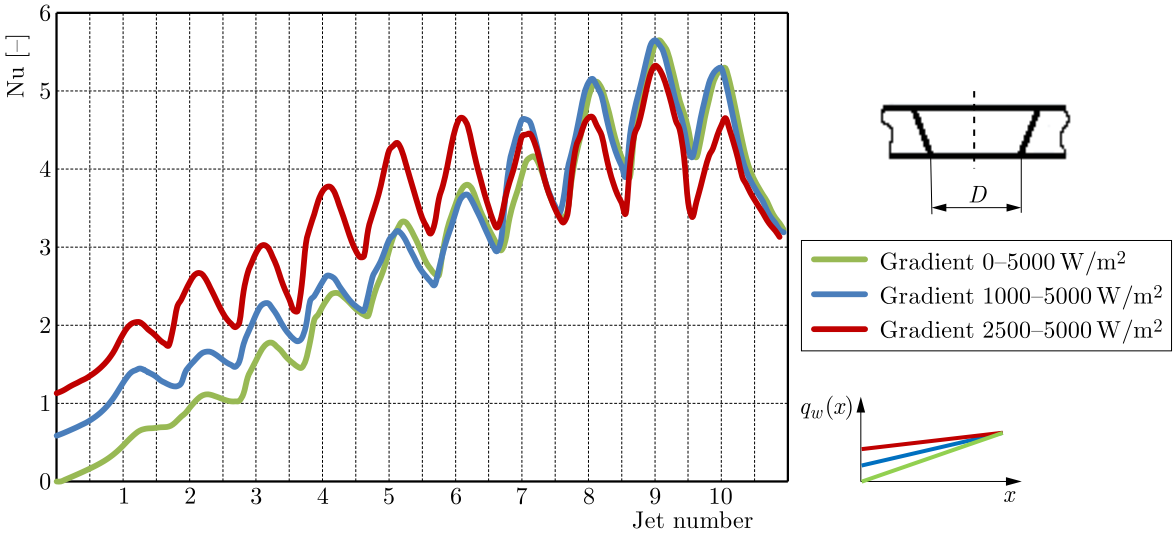

Fig. 5. Area of the averaged Nusselt number $\overline{\mathrm{Nu}}$ for the increasing heat flux $q_w(x)$, convergent nozzles

Figure 6 presents the Nusselt number corresponding to the usage of ten convergent nozzles with a variable heat flux $q_w(x)$ decreasing in the direction of the flow. The wall, the jet impinged onto, is heated with the heat flux represented by three different linear functions (Table 3). The first one represents the heat flux $q_w = 5000\ \mathrm{W/m^2}$ at the beginning of the cooled surface and $q_w = 0\ \mathrm{W/m^2}$ at the end of the cooled surface. The second one represents the heat flux $q_w = 5000\text{-}{-}1000\ \mathrm{W/m^2}$. The third one represents the heat flux $q_w = 5000\text{-}2500\ \mathrm{W/m^2}$. It can be seen that the line of the averaged Nusselt number decreases in the direction of the flow in the distribution tube for the first and the second heat flux function. The heat flux $q_w = 5000\text{-}2500\ \mathrm{W/m^2}$ represents similar values of the Nusselt number Nu_o in the stagnation region for all of the jets. The average difference of the Nusselt number Nu_o is 13%.

In Fig. 7, the Nusselt number corresponding to incorporation of ten divergent nozzles with a variable heat flux $q_w(x)$ increasing in the direction of the flow is presented. The wall, the jet impinged onto, is heated with the heat flux represented by three different linear functions (Table 2). The first one represents the heat flux $q_w = 0\ \mathrm{W/m^2}$ at the beginning of the cooled surface and $q_w = 5000\ \mathrm{W/m^2}$ at the end of the cooled surface. The second one represents the heat flux $q_w = 1000\text{-}5000\ \mathrm{W/m^2}$. The third one represents the heat flux $q_w = 2500\text{-}5000\ \mathrm{W/m^2}$. It can

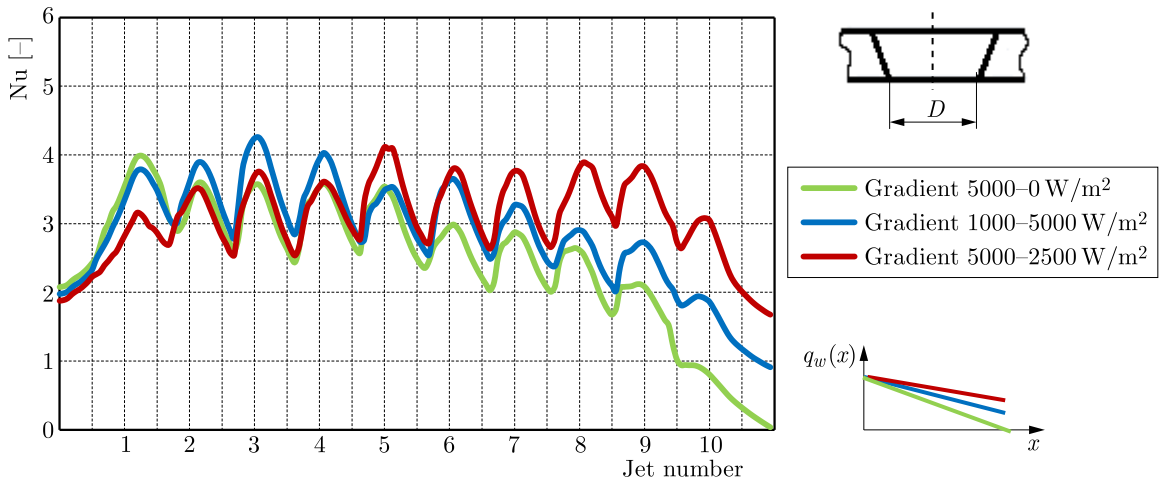

Fig. 6. Area of the averaged Nusselt number $\overline{\mathrm{Nu}}$ for the decreasing heat flux $q_w(x)$, convergent nozzles

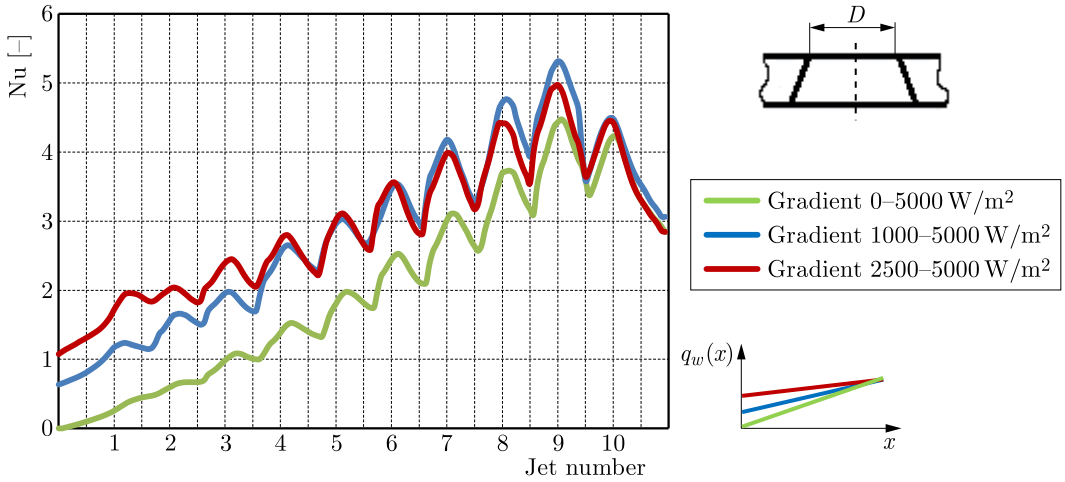

Fig. 7. Area of the averaged Nusselt number $\overline{\mathrm{Nu}}$ for the increasing heat flux $q_w(x)$, divergent nozzles

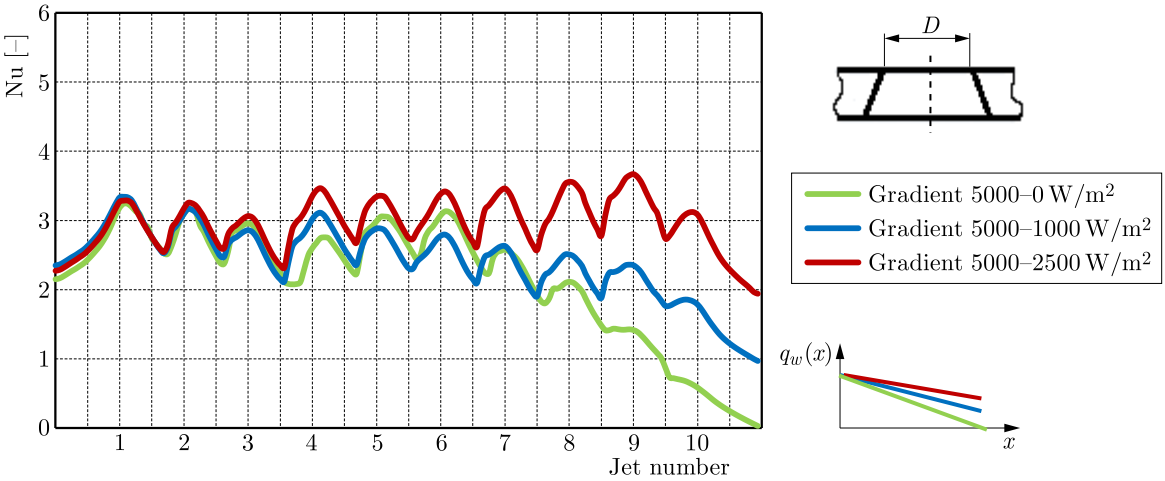

Fig. 8. Area of the averaged Nusselt number $\overline{\mathrm{Nu}}$ for the decreasing heat flux $q_w(x)$, divergent nozzles

be seen that the line of the averaged Nusselt number has a trend to increases in the direction of the flow in the distribution tube for all three heat flux functions. For $q_w = 2500\text{-}5000\,\mathrm{W/m^2}$, the average difference of the Nusselt number Nu_o is 34.3%.

Figure 8 presents the Nusselt number corresponding to application of ten divergent nozzles with a variable heat flux $q_w(x)$ decreasing in the direction of the flow. The wall, the jet impinged onto, is heated with the heat flux represented by three different linear functions (Table 3). The first one represents the heat flux $q_w = 5000\,\mathrm{W/m^2}$ at the beginning of the cooled surface and $q_w = 0\,\mathrm{W/m^2}$ at the end of the cooled surface. The second one represents the heat flux $q_w = 5000\text{-}1000\,\mathrm{W/m^2}$. The third one represents the heat flux $q_w = 5000\text{-}2500\,\mathrm{W/m^2}$. It can be seen that the line of the averaged Nusselt number decreases in the direction of the flow in the distribution tube for the first and the second heat flux functions. The heat flux $q_w = 5000\text{-}2500\,\mathrm{W/m^2}$ represents similar values of the Nusselt number Nu_o in the stagnation region for all of the jets. The average difference of the Nusselt number Nu_o is 9.1%.

6. Conclusions

The aim of the work is numerical analysis of the Nusselt number distribution of an array of ten impingement jets when the cooling surface posses both decreasing and increasing linear temperature distributions (see Tables 2 and 3). Cylindrical, convergent and divergent geometry of the nozzles are taken into consideration. The making use of an array of cooling jets resulted in a uniform distribution of the mass flow among the nozzles. The results indicate that cylindrical geometry of the nozzles results in the highest Nusselt numbers along the cooled surface. The results are convergent with a situation when temperature of the cooled surface is constant (Marzec and Kucaba-Piętal, 2014).

Taking into consideration the heat flux functions $q_w(x)$, the line of the averaged Nusselt number has a trend to increase in the direction of the flow for the cooling system with increasing values of the surface heat flux. This tendency can be observed for all presented shapes of the jets. On the other hand, for the decreasing functions of the heat flux $q_w(x)$, the Nusselt number distribution is more uniform. It can be observed for all types of the nozzles. For the non-uniform heat flux $5000\text{-}2500\,\mathrm{W/m^2}$, very similar values of the Nusselt number Nu_o along the cooled surface can be noticed. For constant values of the heat flux $q_w(x)$=$5000\,\mathrm{W/m^2}$, the line of the averaged Nusselt number has a trend to increase slightly in the direction of the flow. The presented results prove that the shape of the nozzles as well as an the inlet of the system have an impact on the Nusselt number distribution on the cooled plate. It can be interesting for designers of cooling systems who have to handle with the considered problem.

Acknowledgements

The calculations have been performed at ICM UW, Grant G64-0.

References

1. Ahmed F.B., Weigand B.. Meier K., 2010, Heat transfer and pressure drop characteristic for a turbine casing impingement cooling system, *Procedings of 14th International Heat Transfer Conference*, Washington, **5**

2. Al-Hadhrami L.M., 2010, Study of a heat transfer distribution in a channel with inclined target surface cooled by a single array of staggered impinging jets, *Heat Transfer Engineering*, **31**, 234-242

3. Al-Hadhrami L.M., Shaahid S.M., Mubarak A., 2007, Heat transfer in a channel with inclined target surface cooled by a single array of staggered impinging jets, *Proceedings of the ASME Turbo Expo*, Montreal, Canada, 35-42

4. Andreini A., da Soghe R., Facchini B., Maiuolo F., Tarchi L., Coutandin D., 2013, Experimental and numerical analysis of multiple impingement jet arrays for an active clearance control system, *Journal of Turbomachinery*, **135**

5. ASME, 2008, Procedure for estimation and reporting of uncertainty due to discretization in CFD applications, *Journal of Fluids Engineering*, **130**

6. Błoński S., 2009, Laminar-turbulent flow analysis in micro-channels, PhD Thesis, Polish Academy of Science, Institute of Fundamental Technological Research, http://www.ippt.pan.pl/_download/doktoraty/blonski_doktorat.pdf

7. Ee-Mahghany W.M., Hanafy A.A., Khaled M.A., Mohamed A.T., 2012, Numerical simulation for confined rectangular slot jets impingement on isothermal horizontal plate, *European Journal of Science Research*, **76**, 553-566

8. Goordo M., Jongmyung P., Ligrani P., Fox M., Hee-Koo M., 2007, Effects of Mach number and Reynolds number on jet array impingement, *International Journal of Heat and Mass Transfer*, **50**, 367-380

9. Marzec K., Kucaba-Piętal A., 2013, Applications of computer science in impingement cooling system design, *Pre-Proceedings of 9th International Conference on Applied Mathematics*, Baia Mare, Romania

10. Marzec K., Kucaba-Piętal A., 2014, Heat transfer characteristic of an impingement cooling system with different nozzle geometry, *Journal of Physics: Conference Series*, **530**

11. Marzec K., Kucaba-Piętal A., 2016, Numerical investigation of heat transfer characteristics of an impingement cooling system with non-uniform temperature on a cooled surface, *Journal of Physics, Conference Series*, **745**

12. Mubarak A., Shaahid S.M., Al-Hadhrami M., 2011, Impact of jet Reynolds number and feed channel geometry on heat transfer in a channel with inclined target surface cooled by single array of centered impinging jets with outflow in both directions, *Proceedings of International Conference of Mechanical Engineering*, London, UK, 6-8

13. Nirmalkumar M., Katti V., Prabhu S.V., 2011, Local heat transfer distribution on a smooth flat plate impinged by a slot jet, *International Journal of Heat and Mass Transfer*, **54**, 727-738

14. Royne A., Dey Ch., 2006, Effect of nozzle geometry on pressure drop and heat transfer in submerged jet arrays, *International Journal of Heat and Mass Transfer*, **49**, 800-804

15. Royne A., Dey Ch., Mills D., 2005, Cooling of photovoltaic cells under concentrated illumination: a critical review, *Solar Energy Materials and Solar Cells*, **86**, 451-483

16. Ruiz R., Alberts B., Sak W., Seitzer K., Steinetz B., 2006, Benefits of improved HP turbine active clearance control, NASA/CP2007-214995/Vol 1 Air System Workshop, Cleveland, OH

17. San J., Shiao W., 2006, Effect of jet plate size and plate spacing on the stagnation Nusselt number for a confined circular air jet impinging on a flat surface, *International Journal of Heat and Mass Transfer*, **49**, 3477-3486

18. Tarabsheh A., Voutetakis S., Papadopoulos A., Seferlis P., Etier I., Saraereh O., 2013, Investigation of temperature effects in efficiency improvement of non-uniformly cooled photovoltaic cells, *Chemical Engineering Transactions*, **35**

19. Vinze R., Chandel S., Limaye M.D., Prabhu S.V., 2016, Influence of jet temperature and nozzle shape on the heat transfer distribution between a smooth plate and impinging air jets, *International Journal of Thermal Sciences*, **99**, 136-151

20. Xu Sh., Wang W., Guo Z., Hu X., Guoa W., 2014, Multi-channel cooling system for multiple heat source, *Thermal Science Online Issue*, **00**, 123

21. Zuckerman N., Lior N., 2006, Jet impingement heat transfer: physics, correlations and numerical modeling, *Advanced in Heat Transfer*, **39**

22. Żukowski M., 2013, Heat transfer performance of a confined single slot jet if air impinging on a flat surface, *International Journal of Heat and Mass Transfer*, **57**, 484-490

Manuscript received March 19, 2017; accepted for print June 5, 2017

JOURNAL OF THEORETICAL AND APPLIED MECHANICS
55, 4, pp. 1325-1339, Warsaw 2017
DOI: 10.15632/jtam-pl.55.4.1325

DESIGN AND DEVELOPMENT OF 3-STAGE DETERMINATION OF DAMAGE LOCATION USING MAMDANI-ADAPTIVE GENETIC-SUGENO MODEL

Sasmita Sahu

School of Mechanical Engineering, Kalinga Institute of Industrial Technology, KIIT University, Bhubaneswar, Odisha, India; e-mail: gudusasmita@gmail.com

Priyadarshi Biplab Kumar, Dayal R. Parhi

Department of Mechanical Engineering, National Institute of Technology, Rourkela, Odisha, India
e-mail: p.biplabkumar@gmail.com; dayalparhi@yahoo.com

Damage detection in structural elements like beams is one of important research areas for health monitoring. Initiation of a fault in the form of a crack or any damage puts a limitation on the service life of a structural member. So, in this paper, a method is proposed which uses the advantages of soft computing techniques like Fuzzy Inference Systems (Mamdani and Sugeno) and Adaptive Genetic Algorithm for three stage refinement of the data base generated using dynamic responses from a cracked fixed-free aluminum alloy beam element. For the crack element reference, a finite element model of a single transverse crack has been considered. The proposed method describes both Mamdani and Sugeno Fuzzy Inference Systems for training of damage parameters. In the Adaptive Genetic Algorithm, a statistics based method has been incorporated to limit the randomness of the search process. Finally, the results from the Mamdani-Adaptive Genetic-Sugeno model (MAS) are validated with the results from the experimental analysis.

Keywords: damage, Mamdani FIS, Sugeno FIS, Adaptive Genetic Algorithm, vibration, natural frequencies

1. Introduction

Cracks in structural and machine members indicate the amount of serviceability of the structures. Crack initiation is obvious in most of engineering structures due to environmental and working conditions. Usually, a hairline crack is visible and can be inspected using a crack gauge, fiber optical sensor or laser sensor. But, it becomes very difficult to detect a very small crack whose location is very dangerous for the structural element (Jaiswal and Pande, 2015). Cracks change dynamic responses of structures like natural frequencies and mode shapes (Pawar *et al.*, 2007). These changes in the dynamic properties can be used to detect the presence of the crack (Fegade *et al.*, 2014). So, the vibration based methods are gently getting popularized for crack detection. These methods have the ability of convenience measurement by collecting the variation in modal properties (Waghulde and Kumar, 2014). The analytical methods used for damage detection cost time and are subjected to human error. With the invention and development of finite element analysis, many of the researchers are using this method for the analysis of dynamics of cracked beams (Ranjbaran and Ranjbaran, 2013). Though finite element analysis is an approximation method, it can give great data with less time consumption. So, this paper uses finite element analysis for modeling of the crack. Yuan *et al.* (2014) have recently proposed one of the methods to make re-meshing easier for analyzing crack propagation area by incorporating a radial point interpolation method. The artificial intelligence techniques with vibration based methods can make a powerful tool for online detection of the damage. These techniques can learn offline

vibration signatures to evaluate the condition monitoring status of large complex structures both in static and dynamic conditions.

In this research work, a knowledge based computational method and an evolutionary working on the "Natural Selection" is addressed for vibration analysis of the cracked structural element. From the invention of this logic, it has been successfully applied to different research fields. Many researchers have also used Fuzzy Logic and its advance versions in the field of damage detection and localization (Verma *et al.*, 2013). From the vast literature available, it can be observed that most of the researchers have used Mamdani fuzzy inference system for their analyses. Chandrashekhar and Ganguli (2009) proposed one of the analytical methods for modal analysis using Modal Curvature and Fuzzy Logic. Zhu and Wu (2014) depicted a method for rapid structural damage detection using ANFIS and interval modeling technique, in which the ANFIS model has been designed using Sugeno FIS.

In the first Section of the paper, both Mamdani and Sugeno FIS are described for crack detection. Here, Fuzzy Logic has been used to learn the dynamics of the cracked structure for damage detection. Two types of membership functions have been proposed to design variables of the current problem. In the second part of the paper, an Adaptive Genetic Algorithm method has been narrated. The main notion of this adaptive search algorithm is to simulate the process necessary for evolution (Shahidi *et al.*, 2015). This stochastic search algorithm provides an intelligent exploitation of search space to solve a problem. Khaji and Mehrjoo (2014) proposed a new method using Genetic Algorithm for the determination of the crack locations of an arbitrary number of transverse cracks. The Search Space in GA plays an important role in finding the absolute solution as; Genetic Algorithms (GAs) are random search algorithms. These algorithms can be applied to many real world problems of complex and intricate nature which are tough to be solved by traditional or conventional methods. Various statistical methods are also incorporated in damage detection problems to control the randomness and nonlinearity of the damage indices which are trained in different techniques (Niezrecki, 2015). Therefore, in this paper, Regression Analysis has been incorporated for the data analysis of the problem, which makes the problem more adaptive (Dervilis *et al.*, 2015). Finally, in the third part, the data base generated from the finite element analysis and experimental analysis is trained in the proposed method using the 3-stage Mamdani-Adaptive Genetic-Sugeno model.

The first three natural frequencies are extracted from FEA and converted into relative values. The relative values of the natural frequencies (rff, rsf, rtf) are found out by comparing the natural frequencies of the uncracked beam and the cracked beam. Relative values of the crack depth and crack location (rcd, rcl) are also found out using the similar method. This work considers only the natural frequencies because they are less prone to error while calculating. The relative first natural frequency (rff), relative second natural frequency (rsf) and relative third natural frequency (rtf) are treated as the input variables in the proposed method. The outputs from the system are the relative values of the crack depth (rcd) and crack location (rcl) which, in turn, contains the information of damage severity. The reason behind the idea to take the relative values of the input and output variables is to lessen the coding error and running time of the algorithm when fed to it. The proposed method is a type of inverse analysis problem. Here, by giving the crack depths and crack locations, the natural frequencies are found out using theoretical, finite element and experimental analyses. These set of crack locations and first three natural frequencies are used as the data set.

2. Finite element analysis approach for cracked beam element

The Euler-Bernoulli beam model is assumed for the finite element formulation. The crack in this particular case is assumed to be an open crack, and the damping is not being considered in this

theory. The geometry of the cracked beam is described in Fig. 1 (P_1 – axial load, P_2 – bending moment, L_1 – distance of the crack from the free end of the beam, L – length of the cantilever beam, B – breadth of the cantilever beam, W – width of the cantilever beam, a_1 – crack depth.

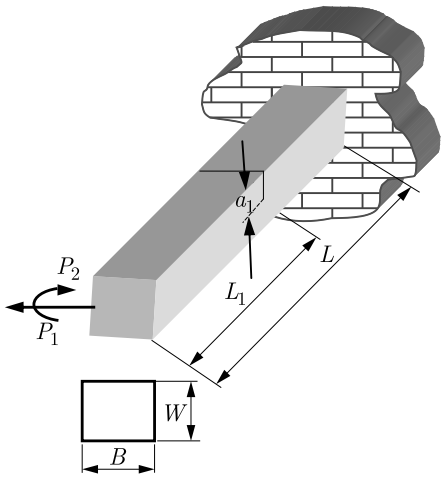

Fig. 1. Geometry of the cracked cantilever beam

The free bending vibration of a Euler-Bernoulli beam of a constant rectangular cross section is given by the following differential equation

$$EI\frac{d^4y}{dx^4} - m\omega_i^2 y = 0 \tag{2.1}$$

where m is the mass of the beam per unit length [kg/m], ω_i – natural frequency of the i-th mode [rad/s], E – modulus of elasticity [N/m^2] and I is the moment of inertia [m^4]. By defining $\lambda^4 = m\omega_i^2/(EI)$, the equation is rearranged as a fourth-order differential equation as follows

$$\frac{d^4y}{dx^4} - \lambda^4 y = 0 \tag{2.2}$$

A general solution to the equation is

$$y = A\cos\lambda_i x + B\sin\lambda_i x + C\cosh\lambda_i x + D\sinh\lambda_i x \tag{2.3}$$

where A, B, C, D are constants and λ_i is a frequency parameter.

The governing differential equation for the system is given as

$$\mathbf{M}\ddot{\mathbf{x}} + \mathbf{C}\dot{\mathbf{x}} + \mathbf{K}\mathbf{x} = \mathbf{F}\sin(\omega t) \tag{2.4}$$

where $\mathbf{M}$, $\mathbf{K}$, $\mathbf{C}$ is the mass, stiffness and damping matrix, respectively, $\mathbf{F}$ is the external force.

But, it is assumed that there is no damping and there is no external force applied to the system. So, the governing equation becomes

$$\mathbf{M}\ddot{\mathbf{x}} + \mathbf{K}\mathbf{x} = \mathbf{0} \tag{2.5}$$

The equation of motion for natural frequencies for undamped free vibration is given in equation (2.5). To solve equation (2.5), it is assumed that

$$\mathbf{x} = \boldsymbol{\phi}\sin(\omega t) \tag{2.6}$$

where $\boldsymbol{\phi}$ is the eigenvector or mode shape, ω – circular natural frequency.

Substituting the differential equation of the assumed solution into Eq. (2.5), the equation of motion will be changed to

$$\omega^2 \mathbf{M}\boldsymbol{\phi}\sin(\omega t) + \mathbf{K}\boldsymbol{\phi}\sin(\omega t) = \mathbf{0} \tag{2.7}$$

After simplification, it becomes

$$(\mathbf{K} - \omega^2 \mathbf{M})\boldsymbol{\phi} = \mathbf{0} \tag{2.8}$$

The equation is called the eigenequation. The basic form of the eigenvalue problem is

$$(\mathbf{A} - \lambda \mathbf{I})\mathbf{x} = \mathbf{0} \tag{2.9}$$

where $\mathbf{A}$ is the square matrix, λ – eigenvalues, $\mathbf{I}$ – identity matrix, $\mathbf{x}$ – eigenvector.

In structural analysis, the eigenequation is written in terms of $\mathbf{K}$, $\mathbf{M}$, and ω with $\omega^2 = \lambda$.

There are two possible solutions to equation (2.8)

1. If $|(\mathbf{K} - \omega^2 \mathbf{M})\boldsymbol{\phi}| \neq 0$ is a trivial solution where $\boldsymbol{\phi} = \mathbf{0}$
2. If $(\mathbf{K} - \omega^2 \mathbf{M})\boldsymbol{\phi} = \mathbf{0}$ is a non-trivial solution where $\boldsymbol{\phi} \neq \mathbf{0}$

$$|(\mathbf{K} - \omega^2 \mathbf{M})| = 0 \qquad |(\mathbf{K} - \lambda \mathbf{M})| = 0 \tag{2.10}$$

The determinant is zero only for discrete eigenvalues

$$|(\mathbf{K} - \omega^2 \mathbf{M})|\phi_i = 0 \qquad i = 1, 2, 3, \ldots \tag{2.11}$$

Adopting Hermitian shape functions, the stiffness matrix of the two-noded beam element without a crack is obtained using the standard integration based on the variation in flexural rigidity

$$\mathbf{K}_c^e = \mathbf{K}^e - \mathbf{K}_c \tag{2.12}$$

Here, $\mathbf{K}_c^e$ is the stiffness matrix of the cracked element, $\mathbf{K}^e$ – element stiffness matrix, $\mathbf{K}_c$ – reduction in the stiffness matrix due to the crack.

According to (Peng *et al.*, 2007), the matrix $\mathbf{K}_c$ is

$$\mathbf{K}_c = \begin{bmatrix} K_{11} & K_{12} & -K_{11} & K_{14} \\ K_{12} & K_{22} & -K_{12} & K_{24} \\ -K_{11} & -K_{12} & K_{11} & -K_{14} \\ K_{14} & K_{24} & -K_{14} & K_{44} \end{bmatrix} \tag{2.13}$$

It is assumed that the crack does not affect the mass distribution of the beam. The consistent mass matrix of the beam element is given as

$$\mathbf{M}^e = \int_0^1 \rho \mathbf{A}\mathbf{H}^{\mathrm{T}}(x)\,\mathbf{H}(x)\,dx \qquad \mathbf{M}^e = \frac{\rho}{20}\mathbf{A}\mathbf{I}\begin{bmatrix} 156 & 221 & 54 & -131 \\ 221 & 41^2 & 131 & -31^2 \\ 54 & 131 & 156 & -221 \\ -131 & -31^2 & -221 & 41^2 \end{bmatrix} \tag{2.14}$$

The natural frequency then can be calculated from relation (2.11).

3. Fuzzy logic approach for structural damage detection

Fuzzy logic can operate on imprecise, noisy inputs, but the output is a very smooth unit. It incorporates a simple rule based approach to solve control problems rather than solving it mathematically. The fuzzy logic controller model is empirically based on the designer's experience rather than the technical understanding of the system. In this work, the natural frequencies from the damaged beam element are used as the input to the fuzzy controller as shown in Fig. 2, and the outputs from the fuzzy controller are the crack depth and crack location.

3.1. Fuzzy inference systems

Fuzzy Inference Systems (FIS) are of two types, i.e., Mamdani FIS and Takagi-Sugeno FIS. In this work, the Mamdani FIS consists of the following steps. Figure 2 describes a fuzzy controller using shuffled membership functions.

1. Fuzzification (use of the membership function for graphical presentation of the database)
2. Rule evaluation (implementation of the rules)
3. Defuzzification (obtaining the crisp values of the results)

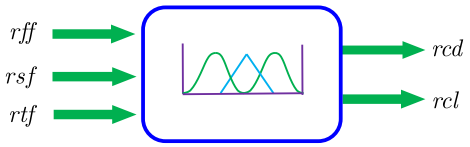

Fig. 2. Fuzzy logic controller using input and output membership functions

3.1.1. Mamdani fuzzy inference system for crack detection

The fuzzy logic system consisting of the Mamdani fuzzy inference model is implemented through the following steps.

1) *Fuzzification:* First, the crisp input and output variables are fuzzified using fuzzy sets. The degrees of membership of these variables are defined.
2) *Rule aggregation and evaluation:* The fuzzified variables are used to form fuzzy rules. If a fuzzy rule consists of many antecedent parts, they are joined by fuzzy operators (AND or NOT). For the Mamdani fuzzy inference, the i-th rule can be mathematically expressed as

$$R_i: \quad \Omega \;\; x_1 = A_{i1} \;\wedge\; x_2 = A_{i2} \;\wedge\; \ldots \;\wedge\; x_n = A_{in} \;\Rightarrow\; y_1 = B_{i1} \;\wedge\; y_2 = B_{i2} \tag{3.1}$$

   where $A_{i1}, A_{i2}, \ldots, A_{in}$ and B_{i1}, B_{i2} are the fuzzy sets.

   The membership values of all rule consequents are combined into a single fuzzy set.
3) *Defuzzification:* The most common type of the defuzzification method is the centroid method. This defuzzifier method has been used in all the fuzzy logic system of this research work. This method finds a point representing the COG (centre of gravity) of the aggregated fuzzy set A in the interval $[a, b]$. The following figure shows the Mamdani FIS applied in this work.

The other types of defuzzification methods are the mean of maximum, weighted average method, height method, etc.

3.1.2. Sugeno fuzzy inference system for crack detection

Steps used in the Takagi-Sugeno fuzzy inference modeling for damage detection are as follows.

1. General structure of the Sugeno fuzzy inference begins with fuzzification of the input (*rff*, *rsf*, *rtf*) and output variables (*rcd*, *rcl*) within the defined range using different types of membership functions (triangular, trapezoidal, Gaussian, etc.) the like Mamdani FIS.

   For the current problem, let x_1, x_2, x_3 be input variables defined on the reference sets X_1, X_2, X_3 and let y_1 and y_2 be output variable defined on the reference sets Y_1 and Y_2.

Then FIS has three input variables and two output variables. Further, each set X_j, $j = 1, 2, 3$, can be divided into $i = 1, 2, \ldots, n$ fuzzy sets

$$\mu_{j,1}(x), \mu_{j,2}(x), \ldots, \mu_{j,i}(x), \ldots, \mu_{j,n}(x) \tag{3.2}$$

where μ is the membership function value.

2. The next step comprises of the formation of the fuzzy base rules. The l-th if-then rule R_k in Sugeno FIS can be written in the following form

$$\begin{aligned} R_l: \quad & \Omega \;\; x_1 = L_{1,i(1,l)} \;\wedge\; x_2 = L_{2,i(1,l)} \;\wedge\; x_3 = L_{3,i(1,l)} \\ & \Rightarrow \;\; y_1 = f_1(x_1, x_2, x_3) \;\wedge\; y_2 = f_2(x_1, x_2, x_3) \end{aligned} \tag{3.3}$$

where $L_{1,i(1,l)}, L_{2,i(1,l)}, L_{3,i(1,l)}$ are the linguistic variables.
$y_1 = f_1(x_1, x_2, x_3)$, $y_2 = f_2(x_1, x_2, x_3)$ are linear polynomial functions, $l = 1, 2, \ldots, N$

$$R_l: \quad \Omega \;\; x_1 = L_{1,i(1,l)} \;\wedge\; x_2 = L_{2,i(1,l)} \;\wedge\; x_3 = L_{3,i(1,l)} \;\Rightarrow\; y_1 = k_1 \;\wedge\; y_2 = k_2 \tag{3.4}$$

where k_1, k_2 are constants. Equation (3.4) describes the zero order Sugeno FIS rule.

3. The third step describes the defuzzification procedure in the Sugeno FIS. The output weight of y_l of each of the l-th if-then rule R_l is aggregated by

$$w_l = \mu(x_1) \;\wedge\; \mu(x_2) \;\wedge\; \mu(x_3) \tag{3.5}$$

The final output after aggregation of N rules is computed as

$$y = \frac{\sum_{l=1}^{N} y_l w_l}{\sum_{l=1}^{N} w_l} \tag{3.6}$$

4. Adaptive genetic algorithm for damage detection

Genetic Algorithms (GAs) are based on the evolution of natural selection and genetics. This algorithm was first developed by Holland (1992). This is a heuristic search algorithm. The main notion of this adaptive search algorithm is to simulate the process necessary for evolution. This stochastic search algorithm provides an intelligent exploitation of search space to solve a problem. The search space in GA plays an important role in finding the absolute solution as; genetic algorithms (GAs) are random search algorithms. Although GAs can be used to find solutions to very complicated real world problems, they are very much simple to use and understand. It is able to search through a variety and huge combination of parameters to find the best match. But, sometimes, the GA becomes unidirectional without expediting the entire search space. The accessibility to the better solution in the search space becomes easier if there exists a relationship between the independent and dependent variables in a problem. Therefore, in this work, regression analysis has been incorporated for the data analysis of the problem, which makes the problem more adaptive.

The operators and procedure or the natural evolution process is similar to the simple genetic algorithm. The domain containing viable solutions is called the search space. Each individual point in the search space is a feasible solution. These solutions are ranked by their fitness values for selection. The important features of the algorithm are the genetic operators. These operators try to imitate the process of natural selection of the evolution process. The genetic operators,

crossover and mutation perform two different roles. Crossover tries to direct the population towards a local solution which leads to premature convergence of the algorithm. But, mutation is a divergence operation that tries to introduce diversity in the population, so that there will be more exploitation of the search space. This paves the way towards achieving a better solution. But the mutation amount in every generation is kept small and should affect a few members of a population. Otherwise, the entire solution space will be changed, and the algorithm will become directionless.

4.1. Regression analysis for the generation of the data pool for GA

Regression analysis comes under the category of supervised learning based on the statistical modeling of the problem. Regression analysis is used to find the relationship between two variables. This method is mainly a statistics based method. It can be described in the form of cause (independent variable) and effect (dependent variable). Several researchers have used regression analysis for the data base analysis of damage detection problems, but no one has combined it with genetic algorithms.

This analysis mainly related to dynamic responses of a cracked structural element with a damage extent. It is often realized that damage parameters are often scalar values, so univariate statistical tests can be utilized to find out possible changes among parameter vectors associated with a definite location. It is also expected that the computational cost of such statistical testing is less than that of the parameter extraction. The present problem is a case of multiple regression analysis due to the presence of multiple input and output variables.

For the present analysis, $Y = rff, rsf, rtf$ and $X = rcd, rcl$.

The linear equations for the current problem relating the dependent and independent variables are as in the following

$$\begin{aligned} Y_1 &= p_1 + q_1(X_1) + q_2(X_2) + q_3(X_3) \\ Y_2 &= p_1 + q_4(X_1) + q_5(X_2) + q_6(X_3) \end{aligned} \tag{4.1}$$

For the data extraction using the regression analysis method, direct values of the variables are used. After analysis, the values of the data are converted to the relative values.

4.2. Implementation of adaptive genetic algorithm for fault detection in cracked structures

As we know Genetic Algorithm (GA) is a search algorithm, it can be well applied to the current problem. In this problem, it is required to find the relative crack depth and relative crack location to a corresponding set of relative natural frequencies from the field signals. For this, first, a database is prepared from the results of theoretical, finite element and experimental analyses. Then rest of the steps are done according to the genetic algorithm. For all types of evolutionary algorithms, the encoding is a must. The advancement of the algorithm and the application of the operators mainly depend on the representation scheme adapted for the algorithm.

The encoding of chromosomes used in the current problem is the bit string/binary encoding. Each gene of the chromosome may be either 0 or 1. The gene/bit strings contain the information about the solution. In this approach, each chromosome contains five genes (*rff*, *rsf*, *rtf*, *rcd* and *rcl*). Each gene contains four bits, so each chromosome contains twenty bits. After the assignment of the representation scheme to the chromosomes, the problem proceeds towards the algorithm.

Following are the steps used in the genetic algorithm.

1) First of all, the variables and fitness functions are selected.

   The GA begins by defining input variables whose values are to be optimized using the fitness function and output variables whose values are to be anticipated using genetic operators.

The fitness function to be minimized is defined as

$$\text{Fitness Function} = \sqrt{(rff_{fd} - rff_{x_1,i})^2 + (rsf_{fd} - rsf_{x_1,i})^2 + (rtf_{fd} - rtf_{x_1,i})^2} \quad (4.2)$$

where rff_{fd} is the first natural frequency of the field, rff_x – relative first natural frequency, rsf_{fd} – second natural frequency of the field, rsf_x – relative second natural frequency, rtf_{fd} – third natural frequency of the field, rtf_x – relative third natural frequency, i – number of iterations.

The less the difference between the field and random frequency, the higher rank will be acquired by chromosome.

2) A data pool (initial population) containing ten numbers of data sets (individuals) is created. This data pool is acquired from FEA and theoretical analysis.

3) Two parents (i.e., two data set) from data pool (i.e., from ten data sets) using the fitness function are selected.

4) The selected parents undergo crossover. Here, two-point crossovers are used. As the chromosomes contain five parameters, and each parameter contains four bits, so the chromosome contains twenty bits. The crossover points are chosen four bits left of the chromosome and four bits right of the chromosome. Figure 3 shows the presentation of the parent with crossover points.

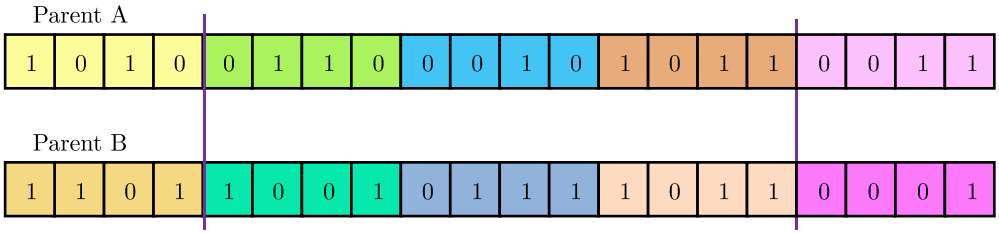

Fig. 3. Parent chromosomes with crossover points

5) The children (two numbers) from the parents are found out. Figure 4 describes the application of two-point crossover points in the genetic algorithm for damage detection.

6) After crossover, mutation is performed. In the proposed paper, as we have used binary encoding, the mutation rate used is 0.1% of the string. As the chromosome consists of 20 bits, only two bits at a time are flipped or altered. Figure 5 describes the application of the tossing type of mutation in the genetic algorithm for damage detection.

7) Again, fitness evaluation of the parents and the offspring is done. Then, the fitness values of the parents and children are compared to find out the best fit member.

8) If the child comes as the best fit, then it is added to the data pool, and a new set of the data pool is created. If a parent comes as the best fit, then the desired output (rcd, rcl), is the output belonging to that set.

9) Steps from 2-8 are repeated in each iteration till the algorithm meets the threshold values.

The algorithm terminates when it meets the threshold values. The threshold values for GA to stop are as below. The algorithm stops when it meets any of the criteria first.

i. 50 generations
ii. Maximum time elapsed (running time of the algorithm, i.e., two minutes)

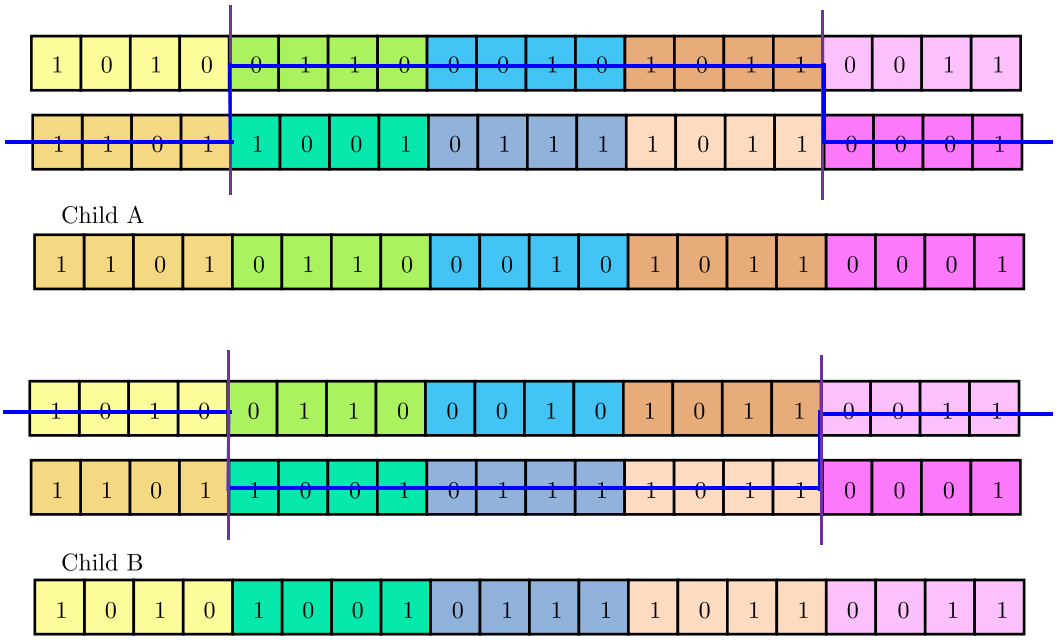

Fig. 4. Two-point crossover used for producing the off-springs

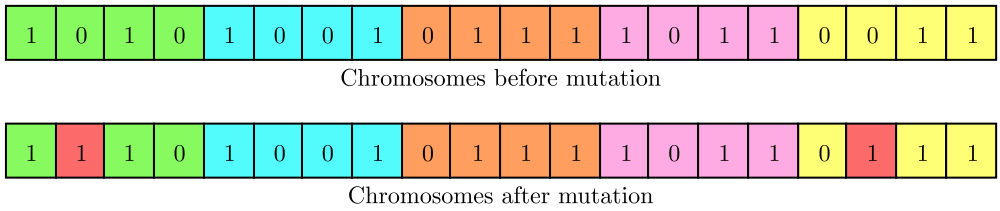

Fig. 5. Description of the mutation process implemented in damage detection

5. Analysis of 3-stage determination of damage location using Mamdani-Adaptive Genetic-Sugeno model

From the vast literature available in the structural damage detection using Fuzzy Logic and Genetic Algorithm for following conclusions have been drawn.

Several authors have used fuzzy logic for damage detection using the Mamdani FIS. The membership functions used in the Mamdani FIS are also different. Some have used simple membership functions (Saridakis *et al.*, 2008) while others have used combinations of membership functions (Parhi *et al.*, 2011; Thatoi *et al.*, 2014). It has been noticed by the researchers that the Mamdani FIS using a combination of membership functions gives better results than the simple membership functions. Fewer researchers have used the Sugeno model for damage detection. Most of the researchers have used Sugeno model with an artificial neural network for damage detection. When the results of the Mamdani FIS and Sugeno FIS are compared, it has been observed that the Sugeno FIS gives better results than the Mamdani FIS. Likewise, many researchers have used genetic algorithms (Vakil-Baghmisheh *et al.*, 2008) for damage detection. A simple Genetic Algorithm is very easy to understand and simple to apply, once the designer has understood the dynamics of the problem. Though it is very widely used in many of engineering fields, it has some shortcomings like attainment of global solution (optimization). This occurs mainly due to the random search of the solution space which is also time consuming. So, in the proposed adaptive genetic algorithm, regression analysis has been incorporated to the statistical modeling of the variable relationship, so that the genetic algorithm will take less time to cover the entire solution space.

After analyzing all the above stated factors, the current method is proposed. In the proposed method, 3-stage treatment of the data generated is done.

5.1. Design and development of 3-stage determination of damage location using the Mamdani-Adaptive Genetic-Sugeno (MAS) model

The previous Sections of this paper have discussed the benefits of the Mamdani FIS, Sugeno FIS and the adaptive genetic algorithm. So, in this Section, a method comprising 3-stage treatment of the data is used for damage detection in beams with two end conditions (fixed-free, fixed-fixed). The data pool which is to be treated in multiple stages, finally to give the crack location (rcd, rcl), is generated from the theoretical, finite element analysis and experimental analysis.

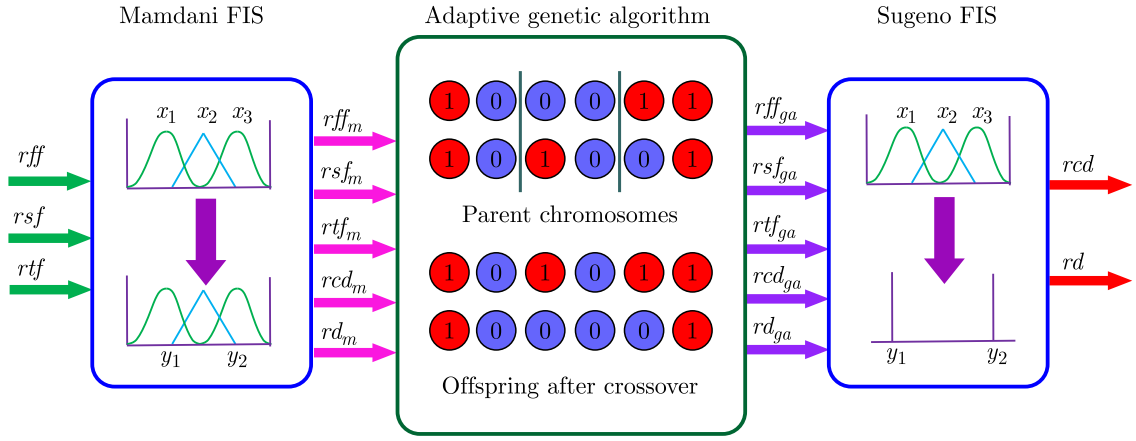

Fig. 6. Presentation of 3-stage determination of damage location using the Mamdani-Adaptive Genetic-Sugeno (MAS) model

In the first stage, the data pool is treated in the fuzzy Mamdani FIS. Here, the Mamdani FIS has been designed using shuffled membership functions comprising of triangular and Gaussian MFs. The efficiency of the Mamdani FIS using shuffled membership functions has already been noticed in Section 3 of this paper. Also from the works of other researchers, it has been observed that a combination of membership functions gives better results than the simple membership functions. In the Mamdani FIS, by changing the input values, the output values are obtained for at least hundred runs. After the training of the data pool in the Mamdani segment, the transit data is generated with the crack location as rcd_m and rcl_m. After obtaining the first set of data from the Mamdani FIS; it is treated in the adaptive genetic algorithm segment as described in Section 4 of this paper.

During the treatment of the data in this segment, the results get closer towards the global solution due to the treatment of the data in regression analysis. After applying regression analysis to the hundred data sets, half of the data sets are taken to be trained in the genetic algorithm. The crack locations from the genetic algorithm are named as rcd_ga and rcl_ga. The GA is then run for hundred times. Out of the hundred runs, fifty different data sets are taken to make the second data pool.

The second data pool is then trained in the Sugeno FIS after the second stage treatment of the data pool; the data gets more refined. After the training of the second data pool in the Sugeno FIS, the final results of the 3-stage training of the data are obtained with better crack location parameters. Due to the achievement of better results from the Sugeno FIS, it has been kept in the last segment of the training procedure after the adaptive genetic algorithm segment. Figure 6 depicts a pictorial presentation of the stages of the 3-stage determination of damage location using the Mamdani-Adaptive Genetic-Sugeno model.

6. Experimental set-up used in the fault detection of a cracked beam

The instruments used in the free vibration analysis of the fixed-free beam are an impact hammer, vibration pick-up, vibration analyzer and vibration indicator (Fig. 7). Using the impact hammer, the cracked fixed-free beam is excited in the free vibration mode. The vibration analyzer is PULSE LAB Prolite 3560. The excitation parameters are picked up by the vibration pick-up or an accelerometer. Then, these parameters are fed to the vibration analyzer, where the parameters are analysed and the results are shown in the vibration indicator.

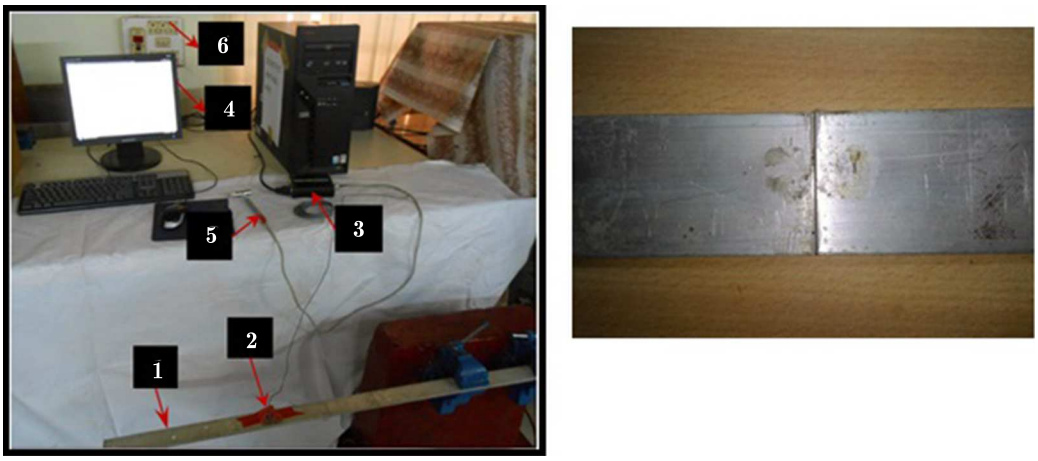

Fig. 7. Experimental set-up with the cracked beam; 1 – cracked fixed-fixed beam with a single crack, 2 – vibration pick-up, 3 – vibration analyzer, 4 – vibration indicator, 5 – impact hammer, 6 – power distribution

Several tests have been conducted using the experimental setup on aluminium alloy beam specimens (800 mm×38 mm×8 mm) with a transverse crack for determining the natural frequencies at different crack locations and crack depths. These specimens are given vibration by impact hammer, and the 1st, 2nd and 3rd natural frequencies are recorded in the vibration indicator.

7. Result and discussions

The percentage error is calculated using the following formula

$$\begin{aligned}&[(\text{FEA result} - \text{result from the proposed technique})/(\text{FEA result})] \cdot 100\\ &[(\text{Exp. result} - \text{result from the proposed technique})/(\text{Exp. result})] \cdot 100\\ &\text{Total error in } \% = (\% \text{ error in } rcd + \% \text{ error in } rcl)/2\end{aligned} \tag{7.1}$$

The present work describes the damage detection method for cracked structural elements. First, the transverse hairline crack has been modeled using the finite element method. In the finite element analysis, the cracked structure has been modeled assuming the Euler-Bernoulli beam model. Then, the vibration parameters which are the indices of damage are extracted from the finite element analysis. Then, a data base consisting of the cause (crack depth, crack location) and effect (change in first three natural frequencies) of initiation of the crack is made. Then, the data base is trained in different computational techniques (fuzzy logic (Mamdani FIS and Sugeno FIS), adaptive genetic algorithm and Mamdani-Adaptive Genetic-Sugeno model) to find the crack location.

Though with the invention of soft computing methods have made it easier to find good results at the fingertip by just running a program, finding a global optimization method remains a major challenge in engineering. Performances of these methods are hampered by some limitations

which include huge computational time consumption. So in this work, a 3-stage determination of damage location using the Mamdani-Adaptive Genetic-Sugeno model has been proposed. The work also tries to compare the performances of individual methods, and the results are described in tables.

From Tables 1-3 the results of the individual methods are given respectively. These tables compare the results from these methods with those from the finite element analysis. Tables 4 and 5 give the comparison of the results from the 3-stage Mamdani-Adaptive Genetic-Sugeno model with finite element analysis and experimental analysis respectively. For the validation of the results from the Mamdani-Adaptive Genetic-Sugeno model, they are compared with the results from the experimental analysis. Two sets of data are used for two different comparisons due to the availability of different data sets from the two analyses. The performance comparison is done in terms of the percentage error. The percentage error has been determined using equations (7.1).

The following table shows the results of the proposed technique (3-stage Mamdani-Adaptive Genetic-Sugeno model).

Table 1. Comparison of the results of FLS (Mamdani FIS) with FEA for a cantilever beam

No.	*rff* from FEA	*rsf* from FEA	*rtf* from FEA	*rcd* from FEA	*rcl* from FEA	rcd using the FLS techique	rcl using the FLS technique	percent. error *rcd*	percent error *rcl*	Total error
1	0.9923	0.9912	0.9966	0.325	0.21875	0.307148	0.206701	5.493	5.508	5.5005
2	0.9931	0.9926	0.9978	0.300	0.20625	0.283536	0.194884	5.488	5.511	5.4995
3	0.9946	0.9942	0.9972	0.2875	0.23125	0.271607	0.218550	5.528	5.492	5.5100
4	0.9959	0.99772	0.9990	0.125	0.21875	0.118106	0.206728	5.515	5.496	5.5055
5	0.9974	0.9977	0.9965	0.275	0.36250	0.259867	0.342505	5.503	5.516	5.5095

Table 2. Comparison of the results of FLS (Sugeno FIS) with FEA for a cantilever beam

No.	*rff* from exp. analysis	*rsf* from exp. analysis	*rtf* from exp. analysis	*rcd* from exp. analysis	*rcl* from exp. analysis	rcd using the FLS techique	rcl using the FLS technique	percent. error *rcd*	percent, error *rcl*	Total error
1	0.9923	0.9912	0.9966	0.325	0.21875	0.307795	0.207152	5.294	5.302	5.2980
2	0.9931	0.9926	0.9978	0.300	0.20625	0.284136	0.195321	5.288	5.299	5.2935
3	0.9946	0.9942	0.9972	0.2875	0.23125	0.272211	0.219008	5.318	5.294	5.3060
4	0.9959	0.99772	0.9990	0.125	0.21875	0.118373	0.207123	5.302	5.315	5.3085
5	0.9974	0.9977	0.9965	0.275	0.36250	0.260403	0.343284	5.308	5.301	5.3045

Table 3. Comparison of the results of Adaptive Genetic Algorithm (AGA) with FEA for a cantilever beam

No.	*rff* from FEA	*rsf* from FEA	*rtf* from FEA	*rcd* from FEA	*rcl* from FEA	rcd using the AGA techique	rcl using the AGA technique	percent. error *rcd*	percent. error *rcl*	Total error
1	0.9923	0.9912	0.9966	0.325	0.21875	0.308016	0.207342	5.226	5.215	5.2205
2	0.9931	0.9926	0.9978	0.300	0.20625	0.284406	0.195535	5.198	5.195	5.1965
3	0.9946	0.9942	0.9972	0.2875	0.23125	0.272585	0.219207	5.188	5.208	5.1980
4	0.9959	0.99772	0.9990	0.125	0.21875	0.118520	0.207351	5.184	5.211	5.1975
5	0.9974	0.9977	0.9965	0.275	0.36250	0.260678	0.343690	5.208	5.189	5.1985

Table 4. Comparison of the results of MAS with FEA for a cantilever beam

No.	*rff* from FEA	*rsf* from FEA	*rtf* from FEA	*rcd* from FEA	*rcl* from FEA	rcd using the MAS techique	rcl using the MAS technique	percent. error *rcd*	percent. error *rcl*	Total error
1	0.9923	0.9912	0.9966	0.325	0.21875	0.309969	0.208659	4.625	4.613	4.619
2	0.9931	0.9926	0.9978	0.300	0.20625	0.286233	0.196756	4.589	4.603	4.596
3	0.9946	0.9942	0.9972	0.2875	0.23125	0.274261	0.220643	4.605	4.587	4.596
4	0.9959	0.9977	0.9990	0.125	0.21875	0.119255	0.208655	4.596	4.615	4.6055
5	0.9974	0.9977	0.9965	0.275	0.36250	0.262259	0.345865	4.633	4.589	4.611

Table 5. Comparison of the results of MAS with experimental analysis for a cantilever beam

No.	*rff* from exp. analysis	*rsf* from exp. analysis	*rtf* from exp. analysis	*rcd* from exp. analysis	*rcl* from exp. analysis	rcd using the MAS techique	rcl using the MAS technique	percent. error *rcd*	percent error *rcl*	Total error
1	0.9973	0.9914	0.9995	0.34375	0.46875	0.327862	0.447131	4.622	4.612	4.617
2	0.9974	0.9890	0.9999	0.375	0.5	0.357795	0.47691	4.588	4.618	4.603
3	0.99816	0.9982	0.9979	0.25	0.375	0.238495	0.35778	4.602	4.592	4.597
4	0.9988	0.9981	0.9989	0.21875	0.40625	0.208659	0.387502	4.613	4.615	4.614
5	0.9892	0.9996	0.9981	0.35	0.1875	0.333862	0.178879	4.611	4.598	4.6045

8. Conclusions

The conclusions drawn from the proposed work can be depicted as follows.

From Tables 1-4, we can get results of the individual methods as well as results from the proposed Mamdani-Adaptive Genetic-Sugeno model. From the comparison of the results of the three individual methods, it can be observed that the adaptive genetic algorithm gives better results as compared to the other two methods (Mamdani FIS and Sugeno FIS). The average total error for the Mamdani FIS is 5.5031%, for the Sugeno FIS is 5.30175%, for the adaptive genetic algorithm is 5.2022%. After analyzing the average total error values of these three methods, it can be said that the adaptive genetic algorithm performs better than the other two methods. From the two of the methods (Mamdani FIS and Sugeno FIS), the Sugeno FIS performs better than the Mamdani FIS. The Sugeno type FIS was designed in order to achieve higher computational effectiveness as compared to the Mamdani FIS. This is possible as the defuzzification of outputs is avoided. Its advantage also lies in involving the functional dependencies of output variables on input variables.

Tables 4 and 5 give the comparison of the results from the 3-stage Mamdani-Adaptive Genetic-Sugeno model with finite element analysis and experimental analysis respectively. The results from the 3-stage analysis are compared with the results from the experimental analysis, for validation of the results from the proposed method. The average total error is found to be 4.6055% and 4.6071% when compared with the results from the finite element analysis and experimental analysis respectively. It is also noticed that the proposed method gives better results as compared to the individual methods. From the analysis of the results and the method, it can be said that the proposed method and all the individual methods can be treated as a robust tool for structural damage detection. The proposed method can be analyzed using different compatible commercial software packages as a future work so that the best method can be found out, which can handle the time consumption and the human error during calculation.

After a thorough literature survey on damage detection, it has been observed that the Artificial Intelligence (AI) techniques are emerging as a powerful tool for damage detection. Lots of work have been done using standalone methods. From different research works, it has been noticed that hybridized methods give better results as compared to standalone methods. This

happens because the hybridized methods retain the goodness of their elementary algorithms. The hybridized algorithms are so designed and developed that each component of the algorithm tries to overcome shortcomings of other components.

In the current research work, Fuzzy Logic (FL) and Genetic Algorithm (GA) have been considered. Lots of research work have been carried away using fundamental FL and GA. Many researchers have also provided shortcomings of these methods. So, this work tries to overcome the shortcomings of the fundamental methods. Fuzzy Logic consists of two types of inference engines, and both of them are good but when the results and procedures are compared, T-S FIS gives better results. Genetic Algorithm is one of the unique evolutionary algorithms based on Darwin's theory of natural selection and evolution. One of the foremost shortcoming of the algorithm is that it could not provide a global solution. The algorithm sometimes gets stuck in the local solution. So to get rid of the above stated problem, regression analysis has been added. This data analysis process generates a relation between the input and output variables. Out of the three steps, the T-S FIS gives best results, so it has been put in the final step. The other two methods are also organized according to their efficiency.

References

1. Chandrashekhar M., Ganguli R., 2009, Structural damage detection using modal curvature and fuzzy logic, *Structural Health Monitoring*, **8**, 4, 267-282
2. Dervilis N., Worden K., Cross E.J., 2015, On robust regression analysis as a means of exploring environmental and operational conditions for SHM data, *Journal of Sound and Vibration*, **347**, 279-296
3. Fegade P.V., Mahajan J.A., Bhole G.P., 2014, Study on vibration analysis of an uncrack and cracked cantilever beam, *International Association of Scientific Innovation and Research*, **10**, 4, 340-343
4. Jaiswal N.G., Pande D.W., 2015, Sensitizing the mode shapes of beam towards damage detection using curvature and wavelet transform, *International Journal Of Scientific and Technology Research*, **4**, 4, 266-272
5. Holland J.H., 1992, Genetic algorithms, *Scientific American*, 66-72
6. Khaji N., Mehrjoo M., 2014, Crack detection in a beam with an arbitrary number of transverse cracks using genetic algorithms, *Journal of Mechanical Science and Technology*, **28**, 3, 823-836
7. Niezrecki C. (Edit.), 2015, *Structural Health Monitoring and Damage Detection, Volume 7, Proceedings of the 33rd IMAC, A Conference and Exposition on Structural Dynamics*, ISBN 978-3--319-15230-1
8. Parhi D.R., Choudhury S., 2011, Intelligent fault detection of a cracked cantilever beam using fuzzy logic technology with hybrid membership functions, *International Journal of Artificial Intelligence and Computational Research*, **3**, 1, 9-16
9. Pawar P.M., Reddy K.V., Ganguli R., 2007, Damage detection in beams using spatial Fourier analysis and neural networks, *Journal of Intelligent Material Systems and Structures*, **18**, 4, 347-359
10. Peng Z.K., Lang Z.Q., Billings S.A., 2007, Crack detection using nonlinear output frequency response functions, *Journal of Sound and Vibration*, **301**, 3, 777-788
11. Ranjbaran A., Ranjbaran M., 2013, New finite-element formulation for buckling analysis of cracked structures, *Journal of Engineering Mechanics*, **140**, 5
12. Saridakis K.M., Chasalevris A.C., Papadopoulos C.A., Dentsoras A.J., 2008, Applying neural networks, genetic algorithms and fuzzy logic for the identification of cracks in shafts by using coupled response measurements, *Computers and Structures*, **86**, 11, 1318-1338

13. Shahidi S.G., Nigro M.B., Pakzad S.N., Pan Y., 2015, Structural damage detection and localisation using multivariate regression models and two-sample control statistics, *Structure and Infrastructure Engineering*, **11**, 10

14. Thatoi D., Choudhury S., Jena P.K., 2014, Fault diagnosis of beam-like structure using modified fuzzy technique, *Advances in Acoustics and Vibration*

15. Vakil-Baghmisheh M.T., Peimani M., Sadeghi M.H., Ettefagh M.M., 2008, Crack detection in beam-like structures using genetic algorithms, *Applied Soft Computing*, **8**, 2, 1150-1160

16. Verma P., Rathore M., Gupta R., 2013, Vibration control of cantilever beam using fuzzy logic controller, *International Journal of Science Engineering and Technology Research*, **2**, 4, 906-909

17. Waghulde K.B., Kumar B., 2014, Vibration analysis of cracked cantilever beam with suitable boundary conditions, *International Journal of Innovative Science, Engineering and Technology*, **1**, 10, 20-24

18. Yuan H., Peng C., Lin Q., Zhang B., 2014, Simulation of tensile cracking in earth structures with an adaptive RPIM-FEM coupled method, *KSCE Journal of Civil Engineering*, **18**, 7, 2007-2018

19. Zhu F., Wu Y., 2014, A rapid structural damage detection method using integrated ANFIS and interval modeling technique, *Applied Soft Computing*, **25**, 473-484

Manuscript received April 7, 2017; accepted for print June 21, 2017

JOURNAL OF THEORETICAL AND APPLIED MECHANICS
55, 4, pp. 1341-1353, Warsaw 2017
DOI: 10.15632/jtam-pl.55.4.1341

AN ANALYTICAL APPROACH TO PREDICTION OF INTERNAL DEFECTS DURING THE FLAT ROLLING PROCESS OF STRAIN-HARDENING MATERIALS

Parvaneh Amjadian, Heshmatollah Haghighat
Razi University, Mechanical Engineering Department, Kermanshah, Iran
e-mail: hhaghighat@razi.ac.ir

In this paper, the upper bound method has been used in analysis of the flat rolling process and prediction of internal defects for a strain-hardening material. The arc of contact has been replaced by a chord. The inlet shear boundary of the deformation zone has been assumed as an exponential curve and the boundary at the exit has been assumed as a cylindrical surface. A kinematically admissible velocity field has been proposed and internal, shear and frictional power terms have been derived. By minimizing the total power with respect to the neutral point position and the shape of the inlet shear boundary, the rolling torque has been determined. A criterion has been presented to predict the occurrence of the internal defects for given rolling conditions. Comparison of the analytically developed approach for rolling torque and internal defects with published theoretical and experimental data shows generally good agreement.

Keywords: upper bound, flat rolling, internal defects, strain-hardening exponent

1. Introduction

Flat rolling is the process of reducing thickness of a long sheet by torques applied through a set of rolls. The rolling process widely is used in production of industrial components, so concentrating on the final quality of the parts produced by this process is very important. Internal central bursts are common rolling processing defects. Ignoring their prediction causes both losses of physical injury and property damage or reducing quality of the final products. Usually, it is very difficult to detect central bursting defects by surface inspection. The investigations on flat rolling have been conducted for decades and various aspects of these processes have been studied. Dyja and Pietrzyk (1983) analyzed an asymmetric dual hot-rolled sheet using minimum energy, and replaced the arc of contact by a chord. Avitzur *et al.* (1988) modeled the flat rolling process by using upper bound analysis for rigid perfectly plastic materials to predict internal defects. Takuda *et al.* (1989) analyzed the strip rolling process by assuming a simple velocity field by considering free deformation zones in front and behind the roll gap. Turczyn and Pietrzyk (1992) analyzed the effect of deformation zone geometry on the internal defect in the flat rolling process. They used the upper bound method and took into consideration velocity boundaries. Discontinuity circular arcs were present and uniform velocity fields for internal defects assumed. Prakash and Dixit (1995) proposed a model for steady state plane strain cold rolling of a strain-hardening material which could predict the roll force and torque with reasonable engineering accuracy over the usual range of process variables. Turczyn (1996) analyzed the effect of deformation zone geometry on the internal defects in rolling process using the upper bound method. Martins and Barata (1999) presented an approach for analyzing plane strain rolling. They used the upper bound method to estimate the rolling torque and to model the material flow within the region of deformation between the rolls. Dogruoglu (2001) introduced a

systematic method for constructing kinematically admissible velocity fields, which was necessary in the analysis of the plastic forming process by the upper bound method. Gosh and Gardiner (2004) identified various modeling issues that were necessary for successful simulation of the cold rolling process by comparing it with experiments on aluminum alloys. Rajak and Reddy (2005) analyzed internal defects in the plane strain rolling process with the finite element method. They used critical damage criteria. Serajzadeh and Mahmoodkhani (2008) presented a combined upper bound and finite element model for prediction of velocity and temperature fields during the hot rolling process. The closing behavior of internal defects in the central part of a continuous casting steel slab during rough transverse rolling was investigated by using FE-code, ANSYS/LS-DYNA by Deng *et al.* (2009). Misicko *et al.* (2009) observed and analyzed by computer simulation behavior of artificial surface defects inside flat steel samples during the hot rolling process by selected parameters. Cao *et al.* (2015) investigated the prediction of damage for the ultimate wire flat rolling process of high carbon steel using three different approaches of ductile damage. Haghighat and Saadati (2015) presented the kinematically admissible velocity field for the rolling of sandwich sheets, non-bonded before rolling, and discussed some mathematical aspects by the upper bound method. Haghighat and Pargzadeh (2017) investigated the effect of strain hardening on the central bursting defects in rod extrusion process. In this paper, analyses of plastic deformation and prediction of internal defects in flat rolling process of a strain-hardening material using the upper bound method is considered. The arc of contact between the roll and the sheet is replaced by a chord. Based on the FEM, it is observed that the inlet and outlet shear boundaries are not circular and in any condition such as inlet thickness and reduction in area are deferent, then we present arbitrary exponential shear boundaries and velocity field that can predict rolling torque and internal defects. Then a kinematically admissible velocity field is proposed and internal, shear and frictional power terms are derived. By minimizing the total power with respect to the neutral point position and the shape of the inlet shear boundary, the rolling torque and the occurrence of internal defects is investigated. The effect of the friction factor, strain-hardening exponent and reduction in the area on the rolling torque and safe and unsafe domains are investigated.

2. Upper bound analysis

Figure 1 shows flat rolling process parameters in a schematic diagram. Because of symmetry of the process, only half of the section is considered. An important subject in the upper bound analysis is the assumption of shear boundaries and a kinematically admissible velocity field satisfying volume constancy in the deformation zone and boundary conditions. In order to determine the velocity field, the arc of contact is replaced by a chord. The material starts as a sheet of thickness t_i and then is deformed into a sheet of thickness $2t_f$, v_i is the initial velocity of the sheet and v_f is the velocity of the product, α is the angle of the line connecting the initial point to the final point of the contact arc with the axis of symmetry. R is radius, and ω is angular velocity of the roll.

2.1. Velocity zones

To analyze the process, the material under deformation is divided into three deformation zones, as shown in Fig. 1. In zones I and III, the material moves rigidly with the velocity v_i and v_f, respectively. Zone II is the deformation zone and is surrounded by two shear surfaces S_1 and S_2 and the contact surface S_3. The shear boundary S_2 at the exit from the deformation zone is assumed to be a cylindrical surface with its center at the apex O. The shear boundary S_1

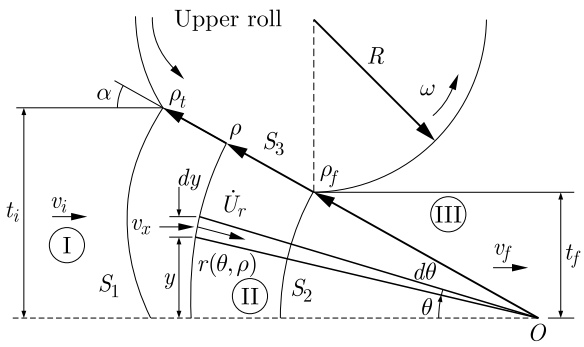

Fig. 1. Geometry of the sheet, roll, deformation zone and the shear boundaries

is assumed to be an arbitrarily curved surface. Using this description, mathematical equations of the shear boundaries S_1 and S_2 are defined in the cylindrical coordinates by

$$r_i(\theta,\rho_i) = \rho_i \exp\Big[\frac{b(\theta-\alpha)}{\alpha}\Big] \qquad r_f(\theta,\rho_f) = \rho_f \tag{2.1}$$

where r_i and r_f are the radial position of inlet and outlet shear boundary, respectively, and the radial position in the deformation zone is

$$r(\theta,\rho) = \rho \exp\Big[\frac{b(\theta-\alpha)}{\alpha}\frac{\rho-\rho_f}{\rho_i-\rho_f}\Big] = \rho g(\theta,\rho) \tag{2.2}$$

where ρ_i and ρ_f are the radial distances from the virtual apex to inlet and outlet shear boundaries on the roll surface shown in Fig. 1, b is the shape factor of the shear boundary at the inlet of deformation zone II, θ is the peripheral position and ρ is the radial position on the contact surface, and g is an arbitrary shape function

$$g(\theta,\rho) = \exp\Big[\frac{b(\theta-\alpha)}{\alpha}\frac{\rho-\rho_f}{\rho_i-\rho_f}\Big] \tag{2.3}$$

b can be negative, zero or positive. When b is negative, the shear boundary moves away from the origin O, when b is positive the shear boundary moves towards the apex O, when b is zero, the inlet shear boundary is a cylindrical surface (i.e. $g = 1$). In zone I and III, the material moves as a rigid body in the axial direction. In zone III, the velocity v_f from the volume flow balance is

$$v_f = v_i\frac{\rho_i}{\rho_f} \tag{2.4}$$

With regard to the equilibrium of volume flow, the admissible velocity filed in deformation zone II can be obtained as

$$v_x(dy) = -\dot{U}_r(rd\theta) \tag{2.5}$$

v_x is the horizontal velocity component in the deformation zone, $\dot{U}_r$ is the radial component of velocity and y is the vertical position.

So, the radial velocity component of the velocity field is

$$\dot{U}_r = -\frac{v_x}{r}\frac{dy}{d\theta} = -v_i\frac{\rho_i}{\rho}\Big(\cos\theta + \frac{1}{g}\frac{\partial g}{\partial\theta}\sin\theta\Big) \tag{2.6}$$

The volume constancy in the cylindrical coordinates system is defined as

$$dot\varepsilon_{rr} + \dot{\varepsilon}_{\theta\theta} + \dot{\varepsilon}_{zz} = 0 \tag{2.7}$$

where $\dot{\varepsilon}_{rr}$, $\dot{\varepsilon}_{\theta\theta}$, $\dot{\varepsilon}_{zz}$ are normal strain rate components.

According to the cylindrical coordinates strain rates components and the assumption of the plane strain process, $\dot{U}_z = 0$ (lateral velocity component), the peripheral velocity component ($\dot{U}_\theta$) is

$$\dot{U}_\theta = v_i \rho_i \frac{\partial g}{\partial r} \sin\theta \tag{2.8}$$

where

$$\frac{\partial g}{\partial r} = \frac{\partial g}{\partial \rho}\frac{\partial \rho}{\partial r} = \frac{b(\theta-\alpha)}{\alpha}\frac{1}{\rho_i - \rho_f}\frac{1}{1+\frac{b(\theta-\alpha)}{\alpha}\frac{\rho}{\rho_i-\rho_f}} \tag{2.9}$$

The velocity components in deformation zone II are given as

$$\dot{U}_r = -v_i \frac{\rho_i}{\rho}\Big(\cos\theta + \frac{1}{g}\frac{\partial g}{\partial \theta}\sin\theta\Big) \qquad \dot{U}_\theta = v_i \rho_i \frac{\partial g}{\partial r}\sin\theta \qquad \dot{U}_z = 0 \tag{2.10}$$

As it is clear from Eqs. (2.10), on the axis of symmetry $\dot{U}_\theta = 0$, and on the contact surface between the roll and sheet $\dot{U}_\theta = 0$, so the incompressibility condition is satisfied. Nonzero strain rate components in the deformation zone are

$$\begin{aligned}
\dot{\varepsilon}_{rr} &= v_i \frac{\rho_i}{\rho^2}\frac{1}{g}\Big[\Big(1-\rho\frac{\partial g}{\partial r}\Big)\cos\theta + \Big(\frac{1}{g}\frac{\partial g}{\partial \theta} - \rho\frac{\partial^2 g}{\partial r \partial \theta}\Big)\sin\theta\Big] \\
\dot{\varepsilon}_{\theta\theta} &= -v_i \frac{\rho_i}{\rho^2}\frac{1}{g}\Big[\Big(1-\rho\frac{\partial g}{\partial r}\Big)\cos\theta + \Big(\frac{1}{g}\frac{\partial g}{\partial \theta} - \rho\frac{\partial^2 g}{\partial r \partial \theta}\Big)\sin\theta\Big] \\
\dot{\varepsilon}_{r\theta} &= \frac{1}{2}v_i \frac{\rho_i}{\rho^2}\frac{1}{g}\Big\{\Big[\rho^2\frac{\partial^2 g}{\partial r^2} + \frac{1}{g^2}\Big(\frac{\partial g}{\partial \theta}\Big)^2 - \frac{1}{g}\frac{\partial^2 g}{\partial \theta^2} + 1\Big]\sin\theta + \frac{1}{g}\frac{\partial g}{\partial \theta}\cos\theta\Big\}
\end{aligned} \tag{2.11}$$

2.2. Determinations of power terms

The internal power in the upper bound analysis for a perfectly elasic von Mises material in the deformation zone is

$$\dot{W}_i = \frac{2}{\sqrt{3}}\sigma_0 \int\limits_V \sqrt{\frac{1}{2}\dot{\varepsilon}_{ij}\dot{\varepsilon}_{ij}}\, dV \tag{2.12}$$

where $\dot{W}_i$ is internal power of deformation, σ_0 is the average flow stress and dV is a differential volume of the deformation zone.

After substitution and simplification, the internal power of region II is given by

$$\dot{W}_i = \frac{2\sigma_0}{\sqrt{3}}\int\limits_0^\alpha \int\limits_{\rho_f}^{\rho_i} \sqrt{\dot{\varepsilon}_{rr}^2 + \dot{\varepsilon}_{r\theta}^2}\,\rho g\Big(g + \rho\frac{\partial g}{\partial \rho}\Big)\, d\rho\, d\theta \tag{2.13}$$

The shear power loss at the shear boundary is

$$\dot{W}_S = \frac{\sigma_0}{\sqrt{3}}\int\limits_{S_1,S_2} |\Delta v|\, dS \tag{2.14}$$

where $\dot{W}_S$ is the shear power loss along the shear boundary, Δv is the velocity difference and dS_1, dS_2 are differential areas of shear surfaces. For calculation of the power consumption on

each surface of velocity discontinuity, the area of discontinuity and the amount of velocity discontinuity must be determined. With attention to Fig. 1

$$\begin{aligned} dS_1 &= \rho_i g(\theta,\rho_i)\sqrt{1+\Big(\frac{b}{\alpha}\Big)^2}\,d\theta \\ |\Delta v_1| &= \Big|v_i\Big(1-\rho_i\frac{\partial g}{\partial r}\frac{1}{1+(b/\alpha)^2}\Big)\sqrt{1+\Big(\frac{b}{\alpha}\Big)}\sin\theta\Big| \end{aligned} \tag{2.15}$$

thus the shear power loss on the shear surface S_1 is obtained as

$$\dot{W}_{S_1} = \frac{\sigma_0}{\sqrt{3}}v_i\rho_i\Big[1+\Big(\frac{b}{\alpha}\Big)^2\Big]\int_0^{\alpha} g(\theta,\rho_i)\Big|1-\rho_i\frac{\partial g}{\partial r}\frac{1}{1+(b/\alpha)^2}\Big|\sin\theta\;d\theta \tag{2.16}$$

also for the shear surface S_2, the differential area and the amount of velocity discontinuity can be obtained respectively by

$$dS_2 = \rho_f d\theta \qquad |\Delta v_2| = |v_f\sin\theta| \tag{2.17}$$

the shear power loss on the shear surface S_2 is obtained as

$$\dot{W}_{S_2} = \frac{\sigma_0}{\sqrt{3}}v_f\rho_f\int_0^{\alpha}\sin\theta\;d\theta \tag{2.18}$$

The friction power loss at the interface of the sheet and the roll in S_3 and its general relation is

$$\begin{aligned} \dot{W}_f &= \frac{m\sigma_0}{\sqrt{3}}\int_{S_3}|\Delta v|\;dS \qquad dS_3 = d\rho \\ \Delta v &= \Big|\dot{U}_r|_{\theta=\alpha}+R\omega\Big| = \Big|-v_i\frac{\rho_i}{\rho}\Big(\cos\alpha+\frac{b}{\alpha}\frac{\rho-\rho_f}{\rho_i-\rho_f}\sin\alpha\Big)+R\omega\Big| \end{aligned} \tag{2.19}$$

where $\dot{W}_f$ is the friction power loss, dS_3 is a differential area of the frictional surface and m is the friction factor after simplification

$$\dot{W}_f = m\frac{\sigma_0}{\sqrt{3}}v_i\rho_i\int_{\rho_f}^{\rho_i}\frac{1}{\rho}\Big|\cos\alpha+\frac{b}{\alpha}\frac{\rho-\rho_f}{\rho_i-\rho_f}\sin\alpha-\frac{R\omega\rho}{v_i\rho_i}\Big|\,d\rho \tag{2.20}$$

In the rolling process, there is only one point along the surface of contact between the roll and the sheet at which the surface velocity of the roll equals to the velocity of the sheet. This point is called the neutral point. Between the inlet shear surface and the neutral point the sheet is moving slower than the roll surface and on the exit side of the neutral point, the sheet moves faster than the roll surface. The position of the neutral point is where the relative velocity is zero, then

$$v_i\frac{\rho_i}{\rho_N}\Big(\cos\alpha+\frac{b}{\alpha}\frac{\rho_N-\rho_f}{\rho_i-\rho_f}\sin\alpha\Big)-R\omega = 0 \tag{2.21}$$

where ρ_N is the radial position of the neutral point on the contact surface.

2.3. Effective flow stress

Since actual metals exhibit strain-hardening behavior and the upper bound method is based on the assumption of perfectly elastic material, amendments must be made to match the theoretical and actual behavior. For a plastic material, the mean flow stress of the material σ_0 is given by

$$\sigma_0 = \frac{1}{\overline{\varepsilon}} \int_0^{\overline{\varepsilon}} \overline{\sigma}\, d\overline{\varepsilon} \qquad \overline{\varepsilon} = \frac{2}{\sqrt{3}} \ln \frac{t_i}{t_f} \tag{2.22}$$

In this paper, a modified upper bound method is used and behavior of the material is considered as

$$\overline{\sigma} = K(\overline{\varepsilon})^n \tag{2.23}$$

where K is the strength coefficient, n is the strain-hardening exponent, $\overline{\sigma}$ is the effective flow stress and $\overline{\varepsilon}$ is effective strain. Inserting Eqs. (2.23) into Eq. (2.22), the mean flow stress of the material is given by

$$\sigma_0 = \frac{1}{n+1} K \Big(\frac{2}{\sqrt{3}} \ln \frac{t_i}{t_f} \Big)^n \tag{2.24}$$

According to Fig. 1, in all three zones each particle of the material undergoes different strains. The material in zone I has no strain-hardening, at the inlet shear boundary it has a strain due to discontinuity of velocity, in zone II the material undergoes strain due to deformation, after it, at the outlet shear boundary the material undergoes strain due to discontinuity of velocity and, finally, it exits from zone III with no deformation. By integrating the incremental strain along a stream line, the equivalent strain in the product is calculated. It has an angle of inclination θ to the axis in the deformation zone. At the shear surface, the engineering shear strain γ_S is

$$\gamma_S = \frac{|\Delta v|}{\dot{U}_r} \tag{2.25}$$

and the effective strain on the shear boundary is

$$\overline{\varepsilon}_S = \frac{1}{\sqrt{3}} \gamma_S \tag{2.26}$$

At the inlet and outlet shear boundaries, the effective strains are, respectively

$$\begin{aligned} \overline{\varepsilon}_{S_1} &= \frac{1}{\sqrt{3}} \gamma_{S_1} = \frac{1}{\sqrt{3}} \frac{\left| \Big(1 - \rho_i \frac{\partial g}{\partial r} \frac{1}{1+(b/\alpha)^2} \Big) \sqrt{1 + \Big(\frac{b}{\alpha} \Big)^2} \sin\theta \right|}{\cos\theta + \frac{1}{g} \frac{\partial g}{\partial \theta} \sin\theta} \\ \overline{\varepsilon}_{S_2} &= \frac{1}{\sqrt{3}} \gamma_{S_2} = \frac{1}{\sqrt{3}} \tan\theta \end{aligned} \tag{2.27}$$

In the deformation zone, the effective strain is expressed by

$$\overline{\varepsilon}_d = \int_{r_f}^{r_i} d\overline{\varepsilon} = \int_{r_f}^{r_i} \frac{d\overline{\varepsilon}}{dt} \frac{dt}{dL}\, dL \tag{2.28}$$

where

$$\frac{d\overline{\varepsilon}}{dt} = \dot{\overline{\varepsilon}} = \sqrt{\frac{2}{3}(\dot{\varepsilon}_{rr}^2 + \dot{\varepsilon}_{\theta\theta}^2 + 2\dot{\varepsilon}_{r\theta}^2)} = \frac{2}{\sqrt{3}} \sqrt{\dot{\varepsilon}_{rr}^2 + \dot{\varepsilon}_{r\theta}^2} \qquad \frac{dt}{dL} = \frac{1}{\sqrt{\dot{U}_r^2 + \dot{U}_\theta^2}} \tag{2.29}$$

where

$$dL = dr\sqrt{1 + r^2\Big(\frac{d\theta}{dr}\Big)^2} \tag{2.30}$$

then

$$\overline{\varepsilon}_d = \frac{2}{\sqrt{3}}\int\limits_{r_f}^{r_i}\sqrt{\frac{\dot{\varepsilon}_{rr}^2 + \dot{\varepsilon}_{r\theta}^2}{\dot{U}_r^2 + \dot{U}_\theta^2}\Big[1 + r^2\Big(\frac{d\theta}{dr}\Big)^2\Big]}\,dr \tag{2.31}$$

Along the stream line, the equivalent strain in the deformed material is

$$\overline{\varepsilon}(\theta) = \overline{\varepsilon}_{S_1}(\theta) + \overline{\varepsilon}_d(\theta) + \overline{\varepsilon}_{S_2}(\theta) \tag{2.32}$$

After obtaining the total strain from Eq. (2.32) and substituting in the power law, one can rewrite the power terms in order to modify the upper bound method with considering the strain-hardening. So the internal power, shear loss powers on S_1 and S_2 surfaces and the frictional power, respectively, are

$$\begin{aligned}
\dot{W}_i &= \int\limits_V \overline{\sigma\dot{\varepsilon}}\,dV = \frac{2}{\sqrt{3}}\int\limits_V K(\overline{\varepsilon})^n\sqrt{\frac{1}{2}\dot{\varepsilon}_{ij}\dot{\varepsilon}_{ij}}\,dV \\
\dot{W}_S &= \int\limits_{S_v}\tau|\Delta v|\,dS = \frac{1}{\sqrt{3}}\int\limits_V K(\overline{\varepsilon})^n|\Delta v|\,dS \\
\dot{W}_f &= \int\limits_{S_f}\tau|\Delta v|\,dS = \frac{m}{\sqrt{3}}\int\limits_V K(\overline{\varepsilon})^n|\Delta v|\,dS
\end{aligned} \tag{2.33}$$

2.4. The required rolling torque

By make use of the upper bound method, the externally supplied power is less than or equal to the sum of the powers described in the previous Sections. The total power J^* is

$$J^* = \dot{W}_i + \dot{W}_{S_1} + \dot{W}_{S_2} + \dot{W}_f \tag{2.34}$$

The rolling torque T is given by

$$T = \frac{J^*}{\omega} \tag{2.35}$$

where T is the required rolling torque per unit width of the sheet. The rolling torque is a function of b (shape factor) and ρ_N (position of the neutral point). The shape factor b determines the inlet shear boundary shape. The minimum value of rolling torque with respect to b is the required torque for the rolling process in the upper bound analysis. Integrals appearing in the above equations do not have analytical solutions and they have been solved numerically with MATLAB software.

3. Internal defects prediction criteria

The external torque is a function of several parameters including roll radius, area reduction, friction factor and shape factor b. In the upper bound analysis, the minimum value of the external power with respect to b is the required power for the rolling process. According to the

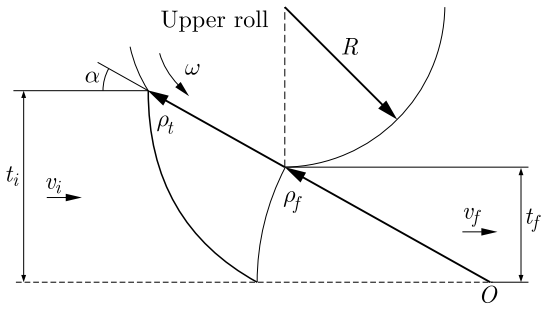

Fig. 2. Geometrical condition to initiate the internal defect

geometrical condition, for the critical value of shape factor b (b_{cr}), the inlet shear boundary intersects the outlet shear boundary in the centerline, see Fig. 2.

In this study, it can be taken that

$$r_i(\theta = 0, \rho_i) = r_f(\theta = 0, \rho_f) \tag{3.1}$$

thus

$$\rho_i \exp(-b) = \rho_f \tag{3.2}$$

so, the critical value of b can be obtained as

$$b_{cr} = \ln \frac{\rho_i}{\rho_f} = \ln \frac{t_i}{t_f} \tag{3.3}$$

So, if the shape parameter obtained from the optimization of the external power is equal or greater than the b_{cr}, the internal defects initiate.

4. Results and discussion

The flat rolling process has been analyzed using the proposed approach. In order to obtain numerical boundaries that can be applied to the prediction and prevention of the occurrence of internal defects in industry, finite element simulations using the proposed approach have been carried out for many combinations of reduction in the area and relative thickness. This means that no internal defects occur under this combination of process parameters. FEM simulations are conducted on the available commercial explicit/FEM software, ABAQUS, to verify the analytical model and study the effects of the upper bound method assumptions on the obtained results. Due to symmetry of the process, finite element meshes are generated on the upper half cross section of the sheet. The sheet is meshed by 2D plane strain, linear, four-noded CPE4R elements. The sheet model contains 460 elements. In this model, the rolls are modeled as rigid bodies. The rolls are rotated by a constant angular velocity about their axes. For verification of the theoretical study, the results of rolling torque are extracted from FEM simulations. In order to verify the validity of the upper bound approach for the flat rolling process presented in the previous Sections, the results obtained from the theoretical model are compared with the available experimental of data of Martins and Barata (1999) as well as with the results of finite element simulations. The calculation has been carried out under various rolling conditions and geometrical data utilized in the rolling analysis summarized in Table 1. During theoretical analysis and numerical simulations, m is set at 0.3 for the contact surface between the roll and sheet, radius of the rolls is $R = 79.375$ mm, and the flow stress for aluminum at room temperature is $\overline{\sigma} = 50.3(1 + \overline{\varepsilon}/0.05)^{0.26}$ MPa. The comparisons between the computed results,

Table 1. Geometrical data used for computations (Martins and Barata, 1999)

Case	$2t_0$ [mm]	$2t_f$ [mm]	Reduction [%]
1	6.274	5.385	14.17
2	6.274	4.902	21.86
3	6.274	4.445	29.40
4	6.274	4.115	34.41

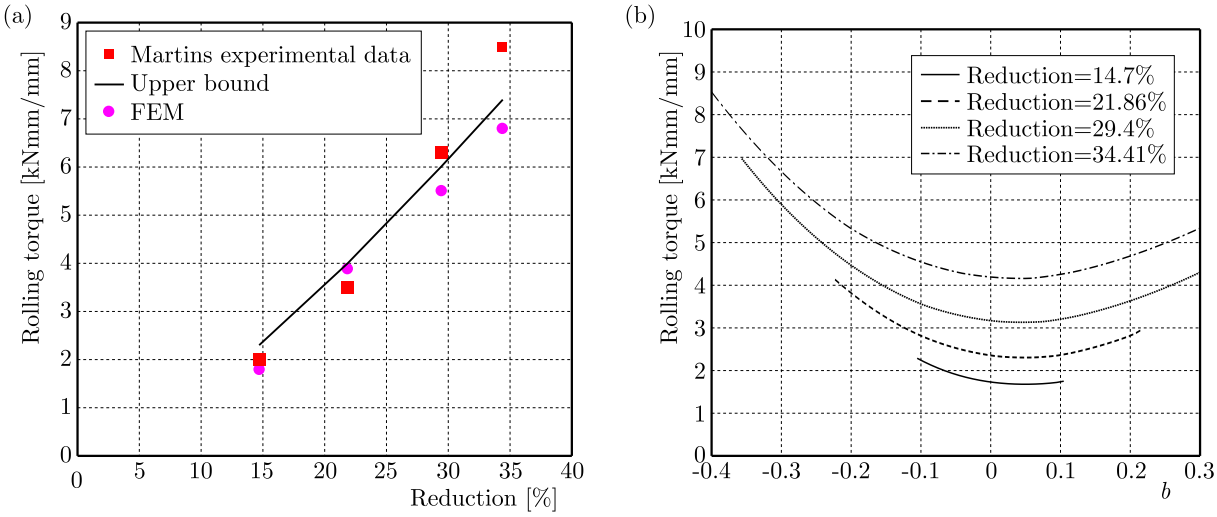

Fig. 3. (a) Comparison of analytical, FEM and Martins experimental data (Martins and Barata, 1999) of rolling torque (per unit of width) as a function of the percentage of reduction. (b) Variation of rolling torque per unit width versus parameter b

FEM simulation and the experimental values of Martins and Barata (1999) for the rolling torque as a function of the rolling reduction are shown in Fig. 3a. It is observed that the proposed velocity field leads to a computationally efficient procedure which gives a good agreement with the experimental data. From Fig. 3a, it can be seen that the calculated torques are basically in agreement with the measured ones. As expected, the predicted rolling torques are always greater than the experimental and FEM results, because the present theoretical values are the upper bound solutions. The reason for such discrepancies may be attributed to the assumption of rigid rolls as well as to difficulties in the modeling of friction in the contact surface between the rolls and the deforming sheet. It can be checked from Fig. 3a that the rolling torque increases with an increase in reduction. Figure 3b shows variation of the rolling load versus the shape parameter b for several reductions of the area according to Table 1. The internal defects criterion is achieved after obtaining the shape parameter from both geometrical and analytical conditions and by comparing them. In Fig. 4, the velocity components obtained from the upper bound solution are compared with the FEM simulation results in $\theta = \alpha/2$ in the deformation zone. The results show a good agreement between the upper bound data and the FEM results. It can be seen that the peripheral velocity components are very small with respect to the radial velocity components. To compare the numerical results with the experimental results of Ghos and Gardiner (2004), the analysis performed on Aluminum 6061-T6 whose mechanical and physical properties are shown in Table 2.

The flow stress for aluminum at room temperature is $\overline{\sigma} = 410(\overline{\varepsilon})^{0.05}$ MPa (Turczyn, 1996). The initial thickness is $t_i = 10$ mm, roll radius $R = 100$ mm, angular velocity $\omega = 0.167\,\mathrm{s}^{-1}$ and friction factor $m = 0.3$. Figure 5 shows the conditions of area reduction and relative thickness for preventing internal defects in Aluminum 6061-T6 for both conditions of strain-hardening

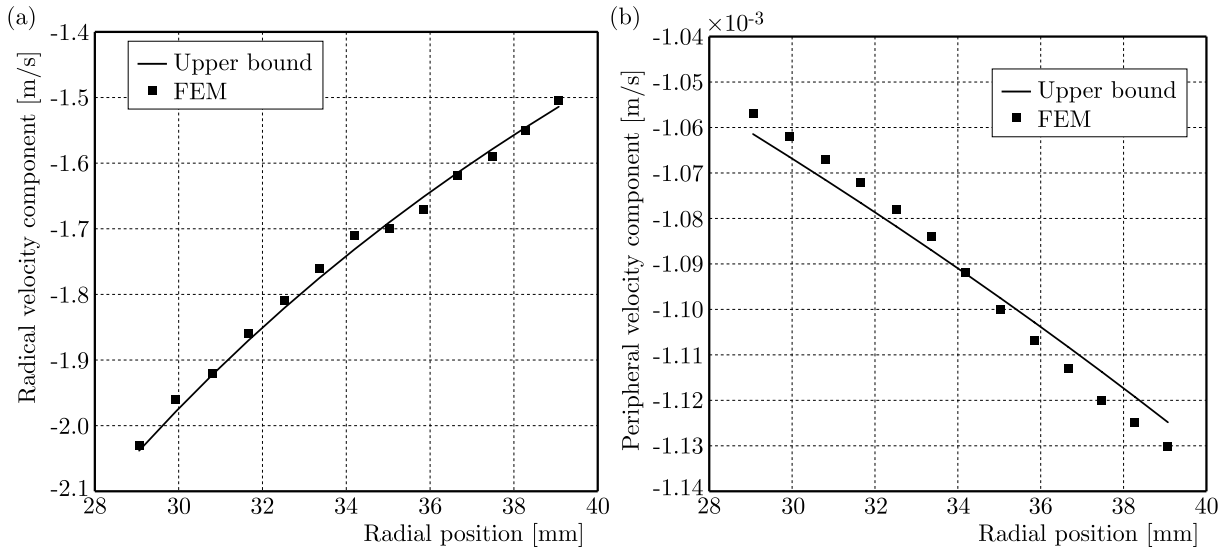

Fig. 4. Comparison of the upper bound and FEM of velocity components (a) radial and (b) peripheral velocity components for 30% reduction in the area

Table 2. Mechanical properties of Aluminum 6061-T6 (Turczyn, 1996)

Young's modulus [GPa]	Poisson's ratio (ν)	Yield stress [MPa]	Density [kg/m^3]	Strength coefficient [MPa]	Strain--hardening exponent
68.9	0.33	276	2700	410	0.05

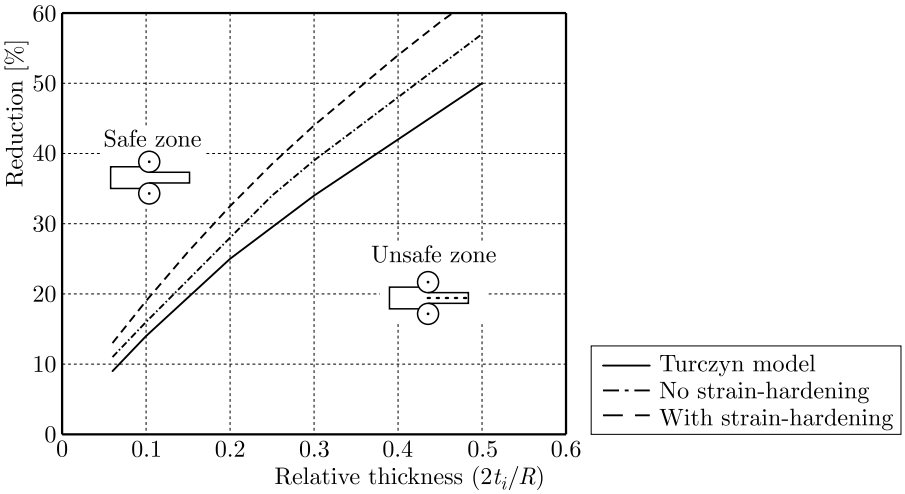

Fig. 5. Comparison of safe and unsafe zones predicted by the present model and the model by Turczyn (1996)

and perfectly plastic materials. Also, these results are compared with the experimental data by Turczyn (1996). It is observed that the safe domain is decreased by including the strain-hardening behavior of the material in the analysis.

Figure 6a shows the velocity field in the flat rolling process with relative thickness $2t_i/R = 0.2$ and 40% reduction in area. The velocity field shows that in this case the internal defects do not occurr. In another model, see Fig. 6b, the reduction of the area is changed to 20% and the relative thickness is $2t_i/R = 0.4$, so that it locates in the unsafe zone. Also, Fig. 6b shows that the internal defects occurr.

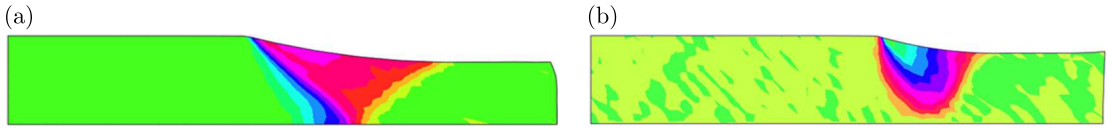

Fig. 6. Deformation zone, (a) for $2t_i/R = 0.2$ and 40% reduction in the area, (b) for $2t_i/R = 0.4$ and 20% reduction in the area

Figure 8 shows the effect of friction factor on internal defects initiation situations for Aluminum 6061-T6. It can be seen that with an increase in the friction factor, the safe zone size decreases. The effect of the strain-hardening exponent on the inlet shear boundary is shown in Fig. 8. From this figure, it can be noticed that with an increase in the strain-hardening exponent, the intersection point of the inlet shear boundary with the axis of symmetry moves towards the outside of the rolls, and the tendency of central bursting defects is decreased. Also, the criterion applied for different strain-hardening exponents is illustrated in Fig. 9a. This figure shows that with an increase in the strain-hardening exponent value, the safe domain increases. Figure 9b shows the effect of strain-hardening exponent on the rolling torque for the upper bound approach and the FEM. This figure illustrates that by increasing the strain-hardening exponent, the rolling torque decreases. Figure 9b also shows that the theoretically predicted rolling torque is higher than that from the FEM results, which is due to the nature of the upper bound theory.

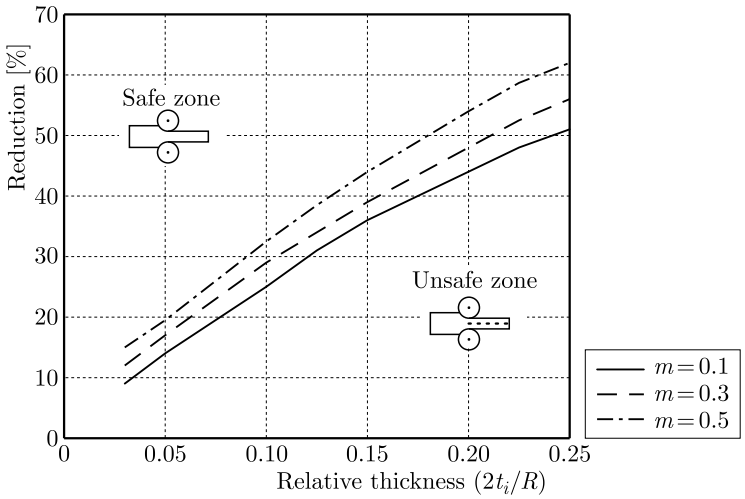

Fig. 7. Effect of the friction factor on size of the safe and unsafe zones

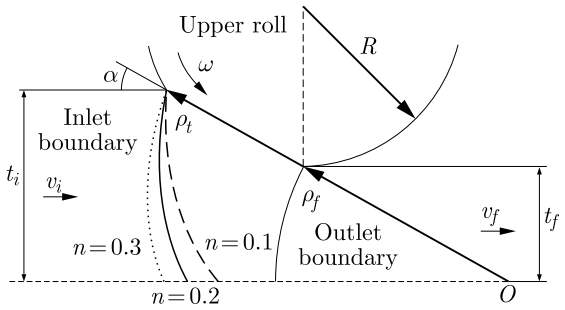

Fig. 8. Effect of the strain-hardening exponent on the inlet shear boundary

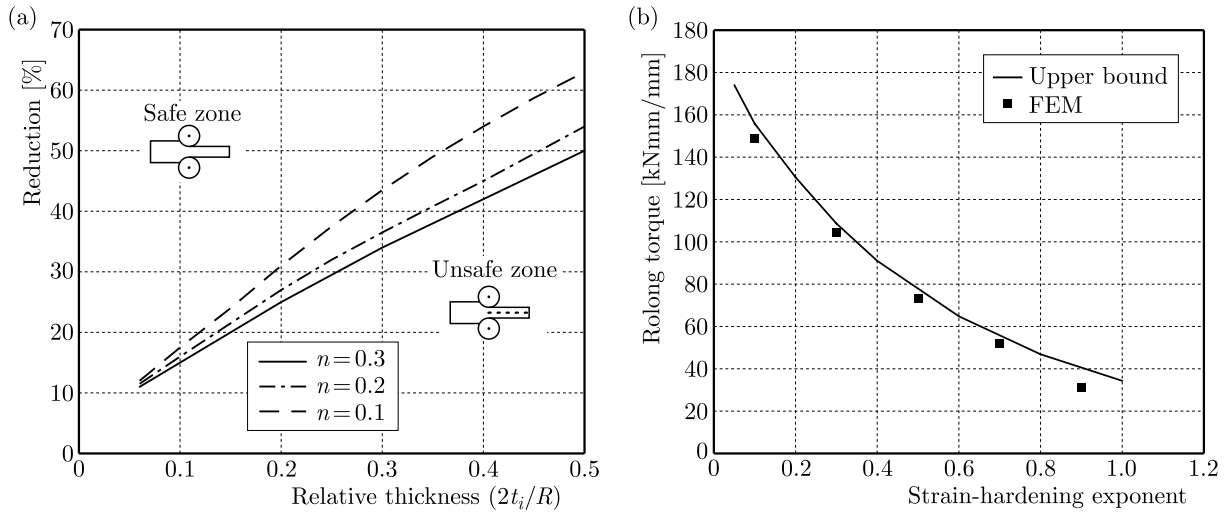

Fig. 9. Effect of the strain-hardening exponent (a) on size of the safe and unsafe zones and (b) on the rolling torque for 30% reduction in the area

5. Conclusions

In this paper, an analytical approach based on the upper bound method, is presented for prediction of rolling torque and occurrence of internal defects in the flat rolling process. The advantages of the presented criterion are the generality of the proposed inlet shear boundary and a new kinematically admissible velocity field. In addition, the presented criterion predicts central bursting defects in simpler mathematical equations than in other criteria, and the effect of the strain hardening exponent of the sheet material on the rolling torque and prediction of internal defects are investigated. It has been concluded that internal defects are affected primarily by the strain-hardening exponent. By increasing the strain-hardening exponent, the rolling torque and the possibility of internal defects decreases. By increasing the strain-hardening exponent, the safe zone size is increased and the internal defects occur in thick sheets with a small reduction. Criteria curves for the safe domains are presented for a wide range of process variables. By using these criteria in the rolling practice, it has become possible to predict necessary rolling conditions in order to avoid internal defects.

References

1. Avitzur B., Van Tyne C., Turczyn S., 1988, The prevention of central bursts during rolling, *Journal of Engineering for Industry*, 110-173

2. Caoa T., Bobadillab C., Montmitonneta P., Bouchard P., 2015, A comparative study of three ductile damage approaches for fracture prediction in cold forming processes, *Journal of Materials Processing Technology*, **216**, 385-404

3. Deng W., Zhao D., Qin X., Du L., Gao X., Wang G., 2009, Simulation of central crack closing behavior during ultra-heavy plate rolling, *Computational Materials Science*, **47**, 439-447

4. Dogruoglu A., 2001, On constructing kinematically admissible velocity fields in cold sheet rolling, *Journal of Materials Processing Technology*, **110**, 287-299

5. Dyja H., Pietrzyk M., 1983, On the theory of the process of hot rolling of bimetal plate and sheet, *International Journal of Mechanical Working Technology*, **8**, 309-325

6. Ghosh S., Li M., Gardiner D., 2004, A computational and experimental study of cold rolling of aluminum alloys with edge cracking, *Transactions of the ASME*, **126**, 74-82

7. Haghighat H., Amjadian P., 2013, A generalized upper bound solution for extrusion of bimetallic rectangular cross-section bars through dies of any shape, *Journal of Theoretical and Applied Mechanics*, **51**, 105-116
8. Haghighat H., Parghazeh A., 2017, An investigation into the effect of strain hardening on the central bursting defects in rod extrusion process, *The International Journal of Advanced Manufacturing Technology*, accepted for publication
9. Haghighat H., Saadati P., 2015, An upper bound analysis rolling process of non-bonded sandwich sheets, *Transaction of Nonferrous Metals Society of China*, **25**, 1605-1613
10. Martins P., Barata M., 1999, Upper bound analysis of plane strain rolling using a flow function and the weighted residuals method, *International Journal for Numerical Methods in Engineering*, **44**, 1671-1683
11. Misicko R., Kvackaj T., Vlado M., Gulova L., Luptak M., Bidulska J., 2009, Defects simulation of rolling strips, *Materials Engineering*, **16**, 7-12
12. Prakash R., Dixit P., 1995, Steady state plane strain cold rolling of a strain-hardening material, *Journal of Materials Processing Technology*, **52**, 338-358
13. Rajak S., Reddy N., 2005, Prediction of internal defects in plane strain rolling, *Journal of Materials Processing Technology*, **159**, 409-417
14. Serajzadeh S., Mahmoodkhani Y., 2008, A combined upper bound and finite element model for prediction of velocity and temperature fields during hot rolling process, *International Journal of Mechanical Sciences*, **50**, 1423-1431
15. Takuda H., Kyoto H., Lippmann H., Kokado J., 1989, Upper bound approach to plane strain strip rolling with free deformation zones, *Ingenieur-Archiv*, **59**, 274-284
16. Turczyn S., 1996, The effect of the roll-gap shape factor on internal defects in rolling, *Journal of Materials Processing Technology*, **60**, 275-282
17. Turczyn S., Pietrzyk M., 1992, The effect of deformation zone geometry on internal defects arising in plane strain rolling, *Journal of Materials Processing Technology*, **32**, 509-518

Manuscript received March 21, 2017; accepted for print June 24, 2017

JOURNAL OF THEORETICAL AND APPLIED MECHANICS
55, 4, pp. 1355-1368, Warsaw 2017
DOI: 10.15632/jtam-pl.55.4.1355

FINITE ELEMENT ANALYSIS OF A SUPERELASTIC SHAPE MEMORY ALLOY CONSIDERING THE EFFECT OF PLASTICITY

Xiangjun Jiang

Xidian University, Key Laboratory of Electronic Equipment Structural Design, Xi'an, China

State Key Laboratory of Structural Analysis for Industrial Equipment, Dalian University of Technology, Dalian, China

State Key Laboratory for Manufacturing Systems Engineering, Xi'an Jiaotong University, Xi'an, China

Baotong Li

Xi'an Jiaotong University, State Key Laboratory for Manufacturing System, Xi'an, China

e-mail: baotong.me@mail.xjtu.edu.cn (corresponding author)

In the present study, a shape memory alloy (SMA) phenomenological constitutive model is proposed that is capable of describing SMA superelastic behavior and the plasticity effect. The phase transformation constitutive model, by using strain and temperature as control variables to judge the phase transformation points in order to avoid the complexity of transformation correction, incorporates plasticity described by the von Mises isotropic hardening model. Further, the proposed model is implemented into the finite element package ANSYS by the user subroutine USERMAT. The results produced by the proposed model of simulated superelastic and plasticity behavior are compared with experimental data taken from the literature.

Keywords: SMAs, superelasticity, plasticity, constitutive law, finite element analysis

1. Introduction

SMA is a kind of functional material which has the function of sensing and driving. It has been applied to many fields because of its shape memory, super elasticity and so on. Until recently, there are very few constitutive models suitable to consider both of stress-induced martensite transformation and plastic deformation of martensite. McKelvey and Ritchie (2001) found that plastic strain of the stress-induced martensite phase occurred if the applied stress was high enough. Lazghab (2001) carried out a theoretical study to SMAs with plastic deformation of martensite, although it was not available to implement into a commercial finite element software. Yan *et al.* (2003) developed a constitutive model to quantify the effect of plasticity on the reverse transformation and examined the influence of hydrostatic stress on the transformation. Bo and Lagoudas (1999) proposed several constitutive models considering the evolution of plastic strain under cyclic thermal induced transformation cycles with micromechanical analyses by a representative volume element. However, those models cannot be utilized to analyze the combination of super-elastic and plastic behavior due to their limitations in the description of martensite plasticity.

Some works have been carried out to implement the super-elastic constitutive model into the finite element model (Auricchio and Taylor, 1997). The super-elastic constitutive model proposed by Auricchio and Taylor (1997) has been successfully implemented into finite element codes such as ABAQUS and ANSYS. However, that model cannot describe plasticity of the martensite. In a more recent work, Kan *et al.* (2010) and Yan *et al.* (2003) developed a temperature-dependent three-dimensional phenomenological constitutive model considering the local plastic yield of martensite under a high stress, and successfully implemented into the finite

element package ABAQUS. Moreover, the nonlinear problem was solved within a framework of the updated Lagrangian formulation using a return mapping algorithm (Lagoudas *et al.*, 1996; Cisse *et al.*, 2016) to update the stress value according to the current strain. However, the phase transformation starting conditions in that model using the phase diagram (σ, T) to determine the SMA phase state (Bouvet *et al.*, 2004; Saint *et al.*, 2009) is complex and not suitable for identifying.

In the present work, a modified constitutive model having temperature and the strain tensor as control variables, is developed. It analyzes thermomechanical behavior of 3D SMA structures with a feature of combination of superelasticity and plasticity, which is particularly suitable for finite element implementation. Moreover, the finite element analysis of a SMA structure considers nonlinearities associated with phase transformation and plasticity. The modified constitutive model is particularly suitable for identifying the starting conditions of phase transformation and plasticity, and for finite element implementation. However, some other phenomena observed in SMAs including re-orientation of the martensite phase and a non-linear transformation hardening function are not taken into account in the construction of the constitutive model.

2. Constitutive model

2.1. Thermodynamic state equation and internal variable

The constitutive model in this work will be constructed under the generalized plasticity theory. Lubliner and Auricchio applied this theory to study SMAs, and proposed a three-dimensional thermo-dynamic constitutive model which can be used to simulate the effect of super elasticity and shape memory effect of SMA (Lubliner and Auricchio, 1996). The following is a brief description of the generalized plastic theory.

On the infinitesimal strain assumption, the additively decomposition of the total strain $\boldsymbol{\varepsilon}$ into an elastic strain $\boldsymbol{\varepsilon}_e$ and an inelastic strain $\boldsymbol{\varepsilon}_{in}$ yields

$$\boldsymbol{\varepsilon} = \boldsymbol{\varepsilon}_e + \boldsymbol{\varepsilon}_{in} \tag{2.1}$$

It is assumed that the Helmholtz free energy can also be additively contributed to elastic and inelastic parts as follows

$$\boldsymbol{\psi} = \boldsymbol{\psi}_e(\boldsymbol{\varepsilon} - \boldsymbol{\varepsilon}^{in}, \xi, T) + \boldsymbol{\psi}_{in}(\xi, \eta, T) \tag{2.2}$$

in which ξ and η depict phase transformation and plastic yield behavior, respectively.

The elastic free energy $\boldsymbol{\psi}_e$ is different from that of the classical elastic, plastic or visco-elastic theory, which is related to the internal variable ξ, and is shown as follows

$$\boldsymbol{\psi}_e = \frac{1}{2}(\boldsymbol{\varepsilon} - \boldsymbol{\varepsilon}^{in}) : \mathbf{D}(\xi) : (\boldsymbol{\varepsilon} - \boldsymbol{\varepsilon}^{in}) \tag{2.3}$$

in which $\mathbf{D}(\xi)$ is the elastic stiffness matrix.

The stress can be derived from the thermodynamic state equation

$$\boldsymbol{\sigma} = \frac{\partial \boldsymbol{\psi}_e}{\partial \boldsymbol{\varepsilon}^e} = \mathbf{D}(\xi) : (\boldsymbol{\varepsilon} - \boldsymbol{\varepsilon}^{in}) \tag{2.4}$$

The above process can be directly extended into construction of the constitutive model of the SMA.

2.2. Main equations of the constitutive model

Based on the assumption of small deformation, the total inelastic strain $\boldsymbol{\varepsilon}_{in}$ can be divided into two parts: stress-induced martensitic transformation $\boldsymbol{\varepsilon}_t$ and irreversible plastic strain $\boldsymbol{\varepsilon}_p$, in which $\boldsymbol{\varepsilon}_p$ includes austenite plastic strain $\boldsymbol{\varepsilon}_p^A$ in a high temperature and martensite plastic strain $\boldsymbol{\varepsilon}_p^M$ under a high stress. As a result, the total strain is

$$\boldsymbol{\varepsilon} = \boldsymbol{\varepsilon}_e + \boldsymbol{\varepsilon}_{in} = \boldsymbol{\varepsilon}_e + \boldsymbol{\varepsilon}_t + \boldsymbol{\varepsilon}_p \tag{2.5}$$

in which $\boldsymbol{\varepsilon}_p = \boldsymbol{\varepsilon}_p^A + \boldsymbol{\varepsilon}_p^M$.

After discretizing the equations, the expressions are as follows

$$\Delta\boldsymbol{\varepsilon}_{in} = \Delta\boldsymbol{\varepsilon}_t + \Delta\boldsymbol{\varepsilon}_p \qquad \Delta\boldsymbol{\varepsilon}_p = \Delta\boldsymbol{\varepsilon}_{Ap} + \Delta\boldsymbol{\varepsilon}_{Mp} \qquad \Delta\boldsymbol{\varepsilon}_e = \Delta\boldsymbol{\varepsilon} - \Delta\boldsymbol{\varepsilon}_t - \Delta\boldsymbol{\varepsilon}_p \tag{2.6}$$

For the super-elastic NiTi alloy, the stress-induced martensitic transformation and its reverse transformation can be expressed by the volume fraction of martensite, which can be defined by the internal variable ξ, so the elastic stress-strain relation can be expressed as

$$\boldsymbol{\sigma} = \boldsymbol{\sigma}^* - \mathbf{D}^e(\xi) : \Delta\boldsymbol{\varepsilon}_{in} \tag{2.7}$$

in which $\boldsymbol{\sigma}^* = \mathbf{D}^e(\xi) : \Delta\boldsymbol{\varepsilon}$ is the trial stress, and $\mathbf{D}^e(\xi)$ is the equivalent elastic tensor. It can be changed with a change of the phase transformation, which is different than in general metal materials, from the initial austenite to the final martensite.

The simple form for the equivalent elastic tensor as $\mathbf{D} = \mathbf{D}_A = \mathbf{D}_M$ has been used in some researches because of its close proximity to the real elastic modulus of austenite and martensite (Tanaka, 1986; Liang and Rogers, 1990). In this paper, a scheme describing the equivalent elastic tensor is proposed to simplify the calculation as

$$\mathbf{D}^e(\xi) = \frac{1}{2}(\mathbf{D}_A + \mathbf{D}_M) \tag{2.8}$$

in which $\mathbf{D}_A$ and $\mathbf{D}_M$ are the elastic tensors of austenite and martensite, respectively. The experiment demonstrated that the effect of the difference between the elastic modulus of austenite and martensite could be ignored.

Metal materials are generally irrecoverably plastic. Their characteristics are independent of hydrostatic pressure. Therefore, the plastic yield surface can only consider the stress tensor. Considering the deviatoric stress of the above equation, we get $\mathbf{D}^e : \Delta\boldsymbol{\varepsilon}_{in} = 2G\Delta\boldsymbol{\varepsilon}_{in}$, and

$$\mathbf{s} = \mathbf{s}^* - 2G\Delta\boldsymbol{\varepsilon}_{in} \tag{2.9}$$

in which $\mathbf{s}^*$ is the deviatoric stress of $\boldsymbol{\sigma}^*$, $G = E/(1+\nu)$ is the shear elastic modulus in which ν is the Poisson ratio, and E is the equivalent elastic modulus expressed as $E = (E_A + E_M)/2$. Therefore, the shear elastic modulus G is independent of the volume fraction of martensite.

2.3. Evolution rule of phase transformation strain

The isotropic behavior of metal materials can be described by the von Mises yield surface. The expression of the yield behavior is as follows

$$F(\boldsymbol{\sigma}, q) = \sigma_{eq} - \sigma_y(q) = 0 \tag{2.10}$$

in which $\sigma_{eq} = [\frac{3}{2}\mathbf{s} : \mathbf{s}]^{1/2}$ is the von Mises equivalent stress, σ_y is the monotonic tensile plastic yield stress of the metal material, q is the cumulative plastic strain.

Similarly to the plastic yield surface of a metal material, the phase transformation function to describe the forward transformation and the reverse transformation are introduced as follows:

— forward phase transformation

$$F_{AM}(\boldsymbol{\sigma},\xi)=\sigma_{eq}-\sigma_{s,T}^{AM}(\xi)=0 \tag{2.11}$$

— reverse phase transformation

$$F_{MA}(\boldsymbol{\sigma},\xi)=\sigma_{eq}-\sigma_{s,T}^{MA}(\xi)=0 \tag{2.12}$$

where $\sigma_{s,T}^{AM}=\sigma_{s_0,T}^{AM}+h_{AM}\varepsilon_L\xi$ and $\sigma_{s,T}^{MA}=\sigma_{s_0,T}^{MA}+h_{MA}\varepsilon_L\xi$ are the initial stresses of the forward phase transformation and the reverse phase transformation, respectively. $\sigma_{s_0,T}^{AM}$ and $\sigma_{s_0,T}^{MA}$ are the initial stress of the forward phase transformation and the reverse phase transformation, respectively. h_{AM} and h_{MA} are the hardening modulus of the martensitic transformation and the reverse transformation, respectively.

In this paper, the volume fraction of martensite is

$$\xi=\frac{\overline{\varepsilon}_t}{\varepsilon_L} \tag{2.13}$$

in which ε_L is the maximum phase transformation strain under uniaxial tension, which can be determined by experimental results under monotonic loading and unloading. $\overline{\varepsilon}_t=[\frac{2}{3}\boldsymbol{\varepsilon}_t:\boldsymbol{\varepsilon}_t]^{1/2}$ is the equivalent phase transformation strain. When the phase transformation does not occur, the equivalent transformation strain is zero. This means that the volume fraction of martensite is $\xi=0$. With an increase in the equivalent transformation strain, the martensite volume fraction increases linearly and eventually the maximum value $\xi=1$ is achieved.

Equation (2.13) shows that the phase transformation strain is proportional to the volume fraction of martensite. As a result, the phase transformation strain rate can be given in the form similar to the plastic theory:

— forward phase transformation

$$\dot{\boldsymbol{\varepsilon}}_t=\dot{\boldsymbol{\varepsilon}}_t^{AM}=\dot{\lambda}_{AM}\frac{\partial F_{AM}(\boldsymbol{\sigma},\xi)}{\partial\boldsymbol{\sigma}}=\sqrt{\frac{3}{2}}\varepsilon_L\dot{\xi}\mathbf{n}_{AM}\qquad\dot{\xi}>0 \tag{2.14}$$

— reverse martensitic transformation

$$\dot{\boldsymbol{\varepsilon}}_t=\dot{\boldsymbol{\varepsilon}}_t^{MA}=\dot{\lambda}_{MA}\frac{\partial F_{MA}(\boldsymbol{\sigma},\xi)}{\partial\boldsymbol{\sigma}}=\sqrt{\frac{3}{2}}\varepsilon_L\dot{\xi}\mathbf{n}_{MA}\qquad\dot{\xi}<0 \tag{2.15}$$

λ_{AM} and λ_{MA} are the transformation multipliers of the martensitic transformation and the reverse transformation, respectively (similar to the plastic multiplier in the plastic theory). $\mathbf{n}_{AM}$ and $\mathbf{n}_{MA}$ are the direction vectors of the forward and reverse phase transformation, respectively

$$\mathbf{n}_{AM}=\frac{\partial F_{AM}(\boldsymbol{\sigma},\xi)}{\partial\boldsymbol{\sigma}}=\sqrt{\frac{3}{2}}\frac{\mathbf{s}}{\sigma_{eq}}\qquad\mathbf{n}_{MA}=\frac{\partial F_{MA}(\boldsymbol{\sigma},\xi)}{\partial\boldsymbol{\sigma}}=\sqrt{\frac{3}{2}}\frac{\mathbf{s}}{\sigma_{eq}} \tag{2.16}$$

In this paper, the phase transformation, austenite and martensite yield behavior under different temperature are considered in the process of implicit solution of the stress integral. In general, the plastic strain produced during the phase transformation ratcheting under cyclic loadings should not be ignored regarding the experiments by Kang *et al.* (2009). However, it is assumed that there is no interaction between them in a single cycle of loading and unloading. The stress-induced martensitic transformation and the plastic behavior of austenite and martensite are independent of each other. The plastic behavior is not considered in the course of implicit stress integration of the phase transformation in our research. The isotropic elastic-plastic constitutive model with the implicit stress integration method is extended to that method of the constitutive modeling of SMA. The transformation strain increment and the plastic strain

increment are calculated by the backward Euler difference method respectively, and the transformation strain and the plastic strain are updated further.

According to the above assumptions, Eq. (2.9) can be further expressed as follows for the implicit stress integration process of the phase change behavior

$$\mathbf{s} = \mathbf{s}^* - 2G\Delta\boldsymbol{\varepsilon}_t \tag{2.17}$$

By Eqs. (2.16), it can be obtained:
— forward phase transformation

$$\Delta\boldsymbol{\varepsilon}_t^{AM} = \sqrt{\frac{3}{2}}\varepsilon_L \Delta\xi \mathbf{n}_{AM} \qquad \Delta\xi > 0 \tag{2.18}$$

— reverse phase transformation

$$\Delta\boldsymbol{\varepsilon}_t^{MA} = \sqrt{\frac{3}{2}}\varepsilon_L \Delta\xi \mathbf{n}_{MA} \qquad \Delta\xi < 0 \tag{2.19}$$

in which

$$\mathbf{n}_{AM} = \mathbf{n}_{MA} = \mathbf{n}_t = \sqrt{\frac{3}{2}}\frac{\mathbf{s}}{\sigma_{eq}} \tag{2.20}$$

Substituting Eqs. (2.18) and (2.19) into Eq. (2.17), we obtain

$$\mathbf{s} = \mathbf{s}^* - 3G\varepsilon_L \Delta\xi \frac{\mathbf{s}}{\sigma_{eq}} \tag{2.21}$$

It is further converted to

$$\mathbf{s}\Big(1 + 3G\frac{\varepsilon_L \Delta\xi}{\sigma_{eq}}\Big) = \mathbf{s}^* \tag{2.22}$$

If we take the contracted tensor product of each side of this with itself, we obtain

$$\Big(1 + 3G\frac{\varepsilon_L \Delta\xi}{\sigma_{eq}}\Big)^2 \mathbf{s} : \mathbf{s} = \mathbf{s}^* : \mathbf{s}^* \tag{2.23}$$

Defining $\sigma_{eq}^* = [\frac{3}{2}\mathbf{s}^* : \mathbf{s}^*]^{1/2}$ as the equivalent stress, Eq. (2.23) can be further transformed into

$$\Big(1 + 3G\frac{\varepsilon_L \Delta\xi}{\sigma_{eq}}\Big)\sigma_{eq} = \sigma_{eq}^* \qquad \text{or} \qquad \sigma_{eq} + 3G\varepsilon_L \Delta\xi = \sigma_{eq}^* \tag{2.24}$$

This is a non-linear equation in $\Delta\xi$ which may be solved by the Newton-Raphson iterative method. Therefore, the martensite volume fraction increment is given as

$$\mathrm{d}\Delta\xi = \frac{\sigma_{eq}^* - 3G\varepsilon_L \Delta\xi - r - \sigma_y}{3G\varepsilon_L + h\varepsilon_L} \tag{2.25}$$

in which σ_y is the initial stress of the forward phase transformation σ_{s,T_0}^{AM} or the reverse phase transformation σ_{s,T_0}^{MA}. h indicates the hardening modulus, and r is the isotropic hardening function. The experimental results show that the stress increase caused by the phase transformation strain can be considered as linear hardening, and the gradient value h is a constant parameter which can be expressed as follows:
— forward phase transformation

$$h = h_{AM} = \frac{\sigma_{f,T}^{AM} - \sigma_{s,T}^{AM}}{\varepsilon_L} \qquad \Delta\xi > 0 \tag{2.26}$$

— reverse phase transformation

$$h = h_{MA} = \frac{\sigma_{s,T}^{MA} - \sigma_{f,T}^{MA}}{\varepsilon_L} \qquad \Delta\xi < 0 \tag{2.27}$$

For linear hardening $r = h\varepsilon_L\xi$. Therefore, $\partial r/\partial\xi = h\varepsilon_L$. From the experimental results, it is found that the start stress of phase transformation with temperature is basically linear, which dose not consider the influence of plasticity on the final stress of the austenite reverse transformation for simplicity. Therefore, the evolution of transformation stress with temperature can be described with the use of the following equation

$$\begin{aligned} \sigma_{s,T}^{MA} &= \sigma_{s,T_0}^{MA} + (T - T_0)C_{AM} \qquad & \sigma_{f,T}^{MA} &= \sigma_{f,T_0}^{MA} + (T - T_0)C_{AM} \\ \sigma_{s,T}^{AM} &= \sigma_{s,T_0}^{AM} + (T - T_0)C_{MA} \qquad & \sigma_{f,T}^{AM} &= \sigma_{f,T_0}^{AM} + (T - T_0)C_{MA} \end{aligned} \tag{2.28}$$

in which C_{AM} and C_{MA} are material parameters which depict the slope of the phase transformation stress with temperature.

2.4. Plastic strain evolution rule

After finishing the stress-induced phase transformation, if the loading is continued up to exceed the martensite plastic yield stress, the plastic deformation of martensite will occur. As temperature is increased, the initial stress of the forward phase transformation increases. As the martensitic start stress is higher than the austenite plastic yield stress, the SMA will begin to undergo the austenite plastic deformation firstly. In this paper, it is assumed that the plastic yield behavior of austenite and martensite is subject to the von Mises yield criterion, and the plastic yield condition can be expressed as:

— austenitic plastic yield

$$F_{Ap}(\boldsymbol{\sigma}, p) = \sigma_{eq} - \sigma_y^A(p) = 0 \tag{2.29}$$

— martensite plastic yield

$$F_{Mp}(\boldsymbol{\sigma}, p) = \sigma_{eq} - \sigma_y^M(p) = 0 \tag{2.30}$$

in which the internal variable p is the cumulative plastic strain

$$\dot{p} = \left[\frac{2}{3}\dot{\boldsymbol{\varepsilon}}_p : \dot{\boldsymbol{\varepsilon}}_p\right]^{\frac{1}{2}}$$

and $\sigma_y^A = \sigma_{y0}^A + h_A^p p$ and $\sigma_y^M = \sigma_{y0}^M + h_M^p p$ are the plastic yield stress of austenite and martensite, respectively. σ_{y0}^A and σ_{y0}^M are the initial plastic yield stress of austenite and martensite, respectively, and h_M^p are the plastic yield modulus of austenite and martensite, respectively.

The plastic strain rate can be expressed as

$$\dot{\boldsymbol{\varepsilon}}_p = \begin{cases} \dot{\boldsymbol{\varepsilon}}_p^A = \dot{\lambda}_A \dfrac{\partial F_{Ap}(\boldsymbol{\sigma}, \xi)}{\partial \boldsymbol{\sigma}} = \sqrt{\dfrac{3}{2}}\dot{p}\mathbf{n}_A & \text{austenitic plastic yield} \\ \dot{\boldsymbol{\varepsilon}}_p^M = \dot{\lambda}_M \dfrac{\partial F_{Mp}(\boldsymbol{\sigma}, \xi)}{\partial \boldsymbol{\sigma}} = \sqrt{\dfrac{3}{2}}\dot{p}\mathbf{n}_M & \text{martensite plastic yield} \end{cases} \tag{2.31}$$

where λ_A and λ_M are plastic multipliers of the austenitic and martensite plastic yield, respectively. $\mathbf{n}_A$ and $\mathbf{n}_M$ are the direction vectors of the austenitic and martensite plastic yield, respectively

$$\mathbf{n}_A = \mathbf{n}_M = \sqrt{\frac{3}{2}}\frac{\mathbf{s}}{\sigma_{eq}} \tag{2.32}$$

The solutions for a plastic strain increment and the renewal of plastic strain are considered in the following. The plastic strain includes plastic strain of austenite and martensite. The course of the implicit stress integration is similar for both of them.

The implicit stress integral of plastic yield behavior can be solved by the method discussed in Section 2.3 for the phase transformation, which is similar to the equation of the deviatoric stress increment in Eq. (2.17)

$$\mathbf{s} = \mathbf{s}^* - 3G\Delta\overline{\varepsilon}_p \frac{\mathbf{s}}{\sigma_{eq}} \tag{2.33}$$

in which $\overline{\varepsilon}_p$ is the equivalent phase transformation strain. We take the contracted tensor product of each side of Eq. (2.33) with itself

$$\sigma_{eq} + 3G\Delta p = \sigma^*_{eq} \tag{2.34}$$

The expression form of the current equivalent plastic strain increment can be obtained by using the Newton-Raphson iteration method

$$\mathrm{d}\Delta p = \frac{\sigma^*_{eq} - 3G\Delta p - r - \sigma_y}{3G + h} \tag{2.35}$$

In the above equations, σ_y is the plastic yield stress of austenite σ_y^A or martensite σ_y^M. h is the plastic hardening modulus, which is the stress increment for the unit equivalent plastic strain increment. This modulus is also expressed as a linear hardening function. It means that the gradient value h is constant, the expression for it is as follows

$$h = \begin{cases} h_A^p & \text{austenitic plastic hardening modulus} \\ h_M^p & \text{martensitic plastic modulus of hardening} \end{cases} \tag{2.36}$$

2.5. Transformation initial conditions

In many constitutive laws, researchers use stress tensors and temperature data as control variables. In this work, an effective criterion proposed in (Ben Jaber *et al.*, 2008) using strain and temperature as control variables is used to judge the phase transformation points in order to avoid the complexity of transformation correction. To start the transformation, the following conditions should be satisfied.

The conditions for A-M transformation are

$$\varepsilon_s^{AM} < \overline{\varepsilon}_t^{AM} < \varepsilon_f^{AM} \qquad \dot{\varepsilon}_t^{AM} > 0 \qquad 0 < \xi < 1 \qquad \sigma_{eq} > \sigma_{s,T}^{AM}$$

The M-A transformation conditions are expressed as follows

$$\varepsilon_s^{MA} < \overline{\varepsilon}_t^{MA} < \varepsilon_f^{MA} \qquad \dot{\varepsilon}_t^{MA} < 0 \qquad 0 < \xi < 1 \qquad \sigma_{eq} < \sigma_{s,T}^{MA}$$

in which $\overline{\varepsilon}_t^{AM}$ and $\overline{\varepsilon}_t^{MA}$ are the equivalent phase transformation strain in A-M stage and M-A stage, respectively.

The parameters of the initial and final strain for this transformation criterion are deduced from those of the stress phase transformation as follows.

The strain ε_s^{AM} marking the beginning of the transformation band A-M

$$\varepsilon_s^{AM} = \begin{cases} \varepsilon_{scr}^{AM} + C_{AM}^*(T - T_s^{AM}) & \text{if} \quad T_0 > T_s^{AM} \\ \varepsilon_{scr}^{AM} & \text{if} \quad T_0 < T_s^{AM} \end{cases} \tag{2.37}$$

The strain $\boldsymbol{\varepsilon}_f^{AM}$ marking the end of the transformation band A-M

$$\boldsymbol{\varepsilon}_f^{AM} = \begin{cases} \boldsymbol{\varepsilon}_{fcr}^{AM} + C_{AM}^*(T - T_s^{AM}) & \text{if } T_0 > T_s^{AM} \\ \boldsymbol{\varepsilon}_{fcr}^{AM} \text{if} & T_0 < T_s^{AM} \end{cases} \tag{2.38}$$

in which $C_{AM}^* = C_{AM}/E_M$, $\boldsymbol{\varepsilon}_{scr}^{AM} = \sigma_{s,T_0}^{AM}/E_A$, $\boldsymbol{\varepsilon}_{fcr}^{AM} = \sigma_{f,T_0}^{AM}/E_M + \varepsilon_L$, and T_0 denotes the specified temperatures, i.e., room temperature.

It should be noted that E_A and E_M are temperature-dependent elastic moduli of austenite and martensite, which can be expressed by the following equation at a certain temperature

$$\begin{aligned} E_A &= E_A^{T_0} + kE_A^{T_0}\ln(T - T_0 + 1) \\ E_M &= E_M^{T_0} + kE_M^{T_0}\ln(T - T_0 + 1) \end{aligned} \tag{2.39}$$

where $E_A^{T_0}$ and $E_M^{T_0}$ are the elastic moduli of austenite and martensite at specified temperatures, i.e., room temperature. k is a material parameter which depicts the increasing rate of the elastic modulus with temperature and is obtained from experimental results.

The state functions of the beginning strain $\boldsymbol{\varepsilon}_s^{MA}$ and the end strain $\boldsymbol{\varepsilon}_f^{MA}$ of the transformation band M-A are

$$\boldsymbol{\varepsilon}_s^{MA} = C_{MA}^*(T - T_s^{MA}) + \varepsilon_L \qquad \boldsymbol{\varepsilon}_f^{MA} = C_{MA}^*(T - T_f^{MA}) \tag{2.40}$$

in which $C_{MA}^* = C_{MA}/E_A$.

3. Finite element implementation

3.1. Consistent tangent modulus of phase transformation

After differentiation of Eqs. (2.24), it can be derived

$$\begin{aligned} &\Big(1 + 3G\frac{\varepsilon_L \Delta\xi}{\sigma_{eq}}\Big)\delta\mathbf{s} - \frac{3G\varepsilon_L}{\sigma_{eq}}\delta\Delta\xi\mathbf{s} - \frac{3G\varepsilon_L\Delta\xi}{\sigma_{eq}^2}\delta\sigma_{eq}\mathbf{s} = \delta\mathbf{s}^* \\ &\delta\sigma_{eq} + 3G\varepsilon_L\delta\Delta\xi = \delta\sigma_{eq}^* \end{aligned} \tag{3.1}$$

To differentiate Eq. (2.10), we put $\delta F = \delta\sigma_{eq} - \delta r = 0$. Therefore, it can be obtained $\delta\sigma_{eq} = \delta r = h\varepsilon_L\delta\xi = h\varepsilon_L\delta\Delta\xi$. So, we may write Eq. $(3.1)_2$ as

$$h\varepsilon_L\delta\Delta\xi + 3G\varepsilon_L\delta\Delta\xi = \delta\sigma_{eq}^* \qquad \text{or} \qquad \delta\Delta\xi = \frac{\delta\sigma_{eq}^*}{(h + 3G)\varepsilon_L} \tag{3.2}$$

Combining with $(3.1)_2$ it gives

$$\delta\sigma_{eq} = \delta\sigma_{eq}^*\Big(1 - \frac{3G}{h + 3G}\Big) \tag{3.3}$$

We now use Eqs. $(3.2)_2$ in Eq. $(3.1)_1$ to eliminate $\delta\sigma_{eq}$, $\delta\Delta\xi$ and $\Delta\xi$, respectively, to give

$$\frac{\sigma_{eq}^*}{\sigma_{eq}}\delta\mathbf{s} + \frac{\delta\sigma_{eq}^*}{\sigma_{eq}\sigma_{eq}}\Big(\sigma_{eq} - \frac{3G\sigma_{eq}^*}{h + 3G}\Big)\mathbf{s} = \delta\mathbf{s}^* \tag{3.4}$$

Consider the term

$$\delta\sigma_{eq}^* = \frac{3}{2}\frac{1}{\sigma_{eq}^*}\mathbf{s}^* : \delta\mathbf{s}^* \tag{3.5}$$

Substituting this together with the expression for $\mathbf{s}$ in Eq. (2.22) into Eq. (3.4) gives

$$\delta\mathbf{s} = \frac{3}{2}\Big(\frac{\mathbf{s}^*}{\sigma^*_{eq}} \otimes \frac{\mathbf{s}^*}{\sigma^*_{eq}}\Big)\Big(\frac{3G}{h+3G} - \frac{\sigma_{eq}}{\sigma^*_{eq}}\Big) : \delta\mathbf{s}^* + \frac{\sigma_{eq}}{\sigma^*_{eq}}\delta\mathbf{s}^* \tag{3.6}$$

If we write

$$Q = \frac{3}{2}\Big(\frac{3G}{h+3G} - \frac{\sigma_{eq}}{\sigma^*_{eq}}\Big) \qquad R = \frac{\sigma_{eq}}{\sigma^*_{eq}}$$

then Eq. (3.6) becomes

$$\delta\mathbf{s} = \Big[Q\Big(\frac{\mathbf{s}^*}{\sigma^*_{eq}} \otimes \frac{\mathbf{s}^*}{\sigma^*_{eq}}\Big) + R\mathbf{I}\Big] : \delta\mathbf{s}^* \tag{3.7}$$

in which $\mathbf{I}$ is the fourth-order identity tensor.

We are trying to relate $\delta\mathbf{s}$ and $\delta\boldsymbol{\varepsilon}$ to derive the Jacobian. The deviatoric trial stress in terms of the deviatoric strain may be written as follows with applying the differential operator

$$\delta\mathbf{s}^* = 2G\Big(\delta\boldsymbol{\varepsilon} - \frac{1}{3}\mathbf{I}\otimes\mathbf{I} : \delta\boldsymbol{\varepsilon}\Big) \tag{3.8}$$

Substituting into Eq. (3.7) gives

$$\begin{aligned}\delta\mathbf{s}^* = 2G\Big[Q\Big(\frac{\mathbf{s}^*}{\sigma^*_{eq}} \otimes \frac{\mathbf{s}^*}{\sigma^*_{eq}}\Big) + R\mathbf{I}\Big] : \Big[\delta\boldsymbol{\varepsilon} - \frac{1}{3}\Big(\mathbf{I}\otimes\mathbf{I}\Big) : \delta\boldsymbol{\varepsilon}\Big] = 2GQ\Big(\frac{\mathbf{s}^*}{\sigma^*_{eq}} \otimes \frac{\mathbf{s}^*}{\sigma^*_{eq}}\Big) : \delta\boldsymbol{\varepsilon} \\ + 2GR\delta\boldsymbol{\varepsilon} - \frac{1}{3}Q\Big(\frac{\mathbf{s}^*}{\sigma^*_{eq}} \otimes \frac{\mathbf{s}^*}{\sigma^*_{eq}}\Big) : [(\mathbf{I}\otimes\mathbf{I}) : \delta\boldsymbol{\varepsilon}] - \frac{2}{3}GR\mathbf{I} : [(\mathbf{I}\otimes\mathbf{I}) : \delta\boldsymbol{\varepsilon}]\end{aligned} \tag{3.9}$$

The stress can be given in terms of its deviatoric tensor as

$$\delta\boldsymbol{\sigma} = \delta\mathbf{s} + \frac{1}{3}(\mathbf{I}\otimes\mathbf{I}) : \delta\boldsymbol{\sigma} = \delta\mathbf{s} + K(\mathbf{I}\otimes\mathbf{I}) : \delta\boldsymbol{\varepsilon} \tag{3.10}$$

in which $K = E/[3(1-2\nu)]$ is the bulk modulus.

Substituting into (3.9) gives

$$\frac{\delta\boldsymbol{\sigma}}{\delta\boldsymbol{\varepsilon}} = 2GQ\Big(\frac{\mathbf{s}^*}{\sigma^*_{eq}} \otimes \frac{\mathbf{s}^*}{\sigma^*_{eq}}\Big) + 2GR\mathbf{I} + \Big(K - \frac{2}{3}GR\Big)(\mathbf{I}\otimes\mathbf{I}) \tag{3.11}$$

This is the consistent tangential modulus for the forward and reverse phase transformation.

3.2. Consistent tangent modulus of plastic deformation

The solving process for the consistent tangent modulus of the plastic strain behavior of the NiTi alloy is similar to that of the previous phase transformation behavior. By differentiating Eq. (2.33), we obtain

$$\begin{aligned}&\Big(1 + 3G\frac{\Delta p}{\sigma_{eq}}\Big)\delta\mathbf{s} - \frac{3G\delta\Delta p}{\sigma_{eq}}\mathbf{s} - \frac{3G\Delta p}{\sigma^2_{eq}}\delta\sigma_{eq}\mathbf{s} = \delta\mathbf{s}^* \\ &\delta\sigma_{eq} + 3G\delta\Delta p = \delta\sigma^*_{eq}\end{aligned} \tag{3.12}$$

and $\delta\sigma_{eq} = \delta r = h\delta p = h\delta\Delta p$.

The consistent tangent modulus expression of the plastic strain behavior is the same as Eq. $(3.12)_2$. The difference from the phase transformation strain behavior is the expression of the plastic hardening modulus h. A reverse mapping algorithm is described in Algorithm 1.

Algorithm 1: Iteration procedure

Begin
Step1 Initialize variables
Step2 Calculate $\dot{\varepsilon}_t^{AM}$, $\overline{\varepsilon}_t^{AM}$, $\dot{\varepsilon}_{eq}$, ε_{eq}, σ_{eq} and ξ
if $\xi = 1$, **goto Step5**
elseif $\dot{\varepsilon}_t^{AM} > 0$, $\varepsilon_s H^{AM} < \overline{\varepsilon}_t^{AM} < \varepsilon_f^{AM}$ and $\sigma_{eq} > \sigma_{s,T}^{AM}$ **goto Step3**
elseif $\sigma_{eq} > \sigma_y^M$ and $\dot{\varepsilon}_{eq} > 0$, **goto Step7**
else goto Step10
endif
Step3 Calculate $\mathrm{d}\Delta\xi$
if $|\mathrm{d}\Delta\xi/\Delta\xi| < toler$
obtaining $\Delta\xi$, and calculating $\Delta\boldsymbol{\varepsilon}^{tr} = \sqrt{3/2}\varepsilon_L \Delta\xi \mathbf{n}_{AM}$, updating elastic strain $\boldsymbol{\varepsilon}^e$, transformation strain $\boldsymbol{\varepsilon}^{tr}$, martensite volume fraction ξ and stress tensor $\boldsymbol{\sigma}$ **goto Step4**
endif
Step4 Calculate consistent tangent modulus of martensite phase transformation, **goto Step5**
Step5 Calculate $\dot{\varepsilon}_t^{MA}$, $\overline{\varepsilon}_t^{MA}$, $\dot{\varepsilon}_{eq}$, ε_{eq}, σ_{eq} and ξ
if $\xi = 0$, **goto Step10**
elseif $\dot{\varepsilon}_t^{MA} < 0$, $\varepsilon_s^{MA} < \overline{\varepsilon}_t^{MA} < \varepsilon_f^{MA}$ and $\sigma_{eq} < \sigma_{s,T}^{MA}$ **goto Step6**
else goto Step10
endif
Step6 Calculate $\mathrm{d}\Delta\xi$
if $|\mathrm{d}\Delta\xi/\Delta\xi| < toler$
obtaining $\Delta\xi$, and calculating $\Delta\boldsymbol{\varepsilon}^{tr} = \sqrt{3/2}\varepsilon_L \Delta\xi \mathbf{n}_{MA}$, updating elastic strain $\boldsymbol{\varepsilon}^e$, transformation strain $\boldsymbol{\varepsilon}^{tr}$, martensite volume fraction ξ and stress tensor $\boldsymbol{\sigma}$
endif
Step7 Calculate $\dot{\varepsilon}_{eq}$, ε_{eq}, σ_{eq}
if $\sigma_{eq}\sigma_y^M$ and $\dot{\varepsilon}_{eq} > 0$, **goto Step8**
else goto Step10
endif
Step8 Calculate $\mathrm{d}\Delta p$
if $|\mathrm{d}\Delta p/\Delta p| < toler$
obtaining Δp, and calculating $\Delta\boldsymbol{\varepsilon}^p = \sqrt{3/2}\Delta p \mathbf{n}_M$, updating elastic strain $\boldsymbol{\varepsilon}^e$, martensite plastic strain $\boldsymbol{\varepsilon}^p$, cumulated plastic strain p and stress tensor $\boldsymbol{\sigma}$
endif
Step9 Calculate consistent tangent modulus of martensite plasticity, **goto Step10**
Step10 Updating status variables
End

4. Verification of the proposed model

The constitutive model outlined in Section 2 has been implemented as a user subroutine for the finite element code ANSYS (2004) to analyze the phase transformation and plastic deformation under the uniaxial tension and unloading condition. In the following, the results of simulations by the proposed model are compared with the experimental data by Kang *et al.* (2009). From the experimental stress-strain curve under different temperatures, the following material parameters can be used. A SMA phase transformation and plasticity behavior diagram is presented in Fig. 1 to identify the parameters: $E_A^{T_0} = 41.0\,\mathrm{GPa}$, $E_M^{T_0} = 37.0\,\mathrm{GPa}$; $v_A = v_M = 0.33$; $C_{AM} = 8.0\,\mathrm{MPa/K}$, $C_{MA} = 8.8\,\mathrm{MPa/K}$; $k = 0.16$; $\sigma_{s,T0}^{AM} = 53.0\,\mathrm{MPa}$, $\sigma_{f,T0}^{AM} = 381.0\,\mathrm{MPa}$, $\sigma_{s,T0}^{MA} = 141.0\,\mathrm{MPa}$, $\sigma_{f,T0}^{MA} = 122.0\,\mathrm{MPa}$; $\varepsilon_L = 0.035$; $T_0 = 295\,\mathrm{K}$; $h_{AM} = 0.8\,\mathrm{GPa}$; $h_{MA} = 1.3\,\mathrm{GPa}$; $h_M^p = 6.7\,\mathrm{GPa}$; $\sigma_y^M = 1.7\,\mathrm{GPa}$.

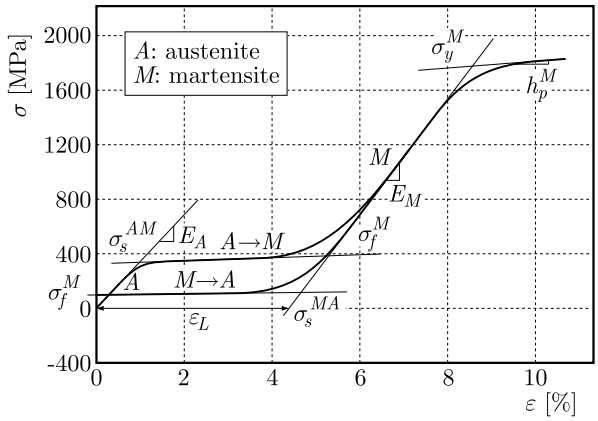

Fig. 1. SMA phase transformation and plasticity behavior diagram

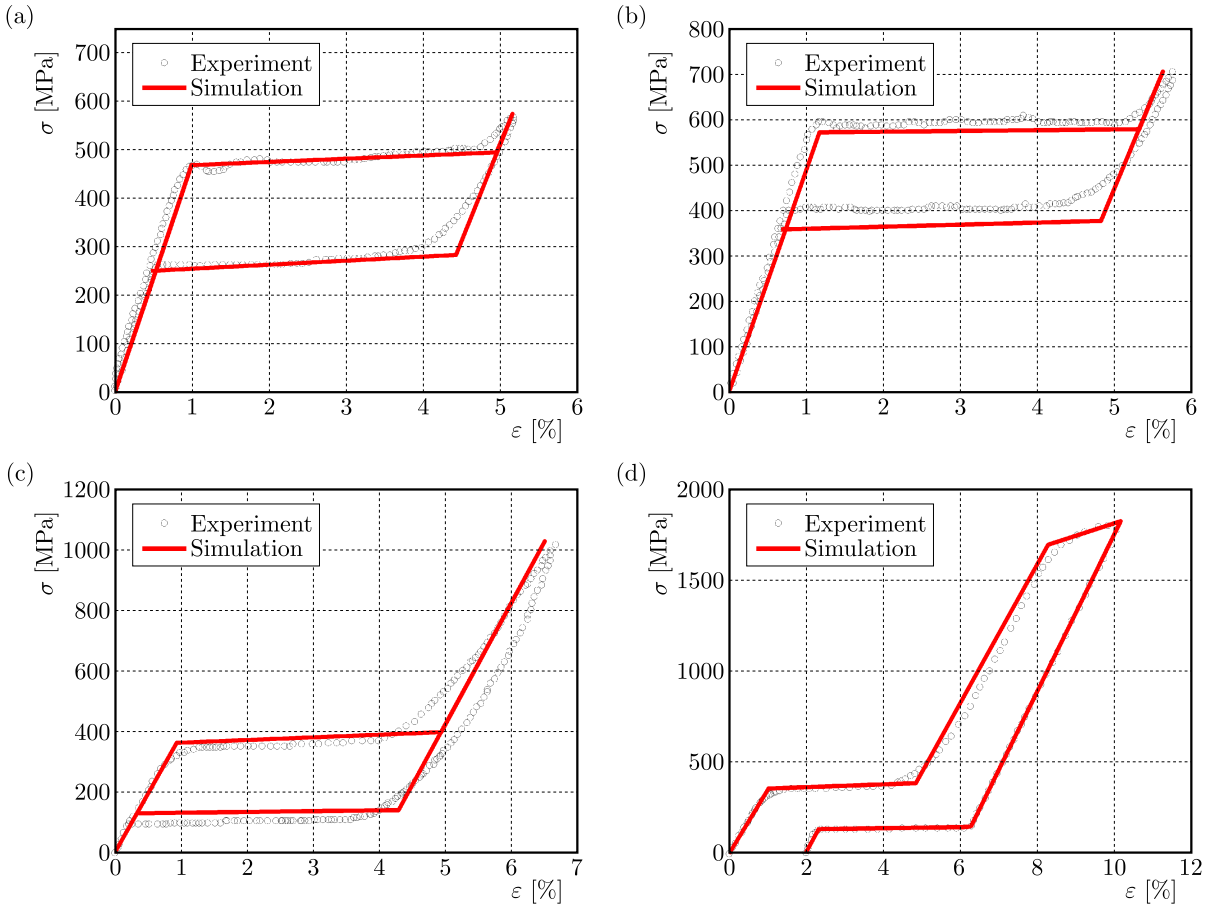

Fig. 2. Stress-strain curves during tension and unloading at various temperatures under strain controlled loading: (a) 309 K, (b) 323 K, (c) 295 K, peak strains at 6.6%, (d) 295 K, peak strains at 10%

The uniaxial tension and unloading case of the material has been calculated using ANSYS based on the proposed model and employed a 3D 8-node iso-parametric brick element. The simulation results are shown in Fig. 2. It can be seen that the stress-induced martensitic transformation occurs at low temperatures, such as 295K, when the stress is applied to the forward phase transformation stress $\sigma_{s,T}^{AM}$. When the stress reaches the end of the forward phase transformation $\sigma_{f,T}^{AM}$, the phase transformation strain can reach the maximum phase transformation strain ε_L, and the martensitic transformation is over. During unloading, once the stress reaches

the initial stress $\sigma_{s,T}^{MA}$ of martensite to austenite, the martensite gradually transforms to austenite. As the load is lower than the phase transformation final stress $\sigma_{f,T}^{MA}$, the elastic unloading of austenite takes place in the aftermath. It can be seen in Fig. 2 that the phase transformation stress is increased with an increase in temperature. The elastic modulus also increases with the increase in temperature.

Figures 2c,d show the stress-strain curves obtained in the tension-unloading with high peak strains at 295 K. It can be seen in Fig. 2c that the response peak stress is about 1000 MPa, and the martensite can still be completely transformed into austenite when undergoing unloading. However, with a higher applied peak strain, an apparent residual strain can be observed which is caused by the plastic deformation of martensite, as shown in Fig. 2d. The simulated results show a good agreement with the experimental ones. The results show that the proposed constitutive model can predict the thermodynamic behavior in the super-elastic NiTi alloy. It can be predicted that the model can also give reasonable prediction results for other working conditions and other experimental results in the temperature range.

Figure 3 shows a finite element model of an SMA rod with multiple elements, with length of 10 mm and radius of 0.5 mm. The fixed boundary conditions are applied at one end, at the other side $\Delta l = 0.1$ mm, 0.3 mm, 0.5 mm and 0.7 mm (direction along the Z axis), and then a total torque load $T_M = 25$ Nm is applied to the peripheral node of this side at $T_0 = 295$ K. The stress-strain curves in the tension-torque loading is calculated based on the data at the Gauss point of the picked element. It can be seen in Fig. 3a that the tension stress exhibits three inflection points. One is the phase transformation starting point A, another one is the phase transformation ending point B, and last one is the yield point C. It can be concluded that the phase transformation and plasticity lead to a decrease in the tension stress for the exact tension strain value. From Fig. 3b it can be found that as the tension strain is small, the tension rod dose not go enough through the phase transformation in the tension stage, such as in the $T_M = 25$ Nm and $\Delta l = 0.1$ mm or $\varepsilon = 0.01$ case. As the total torque load continues to be applied, the tension rod would go through the phase transformation and martensite plasticity stages, which implies the non-homogeneous stress status including both tensile and shear stresses. When the tension strain is high enough, such as in the $T_M = 25$ Nm and $\Delta l = 0.7$ mm or $\varepsilon = 0.07$ case, the tension rod finishes phase transformation in this stage. Then, as the total torque load is applied enough high, the tension rod would just go through the martensite plasticity stage. In this case, the plastic transform point mapped by the shear stress shown in Fig. 3b presents a decrease as the tension strain increases.

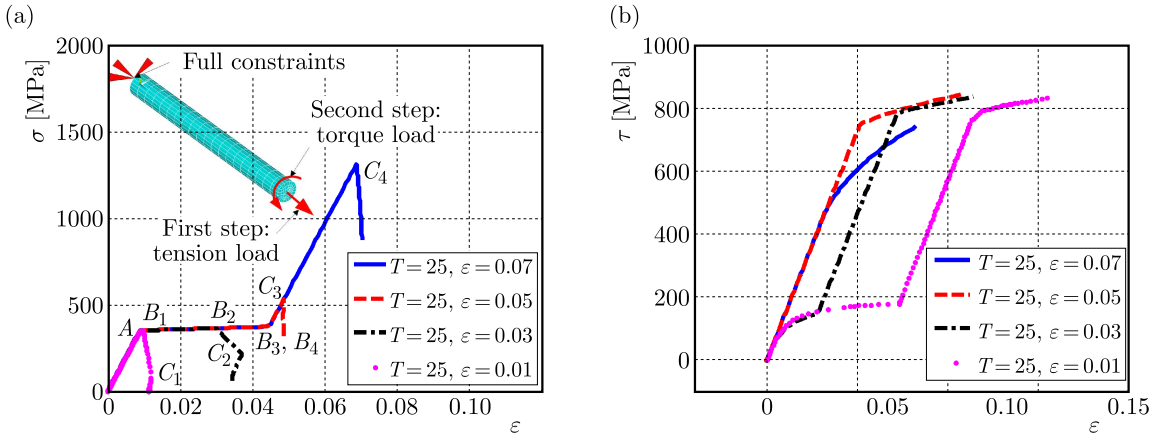

Fig. 3. Finite element analysis of the SMA rod with multiple elements: (a) tension stress, (b) shear stress

5. Conclusions

A shape memory alloy (SMA) phenomenological constitutive model is proposed in the general inelastic framework. Transformation hardening, reverse transformation, temperature dependence of transformation strain for each phase and plasticity hardening are considered in the proposed model. The model is implemented into the finite element code ANSYS by USERMAT user subroutine. The numerical results show that good simulation results can be obtained for uniaxial tensile-unloading stress-strain curves. The simulation results of the proposed model show a good agreement with the experimental ones at different temperatures for the super-elastic behavior of NiTi alloy. Finally, the accuracy of the implementation is verified by numerical tests considering non-homogeneous deformation of the structure.

Acknowledgments

We would like to thank for the financial support of this work by the National Natural Science Foundation of China (NSFC) under Grant Number 51775406 and 51405371, Open Research Fund of State Key Laboratory for Manufacturing Systems Engineering (Grant No. sklms2016007), Open Research Fund of State Key Laboratory of Structural Analysis for Industrial Equipment (Grant No. GZ1612), 111 Project B14042, Fundamental Research Funds for the Central Universities (Grant No. JB160403), Natural Science Foundation of Shanxi Province of China (Grant No. 2017JM5035), the Natural Science Foundation of Guangxi Province of China (Grant No. 2016GXNSFBA380230), and Natural Science Foundation of Hunan Province of China (Grant No. 2015JJ2054).

References

1. ANSYS Structural Analysis Guide, 2004, Version 8.0
2. Auricchio F., Taylor R.L., 1997, Shape-memory alloy modeling and numerical simulations of the finite-strain superelastic behavior, *Computer Methods of Application Mechanics and Engineering*, **143**, 175-194
3. Ben Jaber M., Smaoui H., Terriault P., 2008, Finite element analysis of a shape memory alloy three-dimensional beam based on a finite strain description, *Smart Materials and Structures*, **17**, 4, 5202-5228
4. Bo Z., Lagoudas D.C., 1999, Thermomechanical modeling of polycrystalline SMAs under cyclic loading, Part I: theoretical derivations, *International Journal of Engineering Science*, **37**, 1089-1140
5. Bouvet C., Calloch S., Lexcellent C., 2004, A phenomenological model for pseudoelasticity of shape memory alloys under multi-axial proportional and nonproportional loadings, *European Journal of Mechanics A-Solids*, **23**, 37-61
6. Cisse C., Zaki W., Zineb T. B., 2016, A review of constitutive models and modeling techniques for shape memory alloys, *International Journal of Plasticity*, **76**, 244-284
7. Kan Q.H., Kang G.Z., Qian L.M., 2010, Super-elastic constitutive model considering plasticity and its finite element implementation, *Acta Mechanica Solida Sinica*, **23**, 2, 95-105
8. Kang G.Z., Kan Q.H., Qian L.M., Liu Y.J., 2009, Ratchetting deformation of super-elastic and shape-memory NiTi alloys, *Mechanics of Materials*, **41**, 139-153
9. Lagoudas D.C., Bo Z., Qidwai, M.A., 1996, A unified thermodynamic constitutive model for SMA and finite element analysis of active metal matrix composites, *Mechanics of Composite Materials and Structures*, **3**, 2, 153-179
10. Lazghab T., 2001, Modeling of shape memory alloys with plasticity, Ph.D. Thesis, Florida International University, Florida
11. Liang C., Rogers C., 1990. One-dimensional thermomechanical constitutive relations for shape memory materials, *Journal of Intelligent Material Systems and Structures*, **1**, 207-234

12. Lubliner J., Auricchio F., 1996, Generalized plasticity and shape memory alloys, *International Journal of Solids and Structures*, **33**, 991-1003

13. McKelvey A.L., Ritchie R.O., 2001, Fatigue-crack growth behavior in the superelastic and shape-memory alloy Nitinol, *Metallurgical and Materials Transactions A*, **32**, 3, 731-743

14. Saint S., Chirani S.A., Calloeh S., 2009. A 3D super-elastic model for shape memory alloys taking into account Progressive strain under cyclic loadings, *Mechanics of Materials*, **41**, l, 12-26

15. Tanaka T., 1986, A thermomechanical sketch of shape memory effect: one dimensional tensile behavior, *Res Mechanica*, **18**, 251-263

16. Yan W., Wang C.H., Zhang X.P., Mai Y.W., 2003, Theoretical modelling of the effect of plasticity on reverse transformation in superelastic shape memory alloys, *Materials Science and Engineering A*, **354**, 1, 146-157

Manuscript received August 4, 2016; accepted for print June 24, 2017

JOURNAL OF THEORETICAL AND APPLIED MECHANICS
55, 4, pp. 1369-1380, Warsaw 2017
DOI: 10.15632/jtam-pl.55.4.1369

THERMOELASTIC STRAIN AND STRESS FIELDS DUE TO A SPHERICAL INCLUSION IN AN ELASTIC HALF-SPACE

Kuldip Singh, Renu Muwal

Guru Jambheshwar University of Science and Technology, Department of Mathematics, Hisar, Haryana, India
e-mail: renumuwal66@gmail.com

In this paper, closed form analytical expressions for thermoelastic strain and stress components due to a spherical inclusion in an elastic half-space are obtained. These expressions are derived in the context of steady-state uncoupled thermoelasticity using thermoelastic displacement potential functions. The thermal strain and stress fields are generated due to differences in the coefficients of linear thermal expansion between a subregion and the surrounding material. The strain and stress components for exterior points of the spherical inclusion are same as those of the center of dilatation. Variations of strain and stress components for exterior and interior points of the spherical inclusion are shown graphically.

Keywords: uncoupled thermoelasticity, strain and stress fields, potential functions, spherical inclusion

1. Introduction

Thermoelasticity is an extension of theory of elasticity to include thermal effects. Theory of thermoelasticity is concerned with the interaction between the thermal field and elastic bodies. Comprehensive treatises on the topics of thermoelasticity have been covered in the classical texts (Nowinski, 1978; Truesdell, 1984; Nowacki, 1986; Boley and Weiner, 1997; Boresi *et al.*, 2011; etc.). The study of thermoelasticity has begun with Duhamel (1837) and Neumann (1885), who postulated equations of linear thermoelasticity for isotropic bodies. Goodier (1937) studied the static problem of uncoupled thermoelasticity by employing the method of superposition using displacement potential functions. With the help of Goodier's method, Mindlin and Cheng (1950) obtained the thermal stress in a semi-infinite elastic solid with the traction free surface for the centre of dilatation using Galerkin's vector stress function. The result was then applied to the case of a spherical inclusion in a semi-infinite medium. Nowacki (1957) considered the problem of an instantaneous source of heat in an infinite isotropic elastic space and determined the state of stress using the potential of thermoelastic strain. Also, stress components in a semi-infinite elastic space due to an instantaneous source of heat was obtained using the method of Galerkin's displacement function and the Fourier integral under stress free surface boundary conditions. Sen (1957) presented a direct method for solving problems of circular holes in an isotropic elastic plate having prescribed displacements on the edge. The problem of deformation in an infinite isotropic plate due to the centre of dilatation in the form of a nucleus of thermoelastic strain at a finite distance from the hole was also discussed. Sharma (1957) obtained deformation and stress fields due to a nucleus of thermoelastic strain in an infinite solid having a spherical cavity using interior and exterior spherical harmonics. Another problem of a solid sphere at zero temperature having a heated nucleus inside was also discussed. Biharmonic solutions to steady state thermoelastic problems in three dimensions were derived by Nowinski (1961). Nowinski (1963) proved a mean value theorem for an arbitrary steady-state thermoelastic problem for an

isotropic elastic solid sphere. The stress components at the center of the sphere were expressed in terms of temperature on the surface of the sphere.

Guell and Dundurs (1967) obtained elastic fields due to a subregion between two joined half--spaces by differentiation from the corresponding fields for the whole space using the solutions for the center of dilatation. The Papkovich-Neuber displacement potentials were used when the interface between two joined half-spaces was a smooth interface and perfectly bonded. Those results were then applied to a spherical inclusion. The case of the force on the center of dilatation was also discussed. Hu (1989) considered the problem of a parallelepipedic thermal inclusion in a three-dimensional half-space and derived analytical solution using Goodier's method of the nucleus of thermal strain or the center of dilatation. Wang and Huang (1991) studied some thermoelastic problems in the half-space by using Goodier's thermoelastic potential functions and general solutions of elasticity based on the Boussinesq solutions (consisting of different harmonic functions). Yu *et al.* (1992) and Yu and Sanday (1992), respectively, derived analytical solutions for thermoelastic displacements and stresses due to an inclusion in a dissimilar medium consisting of two joined semi-infinite elastic solids and for the centre of dilatation in a plate. The stress-deformation state of an elastic half-space due to an inhomogeneous spheroidal thermal inclusion in the form of a prolate or oblate ellipsoid of revolution under stress-free surface boundary conditions was discussed by Kolesov *et al.* (1992) using thermoelastic displacement potential functions and the Teredzave method. Yu *et al.* (2002) calculated thermal stresses induced by an ellipsoidal inclusion with uniform dilatational eigenstrains in one of the two perfectly bonded semi-infinite solids using the method of dilatation centres and potential functions. Davies (2003) derived the elastic field due to a non-uniform temperature or a coherently misfitting inclusion in a semi-infinite region from the corresponding field in an infinite region.

Using Green's function method and series expansion techniques, closed form solutions for displacement and stress fields due to a hemispherical inclusion with a uniform eigenstrain in a semi-infinite isotropic elastic medium were obtained by Linzhi (2003). Liu and Wang (2005) obtained the elastic field caused by eigenstrains in a half-space using two types of numerical techniques – discrete correlation and fast Fourier transform as well as discrete convolution and fast Fourier transform. To obtain that field, analytical solutions for influence coefficients were expressed in terms of derivatives of four key integrals. Zhou *et al.* (2009) introduced a fast method for solving the problem of three-dimensional arbitrarily shaped inclusions in an isotropic half-space using a combination of 2D and 3D fast Fourier transform. A fast method for solving contact problems for a half-space containing multiple inhomogeneities such as voids, cavities, inclusions and fibers was presented by Leroux *et al.* (2010). The displacement and stress fields due to eigenstrains of all spherical inclusion were obtained using Eshelby's equivalent inclusion method along with 2D and 3D fast Fourier transforms. Itou (2014) derived basic equations for thermoelastic plane stress conditions and thermoelastic plane strain conditions. Two problems were solved using thermoelastic displacement potential functions: (i) axisymmetric thermal stresses for a hollow thin disk, (ii) thermal stresses for an infinite thin plate with a circular hole under uniform heat flow. Kumagai *et al.* (2014) presented different representations of a seismic spherical source. Those different representations consisted of a spherical source (S1), spherical crack source (S2), isotropic source of three mutually perpendicular vector dipoles (S3) or three mutually perpendicular tensile cracks (S4), Eshelby's spherical source with stress-free strain (S5) and Eshelby's spherical source with strain-free stress (S6). Static displacement fields due to those sources in an infinite medium and in a half-space were also derived.

In the present paper, we obtain thermoelastic strain and stress fields due to a spherical inclusion in an elastic half-space in the context of steady-state uncoupled thermoelasticity. Following the method opted by Davies (2003), we derive thermoelastic strain and stress components for an infinite region from which corresponding fields can be derived in the semi-infinite region. The expressions for these fields are obtained for the axisymmetric problem in cylindrical coordinates

using thermoelastic displacement potential functions. These results are in good agreement with the results found by Mindlin and Cheng (1950).

2. Theory

In the linear theory of thermoelasticity, the total strain can be written as the sum of mechanical and thermal strains (Goodier, 1937; and Nowinski, 1978)

$$e_{ij} = e_{ij}^{(M)} + e_{ij}^{(T)} \tag{2.1}$$

in which for an isotropic material, the thermal strain takes the form $e_{ij}^{(T)} = \alpha T \delta_{ij}$, where α is the coefficient of linear thermal expansion, T is temperature difference, δ_{ij} is Kronecker delta. Then in the context of uncoupled linear thermoelasticity, the displacement-temperature equation of equilibrium in the absence of body forces can be written as

$$\nabla^2 \mathbf{u} + \frac{1}{1-2\nu}\nabla(\nabla \cdot \mathbf{u}) = \frac{2(1+\nu)}{1-2\nu}\alpha \nabla T \tag{2.2}$$

where e_{ij} are components of the strain tensor; $\mathbf{u}$ is the displacement vector and ν is Poisson's ratio.

The uncoupled heat conduction equation for a steady state temperature field T with Q as the heat supply and λ_0 as the thermal conductivity can be written as

$$\nabla^2 T = \frac{-Q}{\lambda_0} \tag{2.3}$$

The solution to inhomogeneous equation (2.2) can be expressed as

$$\mathbf{u} = \mathbf{u}^c + \mathbf{u}^p \tag{2.4}$$

where $\mathbf{u}^c$ is the complementary function satisfying the homogeneous equation of (2.2) and $\mathbf{u}^p$ represents the particular solution to the displacement field generated by the temperature field T.

According to Goodier's method (Timoshenko and Goodier, 1951), the displacement $\mathbf{u}^{(\infty)}(\mathbf{r})$ for an infinite solid is given by $\mathbf{u}^{(\infty)} = \nabla\varphi$, where the potential function φ satisfies Poisson's equation

$$\nabla^2 \varphi = \frac{1+\nu}{1-\nu}\alpha T(\mathbf{r}) \tag{2.5}$$

Then the function φ is obtained as

$$\varphi(\mathbf{r}) = \frac{-1}{4\pi}\frac{1+\nu}{1-\nu}\alpha \int \frac{T(\mathbf{r}')}{|\mathbf{r}-\mathbf{r}'|} d^3(\mathbf{r}') \tag{2.6}$$

where $|\mathbf{r}-\mathbf{r}'| = |(x,y,z)-(\xi,\eta,\varsigma)| = \sqrt{(x-\xi)^2+(y-\eta)^2+(z-\varsigma)^2}$ is the distance between the points (x,y,z) and (ξ,η,ς).

Then the displacement, strain and stress components in the cylindrical polar coordinates (r,θ,z) are expressed in terms of the potential function φ as (Barber, 2002; Sadd, 2005)

$$u_r = \frac{\partial \varphi}{\partial r} \qquad u_\theta = \frac{1}{r}\frac{\partial \varphi}{\partial \theta} \qquad u_z = \frac{\partial \varphi}{\partial z} \tag{2.7}$$

and

$$\begin{aligned} e_{rr} &= \frac{\partial u_r}{\partial r} & e_{\theta\theta} &= \frac{1}{r}\Big(u_r + \frac{\partial u_\theta}{\partial \theta}\Big) & e_{r\theta} &= \frac{1}{2}\Big(\frac{1}{r}\frac{\partial u_r}{\partial \theta} + \frac{\partial u_\theta}{\partial r} - \frac{u_\theta}{r}\Big) \\ e_{zz} &= \frac{\partial u_z}{\partial z} & e_{\theta z} &= \frac{1}{2}\Big(\frac{\partial u_\theta}{\partial z} + \frac{1}{r}\frac{\partial u_z}{\partial \theta}\Big) & e_{zr} &= \frac{1}{2}\Big(\frac{\partial u_r}{\partial z} + \frac{\partial u_z}{\partial r}\Big) \end{aligned} \tag{2.8}$$

and

$$\begin{aligned}
&\frac{1}{2\mu}\sigma_{rr} = \frac{\partial^2\varphi}{\partial r^2} - \nabla^2\varphi \qquad \frac{1}{2\mu}\sigma_{\theta\theta} = \frac{1}{r}\frac{\partial\varphi}{\partial r} + \frac{1}{r^2}\frac{\partial^2\varphi}{\partial\theta^2} - \nabla^2\varphi \qquad \frac{1}{2\mu}\sigma_{zz} = \frac{\partial^2\varphi}{\partial z^2} - \nabla^2\varphi \\
&\frac{1}{2\mu}\sigma_{r\theta} = \frac{\partial}{\partial r}\Big(\frac{1}{r}\frac{\partial\varphi}{\partial\theta}\Big) \qquad \frac{1}{2\mu}\sigma_{\theta z} = \frac{1}{r}\frac{\partial^2\varphi}{\partial\theta\partial z} \qquad \frac{1}{2\mu}\sigma_{zr} = \frac{\partial^2\varphi}{\partial z\partial r}
\end{aligned} \tag{2.9}$$

where the Laplacian operator in the cylindrical polar coordinates (r, θ, z) is given by

$$\nabla^2\varphi = \Big(\frac{\partial^2}{\partial r^2} + \frac{1}{r}\frac{\partial}{\partial r} + \frac{1}{r^2}\frac{\partial^2}{\partial\theta^2} + \frac{\partial^2}{\partial z^2}\Big)\varphi \tag{2.10}$$

3. Formulation and solution of the problem

We consider an axisymmetric problem of a spherical inclusion in the upper half-space ($z \geqslant 0$) having a different coefficient of thermal expansion to that of the half-space but the same elastic constants as in Wang and Huang (1991). Due to this difference in the coefficients of thermal expansion between the sub region and its surrounding material, say η_0, a thermoelastic stress field is generated. Let radius of the spherical inclusion be a and center of it be located at the point $r = 0$ and $z = h$, where $h > a$, as shown in Fig. 1. The surface $z = 0$ is taken as traction free surface. We take the axis of symmetry as the z axis, then for the axisymmetric problem in the cylindrical coordinates (r, θ, z), all quantities are independent of θ. Then using Eq. (2.7), the displacement vector $\mathbf{u}$ has the form $\mathbf{u} = (u_r, 0, u_z)$. Therefore, the components of the strain and stress tensor can be written in the following form, see equations (2.8) and (2.9)

$$\begin{aligned}
&e_{rr} = \frac{\partial u_r}{\partial r} \qquad e_{\theta\theta} = \frac{u}{r} \qquad e_{zz} = \frac{\partial u_z}{\partial z} \\
&e_{zr} = \frac{1}{2}\Big(\frac{\partial u_r}{\partial z} + \frac{\partial u_z}{\partial r}\Big) \qquad e_{r\theta} = 0 \qquad e_{\theta z} = 0
\end{aligned} \tag{3.1}$$

and

$$\begin{aligned}
&\frac{1}{2\mu}\sigma_{rr} = \frac{\partial^2\varphi}{\partial r^2} - \nabla^2\varphi \qquad \frac{1}{2\mu}\sigma_{\theta\theta} = \frac{1}{r}\frac{\partial\varphi}{\partial r} - \nabla^2\varphi \qquad \frac{1}{2\mu}\sigma_{zz} = \frac{\partial^2\varphi}{\partial z^2} - \nabla^2\varphi \\
&\frac{1}{2\mu}\sigma_{zr} = \frac{\partial^2\varphi}{\partial z\partial r} \qquad \sigma_{r\theta} = 0 \qquad \sigma_{\theta z} = 0
\end{aligned} \tag{3.2}$$

where

$$\nabla^2\varphi = \Big(\frac{\partial^2}{\partial r^2} + \frac{1}{r}\frac{\partial}{\partial r} + \frac{\partial^2}{\partial z^2}\Big)\varphi \tag{3.3}$$

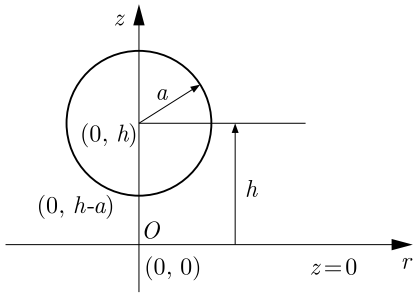

Fig. 1. A spherical inclusion in a thermoelastic half-space

Then according to Wang and Huang (1991), the thermoelastic potential function φ satisfies the following Poisson's equations, when temperature of the semi-infinite region increases up to T_0

$$\nabla^2\varphi = \begin{cases} \dfrac{1+\nu}{1-\nu}\alpha T = \dfrac{1+\nu}{1-\nu}\eta_0 T_0 & \text{for} \quad R_1 \leqslant a \\ 0 & \text{for} \quad R_1 > a \end{cases} \tag{3.4}$$

where $R_1^2 = r^2 + (z-h)^2$ is the distance of the point (r, z) from $(0, h)$. Then, the function φ for this problem is taken as (Wang and Huang 1991)

$$\varphi = \begin{cases} \dfrac{1}{6}KR_1^2 & \text{for} \quad R_1 \leqslant a \\ \dfrac{1}{6}K\Big(3a^2 - 2\dfrac{a^3}{R_1}\Big) & \text{for} \quad R_1 > a \end{cases} \tag{3.5}$$

where

$$K = \frac{1+\nu}{1-\nu}\eta_0 T_0 \tag{3.6}$$

Considering the boundary conditions, we assume that the boundary $z = 0$ of the half-space is traction free surface i.e.

$$\sigma_{zz} = \sigma_{rz} = 0 \qquad \text{at} \quad z = 0 \tag{3.7}$$

Now according to Davies (2003), the strain and stress components within the semi-infinite region $z \geqslant 0$ with the traction free surface in terms of strain and stress components for an infinite region for the axisymmetric problem in the rz-plane can be reduced to the form

$$\begin{aligned} e_{rr} &= e_{rr}^{(\infty)} + (3-4\nu)\overline{e}_{rr}^{(\infty)} + 2z\frac{\partial}{\partial z}\overline{e}_{rr}^{(\infty)} & e_{\theta\theta} &= e_{\theta\theta}^{(\infty)} + (3-4\nu)\overline{e}_{\theta\theta}^{(\infty)} + 2z\frac{\partial}{\partial z}\overline{e}_{\theta\theta}^{(\infty)} \\ e_{zz} &= e_{zz}^{(\infty)} - (1-4\nu)\overline{e}_{zz}^{(\infty)} + 2z\frac{\partial}{\partial z}\overline{e}_{zz}^{(\infty)} & e_{rz} &= e_{rz}^{(\infty)} - \overline{e}_{rz}^{(\infty)} - 2z\frac{\partial}{\partial z}\overline{e}_{rz}^{(\infty)} \\ e_{r\theta} &= 0 = e_{\theta z} \end{aligned} \tag{3.8}$$

and

$$\begin{aligned} \sigma_{rr} &= \sigma_{rr}^{(\infty)} + (3-4\nu)\overline{\sigma}_{rr}^{(\infty)} - 4\nu\overline{\sigma}_{zz}^{(\infty)} + 2z\frac{\partial}{\partial z}\overline{\sigma}_{rr}^{(\infty)} \\ \sigma_{\theta\theta} &= \sigma_{\theta\theta}^{(\infty)} + (3-4\nu)\overline{\sigma}_{\theta\theta}^{(\infty)} - 4\nu\overline{\sigma}_{zz}^{(\infty)} + 2z\frac{\partial}{\partial z}\overline{\sigma}_{\theta\theta}^{(\infty)} & \sigma_{r\theta} &= 0 = \sigma_{\theta z} \\ \sigma_{zz} &= \sigma_{zz}^{(\infty)} - \overline{\sigma}_{zz}^{(\infty)} + 2z\frac{\partial}{\partial z}\overline{\sigma}_{zz}^{(\infty)} & \sigma_{rz} &= \sigma_{rz}^{(\infty)} - \overline{\sigma}_{rz}^{(\infty)} - 2z\frac{\partial}{\partial z}\overline{\sigma}_{rz}^{(\infty)} \end{aligned} \tag{3.9}$$

Then the displacement, strain and stress fields in the infinite region and those at the image point for exterior points ($R_1 > a$) of the spherical inclusion (where $\nabla^2\varphi = 0$) are obtained using $\mathbf{u}^{(\infty)} = \nabla\varphi$ and equations (3.1)-(3.3)

$$u_r^{(\infty)} = \frac{\partial\varphi}{\partial r} = \frac{1}{3}Ka^3\Big(\frac{r}{R_1^3}\Big) \qquad u_\theta^{(\infty)} = \frac{1}{r}\frac{\partial\varphi}{\partial\theta} = 0 \qquad u_z^{(\infty)} = \frac{\partial\varphi}{\partial z} = \frac{1}{3}Ka^3\Big(\frac{z-h}{R_1^3}\Big) \tag{3.10}$$

$$\begin{aligned} e_{rr}^{(\infty)} &= \frac{\partial^2\varphi}{\partial r^2} = \frac{1}{3}Ka^3\Big(\frac{1}{R_1^3} - \frac{3r^2}{R_1^5}\Big) & e_{\theta\theta}^{(\infty)} &= \frac{u_r}{r} = \frac{1}{3}Ka^3\Big(\frac{1}{R_1^3}\Big) & e_{r\theta}^{(\infty)} &= e_{\theta z}^{(\infty)} = 0 \\ e_{zz}^{(\infty)} &= \frac{\partial^2\varphi}{\partial z^2} = \frac{1}{3}Ka^3\Big(\frac{1}{R_1^3} - \frac{3(z-h)^2}{R_1^5}\Big) & e_{rz}^{(\infty)} &= e_{zr}^{(\infty)} = \frac{\partial^2\varphi}{\partial r\partial z} = -Ka^3\frac{r(z-h)}{R_1^5} \end{aligned} \tag{3.11}$$

$$\frac{1}{2\mu}\sigma_{rr}^{(\infty)} = \frac{1}{3}Ka^3\Big(\frac{1}{R_1^3} - \frac{3r^2}{R_1^5}\Big) \qquad \frac{1}{2\mu}\sigma_{\theta\theta}^{(\infty)} = \frac{1}{3}Ka^3\Big(\frac{1}{R_1^3}\Big) \qquad \sigma_{r\theta}^{(\infty)} = 0 = \sigma_{\theta z}^{(\infty)}$$
$$\frac{1}{2\mu}\sigma_{zz}^{(\infty)} = \frac{1}{3}Ka^3\Big(\frac{1}{R_1^3} - \frac{3(z-h)^2}{R_1^5}\Big) \qquad \frac{1}{2\mu}\sigma_{rz}^{(\infty)} = -Ka^3\frac{r(z-h)}{R_1^5} \tag{3.12}$$

$$\overline{u}_r^{(\infty)} = \frac{1}{3}Ka^3\Big(\frac{r}{R_2^3}\Big) \qquad \overline{u}_\theta^{(\infty)} = 0 \qquad \overline{u}_z^{(\infty)} = \frac{-1}{3}Ka^3\Big(\frac{z+h}{R_2^3}\Big) \tag{3.13}$$

$$\overline{e}_{rr}^{(\infty)} = \frac{1}{3}Ka^3\Big(\frac{1}{R_2^3} - \frac{3r^2}{R_2^5}\Big) \qquad \overline{e}_{\theta\theta}^{(\infty)} = \frac{1}{3}Ka^3\Big(\frac{1}{R_2^3}\Big) \qquad \overline{e}_{r\theta}^{(\infty)} = \overline{e}_{\theta z}^{(\infty)} = 0$$
$$\overline{e}_{zz}^{(\infty)} = \frac{1}{3}Ka^3\Big(\frac{1}{R_2^3} - \frac{3(z+h)^2}{R_2^5}\Big) \qquad \overline{e}_{rz}^{(\infty)} = Ka^3\frac{r(z+h)}{R_2^5} \tag{3.14}$$

$$\frac{1}{2\mu}\overline{\sigma}_{rr}^{(\infty)} = \frac{1}{3}Ka^3\Big(\frac{1}{R_2^3} - \frac{3r^2}{R_2^5}\Big) \qquad \frac{1}{2\mu}\overline{\sigma}_{\theta\theta}^{(\infty)} = \frac{1}{3}Ka^3\Big(\frac{1}{R_2^3}\Big) \qquad \overline{\sigma}_{r\theta}^{(\infty)} = 0 = \overline{\sigma}_{\theta z}^{(\infty)}$$
$$\frac{1}{2\mu}\overline{\sigma}_{zz}^{(\infty)} = \frac{1}{3}Ka^3\Big(\frac{1}{R_2^3} - \frac{3(z+h)^2}{R_2^5}\Big) \qquad \frac{1}{2\mu}\overline{\sigma}_{rz}^{(\infty)} = Ka^3\frac{r(z+h)}{R_2^5} \tag{3.15}$$

where $(0,-h)$ is the image of point $(0,h)$ and $R_2^2 = r^2 + (z+h)^2$ is the distance of the point (r,z) from $(0,-h)$.

Substituting equations (3.11), (3.14) and (3.12), (3.15) into (3.8) and (3.9), respectively, the strain and stress components in the thermoelastic half-space for exterior points ($R_1 > a$) of the spherical inclusion can be expressed as

$$e_{rr} = \frac{1}{3}Ka^3\Big[\frac{1}{R_1^3} + \frac{3-4\nu}{R_2^3} - \frac{6z(z+h)}{R_2^5} - 3r^2\Big(\frac{1}{R_1^5} + \frac{3-4\nu}{R_2^5} - \frac{10z(z+h)}{R_2^7}\Big)\Big]$$
$$e_{\theta\theta} = \frac{1}{3}Ka^3\Big(\frac{1}{R_1^3} + \frac{3-4\nu}{R_2^3} - \frac{6z(z+h)}{R_2^5}\Big)$$
$$e_{zz} = \frac{1}{3}Ka^3\Big(\frac{1}{R_1^3} - \frac{1-4\nu}{R_2^3} - \frac{18z(z+h)}{R_2^5} - \frac{3(z-h)^2}{R_1^5} + \frac{3(1-4\nu)(z+h)^2}{R_2^5} + \frac{30z(z+h)^3}{R_2^7}\Big) \tag{3.16}$$
$$e_{rz} = -Ka^3r\Big(\frac{z-h}{R_1^5} + \frac{3z+h}{R_2^5} - \frac{10z(z+h)^2}{R_2^7}\Big)$$

and

$$\sigma_{rr} = 2\mu\frac{Ka^3}{3}\Big[\frac{1}{R_1^3} + \frac{3-8\nu}{R_2^3} - \frac{6z(z+h)}{R_2^5} + \frac{12\nu(z+h)^2}{R_2^5} - 3r^2\Big(\frac{1}{R_1^5} + \frac{3-4\nu}{R_2^5} - \frac{10z(z+h)}{R_2^7}\Big)\Big]$$
$$\sigma_{\theta\theta} = 2\mu\frac{Ka^3}{3}\Big(\frac{1}{R_1^3} + \frac{3-8\nu}{R_2^3} - \frac{6z(z+h)}{R_2^5} + \frac{12\nu(z+h)^2}{R_2^5}\Big)$$
$$\sigma_{zz} = 2\mu\frac{Ka^3}{3}\Big(\frac{1}{R_1^3} - \frac{1}{R_2^3} - \frac{18z(z+h)}{R_2^5} - \frac{3(z-h)^2}{R_1^5} + \frac{3(z+h)^2}{R_2^5} + \frac{30z(z+h)^3}{R_2^7}\Big) \tag{3.17}$$
$$\sigma_{rz} = -2\mu Ka^3r\Big(\frac{z-h}{R_1^5} + \frac{3z+h}{R_2^5} - \frac{10z(z+h)^2}{R_2^7}\Big)$$

Further, from equation (3.17), we can see that $\sigma_{zz} = \sigma_{rz} = 0$ at the boundary $z = 0$ of the half-space, which is in accordance with the boundary conditions as in equation (3.7).

Also, for the interior points ($R_1 \leqslant a$) of the spherical inclusion, as in Mindlin and Cheng (1950)

$$\mathbf{u}_{int} = \mathbf{u}_{ext} + \frac{a^3K\mathbf{R}_1}{3}\Big(\frac{1}{a^3} - \frac{1}{R_1^3}\Big) \tag{3.18}$$

Using this, the following relations between the strain components of the exterior points ($R_1 > a$) and the interior points ($R_1 \leqslant a$) of the spherical inclusion are given by

$$\begin{aligned} e_{rr}^{int} &= e_{rr}^{ext} + \frac{Ka^3}{3}\Big(\frac{1}{a^3} - \frac{1}{R_1^3}\Big) + Ka^3\frac{r^2}{R_1^5} \qquad e_{\theta\theta}^{int} = e_{\theta\theta}^{ext} + \frac{Ka^3}{3}\Big(\frac{1}{a^3} - \frac{1}{R_1^3}\Big) \\ e_{zz}^{int} &= e_{zz}^{ext} + \frac{Ka^3}{3}\Big(\frac{1}{a^3} - \frac{1}{R_1^3}\Big) + Ka^3\frac{(z-h)^2}{R_1^5} \qquad e_{rz}^{int} = e_{rz}^{ext} + Ka^3\frac{r(z-h)}{R_1^5} \end{aligned} \tag{3.19}$$

Also, the relations between the stress components of the exterior points ($R_1 > a$) and the interior points ($R_1 \leqslant a$) of the spherical inclusion are given below, see Guell and Dundurs (1967)

$$\begin{aligned} \sigma_{rr}^{int} &= \sigma_{rr}^{ext} - 2\mu K\Big(\frac{2}{a^3} + \frac{1}{R_1^3} - \frac{3r^2}{R_1^5}\Big) \qquad \sigma_{\theta\theta}^{int} = \sigma_{\theta\theta}^{ext} - 2\mu K\Big(\frac{2}{a^3} + \frac{1}{R_1^3}\Big) \\ \sigma_{zz}^{int} &= \sigma_{zz}^{ext} - 2\mu K\Big(\frac{2}{a^3} + \frac{1}{R_1^3} - \frac{3(z-h)^2}{R_1^5}\Big) \qquad \sigma_{rz}^{int} = \sigma_{rz}^{ext} + 6\mu K\frac{r(z-h)}{R_1^5} \end{aligned} \tag{3.20}$$

Substituting equations (3.16) and (3.17) into (3.19) and (3.20), respectively, the strain and stress components in the thermoelastic half-space for the interior points ($R_1 \leqslant a$) of the spherical inclusion can be expressed as

$$\begin{aligned} e_{rr} &= \frac{1}{3}Ka^3\Big[\frac{1}{a^3} + \frac{3-4\nu}{R_2^3} - \frac{6z(z+h)}{R_2^5} - 3r^2\Big(\frac{3-4\nu}{R_2^5} - \frac{10z(z+h)}{R_2^7}\Big)\Big] \\ e_{\theta\theta} &= \frac{1}{3}Ka^3\Big(\frac{1}{a^3} + \frac{3-4\nu}{R_2^3} - \frac{6z(z+h)}{R_2^5}\Big) \\ e_{zz} &= \frac{1}{3}Ka^3\Big(\frac{1}{a^3} - \frac{1-4\nu}{R_2^3} - \frac{18z(z+h)}{R_2^5} + \frac{3(1-4\nu)(z+h)^2}{R_2^5} + \frac{30z(z+h)^3}{R_2^7}\Big) \\ e_{rz} &= -Ka^3r\Big(\frac{3z+h}{R_2^5} - \frac{10z(z+h)^2}{R_2^7}\Big) \end{aligned} \tag{3.21}$$

and

$$\begin{aligned} \sigma_{rr} &= 2\mu\frac{Ka^3}{3}\Big[\frac{-2}{a^3} + \frac{3-8\nu}{R_2^3} - \frac{6z(z+h)}{R_2^5} + \frac{12\nu(z+h)^2}{R_2^5} - 3r^2\Big(\frac{3-4\nu}{R_2^5} - \frac{10z(z+h)}{R_2^7}\Big)\Big] \\ \sigma_{\theta\theta} &= 2\mu\frac{Ka^3}{3}\Big(\frac{-2}{a^3} + \frac{3-8\nu}{R_2^3} - \frac{6z(z+h)}{R_2^5} + \frac{12\nu(z+h)^2}{R_2^5}\Big) \\ \sigma_{zz} &= 2\mu\frac{Ka^3}{3}\Big(\frac{-2}{a^3} - \frac{1}{R_2^3} - \frac{18z(z+h)}{R_2^5} + \frac{3(z+h)^2}{R_2^5} + \frac{30z(z+h)^3}{R_2^7}\Big) \\ \sigma_{rz} &= -2\mu Ka^3r\Big(\frac{3z+h}{R_2^5} - \frac{10z(z+h)^2}{R_2^7}\Big) \end{aligned} \tag{3.22}$$

The results obtained above are in good agreement to those of Mindlin and Cheng (1950) for the spherical inclusion in the interior of a thermoelastic semi-infinite solid using the usual thermoelastic relation.

4. Numerical results and discussion

In this Section, graphical representations of the strain and stress components at the points $(0, 0)$ and $(0, h - a)$ just outside the spherical inclusion in the thermoelastic half-space are obtained using MATLAB software programming. The numerical computations are carried out for Poisson's ratios $\nu = 0.1$ to 0.5. Figures 2a and 2b respectively show the variation of strain

components $e_{rr}(= e_{\theta\theta})$ and e_{zz} at the point $(0, 0)$ for exterior points of the spherical inclusion along the distance and varying Poisson's ratio from 0.1 to 0.5. From Fig. 2a, we observe that the strain $e_{rr}(= e_{\theta\theta})$ decreases smoothly with increasing values of the distance h/a, and it vanishes at infinitely large values of h/a. Also, as Poisson's ratio ν increases from 0.1 to 0.5, this strain increases quantitatively. From Fig. 2b, we observe that the strain e_{zz} assumes negative values for all the values of Poisson's ratio ν ranging from 0.1 to 0.5. Further, it continuously increases with the increasing distance h/a assuming the value of zero at infinitely large values of h/a. In Figs. 3a and 3b, respectively, the variation of strain components $e_{rr}(= e_{\theta\theta})$ and e_{zz} at the point $(0, h - a)$ just outside the spherical inclusion are presented for exterior points. From Fig. 3b, it can be seen that the strain e_{zz} first increases and then decreases continuously as the distance h/a increases. Further, this strain approaches a finite negative value (depending on Poisson's ratio) at infinitely large values of the distance h/a.

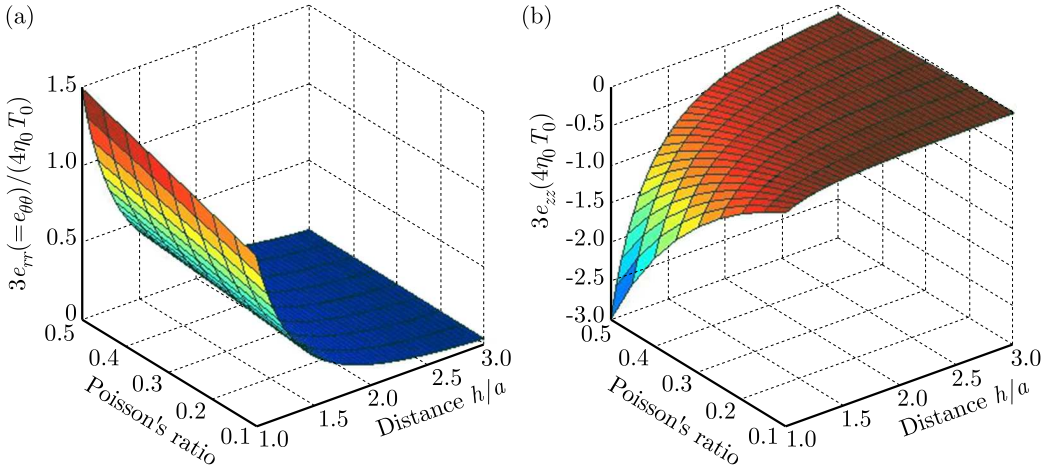

Fig. 2. (a) Strain component $e_{rr}(= e_{\theta\theta})$ at the point $(0, 0)$ for exterior points of the spherical inclusion, (b) strain component e_{zz} atthe point $(0, 0)$ for exterior points of the spherical inclusion

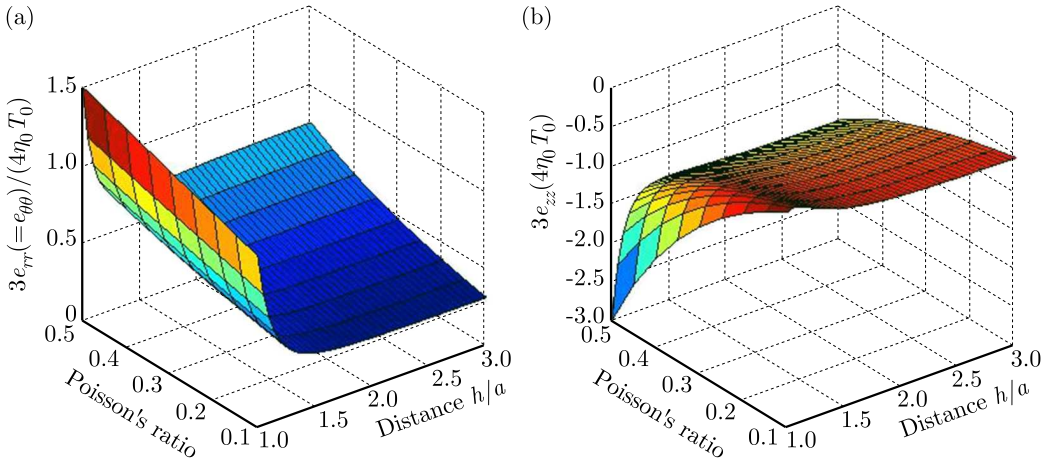

Fig. 3. (a) Strain component $e_{rr}(= e_{\theta\theta})$ at the point $(0, h - a)$ just outside the spherical inclusion for exterior points, (b) strain component e_{zz} at the point $(0, h - a)$ just outside the spherical inclusion for exterior points

Figure 4 shows the variation of the stress component $\sigma_{rr}(= \sigma_{\theta\theta})$ at the point $(0, 0)$ for exterior points of the spherical inclusion in the thermoelastic half-space. From Fig. 4, we observe that the stress component $\sigma_{rr}(= \sigma_{\theta\theta})$ decreases gradually as the distance h/a increases and it vanishes at infinitely large of h/a. Also, as Poisson's ratio ν increases from 0.1 to 0.5, this stress increases

quantitatively as shown in the figure. Figures 5a and 5b, respectively, show the variation of the stress component $\sigma_{rr}(=\sigma_{\theta\theta})$ and σ_{zz} at the point $(0, h-a)$ just outside the spherical inclusion in the thermoelastic half-space. From Fig. 5a, we observe that the stress component $\sigma_{rr}(=\sigma_{\theta\theta})$ also decreases gradually with the increasing distance h/a but it assumes finite positive values (depending on Poisson's ratio) at infinitely large values of the distance h/a. From Fig. 5b, we observe that as Poisson's ratio increases from 0.1 to 0.5, the stress decreases more rapidly with increasing values of the distance h/a and tends to finite negative values (depending on Poisson's ratio) at infinitely large values of the distance h/a.

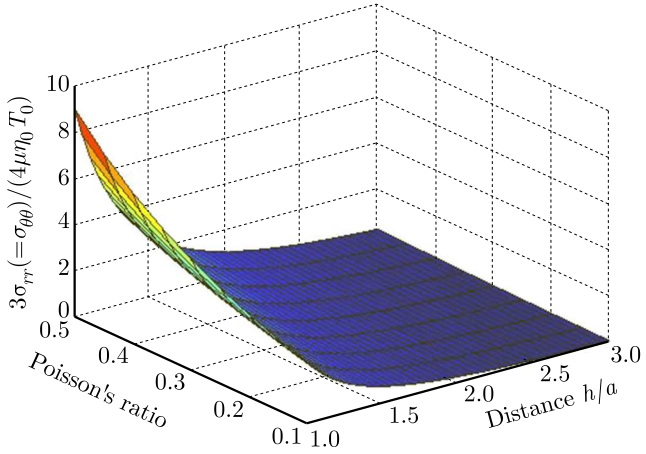

Fig. 4. Stress component $\sigma_{rr}(=\sigma_{\theta\theta})$ at the point $(0, 0)$ for exterior points of the spherical inclusion

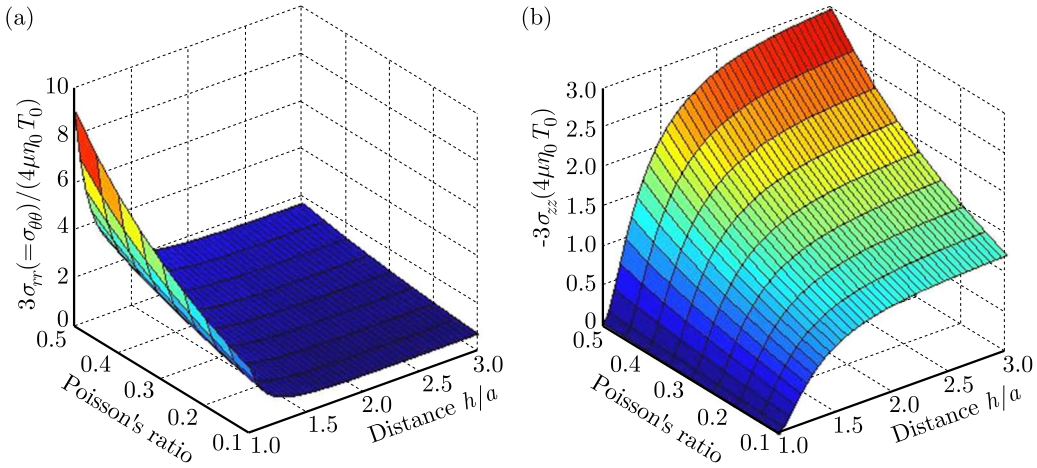

Fig. 5. (a) Stress component $\sigma_{rr}(=\sigma_{\theta\theta})$ at the point $(0, h-a)$ just outside the spherical inclusion for exterior points, (b) stress component σ_{zz} at the point $(0, h-a)$ just outside a spherical inclusion for exterior points

Figures 6a and 6b, respectively, show the variation of strain components $e_{rr}(=e_{\theta\theta})$ and e_{zz} at the point $(0, h)$ for interior points of the spherical inclusion. As observed from Fig. 6a, the strain $e_{rr}(=e_{\theta\theta})$ increases continuously with the increasing distance h/a and with increasing values of Poisson's ratio ν from 0.1 to 0.5. From Fig. 6b, we observe that the strain e_{zz} decreases gradually for all values of Poisson's ratio $\nu = 0.1$ to 0.5 as the distance h/a increases. It is noticed from Figs. 6a and 6b that these strains assume finite positive values (depending on Poisson's ratio) at infinitely large values of the distance h/a. Figures 7a and 7b, respectively, show the variation of stress components $\sigma_{rr}(=\sigma_{\theta\theta})$ and σ_{zz} at the point $(0, h)$ for interior points of the spherical inclusion. It is noticed from Figs. 7a and 7b that the stresses decrease continuously

as the distance h/a increases and these assume finite negative values (depending on Poisson's ratio) at infinitely large values of distance h/a.

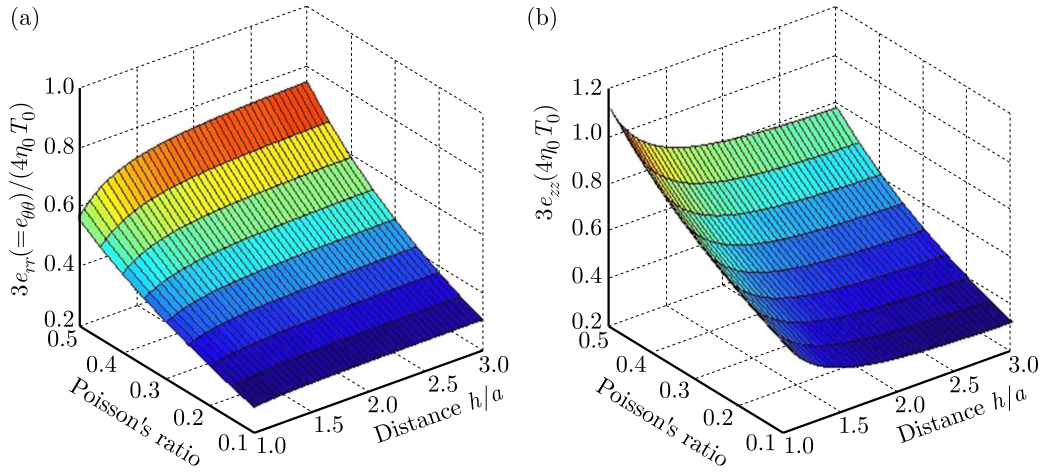

Fig. 6. (a) Strain component $e_{rr}(= e_{\theta\theta})$ at the point $(0, h)$ for interior points of the spherical inclusion, (b) strain component e_{zz} at the point $(0, h)$ for interior points of the spherical inclusion

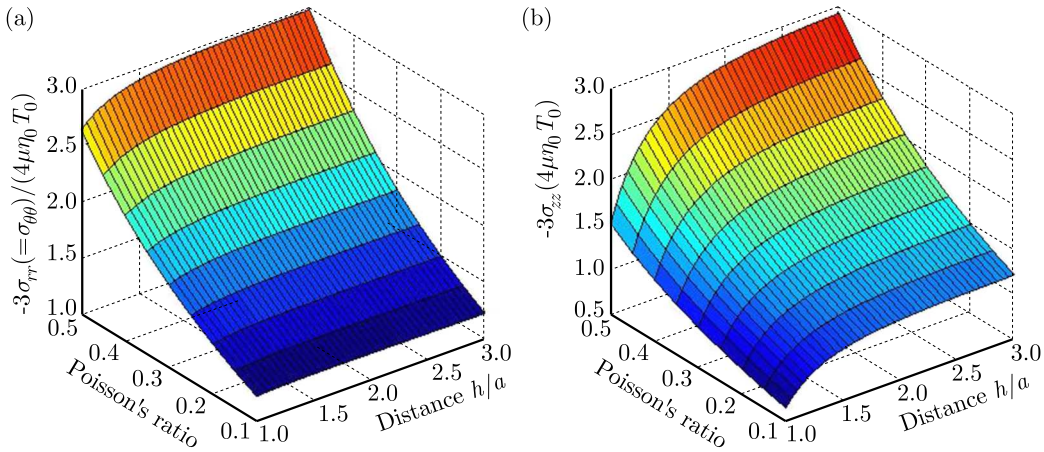

Fig. 7. (a) Stress component $\sigma_{rr}(= \sigma_{\theta\theta})$ at the point $(0, h)$ for interior points of the spherical inclusion, (b) stress component σ_{zz} at the point $(0, h)$ for interior points of the spherical inclusion

5. Conclusion

In this paper, closed form analytical expressions for thermoelastic strain and stress components due to a spherical inclusion in a thermoelastic half-space are obtained. These expressions are derived in axisymmetric cylindrical coordinates in the context of steady-state uncoupled thermoelasticity using thermoelastic displacement potential functions. The thermoelastic strain and stress components for the exterior points of the spherical inclusion are the same as those of the center of dilatation. The variations of the thermoelastic strain and stress components for the exterior and interior points of the spherical inclusion are also shown graphically for different values of Poisson's ratios. It is observed that the strain and stress components at the points $(0, h-a)$ and $(0, h)$ approach finite values depending on Poisson's ratio at infinitely large values of the distance h/a, whereas at the point $(0, 0)$ these quantities tend to zero as h/a tends to infinity. Thus, Poisson's ratio has a significant effect on the strain and stress components due to the spherical inclusion in the thermoelastic half-space.

Acknowledgement

We are thankful to the University Grants Commission, New Delhi, for financial support. We also thank the reviewer for useful suggestions in the improvement of our paper.

References

1. Barber J.R., 2002, *Elasticity*, Second Edition, Kluwer Academic Publishers, Dordrecht
2. Boley B.A., Weiner J.H., 1997, *Theory of Thermal Stresses*, Dover Publications, New York
3. Boresi A.P., Chong K.P., Lee J.D., 2011, *Elasticity in Engineering Mechanics*, Third Edition, John Wiley & Sons, Inc., Hoboken, New Jersey
4. Davies J.H., 2003, Elastic field in a semi-infinite solid due to thermal expansion or a coherently misfitting inclusion, *Journal of Applied Mechanics*, **70**, 5, 655-660
5. Duhamel J.M.C., 1837, Second mémoire sur les phénomènes thermo-mécaniques, *Journal de l'Ecole Polytechnique*, **15**, 25, 1-57
6. Goodier J.N., 1937, On the integration of the thermoelastic equations, *Philosophical Magazine*, **7**, 23, 1017-1032
7. Guell D.L., Dundurs J., 1967, Further results on center of dilatation and residual stresses in joined elastic half-spaces, [In:] *Developments in Theoretical and Applied Mechanics*, W.A. Shaw (Edit.), **3**, 105-115, Pergamon Press, Oxford
8. Hu S.M., 1989, Stress from a parallelepipedic thermal inclusion in a semispace, *Journal of Applied Physics*, **66**, 6, 2741-2743
9. Itou S., 2014, Plane strain and plane stress problems in thermoelasticity, [In:] *Encyclopedia of Thermal Stresses*, Richard B. Hetnarski (Eds.), Springer Netherlands, 3921-3930
10. Kolesov V.S., Vlasov N.M., Tisovskii L.O., Shatskii I.P., 1992, The stress-deformation state of an elastic half-space with a spheroidal thermal inclusion, *International Applied Mechanics*, **28**, 7, 426-434
11. Kumagai H., Maeda Y., Ichihara M., Kame N., Kusakabe T., 2014, Seismic moment and volume change of a spherical source, *Earth Planets and Space*, **66**, 7, 1-10
12. Leroux J., Fulleringer B., Nelias D., 2010, Contact analysis in presence of spherical inhomogeneities within a half-space, *International Journal of Solids and Structures*, **47**, 3034-3049
13. Linzhi W., 2003, The elastic field induced by a hemispherical inclusion in the half-space, *Acta Mechanica Sinica*, **19**, 3, 253-262
14. Liu S., Wang Q., 2005, Elastic fields due to eigenstrains in a half-space, *Journal of Applied Mechanics*, **72**, 871-878
15. Mindlin R.D., Cheng D.H., 1950, Thermoelastic stress in the semi-infinite solid, *Journal of Applied Physics*, **21**, 931-933
16. Neumann F., 1885, *Vorlesungen über die Theorie der Elasticität der festen Körper und des Lichtäthers*, B.G. Teubner, Leipzig
17. Nowacki W., 1957, State of stress in an infinite and semi-infinite elastic space due to an instantaneous source of heat, *Bulletin de L'Academic Polonaise des Sciences*, **IV**, 5, 2, 77-86
18. Nowacki W., 1986, *Thermoelasticity*, Second Edition, Pergamon Press, PWN-Polish Scientific Publishers, Warszawa
19. Nowinski J., 1961, Biharmonic solutions to the steady-state thermoelastic problems in three dimensions, *Zeitschrift für angewandte Mathematik und Physik (ZAMP)*, **XII**, 2, 132-149
20. Nowinski J.L., 1963, A mean value theorem for an arbitrary steady-state thermoelastic problem for a solid sphere, *Journal of the Society for Industrial and Applied Mathematics*, **11**, 3, 623-631

21. Nowinski J.L., 1978, *Theory of Thermoelasticity with Applications*, Alphen Aan Den Rijn Sijthoff and Noordhoff International Publishers

22. Sadd M.H., 2005, *Elasticity – Theory, Applications and Numerics*, Elsevier Academic Press Inc., UK

23. Sen B., 1957, Note on a direct method of solving problems of elastic plates with circular boundaries having prescribed displacement, *Kurze Mitteilungen-Brief Reports-Communications breves*, **VIII**, 307-309

24. Sharma B.D., 1957, Stresses due to a nucleus of thermo-elastic strain (i) in an infinite elastic solid with spherical cavity and (ii) in a solid elastic sphere, *Zeitschrift für angewandte Mathematik und Physik (ZAMP)*, **VIII**, 142-150

25. Timoshenko S., Goodier J.N., 1951, *Theory of Elasticity*, Second Edition, McGraw-Hill, New York

26. Truesdell C. (Edit.), 1984, *Mechanics of Solids, Volume II, Linear Theories of Elasticity and Thermoelasticity*, Springer-Verlag Berlin Heidelberg.

27. Wang M., Huang K., 1991, Thermoelastic problems in the half space – An application of the general solution in elasticity, *Applied Mathematics and Mechanics*, **12**, 9, 849-862

28. Yu H.Y., Sanday S.C., 1992, Centre of dilatation and thermal stresses in an elastic plate, *Proceedings of the Royal Society of London A*, **438**, 103-112

29. Yu H.Y., Sanday S.C., Rath B.B., 1992, Thermoelastic stresses in bimaterials, *Philosophical Magazine A*, **65**, 5, 1049-1064

30. Yu J.H., Kuang Z.B., Gu M.Y., 2002, Thermal stresses in joined semi-infinite solids, *Journal of Thermal Stresses*, **25**, 9, 889-905

31. Zhou K., Chen W.W., Keer L.M., Wang Q. J., 2009, A fast method for solving three-dimensional arbitrarily shaped inclusions in a half space, *Computer Methods in Applied Mechanics and Engineering*, **198**, 9-12, 885-892

Manuscript received December 13, 2016; accepted for print June 24, 2017

JOURNAL OF THEORETICAL AND APPLIED MECHANICS
55, 4, pp. 1381-1395, Warsaw 2017
DOI: 10.15632/jtam-pl.55.4.1381

POROUS MATERIAL EFFECT ON GEARBOX VIBRATION AND ACOUSTIC BEHAVIOR

Mohamed Riadh Letaief, Lassaad Walha, Mohamed Taktak,
Fakher Chaari, Mohamed Haddar

Mechanical, Modeling and Manufacturing Laboratory LA2MP, National School of Engineers of Sfax, Sfax, Tunisia
e-mail: walhalassaad@yahoo.fr

In this paper, we define a resolution method to study the effect of a porous material on vibro-acoustic behavior of a geared transmission. A porous plate is coupled with the gearbox housing cover. The developed model depends on the gearbox characteristic and poroelastic parameters of the porous material. To study the acoustic effect of the housing cover, the acoustic transmission loss is computed by simulating numerically the elastic-porous coupled plate model, and the numerical implementation is performed by directly programming the mixed displacement-pressure formulation. To study the vibration effect, the bearing displacement is computed using a two-stage gear system dynamical model and used as the gearbox cover excitation. Numerical implementation is performed by direct programming of the Leclaire formulation.

Keywords: porous material, gearbox, vibro-acoustic behavior

1. Introduction

Controlling the vibro-acoustic behavior of rotating machinery has become a quality factor to improve the comfort by reducing noise and vibration levels. One of the major noise and vibration sources are geared transmissions (gears, shafts, roller bearings and the housing). The generalized forces which generate the vibration response of the gearbox housing are multiple, as expressed by Remond *et al.* (1993). Sources of vibration excitations generated by geared transmissions can be divided into two categories, first the internal excitation sources like the static transmission error under load, elastic deformations of teeth, fluctuation in the frictional force developed by Houser (1991), Aziz and Seirg (1994), schock phenomenon and the projection or flows of the lubricant on walls of the housing according to Houser (1991) and Houjoh and Umezawa (1992). External sources of excitation can be associated with the fluctuations in engine torque and load inertia.

Regardless of directivity of the source, larger walls of the housing are more flexible and contribute most to noise radiation. A parametric study performed by Sibe (1997) shows that the more walls are heavy, stiff and thick, the higher is the acoustic transmission loss of the housing. An increase in the thickness of the housing is unfortunately contrary to the desire of manufacturers who always want to increase the specific power of their transmissions. Note that in the majority of gearboxes, their housings covers are more flexible than other parts body of the housing and have the largest surface of acoustic radiation while looking for a method how to decrease their acoustic emission, some research work as that carried out by Guezzen (2004), confirmed effects of structure of the gearbox cover on noise radiation. In this context, we study a housing cover of a gearbox coupled with a porous material plate to isolate sources of noise radiation.

Various models have been developed to describe the acoustic propagation in porous media. One of the best known and the easiest to implement is the model of Delany and Bazley (1970).

However, this model is limited because it represents only tested materials and does not express the phenomenon related to skeleton vibrations. To model more accurately the dissipative effects, unlike in the model developed by Johnson *et al.* (1987), one may introduce a function of viscous form which is not limited by the geometric nature of the skeleton. Modeling of the variation of the viscous dissipation modulus may require introduction of the viscous characteristic length which is an intrinsic parameter of the material that can be obtained through experience. Similarly, Champoux and Allard (1991) defined the thermal characteristic length as an intrinsic parameter expressing thermal effects. Lafarge *et al.* (1997) introduced thermal permeability to improve thermal effects at low frequencies. However, the model with a rigid structure is not suitable when the skeleton of the material is deformed or mobile: this is the case in many applications where a porous material is directly subjected to a mechanical or acoustic wave excitation which is the subject of our paper. Allard (1993) adapted a model for acoustic applications by integrating various contributions previously cited, see Johnson *et al.* (1987), Champoux and Allard (1991) and Lafarge *et al.* (1997). This model, commonly called the Biot-Allard model is used in our study since porous materials are subjected to the imposed displacement or acoustic pressure.

In Section 2, we describe equations of motion for the dynamic model of gearbox and the housing cover (elastic and porous coupled plate) implementing porous models. In Section 3, we present the resolution method (input and output, geometry, implemented porous and boundary conditions). In Section 4, we describe the porous plate effect on vibration and the acoustic transmission loss of our gearbox housing cover by a study case.

2. Gearbox modelling

In most gearboxes, especially those having reduced sizes, the wheel axis is in the same plane between the two parts of the gearbox (Fig. 1) that enables easy assembling of the wheels.

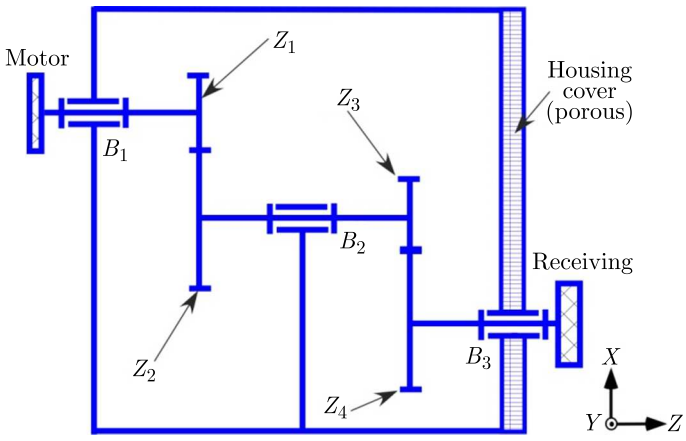

Fig. 1. Plane configuration of a two-stage gear system and the porous housing cover

We defined a fixed reference frame (O, X_0, Y_0) in the model. α_i are pressure angles of two gearmesh contact. In this paper, these angles are equal to 20° in the case of the gearings with right teeth.

2.1. Dynamic model of a two-stage gear system

A two-stage gear system is composed of two trains of gearings. Every train links two blocks. So, the gear system has in total three blocks ($j = 1, 2, 3$). Every block is supported by a flexible bearing whose bending stiffness is k_{xj} and the traction compression stiffness is k_{yj}. The dynamic

model developed has twelve degrees of freedom: six angular movements γ_{ji} and six linear movements x_j and y_j (Fig. 2). The motor and receiving wheels are introduced by inertias I_m and I_r as expressed by Miller (1999) with the assumption that we use short shafts. The other spur gears constitute the gearbox. The gearmeshes are modeled by a linear spring $ks(t)$ $(s = 1, 2)$ along the lines of action represented in Fig. 2. α_i are pressure angles of two gearmesh contact. The angular displacements of every wheel are noticed by γ_{ji} with the indices $j = 1$ to 3 designating the number of the block, and $i = 1, 2$ designating the two wheels of each block. Besides, the linear displacements of the bearing denoted by x_j and y_j are measured in the plane which is orthogonal to the axis of wheel rotation.

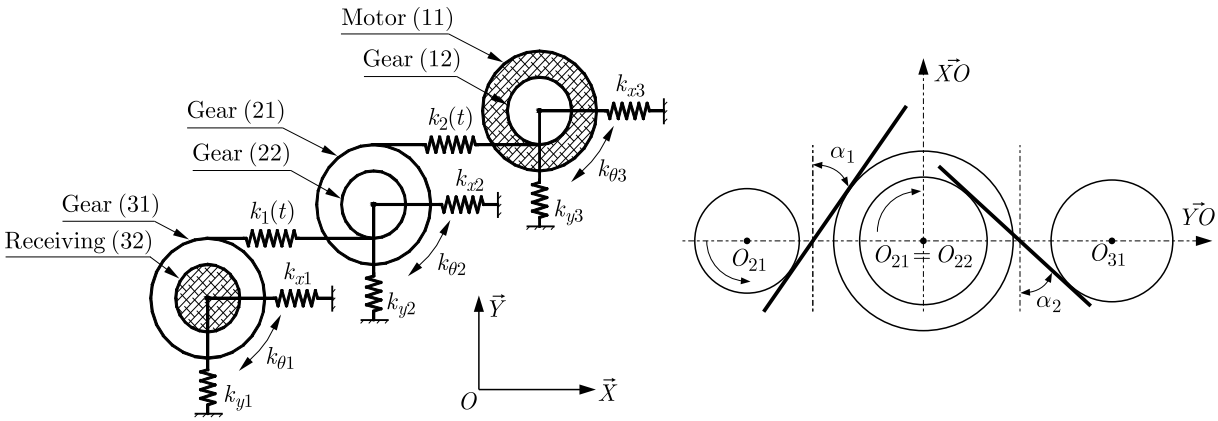

Fig. 2. Model of the two-stage gear system developed by Walha *et al.* (2009)

2.2. Modeling of the mesh stiffness

Generally, we can model variation of the gearmesh stiffness $k_i(t)$ by a square wave which was developed by Velex (1988). The variation in stiffness comes from the fact that during meshing there is a change in the number of contacting pairs. For spur gears, there is a change for two pairs of teeth in contact for a period of meshing. The square wave variation is the best representative of the real phenomenon, and is represented in Fig. 3.

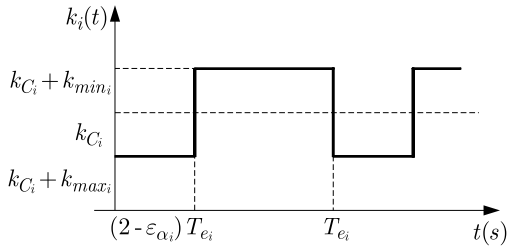

Fig. 3. Modeling of the mesh stiffness variation

The gearmesh stiffness variation can be decomposed into two components: an average component denoted by k_{c_i}, and a time-dependent one denoted by $k_{v_i}(t)$.

The extreme values of the mesh stiffness are defined by

$$k_{min_i} = -\frac{k_c}{2\varepsilon_{\alpha i}} \qquad k_{max_i} = -k_{min_i}\frac{2 - \varepsilon_{\alpha i}}{\varepsilon_{\alpha i} - 1} \tag{2.1}$$

The terms $\varepsilon_{\alpha i}$ are the contact ratio corresponding to the two gearmesh contacts.

2.3. Equations of motion

Applying the Lagrange equations, we obtain a system of differential equations governing the dynamic behavior. It can be written in the following usual matrix form

$$\mathbf{M}\ddot{\mathbf{q}} + [\mathbf{K}_s + \mathbf{K}(t)]\mathbf{q} = \mathbf{F}_0 \tag{2.2}$$

where $\mathbf{q}$ is the generalized coordinate vector, $\mathbf{M}$ is the mass matrix expressed by

$$\mathbf{M} = \text{diag}\,(m_1, m_1, m_2, m_2, m_3, m_3, I_m, I_{12}, I_{21}, I_{22}, I_{31}, I_r)$$

m_j is mass of the block j, I_m is the polar inertia of the motor wheel, I_r is the polar inertia of the receiving wheel.

The matrix of average stiffness of the structure is defined by

$$\mathbf{K}_s = \begin{bmatrix} \mathbf{K}_p & \mathbf{0} \\ \mathbf{0} & \mathbf{K}_\theta \end{bmatrix}$$

$$\mathbf{K}_p = \begin{bmatrix} k_{x1} & 0 & 0 & 0 & 0 & 0 \\ 0 & k_{y1} & 0 & 0 & 0 & 0 \\ 0 & 0 & k_{x2} & 0 & 0 & 0 \\ 0 & 0 & 0 & k_{y2} & 0 & 0 \\ 0 & 0 & 0 & 0 & k_{x3} & 0 \\ 0 & 0 & 0 & 0 & 0 & k_{y3} \end{bmatrix}$$

$$\mathbf{K}_\theta = \begin{bmatrix} k_{\theta1} & -k_{\theta1} & 0 & 0 & 0 & 0 \\ -k_{\theta1} & k_{\theta1} & 0 & 0 & 0 & 0 \\ 0 & 0 & k_{\theta2} & -k_{\theta2} & 0 & 0 \\ 0 & 0 & -k_{\theta2} & k_{\theta2} & 0 & 0 \\ 0 & 0 & 0 & 0 & k_{\theta3} & -k_{\theta3} \\ 0 & 0 & 0 & 0 & -k_{\theta3} & k_{\theta3} \end{bmatrix}$$

where $\mathbf{K}_p$ is the bearing stiffness matrix and $\mathbf{K}_\theta$ is the shaft torsional stiffness matrix.

$\mathbf{K}(t)$ is the stiffness matrix of the engagement which is variable over time

$$\mathbf{K}(t) = \begin{bmatrix} \mathbf{K}_1(t) & \mathbf{K}_{12}(t) \\ \mathbf{K}_{12}^{\mathrm{T}}(t) & \mathbf{K}_2(t) \end{bmatrix}$$

where

$$\mathbf{K}_1(t) = \begin{bmatrix} k_1 s_1^2 & -k_1 s c_1 & -k_1 s_1^2 & k_1 s c_1 & 0 & 0 \\ -k_1 s c_1 & k_1 c_1^2 & k_1 s c_1 & -k_1 c_1^2 & 0 & 0 \\ -k_1 s_1^2 & k_1 s c_1 & k_1 s_1^2 + k_2 s_2^2 & -k_1 s c_1 - k_2 s c_2 & -k_2 s_2^2 & k_2 s c_2 \\ k_1 s c_1 & -k_1 c_1^2 & -k_1 s c_1 - k_2 s c_2 & k_1 c_1^2 + k_2 c_2^2 & k_2 s c_2 & -k_2 c_2^2 \\ 0 & 0 & -k_2 s_2^2 & k_2 s c_2 & k_2 s_2^2 & -k_2 s c_2 \\ 0 & 0 & k_2 s c_2 & -k_2 c_2^2 & -k_2 s c_2 & k_2 c_2^2 \end{bmatrix}$$

$$\mathbf{K}_{12}(t) = \begin{bmatrix} 0 & -k_1 r_{b12} s_1 & -k_1 r_{b21} s_1 & k_1 s c_1 & 0 & 0 \\ 0 & k_1 r_{b12} c_1 & k_1 r_{b21} c_1 & -k_1 c_1^2 & 0 & 0 \\ 0 & k_1 r_{b12} s_1 & k_1 r_{b12} s_1 & -k_1 s c_1 - k_2 s c_2 & -k_2 s_2^2 & k_2 s c_2 \\ 0 & -k_1 r_{b12} c_1 & -k_1 s c_1 - k_2 s c_2 & k_1 c_1^2 + k_2 c_2^2 & k_2 s c_2 & -k_2 c_2^2 \\ 0 & 0 & -k_2 s_2^2 & k_2 s c_2 & k_2 s_2^2 & -k_2 s c_2 \\ 0 & 0 & k_2 s c_2 & -k_2 c_2^2 & -k_2 s c_2 & k_2 c_2^2 \end{bmatrix}$$

$$\mathbf{K}_2(t) = \begin{bmatrix} 0 & 0 & 0 & 0 & 0 & 0 \\ 0 & k_1 r_{b12}^2 & k_1 r_{b12} r_{b21} & 0 & 0 & 0 \\ 0 & k_1 r_{b12} r_{b21} & k_1 r_{b21}^2 & 0 & -k_2 s_2^2 & 0 \\ 0 & 0 & 0 & k_2 r_{b22}^2 & k_2 r_{b22} r_{b31} & 0 \\ 0 & 0 & 0 & k_2 r_{b22} r_{b31} & k_2 r_{b31}^2 & 0 \\ 0 & 0 & 0 & 0 & 0 & 0 \end{bmatrix}$$

where r_b is the base radius; s_i, sc_i and c_i^2 are simplifications of the functions: $s_i = \sin^2 \phi_i$, $sc_i = \sin \phi_i \cos \phi_i$ and $c_i^2 = \cos^2 \phi_i$, respectively. $\mathbf{F}_0$ is the vector of external static forces and can be expressed as

$$\mathbf{F}_0 = [0, 0, 0, 0, 0, 0, C_m, 0, 0, 0, 0, -C_r]^{\mathrm{T}}$$

C_m and C_r are the motor and receiving wheel torques, respectively.

3. Modelling of the housing cover

In our study, the housing cover is modeled as an elastic and porous coupled plate. In fact, two porous models are implemented.

3.1. Leclaire's formulation

Leclaire's formulation is based on the classical theory of homogeneous plates and on the Biot stress-strain relations in an isotropic porous medium with a uniform porosity. The vibrations of a rectangular porous plate can be described by two coupled dynamic equations of equilibrium relating the plate deflection w_s and the fluid/solid relative displacement w.

In the case of a plate with thickness h and subjected to a load q, these two equations can be expressed as

$$\begin{aligned} &\Big(D + \frac{\phi^2 \widetilde{\lambda}^f h^3}{12\phi^2}\Big)\nabla^4 w_s + h(\rho_1 \ddot{w}_s + \rho_0 \ddot{w}) = q \\ &\frac{\widetilde{\lambda}^f h}{\phi}\nabla^2 w_s - h(\rho_0 \ddot{w}_s + m\ddot{w}) = 0 \end{aligned} \tag{3.1}$$

where D is the flexural rigidity, ρ_0 – density of the fluid, ρ_1 – density of the frame, ϕ – porosity, $\widetilde{\lambda}^f$ – material expansion coefficient and m is the mass parameter introduced by Biot (1962) given by

$$m(\omega) = \frac{\tau(\omega)}{\phi}\rho_0 \tag{3.2}$$

where ω is the pulsation, $\tau(\omega)$ is the dynamic tortuosity expressed as folows

$$\tau(\omega) = \tau_\infty - j\frac{\sigma\phi}{\rho_0}F(\omega)\sqrt{1 + \frac{4\eta\alpha_\infty^2\rho_0}{\sigma^2\Lambda^2\phi^2}j\omega} \qquad F(\omega) = \sqrt{1 - \mathrm{i}\frac{4\tau_\infty^2\kappa^2\rho_0\omega}{\eta\Lambda^2\phi^2}} \tag{3.3}$$

where $F(\omega)$ is the viscosity correction function introduced by Johnson *et al.* (1987), α_∞ is the tortuosity of pores, η is the damping coefficient, Λ is the characteristic dimension of pores, σ is the flow resistivity.

The space derivatives are written with the help of the operators $\nabla^4 = \nabla^2(\nabla^2)$ and $\nabla^2 = \partial^2/prtx^2 + \partial^2/\partial y^2$ of the system of co-ordinates (x, y) while the double dots denote the second time derivative.

In the first equation of equilibrium (or plate equation) $[D+\phi^2\widetilde{\lambda}^f h^3/(12\phi^2)]\nabla^4 w_s$ represents the internal potential force (per unit surface) within the fluid-saturated plate, while the inertia terms $h\rho_1\ddot{w}_s$ and $h\rho_0\ddot{w}$ and the load q are considered as external forces. Similarly, the internal force associated with the fluid-solid relative displacement may be defined, and is given by $(\widetilde{\lambda}^f h/\phi)\nabla^2 w_s$ while the external forces can be taken as $hm\ddot{w}$ and $h\rho_0\ddot{w}_s$.

We note that the Leclaire formulation is a 2D one and the unknown variables are w_s and w. All terms used in this formulation are based on poroelastic material characteristics.

3.2. The mixed formulation

In order to reduce the computation time enlarged by complexity of the problem, mixed formulations (u,p) have been implemented. This formulation was developed by Atalla *et al.* (1998) using the classical equations of Biot where u represents displacement field of the solid phase and p is the pore pressure. Replacing the displacement of the fluid phase by its pressure allows us to reduce degrees of freedom from 6 to 4 per node, valid only for harmonic motion. It is also accurate in the classical formulation (u,U). The modified equations of equilibrium (for small harmonic oscillations) are expressed as follows

$$\widehat{\sigma}^s_{ij/j}S+\omega^2\widetilde{\rho}u_i+\widetilde{\gamma}p_{/i}=0 \qquad -\omega^2\frac{\widetilde{\rho}_{22}\widetilde{\gamma}}{\phi^2}u_{i/i}+\omega^2\frac{\widetilde{\rho}_{22}}{\widetilde{\lambda}^f}p+p_{/ii}=0 \tag{3.4}$$

where $\widehat{\sigma}^s_{ij}$ is the stress tensor of the material "in vacuo" (does not depend on the fluid phase). It is written by

$$\widehat{\sigma}^s_{ij}=\hat{\widetilde{\lambda}}^s\varepsilon^s_{kk}\delta_{ij}+2\mu^s\varepsilon^s_{ij} \qquad \varepsilon^s_{ij}=\frac{1}{2}(u_{i/j}+u_{j/i}) \tag{3.5}$$

where ε^s_{ij} is the strain tensor of the skeleton, μ^s is the shear modulus of the porous material. The above equations depend on certain factors: $\hat{\widetilde{\lambda}}^s$, $\widetilde{\rho}$, $\widetilde{\gamma}$ and $\widetilde{\lambda}^f$. These are based on intrinsic poroelastic characteristics introduced by Horoshenkov and Swift (2001) and Umnova *et al.* (2001).

4. Resolution method

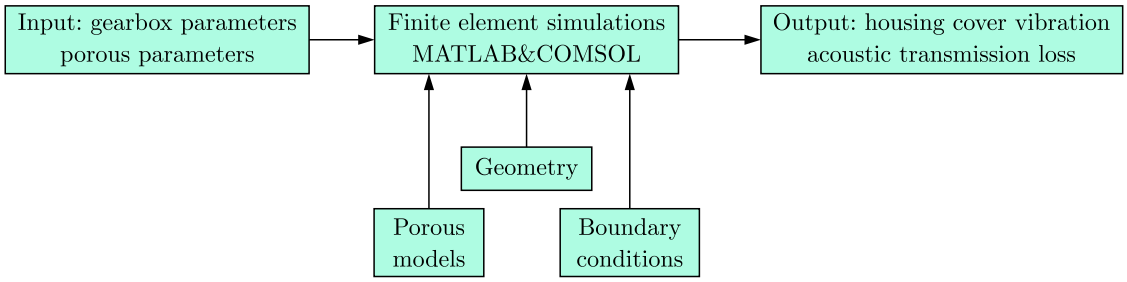

Fig. 4. SADT diagram

For the two cases of study (acoustic and vibration behavior), the implemented porous models are analysed by the finite element software COMSOL and MATLAB. The equations of motion are introduced by the EDP module of COMSOL software.

4.1. Porous models

In COMSOL, the general form of PDE (for a temporal analysis) must be expressed in the following matrix form

$$\mathbf{\Gamma} \cdot \nabla = \mathbf{F} \tag{4.1}$$

where $\mathbf{\Gamma}$ is the matrix of the flux vectors and $\mathbf{F}$ is the right part of the vector. In Cartesian coordinates, the gradient/divergence operator vector ∇ is defined as follows

$$\nabla = \begin{bmatrix} \dfrac{\partial}{\partial x} \\ \dfrac{\partial}{\partial y} \end{bmatrix} \tag{4.2}$$

4.1.1. Leclaire's formulation

If we adapt Leclaire's formulation, Eqs. (3.1), to the EDP form in COMSOL, we obtain the following equations

$$\mathbf{\Gamma} = \begin{bmatrix} \dfrac{\partial z}{\partial x} & \dfrac{\partial z}{\partial y} \\ \dfrac{\partial w_s}{\partial x} & \dfrac{\partial w_s}{\partial y} \\ \dfrac{\partial w}{\partial x} & \dfrac{\partial w}{\partial y} \end{bmatrix} \qquad \mathbf{F} = \begin{bmatrix} \dfrac{1}{D + \alpha^2 M h^3/12} \left(q + h\omega^2(\rho w_s + \rho_f w)\right) \\ \dfrac{1}{\alpha M h} \left(\Delta P - h\omega^2(\rho_f w_s + m w)\right) \\ z \end{bmatrix} \tag{4.3}$$

4.1.2. The mixed formulation

If we adapt „the mixed formulation", equations (3.4),to the EDP form of COMSOL, we obtain the following equations

$$\mathbf{\Gamma} = \begin{bmatrix} \Gamma_{ij} \\ \Gamma_{4i} \end{bmatrix} = \begin{bmatrix} \mu^S(u_{i/j} + u_{j/i}) + \widetilde{\lambda}^S u_{k/k}\delta_{ij} \\ p_{/i} \end{bmatrix} \qquad \mathbf{F} = \begin{bmatrix} F_i \\ F_4 \end{bmatrix} = \begin{bmatrix} -\omega^2 \rho_e u_i - \gamma p_{/i} \\ -\omega^2 \dfrac{\widetilde{\rho}_{22}}{\widetilde{\lambda}^f} p + \omega^2 \dfrac{\widetilde{\rho}_{22}\widetilde{\gamma}}{\phi^2} u_{i/i} \end{bmatrix} \tag{4.4}$$

4.2. Geometry

The geometry of the structure used in the numerical simulation is represented by a coupled porous plate (Fig. 5) with dimensions $a = b$. Thickness of the porous plate is hp, of the elastic plate hs. The system is loaded by the imposed displacement.

4.3. Input parameters

The input parameters are the gear system parameters: motor torque C_m and speed N_m, bearing and shaft stiffnesses kx_s, ky_s, $k\theta_s$, teeth number, width and module Z, b, m, average mesh stiffness k_{c1}, contact ratio $\varepsilon_{\alpha 1}$, pressure angle α and 9 poroelastic parameters: porosity ϕ, tortuosity α_∞, flow resistivity σ, thermal and viscous characteristic dimensions of pores, modulus of elasticity Λ and Λ', density of the skeleton ρ_1, skeleton Poisson's coefficient ν, damping coefficient η and the skeleton elasticity modulus E.

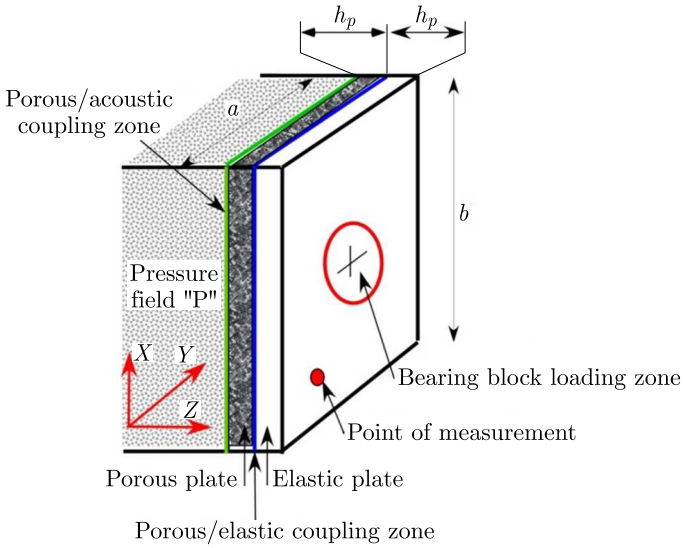

Fig. 5. System of co-ordinates in the plate

4.4. Output parameters

The first output is the normal incidence transmission loss T_L, as introduced by Rossing (2007)

$$T_L = 10 \log \frac{1}{|T_a|^2} \tag{4.5}$$

where $|T_a|^2$ is the normal incidence power transmission coefficient for an anechoically-terminated sample, that is the ratio of the sound power transmitted by the sample to the sound power incident on the sample. In the case of perfectly anechoic termination $T_a = C/A$

$$A = \frac{j(P_1 e^{jkx_2} - P_2 e^{jkx_1})}{2\sin[k(x_1 - x_2)]} \qquad C = \frac{j(P_3 e^{jkx_4} - P_4 e^{jkx_3})}{2\sin[k(x_3 - x_4)]} \tag{4.6}$$

with P_1 to P_4 are complex sound pressures at x_1 to x_4, and k is the wave number.

The second output is the bearing block load

$$F_b = K_{x3} x_3 + K_{y3} y_3 \tag{4.7}$$

x and y are bearing displacements, K is the bearing stiffness and F_b is the bearing block load.

4.5. Boundary conditions

The boundary conditions for EDP in COMSOL in their general form are as follows

$$\mathbf{0} = \mathbf{R} \qquad -\mathbf{\Gamma n} = \mathbf{G} + \left[\frac{\partial \mathbf{R}}{\partial u}\right]^{\mathrm{T}} \mu \tag{4.8}$$

The vector $\mathbf{R}$ and matrix $\mathbf{\Gamma}$ may be functions of the spatial co-ordinates with $\mathbf{n}$ being the normal unit vector leaving the boundary surface. These are the boundary conditions of Dirichlet and Neumann, respectively. The term μ in the Neumann boundary conditions is synonymous with the Lagrange multiplier.

There are several boundary conditions to be respected since there are two clamped coupled plates with four sides and poroelastic/acoustic as well as poroelastic/elastic coupling zones. Using the Biot-Allard formulation, the boundary conditions are discussed below.

- Imposed pressure field

The imposed pressure field $\overline{p}$ on the boundary of the porous medium allows us to write the following relations

$$\sigma_{ij}^t n_j = -\overline{p} n_i \qquad p = \overline{p} \tag{4.9}$$

which express the continuity of the total normal stress and continuity of pressure across the interface of the border. The total stress is equal to

$$\begin{aligned} \sigma_{ij}^t &= \sigma_{ij}^S + \sigma_{ij}^f = \sigma_{ij}^S - \phi p \delta_{ij} = \widehat{\sigma}_{ij}^S - \phi\Big(1 + \frac{\widetilde{\lambda}^{fS}}{\widetilde{\lambda}^f}\Big) p \delta_{ij} \\ &= \mu^S (u_{i/j} + u_{j/i}) + \widetilde{\lambda}^S u_{k/k} \delta_{ij} - \phi\Big(1 + \frac{\widetilde{\lambda}^{fS}}{\widetilde{\lambda}^f}\Big) p \delta_{ij} \end{aligned} \tag{4.10}$$

Using the second boundary condition of Eq. (4.9), the first one can be expressed as follows

$$-[\mu^S (u_{i/j} + u_{j/i}) + \widetilde{\lambda}^S u_{k/k} \delta_{ij}] n_j = \Big[1 - \phi\Big(1 + \frac{\widetilde{\lambda}^{fS}}{\widetilde{\lambda}^f}\Big)\Big] \overline{p} n_i \tag{4.11}$$

After identification, the terms $\mathbf{R}$ and $\mathbf{G}$ are as follows

$$\mathbf{R} = \begin{bmatrix} R_i \\ R_4 \end{bmatrix} = \begin{bmatrix} 0 \\ \overline{p} - p \end{bmatrix} \qquad \mathbf{G} = \begin{bmatrix} G_i \\ G_4 \end{bmatrix} = \begin{bmatrix} \Big[1 - \phi\Big(1 + \dfrac{\widetilde{\lambda}^{fS}}{\widetilde{\lambda}^f}\Big)\Big] \overline{p} n_i \\ 0 \end{bmatrix} \tag{4.12}$$

When a portion of the surface of the porous medium is coupled to an infinite acoustic medium, the condition of a free edge can be applied. This is assuming that $\overline{p} = 0$.

- Imposed displacement field

In the case of the imposed displacement field $\overline{u}_i$, the boundary conditions can be expressed by

$$u_i = \overline{u}_i \qquad v_i n_i - u_i n_i = 0 \tag{4.13}$$

The first term in Eq. (4.13) expresses the continuity between the imposed displacements and the solid phase displacements, while the second term describes the continuity of the normal displacement between the fluid and solid phase. In this second condition, it is necessary to replace the displacement of the fluid phase by the fluid pressure

$$v_i = \frac{\phi}{\omega^2 \widetilde{\rho}_{22}} p_{/i} - \frac{\widetilde{\rho}_{12}}{\widetilde{\rho}_{22}} u_i \tag{4.14}$$

which yields

$$p_{/i} n_i = \frac{\omega^2}{\phi} (\widetilde{\rho}_{12} + \widetilde{\rho}_{22}) u_i n_i \tag{4.15}$$

such as

$$\frac{\omega^2}{\phi} (\widetilde{\rho}_{12} + \widetilde{\rho}_{22}) = \frac{\omega^2}{\phi} (\rho_{12} + \rho_{22}) = \omega^2 \rho_0 \tag{4.16}$$

After identification, the terms $\mathbf{R}$ and $\mathbf{G}$ are as follows

$$\begin{aligned} R_i &= \overline{u}_i - u_i \qquad & R_4 &= 0 \\ G_i &= 0 \qquad & G_4 &= -\frac{\omega^2}{\phi} (\widetilde{\rho}_{12} + \widetilde{\rho}_{22}) u_i n_i \end{aligned} \tag{4.17}$$

Applying that $\overline{u}_i = 0$ implies the fact that our porous domain is embedded to a rigid wall.

- Acoustic – poroelastic coupling

In this case, the equations for continuity of the total normal stresses, acoustic pressure and fluid flow are as follows

$$\begin{aligned} &\sigma_{ij}^t n_j = -p^a n_j \qquad p = p^a \\ &(1-\phi)u_i n_i + \phi v_i n_i = \frac{1}{\rho_0 \omega^2}\nabla p^a n_i \end{aligned} \tag{4.18}$$

where p^a is pressure in the acoustic medium, ρ_0 its density and σ^t the total stress tensor in the poroelastic material. The vectors $\mathbf{G}$ and $\mathbf{R}$ will have the following components

$$\begin{aligned} &R_i = 0 \qquad R_4 = p - p^a \\ &G_i = \Big[1 - \phi\Big(1 + \frac{\widetilde{\lambda}^{fS}}{\widetilde{\lambda}^f}\Big)\Big]p^a n_i \qquad G_4 = 0 \end{aligned} \tag{4.19}$$

In addition, the continuity of the fluid flow at the coupling interface can be expressed as an imposed acceleration on the fluid in the acoustic environment. Replacing v_i by its expression, the normal acceleration can be obtained by

$$\frac{1}{\rho_0}\nabla p^a n_i = \omega^2\Big[u_i n_i\Big(1 - \phi\Big(1 + \frac{\widetilde{\rho}_{12}}{\widetilde{\rho}_{22}}\Big)\Big)\Big] + \omega^2\Big[\nabla p n_i\Big(\frac{\phi^2}{\omega^2\widetilde{\rho}_{22}}\Big)\Big] \tag{4.20}$$

For the Leclaire formulaion, a boundary condition can be considered. It is discussed below

- Clamped plate

At the boundary conditions, an embedding condition is introcuced

$$w_s = 0 \qquad U_f = 0 \tag{4.21}$$

The relative solid-fluid displacement is defined as follows

$$w = \phi\Big(U_f - w_s\Big) \qquad U_f = \frac{1}{\phi}w + w_s \tag{4.22}$$

where w_s is the solid displacement and U_f is the fluid displacement.

Subsequently, $\mathbf{R}$ and $\mathbf{G}$ are expressed by

$$\mathbf{R} = \begin{bmatrix} w_s \\ \dfrac{1}{\phi}w + w_s \\ 0 \end{bmatrix} \qquad \mathbf{G} = \begin{bmatrix} 0 \\ 0 \\ 0 \end{bmatrix} \tag{4.23}$$

The loading conditions q and ΔP are fixed according to the type of solicitation (pressure, force,...). For the surface pressure, a value of 0.1 is assumed

$$\Delta P = q = 0.1\,\text{bars} \tag{4.24}$$

5. Study case

The numerical parameters of the two-stage gear system are summarized in Table 1.

Table 3 describes numerical values of parameters of the poroelastic materials.

Table 1. Geared transmission parameters

External inputs	Motor torque and speed	$C_m = 1000\,\text{Nm}$, $N_m = 3000\,\text{tr/mn}$
Structure characteristics	Bearing and shaft stiffness	$x_s = ky_s = 10^9\,\text{N/m}$, $k\theta_s = 10^5\,\text{Nm/rad}$

Gear characteristics material: 42CrMo4, $\rho = 7860\,\text{kg/m}^3$		
	First stage	Second stage
Teeth width and module [mm]	$b = 20$, $m = 4$	$b = 20$, $m = 4$
Teeth number	$Z(12) = 26$, $Z(21) = 39$	$Z(12) = 26$, $Z(21) = 39$
Average mesh stiffness	$k_{c1} = 1.4 \cdot 10^8\,\text{N/m}$	$k_{c2} = 1.4 \cdot 10^8\,\text{N/m}$
Contact ratio and pressure angle	$\varepsilon_{\alpha 1} = 1.57$, $\alpha = 20^\circ$	$\varepsilon_{\alpha 2} = 1.53$, $\alpha = 20^\circ$

Table 2. First eigenfrequency of the geared transmission

ω_i [rad]	1823	4095	6016	16063	17353	27365
f_i [Hz]	290	652	957	2557	2763	4357

Table 3. Poroelastic parameters for validation of the models

Parameter	Unity	Porous material
ρ_1	kg/m^3	90
ϕ	–	0.7
σ	Ns/m^4	22250
α_∞	–	1.3
ν	–	0.05
Λ	μm	75
Λ'	μm	87
E	N/m^2	2980000
η	–	0.12

5.1. Porous plate effect on vibration level

Figure 6 shows the displacement along the axis x of the output bearing at the housing cover. The displacement amplitude is about $2 \cdot 10^{-6}$. The periodicity of the bearing displacement comes from domination of the gearmesh frequency.

Figure 7 shows that the RMS bearing displacement increases with the meshing frequency as it is shown in Fig. 8. The results show that the gearmesh frequency and its harmonics dominate the RMS bearing displacement with higher amplitudes when the gearmesh frequency or one of its harmonics is close to the eigenfrequency. The first peak is close to the first eigenfrequency (290 Hz) the second one is close to the third eigenfrequency (957 Hz). The third peak is close to the sum of the first and the third eigenfrequency (1608 Hz).

Figure 9 shows that the gearmesh frequency and its harmonics dominate the point plate displacement. The absence of a negative displacement is due to the elastic effect of the plate at the measurement point. Due to the same reason, there are no positive displacements in the other half of the plate.

As it is shown in Fig. 10, the gearmesh frequency dominates the point plate displacement. The absence of a negative displacement is due to the elastic effect of the plate at the measurement point. Due to the same cause, there are no positive displacements in the other half of the plate.

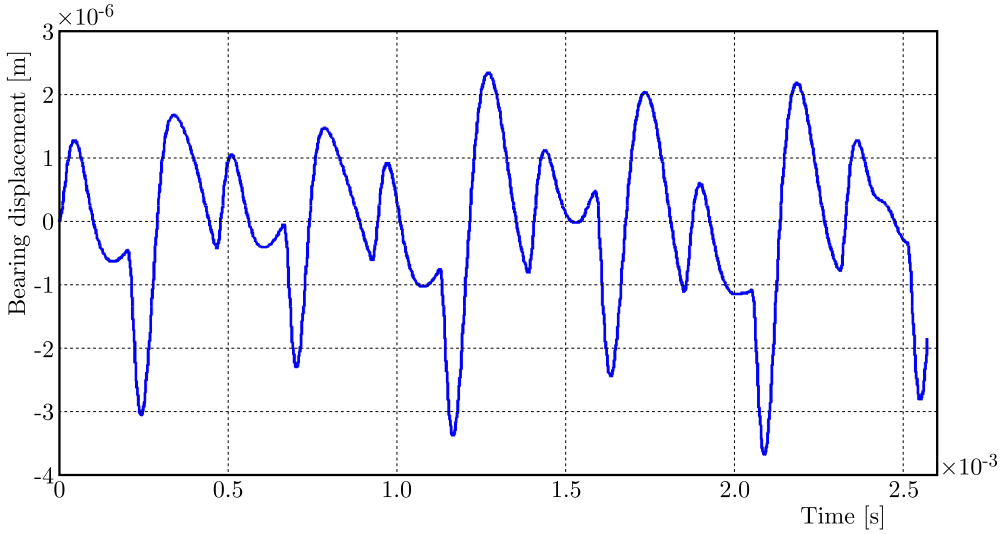

Fig. 6. Output bearing displacement in the x direction

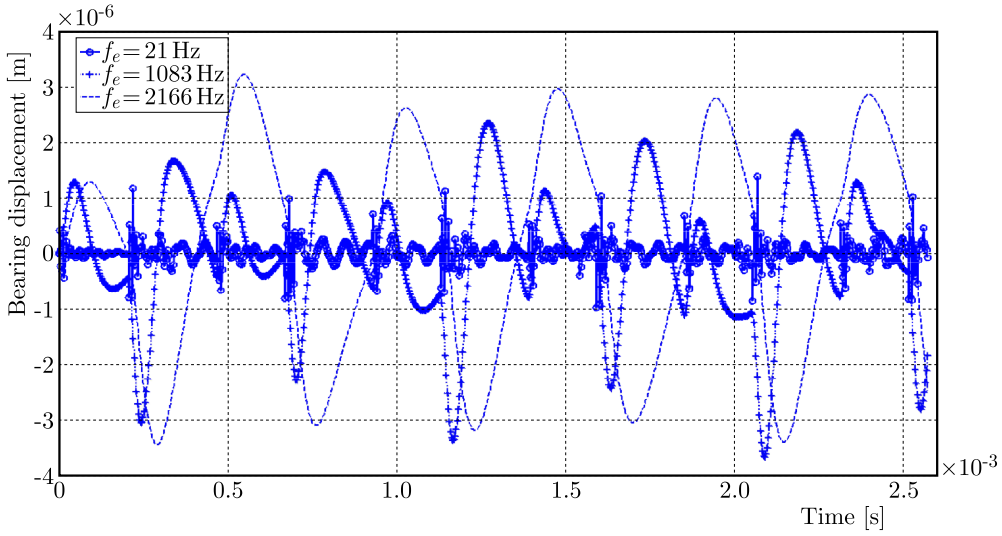

Fig. 7. Output bearing displacement in the x direction for three gearmesh frequencies

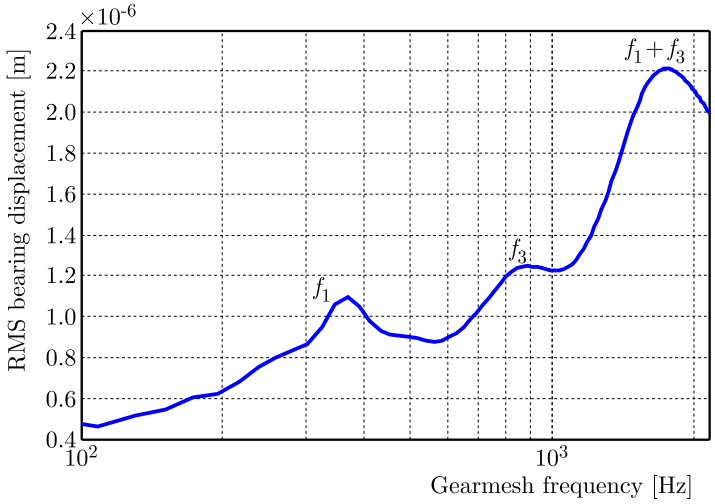

Fig. 8. RMS bearing displacement

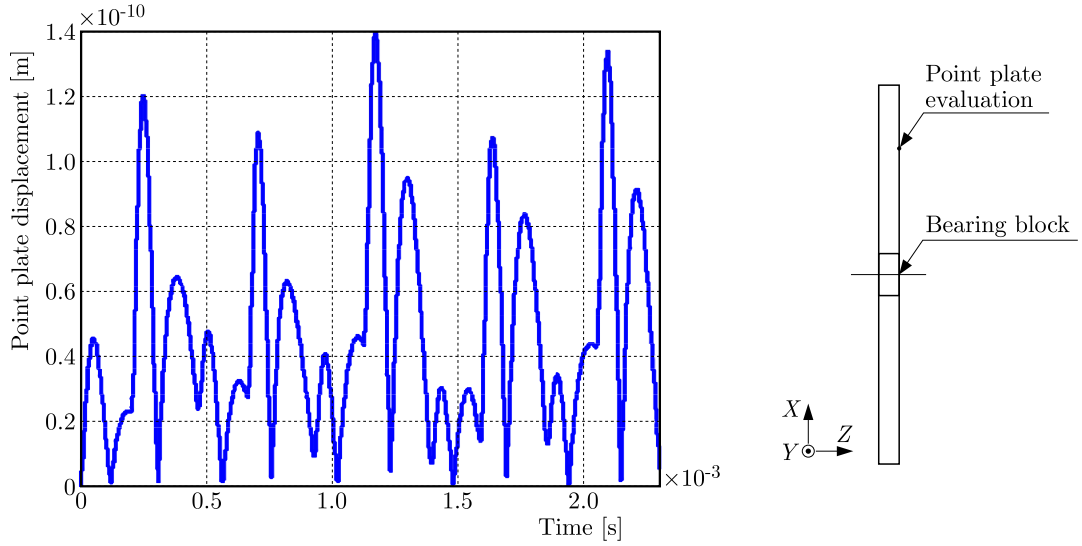

Fig. 9. Displacement along the axis x at a point with coordinates $(0.15, 0.24)$ on the elastic plate

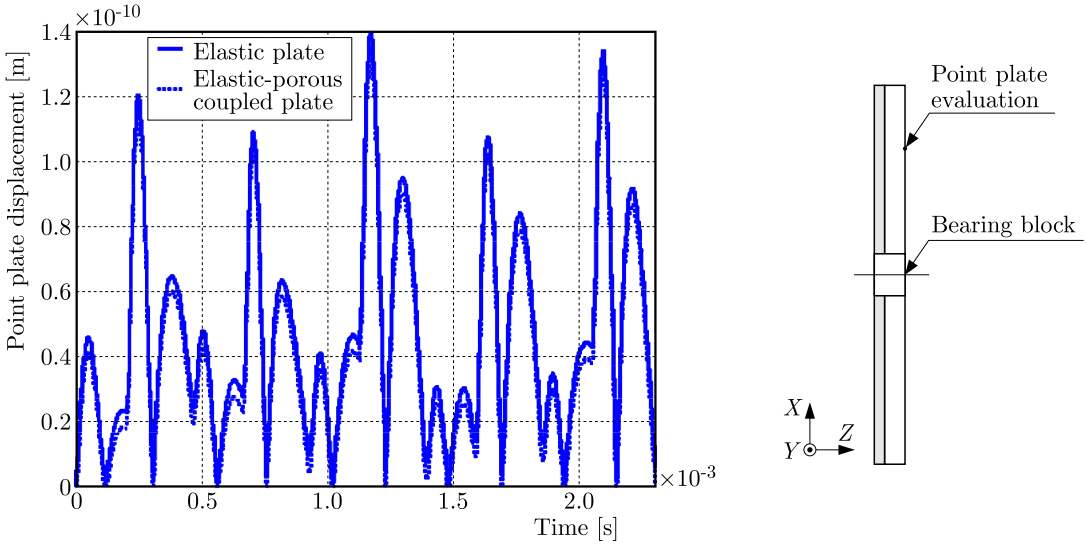

Fig. 10. Point displacements (solid line: elastic plate, dashed: elastic and porous coupled plate)

5.2. Acoustic effect of the porous plate

Figure 11 shows the transmission loss T_L of the elastic-porous coupled plate. The calculation is conducted for the porous plate with a characteristic defined in Table 3 and thickness 10 mm. T_L increases along the frequency axis and is dominated by the resonance frequency of the plate where T_L decreases with the frequency converging to 67 dB, 54 dB and 83 dB at, respectively, natural frequencies 620 Hz, 1240 Hz and 1900 Hz. Figure 11 shows the dependence of the sound transmission loss on the flow resistivity which is one of the characteristic of the porous material but is still dominated by the natural frequencies.

6. Conclusion

A resolution method to determine the porous plate effect on a gearbox hosing cover is discusseg in the paper. The developed model depends on several parameters: gearbox and porous plates parameters. It is found that coupling of the porous plate to the housing cover reduces the

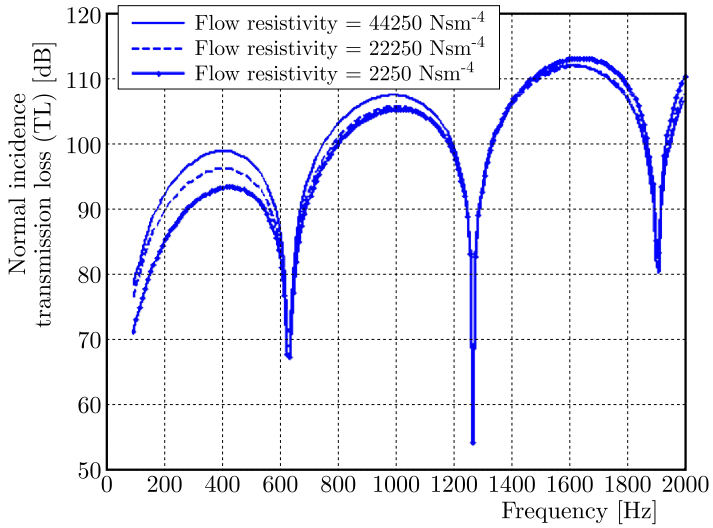

Fig. 11. Sound transmission loss T_L for different flow resistivity σ

vibration level and is dominated by the gearmesh frequency. For the acoustic effect, poroelastic materials have major capacity to mitigate the noise level caused by the geared transmission. The vibration and the acoustic behavior are heavily dependent on poroelastic characteristics. These results were validated by Tewes (2005), who computed the transmission loss of an infinite double wall partition for various angles of incidence and for various mass ratios. The developed method helps one to make decisions in the robust design and lessens the enormous computing time.

References

1. Allard J.F., 1993, *Propagation of Sound in Porous Media*, Elsevier Science, Essex, UK
2. Allard J.F., Champoux Y., 1992, New empirical equations for sound propagation in rigid frame fibrous materials, *Journal of the Acoustical Society of America*, **91**, 3346-3353
3. Allard J.F., Herztog P., Lafarge D., 1993, Recent topics concerning the acoustics of fibrous and porous materials, *Applied Acoustics*, **39**, 3-21
4. Atalla N., Panneton R., Debergue P., 1998, A mixed displacement-pressure formulation for poroelastic materials, *Journal of the Acoustical Society of America*, **104**, 3, 1444-1452
5. Aziz S.M.A., Seirg A., 1994, Parametric study of frictional noise in gear, *Wear*, **176**, 1, 25-28
6. Biot M.A., 1962, Mechanics of deformation and acoustics propagation in porous media, *Journal of Applied Physics*, **33**, 1482-1498
7. Champoux Y., Allard J.F., 1991, Dynamic tortuosity and bulk modulus in air-saturated porous media, *Applied Physics*, **70**, 4, 1975-1979
8. Champoux M., Stinson M.R., 1992, On acoustical models for sound propagation in rigid frame porous materials and the influence of shape factors, *Journal of the Acoustical Society of America*, **92**, 1120-1131
9. Chedly S., Chettah A., Bonnnefoy H., Ichchou M., 2008, A robust shock and noise models for the manufacturing of moulded LDPE foams, *Polymer Engineering and Science*
10. Delany M.E., Bazley E.N., 1970, Acoustic properties of fibrous absorbent materials, *Applied Acoustics*, **3**, 105-116
11. Guezzen S., 2004, Vibro-acoustic behavior study of rib structures (in French), Thesis, INSA Lyon, France, http://theses.insa-lyon.fr/publication/2004ISAL0092/these.pdf

12. Hentati T., Bouazizi L., Taktak M., Trabelsi H., Haddar M., 2016, Multi-levels inverse identification of physical parameters of porous materials, *Applied Acoustics*, **108**, 26-30
13. Horoshenkov K.V., Swift M.J., 2001, The acoustic properties of granular materials with pore size distribution close to log-normal, *Journal of the Acoustical Society of America*, **110**, 2371-2378
14. Houjoh H., Umezawa K., 1992, A generation mechanism of aerodynamic sound of spur gears, *Proceedings of the 6th International Power Transmission and Gearing Conference*, Scottsdale, **2**, 597-604
15. Houser D., 1991, *Gear Noise, Dudley's Gear Handbook*, 2nd Edition, McGraw Hill
16. Johnson D.L., Koplik J., Dashen R., 1987, Theory of dynamic permeability and tortuosity in fluid-saturated porous media, *Journal of Fluid Mechanics*, **176**, 379-402
17. Lafarge D., Lemarinier P., Allard J.F., Tarnow V., 1997, Dynamic compressibility of air in porous structures at audible frequencies, *Journal of the Acoustical Society of America*, **102**, 4, 1995-2006
18. Leclaire P., Horoshenkov V., Cummings A., 2001, Transverse vibrations of a thin rectangular porous plate saturated by a fluid, *Journal of Sound and Vibration*, **247**, 1-18
19. Miller A.J., 1999, A new wavelet basis for the decomposition of gear motion error signals and its application to gearbox diagnostics, M.Sc. Thesis, The Pennsylvania State University, Pennsylvania, PA, USA
20. Othmani C., Hentati T., Taktak M., Elnady T., Haddar M., 2015, Effect of liner characteristics on the acoustic performance of duct systems, *Technical Note*, **40**, 1, 117-127
21. Phong V., 2012, Acoustic transmission loss of perforated plates, *AIAA/CEAS Aeroacoustics Conference*, Colorado Springs
22. Phong V., 2015, Normal incidence acoustic transmission loss of perforated plates with Bias flow, *53rd AIAA Aerospace Sciences Meeting*, Kissimmee, Florida
23. Putra A., Ismail A.Y., Ramlan R., Ayob Md.R., Py M.S., 2013, Normal incidence of sound transmission loss of a double-leaf partition inserted with a microperforated panel, *Advances in Acoustics and Vibration*, ID 216493
24. Rossing T., 2007, *Handbook of Acoustic*, Springer, LLC New York, ISBN 978-0-387-30425-0
25. Sibe A., 1997, Study of the acoustic transparency of transmission housings of gears (in French), Thesis, http://bibli.ec-lyon.fr/exl-doc/TH_T1701_pducret.pdf
26. Tewes S., 2005, Active trim panel attachments for control of sound transmission through aircraft structures, Dissertation, https://mediatum.ub.tum.de/doc/601937/document.pdf
27. Umnova O., Attenborough K., Li K.M., 2001, A cell model for the acoustical properties of packings of spheres, *Acta Acustica*, **87**, 226-235
28. Velex P., 1988, Contribution to the analysis of the dynamic behavior of parallel axis gears (in French), Thesis, INSA Lyon, France, No. 88, ISAL 0032, 188 p.
29. Velex P., Sainsot P., 2002, An analytical study of tooth friction excitations in errorless spur and helical gears, *Mechanism and Machine Theory*, **37**, 641-658
30. Walha L., Fakhfakh T., Haddar M., 2009, Nonlinear dynamics of a two-stage gears system with mesh stiffness fluctuation, bearing flexibility and backlash, *Mechanism and Machine Theory*, **44**, 1058-1069
31. Wilson D.K., 1997, Simple relaxational models for the acoustical properties of porous media, *Applied Acoustics*, **50**, 171-188
32. Zielinski T.G., Gallad M.A., Ichchou M., 2012, Fully coupled finite-element modeling of active sandwich panels with poroelastic core, *Journal of Vibration and Acoustics*, **134**, 021007, 1-10

Manuscript received February 29, 2016; accepted for print July 10, 2017

JOURNAL OF THEORETICAL AND APPLIED MECHANICS
55, 4, pp. 1397-1408, Warsaw 2017
DOI: 10.15632/jtam-pl.55.4.1397

EXPERIMENTAL STUDY ON SUPPRESSION OF VORTEX STREET BEHIND PERFORATED SQUARE CYLINDER

Amir Teimourian, Hasan Hacışevki, Arian Bahrami

Aerodynamic Laboratory, Department of Mechanical Engineering, Eastern Mediterranean University, Northern Cyprus, Famagusta, Turkey; e-mail: amir.teimourian@cc.emu.edu.tr

In this study, the effects of entrainment of a fluid through a perforated surface on suppression of the vortex street behind a perforated square cylinder have been studied experimentally. The wake region has been investigated in terms of coherent flow structure, time averaged properties and effectiveness of different perforations. The quantitative measurements revealed that the perforated surfaces are only effective within a width interval of $y/D = \pm 1.0$. It has been observed that in the near wake region up to approximately $1.5D$ downstream the wake, the shedding phenomenon has been suppressed significantly. It has been also demonstrated that velocity profiles and flow structure have been affected by different perforated surfaces and, as a result, coherent structures have been diminished considerably.

Keywords: vortex shedding, flow control, coherent flow structure, perforated square cylinder

Nomenclature

u, v	–	streamwise and transverse velocity component
U_∞	–	free stream velocity
D	–	square cylinder width
f	–	shedding frequency
$\langle u \rangle, \langle v \rangle$	–	phase averaged streamwise and transverse velocity
$\langle \overline{u} \rangle, \langle \overline{v} \rangle$	–	phase averaged time-mean streamwise and transverse velocity
$\langle \overline{u}'^2 \rangle, \langle \overline{v}'^2 \rangle$	–	incoherent streamwise and transverse Reynolds normal stress
$\langle \widetilde{u} \rangle, \langle \widetilde{v} \rangle$	–	coherent phase averaged streamwise and transverse velocity
TKE	–	Turbulent Kinetic Energy
T	–	vortex shedding period
$x/D, y/D$	–	normalized streamwise and transverse coordinate
t/T	–	normalized time
ν	–	kinematic viscosity

1. Introduction

The vortex shedding phenomenon from bluff bodies has been investigated on geometries and arrangements having different applications in civil engineering, wind engineering and aerospace engineering. The unsteady loading behavior which is induced by vortex shedding in the wake region requires great consideration and, as a result, has attracted many researchers. Such fluctuating forces are the main concern during design stages of industrial systems where the vortex-induced vibration can have an undesirable effect on the structure. In the context of a square cylinder, Okajima (1982), Saha *et al.* (2000), Saha (2013), Hacışevki and Teimourian (2015), Sohankar *et al.* (2015b) and many other researchers conducted extensive studies on the vortex shedding phenomenon. They investigated different features of vortex shedding behind square

cylinders and reported wake flow structures, Strouhal number variation and other aerodynamic parameters.

The fluctuating forces are derived from the wake structure and, therefore, any endeavor for suppression of the vortex street to reduce such a destructive feature is valuable. For this purpose, various passive and active flow-control methods have been employed by engineers to protect the structures against the damaging fluid forces acting on the bluff bodies. Sakamoto *et al.* (1997), Alam *et al.* (2002), Malekzadeh and Sohankar (2012) and Igarashi (1997) investigated passive flow control by employing a control plate or a rod upstream a square cylinder as a means of controlling the vortex shedding. They all reported a considerable reduction on the mean and the fluctuating forces acting on the square cylinder. It was observed that while the drag force on the square cylinder was significantly reduced, the fluctuating lift was also suppressed.

On the other hand, Çuhadaroğlu *et al.* (2007), Çuhadaroğlu and Turan (2009), Çuhadaroglu (2009), Turhal and Çuhadaroğlu (2010) and Sohankar *et al.* (2015a) employed an active control method with injection of a fluid through the surface of the square cylinder to reduce the damaging effect of the vortex shedding phenomenon. Çuhadaroğlu *et al.* (2007) conducted an experimental study to investigate the injection effects on the pressure coefficient and drag coefficient of a perforated square cylinder at high Reynolds numbers between $\mathrm{Re} = 10\,000$ and $24\,000$. Different configurations of injection through the front, top and rear surfaces of the cylinder have been employed. The results revealed that injection through the rear face decreased the drag force. However, injection of the fluid through the front face demonstrated opposite results and caused an increase in drag force. Moreover, injection through other faces demonstrated negligible effects. Turhal and Çuhadaroğlu (2010) experimentally studied variation of the pressure coefficient, drag coefficient and Strouhal number of a perforated square cylinder (horizontal and diagonal) with having the fluid injected through various surfaces at high Reynolds numbers. The result revealed that in the case of a diagonal square cylinder, the surface injection through the top-rear, rear and all surfaces reduced the drag coefficient. However, only the injection through all surfaces of a horizontal square cylinder could result in a reduction of the drag coefficient. Numerical study on control of fluid flow of by injection through surfaces of a square cylinder, which were reported by Sohankar *et al.* (2015a), is one of the latest studies in this context. The simulation demonstrated that in the case of fluid injection through the front surface, the Strouhal number decreased by increasing the injection parameter, while aerodynamic force fluctuations were increased. On the other hand, the injection of fluid through the rear face caused a reduction in the Strouhal number and drag coefficient.

To sum up, the review shows that even though various passive and active flow control over a square cylinder have been investigated, there is still a gap in the literature. The previous studies tackled the problem of the perforated square cylinder together with active control theory. Although, the ultimate aim of these studies was the suppression of vortex shedding in the wake region of the square cylinder, most of the investigations reported variation of aerodynamic parameters such as the drag and pressure coefficient, and very limited results are available in terms of the wake flow structure and vortex street. Therefore, the objective of this study is to investigate the effects of perforating a square cylinder on the flow structure and suppression of vortex shedding. The suppression of vortex shedding has been studied by employing a triple decomposition technique rather than classical Reynolds decomposition to distinguish the incoherent turbulent flow fluctuation from the coherent vortex shedding structure for a better understanding of this phenomenon. The downstream wake behind the perforated square cylinder has been measured quantitatively by employing hotwire anemometry, and phase averaged properties have been presented. Moreover, coherent and incoherent structures of the downstream wake behind perforated square cylinders have been identified. The effectiveness of suppression of the vortex street in the wake region have been probed.

2. Experimental set-up and methodology

The investigations have been conducted in an open-return subsonic wind tunnel with a 0.5 m×0.5 m test section and 1.0 m length available at Aerodynamic Laboratory of Eastern Mediterranean University. The wind tunnel speed was controlled by a Danfoss frequency controller with the maximum speed of 30 m/s. The experiment was conducted at a free stream velocity $U_\infty = 10.5 \pm 2\%$ m/s with a measured turbulence intensity of 0.6% at this speed. A perforated hollow square cylinder with a cross section of 25 mm×25 mm with the corresponding blockage ratio of 5% was selected for the experiment.

The square cylinder model was constructed from aluminum, and four different perforations have been drilled with a CNC machine with accuracy ±0.001 mm. The experimental setup and schematic of the perforated square cylinders are illustrated in Figs. 1 and 2, respectively. Each face of the square cylinder was perforated with holes $\phi = 2$ mm in diameter uniformly distributed on the perforated surface. The Reynolds number of the experiment was Re = 18500 (Re = $(U_\infty D)/\nu$) based on the side-length of the square cross-section of the cylinder, which resulted in turbulent vortex shedding behind the square cylinder in the domain of interest ($0.5 < x/D < 4.0$).

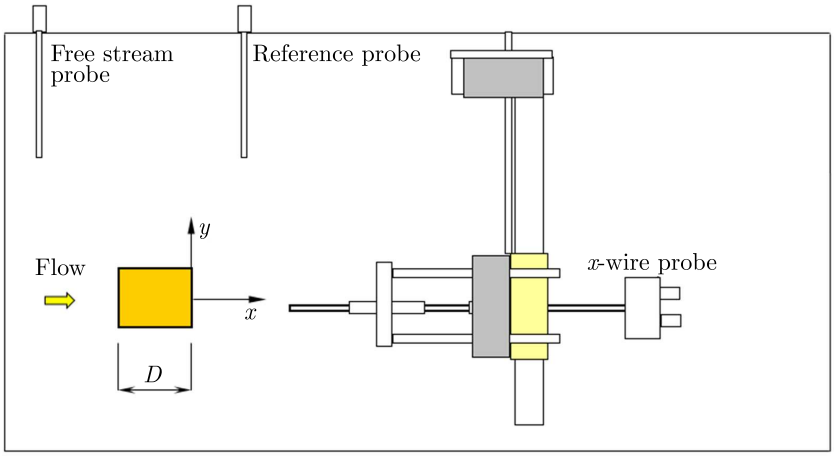

Fig. 1. Experimental setup and coordinates (top view)

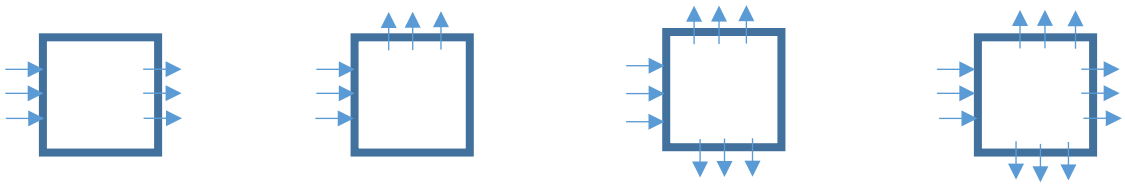

Fig. 2. Schematic of perforated square cylinders

Velocity field measurements have been acquired by employing TSI FlowPoint 1500 constant temperature anemometry hotwire system by means of two S types (1210-T1.5) and one X type (1240-T1.5) hotwires. Two velocity components (u and v) were acquired by means of an X hotwire probe, while free stream velocity and reference signal of periodic shedding were acquired by means of S hotwire probes. The X probe was mounted on a three-axis traverse mechanism to traverse in the xy domain during data acquisition with an accuracy of ±0.25 mm. The velocity components for a given streamwise location x/D, were acquired at various lateral locations y/D within ±2.6. All the measurements were carried out at the midpoint of the test section in the z-direction. The acquired data was filtered by considering the frequency of shedding with the

reference waveform by implementing MATLAB/Simulink to produce the characteristic vortex shedding waveform. Finally, the filtered data was analyzed by implementing the triple decomposition and ensemble averaging method (Hussain, 1986; Reynolds and Hussain, 1972) to produce the phase averaged properties. This technique provides a better understanding to distinguish the coherent structure and incoherent turbulent fluctuations. The instantaneous velocity u, can be decomposed into time-mean averaged component $\overline{u}$, coherent component $\widetilde{u}$ and incoherent component (turbulent fluctuations) u'

$$u = \overline{u} + \widetilde{u} + u' \qquad v = \overline{v} + \widetilde{v} + v' \tag{2.1}$$

The purpose is to obtain the dependence of these components on time (normalized with respect to total period T) during one complete cycle of vortex shed. A reference signal (the periodic vortex shedding velocity fluctuation in the present study) has been selected and the velocity signals (u and v component) at the selected domain point have been acquired. The phase averages are then computed by sorting the instantaneous velocity components into 60 different bins of different phases obtained by equally subdividing the intervals between peaks of the output of the phase detector probe. Then, corresponding to same t/T of consecutive reference cycles, the acquired velocity components at the same instant are summed and averaged. This process is repeated for different times during one cycle to construct the variation of properties $\langle u\rangle$, $\langle v\rangle$, $\langle\overline{u}\rangle$, $\langle\overline{v}\rangle$, $\langle\overline{u}'^2\rangle$, $\langle\overline{v}'^2\rangle$, $\langle\widetilde{u}\rangle$, $\langle\widetilde{v}\rangle$ and TKE ($\langle\widetilde{u}^2\rangle+\langle\widetilde{v}^2\rangle$) across one complete cycle of vortex shedding. A modified Navier-Stokes equation was obtained by substituting the triple decomposition of the u and v components of velocity and by applying phase averaging techniques as shown below

$$\langle u\rangle = \frac{1}{n}\sum_{1}^{n} u \qquad \langle\widetilde{u}\rangle = \frac{1}{n}\sum_{1}^{n}\widetilde{u} \qquad \langle u'\rangle = \frac{1}{n}\sum_{1}^{n} u'_i \tag{2.2}$$

where n is the number of cycles used for phase averaging and $\widetilde{u}$ is the value of coherent component and u' is the value of incoherent component at the same normalized time successive cycles

$$\langle\overline{u}\rangle = \frac{1}{m}\sum_{1}^{m}\langle u\rangle \qquad \langle\overline{\widetilde{u}}\rangle = \frac{1}{m}\sum_{1}^{m}\langle\widetilde{u}\rangle \qquad \langle\overline{u'}\rangle = \frac{1}{m}\sum_{1}^{m}\langle u'\rangle \tag{2.3}$$

where m is the number of phase averages used in one cycle to construct phase averages of the successive cycles. Such a definition can be applied for any velocity components or product of velocity components. Consequently, applying the phase averaging concept to the Navier-Stokes momentum equation will result in the modified Navier-Stokes equation. Furthermore, the coherent Turbulence Kinetic Energy (TKE) can be defined as the following equation

$$\text{TKE} = \frac{1}{2}\overline{\widetilde{u}_i\widetilde{u}_i} = \frac{1}{2}(\overline{\widetilde{u}_1\widetilde{u}_1 + \widetilde{u}_2\widetilde{u}_2}) = \frac{1}{2}(\overline{\widetilde{u}\widetilde{u} + \widetilde{v}\widetilde{v}}) \tag{2.4}$$

3. Spectral analysis

In order to identify the vortex shedding frequency and quantitative comparison between different perforated square cylinders, Fast Fourier Transform (FFT) has been implemented on the acquired velocity data. Therefore, the dominant shedding frequency f can be observed as a single peak corresponding to the Strouhal number, $\text{St} = fD/U_\infty$, in the wake behind the cylinder. The instantaneous velocity has been acquired at various x/D downstream the wake and various transverse directions have been used for frequency spectra determination. The dominant shedding frequency has been found as $f = 43.9\,\text{Hz}$ that gives the Strouhal number $\text{St} = 0.104$, identical to the corresponding Strouhal number of the non-perforated square cylinder. These dominant shedding frequencies have been acquired at positions outside the effective wake width of

the perforated surface. Similarly, the shedding frequencies obtained by Turhal and Çuhadaroğlu (2010) at a similar position for the perforated square cylinder with injection demonstrated an insignificant alternation in the shedding frequency. However, the measurement inside the effective width of perforation were influenced by entrainment of the fluid through the perforated surfaces. It would be impossible to present all the power spectra due to space limitation. Therefore, for the sake of brevity, only a comparison between different perforated square cylinders and detailed investigation on perforated square cylinder P3 have been presented in Figs. 3 and 4, respectively.

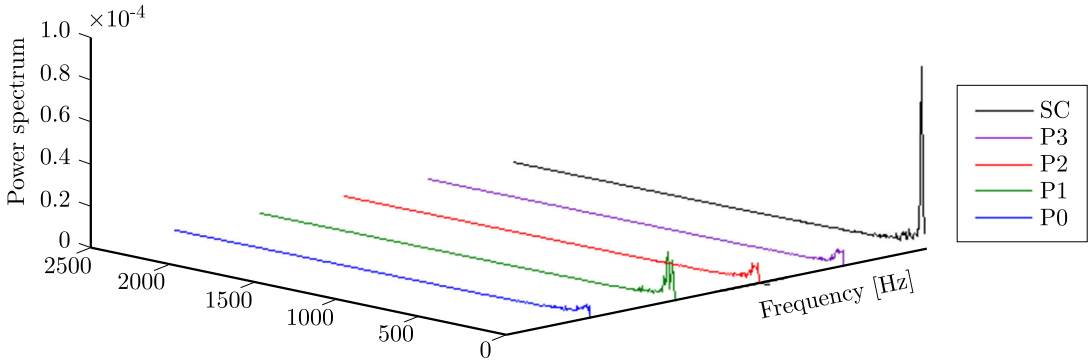

Fig. 3. Comparison of PSD of total transverse velocity fluctuations at $x/D = 0.5$ and $y/D = 0$ for perforated square cylinders P0, P1, P2, P3 and non-perforated square cylinders (SC)

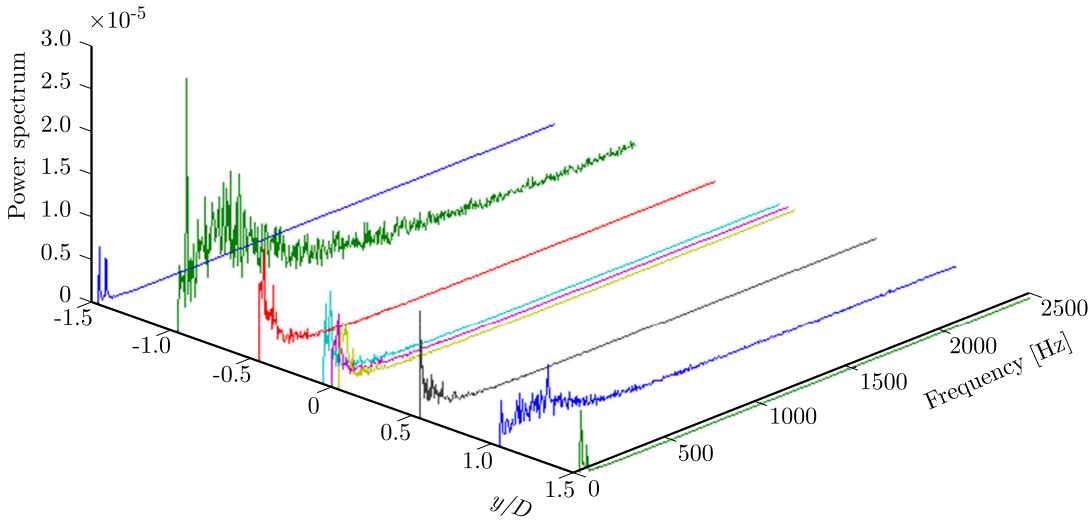

Fig. 4. PSD of perforated square cylinder P3 at $x/D = 0.5$ for various transverse locations

Power Spectrum Density (PSD) analysis of total (i.e. random and coherent) transverse velocity fluctuations for different perforated square cylinders (P0, P1, P2 and P3) and non-perforated square cylinder (SC) measured at $x/D = 0.5$ and $y/D = 0$ (along centerline) in the downstream wake has been demonstrated in Fig. 3. As it can be seen from the figure, the frequency spectrum is clearly evident as a single strong peak in the wake of the non-perforated square cylinder. By contrast, in the wake region behind the perforated square cylinder, no dominant shedding frequency along the centerline is evident. Such an observation implied that the vortex shedding has been partially suppressed by fluid entrainment through the perforated surfaces.

Further investigations of PSD of total transvers velocity fluctuations acquired within the transverse direction interval $y/D = \pm 1.5$ for perforated square cylinder P3 have been illustrated in Fig. 4. It can be seen that the dominant shedding frequency is clearly evident for the wake region outside the interval $y/D = \pm 0.5$. However, inside this interval, where the perforated

surfaces are effective, the power spectrum demonstrated evidence of no-single dominant peak with multiple peaks in the spectra. These multiple peaks indicated formation of the secondary vortex and suppression of the primary shedding due to entrainment of the fluid through the perforated surfaces.

4. Phase averaged properties

The objective of this study is to investigate the formation of the vortex shedding phenomenon in the wake region behind the perforated square cylinders. Development of the vortex street in the wake region behind perforated square cylinder P0 has been demonstrated in Fig. 5. The figure illustrates the variation of phase averaged streamwise velocity contours $\langle u \rangle$ versus normalized time t/T during one complete cycle of oscillation for various x/D downstream the wake region.

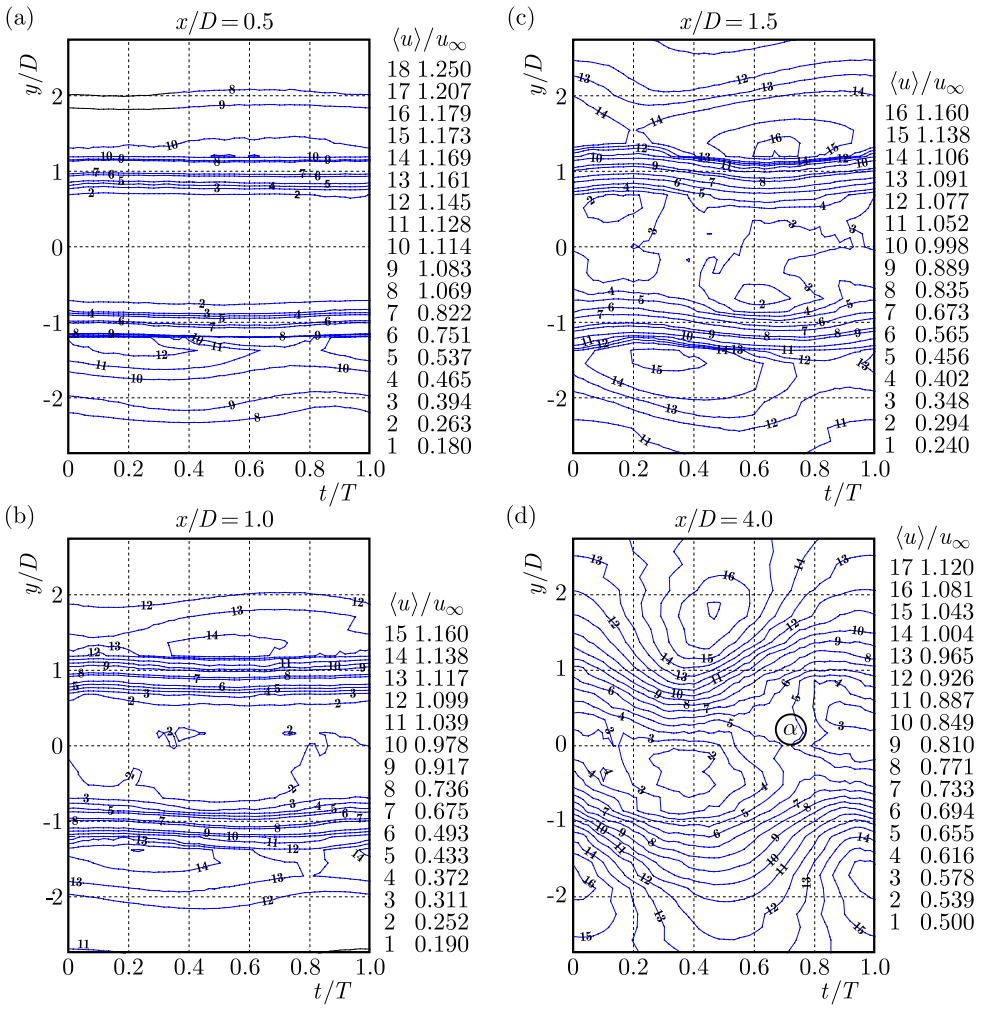

Fig. 5. Comparison of phase averaged streamwise velocity $\langle u \rangle$ for perforated square cylinder P0 acquired at: (a) $x/D = 0.5$, (b) $x/D = 1.0$, (c) $x/D = 1.5$, (d) $x/D = 4.0$

It can be seen from the figure that the vortex shedding has been completely suppressed by the entrainment of the fluid into the wake region through the perforated surfaces in the wake region up to approximately $x/D = 1.5$. In the near wake region of the perforated square cylinder, i.e. $x/D = 0.5$, while within the interval $y/D = \pm 1$ there is no evidence of vortex shedding, some vortices are being rolled beyond the edges of the square cylinder. As the probe moves downstream the wake, the vortex shedding process is being developed and at $x/D = 1.5$, the $\langle u \rangle$

contours exhibit patterns corresponding to vortices being shed periodically. In addition to two peaks beyond the edges of the perforated square cylinder, two low level zone phase drifted by half the period corresponding to edges of the perforated square cylinder are also evident. Eventually, the streamwise phase average velocity contours at $x/D = 4.0$, where the perforated surfaces are no more effective, demonstrate classical vortex shedding. Through such development, the peaks drift away from the centerline. In contrast, the two low level zones are shifted towards the centerline behind the perforated square cylinder. Such a flow pattern is comparable to the streamwise velocity in the wake region of the square cylinder as reported by Hacışevki and Teimourian (2015).

Figure 6 illustrates the phase averaged transverse velocity component contours at two different distances downstream the wake region. Similarly to the streamwise velocity component, the peaks occur during a half of the period phase ($t/T = 0.5$). However, comparison between streamwise and transverse velocity component measured at $x/D = 4.0$ reveals that the transverse velocity peaks (point α as illustrated in Fig. 6) lag behind the streamwise velocity peaks with a phase shift equal to 1/4 of the cycle. Therefore, the point α as illustrated in Fig. 5, corresponds to normalized time at which the transverse velocity reaches the peak value in Fig. 6. The contours around this peak region imply a remarkable lateral momentum transfer towards the growing vortex on the other edge of the square cylinder. However, such a phenomenon has been suppressed by the perforated surface near the wake, i.e. $x/D = 1.0$, where the perforated surfaces are effective.

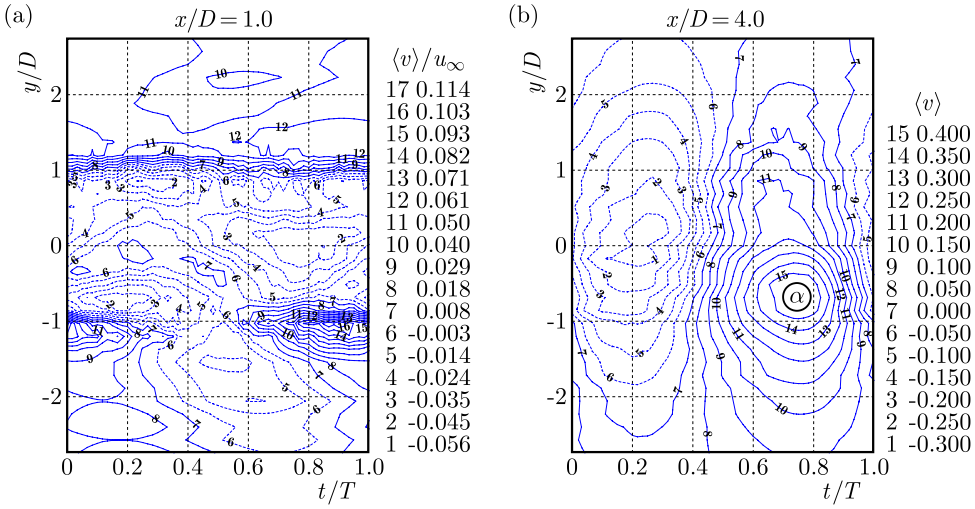

Fig. 6. Comparison of the phase averaged transverse velocity $\langle v \rangle$ for perforated square cylinder P0 acquired at (a) $x/D = 1.0$ and (b) $x/D = 4.0$

Furthermore, a comparison between the phase averaged streamwise velocities in the wake region of the non-perforated square cylinder and four different perforated square cylinders measured at $x/D = 1.5$ have been presented in Fig. 7. From this figure it can be observed that while in the wake region of the non-perforated square cylinder the rolling vortices are clearly apparent with periodic flow patterns, the development of the vortex shedding phenomenon in the wake region behind perforated square cylinders have been delayed. Moreover, it can be observed that perforated square cylinders P0 and P3 delayed such development more effectively as a result of entraining the fluid particle directly into the wake region by employing the perforated rear face.

As discussed previously, triple decomposition would provide a better illustration of the vortex shedding phenomenon. Therefore, to investigate the development of a coherent structure of the shedding phenomenon, coherent Turbulent Kinetic Energy production in the wake region behind perforated square cylinder P1 has been depicted in Fig. 8.

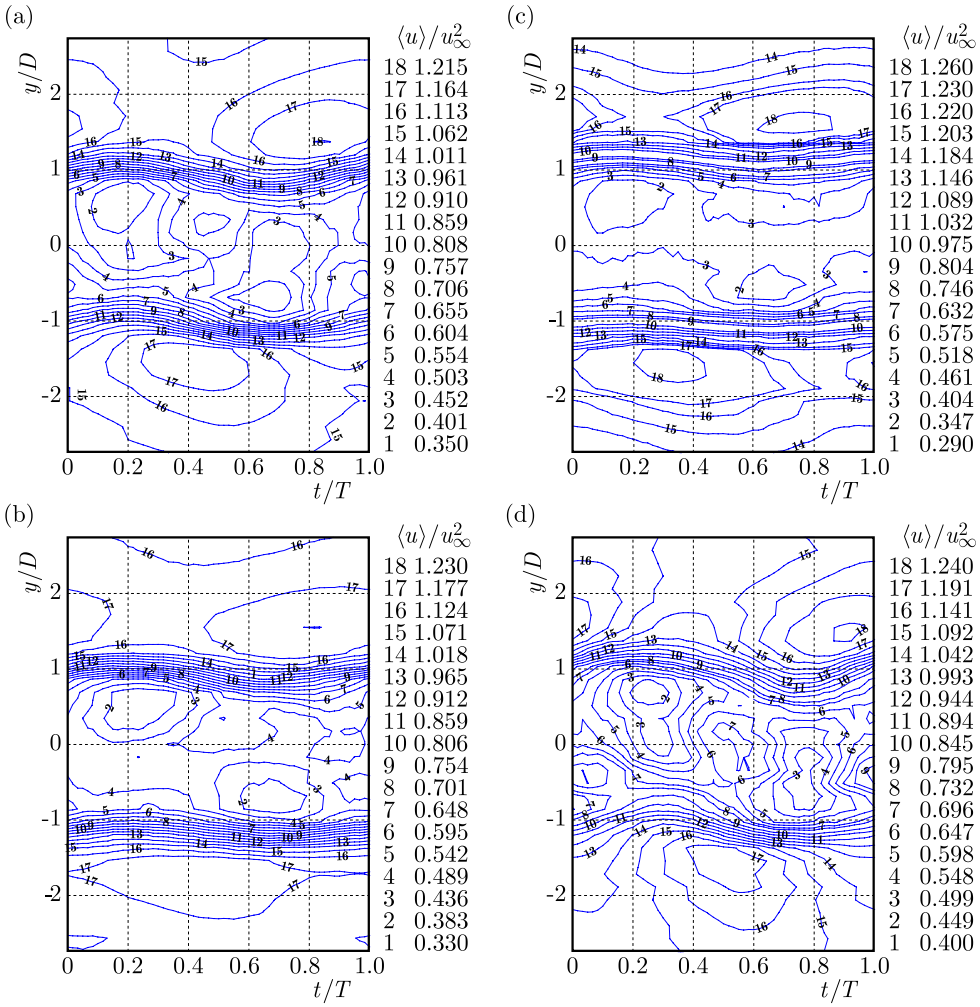

Fig. 7. Comparison of phase averaged streamwise velocity $\langle u\rangle$ acquired at $x/D = 1.5$ for perforated square cylinder: (a) P1, (b) P2, (c) P3 and (d) non-perforated square cylinder (SC)

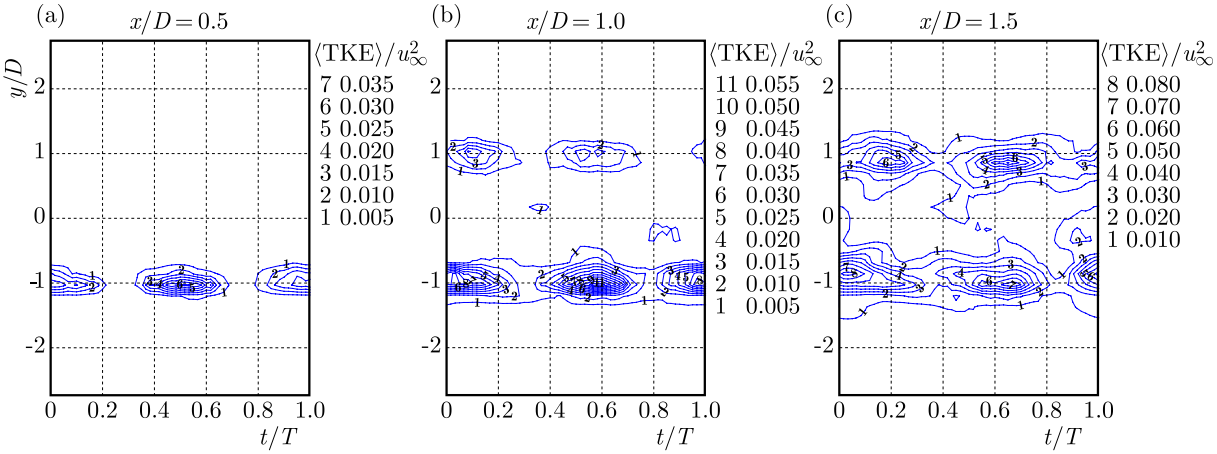

Fig. 8. Coherent Turbulent Kinetic Energy production in the wake region of perforated square cylinder P1 acquired at: (a) $x/D = 0.5$, (b) $x/D = 1.0$, (c) $x/D = 1.5$

It can be seen from the figure that near the wake region while coherent structures have been formed beyond the right edge, the wake of the left edge shows no evidence of the coherent structure. As the probe moved downstream, the perforated surface is losing its effectiveness and, as a result, the first evidence of the coherent structure on the left edge has been also developed. Farther downstream the wake (i.e. $x/D = 4.0$), the two coherent structures are combined and form a larger structure as wide as the wake.

The relative reduction in coherent TKE production with respect to the non-perforated cylinder can be a measure of effectiveness of such perforation. As a result, the relative reduction in coherent TKE peak production for P1 (compared with the non-perforated square cylinder) varies form 66% to 27% between $x/D = 0.5$ to 1.5 downstream the wake, and beyond $x/D = 1.5$ the effectiveness drops significantly to approximately 7% at $x/D = 3.0$. The effectiveness of other perforated surfaces for coherent streamwise and transverse velocities and coherent TKE have been illustrated in Table 1.

Table 1. Relative reduction in the coherent structure peak value and TKE with respect to the non-perforated cylinder

	$x/D = 0.5$			$x/D = 1.0$			$x/D = 1.5$		
	$\langle\widetilde{u}\rangle$	$\langle\widetilde{v}\rangle$	TKE	$\langle\widetilde{u}\rangle$	$\langle\widetilde{v}\rangle$	TKE	$\langle\widetilde{u}\rangle$	$\langle\widetilde{v}\rangle$	TKE
P0	65	86	90	52	73	88	36	56	64
P1	42	64	67	24	54	38	7	16	27
P2	69	86	92	52	73	88	21	50	55
P3	81	86	96	64	77	88	39	63	73

5. Time averaged properties

Better understanding of the flow structure also requires knowledge how to quantify development and decay of flow properties such as streamwise velocity, transverse velocity and turbulent stresses downstream the wake region. In this Section, a quantitative comparison of the phase averaged time-mean streamwise velocity and the phase averaged time-mean turbulent stresses measured at various x/D in the wake region have been presented. Phase averaged time-mean properties such as streamwise and transverse velocities are normalized with the free stream velocity U_∞, and the turbulent normal and shear stress are normalized with U_∞^2.

The variation of phase averaged streamwise velocity contours $\langle u\rangle$ versus normalized time t during one complete cycle of oscillation have been presented in the previous Section. At a given y/D, averaging with respect to t/T in one cycle yields the phase averaged time-mean $\langle\overline{u}\rangle$ or, traditionally known, the time mean $\overline{u}$ of the streamwise velocity. For the streamwise velocity, this two averaging techniques result in the same values as both imply the same averaging. The phase averaged time-mean can be obtained by averaging across one cycle with the values obtained across all acquired cycles, while the time mean is computed across all cycles in the direct time averaging process. Variation of the phase averaged time-mean streamwise velocity $\langle\overline{u}\rangle$ against the lateral position y/D for different perforated square cylinders is demonstrated in Fig. 9. In thise figure, symmetrical variation of $\langle\overline{u}\rangle$ profile with respect to the wake axis is clearly apparent. It can be observed that for the case of perforated square cylinder P1 with no perforated surface in the rear face, the u profile measured near the wake ($x/D = 0.5$) decreases up to the centerline and then increases gradually. However, in case of P0 with a perforated rear face, the u profile remains approximately constant with some fluctuation corresponding to the measurement exactly behind the perforations. Moreover, it can be also observed that further downstream the wake, the effect of perforated surfaces decays considerably.

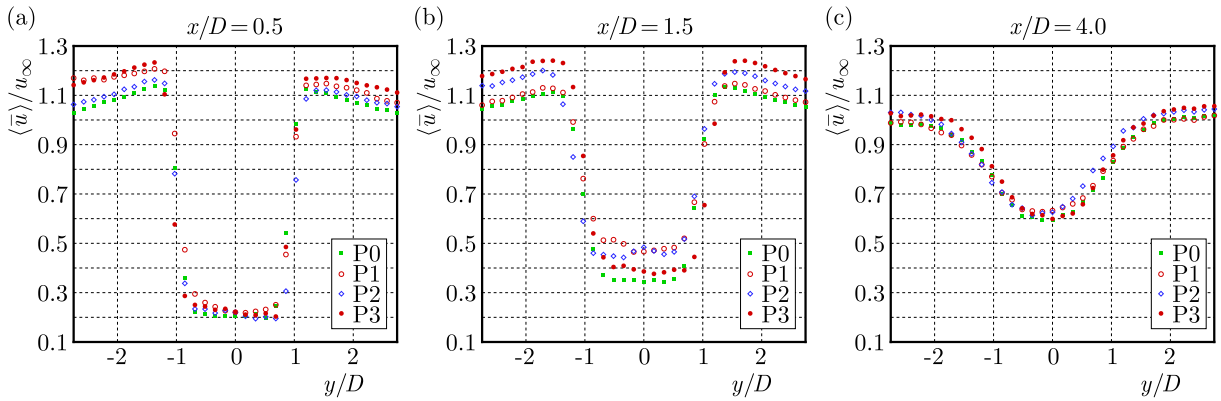

Fig. 9. Comparison of variation of $\langle \overline{u} \rangle$ for different perforated square cylinders acquired at: (a) $x/D = 0.5$, (b) $x/D = 1.5$, (c) $x/D = 4.0$

The phase averaged time-mean incoherent streamwise and transverse stresses downstream the wake for different perforated square cylinders measured at $x/D = 1.0$ and 4.0 are illustrated in Fig. 10. In the figure, it can be observed that both streamwise and transverse normal stresses significantly decay compared with the non-perforated square cylinder (SC) in the interval of $y/D = \pm 1.0$ near the wake. However, further downstream the wake at $x/D = 4.0$, incoherent stresses reach a value close to the non-perforated square cylinder. It can be observed that P0 exhibits the lowest streamwise and transverse normal stress. Such an observation is as a result of direct entrainment of the fluid through the perforated rear side into the wake region together with having the highest entrainment flow rate. Moreover, in the near wake region ($x/D = 1.0$) both streamwise and transverse stresses exhibit double peaks corresponding to the vortex shed from the edges. However, such a profile transforms gradually to a single peak profile as the vortices migrate toward the centerline.

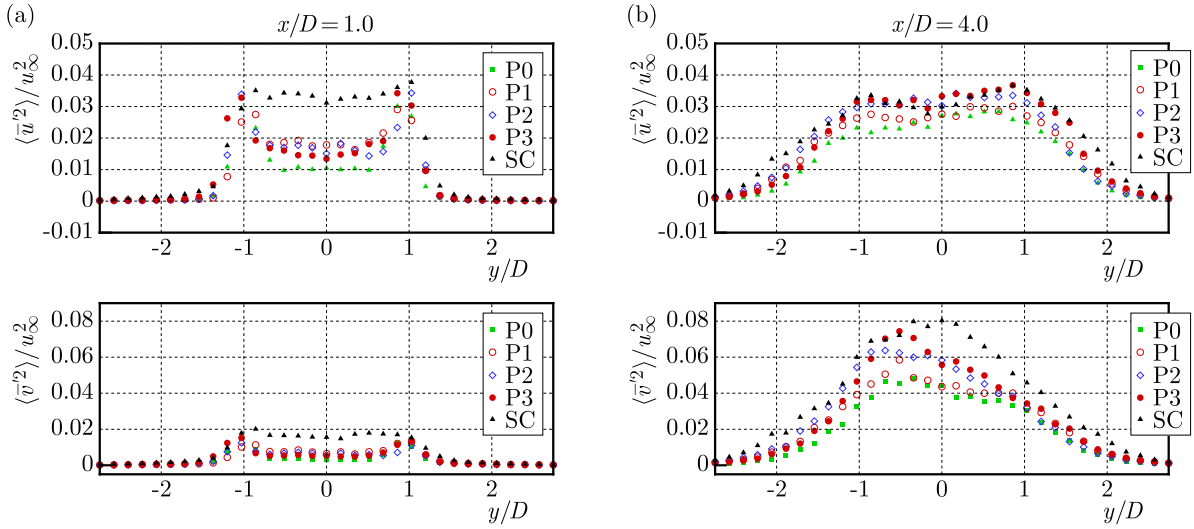

Fig. 10. Comparison of the phase averaged time mean incoherent normal Reynolds stress for different perforations acquired at: (a) $x/D = 1.0$, (b) $x/D = 4.0$

Clearly, an insufficient number of phases during one cycle resulted in discrete variation for phase averaging rather than a continuous variation of the properties. However, in this study with employing 60 phases during one cycle, the time mean phase averaged properties over one cycle are zero within an accuracy of $\pm 1\%$. Such an observation has been illustrated in Fig. 11 for coherent streamwise and transverse velocity components.

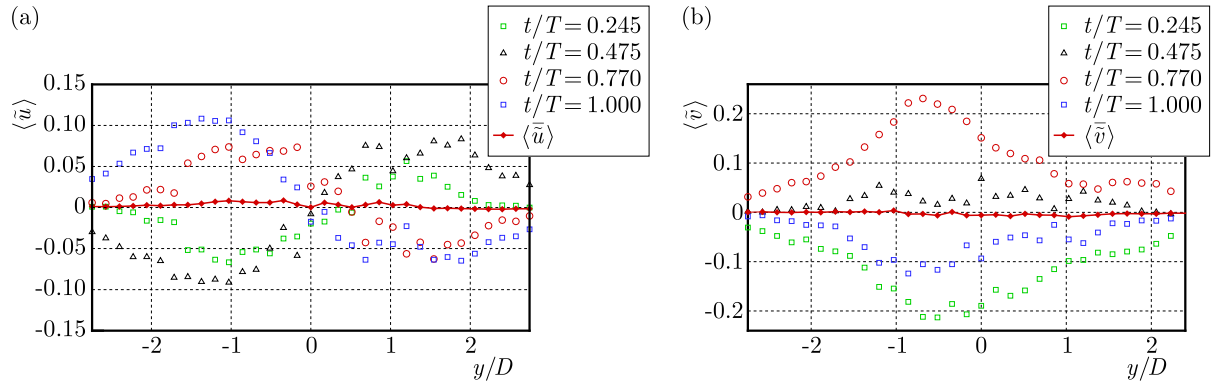

Fig. 11. Phase averaged coherent velocity components profile measured at $x/D = 4.0$ at various normalized times

6. Conclusion

In this study, the effect of entrainment of a fluid through perforated surfaces on suppression of the vortex street behind a perforated square cylinder has been studied experimentally. To probe the vortex formation process, different characteristics and coherent structures in the downstream wake have been analyzed. It has been observed that the perforated surfaces are effective only within the effective width $y/D = \pm 1.0$, and up to $1.5D$ in the downstream wake. Although previous studies reported that high injection through the rear surface is required to decrease the vortex shedding frequency. It has been found that even for a low entrainment flow rate, the shedding phenomenon has been affected significantly. Thus, observation of multiple peaks in the spectra indicates the secondary vortex formation and suppression of the primary shedding due to entrainment of the fluid through the perforated surfaces. The result shows that different perforated surface front-rear, front-one face, front-two faces and all faces have some effects on the velocity profiles, flow structure and vortex street. Asymmetric coherent flow structures behind the perforated square cylinder have been observed and the effectiveness of this perforation has been presented in terms of reduction in the coherent structure peak value. It has been revealed that the square cylinder with all faces perforated, has given the most significant relative reduction in the coherent TKE production compared with other perforations.

References

1. Alam M.M., Moriya M., Takai K., Sakamoto H., 2002, Suppression of fluid forces acting on two square prisms in a tandem arrangement by passive control of flow, *Journal of Fluids and Structures*, **16**, 1073-1092
2. Çuhadaroğlu B., 2009, A numerical study on turbulent flow around a square cylinder with uniform injection or suction, *International Journal of Numerical Methods for Heat and Fluid Flow*, **19**, 708-727
3. Çuhadaroğlu B., Akansu Y.E., Turhal A.Ö., 2007, An experimental study on the effects of uniform injection through one perforated surface of a square cylinder on some aerodynamic parameters, *Experimental Thermal and Fluid Science*, **31**, 909-915
4. Çuhadaroğlu B., Turan O., 2009, Numerical simulation of turbulent flow around a square cylinder with uniform injection or suction and heat transfer, *Numerical Heat Transfer, Part A: Applications*, **55**, 163-184
5. Hacışevki H., Teimourian A., 2015, Comparison of flow structures in the wake region of two similar normal flat plates in tandem and a square cylinder, *Experimental Thermal and Fluid Science*, **69**, 169-177

6. Hussain A., 1986, Coherent structures and turbulence, *Journal of Fluid Mechanics*, **173**, 303-356

7. Igarashi T., 1997, Drag reduction of a square prism by flow control using a small rod, *Journal of Wind Engineering and Industrial Aerodynamics*, **69**, 141-153

8. Malekzadeh S., Sohankar A., 2012, Reduction of fluid forces and heat transfer on a square cylinder in a laminar flow regime using a control plate, *International Journal of Heat and Fluid Flow*, **34**, 15-27

9. Okajima A., 1982, Strouhal numbers of rectangular cylinders, *Journal of Fluid Mechanics*, **123**, 379-398

10. Reynolds W., Hussain A., 1972, The mechanics of an organized wave in turbulent shear flow. Part 3. Theoretical models and comparisons with experiments, *Journal of Fluid Mechanics*, **54**, 263-288

11. Saha A.K., 2013, Unsteady flow past a finite square cylinder mounted on a wall at low Reynolds number, *Computers and Fluids*, **88**, 599-615

12. Saha A., Muralidhar K., Biswas G., 2000, Experimental study of flow past a square cylinder at high Reynolds numbers, *Experiments in Fluids*, **29**, 553-563

13. Sakamoto H., Tan K., Takeuchi N., Haniu H., Suppression of fluid forces acting on a square prism by passive control, *Journal of Fluids Engineering*, **119**, 506-511

14. Sohankar A., Khodadadi M., Rangraz E., 2015a, Control of fluid flow and heat transfer around a square cylinder by uniform suction and blowing at low Reynolds numbers, *Computers and Fluids*, **109**, 155-167

15. Sohankar A., Mohagheghian S., Dehghan A., Manshadi M.D., 2015b, A smoke visualization study of the flow over a square cylinder at incidence and tandem square cylinders, *Journal of Visualization*, **18**, 687-703

16. Turhal A.Ö., Çuhadaroğlu B., 2010, The effects of surface injection through a perforated square cylinder on some aerodynamic parameters, *Experimental Thermal and Fluid Science*, **34**, 725-735

Manuscript received October 14, 2016; accepted for print July 12, 2017

JOURNAL OF THEORETICAL AND APPLIED MECHANICS
55, 4, pp. 1409-1422, Warsaw 2017
DOI: 10.15632/jtam-pl.55.4.1409

DYNAMIC STABILITY OF A STEPPED DRILLSTRING CONVEYING DRILLING FLUID

Guang-Hui Zhao, Song Tang, Zheng Liang, Ju Li

School of Mechanical Engineering, Southwest Petroleum University, Chengdu 610500, China
e-mail: wy_zgh@126.com; m15102835095@163.com; liangz_2242@126.com; littlemj@126.com

Taking into account differences between a drill pipe (DP) and a drill collar (DC), the drillstring in a vertical well is modeled as a stepped pipe conveying a drilling fluid downwards to the bottom inside the string and then upwards to the ground from the annulus. An analytical model that describes lateral vibration of the drillstring and involves the drillstring gravity, weight on bit (WOB), hydrodynamic force and damping force of the drilling fluid is established. By analysis of complex frequencies, the influences of WOB, borehole diameter, DP length, velocity and density of the drilling fluid on the stability of the system are discussed.

Keywords: drillstring, stepped fluid-conveying pipe, complex frequency, stability, FEM

Nomenclature

A_{ch}	–	cross-sectional flow area of annulus, m^2
A_i	–	cross-sectional flow area inside drillstring, m^2
A_o	–	external cross-sectional area of drillstring, m^2
C_f	–	frictional damping coefficient of drilling fluid
D_{ch}	–	borehole diameter, m
D_h	–	hydraulic diameter of annular flow, m
D_i, D_o	–	inner and outer diameter of drillstring, m
EI	–	flexural rigidity, N·m^2
k	–	viscous damping coefficient of drilling fluid
L	–	drillstring length, m
M_t	–	mass per unit length of drillstring, kg/m
M_f	–	mass per unit length of fluid inside drillstring, kg/m
p_i	–	fluid pressure inside drillstring, Pa
p_o	–	fluid pressure in annulus, Pa
S_{tot}	–	wetted area per unit length, m^2
T	–	axial force, N
U_i, U_o	–	flow velocity inside and outside drillstring, m/s
ρ_f	–	drilling fluid density, kg/m^3
χ	–	added mass coefficient
ω	–	complex frequency

Subscripts

1 – DP segment, 2 – DC segment, L – at the borehole bottom

1. Introduction

The drillstring is the most widely used and important part of the drilling rig system of petroleum and natural gas. Working under complex conditions, the drillstring is apt to lose stability and collides with the borehole wall seriously. It would lead to reduction in both the quality of wellbore and the service life of drilling tools, and result in the raise of drilling costs ultimately (Hakimi and Moradi, 2010; Zamani *et al.*, 2016; Navarro-López *et al.*, 2007).

In the recent years, many researches on transverse vibration of the drillstring have been conducted. But most of these works ignored the interaction between the drillstring and drilling mud. The conventional exploitation mode of oil and gas reservoir is through the vertical well, and the studies on dynamic characteristics of the drillstring in the vertical well are the most. The influence of installation sites of stabilizers on lateral vibration of the drillstring was discussed by Zhao *et al.* (2014) and Mongkolcheep *et al.* (2015). Considering the damping effect of the drilling fluid, Ghasemloonia *et al.* (2013, 2014) analyzed the coupled axial-transverse vibration of the drillstring in vibration-assisted rotary drilling, however the flow effect was not included. With the widespread implementation of extended reach wells in offshore and onshore oilfields, the dynamic characteristics of drillstrings in the horizontal and inclined wells also attract attention of the researchers. Considering the drillstring in an inclined well as a simply supported axially moving rotor, Sahebkar *et al.* (2011) derived the kinetic equation of the string by means of Hamilton's principle. Zhu and Di (2011) and Zhu *et al.* (2012) studied the effect of pre-bent deflection on lateral vibration of drill collars in horizontal and inclined wells respectively. Tikhonov and Safronov (2011) and Samuel and Yao (2013) developed a two-dimensional transverse vibration model of the drillstring to three-dimensional circumstances. Because of the complexity of the drillstring system, the influence of drilling fluid flow on the dynamic response of the drillstring was not considered in these studies.

With the whole process of drilling operation, both the hollow drillstring and the annular space between the drillstring and borehole wall are filled with a drilling fluid flowing axially. The drillstring could be regarded as a flexible and slender pipe conveying fluid in the wellbore. Fluid-solid coupling vibration of the fluid-conveying pipe has attracted considerable attention for its extensive engineering applications and rich dynamic responses (Jin and Song, 2005; Xu and Yang, 2006; Panda and Kar, 2007; Wang, 2009; Ni *et al.*, 2015). As early as 1978, Hannoyer and Paidoussis (1978) established a dynamic model of tubular beams simultaneously subjected to internal and external axial flows based on dynamics of cylindrical structures subjected to axial flow (Paidoussis, 1973). Later, Zhang and Miska (2005) reduced the drillstring to a uniform tubular beam, and used the model of fluid-conveying pipe to simulate the dynamic stability of the drillstring system in response to its own weight, WOB and drilling fluid flowing inside and outside the string. In 2008, Paidoussis *et al.* (2008) revised the expression of the frictional viscous force in the normal direction due to the external flow used in the previous studies (Luu, 1983), and discussed the effect of flow velocity on the stability of the drillstring-like system with a floating drill bit by using Galerkin-Fourier method. Meanwhile, Qian *et al.* (2008) studied dynamics of the drill-string-like system in the counterflush drilling process where the drilling fluid flowed downwards to the bottom through the annular region and returned upwards to the ground in the drillstring. The model of the fluid-conveying pipe could reflect the characteristics of fluid-structure interaction of the string system well, which was validated by an experiment (Rinaldi and Paidoussis, 2012). In these analytical models, however, the drillstring was reduced to a uniform pipe that was very different from the actual drillstring. The drillstring is mainly composed of DP and DC. Compared with DP, DC has larger outer diameter and smaller inner diameter which makes both the line density and stiffness of DC much larger than those of DP. Under a given drilling pressure, the dynamic prediction of the uniform string model, whose

neutral point (the point where the axial force is zero) is much higher than that of the actual drillstring, may be inaccurate.

In view of the complexity and diversity of make-up of the string, well path, drilling fluid properties and drilling parameters, it is still impossible to describe the dynamic response of the drillstring system quantitatively. At present, it remains the main way to explore the effect of a single factor on the system and coupling interaction among several factors. The present study is concerned with the dynamics of the drillstring that is in a vertical well and simplified to be a stepped fluid-conveying pipe composed of DP and DC. Considering the drillstring gravity, WOB and drilling fluid flowing inside and outside the string, an analytical model of lateral vibration of drillstring is proposed. The effect of the fluid-pipe interaction and the drillstring structure on the stability of the drillstring system is discussed.

2. Dynamic model

The drillstring that is composed of DP, DC, connector and a variety of accessories plays an important role in conveying drilling fluid, exerting WOB and transmitting power on the bit. In the drilling process using a PDC bit or an impregnated diamond bit, the bottom hole rock is broken by cutting or grinding. So, WOB fluctuates weakly and could be reduced to a constant value. Under the action of drilling pressure and floating weight, the upper part of the drillstring is subjected to tensile stress and the lower part is compressed. To avoid the DP from buckling, the neutral point is generally located at the section of DC. Generally, the drilling fluid is pumped downwards through the inner channel of the drillstring from the well head, flows through the drill bit and returns to the ground along the annular space between the drillstring and borehole wall. Ignoring the influence of tool joints and flexibility of the drilling rig, the drillstring is simplified to be a stepped fluid-conveying pipe composed of DP and DC, which is constrained by a fixed hinge at the well head and a movable hinge at the bottom hole (Fig. 1). The origin of the

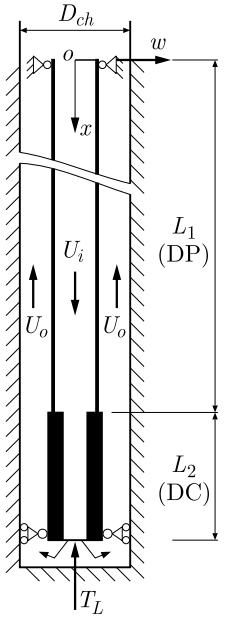

Fig. 1. Sketh of drillstring

coordinate o is located at the well head, x-axis is directed vertically downwards, and the lateral displacement of the drillstring is $w(x,t)$. Considering the drillstring gravity, WOB, constraint of the wellbore and drilling fluid flowing inside and outside the drillstring, the equation of lateral

vibration of the stepped drillstring could be established by doing similar element analysis as the model of Paidoussis *et al.* (2008)

$$\begin{aligned} &EI\frac{\partial^4 w}{\partial x^4}+M_t\frac{\partial^2 w}{\partial t^2}+M_f\Big(\frac{\partial^2 w}{\partial t^2}+2U_i\frac{\partial^2 w}{\partial t\partial x}+U_i^2\frac{\partial^2 w}{\partial x^2}\Big)\\ &\quad+\chi\rho_f A_o\Big(\frac{\partial^2 w}{\partial t^2}-2U_o\frac{\partial^2 w}{\partial t\partial x}+U_o^2\frac{\partial^2 w}{\partial x^2}\Big)-\frac{\partial}{\partial x}(A_o p_o-A_i p_i-T)\frac{\partial w}{\partial x}\\ &\quad-(A_o p_o-A_i p_i-T)\frac{\partial^2 w}{\partial x^2}+\frac{1}{2}C_f\rho_f D_o U_o\frac{\partial w}{\partial t}+k\frac{\partial w}{\partial t}=0 \end{aligned} \tag{2.1}$$

where

$$\chi=\frac{D_{ch}^2+D_o^2}{D_{ch}^2-D_o^2}\qquad D_h=\frac{4A_{ch}}{S_{tot}}\qquad S_{tot}=\pi(D_{ch}+D_o)$$

$$k=\sqrt{2\nu\omega}\pi\rho_f D_o\left(1+\frac{(D_{ch}/D_o)^3}{[1-(D_{ch}/D_o)^2]^2}\right)$$

(symbolic meaning are listed in nomenclature), and

$$\frac{\partial}{\partial x}(A_o p_o-A_i p_i-T)=-[M_t-\rho_f(A_o-A_i)+M_f-\rho_f A_o]g+\frac{1}{2}C_f\rho_f D_o U_o^2\Big(1+\frac{D_o}{D_h}\Big) \tag{2.2}$$

The differences between Eq. (2.1) and the model of the drillstring-like system of Paidoussis *et al.* (2008) are mainly in two aspects: 1) except for the friction damping C_f and density ρ_f, all the physical parameters are different between the DP part and DC part; 2) WOB that is an important factor in the stability of the drillstring is included and the drill bit is constrained by a movable hinge. So, the present model and parameters are more closely related to a real system. In the following equations, subscripts 1 and 2 would be used to indicate the parameters associated with DP and DC, respectively. The term $(A_o p_o - A_i p_i - T)$ in Eq. (2.1) could be obtained by integrating Eq. (2.2) as follows.

For the DP segment

$$\begin{aligned} A_o p_o-A_i p_i-T&=A_{o2}p_{oL}-A_{i2}p_{iL}-T_L\\ &+\Big\{[M_{t2}-\rho_f(A_{o2}-A_{i2})+M_{f2}-\rho_f A_{o2}]g-\frac{1}{2}C_f\rho_f D_{o2}U_{o2}^2\Big(1+\frac{D_{o2}}{D_{h2}}\Big)\Big\}(L-L_1)\\ &+\Big\{[M_{t1}-\rho_f(A_{o1}-A_{i1})+M_{f1}-\rho_f A_{o1}]g-\frac{1}{2}C_f\rho_f D_{o1}U_{o1}^2\Big(1+\frac{D_{o1}}{D_{h1}}\Big)\Big\}(L_1-x) \end{aligned} \tag{2.3}$$

And for the DC segment

$$\begin{aligned} A_o p_o-A_i p_i-T&=A_{o2}p_{oL}-A_{i2}p_{iL}-T_L\\ &+\Big\{[M_{t2}-\rho_f(A_{o2}-A_{i2})+M_{f2}-A_{o2}\rho_f]g-\frac{1}{2}C_f\rho_f D_{o2}U_{o2}^2\Big(1+\frac{D_{o2}}{D_{h2}}\Big)\Big\}(L-x) \end{aligned} \tag{2.4}$$

where p_{iL} and p_{oL} are fluid pressures of the bottom hole inside and outside the drillstring, respectively. They could be calculated based on the following assumptions: fluid pressure in the annulus is zero at the well head, namely, $p_o\big|_{x=0}=0$; the local loss near the joint of DP and DC is ignored, and the variation of pressure p_o with x is approximated as a piecewise linear function. Considering the pressure drop of the drilling fluid flowing through the bit jet (Zhang *et al.*, 2005), one obtains

$$\begin{aligned} p_{oL}&=\rho_f gL+\frac{1}{2A_{o2}}C_f D_{o2}U_{o2}^2(L-L_1)\frac{D_{o2}}{D_{h2}}+\frac{1}{2A_{o1}}C_f D_{o1}U_{o1}^2 L_1\frac{D_{o1}}{D_{h1}}\\ p_{iL}&=p_{oL}+\rho_f U_{o2}(U_{o2}-U_{i2}) \end{aligned} \tag{2.5}$$

Substituting Eqs. (2.2)-(2.5) into Eq. (2.1), the equations of lateral vibration of DP and DC could be obtained. The boundary conditions at the well head and bottom are

$$w(0,t)=\frac{\partial^2 w}{\partial x^2}(0,t)=0 \qquad w(L,t)=\frac{\partial^2 w}{\partial x^2}(L,t)=0 \tag{2.6}$$

For convenience of the analysis, the following dimensionless quantities could be defined based on the parameters of DC

$$\eta=\frac{w}{L} \qquad \xi=\frac{x}{L} \qquad \tau=\frac{t}{L^2}\sqrt{\frac{E_2I_2}{M_{t2}+M_{f2}+\rho_f A_{o2}}} \qquad u_{i1}=\sqrt{\frac{M_{f1}}{E_2I_2}}U_{i1}L$$

$$u_{i2}=\sqrt{\frac{M_{f2}}{E_2I_2}}U_{i2}L \qquad u_{o1}=\sqrt{\frac{\rho_f A_{o1}}{E_2I_2}}U_{o1}L \qquad u_{o2}=\sqrt{\frac{\rho_f A_{o2}}{E_2I_2}}U_{o2}L$$

$$\beta_{i1}=\frac{M_{f1}}{M_{t2}+M_{f2}+\rho_f A_{o2}} \qquad \beta_{o1}=\frac{\rho_f A_{o1}}{M_{t2}+M_{f2}+\rho_f A_{o2}}$$

$$\beta_{i2}=\frac{M_{f2}}{M_{t2}+M_{f2}+\rho_f A_{o2}} \qquad \beta_{o2}=\frac{\rho_f A_{o2}}{M_{t2}+M_{f2}+\rho_f A_{o2}}$$

$$\gamma_1=\frac{[M_{t1}-\rho_f(A_{o1}-A_{i1})+M_{f1}-A_{o1}\rho_f]gL^2}{E_2I_2} \qquad \kappa_1=\frac{k_1L^2}{\sqrt{E_2I_2(M_{t2}+M_{f2}+\rho_f A_{o2})}}$$

$$\gamma_2=\frac{[M_{t2}-\rho_f(A_{o2}-A_{i2})+M_{f2}-A_{o2}\rho_f]gL^2}{E_2I_2} \qquad \kappa_2=\frac{k_2L^2}{\sqrt{E_2I_2(M_{t2}+M_{f2}+\rho_f A_{o2})}}$$

$$\Gamma=\frac{L^2T_L}{E_2I_2} \qquad \Pi_i=\frac{L^2A_{f2}p_{iL2}}{E_2I_2} \qquad \Pi_o=\frac{L^2A_{o2}p_{oL}}{E_2I_2} \qquad c_f=\frac{4C_f}{\pi}$$

$$h_1=\frac{D_{o1}}{D_{h1}} \qquad h_2=\frac{D_{o2}}{D_{h2}} \qquad \varepsilon_1=\frac{L}{D_{o1}} \qquad \varepsilon_2=\frac{L}{D_{o2}} \qquad \lambda=\frac{A_{o1}}{A_{o2}}$$

$$\alpha_1=\frac{E_1I_1}{E_2I_2} \qquad \alpha_2=\frac{M_{t1}+M_{f1}+\rho_f A_{o1}}{M_{t2}+M_{f2}+\rho_f A_{o2}} \qquad \delta=\frac{L_1}{L}$$

By substituting the quantities above into Eq. (2.1), the dimensionless governing equations for DP and DC are obtained, respectively. For the DP segment

$$\begin{aligned}
&\alpha_1\frac{\partial^4\eta}{\partial\xi^4}+[\alpha_2+\beta_{o1}(\chi_1-1)]\frac{\partial^2\eta}{\partial\tau^2}+2\Big(\sqrt{\beta_{i1}}u_{i1}-\chi_1\sqrt{\beta_{o1}}u_{o1}\Big)\frac{\partial^2\eta}{\partial\tau\partial\xi}+\Big(u_{i1}^2+\chi_1u_{o1}^2\Big)\frac{\partial^2\eta}{\partial\xi^2}\\
&\quad-\Big\{-\Gamma-\Pi_{iL}+\Pi_{oL}+\Big[\gamma_2-\frac{1}{2}c_f\varepsilon_2u_{o2}^2(1+h_2)\Big](1-\delta)\\
&\quad+\Big[\gamma_1-\frac{1}{2}c_f\varepsilon_1u_{o1}^2(1+h_1)\Big](\delta-\xi)\Big\}\frac{\partial^2\eta}{\partial\xi^2}+\Big[\gamma_1-\frac{1}{2}c_f\varepsilon_1u_{o1}^2(1+h_1)\Big]\frac{\partial\eta}{\partial\xi}\\
&\quad+\frac{1}{2}c_f\varepsilon_1\sqrt{\beta_{o1}}u_{o1}\frac{\partial\eta}{\partial\tau}+\kappa_1\frac{\partial\eta}{\partial\tau}=0
\end{aligned} \tag{2.7}$$

and for the DC segment

$$\begin{aligned}
&\frac{\partial^4\eta}{\partial\xi^4}+[1+\beta_{o2}(\chi_2-1)]\frac{\partial^2\eta}{\partial\tau^2}+2\Big(\sqrt{\beta_{i2}}u_{i2}-\chi_2\sqrt{\beta_{o2}}u_{o2}\Big)\frac{\partial^2\eta}{\partial\xi\partial\tau}+(u_{i2}^2+\chi_2u_{o2}^2)\frac{\partial^2\eta}{\partial\xi^2}\\
&\quad-\Big\{-\Gamma-\Pi_{iL}+\Pi_{oL}+\Big[\gamma_2-\frac{1}{2}c_f\varepsilon_2u_{o2}^2(1+h_2)\Big](1-\xi)\Big\}\frac{\partial^2\eta}{\partial\xi^2}\\
&\quad+\Big[\gamma_2-\frac{1}{2}c_f\varepsilon_2u_{o2}^2(1+h_2)\Big]\frac{\partial\eta}{\partial\xi}+\frac{1}{2}c_f\varepsilon_2u_{o2}\sqrt{\beta_{o2}}\frac{\partial\eta}{\partial\tau}+\kappa_2\frac{\partial\eta}{\tau}=0
\end{aligned} \tag{2.8}$$

where

$$\begin{aligned} \Pi_{oL} &= \frac{A_{o2}\rho_f g L^3}{E_2 I_2} + \frac{1}{2}c_f \varepsilon_2 u_{o2}^2(1-\delta)h_2 + \frac{1}{2}c_f \varepsilon_1 u_{o1}^2 \delta\lambda h_1 \\ \Pi_{iL} &= \alpha^2 \Pi_{oL} + \alpha u_{o2}(\alpha u_{o2} - u_{i2}) \end{aligned} \tag{2.9}$$

The dimensionless boundary conditions are

$$\eta(0,\tau) = \frac{\partial^2 \eta}{\partial \xi^2}(0,\tau) = 0 \qquad \eta(1,\tau) = \frac{\partial^2 \eta}{\partial \xi^2}(1,\tau) = 0 \tag{2.10}$$

3. Method of solution

It is difficult to solve Eqs. (2.7)-(2.10) of the stepped fluid-conveying pipe by means of the conventional Galerkin method, the multiple scales method and the differential quadrature method. Here, the finite element method that takes the Hermite polynomial as shape function is used.

3.1. The finite element method

The drillstring is divided into n elements by $(n+1)$ nodes. The length of the j-th element is $L_j = \xi_{j+1} - \xi_j$, and the lateral displacement $\eta(\xi)$ is represented by means of cubic Hermite interpolation

$$\eta(\xi) = \mathbf{N}_{ej} \cdot \boldsymbol{\eta}_{ej} \qquad \xi_j \leqslant \xi \leqslant \xi_{j+1} \tag{3.1}$$

where $\mathbf{N}_{ej}$ and $\boldsymbol{\eta}_{ej}$ are primary functions and nodal displacements of the j-th element, respectively, and denoted as

$$\mathbf{N}_{ej} = \begin{bmatrix} \lambda_j^2(\lambda_j + 3\lambda_{j+1}) \\ L_j \lambda_j^2 \lambda_{j+1} \\ \lambda_{j+1}^2(\lambda_{j+1} + 3\lambda_j) \\ -L_j \lambda_{j+1}^2 \lambda_j \end{bmatrix}^{\mathrm{T}} \qquad \boldsymbol{\eta}_{ej} = \begin{bmatrix} \eta_j \\ \varphi_j \\ \eta_{j+1} \\ \varphi_{j+1} \end{bmatrix}$$

where $\lambda_j = (\xi_{j+1} - \xi)/L_j$, $\lambda_{j+1} = (\xi - \xi_j)/L_j$. η_j and φ_j are deflection and rotation angles of the j-th node, respectively. Substituting Eq. (3.1) into Eqs. (2.7)-(2.8) and using the virtual work principle, we obtain the equation of motion of the j-th element as follows

$$\mathbf{M}_{ej}\ddot{\boldsymbol{\eta}}_{ej} + \mathbf{C}_{ej}\dot{\boldsymbol{\eta}}_{ej} + \mathbf{K}_{ej}\boldsymbol{\eta}_{ej} = \mathbf{0} \tag{3.2}$$

where $\mathbf{M}_{ej}$, $\mathbf{C}_{ej}$, and $\mathbf{K}_{ej}$ are the mass matrix, damping matrix and stiffness matrix of the j-th element, respectively. It should be noted that the element matrices of DP are different from those of DC.

Assembling the element matrices in the global coordinate system and using boundary conditions (2.10), the finite element equation of the whole drillstring system could be obtained

$$\mathbf{M}\ddot{\boldsymbol{\eta}} + \mathbf{C}\dot{\boldsymbol{\eta}} + \mathbf{K}\boldsymbol{\eta} = \mathbf{0} \tag{3.3}$$

where $\mathbf{M}$, $\mathbf{C}$ and $\mathbf{K}$ are all global matrices of the order $2n$ corresponding to mass, damping and stiffness, respectively.

The solutions to Eq. (3.3) could be expressed as

$$\boldsymbol{\eta} = \overline{\boldsymbol{\eta}} \mathrm{e}^{\omega\tau} \tag{3.4}$$

Substituting it into Eq. (3.3), gives

$$(\omega^2\mathbf{M} + \omega\mathbf{C} + \mathbf{K})\overline{\boldsymbol{\eta}} = \mathbf{0} \tag{3.5}$$

Equation (3.5) is a generalized eigenvalue problem, and the stability of the drillstring system could be determined by calculating the complex eigenvalues ω of the matrix $\mathbf{E}$

$$\mathbf{E} = \begin{bmatrix} \mathbf{0} & \mathbf{I} \\ -\mathbf{M}^{-1}\mathbf{K} & -\mathbf{M}^{-1}\mathbf{C} \end{bmatrix} \tag{3.6}$$

$\mathrm{Re}(\omega)$ and $\mathrm{Im}(\omega)$ are the real and imaginary parts of ω, respectively. $\mathrm{Re}(\omega)$ is related to modal damping of the system, and $\mathrm{Im}(\omega)$ is the natural frequency. In the case of $\mathrm{Re}(\omega) \geqslant 0$ and $\mathrm{Im}(\omega) \neq 0$ flutter instability occurs, and the fluid velocity at which $\mathrm{Re}(\omega)$ increases to zero from negative values is called the critical flutter velocity u_{cf}. Buckling instability happens when $\mathrm{Im}(\omega) = 0$, and the corresponding flow rate is the critical buckling velocity u_{cd}. In this paper, u_{cf} and u_{cd} are all defined based on the internal flow of the DP segment.

3.2. Model validation

The correctness of the finite element method and the numerical model is verified by comparing the present results with those given by Dai *et al.* (2013) and Paidoussis *et al.* (2008).

Firstly, the present model is reduced into a fluid-conveying cantilevered pipe that consists of an aluminum segment and a steel segment according to Dai *et al.* (2013). These two segments have the same cross section and length, and the end of the aluminum segment is fixed. For the cantilever beam, the rows and columns that are associated with the fixed end in the global matrices of the present model are set to zero. The evolution of the first four complex frequencies with the flow velocity is illustrated in Fig. 2. The dimensionless critical flutter velocity of the second mode is $u_{cf} = 7.8$, which is completely consistent with literature (Dai *et al.*, 2013), and shows correctness of the finite element method.

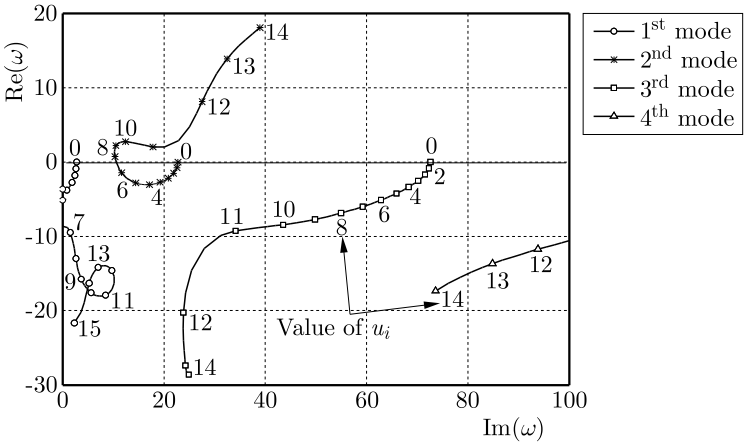

Fig. 2. The present result of the first four dimensionless complex frequencies as functions of u_i

Secondly, in accordance with Paidoussis *et al.* (2008), the stepped pipe is reduced to a uniform tubular column and the parameters are: $L_1 = 0\,\mathrm{m}$, $L_2 = 1000\,\mathrm{m}$, $D_{i2} = 0.45\,\mathrm{m}$, $D_{o2} = 0.5\,\mathrm{m}$, $D_{ch} = 10\,\mathrm{m}$, $\rho_f = 998\,\mathrm{kg/m^3}$, $\rho_t = 7830\,\mathrm{kg/m^3}$, $C_f = 0.0125$, and $\nu = 10^{-6}\,\mathrm{m^2/s}$. By using the finite element method, we obtain the first three complex frequencies varying with the flow rate u_i (Fig. 3). This result can be compared to that given by Paidoussis *et al.* (2008) through the hybrid Galerkin-Fourier method. It needs to be pointed out that the definition of ω in this literature is different from that in the present paper. Denoting ω in Paidoussis *et al.* (2008) as ω^*,

the relationships between ω^* and ω in this paper are: $\mathrm{Re}(\omega^*) = \mathrm{Im}(\omega)$ and $\mathrm{Im}(\omega^*) = -\mathrm{Re}(\omega)$. As shown in Fig. 3, the present results agree with those of Paidoussis *et al.* (2008) very well, and the dimensionless critical flutter velocity of the second and third modes are $u_{cf} = 2.2$ and $u_{cf} = 2.56$, respectively. Compared with the result of Paidoussis *et al.* (2008), the relative errors are only 3.8% and 0.4%. It demonstrates correctness of the present model. So, the present model and algorithm would be used to analyze the stability of the stepped drillstring system composed of DP and DC.

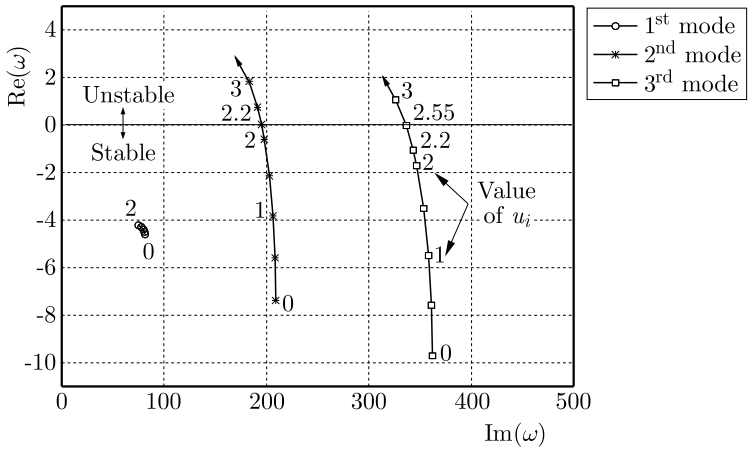

Fig. 3. The first three complex frequencies as functions of the velocity of fluid u_i

4. Dynamic stability of drillstring system

The drillstring system in the vertical well with well depth $L = 1000\,\mathrm{m}$ is studied. The parameters are, for DP: $L_1 = 948\,\mathrm{m}$, $D_{i1} = 0.127\,\mathrm{m}$, $D_{o1} = 0.1016\,\mathrm{m}$, $m_{t1} = 43.75\,\mathrm{kg/m}$; and for DC: $L_2 = 52\,\mathrm{m}$, $D_{i2} = 0.203\,\mathrm{m}$, $D_{o2} = 0.07144\,\mathrm{m}$, $m_{t2} = 228.28\,\mathrm{kg/m}$; in addition, $T = 50\,\mathrm{kN}$, $D_{ch} = 0.314\,\mathrm{m}$, $\rho_f = 1200\,\mathrm{kg/m^3}$, $\nu = 10^{-6}\,\mathrm{m^2/s}$. The viscosity damping coefficient C_f of the drilling fluid is a semi-empirical value of 0.0125, and k could be calculated iteratively for each natural frequency.

Figure 4 illustrates the first four complex frequencies of this DP-DC system varying with the flow rate U_{i1}, and indicates that the system is in the stable state for $U_{i1} \leqslant 110\,\mathrm{m/s}$. With an increase in U_{i1}, $\mathrm{Re}(\omega)$ and $\mathrm{Im}(\omega)$ all decrease gradually, and stability of the DP-DC system deteriorates.

In order to show the difference between the present stepped model and the uniform column model (Zhang and Miska, 2005), the drillstring is also simplified as a uniform DP model, i.e. $L_1 = 1000\,\mathrm{m}$, $L_2 = 0$, the other parameters are chosen as the DP-DC model above. For this DP model, the first four complex frequencies ω that are functions of U_{i1} are obtained and shown in Fig. 5. The system loses stability by buckling in its first mode at $U_{i1} = 43.7\,\mathrm{m/s}$, namely, $u_{cd} = 43.7\,\mathrm{m/s}$.

By comparing Fig. 5 to Fig. 4, one could find that the stability characteristics of these two models are very different. Both natural frequency and critical buckling velocity of the stepped DP-DC model are all much higher than those given by the uniform DP model. Compared with DP model, DP-DC model has a lower neutral point and a higher stiffness of the compression section because the linear density and stiffness of DC are all larger than those of DP. This is consistent with the realistic well condition. As a result, DC could improve the stability of the drillstring system significantly, and the stepped DP-DC model could describe the stability of the drillstring system better.

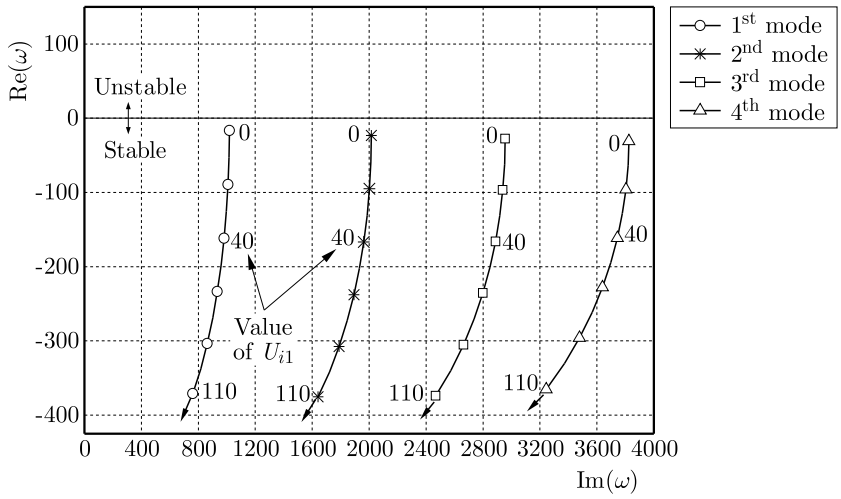

Fig. 4. The first four complex frequencies as functions of U_{i1} by the stepped DP-DC model ($D_{ch} = 0.314\,\mathrm{m}$)

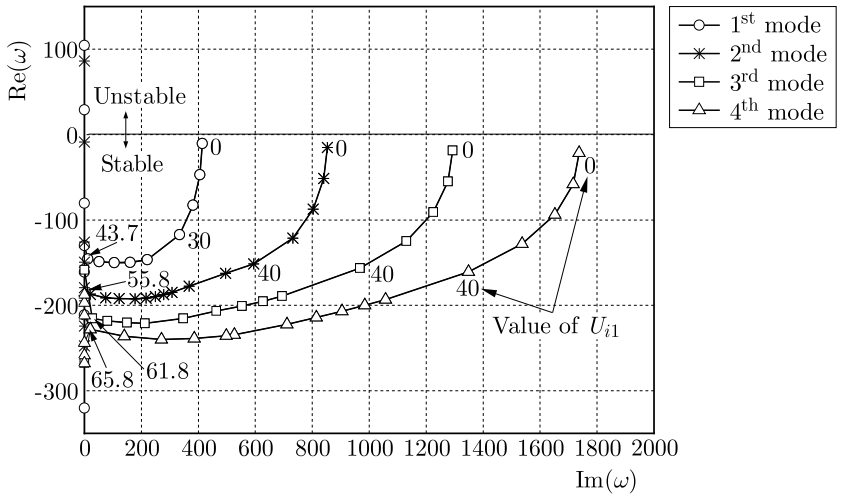

Fig. 5. The first four complex frequencies as functions of U_{i1} by the uniform DP model

5. The effect of parameters on stability

In addition to the internal flow rate U_i, the parameters such as WOB T_L, borehole size D_{ch}, well depth L and drilling fluid density ρ_f also have effects on the stability of the drillstring system.

5.1. WOB

WOB is an important drilling parameter which influences drilling speed greatly and could be controlled by adjusting the hook load. With an increase in WOB, the neutral point gradually moves up. In order to avoid the DP from compression, the neutral point should be located in the drill collar. As a result, WOB should not exceed 98kN for the drillstring system at hand. Figure 6 shows the variation of the first four dimensionless complex frequencies with WOB (T_L) for $U_{i1} = 5\,\mathrm{m/s}$. It means that the drillstring system is stable under the normal drilling condition ($T_L \leqslant 98\,\mathrm{kN}$). Along with T_L increasing, $\mathrm{Re}(\omega)$ increases and $\mathrm{Im}(\omega)$ decreases. It means that WOB is the instability drive of the drillstring system. As the WOB increases further, the buckling instability will occur eventually.

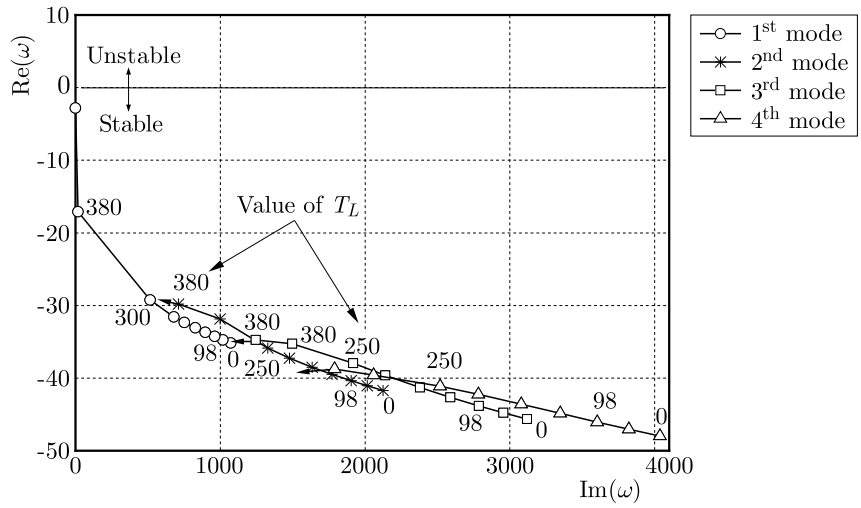

Fig. 6. The first four dimensionless complex frequencies as functions of T_L at $U_{i1} = 5\,\mathrm{m/s}$

5.2. Borehole size

Borehole diameter D_{ch} can be approximated to the bit diameter. In order to ensure implement of wash over fishing operation, 8-in (0.203 m) DC should be equipped with the bit not smaller than 91/2-in (0.2413 m) (NDRC, 2007). The borehole size affects the annular flow velocity. Under the conditions of $D_{ch} = 0.2669\,\mathrm{m}$, 0.2413 m and 0.314 m, the variation of complex frequencies of the drillstring with fluid velocity of U_{i1} are obtained and shown in Fig. 4, Fig. 7 and Fig. 8, respectively. It could be concluded by comparative analysis of these three cases that: Im(ω) of the first four modes decreases along with increasing U_{i1}; the critical buckling velocity (u_{cd}) exceeds 110 m/s for $D_{ch} = 0.314\,\mathrm{m}$ (as shown in Fig. 4), $u_{cd} = 102.2\,\mathrm{m/s}$ for $D_{ch} = 0.2669\,\mathrm{m}$ (Fig. 7) and $u_{cd} = 70.9\,\mathrm{m/s}$ for $D_{ch} = 0.2413\,\mathrm{m}$ (Fig. 8), respectively. It is shown that the drillstring system is more stable for the wellbore with larger size. Therefore, an increase in the fluid velocity, both inside and outside the drillstring, will drive the drillstring system buckling instability.

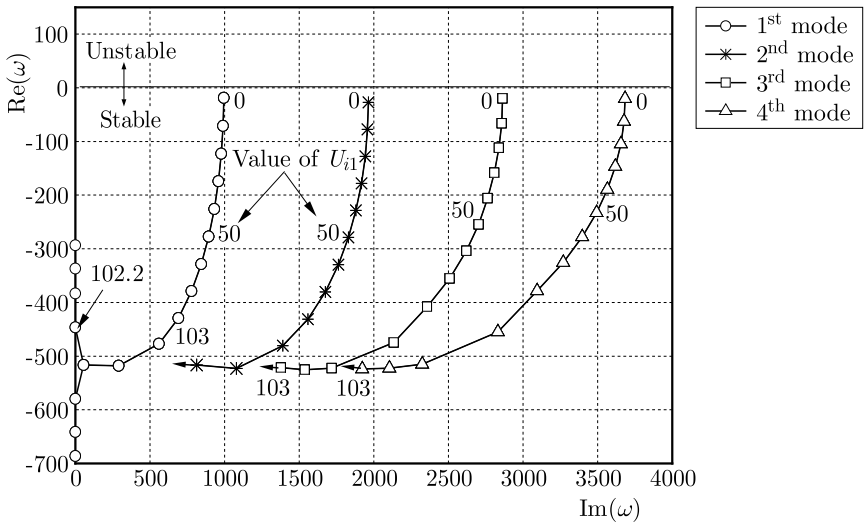

Fig. 7. The first four complex frequencies as functions of U_i for $D_{ch} = 0.2669\,\mathrm{m}$

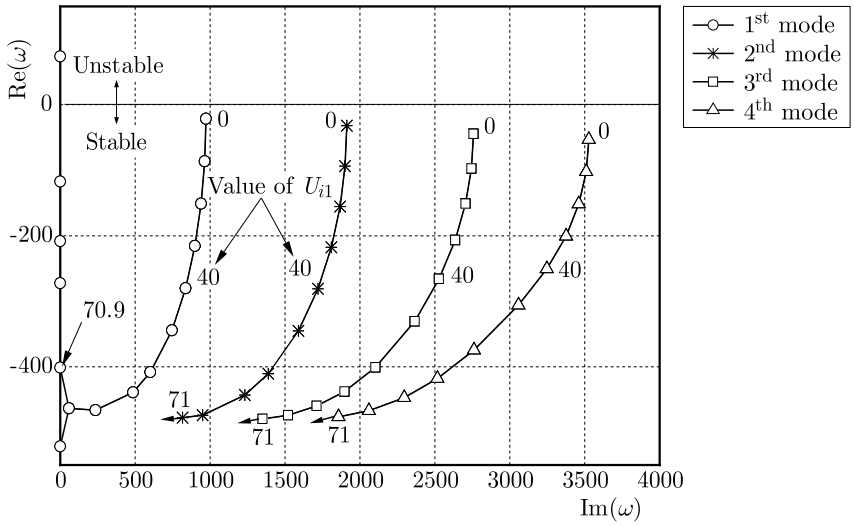

Fig. 8. The first four complex frequencies as functions of U_i for $D_{ch} = 0.2413\,\mathrm{m}$

5.3. Drillstring length

In the actual drilling operation, the structure and length of DC are determined according to the design WOB and remain constant, while length of DP increases in the drilling process. Keeping $L_2 = 52\,\mathrm{m}$, $\mathrm{Im}(\omega)$ of the first four modes that varies along with length of the drillstring is illustrated in Fig. 9. It shows that the relationship between $\mathrm{Im}(\omega)$ and L is similar to a parabola. As the well depth increases, the stability of the drillstring system becomes worse, but the effect of the drillstring length on the stability is smaller and smaller.

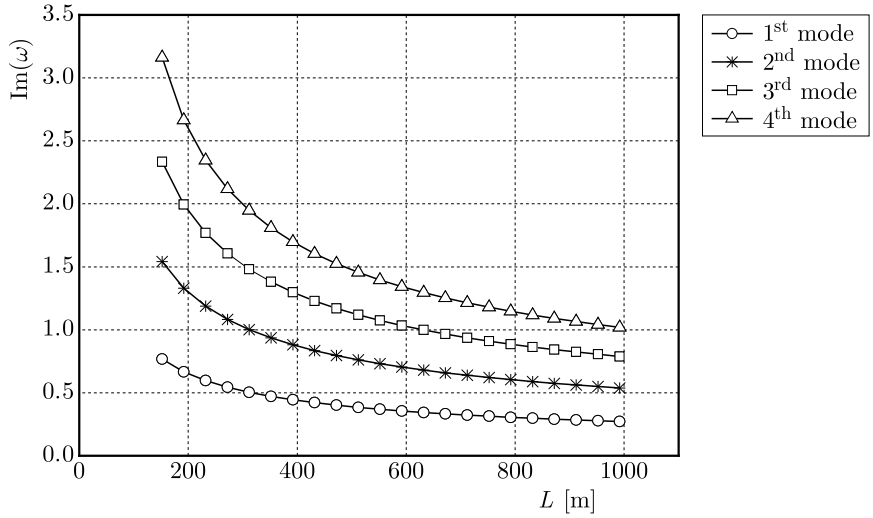

Fig. 9. The effect of the drillstring length on natural frequencies

5.4. Drilling fluid density

In addition to carrying cuttings, cooling and lubricating bit, the drilling fluid plays important roles in stabilizing the borehole wall and balancing the formation pressure. The formation pressure is changing with the drilling depth and needs to be balanced by adjusting the drilling fluid density. The density ρ_f exerts influence on its hydrodynamic characteristic and the buoyant weight of drillstring. Varying ρ_f from $800\,\mathrm{kg/m^3}$ to $1800\,\mathrm{kg/m^3}$, the first four natural

frequencies are shown in Fig. 10. With an increase in ρ_f, the natural frequencies of the system increase slightly, and the stability improves in a minor way.

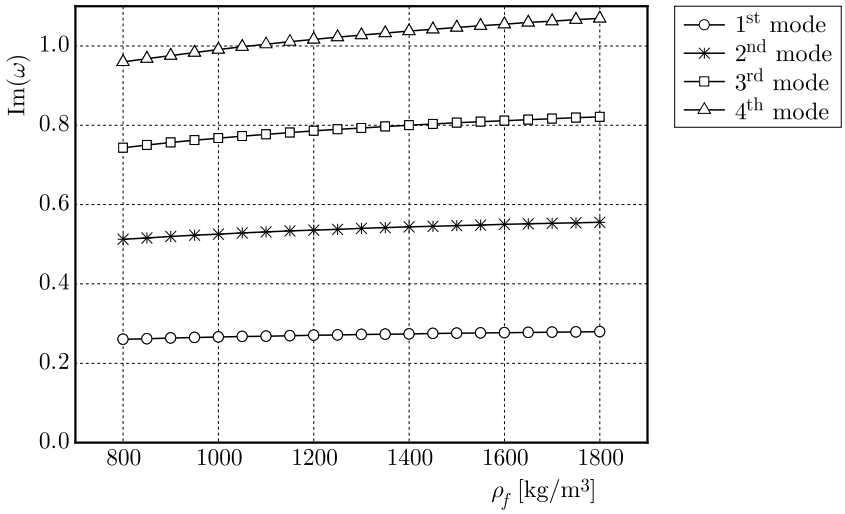

Fig. 10. The effect of drilling fluid density on natural frequencies

6. Conclusion

The drillstring in a vertical well is reduced to a stepped fluid-conveying pipe composed of DP segment and DC segment. Considering the interaction among drillstring gravity, WOB, and drilling fluid that flows inside and outside the drillstring, we propose an analytical model of lateral vibration of the drillstring, discuss the dynamic stability by means of complex frequencies and come to the following conclusions:

- The DC segment whose linear density and stiffness are much larger than that of the DP, could improve the drillstring stability significantly and has a great effect on the dynamics of the whole system. Compared with the uniform string model, the stepped DP-DC model could reflect the dynamic characteristics of the drillstring system better.
- Both WOB and delivery capacity are sources of instability in the drillstring system, and they have a significant effect on the stability of the drillstring system. Buckling instability occurs eventually as these two parameters increase further.
- Along with the increasing well depth, natural frequencies decrease parabolically and the drillstring stability becomes worse. But this influence is smaller and smaller with an increase in the drilling depth.
- Drilling fluid density has a positive effect on the drillstring stability, yet in a minor way.

In the course of drilling operation, one could improve the dynamic stability of the drillstring system by taking actions such as increasing the DC length properly, optimizing the structure of BHA, reducing flow rate under the condition of ensuring cuttings carrying, adopting underbalanced drilling technology, and so on. With the development of logging-while-drilling and controlling technology, the dynamics of drillstring systems with feedback control may be the focus of research in the future.

Acknowledgments

This project was supported by the Open Fund (OGE201403-10) of Key Laboratory of Oil and Gas Equipment, Ministry of Education (SWPU), and the National Natural Science Foundation (51134004) and CSC of China. We also acknowledge association with UNSW.

References

1. Chen S.L., Geradin M., 1995, An improved transfer matrix technique as applied to BHA lateral vibration analysis, *Journal of Sound and Vibration*, **185**, 1, 93-106
2. Dai H.L., Wang L., Ni Q., 2013, Dynamics of a fluid-conveying pipe composed of two different materials, *International Journal of Engineering Science*, **73**, 67-76
3. Ghasemloonia A., Geoff Rideout D., Butt S.D., 2013, Vibration analysis of a drillstring in vibration-assisted rotary drilling: finite element modeling with analytical validation, *Journal of Energy Resources Technology*, **135**, 3, 1-18
4. Ghasemloonia A., Geoff Rideout D., Butt S.D., 2014, Analysis of multi-mode nonlinear coupled axial-transverse drillstring vibration in vibration assisted rotary drilling, *Journal of Petroleum Science and Engineering*, **116**, 36-49
5. Hakimi H., Moradi S., 2010, Drillstring vibration analysis using differential quadrature method, *Journal of Petroleum Science and Engineering*, **70**, 3-4, 235-242
6. Hannoyer M.J., Paidoussis M.P., 1978, Instabilities of tubular beams simultaneously subjected to internal and external axial flows, *Journal of Mechanical Design*, **100**, 328-336
7. Jin J.D., Song Z.Y., 2005, Parametric resonances of supported pipes conveying pulsating fluid, *Journal of Fluids and Structures*, **20**, 763-783
8. Lian Z.H., Zhang Q., Lin T.J., Wang F.H., 2015, Experimental and numerical study of drill string dynamics in gas drilling of horizontal wells, *Journal of Natural Gas Science and Engineering*, **27**, 3, 1412-1420
9. Luu T.P., 1983, On the dynamics of three systems involving tubular beams conveying fluid, M. Eng. Thesis, McGill University, Canada
10. Mongkolcheep K., Ruimi A., Palazzolo A., 2015, Modal reduction technique for predicting the onset of chaotic behavior due to lateral vibrations in drillstrings, *Journal of Vibration and Acoustics*, **137**, 2, 1-11
11. Navarro-López E.M., Cortés D., 2007, Avoiding harmful oscillations in a drillstring through dynamical analysis, *Journal of Sound and Vibration*, **307**, 152-171
12. NDRC, 2007, Practice for selection and use of drill pipe and drill collar (SY/T 6288-2007) (in Chinese), Petroleum Industry Press, Beijing
13. Ni Q., Wang Y.K., Tang M., Luo Y.Y., Yan H., Wang L., 2015, Nonlinear impacting oscillations of a fluid-conveying pipe subjected to distributed motion constraints, *Nonlinear Dynamics*, **81**, 893-906
14. Paidoussis M.P., 1973, Dynamics of cylindrical structures subjected to axial flow, *Journal of Sound and Vibration*, **29**, 3, 365-385
15. Paidoussis M.P., Luu T.P., Prabhakar S., 2008, Dynamics of a long tubular cantilever conveying fluid downwards, which then flows upwards around the cantilever as a confined annular flow, *Journal of Fluids and Structures*, **24**, 111-128
16. Panda L.N., Kar R.C., 2007, Nonlinear dynamics of a pipe conveying pulsating fluid with parametric and internal resonances, *Nonlinear Dynamics*, **49**, 9-30
17. Qian Q., Wang L., Ni Q., 2008, Vibration and stability of vertical upward-fluid-conveying pipe immersed in rigid cylindrical channel, *Acta Mechanica Solida Sinica*, **21**, 431-440
18. Rinaldi S., Paidoussis M.P., 2012, Theory and experiments on the dynamics of a free-clamped cylinder in confined axial air-flow, *Journal of Fluids and Structures*, **28**, 167-179
19. Sahebkar S.M., Ghazavi M.R., Khadem S.E., Ghayesh M.H., 2011, Nonlinear vibration analysis of an axially moving drillstring system with time dependent axial load and axial velocity in inclined well, *Mechanism and Machine Theory*, **46**, 743-760

20. Samuel R., Yao D.P., 2013, Drillstring vibration with hole-enlarging tools: analysis and avoidance, *Journal of Energy Resources Technology*, **135**, 3, 1-13

21. Tikhonov V.S., Safronov A.I., 2011, Analysis of postbuckling drillstring vibrations in rotary drilling of extended-reach wells, *Journal of Energy Resources Technology*, **133**, 4, 043102-043109

22. Wang L., 2009, A further study on the non-linear dynamics of simply supported pipes conveying pulsating fluid, *International Journal of Non-Linear Mechanics*, **44**, 115-121

23. Xu J., Yang Q.B., 2006, Flow-induced internal resonances and mode exchange in horizontal cantilevered pipe conveying fluid, *Applied Mathematics and Mechanics*, **27**, 1, 943-951

24. Zamani S.M., Hassanzadeh-Tabrizi S.A., Sharifi H., 2016, Failure analysis of drill pipe: a review, *Engineering Failure Analysis*, **59**, 605-623

25. Zhang Q., Miska S., 2005, Effects of flow–pipe interaction on drill pipe buckling and dynamics, *Journal of Pressure Vessel Technology*, **127**, 129-136

26. Zhao M., Zhu X.Z., Wang C.L., 2014, Nonlinear dynamic analysis of drill string system for horizontal oil well with different positions of stabilizers, *Applied Mechanics and Materials*, **716-717**, 615-618

27. Zhu W.P., Di Q.F., 2011, Effect of prebent deflection on lateral vibration of stabilized drill collars, SPE-120455-PA

28. Zhu X.Z., He Y.D., Chen L., Yuan H.Q., 2012, Nonlinear dynamics analysis of a drillstring-bit-wellbore system for horizontal oil well, *Advanced Science Letters*, **16**, 13-19

Manuscript received October 10, 2016; accepted for print July 15, 2017

JOURNAL OF THEORETICAL AND APPLIED MECHANICS
55, 4, pp. 1423-1435, Warsaw 2017
DOI: 10.15632/jtam-pl.55.4.1423

A MODEL FOR THE DYNAMIC ANALYSIS OF A BELT TRANSMISSION USING THE DAHL FRICTION MODEL

Krzysztof Kubas
University of Bielsko-Biala, Faculty of Mechanical Engineering and Computer Science, Bielsko-Biała, Poland
e-mail: kkubas@ath.bielsko.pl

The paper presents a two-dimensional model of a belt transmission for dynamic analysis. It is assumed that the belt is modelled by links joined by spring-damping elements with its rotational and translational stiffness. Normal forces in the contact between the belt and the pulleys are implemented by assuming its stiffness and damping, whereas friction is modelled by the Dahl friction model. The calculation results are also presented in two specific cases of load of the belt transmission.

Keywords: belt transmission, dynamic analysis, Dahl friction model

1. Introduction

In the author's earlier papers, two-dimensional models of belt transmissions using the Threlfall friction model (Kubas, 2015) and a model including microslip were developed (Kubas, 2014). In the paper (Kubas, 2014), assumptions and requirements made during the process of model development were presented. In the present paper, the Dahl friction model (Dahl, 1968) is assumed as one in the group of dynamic friction models that allows one to include stiffness of contact areas.

Papers should be mentioned here in which friction was modelled between rubber and other materials. The most well known are works related to automotive engineering, especially those dealing with the modelling of friction between the tyre and the road, see e.g. often cited work by Canudas de Wit *et al.* (2003). Among the proposed friction models, also presented in the paper above was the Dahl friction model. The paper (Canudas de Wit *et al.*, 2003) introduced another dynamic friction model – the LuGre model, which allows one to include the Stribeck effect.

Leamy and Wasfy (2002a,b) presented belt transmission models with a piecewise linear friction model with the possibility of predicting belt creep. It is called the Coulomb-like tri-linear creep-rate-dependent friction model. Another sample model was presented in (Kim *et al.*, 2011) and was called the elastic/perfectly-plastic friction law (EPP).

A group of papers should also be mentioned in which the Dahl friction model is applied as a way of modelling friction in the revolute joint of a belt tensioner, see e.g. Bastien *et al.* (2007) and Chatlet *et al.* (2008).

The changing belt and chain transmissions research objectives over the centuries and more important works were presented by Fawcett (1981).

2. Mathematical model

The model presented in an earlier paper (Kubas, 2014) of a belt transmission was modified by changing it into a friction model. As presented in the above-mentioned work, it was assumed that the belt would be divided into n_b bodies. Each neighbouring pair of bodies was joined by the SDE with proper translational and bending stiffness and damping parameters (Fig. 1).

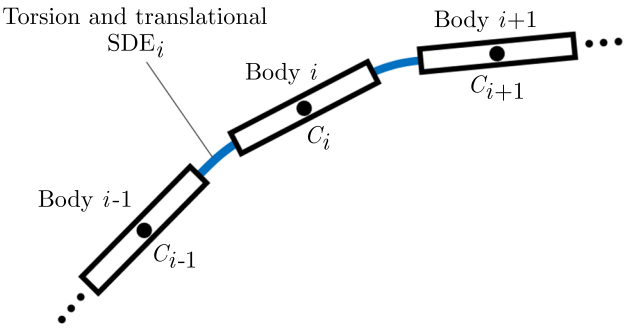

Fig. 1. Assumed belt model with translational and torsion SDEs

For each body i ($i = 1, \ldots, n_b$), it was assumed that there were three generalised coordinates (Fig. 2): translations x_i and y_i and rotation by an angle φ_i relative to the mass centre. The generalised coordinates in the body i are presented in Fig. 2.

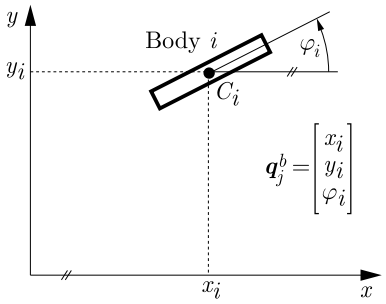

Fig. 2. Generalised coordinates of the belt body i

It was also assumed that there were n_p pulleys in the transmission "lying" in the xy plane and rotating around the axis parallel to z with a rotation angle θ_j ($j = 1, \ldots, n_p$). Therefore, the vector of the generalised coordinates takes the form

$$\mathbf{q}^{\mathrm{T}} = \left[\mathbf{q}_1^{b\,\mathrm{T}}, \ldots, \mathbf{q}_i^{b\,\mathrm{T}}, \ldots, \mathbf{q}_{n_b}^{b\;\mathrm{T}}, \theta_1, \ldots, \theta_j, \ldots, \theta_{n_p}\right] \tag{2.1}$$

where $\mathbf{q}_i^b$ is the vector of generalised coordinates of the body i (presented in Fig. 2).

2.1. Spring-damping elements

The values of forces and torques in the translational and torsion SDE connecting the body $i-1$ with the body i are described by the Kelvin-Voigt (Voigt, 1892) relations

$$\begin{aligned} F_i^{Ltra} &= F_{i-1}^{Rtra} = c_{tra}\Delta l_i^L + b_{tra}\Delta \dot{l}_i^L \\ M_i^{Ltor} &= M_{i-1}^{Rtor} = c_{tor}(\varphi_i - \varphi_{i-1}) \end{aligned} \tag{2.2}$$

where F_i^{Ltra}, F_i^{Rtra} are values of translational forces in the left SDE (connecting the body i with the body $i-1$) and the right SDE (connecting the body i with the body $i+1$), respectively; M_i^{Ltor}, M_i^{Rtor} – bending torques in the left SDE and right SDE, respectively; c_{tra}, b_{tra} – translational stiffness and damping coefficients in SDE; c_{tor} – torsional stiffness coefficient in SDE; Δl_i^L, $\Delta \dot{l}_i^L$ – translational deformation and deformation speed of SDE.

2.2. Model of the belt-pulley contact

A vector notation of the forces is used to take into account the contact between the belt bodies and pulleys in the transmission. A diagram of the assumed distribution of forces acting on the belt body i at the period of contact with the pulley j is presented in Fig. 3.

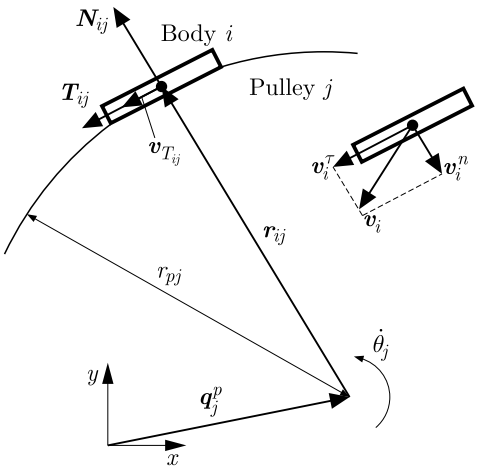

Fig. 3. Assumed configuration of the velocity components of the belt body i and forces acting on this body from the pulley j

It is assumed that the force components, i.e. normal force $\mathbf{N}_{ij}$ and friction force $\mathbf{T}_{ij}$, would be applied to the mass centre of each body which has contact with one of the pulleys.

As is shown in Fig. 3, the vector $\mathbf{r}_{ij}$ is orientated from the centre of the pulley j to the mass centre of the body i. If there is contact between the body and the pulley but the value of the normal force $\mathbf{N}_{ij}$ is still zero, the length of this vector equals an arbitrary value r_{pj}. Thus, at the time of a non-zero normal force, there is an inequality: $r_{ij} < r_{pj}$. The position of the pulley centre in the global coordinate system is specified via the vector $\mathbf{P}_{pj}$.

The vector $\mathbf{r}_{ij}$ can be determined from the following formula

$$\mathbf{r}_{ij} = \mathbf{q}_i^b - \mathbf{q}_j^p \tag{2.3}$$

A versor (unit vector) according to the direction and sense of the vector $\mathbf{r}_{ij}$ equals

$$\overline{\mathbf{r}}_{ij} = \frac{\mathbf{r}_{ij}}{|\mathbf{r}_{ij}|} \tag{2.4}$$

The penetration depth of the belt body i with the pulley j can be determined from the formula

$$p_{ij} = r_{pj} - |\mathbf{r}_{ij}| \tag{2.5}$$

Assuming that the linear velocity of the centre of the pulley is zero, then the value of penetration velocity $\dot{p}_{ij}$ is equal to the value of the normal velocity component $\mathbf{v}_i^n$ (Fig. 3). This value is determined on the basis of the following scalar product

$$\dot{p}_{ij} = |\mathbf{v}_i^n| = -\mathbf{v}_i^{\mathrm{T}} \cdot \overline{\mathbf{r}}_{ij} \tag{2.6}$$

where $\mathbf{v}_i$ is the velocity of the mass centre of the body i.

Since the contact force $\mathbf{N}_{ij}$ formed during contact between the body i and the pulley j has a consistent direction with the direction of the versor $\overline{\mathbf{r}}_{ij}$, then

$$\mathbf{N}_{ij} = N_{ij}\overline{\mathbf{r}}_{ij} \tag{2.7}$$

The value of this force is determined in a similar form as given in the paper (Čepon *et al.*, 2010), in which the authors proved a nonlinear relation between the penetration depth and the normal force

$$N_{ij}(p_{ij}, \dot{p}_{ij}) = c_1 p_{ij}^2 + c_2 p_{ij} + b\dot{p}_{ij} \tag{2.8}$$

where c_1, c_2 are belt-pulley contact stiffness coefficients, b – belt-pulley contact damping coefficient.

2.3. Dahl friction model

The value of the relative velocity $\mathbf{v}_{Tij}$ between the body i and the pulley j is needed to calculate the friction force (shown in Fig. 3). The way of calculating this velocity was presented in an earlier work (Kubas, 2014).

As was mentioned before, the Dahl model is assumed as presented in (Dahl, 1968)

$$\mu_{ij} = \begin{cases} (\mu_{0ij} - \mu_k)\exp\Big(-\frac{\sigma}{\mu_k}(x_{ij} - x_{0ij})\Big) + \mu_k & \text{for} \quad v_{Tij} \geqslant 0 \\ (\mu_{0ij} + \mu_k)\exp\Big(-\frac{\sigma}{\mu_k}(x_{ij} - x_{0ij})\Big) - \mu_k & \text{for} \quad v_{Tij} < 0 \end{cases} \tag{2.9}$$

where v_{Tij} is the relative velocity between two moving parts, x_{0ij} – starting value of displacement at the moment of change of sense of the relative velocity, μ_{0ij} – starting value of the friction coefficient (according to x_{0ij} displacement), x_{ij} – displacement, μ_k – dynamic friction coefficient, σ – stiffness coefficient of the friction joint.

The shape of an exemplary displacement-dependent friction characteristic is presented in Fig. 4.

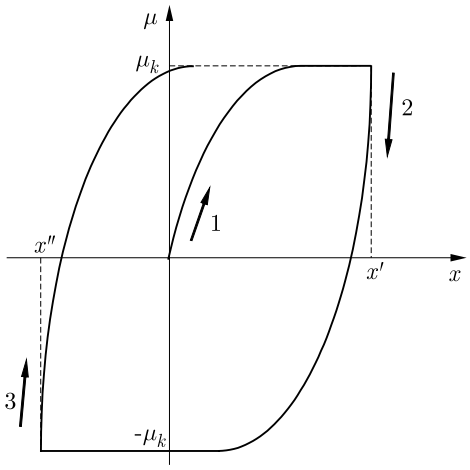

Fig. 4. Exemplary shape of a Dahl friction characteristic as a function of displacement

First, the starting value of displacement is x_{0ij} and the starting value of friction coefficient μ_{0ij} is equal to 0. When the two corresponding layers start to move and the relative velocity $\dot{x}$ is positive (in relation to the assumed local coordinate system), the friction coefficient increases (1st phase shown in Fig. 4) according to equation $(2.9)_1$. Sometimes, as shown in Fig. 4, the relative velocity can reach the value of μ_k (especially when its direction does not change in a relatively long period of time). When the direction of the velocity changes to the opposite (negative values), the starting value of the displacement and the starting value of the friction coefficient should change to the values: $x_{0ij} = x'$, $\mu_{0ij} = \mu_k$. The friction coefficient starts to decrease (2nd phase) according to equation $(2.9)_2$ and can reach an arbitry value of $-\mu_k$ (this situation is shown in Fig. 4). When the velocity changes again into positive values, the friction coefficient increases again (3rd phase), and $x_{0ij} = x''$, $\mu_{0ij} = -\mu_k$.

The value of the friction force can be, therefore, described as

$$T_{ij} = \mu_{ij} N_{ij} \tag{2.10}$$

The direction of the friction force vector is opposite to the relative velocity $\mathbf{v}_{Tij}$.

2.4. Equations of motion

Equations of motion of the body i take the form

$$\begin{aligned} m_i\ddot{x}_i &= \overline{\mathbf{X}}^{\mathrm{T}} \cdot \Big[\mathbf{F}_i^{Ltra} + \mathbf{F}_i^{Rtra} + \sum_{j=0}^{n_p-1}(\mathbf{N}_{ij} + \mathbf{T}_{ij}) + m_i\mathbf{g}\Big] \\ m_i\ddot{y}_i &= \overline{\mathbf{Y}}^{\mathrm{T}} \cdot \Big[\mathbf{F}_i^{Ltra} + \mathbf{F}_i^{Rtra} + \sum_{j=0}^{n_p-1}(\mathbf{N}_{ij} + \mathbf{T}_{ij}) + m_i\mathbf{g}\Big] \\ I_{z_i}\ddot{\varphi}_i &= \overline{\mathbf{Z}}^{\mathrm{T}} \cdot (\mathbf{M}_i^{Ltra} + \mathbf{M}_i^{Rtra} + \mathbf{M}_i^{Ltor} + \mathbf{M}_i^{Rtor}) \end{aligned} \tag{2.11}$$

where $\overline{\mathbf{X}}^{\mathrm{T}} = [1,0,0]$, $\overline{\mathbf{Y}}^{\mathrm{T}} = [0,1,0]$, $\overline{\mathbf{Z}}^{\mathrm{T}} = [0,0,1]$ – versors consistent with the axes x, y, z, respectively, of the global coordinate system, $\mathbf{M}_i^{Ltra} = -\mathbf{l}_i' \times \mathbf{F}_i^{Ltra}$, $\mathbf{M}_i^{Rtra} = \mathbf{l}_i' \times \mathbf{F}_i^{Rtra}$, $\mathbf{g}$ – vector of gravitational acceleration.

It is assumed that the pulleys motion will take place from the set torques. The equation of motion of the pulley j has the form

$$I_{z_j}\ddot{\theta}_j = M_{dj} - \sum_{i=0}^{n_b-1} \overline{\mathbf{Z}}^{\mathrm{T}} \cdot \mathbf{M}_{Tij} \tag{2.12}$$

where I_{z_j} is the mass moment of inertia of the pulley j, M_{dj} – the set torque, $\mathbf{M}_{Tij} = \overline{\mathbf{r}}_{ij} \times \mathbf{T}_{ij}$ – friction torque acting from the belt body i.

The resistance torque acting on the pulley can be included in the assumed model. A negative value of M_{dj} (e.g. constant or dependent on velocity $\dot{\theta}_j$) should be taken in this case.

Case 1: Analysis with a driving torque of 100 Nm

A two-pulley belt transmission with the same radius $r_p = 0.1$ m is taken into analysis. The scheme of the assumed transmission is presented in Fig. 5. The distance between the pulleys is $l_p = 0.290$ m. The analysed belt is 1.2 m in length. The friction coefficient, translational and rotational stiffness and damping coefficients are assumed based on own related works and (Čepon and Boltežar, 2009; Čepon *et al.*, 2009, 2010). The number of belt elements is assumed as $n_b = 60$ and the coefficient as $\sigma = 10000\,\mathrm{m}^{-}1$. One belt element and the neighbouring spring-damping element (on the left side of the belt element) are chosen to show some example calculation results. The selected belt element is also presented in Fig. 5 as case 1.

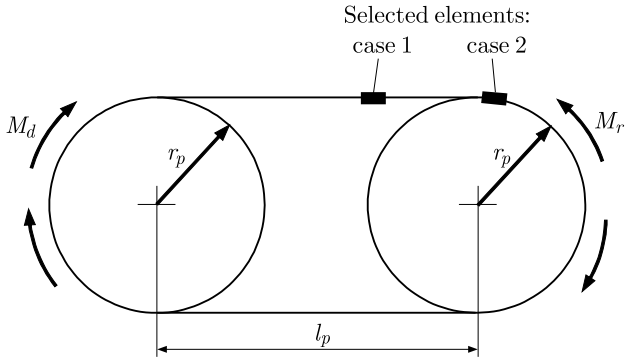

Fig. 5. Assumed belt transmission with a selected belt element

The torque applied in the driving pulley is also assumed as a partially-linear time-depended function. From 0 to 0.3 s, the value of the torque decreased from 0 to −50 Nm. After that moment, it remained constant.

The resistance torque applied in the driven pulley is described as a function of its angular velocity

$$M_{d2} = \frac{100}{2\pi}\dot{\theta}_2 \tag{2.13}$$

All of the presented calculation results omit the stabilisation phase of the analysed model.

The calculated driving and resistance torques are presented in Fig. 6.

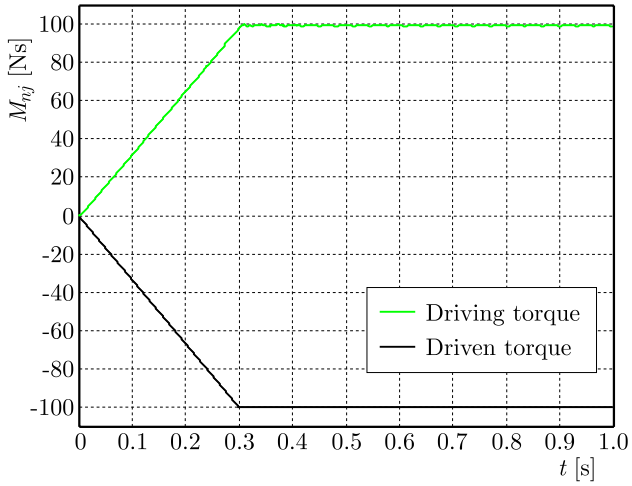

Fig. 6. Driving and driven torques applied to the pulleys in case 1

The achieved angular velocities of the driving and driven pulleys are presented in Fig. 7. As can be observed, after 0.3 s the angular velocities remain constant with a value almost equal to 2π rad/s. Some disturbances can also be observed as a result of the assumed discrete model of the belt. It is worth mentioning that this effect can be reduced even more by assuming more belt elements; this will of course cause an increase in the number of equations of motion.

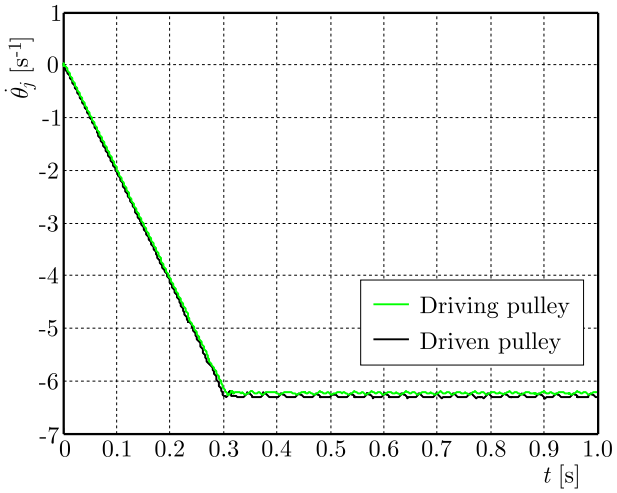

Fig. 7. Calculated values of angular velocities of the pulleys

In the next two figures (Figs. 8a and 8b), the longitudinal deformation and resulting force in a chosen spring-damping element is presented. As has been mentioned, it is located next to the chosen rigid element shown in Fig. 5. As can be observed, this element is located in the passive part of the belt at the moment that the transmission starts. The values of deformation and force decrease. Some disturbances and an increase in the values can be observed just over

0.3 s. From this moment, the rigid element is located on the driven pulley. This situation lasts to about 0.82 s. After this time period, it moves in the active part of the belt.

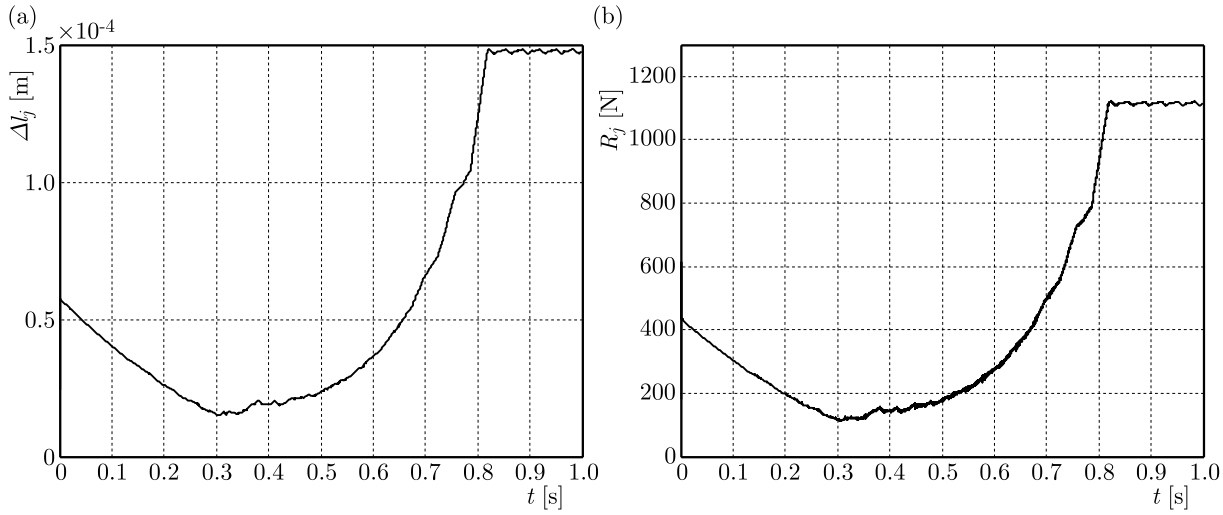

Fig. 8. Longitudinal deformation and reaction force in the selected SDE: (a) longitudinal deformation, (b) reaction force

As can be observed from the shapes in the figures, the reaction force in the spring-damping element mainly depends on the deformation. The dependence on the deformation velocity is negligible.

Figure 9 shows the reaction forces on each element at a chosen time of 0.4 s. Elements with numbers 1-9 and 53-60 are located in the passive top part of the belt. The values of the force in this part are about 120 N. Elements 23-39 are in the active bottom part of the belt. The values of the force in this part are about 1120 N. Elements located in the driven pulley correspond to numbers 10-22 (growing force), whereas those located on the driving pulley correspond to numbers 40-52 (decreasing force).

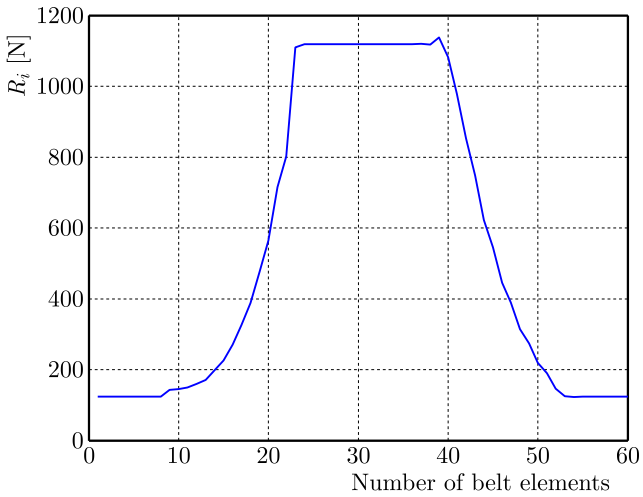

Fig. 9. Reaction forces in all SDEs at a selected time

In Figs. 10a and 10b, the calculated values of normal and friction forces acting on a selected rigid element from the driven pulley are presented. As can be observed, up to about 0.6 s, the friction forces are smaller than the normal forces and do not correspond to the developed friction or slip (which is consistent with the results of the angular velocities shown in Fig. 7). From about 0.6 s, the values start to be equal or almost equal.

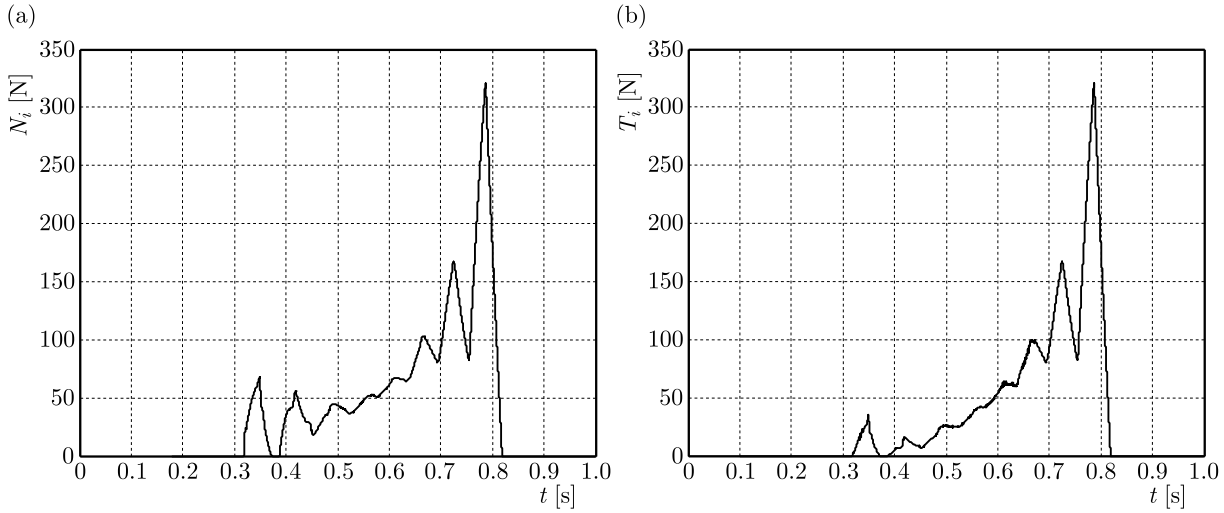

Fig. 10. Normal and friction forces acting on a selected belt element from the driven pulley: (a) normal force, (b) friction force

In Fig. 11a, the calculated values of the friction coefficient of the selected belt element are shown. The values are negative because of the opposite direction of the friction force to the assumed positive direction of the pulley rotation (Fig. 3). As can be observed, when contact between the element and the driven pulley starts, the values of the friction coefficient increase rapidly to a value of about 0.59 and return to zero (from about 0.31 s to 0.38 s). At this moment, the element loses contact with the pulley (this can also be observed in Fig. 10a). At about 0.39 s, the belt element returns to the area of the pulley. Up to about 0.68 s, the values increase to the assumed value μ_k. The values remain constant from this time to about 0.82 s. At about 0.82 s, the element loses contact with the driven pulley and starts moving in the active part of the belt.

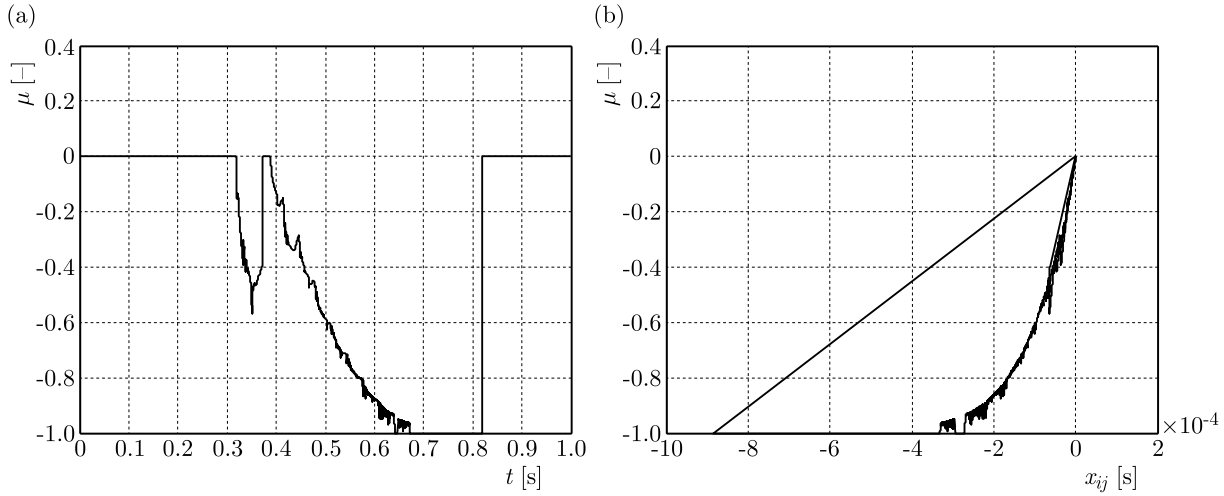

Fig. 11. Change of the friction coefficient: (a) in a selected belt element, (b) presented as a function of displacement

In Fig. 11b, the calculated values of the friction coefficient are shown as a function of displacement. As can be observed, the values asymptotically grow to the assumed value μ_k. Two moments of changing the values to zero, as identified earlier, can be observed.

The disturbances of the changing values of the friction coefficient result from the changing direction of the relative velocity, which is presented in Fig. 12.

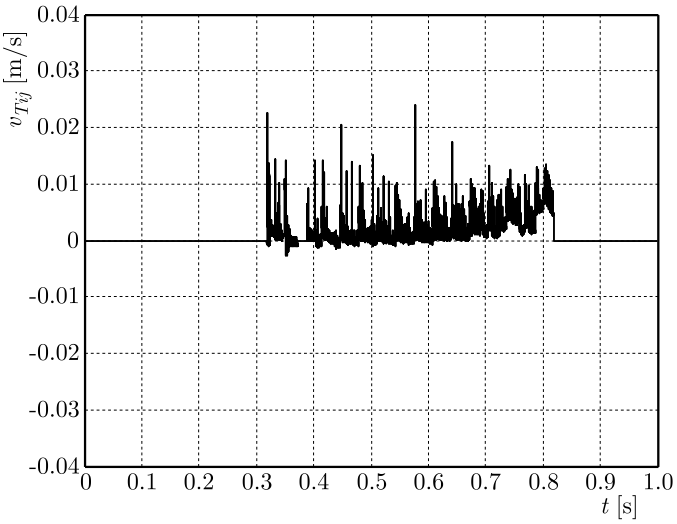

Fig. 12. Calculated relative velocity between a chosen rigid element and the driven pulley

The presented case of load causes a relatively large acceleration of the transmission. After velocity stabilisation, only friction in one direction can be analysed. Calculations with another drive and resistance torques are repeated.

Case 2: Oscillating torque

Next, the torque applied to the driving pulley as shown in Fig. 13 is assumed. As can be observed, first the torque is linear-changing from 0 (at the start) to −50 Nm (at time 0.25 s). Next, the values increase to 50 Nm (at 0.75 s). At the end of analysis, the torque decreases to 0. Simultaneously, the resistance torque of the passive pulley has opposite values.

This kind of torque loads the transmission in two opposite directions with a relatively small movement. The belt is slightly rotated clockwise. The chosen belt element (whose initial position is shown in Fig. 5 as case 2) moves toward the right side of the driven pulley.

The rest of the conditions (initial preload of the belt, dimensions of the transmission, etc.) are the same.

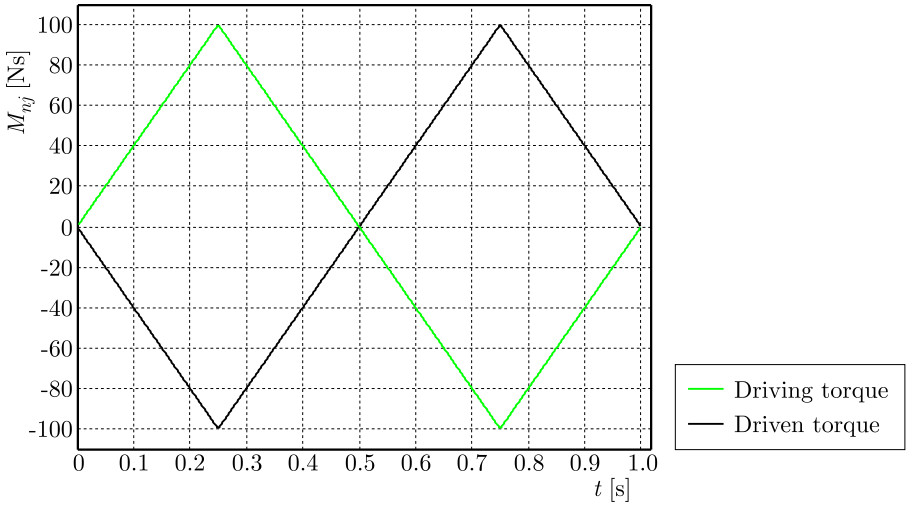

Fig. 13. Driving and driven torques applied to the pulleys in case 2

As shown in Fig. 14, the angular velocities of the driving and driven pulleys differ significantly. It can also be observed that the transmission oscillates in moments of the changing direction of

these velocities (at time 0.25 s and 0.75 s). Just before the oscillations, the velocities differ about 0.1 rad/s.

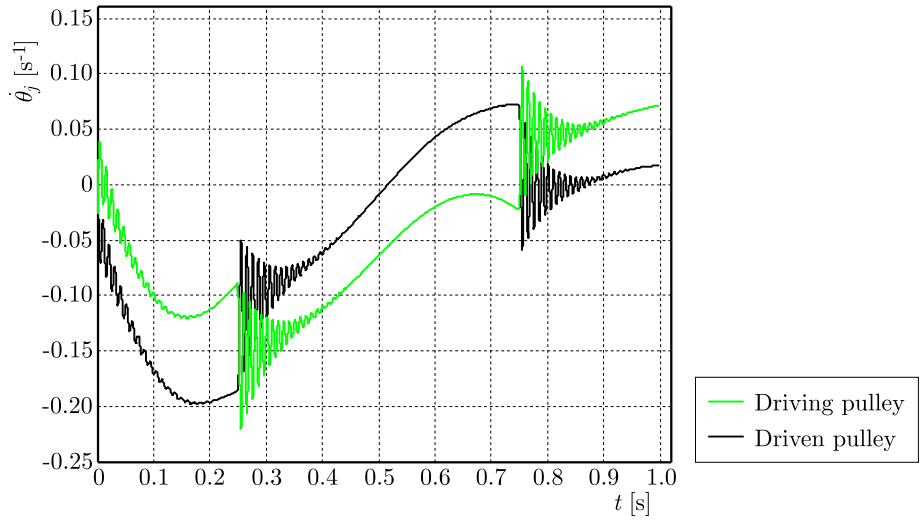

Fig. 14. Calculated angular velocities of the pulleys in case 2

Figure 15 shows the resulting reaction force in the selected spring-damping element. At the beginning, the force is about 420 N and decreases to about 100 N. After changing the direction of the load torques, the force increases to about 1110 N. At the end of the simulation the force achieves a value of about 580 N.

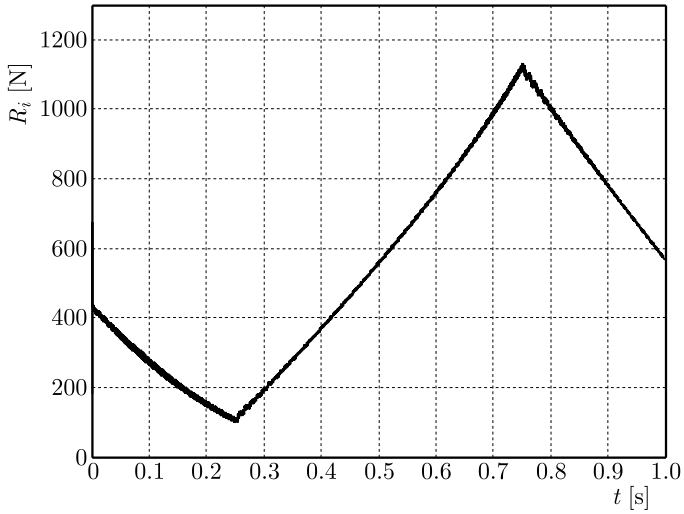

Fig. 15. Calculated values of the reaction force in a selected spring-damping element in case 2

Figure 16 shows the calculated normal and friction forces between the chosen belt element and the pulley. Because the selected belt element moves slowly to the right side of the driven pulley, where the normal force is larger, the absolute friction force also increases to about 190 N.

After 0.75 s, the selected belt element moves back and the absolute values of normal and friction forces start to decrease.

Figure 17a shows the calculated values of the friction coefficient. In this case, the friction between the selected belt element and the pulley achieves values of $-\mu_k$ and μ_k, which means that in particular moments it is fully developed. It corresponds to intervals 0.16 s-0.25 s and 0.66 s-0.76 s, respectively.

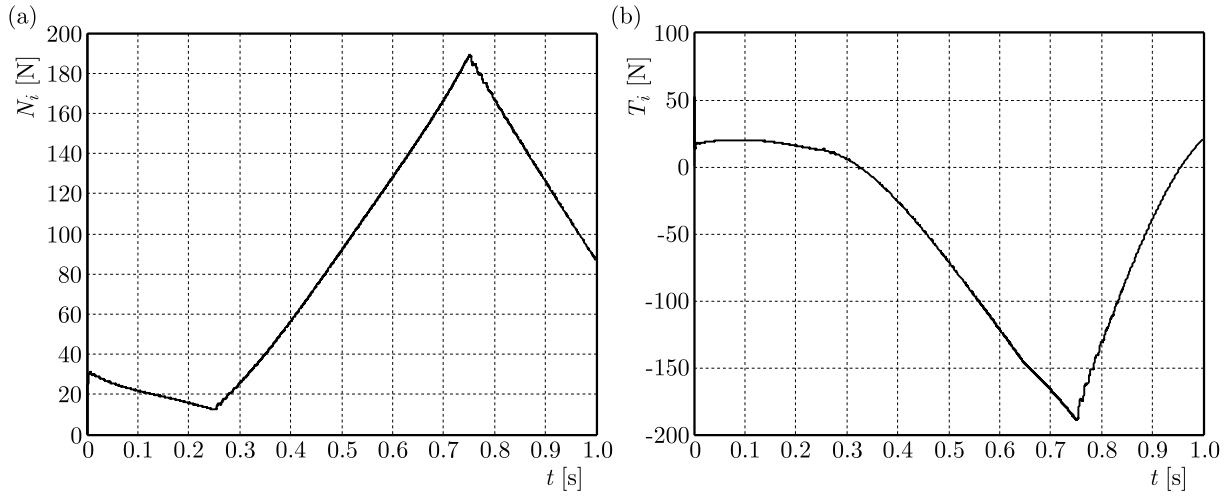

Fig. 16. Normal and friction forces of a selected belt element in case 2

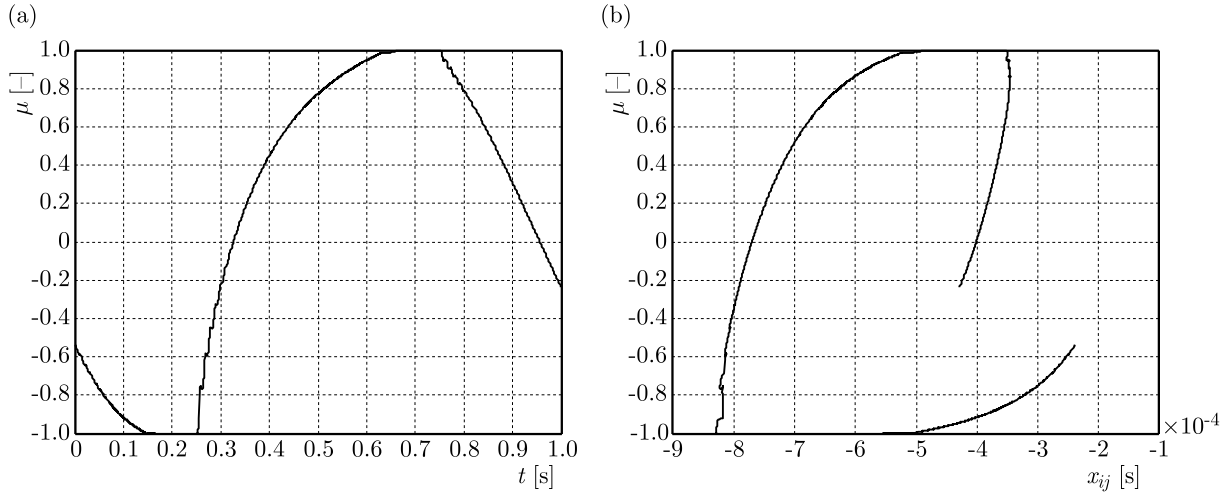

Fig. 17. Change of the friction coefficient: (a) in a selected belt element in case 2, (b) presented as a function of displacement in case 2

Figure 17b shows values of the friction coefficient as a function of displacement acting on a chosen element from the pulley. As can be observed, at the beginning the friction coefficient decreases to an arbitrary value $-\mu_k$ and the displacement is achieved at about 0.83 mm. Then the direction of the relative velocity changes. After this moment, the values increase to a positive value of μ_k. The relative displacement achieves in this phase about 0.45 mm (absolute displacement is about 0.38 mm).

It has been decided to check how much the change in the σ coefficient affected the calculation results. Figure 18 shows the friction coefficient courses as a function of the displacement in two cases: $\sigma = 10000$ and $\sigma = 5000$ as assumed earlier. As can be observed, the slope of the curve has changed.

Figure 19 shows the calculated angular velocities of the pulleys. A comparison of these courses with the courses from Fig. 14 shows slightly larger amplitudes of the vibrations. Because of the assumed smaller value of σ, the system became 'more flexible'. The contact and friction parameters will be investigated on a research stand in the future.

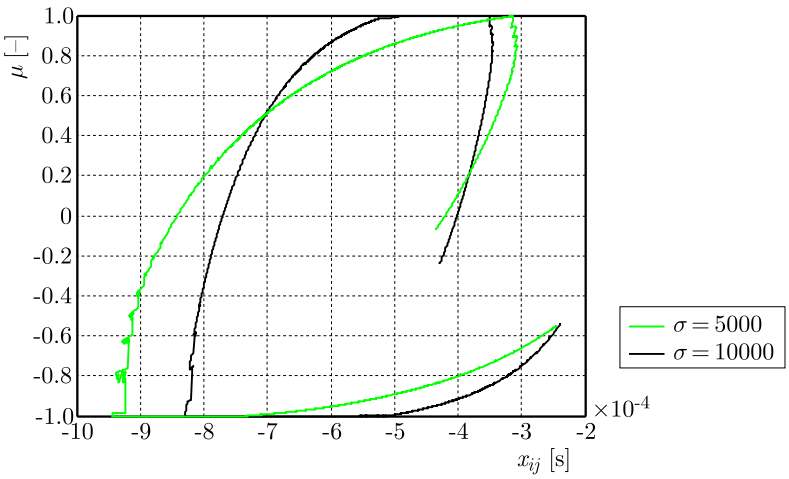

Fig. 18. Change of the friction coefficient presented as a function of displacement in case 2, for two different values of the coefficient σ

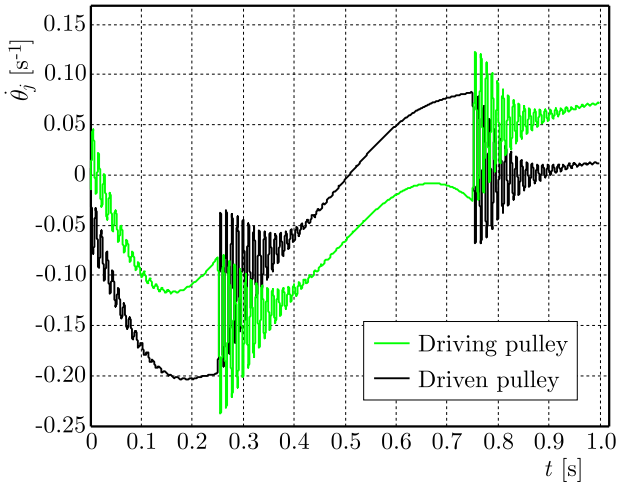

Fig. 19. Calculated angular velocities of pulleys in case 2 with the assumed coefficient $\sigma = 5000$

3. Conclusions

As has been mentioned before, the proposed Dahl model does not include the Stribeck effect. This assumption is possible because the static and dynamic friction coefficients are approximately the same. It would be necessary to assume another friction model if they were different. The LuGre friction model is especially interesting and very popular (Canudas de Wit *et al.*, 1995). In future works, it will be the main subject of investigation in belt transmission applications. It is also important to compare the prepared models with early mentioned models, especially with the EPP friction model, which also includes elasticity of the joint.

Of course, the most important is to compare them with real measurements made on a research stand. As mentioned before, a series of experiments on a specially built research stand is planned. The main subject of these experiments will be to measure the friction parameters between the belt and the pulley. The measurements will be done for a clean belt and with some impurities (oil, water, etc.). It has been noticed from first experiments made on a clean belt that friction between the belt and the pulley cannot be described with a relatively simple Euler formula. Its dependence on the belt preload or wrap angle can be more complicated. The friction can also depend on the rest time between movements of the transmission or belt slip, on the relative velocity between the belt and the pulley surfaces or even on the acceleration.

References

1. Bastien J., Michon G., Manin L., Dufour R., 2007, An analysis of the modified Dahl and Masing models: Application to a belt tensioner, *Journal of Sound and Vibration*, **302**, 4/5, 841-864
2. Canudas de Wit C., Olsson H., Astrom K.J., Lischinsky P., 1995, A new model for control of systems with friction, *IEEE Transactions on Automatic Control*, **40**, 3
3. Canudas de Wit C., Tsiotras P., Velenis E., Basset M., Gissinger G., 2003, Dynamic friction models for road/tire longitudinal interaction, *Vehicle System Dynamics*, **39**, 3, 189-226
4. Chatlet E., Michon G., Manin L., Jacquet G., 2008, Stick/slip phenomena in dynamics: Choice of contact model, *Mechanism and Machine Theory*, **43**, 10, 1211-1224
5. Čepon G., Boltežar M., 2009, Dynamics of a belt-drive system using a linear complementarity problem for the belt-pulley contact description, *Journal of Sound and Vibration*, **319**, 1019-1035
6. Čepon G., Manin L., Boltežar M., 2009, Introduction of damping into the flexible multibody belt-drive model: A numerical and experimental investigation, *Journal of Sound and Vibration*, **324**, 283-296
7. Čepon G., Manin L., Boltežar M., 2010, Experimental identification of the contact parameters between a V-ribbed belt and a pulley, *Mechanism and Machine Theory*, **45**, 1424-1433
8. Dahl P.R., 1968, A Solid Friction Model, Report No. TOR-0158(3107-18)-1, Aerospace Corporation Report
9. Fawcett J.N., 1981, Chain and belt drives – a review, *Shock Vibrations Digest*, **13**, 5, 5-12
10. Kim D., Leamy M.J., Ferri A.A., 2011, Dynamic modeling and stability analysis of flat belt drives using an elastic/perfectly plastic friction law, *ASME Journal of Dynamic Systems, Measurement, and Control*, **133**, 1-10
11. Kubas K., 2014, A two-dimensional discrete model for dynamic analysis of belt transmission with dry friction, *The Archive of Mechanical Engineering*, **61**, 4, 571-593
12. Kubas K., 2015, A model for analysing the dynamics of a belt transmissions with a 5pk belt, *The Archives of Automotive Engineering*, **16**, 1
13. Leamy M.J., Wasfy T.M., 2002, Analysis of belt-drive mechanics using a creep-rate-dependent friction law, *Journal of Applied Mechanics, Transaction of ASME*, **69**, 6, 763-771
14. Leamy M.J., Wasfy T.M., 2002, Transient and steady-state dynamic finite element modeling of belt-drives, *ASME Journal of Dynamic Systems, Measurement, and Control*, **124**, 4, 575-581
15. Voigt W., 1892, Ueber innere Reibung fester Körper, insbesondere der Metalle, *Annalen der Phisik*, **283**, 671-693

Manuscript received September 28, 2016; accepted for print July 18, 2017

JOURNAL OF THEORETICAL
AND APPLIED MECHANICS
55, 4, pp. 1437-1441, Warsaw 2017
DOI: 10.15632/jtam-pl.55.4.1437

SHORT RESEARCH COMMUNICATION

JERK BY AXES IN MOTION ALONG A SPACE CURVE

Michael Tsirlin
ELMO Motion Control, Petah Tiqva, Israel
e-mail: mz695444@gmail.com

In the paper, a formula for calculation of the jerk of a point moving along a space curve is derived. Such a formula is needed for control of motion to calculate jerks (second derivatives of the velocity) by axes of motion. On the basis of this formula, an expression for the maximum admissible velocity on the space curve to satisfy limitation by the jerk is given as well. Such a requirement also arises in the motion control.

Keywords: jerk, motion control, profiler

1. Introduction

In the multi axis motion control, a motion command may contain four kinematics parameters: position, velocity, acceleration and jerk. Such a command must be issued for each axis x, y and z controlled by a servo on each control cycle. While calculation of the velocity and acceleration is trivial, calculation of jerk (that is mainly used for analysis of motion) is a new demand. In a number of papers devoted to the motion control, a tangential jerk along the trajectory is considered while the problem of jerk caused by a high curvature on the transition curve between two line segments is a new one. For a particular case of planar motion, the jerk vector was considered by Shot (1978). In this special case, the jerk can be resolved into tangential and normal components. As will be shown below, in the case of 3D space motion, the jerk vector has three components although the acceleration vector still can be decomposed into tangential and normal.

Consider a space curve in the 3D space defined by a vector function $\boldsymbol{\gamma}(\sigma) = \{\varphi_x(\sigma), \varphi_y(\sigma), \varphi_z(\sigma)\}$. In further considerations, any special nature of the parameter σ (σ – is not time or arc length s) and any special limit of the parameter variation are not supposed. We suppose here that $\boldsymbol{\gamma}(\sigma)$ is a continuous mapping $\sigma \to R_3$, $\sigma \in [a, b]$ with three times differentiable coordinate functions $\varphi_x(\sigma)$, $\varphi_y(\sigma)$, $\varphi_z(\sigma)$ that define geometrical properties of the curve.

As $\boldsymbol{\gamma}'(\sigma) = \{\varphi'_x(\sigma), \varphi'_y(\sigma), \varphi'_z(\sigma)\}$ then the unit tangent vector can be defined as $\boldsymbol{\tau}(\sigma) = \{\varphi'_x(\sigma)/\|\boldsymbol{\gamma}'(\sigma)\|, \varphi'_y(\sigma)/\|\boldsymbol{\gamma}'(\sigma)\|, \varphi'_z(\sigma)/\|\boldsymbol{\gamma}'(\sigma)\|\}$.

The second derivative $\mathbf{a}(\sigma) = \boldsymbol{\gamma}''(\sigma) = \{\varphi''_x(\sigma), \varphi''_y(\sigma), \varphi''_z(\sigma)\}$ with a normal component $\mathbf{a}_n(\sigma) = \mathbf{a}(\sigma) - [\mathbf{a}(\sigma) \cdot \boldsymbol{\tau}(\sigma)]\boldsymbol{\tau}(\sigma)$. Then, the unit normal vector can be defined as $\mathbf{n} = \mathbf{a}_n(\sigma)/\|\mathbf{a}_n(\sigma)\|$.

The binormal unit vector $\mathbf{b}(\sigma)$ can be defined as $\boldsymbol{\tau}(\sigma) \times \mathbf{n}(\sigma)$. Thus, we know the Frenet-Serret frame $\boldsymbol{\tau}(\sigma)$, $\mathbf{n}(\sigma)$ and $\mathbf{b}(\sigma)$ for each parameter value σ.

Consider a point moving along a curve defined by its radius-vector $\mathbf{r}(t)$. For each control cycle (at time t) from the profiler calculations we know the position increment along the curve $s(t)$, velocity along the curve $ds/dt = v(t)$, acceleration along the curve $d^2s/dt^2 = a(t)$ and jerk along the curve $d^3s/dt^3 = J(t)$, where s is a distance along the curve. The value of the curve parameter σ is not known but with the use of numerical methods, the mapping $s \to \sigma$ can be done with any required precision.

2. Vector of jerks for the position increment $s(t)$

The velocity and acceleration vectors of the point moving along the space curve are defined by

$$\begin{aligned}\mathbf{v}(t) &= \frac{d\mathbf{r}}{dt} = \boldsymbol{\tau}\Big(\frac{ds}{dt}\Big)\\ \mathbf{a}(t) &= \frac{d\mathbf{v}}{dt} = \boldsymbol{\tau}\Big(\frac{d^2s}{dt^2}\Big) + \mathbf{n}\Big(\frac{ds}{dt}\Big)^2\frac{1}{\rho(s)} = \boldsymbol{\tau}\Big(\frac{d^2s}{dt^2}\Big) + \mathbf{n}\Big(\frac{ds}{dt}\Big)^2 K_1(s)\end{aligned} \tag{2.1}$$

where $K_1(s)$ and $\rho(s)$ are the curvature and radius of the curvature at point s.

The vector of the third derivative (jerk) can be calculated as $d\mathbf{a}(t)/dt$

$$\mathbf{J}(t) = \frac{d\mathbf{a}}{dt} = \frac{d\boldsymbol{\tau}}{ds}\frac{ds}{dt}\frac{d^2s}{dt^2} + \boldsymbol{\tau}\Big(\frac{d^3s}{dt^3}\Big) + \frac{d\mathbf{n}}{ds}\Big(\frac{ds}{dt}\Big)^3 K_1(s) + \mathbf{n}\frac{d\Big[\Big(\frac{ds}{dt}\Big)^2 K_1(s)\Big]}{dt} \tag{2.2}$$

At first, we consider

$$\mathbf{n}\frac{d\Big[\Big(\frac{ds}{dt}\Big)^2 K_1(s)\Big]}{dt} = \mathbf{n}\Big[2\frac{ds}{dt}\frac{d^2s}{dt^2}K_1(s) + \Big(\frac{ds}{dt}\Big)^2\frac{dK_1(s)}{ds}\frac{ds}{dt}\Big] \tag{2.3}$$

By the Frenet-Serret formulas

$$\frac{d\boldsymbol{\tau}}{ds} = K_1\mathbf{n} \qquad \frac{d\mathbf{n}}{ds} = -K_1\boldsymbol{\tau} + K_2\mathbf{b} \tag{2.4}$$

The curvature K_1 and torsion K_2 for an arbitrary curve parameter σ (which is not necessarily the arc length s) at the parameter point σ are calculated by

$$\begin{aligned}K_1(\sigma) &= \frac{\|\boldsymbol{\gamma}'(\sigma)\times\boldsymbol{\gamma}''(\sigma)\|}{\|\boldsymbol{\gamma}'(\sigma)\|^3}\\ K_2(\sigma) &= \frac{[\boldsymbol{\gamma}'(\sigma),\boldsymbol{\gamma}''(\sigma),\boldsymbol{\gamma}'''(\sigma)]}{\|\boldsymbol{\gamma}'(\sigma)\times\boldsymbol{\gamma}''(\sigma)\|^2} = \frac{[\boldsymbol{\gamma}'(\sigma)\times\boldsymbol{\gamma}''(\sigma)]\cdot\boldsymbol{\gamma}'''(\sigma)}{\|\boldsymbol{\gamma}'(\sigma)\times\boldsymbol{\gamma}''(\sigma)\|^2}\end{aligned} \tag{2.5}$$

where $\boldsymbol{\gamma}'(\sigma)$, $\boldsymbol{\gamma}''(\sigma)$, $\boldsymbol{\gamma}'''(\sigma)$ are known curve derivatives, and the curve parameter σ can be found from the numerical mapping $s\to\sigma$ (if $\sigma\neq s$) that must be done for each point s. We calculate curvature and torsion at the parameter point σ that corresponds to the increment s along the curve. Point s is a point where the profiler calculations have just determined ds/dt, d^2s/dt^2, d^3s/dt^3. So, at the point s, we can use $K_1(\sigma)$ and $K_2(\sigma)$ instead of $K_1(s)$ and $K_2(s)$. Below we use designations K_1 and K_2.

From (2.2)-(2.4), we get

$$\begin{aligned}\mathbf{J}(t) &= K_1\mathbf{n}\frac{ds}{dt}\frac{d^2s}{dt^2} + \boldsymbol{\tau}\Big(\frac{d^3s}{dt^3}\Big) + (-K_1\boldsymbol{\tau} + K_2\mathbf{b})\Big(\frac{ds}{dt}\Big)^3 K_1\\ &+ \mathbf{n}\Big[2\frac{ds}{dt}\frac{d^2s}{dt^2}K_1 + \Big(\frac{ds}{dt}\Big)^2\frac{dK_1(s)}{ds}\frac{ds}{dt}\Big] = \boldsymbol{\tau}\Big[\frac{d^3s}{dt^3} - K_1^2\Big(\frac{ds}{dt}\Big)^3\Big]\\ &+ \mathbf{n}\Big[K_1(s)\frac{ds}{dt}\frac{d^2s}{dt^2} + 2\frac{ds}{dt}\frac{d^2s}{dt^2}K_1 + \Big(\frac{ds}{dt}\Big)^2\frac{dK_1(s)}{ds}\frac{ds}{dt}\Big] + \mathbf{b}\frac{K_2}{\rho}\Big(\frac{ds}{dt}\Big)^3\\ &= \boldsymbol{\tau}\Big[\frac{d^3s}{dt^3} - \Big(\frac{ds}{dt}\Big)^3 K_1^2\Big] + \mathbf{n}\Big[3\frac{ds}{dt}\frac{d^2s}{dt^2}K_1 + \Big(\frac{ds}{dt}\Big)^3\frac{dK_1(s)}{ds}\Big] + \mathbf{b}\Big[K_2\Big(\frac{ds}{dt}\Big)^3 K_1\Big]\end{aligned} \tag{2.6}$$

Since we do not know the function $K_1(s)$ then calculation of its derivative at the point s requires special consideration. $K_1(s) = K_1[s(\sigma)] = K_{1\sigma}(\sigma)$, and by differentiating both sides we get

$$\frac{dK_1(s)}{ds} = \frac{dK_{1\sigma}(\sigma)}{ds} = \frac{dK_{1\sigma}(\sigma)}{d\sigma}\frac{d\sigma}{ds} = \frac{dK_{1\sigma}(\sigma)}{d\sigma}\Big/\frac{ds}{d\sigma} = \frac{dK_{1\sigma}(\sigma)}{d\sigma}\frac{1}{\|\boldsymbol{\gamma}'(\sigma)\|} \tag{2.7}$$

where instead of the unknown $d\sigma/ds$ we used the derivative $ds/d\sigma = \|\boldsymbol{\gamma}'(\sigma)\|$ of the inverse function $s(\sigma)$, that is a curve length function

$$\begin{aligned}\frac{dK_{1\sigma}(\sigma)}{d\sigma} &= \frac{d\frac{\|\boldsymbol{\gamma}'(\sigma)\times\boldsymbol{\gamma}''(\sigma)\|}{\|\boldsymbol{\gamma}'(\sigma)\|^3}}{d\sigma} \\ &= \Big(\frac{d\|\boldsymbol{\gamma}'(\sigma)\times\boldsymbol{\gamma}''(\sigma)\|}{d\sigma}\|\boldsymbol{\gamma}'(\sigma)\|^3 - \|\boldsymbol{\gamma}'(\sigma)\times\boldsymbol{\gamma}''(\sigma)\|\frac{d\|\boldsymbol{\gamma}'(\sigma)\|^3}{d\sigma}\Big)\frac{1}{\|\boldsymbol{\gamma}'(\sigma)\|^6} \\ &= \frac{d\|\boldsymbol{\gamma}'(\sigma)\times\boldsymbol{\gamma}''(\sigma)\|}{d\sigma}\frac{1}{\|\boldsymbol{\gamma}'(\sigma)\|^3} - K_1(\sigma)\frac{d\|\boldsymbol{\gamma}'(\sigma)\|^3}{d\sigma}\frac{1}{\|\boldsymbol{\gamma}'(\sigma)\|^3}\end{aligned} \tag{2.8}$$

Below we assume that for any vector $\mathbf{p}$ the derivative of its Euclidean norm can be calculated as

$$\begin{aligned}\|\mathbf{p}\|' &= \frac{1}{2}(\mathbf{p}'\mathbf{p}+\mathbf{p}\mathbf{p}')\frac{1}{\sqrt{\mathbf{p}\mathbf{p}}} = \frac{\mathbf{p}\mathbf{p}'}{\|\mathbf{p}\|} \\ \frac{d\|\boldsymbol{\gamma}'(\sigma)\times\boldsymbol{\gamma}''(\sigma)\|}{d\sigma} &= \frac{[\boldsymbol{\gamma}'(\sigma)\times\boldsymbol{\gamma}''(\sigma)]\,[\boldsymbol{\gamma}''(\sigma)\times\boldsymbol{\gamma}''(\sigma)+\boldsymbol{\gamma}'(\sigma)\times\boldsymbol{\gamma}'''(\sigma)]}{\|\boldsymbol{\gamma}'(\sigma)\times\boldsymbol{\gamma}''(\sigma)\|} \\ &= \frac{[\boldsymbol{\gamma}'(\sigma)\times\boldsymbol{\gamma}''(\sigma)]\,[\boldsymbol{\gamma}'(\sigma)\times\boldsymbol{\gamma}'''(\sigma)]}{\|\boldsymbol{\gamma}'(\sigma)\times\boldsymbol{\gamma}''(\sigma)\|} \\ \frac{d\|\boldsymbol{\gamma}'(\sigma)\|^3}{d\sigma} &= 3\|\boldsymbol{\gamma}'(\sigma)\|^2\frac{d\|\boldsymbol{\gamma}'(\sigma)\|}{d\sigma} = 3\|\boldsymbol{\gamma}'(\sigma)\|^2\frac{\boldsymbol{\gamma}'(\sigma)\boldsymbol{\gamma}''(\sigma)}{\|\boldsymbol{\gamma}'(\sigma)\|} = 3\|\boldsymbol{\gamma}'(\sigma)\|[\boldsymbol{\gamma}'(\sigma)\boldsymbol{\gamma}''(\sigma)]\end{aligned} \tag{2.9}$$

So, finally we get

$$\frac{dK_{1\sigma}(\sigma)}{d\sigma} = \frac{[\boldsymbol{\gamma}'(\sigma)\times\boldsymbol{\gamma}''(\sigma)]\,[\boldsymbol{\gamma}'(\sigma)\times\boldsymbol{\gamma}'''(\sigma)]}{\|\boldsymbol{\gamma}'(\sigma)\|^3\|\boldsymbol{\gamma}'(\sigma)\times\boldsymbol{\gamma}''(\sigma)\|} - 3K_1(\sigma)\frac{\boldsymbol{\gamma}'(\sigma)\boldsymbol{\gamma}''(\sigma)}{\|\boldsymbol{\gamma}'(\sigma)\|^2} \tag{2.10}$$

Another derivation of (2.10) was given by Angeles (2003, pp. 371-372).

In some cases (cubic spline with iterative adaptation of the parameter σ or PH-curve proposed by Farouki (2010)) we can use the curve parameter close or equal to natural $\sigma = s$. In such cases, the curvature K_1 and its derivative dK_1/ds are defined as

$$\begin{aligned}K_1 &= \|\boldsymbol{\gamma}''(s)\| = \sqrt{[\varphi_x''(\sigma)]^2+[\varphi_y''(\sigma)]^2+[\varphi_z''(\sigma)]^2} \\ \frac{dK_1}{ds} &= \frac{1}{K_1}[\varphi_x''(\sigma)\varphi_x'''(\sigma)+\varphi_y''(\sigma)\varphi_y'''(\sigma)+\varphi_z''(\sigma)\varphi_z'''(\sigma)] = \frac{\boldsymbol{\gamma}''(\sigma)\boldsymbol{\gamma}'''(\sigma)}{\|\boldsymbol{\gamma}''(s)\|}\end{aligned} \tag{2.11}$$

In (2.6), we have come to the vector

$$\mathbf{J}(t) = \boldsymbol{\tau}(\sigma)C_1 + \mathbf{n}(\sigma)C_2 + \mathbf{b}(\sigma)C_3 \tag{2.12}$$

The vectors $\boldsymbol{\tau}(\sigma)$, $\mathbf{n}(\sigma)$ and $\mathbf{b}(\sigma)$ are defined above, and the scalar coefficients C_1, C_2, C_3 are also known from (2.6)

$$\begin{aligned}C_1 &= \frac{d^3s}{dt^3} - \frac{K_1}{\rho}\Big(\frac{ds}{dt}\Big)^3 = J(t) - K_1^2v^3(t) \\ C_2 &= 3\frac{ds}{dt}\frac{d^2s}{dt^2}K_1 + \Big(\frac{ds}{dt}\Big)^3\frac{dK_1(s)}{ds} = 3v(t)a(t)K_1 + v^3(t)\frac{dK_1(\sigma)}{d\sigma}\frac{1}{\|\boldsymbol{\gamma}'(\sigma)\|} \\ C_3 &= \frac{K_2}{\rho}\Big(\frac{ds}{dt}\Big)^3 = K_1K_2v^3(t)\end{aligned} \tag{2.13}$$

3. Applications of the formula

In the case of uniform motion with $ds/dt = V$, $d^2s/dt^2 = 0$ and $d^3s/dt^3 = 0$ we get

$$C_1 = -\frac{K_1}{\rho}\Big(\frac{ds}{dt}\Big)^3 = -K_1^2V^3 \qquad C_2 = \Big(\frac{ds}{dt}\Big)^3\frac{dK_1(s)}{ds} = V^3\frac{dK_1(\sigma)}{d\sigma}\frac{1}{\|\boldsymbol{\gamma}'(\sigma)\|}$$
$$C_3 = \frac{K_2}{\rho}\Big(\frac{ds}{dt}\Big)^3 = K_1K_2V^3 \tag{3.1}$$

In the case of plane 2D motion with $K_2 = 0$

$$C_1 = \frac{d^3s}{dt^3} - \frac{K_1}{\rho}\Big(\frac{ds}{dt}\Big)^3 = J(t) - K_1^2v^3(t)$$
$$C_2 = 3v(t)a(t)K_1 + v^3(t)\frac{dK_1(\sigma)}{d\sigma}\frac{1}{\|\boldsymbol{\gamma}'(\sigma)\|} \qquad C_3 = 0 \tag{3.2}$$

Formulas (3.1) can be used for the estimation of the maximum velocity V admissible on the curve to satisfy condition $\|\mathbf{J}\| \leqslant J_{max}$. While generating the trajectory, instead of $K_1(s)$ and $K_2(s)$ we know $K_1(\sigma)$ and $K_2(\sigma)$ for any parameter value σ. So, in the case of uniform motion with $ds/dt = V$ and designation $\widetilde{K_1} = [dK_1(\sigma)/d\sigma]/\|\boldsymbol{\gamma}'(\sigma)\|$ we get

$$\begin{aligned}\|\mathbf{J}(\sigma)\| &= \sqrt{K_1^4(\sigma)V^6 + V^6\widetilde{K_1}^2 + K_1^2(\sigma)K_2^2(\sigma)V^6}\\ &= V^3\sqrt{K_1^4(\sigma) + \widetilde{K_1}^2 + K_1^2(\sigma)K_2^2(\sigma)} = V^3\sqrt{\Psi(\sigma)}\end{aligned} \tag{3.3}$$

and the maximum velocity admissible at all trajectory points must satisfy

$$V \leqslant \frac{\sqrt[3]{J_{max}}}{\sqrt[6]{\max\Psi(\sigma)}} \tag{3.4}$$

In most applications, the point σ^* that produces $\Psi(\sigma^*) = \max\Psi(\sigma)$ belongs to a small neighborhood of the point σ_p such that $\boldsymbol{\gamma}(\sigma_p)$ can be called the peak of the curve.

In the case of 2D uniform motion, $ds/dt = V$, $K_2(\sigma) = 0$, and we get

$$\|\mathbf{J}(\sigma)\| = V^3\sqrt{K_1^4(\sigma) + \widetilde{K_1}^2} \tag{3.5}$$

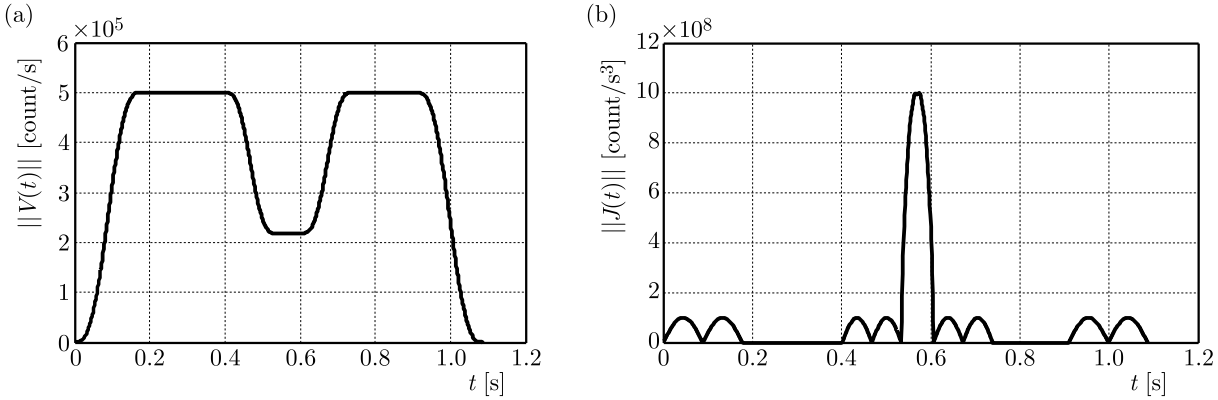

Fig. 1. (a) Velocity vector modulus. (b) Jerk vector modulus

In Fig. 1a, we can see a velocity decrease from $5 \cdot 10^5$ down to 218560.65 to satisfy the condition $\|\mathbf{J}(\sigma)\| \leqslant 10^9$. It happens on the transition curve between two lines constructed as a 3D septic polynomial. In Fig. 1b, we can see that the jerk comes exactly to the limiting value (time is measured in seconds, velocity in count/s, jerk in count/s^3). The calculations have been performed by (3.3) and (3.4).

References

1. Angeles J., 2003, *Fundamentals of Robotic Mechanical Systems: Theory, Methods and Algorithms*, Springer
2. Farouki R.T., 2010, *Pythagorean-Hodograph Curves*, Springer 3
3. Schot S.H., 1978, Jerk: the time rate of change of acceleration, *American Journal of Physics*, **46**, 11, 1090-1105

Manuscript received December 1, 2016; accepted for print June 20, 2017

JOURNAL OF THEORETICAL
AND APPLIED MECHANICS
55, 4, pp. 1443-1448, Warsaw 2017
DOI: 10.15632/jtam-pl.55.4.1443

SHORT RESEARCH COMMUNICATION

EXPERIMENTAL ANALYSIS AND MODELLING OF FATIGUE CRACK INITIATION MECHANISMS

Aneta Ustrzycka, Zenon Mróz, Zbigniew L. Kowalewski

Institute of Fundamental Technological Research, Polish Academy of Sciences, Warsaw, Poland

e-mail: austrzyc@ippt.pan.pl; zmroz@ippt.pan.pl; zkowalew@ippt.pan.pl

The present work is devoted to simulation of fatigue crack initiation for cyclic loading within the nominal elastic regime. It is assumed that damage growth occurs due to action of mean stress and its fluctuations induced by crystalline grain inhomogeneity and the free boundary effect. The macrocrack initiation corresponds to a critical value of accumulated damage. The modelling of damage growth is supported by Electronic Speckle Pattern Interferometry (ESPI) apparatus using coherent laser light.

Keywords: fatigue crack initiation, damage evolution, optical methods

1. Introduction

The process of fatigue damage development and structural degradation is of local nature. The mechanism responsible for damage accumulation during cyclic loading below the yield point remains elusive. The present paper concerns the fatigue crack initiation and evolution in metals subjected to loading at the stress level below the conventional yield strength. During the process of cyclic loading due to an inhomogeneous grain structure, the micro plastic effects develop and can be observed on the macro-scale. Sangid (2013) proposed a physically-based model for prediction of fatigue crack initiation based on the material microstructure. Using the potential offered by the novel experimental techniques, it is possible to identify physical phenomena and to describe mechanisms of degradation and fatigue damage development in modern structural materials. Their identification involves usage of damage detection methods, both destructive and non-destructive to evaluate material behaviour under different loads (Kowalewski *et al.*, 2008). Electronic Speckle Pattern Interferometry (ESPI) is a widely used technique to measure full-field deformation on surfaces of many kinds of objects. The shielding effect on fatigue crack growth at constant amplitude loading and during application of overloads was investigated using ESPI by Vasco-Olmo *et al.*, (2016). The analysis of the plastic processes that governs crack propagation was analysed using ESPI method by Ferretti *et al.*, (2011). However, its application to the study of fatigue damage mechanisms has not been yet explored extensively. Therefore, in this study, ESPI is applied to investigate the distribution of strain fluctuations.

2. Applications of ESPI method

Nowadays, the ESPI method seems to be very attractive in capturing damage growth. Primarily, optical methods are used to analyze strain fields and strain localization on the surface of a specimen. For instance, strain distribution map using ESPI for nickel alloys (C – 0.09%, Cr – 8.8%, Mn – 0.1%, Si – 0.25%, W – 9.7%, Co – 9.5%, Al – 5.7%, Ta+Ti+HF – 5.5%) is presented for an increasing number of load cycles in Fig. 1.

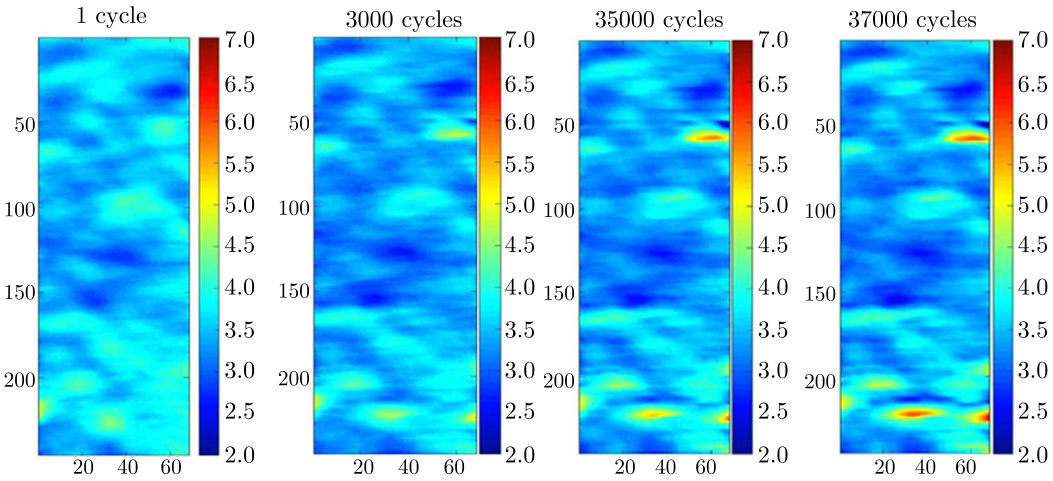

Fig. 1. Strain distribution maps on the plane specimen surface using ESPI for different stages of the fatigue process

During the process of pulsating cyclic loading the material deforms heterogeneously and numerous strain concentration spots are visible. It is expected that the microstructure of the materials plays an important role in strain localization. The strain concentration occurs especially at grain boundaries. It can be expected that cracks start to nucleate in the zones containing large strain accumulation during cyclic loading. Apart from the density and distribution of defects in the volume of tested specimen, the specimen size and location of individual defects are important factors of fatigue damage initiation and its further evolution. The lateral profiles of maximal cross-sectional strain distribution for the increasing number of cycles are presented in Fig. 2. The results are shown for the nickel alloy.

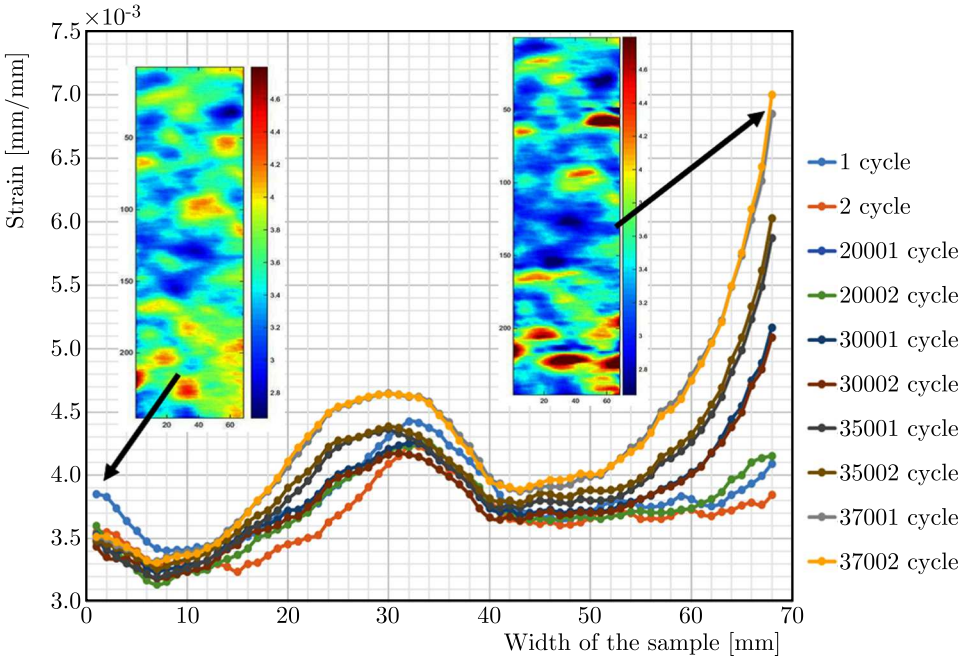

Fig. 2. The lateral profiles of maximal cross-sectional strain evolution

The distribution of strain across the sample at the place of crack initiation and its evolution during the cyclic loading process is shown in Fig. 2. Using ESPI, the strain distributions for the first and last cycle (at the moment of rupture) are included. The strain values evolve faster at

the edge of the sample. Results will serve to verify and calibrate the mathematical description. The results of fatigue tests in the form of stress-strain diagrams exhibiting the permanent strain, stiffness modulus variation and hysteresis loops during selected cycles of fatigue are presented in Fig. 3.

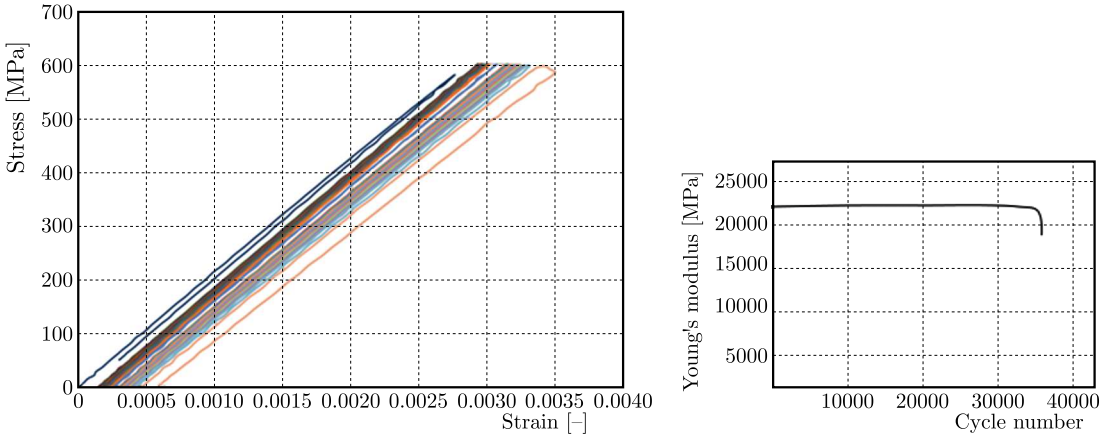

Fig. 3. Development of the fatigue hysteresis loop during selected cycles

The fatigue hysteresis loops are not measurable during the cyclic process indicating that the material globally deforms in the elastic state, and the macroplastic strain developed in the final phase of process is of order 0.1%. The microdamage can evolve within the local zones of strain concentration. The understanding of mechanical properties of materials plays an important role during the fatigue process.

3. Mathematical modelling of fatigue damage evolution, numerical implementation and comparison with ESPI results

In the present paper, the mathematical description of fatigue crack initiation and evolution is formulated. The problem of damage evolution for metals under cyclic loading inducing fatigue crack initiation and propagation within the elastic regime is discussed. The condition of damage accumulation is formulated after Mróz *et al.*, (2004). It is assumed that when the critical stress condition is reached on the material plane, the damage zone Ω is generated. Afterwards, the growth of the damage zone can be described. The mathematical model is applied to study damage evolution under cyclic tension and the predictions are compared with experimental data. The profile of normal strain $\varepsilon(x)$ and stress $\sigma(x)$ along the damage zone Ω is expressed as a sum of the mean $(\overline{\varepsilon}, \overline{\sigma})$ and fluctuation $(\widetilde{\varepsilon}(x), \widetilde{\sigma}(x))$ components

$$\varepsilon(x) = \overline{\varepsilon} + \widetilde{\varepsilon}(x) \qquad \sigma(x) = \overline{\sigma} + \widetilde{\sigma}(x) \tag{3.1}$$

The material is assumed to be linearly elastic, but exhibiting a damage process at the strain concentration zones. In order to illustrate the problem (Fig. 4), the potential damage zone Ω is selected with the largest strain and stress fluctuations.

Damage evolution rule (3.2) was originally formulated by Mróz *et al.* (2004) for brittle materials

$$dD = A\Big(\frac{\sigma - \sigma_0^*}{\sigma_c - \sigma_0}\Big)^n \frac{d\sigma}{\sigma_c^* - \sigma_0^*} \tag{3.2}$$

where A, n and p denote material parameters, σ_0 is the damage initiation threshold, σ_c denotes the failure stress in tension for the damaged material, σ_0^* and σ_c^* are the threshold values for the undamaged material and D denotes the scalar measure of damage $(0 \leqslant D \leqslant 1)$.

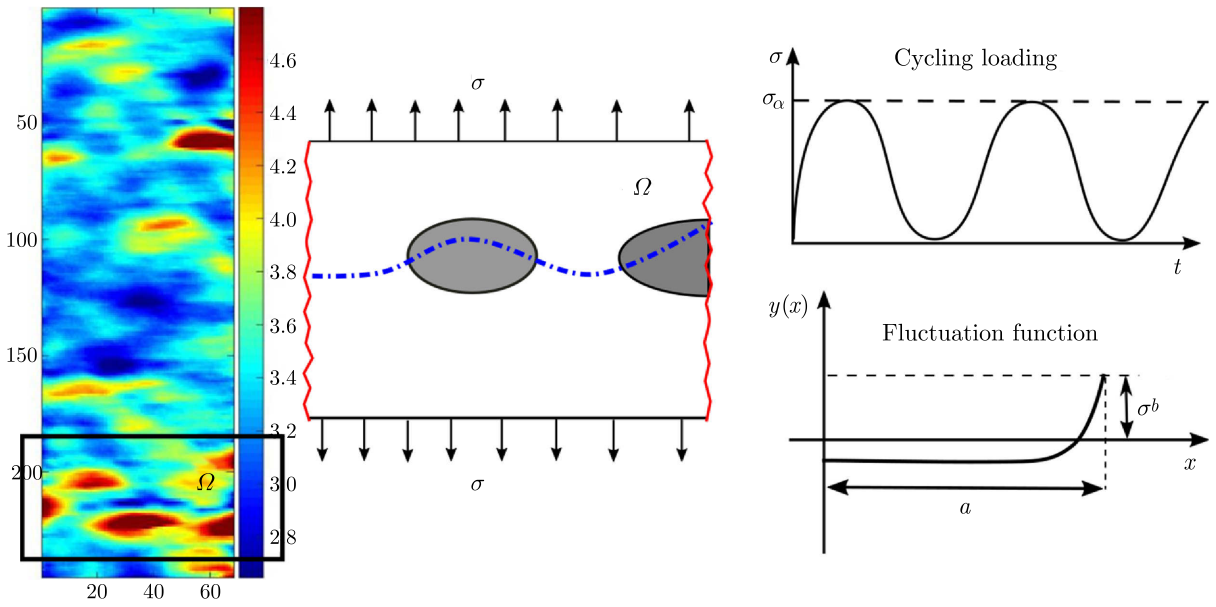

Fig. 4. Damage zone Ω with the major stress fluctuation

The stress value σ increases but the values of σ_0 and σ_c decrease. Both σ_0 and σ_c depend on the damage state according to the formula

$$\sigma_c - \sigma_0 = (\sigma_c^* - \sigma_0^*)(1-D)^p \tag{3.3}$$

The process of cyclic loading is described by the time variation of stress in the following form

$$\sigma(t) = \frac{1}{2}\sigma_a[1+\sin(\omega t)] \qquad \omega = \frac{2\pi}{T} \tag{3.4}$$

where σ_a is the stress amplitude. Substituting σ from Eq. (3.4) into Eq. (3.2) and integrating, the equation for the damage increase in one cycle $\Delta D_s = D_{s+1} - D_s$ is expressed as follows

$$\int_{D_s}^{D_s+\Delta D_s} (1-D)^{np}\, dD = \frac{A\omega\sigma_a}{2(\sigma_c^* - \sigma_0^*)^{n+1}} \int_0^T \Big(\frac{1}{2}\sigma_a(1+\sin(\omega t)) - \sigma_0^*\Big)^n \cos(\omega t)\, dt \tag{3.5}$$

Finally, the damage evolution law for one cycle reads

$$\Delta D_s = \frac{1}{(1-D_s)^{np}} \frac{A}{(\sigma_c^* - \sigma_0)^{n+1}} \frac{1}{n+1} \left[\Big(\frac{1}{2}\sigma_a(1+\sin(\omega T)) - \sigma_0^*\Big)^{n+1} - \Big(\frac{1}{2}\sigma_a - \sigma_0^*\Big)^{n+1} \right] \tag{3.6}$$

The free edges of the sample due to surface irregularities act as a kind of stress concentrators. The influence of edge defects on the damage evolution and crack propagation is significant (see Fig. 2).

In order to account for the edge effect, the stress fluctuation function (see Fig. 4) is introduced and the total stress expressed as follows

$$\sigma(x) = \overline{\sigma} + \widetilde{\sigma}(x) = \overline{\sigma} + \overline{\sigma} y(x) = \overline{\sigma}\Big(1 + \alpha + \beta\Big|\frac{x}{a}\Big|^m\Big) \qquad y(x) = \alpha + \beta\Big|\frac{x}{a}\Big|^m \tag{3.7}$$

where $y(x)$ denotes the fluctuation function, a is width of the sample, β and m are material parameters. The integration of stress fluctuation on $[0,a]$ makes it possible to establish the parameter α

$$\int_0^a \widetilde{\sigma}(x)\, dx = 0 \quad \rightarrow \quad \int_0^a \Big(\alpha + \beta\Big|\frac{x}{a}\Big|^m\Big)\, dx = 0 \quad \rightarrow \quad \alpha = -\frac{\beta}{m+1} \tag{3.8}$$

The boundary condition at the external edge allows one to specify parameter β, thus

$$\widetilde{\sigma}(x=a)=\sigma^b \quad \rightarrow \quad \beta=\frac{\sigma^b}{\overline{\sigma}}\frac{m+1}{m} \tag{3.9}$$

The value of σ^b is assumed to correspond to the measured boundary fluctuation, here $\sigma^b=1.1\overline{\sigma}$.

Finally, the stress distribution is expressed in the following form

$$\sigma(x,t)=\overline{\sigma}\Big(1+\alpha+\beta\Big|\frac{x}{a}\Big|^m\Big)\Big(\frac{1}{2}+\frac{1}{2}\sin(\omega t)\Big) \tag{3.10}$$

According to the mathematical description, numerical analysis of damage evolution (3.2) under mechanical loads (3.10) in elastic-plastic solids has been made. The evolution of damage during the growing number of cycles is shown in Fig. 5. The macro-crack initiation is assumed to occur at the critical value of damage $D_c=0.3$.

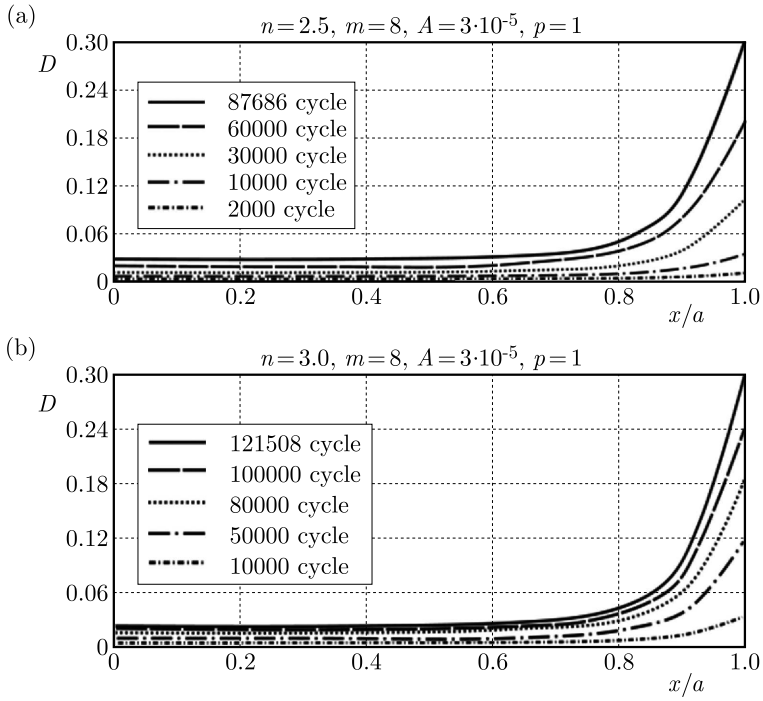

Fig. 5. Damage evolution related to the number of cycles for different values of the parameter n

4. Conclusions

The present paper concerns the damage evolution in elastic-plastic materials subjected to cyclic loading. The mathematical description of crack initiation and propagation under cyclic loading is presented. This model is supported by optical methods of stress and strain monitoring (ESPI) for early detection, localization and monitoring of damage in materials under fatigue loading. The numerical prediction and the experimental results indicate a good correlation.

Acknowledgement

This work has been supported by the National Science Centre through the Grant No. 2014/15/B/ST8/04368.

References

1. Ferretti D., Rossi M., Royer-Carfagni G., 2011, An ESPI experimental study on the phenomenon of fracture in glass. Is it brittle or plastic? *Journal of the Mechanics and Physics of Solids*, **59**, 1338-1354
2. Kowalewski Z.L., Mackiewicz S., Szelążek J., 2008, Evaluation of damage in steels subjected to exploitation loading – destructive and non-destructive methods, *International Journal of Modern Physics B*, **22**, 5533-5538
3. Mróz Z., Seweryn A., Tomczyk A., 2004, Fatigue crack growth prediction accounting for the damage zone, *Fatigue and Fracture of Engineering Materials and Structures*, **28**, 61-71
4. Sangid M.D., 2013, The physics of fatigue crack initiation, *International Journal of Fatigue*, **57**, 58-72
5. Vasco-Olmo J.M., Daz F.A., Patterson E.A., 2016, Experimental evaluation of shielding effect on growing fatigue cracks under overloads using ESPI, *International Journal of Fatigue*, **83**, 117-126

Manuscript received July 18, 2017; accepted for print July 20, 2017

INFORMATION FOR AUTHORS

Journal of Theoretical and Applied Mechanics (***JTAM***) is devoted to all aspects of solid mechanics, fluid mechanics, thermodynamics and applied problems of structural mechanics, mechatronics, biomechanics and robotics. Both theoretical and experimental papers as well as survey papers can be proposed.

We accept articles in English only. The text of a *JTAM* paper should not exceed **12 pages of standard format A4** (11-point type size, including abstract, figures, tables and references), short communications – **4 pages**.

The material for publication should be sent to the Editorial Office via electronic journal system: http://www.ptmts.org.pl/jtam/index.php/jtam

Papers are accepted for publication after the review process. Blind review model is applied, which means that the reviewers' names are kept confidential to the authors. The final decision on paper acceptance belongs to the Editorial Board.

After qualifying your paper for publication we will require LaTeX or TeX or Word document file and figures.

The best preferred form of figures are files obtained by making use of editorial environments employing vector graphics:

- genertaed in CorelDraw (*.cdr), AutoCad and ArchiCad (*.dwg) and Adobe Illustrator (*.ai). We require original fioles saved in the standard format of the given program.
- genertaed by calculation software (e.g. Mathematica) – we need files saved in *.eps or *.pdf formats.
- made in other programs based on vector graphics – we ask for *.eps, *.wmf, *.svg, *.psfiles.

Any figures created without application of vector graphics (scans, photos, bitmaps) are strongly encouraged to be supplied in *.jpg, *.tif, *.png formats with resolution of at least 300 dpi.

Requirements for paper preparation

Contents of the manuscripts should appear in the following order:

- Title of the paper
- Authors' full name, affiliation and e-mail
- Short abstract (**maximum 100 words**) and 3-5 key words (**1 line**)
- Article text (equations should be numbered separately in each section; each reference should be cited in the text by the last name(s) of the author(s) and the publication year)
- References in alphabetical order. See the following:
    1. Achen S.C., 1989, A new boundary integral equation formulation, *Journal of Applied Mechanics*, **56**, 2, 297-303
    2. Boley B.A., Weiner J.H., 1960, *Theory of Thermal Stresses*, Wiley, New York
    3. Canon W., 1955, Vibrations of heated beams, Ph.D. Thesis, Columbia University, New York
    4. Deresiewicz H., 1958, Solution of the equations of thermoelasticity, *Proceedings of Third U.S. National Congress of Applied Mechanics*, 287-305
- Titles of references originally published not in English, should be translated into English and formulated as follows:
    5. Huber M.T., 1904, Specific work of strain as a measure of material effort (in Polish), *Czasopismo Techniczne*, **XXII**, 3, 80-81

All the data should be reported in **SI units**.

Cena 35,00 zł (VAT 5%)

Contents

Suchocki C. — Numerical implementation of finite strain elasto-plasticity without yield surface **1113**

Akbarzadeh Khorshidi M., Shariati M. — A multi-spring model for buckling analysis of cracked Timoshenko nanobeams based on modified couple stress theory **1127**

Najafi H.R., Karimian S.M.H. — Analysis of controlled molecular dynamic flow in a channel with non-equal inlet and outlet cross-sectional areas **1141**

Thakur P., Singh S.B., Pathania D.S., Verma G. — Thermal creep stress and strain analysis in a non-homogeneous spherical shell **1155**

Qian D., Shi Z. — Bandgap properties in locally resonant phononic crystal double panel structures with periodically attached pillars **1167**

Malanchuk N., Slobodyan B., Martynyak R. — Frictional contact of two solids with a periodically grooved surface in the presence of an ideal gas in interface gaps **1181**

Lichota P., Szulczyk J., Noreña D.A., Vallejo Monsalve F.A. — Power spectrum optimization in the design of multisine manoeuvre for identification purposes **1193**

Arslan G., Keskin R.S.O., Ulusoy S. — An experimental study on the shear strength of SFRC beams without stirrups **1205**

Bendarma A., Jankowiak T., Łodygowski T., Rusinek A., Klósak M. — Experimental and numerical analysis of aluminum alloy AW5005 behavior subjected to tension and perforation under dynamic loading **1219**

Levadnyi I., Awrejcewicz J., Loskutov A., Szymanowska O. — On the choice of thickness of the cement mantle in cemented hip arthroplasty **1235**

Shen Y., Chen L., Liu Y., Zhang X. — Analysis of vibration transfer characteristics of vehicle suspension system employing inerter **1245**

Mokhtari M., Madani K., Benzaama H., Malarino S. — Effects of the composite stacking sequence on the failure load of the single lap bonded joint **1257**

Mojzeš M., Kukal J., Lauschmann H. — Comparison of Bayesian and other approaches to the estimation of fatigue crack growth rate from 2D textural features **1269**

Eyvazov E.B., Öge M. — Torsion of a circular anisotropic beam with two linear cracks weakened with a circular cavity **1279**

De Sousa T.L., Kanke F., Pereira J.T., Bavastri C.A. — Property identification of viscoelastic solid materials in nomograms using optimization techniques **1285**

Kammoun N., Jrad H., Bouaziz S., Soula M., Haddar M. — Vibration analysis of three--layered nanobeams based on nonlocal elasticity theory **1299**

Marzec K., Kucaba-Piętal A. — Numerical investigation of local heat transfer distribution on surfaces with a non-uniform temperature under an array of impinging jets with various nozzle shapes **1313**

Sahu S., Kumar P.B., Parhi D.R. — Design and development of 3-stage determination of damage location using Mamdani-Adaptive Genetic-Sugeno model **1325**

Amjadian P., Haghighat H. — An analytical approach to prediction of internal defects during the flat rolling process of strain-hardening materials **1341**

Jiang X., Li B. — Finite element analysis of a superelastic shape memory alloy considering the effect of plasticity **1355**

Singh K., Muwal R. — Thermoelastic strain and stress fields due to a spherical inclusion in an elastic half-space **1369**

Letaief M.R., Walha L., Taktak M., Chaari F., Haddar M. — Porous material effect on gearbox vibration and acoustic behavior **1381**

Teimourian A., Hacışevki H., Bahrami A. — Experimental study on suppression of vortex street behind perforated square cylinder **1397**

Zhao G.-H., Tang S., Liang Z., Li J. — Dynamic stability of a stepped drillstring conveying drilling fluid **1409**

Kubas K. — A model for the dynamic analysis of a belt transmission using the Dahl friction model **1423**

Short Research Communication

Tsirlin M. — Jerk by axes in motion along a space curve **1437**

Ustrzycka A., Mróz Z., Kowalewski Z.L. — Experimental analysis and modelling of fatigue crack initiation mechanisms **1443**